

# **SHEAR STRENGTH OF REINFORCED CONCRETE BRIDGE DECK SLABS**

THÈSE N° 3739 (2007)

PRÉSENTÉE À LA FACULTÉ ENVIRONNEMENT NATUREL, ARCHITECTURAL ET CONSTRUIT

Institut de structures

SECTION DE GÉNIE CIVIL

**ÉCOLE POLYTECHNIQUE FÉDÉRALE DE LAUSANNE**

POUR L'OBTENTION DU GRADE DE DOCTEUR ÈS SCIENCES

PAR

**Rui VAZ RODRIGUES**

Ingénieur civil diplômé  
Instituto Superior Técnico, Lisboa, Portugal

et de nationalité Portugaise

Jury de thèse :

Prof. M. A. Hirt, président du jury  
Prof. A. Muttoni, directeur de thèse  
Dr J.-P. Lebet, rapporteur  
Dr W. Kaufmann, rapporteur  
Prof. A. Pérez Caldentey, rapporteur

Lausanne, EPFL  
2007



*Para a Cátia  
Graciosa, Vítor e Rita*



## Préface

Les dalles de roulement en béton armé ou précontraint sont des éléments très importants et très sollicités des ponts routiers, mais malgré cela plusieurs aspects importants liés à leur calcul, leur dimensionnement et leur vérification restent relativement peu connus. En effet, l'essentiel de la recherche effectuée jusqu'à présent sur les dalles de roulement ne concerne que la flexion, en sorte qu'aussi bien le dimensionnement que la vérification sont effectués sans tenir compte de l'effet de l'effort tranchant. Ce dernier est pourtant très important, compte tenu du fait que l'action du trafic routier sur la dalle est essentiellement introduite sous forme de charges ponctuelles très intenses (réparties sur des surfaces de contact relativement petites entre pneus et revêtement).

La flexion de la dalle, qui résulte généralement d'un calcul élastique pour le dimensionnement et d'un calcul plastique avec mécanismes pour la vérification, est habituellement traitée indépendamment de l'effort tranchant. Pour ce faire, un comportement ductile est admis. En réalité, le comportement réel est assez mal connu et des doutes subsistent quant à l'effet de l'effort tranchant sur la ductilité du système. En outre, les travaux connus se limitent à des essais sur des dalles de taille réduite, en sorte que la pertinence des modèles pour la vérification de la résistance à l'effort tranchant n'a jamais été validée expérimentalement sur des dalles de roulement de grandeur réelle.

La recherche effectuée par M. Vaz Rodrigues représente une contribution importante dans ce domaine encore peu exploré. La partie expérimentale, effectuée sur des bandes de dalles et des porte-à-faux de ponts a donné des résultats très intéressants et dans une certaine mesure surprenants. En effet, la rupture produite par l'effort tranchant a presque toujours été déterminante. Les travaux expérimentaux et théoriques de cette thèse seront suivis du développement d'une méthode simplifiée permettant d'analyser efficacement les cas pratiques et d'une étude paramétrique sur l'influence du système statique de la dalle et de sa configuration sur la capacité portante.

Je tiens ici encore à remercier l'Office Fédéral des Routes et la Fondation Portugaise pour la Science et Technologie (FCT) qui ont soutenu ce projet de recherche ainsi que le « Groupe de Travail Recherche en matière de ponts » de l'avoir suivi avec des discussions et des remarques constructives.

Lausanne, février 2007

Prof. Dr Aurelio Muttoni



## Acknowledgements

This research work was carried out at the Structural Concrete Laboratory (IS-BETON) of the Ecole Polytechnique Fédérale de Lausanne (EPFL) under the supervision of Professor A. Muttoni. To him I would like to express my deep gratitude for his support, guidance and enthusiastic following of the work.

I would also like to acknowledge the members of the jury, namely Professor M. A. Hirt, Dr. W. Kaufmann from dsp Ingenieure & Planer AG, Professor A. Pérez Caldentey from Universidad Politécnica de Madrid and Dr. J.-P. Lebet from the Steel Structures Laboratory (ICOM) of the EPFL.

The research project was supported and financed by the Swiss Federal Roads Authority (FEDRO) and by the Portuguese Foundation for Science and Technology (FCT), grant FCT/BD/13259/2003. Their support is gratefully acknowledged.

Thanks are given to the technical staff for their help on the experimental work, namely S. Demierre, G. Guignet, N. Frey, R. Gysler, F. Perrin, G. Pidoux, H. Reist and G. Oreiller.

The friendly research atmosphere and fruitful discussions provided by all my colleagues in IS-BETON were greatly appreciated. In particular I would like to thank to Dr. O Burdet and Dr. M. Fernández Ruiz for their valuable suggestions and comments on the dissertation. The support of Mrs. Buehl is as well very much appreciated.

A warm thanks to my friends (in alphabetical order) Alexandre, Ana, Bruno, Fátima, Intan, Janina, Luís, Luísa, Mário, Pedro, Stefano and many others. Their company and good mood was essential to help keeping a good spirit during these years.

This work would not be possible without the love and permanent support of my beloved wife Cátia, to her I am deeply grateful. Também queria agradecer muito especialmente aos meus pais Graciosa e Vítor e à minha irmã Rita, que me apoiaram desde sempre. Um grande obrigado também a José, Maria Antónia e Félix Felisberto.





## Summary

Reinforced concrete bridge deck slabs without shear reinforcement can be subjected to concentrated or distributed loads of important magnitude. Under these loads their structural response is not always ductile. In particular under concentrated loads their deformation capacity can be limited by shear or punching shear failures, which prevent them from reaching the ultimate load predicted by pure flexural analysis. This problem has been studied in this research by means of an important experimental program and theoretical modeling.

The limited ductility of bridge decks was investigated by means of full scale tests on bridge deck cantilevers under groups of concentrated loads. Six large scale laboratory tests were performed on two bridge deck cantilevers with a span of 2.8 m and a length of 10.0 m. All slabs failed in a brittle manner, in shear or punching shear. The theoretical flexural failure load estimated using the yield-line method was never attained.

Despite the brittle failures, the results of tests on cantilevers have shown that some amount of yielding can occur before the shear failure and therefore reduce the shear strength. This effect was quantified on eleven full scale tests on slab strips without shear reinforcement with a length of 8.4 m. The results clearly show that the increase of plastic strains in the flexural reinforcement leads to a reduction of the shear strength. The measured rotation capacity of the plastic hinge was thus limited by a shear failure.

A particular problem of bridge deck slabs is the introduction of concentrated loads applied by wheels with pneumatic pressure. Punching shear with these loads is usually treated in a manner similar to punching by a column. A punching shear test was performed with a concentrated load simulating a vehicle wheel with pneumatic pressure to investigate the differences. It appears that punching shear with a wheel with pneumatic pressure is less critical because curvatures tend to be distributed over the surface of the applied load rather than concentrated near the edges of the column.

In order to investigate the experimental results on slab strips without shear reinforcement, a mechanical model is proposed to predict the shear strength and rotation capacity of plastic hinges. The shear strength is formulated as a function of the opening of the shear crack and of the strength of the concrete compression zone. The results of the mechanical model are in good agreement with the measured values, both for the shear strength and for the shear carried across the shear crack. Based on the mechanical model, a simplified equation is proposed. The model can also be used to predict the shear capacity of yield-lines.

A non linear finite element model was implemented during this work and used to correctly predict the measured rotations and load-displacements curves of the tested cantilevers and other full scale tests performed by other researchers. The measured

failure loads are accurately estimated by using the results of the non-linear model and the one-way shear and punching shear criteria proposed by Prof. A. Muttoni (Muttoni 2003).

**Keywords:** Reinforced concrete, ductility, slabs without shear reinforcement, shear and punching shear strengths, yield-line, concentrated loads, wheel loads with pneumatic pressure, plastic hinge, mechanical model, aggregate interlock, non-linear finite element analysis, shear flow.

## Résumé

Les dalles des ponts en béton armé sans armature d'effort tranchant peuvent être sollicitées par des charges importantes, concentrées ou uniformément réparties. Le comportement de la structure sous ces charges n'est pas toujours ductile. En particulier, la capacité de déformation sous charges concentrées peut être limitée par une rupture à l'effort tranchant ou par poinçonnement, sans que la charge de rupture par flexion ne soit atteinte. La recherche présentée aborde cette problématique par un programme expérimental important et par une approche théorique.

Une série d'essais à la rupture, effectuée sur des porte-à-faux de ponts de grande échelle soumis à des groupes de charges concentrées a permis de mieux comprendre le comportement réel et d'évaluer la capacité de déformation des dalles de ponts. Six essais ont été réalisés sur deux porte-à-faux d'une portée libre de 2.8 m et d'une longueur totale de 10.0 m. Le comportement observé a été très fragile avec une rupture par poinçonnement ou par effort tranchant. La charge de rupture par flexion, estimée par la méthode des lignes de rupture, n'a jamais été atteinte.

Les essais sur porte-à-faux de ponts ont montré que les armatures de flexion peuvent atteindre la limite d'écoulement avant la rupture par effort tranchant. La plastification des armatures de flexion peut alors réduire la résistance à l'effort tranchant. Cet effet a été quantifié par onze essais à la rupture effectués sur des poutres sans étriers d'une longueur totale de 8.4 m. Les résultats montrent que la plastification de l'armature de flexion mène à une réduction de la résistance à l'effort tranchant. Ces résultats peuvent aussi être décrits comme une limitation de la capacité de rotation des rotules plastiques provoquée par la rupture à l'effort tranchant.

Un problème particulier aux dalles des ponts est l'introduction des charges concentrées par les pneus des véhicules. Ce cas est aujourd'hui traité de façon similaire au poinçonnement d'une dalle par une colonne. Les différences entre les deux cas ont été investiguées par un essai de poinçonnement d'une dalle soumise à une charge simulant un pneu. Il ressort que le poinçonnement par une charge de roue est moins critique, car les déformations de flexion ont tendance à se répartir plutôt qu'à se concentrer près des bords de la colonne.

Pour l'analyse des résultats expérimentaux sur des poutres sans étriers, un modèle mécanique est proposé pour calculer la résistance à l'effort tranchant et la capacité de rotation des rotules plastiques des poutres sans étriers. La résistance à l'effort tranchant est une fonction de l'ouverture de la fissure critique et de la résistance de la zone comprimée. Les résultats obtenus avec le modèle mécanique sont en bon accord avec les valeurs mesurées, ceci tant pour la résistance à l'effort tranchant et que pour l'effort tranchant transmis au travers de la fissure critique. Sur la base des résultats obtenus avec le modèle mécanique, une équation simplifiée est proposée. Le modèle peut aussi être utilisé pour estimer la résistance à l'effort tranchant des lignes de rupture.

Un modèle non linéaire aux éléments finis a été implémenté durant ce travail. Le modèle non linéaire prédit correctement les rotations et les flèches mesurées lors des essais effectués sur des porte-à-faux dans le cadre de ce travail et lors d'essais à l'échelle 1:1 réalisés par d'autres chercheurs. Les charges de rupture sont calculées d'après les résultats du modèle non linéaire et les critères de rupture au poinçonnement et à l'effort tranchant proposés par le Prof. A. Muttoni (Muttoni 2003). Les charges de rupture mesurées lors des essais sont ainsi estimées avec une bonne précision.

**Mots-clés:** Béton armé, ductilité, dalles sans armature d'effort tranchant, résistance à l'effort tranchant, résistance au poinçonnement, charges concentrées, rotule plastique, modèle mécanique, critère de rupture, effet d'engrènement, analyse non linéaire, flux d'effort tranchant.

## Resumo

As lajes de pontes em betão armado sem armaduras de esforço transverso (estribos) podem ser solicitadas por cargas elevadas, concentradas ou uniformemente repartidas. Sob estas cargas, a ductilidade da estrutura não está sempre garantida. Em particular, a capacidade de deformação das lajes sem estribos pode ser limitada por uma rotura por esforço transverso ou punçoamento, sem que a carga de rotura por flexão seja alcançada. O presente estudo aborda esta problemática na sua vertente experimental através de um elevado número de ensaios de grandes dimensões, e na sua vertente teórica através da modelação física e numérica.

Foram efectuados vários ensaios à rotura sobre lajes de pontes de grandes dimensões sujeitas a grupos de cargas concentradas. Estes ensaios permitiram uma caracterização do comportamento real das lajes e a avaliação da sua capacidade de deformação. Esta série de ensaios consistiu em seis testes efectuados sobre duas consolas com um vão livre de 2.8 m e um comprimento total de 10.0 m. Observou-se sempre um modo de rotura frágil por punçoamento ou esforço transverso. A carga de rotura por flexão, estimada pelo método das linhas de rotura, nunca foi alcançada.

Os ensaios sobre as lajes de pontes mostraram que a cedência das armaduras de flexão pode ocorrer antes da rotura por esforço transverso ou punçoamento, sem que no entanto a carga de rotura por flexão seja alcançada. De modo a poder quantificar a influência que a cedência das armaduras de flexão tem sobre a resistência ao esforço transverso, efectuaram-se onze ensaios à rotura sobre vigas de betão armado sem estribos, com um comprimento total de 8.4 m. Os resultados mostram que a cedência das armaduras reduz a resistência ao esforço transverso (até 50% de redução). Os resultados observados podem também ser descritos como uma limitação da capacidade de rotação das rótulas plásticas devido a uma rotura por esforço transverso.

Um problema particular das lajes de pontes é a aplicação de cargas concentradas por pneus. Este caso é actualmente, na prática corrente, tratado de maneira similar ao punçoamento de uma laje apoiada em coluna de betão. As diferenças entre os dois casos (punçoamento com pneu e com coluna) foram analisadas num ensaio de punçoamento de uma laje solicitada por uma carga concentrada simulando um pneu. Concluiu-se que o punçoamento causado por um pneu é um fenómeno que apresenta maior ductilidade do que o punçoamento causado por uma coluna. A explicação para este facto é a seguinte: as deformações de flexão têm tendência a distribuir-se na zona sob o pneu, em vez de se concentrarem na região da laje junto aos bordos da coluna.

Neste trabalho é proposto um modelo mecânico para o cálculo da resistência ao esforço transverso e da capacidade de rotação das rótulas plásticas em vigas sem estribos. A resistência ao esforço transverso é definida como uma função da abertura da fissura crítica e da resistência da zona comprimida. Os resultados obtidos com o modelo mecânico coincidem bem com os valores medidos, quer para a resistência ao esforço transverso, quer para o esforço transverso transmitido através da fissura crítica. Uma

equação simplificada é proposta com base nos resultados do modelo mecânico. O modelo pode também ser usado para determinar a resistência ao esforço transversal das linhas de rotura em lajes de betão.

Durante este trabalho foi ainda desenvolvido um modelo não linear de elementos finitos. Este modelo foi usado para calcular as rotações e os deslocamentos medidos durante os ensaios de consolas efectuados no âmbito deste trabalho e de outros ensaios à escala 1:1 efectuados por outros investigadores. As cargas de rotura são calculadas usando os resultados do modelo não linear e os critérios de rotura ao punçoamento e esforço transversal propostos pelo Prof. A. Muttoni (Muttoni 2003). As cargas de rotura medidas nos ensaios são assim correctamente estimadas, havendo pouca dispersão entre os valores medidos e calculados.

**Palavras chave:** Betão armado, ductilidade, lajes sem estribos, resistência ao esforço transversal, resistência ao punçoamento, cargas concentradas, rótula plástica, modelo mecânico, critério de rotura, efeito de inter-bloqueamento dos inertes, análise não linear, fluxo de esforço transversal.

## Zusammenfassung

Brückenfahrbahnplatten aus Stahlbeton oder Spannbeton ohne Schubbewehrung können durch Punkt- oder verteilte Lasten von grosser Intensität belastet werden. Unter diesen Lasten ist das Tragwerksverhalten nicht immer duktil. Insbesondere unter Punktlasten kann ihr Verformungsvermögen durch Schub- oder Durchstanzbrüchen begrenzt werden, was sie davon abhält, die nach reiner Biegelehre vorhergesagte Bruchlast zu erreichen. Dieses Problem wird in dieser Forschungsarbeit mittels eines umfangreichen Versuchsprogramms und theoretischer Modellierung untersucht.

Die begrenzte Duktilität von Brückenfahrbahnplatten wurde anhand von Versuchen im Massstab 1:1 an Kragarmplatten unter zwei Gruppen von Punktlasten getestet. Sechs Laborversuche im Massstab 1:1 wurden an zwei Platten mit Spannweite von 2.8 m und Länge von 10.0 m durchgeführt. Alle Platten versagten spröde, auf Schub oder Durchstanzen. Die theoretische Biegebruchlast nach Fliesslinientheorie wurde nie erreicht.

Trotz der spröden Natur der Brüche haben die Ergebnisse der Versuche an den Kragarmen gezeigt, dass Fließen zu einem gewissen Masse vor dem Schubbruch auftreten kann und daher die Schubtragfähigkeit reduziert. Dieser Effekt wurde bei elf Plattenstreifen ohne Schubbewehrung mit einer Länge von 8.4 m quantifiziert. Die Ergebnisse zeigen klar, dass eine Zunahme der plastischen Dehnungen in der Biegebewehrung zu einer Abminderung der Schubtragfähigkeit führt. Die gemessene Rotationskapazität des plastischen Gelenks war daher beschränkt durch einen Schubbruch.

Ein besonderes Problem von Brückenfahrbahnplatten ist die Belastung durch konzentrierte Lasten mittels Reifen mit pneumatischem Druck. Durchstanzen durch eine solche Last wird generell auf ähnliche Weise behandelt wie Durchstanzen durch eine Stütze. Ein Durchstanzversuch wurde mit einer Last, die einen Fahrzeugreifen mit pneumatischem Druck simuliert, durchgeführt, um die Unterschiede zu untersuchen. Es zeigt sich, dass Durchstanzen mit einer Reife mit pneumatischem Druck weniger kritisch ist, weil die Krümmung sich über die Lastfläche verteilt, und sich nicht an den Stützenrändern konzentriert.

Ein mechanisches Modell wird vorgeschlagen, um die Schubtragfähigkeit und die Rotationskapazität von Fliessgelenken vorherzusagen. Die Schubtragfähigkeit wird in Abhängigkeit von der Schubrissöffnung und der Festigkeit der Betondruckzone formuliert. Die Ergebnisse des mechanischen Modells sind in guter Übereinstimmung mit den gemessenen Werten, jeweils für die Schubtragfähigkeit und für den Teil des Schubs, der über den Schubriss hinweg übertragen wird. Basierend auf dem mechanischen Modell wird eine vereinfachte Gleichung vorgeschlagen. Das Modell kann auch zur Vorhersage des Schubtragvermögens von Fliesslinien verwendet werden.

Ein nichtlineares Finite-Elemente-Modell wurde im Rahmen dieser Arbeit entwickelt und benutzt, um mit vernünftiger Übereinstimmung die gemessenen Verdrehungen und Last-Verschiebungskurven der getesteten Kragarme und die von Versuchen anderer Forscher im Massstab 1:1 vorherzusagen. Die gemessenen Bruchlasten werden bei Benutzung der Ergebnisse des nichtlinearen Modells und des Schub- und Durchstanzkriteriums, welches von Prof. A. Muttoni vorgeschlagt wurde (Muttoni 2003), akkurat abgeschätzt.

**Schlüsselwörter:** Stahlbeton, Duktilität, Platten ohne Schubbewehrung, Schub- und Durchstanztragfähigkeit, Fliesslinie, Punktlasten, Reifenlasten mit pneumatischem Druck, plastisches Gelenk, mechanisches Modell, Rissuferverzahnung, nichtlineare Finite-Elemente-Berechnung, Schubfluss



# Table of contents

<b>Préface</b>	i
<b>Acknowledgements</b>	iii
<b>Summary</b>	v
<b>Résumé</b>	vii
<b>Resumo</b>	ix
<b>Zusammenfassung</b>	xi
<b>1. Introduction</b>	<b>1</b>
1.1 Problem statement	1
1.2 Aims	3
1.3 Structure of dissertation	3
<b>2. Literature review</b>	<b>5</b>
2.1 One-way and two-way shear	5
2.2 One-way shear failure	6
2.2.1 Kani's approach	6
2.2.2 Mechanical behavior up to failure	7
2.2.3 Failure criterion (Muttoni 2003)	8
2.3 Punching shear failure	11
2.3.1 Mechanical behavior up to failure	12
2.3.2 Failure criterion (Muttoni 2003)	13
2.4 Experimental studies	14
2.4.1 Shear strength after yielding of reinforced concrete slab strips	15
2.4.2 Bridge deck slabs without shear reinforcement	16
2.5 Flexural failure	19
2.5.1 Lower bound methods	20
2.5.2 Yield line method	24
2.5.3 Exact solutions for flexural failure	25
<b>3. Summary of experimental results</b>	<b>27</b>
3.1 Introduction	27
3.2 Tests on large scale RC bridge cantilevers (appendix A)	27
3.2.1 Results	28
3.3 Tests on RC slab strips without shear reinforcement (appendix B)	32
3.3.1 Layout of experiments	32
3.3.2 Results	33
3.3.3 Analysis of strain fields	35
3.4 Punching shear test with simulation of vehicle wheel (appendix A)	39
3.5 Conclusions	42
<b>4. Mechanical model for the shear failure of plastic hinges</b>	<b>45</b>
4.1 Problem statement	45
4.2 Post-yield behavior of the tension tie	46
	xiii

4.3	Aggregate interlock action	48
4.4	Compression zone action	53
4.5	Dowel action	57
4.6	Model for the internal shear distribution	57
4.7	Formulation of the shear failure criterion	61
4.8	Comparison with the test data	63
4.9	Parametric analysis	64
4.10	Simplified equation	66
4.11	Conclusions	67
<b>5.</b>	<b>Shear assessment of bridge deck slabs under concentrated loads</b>	<b>69</b>
5.1	Introduction	69
5.2	Further assumptions to calculate the punching shear capacity	69
5.3	Further assumptions to calculate the one-way shear capacity	70
5.4	Representation of the flow of transverse shear forces	71
5.5	Linear model for calculation of inner forces	72
5.6	Non linear model for calculation of rotations and displacements	75
5.7	Comparison with large scale tests	78
5.7.1	Punching shear test	78
5.7.2	Test of decommissioned slab bridge	82
5.7.3	Tests on bridge deck cantilevers	85
5.8	Conclusions	99
<b>6.</b>	<b>Conclusions</b>	<b>101</b>
6.1	Synthesis of contributions and conclusions	101
6.2	Recommendations for future research	103
	<b>Bibliography</b>	<b>105</b>
	<b>Notation</b>	<b>113</b>
	<b>Test Reports :</b>	
<b>A</b>	<b>Large Scale Tests on Reinforced Concrete Bridge Deck Slabs</b>	
<b>B</b>	<b>Shear Strength without Stirrups after yielding of RC Slab Strips</b>	

# 1. Introduction

## 1.1 Problem statement

A proper understanding of the structural behavior should translate into correct design, as postulated Emil Mörsh already in 1922 (Mörsh 1922):

“Only an exact knowledge of the structural materials and their behavior up to failure in the individual structural members enables the engineer involved with reinforced concrete design to adapt the conventional calculations methods correctly for the particular problem, and accept the responsibility of designing and executing complex reinforced concrete structures, which fulfill the required safety regulations in all parts without being uneconomic”.

This idea should also apply to the design of reinforced concrete slabs.

Reinforced concrete slabs without shear reinforcement can fail in shear. Figure 1.1 shows reinforced concrete slabs without shear reinforcement that are subjected to various loadings. The first example shows a bridge deck slab subjected to the action of four concentrated loads. These concentrated loads represent the footprints of a heavy truck. The second example shows a flat slab supported by columns. In this case the concentrated loads are the permanently applied reactions of the columns. The third case is a cut-and-cover tunnel subjected to a line load. In each case, it is important to know the type of behavior the structure will exhibit (ductile, brittle) and at what load it will fail.

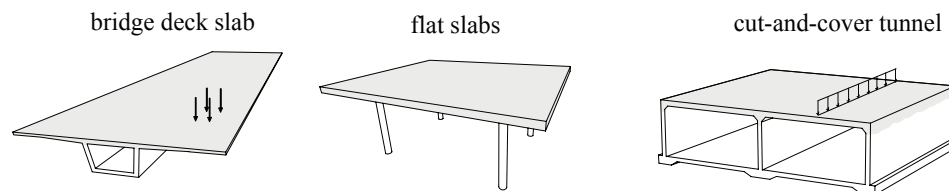


Figure 1.1: Slabs without shear reinforcement

The failure modes of reinforced concrete slabs can be categorized as follows:

- Flexural failure: This failure mode is associated with a ductile behavior of slabs with moderate reinforcement ratios subjected to uniformly distributed loads. Shear stresses in the slab are usually low and the structure can freely undergo plastic strains without a limitation of its capacity.
- Punching shear failure: This failure mode is associated with the local introduction of concentrated loads such as columns or wheel loads. It is brittle and therefore undesirable.
- One-way shear failure. This failure mode is associated with line loads and linear supports with distributed loads. It is also brittle and undesirable.

The actual behavior of slabs is more complex however, because of the two following aspects:

- A shear or punching shear failures may occur either before or after the yielding of flexural reinforcement. In the latter case, this means that a brittle failure type occurs

during the process of yield line formation. The interaction between shear strength and yielding should thus be considered.

- The flow of shear forces in bridge decks is different from either punching shear or one-way shear. Hybrid situations between punching shear and one-way shear failures are commonly found in practical cases (fig. 1.2).

A possible failure type of a bridge deck under concentrated loads is illustrated in figure 1.2. It can be observed that the mode of failure that occurred is somewhere between one-way shear and punching shear (two-way shear). In this case, yielding was reached only just before failure. This shows that the actual behavior may include yielding of flexural reinforcement and intermediate failure types between one-way and two-way shear.

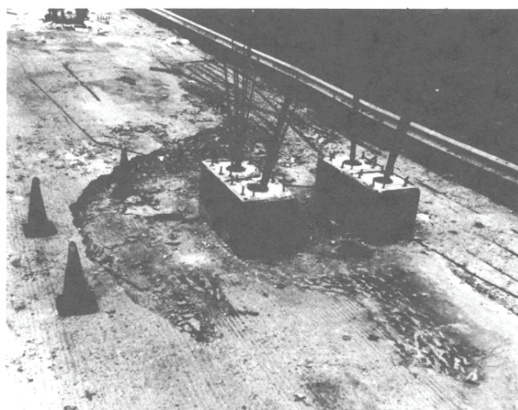


Figure 1.2: Shear failure of full scale bridge deck under concentrated loads (Miller et al. 1994)

This example introduces the main research field of this dissertation. From a conceptual standpoint, it lies at the intersection of three failure types: flexural, punching and one-way shear, as shown in figure 1.3.

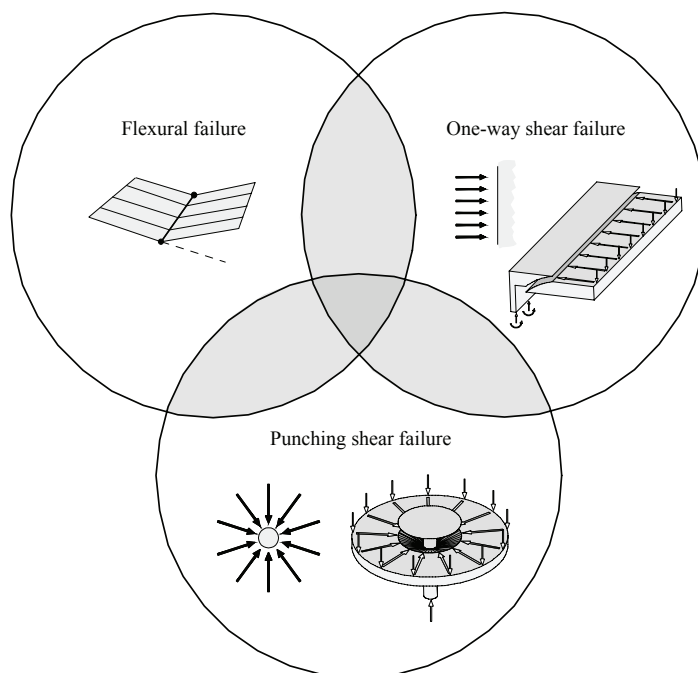


Figure 1.3: Scope of the present research

## 1.2 Aims

The main objectives of this dissertation are:

- To gain a better understanding of the various failure types governing the behavior of concrete bridge decks.
- To provide experimental evidence on the subject.
- To develop a simple and accurate method to assess the load capacity of bridge decks without shear reinforcement.
- To develop a mechanical model able to predict the one-way shear strength after yielding of the flexural reinforcement.

The subject of shear and punching shear strength is an ongoing topic of interest at the Structural concrete laboratory of the EPFL and the present work is based on some aspects previously developed (Muttoni 2003, Guandalini 2005).

## 1.3 Structure of dissertation

This dissertation is organized as follows:

Chapter 2 describes the mechanical behavior up to failure in shear, punching shear and bending. One-way and punching shear models (Muttoni 2003) are presented in detail. A review of previous experimental works on the subject is done, both regarding the effect of yielding on one-way shear and regarding the behavior of bridge decks under concentrated loads. The available methods for calculating the theoretical flexural failure load of bridge deck slabs without shear reinforcement are presented, with an emphasis on cantilever slabs.

Chapter 3 outlines the experimental campaign performed during this dissertation and analyses its results. The full test reports are included in the appendices A and B to the dissertation. The first part of the campaign deals with the shear strength of bridge deck slabs. The second part deals with the shear strength of beams undergoing plastic strains.

Chapter 4 investigates the shear strength of slab strips (beams) without shear reinforcement in the presence of yielding of the longitudinal reinforcement. A mechanical model is developed relating the shear strength to the rotation capacity of the critical section. The predictions of the model are compared with the experimental results.

Chapter 5 investigates the punching shear strength of slabs subjected to concentrated loads. A non-linear model is implemented for estimating the rotations and deflections of reinforced concrete slabs. Its results, in combination with the failure criteria presented in (Muttoni 2003), allow to determine the shear strength of bridge deck slabs. The results from this approach are analyzed and compared to those of the experimental campaign detailed in chapter 3.

Chapter 6 draws conclusions from the present work.



## 2. Literature review

The desired mode of failure for all structures, and more specifically for bridge deck slabs is a ductile failure mode, allowing large deformations and a significant redistribution of inner forces within the structure before collapse. A ductile behavior can usually be expected from a properly designed structure, in which yielding of the reinforcing steel occurs before crushing of concrete. This mode of failure is unfortunately not always guaranteed, as the structure may fail in shear or punching shear before reaching its theoretical flexural strength.

It has been observed that deck cantilevers slabs without shear reinforcement subjected to a concentrated load can fail in shear. This is an undesirable and brittle failure mode, and it prevents the structure from deforming and reaching higher load levels. It is therefore important to investigate and understand the nature of shear failures in deck slabs, which are typically not provided with shear reinforcement.

This chapter reviews contributions on the shear and punching shear strengths of reinforced concrete bridge deck slabs. The various load carrying mechanisms are analyzed both for one-way and punching shear. Contributions pertaining to flexural failure modes are also reviewed.

### 2.1 One-way and two-way shear

In the technical and scientific literature relative to shear and punching shear, these two modes of failure are sometimes referred to as “one-way” and “two-way” shear. This is somewhat of a misnomer as shear, as a mechanical quantity, is inherently unidirectional (it can be represented as a vector). Indeed, at any location shear equilibrium is ensured by two components (typically following the canonical axes:  $v_x$  and  $v_y$ ). It results that there is only one direction for the principal shear, and not two as for moments, which are a tensorial quantity of a higher level, and have at each location two principal directions and two principal moments. Shear is thus exclusively carried in the direction of the principal shear, with no shear being transferred perpendicularly to it. Two-way shear is in that sense a physical impossibility.

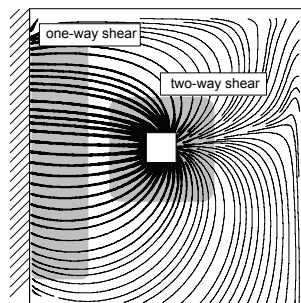


Figure 2.1: Shear flow in a slab : zones of one-way and two-way shear

In fact, “one-way” and “two-way shear” can be better understood by considering the representation of figure 2.1, which shows the flow of shear forces in a cantilever slab subjected to one concentrated load. Zones in which one-way shear is acting are the areas of the plot where the principal shear lines run parallel to one another. This is mostly the case close to the fixed end. Zones in which two-way shear is acting are those in which

the principal shear lines are not running in parallel, as for instance around the point of introduction of the concentrated load.

## 2.2 One-way shear failure

One-way shear failures are generally associated with distributed or line loads and linear supports such as walls or the webs of a bridge girder. In the case shown in figure 2.2, the line load applied at the tip of the cantilever is carried by shear forces to the support along lines running perpendicular to the support (parallel shear flow). A slab without shear reinforcement should be checked against one-way shear failure if this type of flow of inner forces is present. This failure mode is generally brittle and can occur without any indication of an impending collapse.

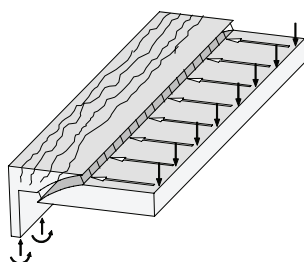


Figure 2.2: Schematic representation of one-way shear failure and associated flow of forces

One-way shear failure models are used to predict the shear failure load of reinforced concrete slabs and beams without shear reinforcement. There has been a great amount of contributions in this field; CEB Bulletin 180 (CEB 1987) summarizes a series of contributions based on the theory of plasticity, fracture mechanics, empirical considerations and numerical simulations.

### 2.2.1 Kani's approach

Kani proposed a rational formulation based on a two regime law, the Kani's shear valley (Kani 1964 and Kani et al. 1979):

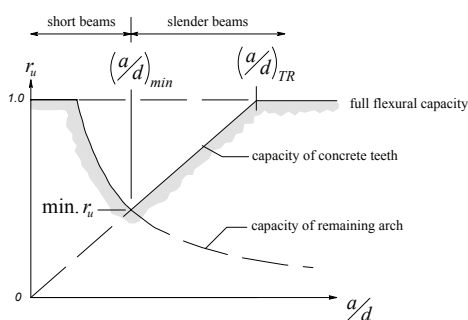


Figure 2.3: Kani's valley of shear failure (adapted from Kani et al. 1979)

Depending on the span-to-depth ratio ( $a/d$ ), the shear capacity is governed either by the capacity of the “remaining arch” or the capacity of the “concrete teeth”. The shear strength is expressed as  $V_R = r_u \cdot M_y / a$ , where  $M_y$  is the yielding moment,  $r_u$  is the reduction factor and  $a$  the shear span. According to this model, the reduction of the flexural capacity is more pronounced for larger depths and increases with the reinforcement ratio.



## 2.2.2 Mechanical behavior up to failure

Several rational models include in their formulation a description of the various load carrying mechanisms and their relationship to the failure load (Fenwick, Paulay 1968). These mechanisms can be represented by strut and tie models (Muttoni, Schwartz 1991). The actual load carrying mechanism depends on the location and the opening of cracks. For a beam with bending cracks, the possible mechanisms include cantilever action, aggregate interlock action and dowel action (fig. 2.4).

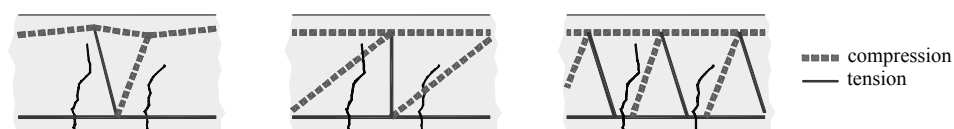


Figure 2.4: Mechanisms of shear transfer without shear reinforcement (Muttoni, Schwartz 1991): Cantilever action, aggregate interlock action and dowel action

In reality, the effects of dowel action, aggregate interlock and cantilever action coexist. When a reinforced concrete beam is loaded to failure, the contribution of the various load carrying mechanisms does not remain constant. Rather, their relative importance depends on the crack pattern and the load level. Figure 2.5 shows the various possible strut and tie models considering the presence of the actual flexural cracks for the slab strip SR3 tested in the framework of this dissertation (see chapter 3). The shape of the bending moment diagram is indicated (fig. 2.5a). These various strut and tie models were discussed by (Guandalini 2005). At the point of zero moment, shear is carried at all load levels by means of a vertical tension tie, entirely relying on the tensile strength of concrete. Before cracking, the state of stresses can be adequately described by using the elasticity theory. After the formation of the first crack under the applied load  $Q_{cr}$ , this is no longer possible. Figure 2.5b) shows a possible strut and tie model for a higher load level ( $0.67 \cdot Q_R$ ). This model assumes that it is not possible to carry a tensile force across a crack. At level of the bottom tie, the shear force is thus carried by the reinforcement through dowel action (fig. 2.4).

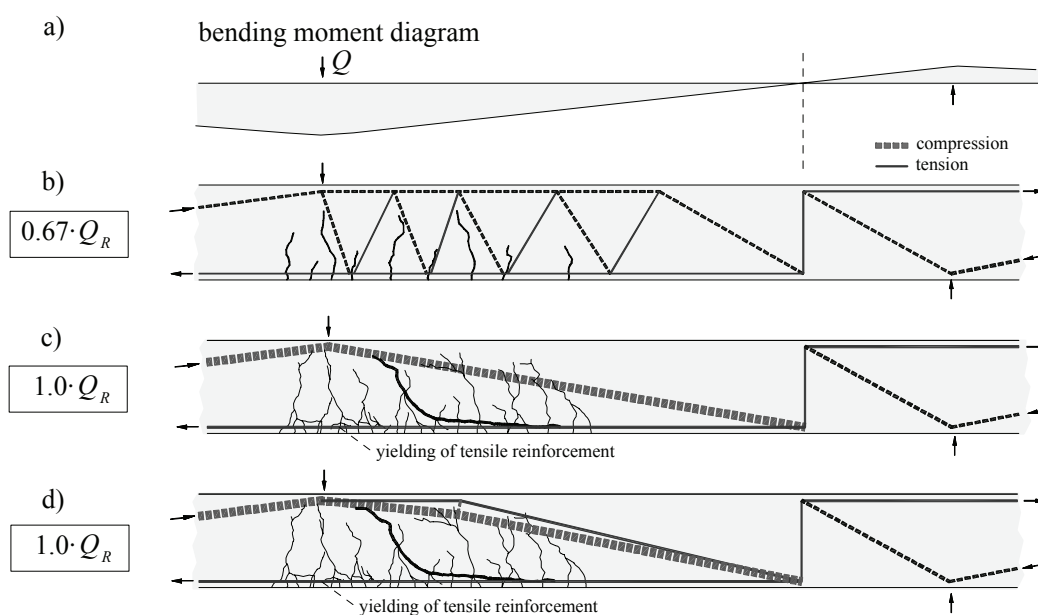


Figure 2.5: Evolution of the load carrying mechanisms up to failure

At  $1.0 \cdot Q_R$  (fig. 2.5c), it can be observed that flexural cracks have propagated not only vertically but also horizontally. This limits the efficiency of the load transfer system depicted in figure 2.5b). A new stress field must therefore develop, compatible with the existing cracks, as shown in figure 2.5c). It consists of an inclined strut from the point of application of the load to the point of zero moment. It can be observed that the compression strut is in part crossed by the shear crack. (Muttoni 1990, Muttoni, Schwartz 1991) showed that, when a strut is crossed by cracks, only a limited amount of compression can be transmitted. This causes the strut to shift towards the top edge of the beam (figure 2.5d). To ensure equilibrium, two additional ties are necessary to equilibrate the deviated strut. These ties will cause the decompression of the top fiber, as shown by experimental observations (Muttoni, Thürlimann 1986). Collapse of the slab strip occurs when the tensile strength of concrete is reached on the tension tie near the concrete surface.

In last two load stages (figs. 2.5c and d), the same shear force is carried. Only the vertical deflection under the point of application of the load increases, which causes the shear crack to propagate toward the point of introduction of the load.

This example clearly shows that the behavior is strongly affected by the location of the critical crack relative to the position of the compression strut. Aggregate interlock also plays an important role since it controls the amount of shear force transmitted across the shear crack. The shear strength of reinforced concrete beams thus depends on the following parameters:

- Concrete compressive and tensile strengths
- Openings of the critical shear crack
- Maximum diameter and strength of the aggregates

### 2.2.3 Failure criterion (Muttoni 2003)

Muttoni proposed a rational model for the shear strength of beams without shear reinforcement (Muttoni 2003). The nominal opening of the cracks in the critical region needs to be known. To that end, the model estimates this opening based on the following hypotheses:

- The critical zone is located at a cross section located at a distance of  $0.5 \cdot d$  from the point of introduction of the load and at  $0.6 \cdot d$  from the extreme compression fiber.
- The crack opening in the critical region is proportional to the product of the section's strains  $\varepsilon$  by the effective depth  $d$ .

Accordingly to these hypotheses and assuming that plane sections remain plane, it follows:

$$\varepsilon = \frac{M}{d \cdot \rho \cdot E_s \cdot (d - x/3)} \cdot \frac{0.6 \cdot d - x}{d - x}, \quad x = d \cdot \rho \cdot \frac{E_s}{E_c} \cdot \left( \sqrt{1 + \frac{2 \cdot E_c}{\rho \cdot E_s}} - 1 \right) \quad (2.1)$$

Where  $x$  is the depth of the compression zone and  $M$  is the bending moment at the critical cross-section.

On the basis of the systematic analysis of 253 shear tests, the one-way shear strength of members without shear reinforcement can be expressed by the following equation:

$$\tau_R = \frac{V_R}{b \cdot d} = \frac{\tau_c}{0.9 + 2.3 \cdot \varepsilon \cdot d \cdot k_{dg}} \quad (2.2)$$

With  $\varepsilon \cdot d \cdot k_{dg}$  in [mm]. The parameter  $k_{dg} = 48 / (D_{max} + 16)$  includes the influence of the maximum aggregate size  $D_{max}$  [mm]. Shear tests on beams without shear reinforcement under concentrated loads are represented in figure 2.6, along with the predictions of this model. The resisting shear force is  $V_R$ , the effective depth is  $d$ , the width of the beam is  $b$  and the concrete compressive strength is  $f_c$ . The nominal shear strength of concrete is  $\tau_c = 0.3 \cdot \sqrt{f_c}$ , with  $f_c$  in [MPa].

As shown in figure 2.6, equation 2.2 predicts well the measured shear strength.

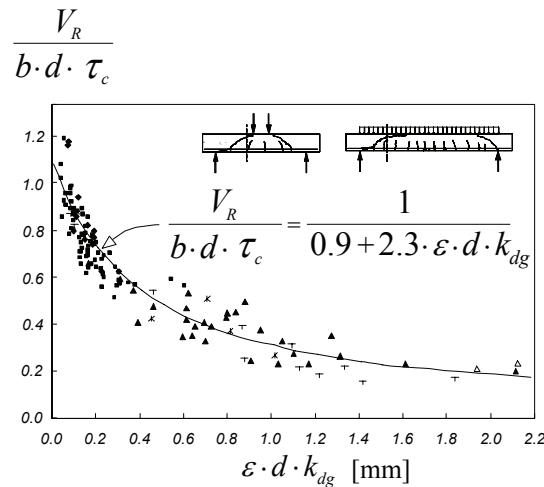


Figure 2.6: Test results from 253 shear tests without shear reinforcement and prediction of equation 2.2 (Muttoni 2003)

It should be noted that the tested beams with low reinforcement ratios, large effective depths (up to 3.0 m) and small diameter aggregates have exhibited very low shear strengths.

### Design equation

As indicated by equation 2.2, the shear strength directly depends on the strains  $\varepsilon$  calculated at the critical cross-section (eq. 2.1). The strains are calculated according to the properties of the cross-section and the acting moment and axial force. As equation 2.2 is too complex for practical applications, a simplified version is included in the Swiss concrete structures code SIA 262 (SIA 2003b). The derivation of the simplified equation is given in SIA D 0182 (SIA 2003c) and Muttoni 2003.

Equation (2.2) can however be applied in design, by introducing the characteristic value of the concrete compressive strength ( $f_{ck}$ ) and the partial safety factor for concrete  $\gamma_c$ .

$$\tau_{Rd} = \frac{V_{Rd,ct}}{b \cdot d} = \frac{\tau_{cd}}{1.0 + 2.5 \cdot \varepsilon \cdot d \cdot k_{dg}} \quad , \quad \tau_{cd} = \frac{0.3}{\gamma_c} \cdot \sqrt{f_{ck}} = 0.2 \cdot \sqrt{f_{ck}} \quad (\gamma_c = 1.5) \quad (2.3)$$

The coefficients on the denominator have been adapted to the design values. The ratio  $V_{R,min} / V_{Rd,ct}$  is 1.25, where  $V_{R,min}$  is the measured shear strength that has probability of 95% of being exceeded.

The section strains  $\varepsilon$  at the critical cross section can be expressed as a function of the strains in the tensile flexural reinforcement  $\varepsilon_s$  and of the depth  $x$  of the compression zone. Assuming that  $x \cong 0.32 \cdot d$ , the following simplified expression is obtained:

$$\varepsilon = \varepsilon_s \cdot \frac{0.6 \cdot d - x}{d - x} \cong 0.41 \cdot \varepsilon_s \quad (2.4)$$

Furthermore, by assuming that the strains in the tensile reinforcement  $\varepsilon_s$  increase linearly with the acting design moment  $m_d$  and that the yielding of the tensile flexural reinforcement occurs when  $m_{Rd}$  is reached, the following expression is obtained:

$$\varepsilon = 0.41 \cdot \frac{f_{sd}}{E_s} \cdot \frac{m_d}{m_{Rd}} \cong 0.0009 \cdot \frac{m_d}{m_{Rd}}, \quad \text{with } f_{sd} = 500 / 1.15 = 435 \text{ MPa} \quad (2.5)$$

Introducing equation (2.5) into equation (2.3) leads to:

$$\tau_{Rd} = \frac{V_{Rd,ct}}{b \cdot d} = \frac{\tau_{cd}}{1 + k_v \cdot d}, \quad \text{with } k_v = 2.2 \cdot \frac{m_d}{m_{Rd}} \quad (2.6)$$

The acting design bending moment  $m_d$  and the resisting bending moment  $m_{Rd}$  should be calculated at the critical cross section.

For a reinforcement with  $f_{sd} > 435$  MPa or an aggregate with a maximum diameter  $D_{max} < 32$  mm, the shear strength predicted by equation 2.6 is to be multiplied respectively by  $f_{sd} / 435$  or  $48 / (D_{max} + 16)$ . For light-weight concrete, the critical crack will cross the aggregates because of their low strength. In his case, a value of  $D_{max} = 0$  should be used.

The hypothesis of a linear relationship between the strains in the tensile reinforcement  $\varepsilon_s$  and the acting bending moment (leading to eq. 2.6) supposes a linear elastic behavior of the reinforcement. If the tensile reinforcement undergoes plastic strains, this assumption is no longer valid. The effect of the yielding of reinforcement should be accounted when the formation of plastic hinges is considered in the design. In this case, the value of the coefficient  $k_v$  should be increased. According to SIA 262 (SIA 2003b), a value of  $k_v = 3$  should be considered after yielding of the tensile reinforcement.

Many tests show that curtailment of the reinforcement inside the critical region leads to a concentration of cracks that induce a reduction of the shear strength. This effect can be considered by increasing  $k_v$  (eq. 2.6) by 50% if the curtailment of the tensile flexural reinforcement lies at a distance  $\leq d$  from the control cross section.

Equation 2.5 implicitly assumes that the strains  $\varepsilon$  are considered along the direction of the flexural reinforcement. In reinforced concrete slabs, it often occurs that the direction of the principal shear force does not coincide with direction of the flexural reinforcement (Marti 2003). If the reinforcement lies parallel to the  $x$  and  $y$  axes, the angle between the direction of the principal shear force and the reinforcement is:

$$\varphi = \tan^{-1} \left( \frac{v_y}{v_x} \right) \quad (2.7)$$

The strains along the direction of the principal shear force can be calculated by multiplying  $k_v$  (eq. 2.6) by the following factor:

$$\frac{1}{\sin^4 \varphi + \cos^4 \varphi} \quad (2.8)$$

As shown in figure 2.7, this factor has a maximum value of 2 when the direction of the principal shear force defines an angle of  $45^\circ$  with the direction of the reinforcement.

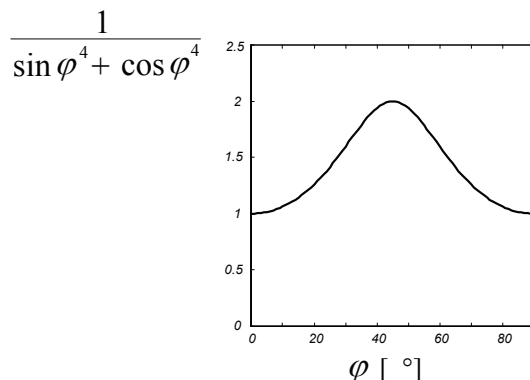


Figure 2.7: Amplification factor for the section strains when the direction of the principal shear force does not coincides with the direction of the reinforcement

## 2.3 Punching shear failure

A punching shear failure is generally associated with the introduction of concentrated loads or punctual supports such as columns. A schematic representation of a symmetrical punching shear failure is shown in fig. 2.8. In this case, the shear forces are introduced in the central support along lines that radiate from the center of a circular column. The failure occurs as the column penetrates across the concrete slab, creating a truncated cone. This failure mode has a nature similar to that of one-way shear, i.e., it is generally brittle and it occurs without signs that the collapse of the slab is impending.

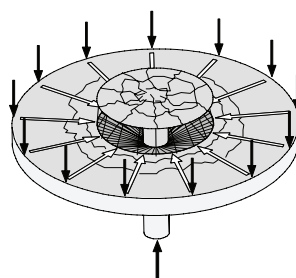


Figure 2.8: Schematic representation of symmetrical punching shear failure and associated force flow

Punching shear failures have in fact always been a major concern in the design of reinforced concrete flat slabs supported by columns (fig. 2.9).



Figure 2.9: Full scale test of slab over columns, 1908, R. Maillart (Maillart 1926)

One of the first mechanical models was proposed by (Kinnunen, Nylander 1960). (FIB 2001), (Guandalini 2005) give an overview of some of the most important contributions on this subject.

### 2.3.1 Mechanical behavior up to failure

The description of the mechanical behavior up to failure has been described by (Muttoni, Schwartz 1991) and (Guandalini 2005).

An understanding of the mechanics of punching shear can be gained from the systematic observation of cracking and of the evolution of deformations in punching shear tests. A major limitation of such observations is that the inner cracks across the slab are invisible. On the contrary, tests on slab strips under one-way shear allow observing the formation of cracks and the development of web deformations up to the shear failure (fig. 2.5).

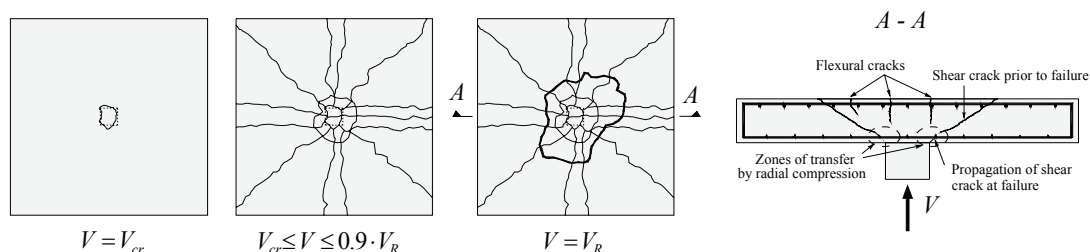


Figure 2.10: Evolution of crack pattern at the top surface (adapted from Guandalini 2005)

In an initial linear elastic phase, the slab deforms elastically until the formation of the first flexural cracks. These cracks appear at low load levels on the top face near the projection of the perimeter of the column (fig. 2.10, at  $V = V_{cr}$ ). The radial cracking moment is reached at those locations. After the first cracking, redistribution of stresses between radial and tangential directions starts. The next cracks are essentially due to the tangential moments. Therefore, these cracks are oriented along lines radiating from the center of the column and dividing the slab into sectors (fig. 2.10, at  $V_{cr} \leq V \leq 0.9 \cdot V_R$ ). Other cracks in tangential direction form at a larger distance from the column (fig. 2.10, at  $V_{cr} \leq V \leq 0.9 \cdot V_R$ ). Inclined cone-shape internal cracks form from the tangential cracks produced by radial bending moments. These inclined cracks tend to propagate toward the column edges (fig. 2.10, cross section  $A - A$ ). After a certain load level and up to failure, no new cracks can be observed, but only an increase of the width of the existing cracks. Failure occurs in a very brittle manner, without significant deformations in case of normally reinforced slabs. The cone-shaped crack between the slab and the punching shear cone suddenly opens and its propagation leads to the collapse. The presence of an important amount of bottom flexural reinforcement can help to suspend the slab after

failure and prevent it from entirely collapsing. The top flexural reinforcement is not effective because it is wrenched from the concrete surface after the punching shear failure.

The analysis of the concrete radial strains at the bottom surface near the column leads to an interesting observation. The compressive strains initially increase up to a load level of  $V = 0.8$  to  $0.9 \cdot V_R$ . Above this load level, the compression strains tend to decrease, and in some cases even tensile strains are measured.

(Muttoni, Schwartz 1991) give an interpretation for this phenomenon based on a stress field (fig. 2.11). The tensile stresses on the bottom surface are necessary to equilibrate the deviated compression strut, in a manner similar to the behavior of slab strips without shear reinforcement under one-way shear.

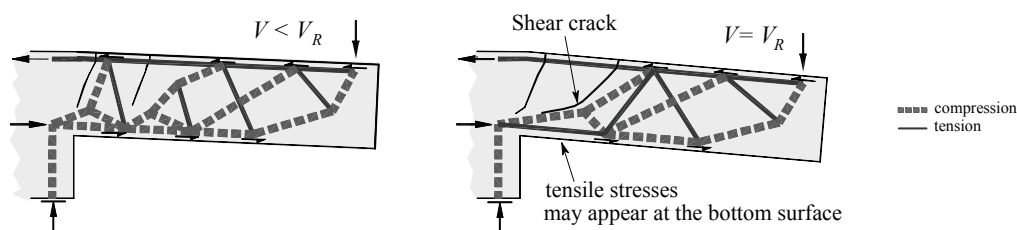


Figure 2.11: Flow of inner forces prior to punching shear failure (adapted from Muttoni, Schwartz 1991 and Guandalini 2005)

### 2.3.2 Failure criterion (Muttoni 2003)

Muttoni proposed a rotation-based model for the symmetric punching of reinforced concrete slabs without shear reinforcement (Muttoni 2003). In a manner similar to slab strips under one-way shear, the shear strength is negatively affected by the propagation of flexural cracks (Muttoni 1990 and Muttoni, Schwartz 1991). The punching shear strength is therefore calculated as a function of the deformations in the critical region. It is observed that the deformations of the slab concentrate in the zone near the column edge. The rotation  $\theta$  of the slab is therefore chosen as the controlling parameter. According to (Muttoni, Schwartz 1991) the width of the critical crack is strongly correlated with  $\theta \cdot d$  (fig. 2.12). The shear strength can be expressed as a function of  $\theta \cdot d$ , as indicated by the equation 2.9:

$$\tau_R = \frac{V_R}{u \cdot d} = \frac{\tau_c}{0.4 + 0.125 \cdot \theta \cdot d \cdot k_{dg}} \quad (2.9)$$

With  $\theta \cdot d \cdot k_{dg}$  in [mm]. The parameter  $k_{dg} = 48 / (D_{max} + 16)$  includes the influence of the maximum aggregate size  $D_{max}$  [mm]. Punching shear tests on slabs without shear reinforcement are shown in figure 2.14, along with the predictions of the model. The resisting punching shear force is  $V_R$ , the effective depth is  $d$ , the length of the control perimeter is  $u$  (see fig. 2.13), and the concrete compressive strength is  $f_c$ . The nominal shear strength of concrete is  $\tau_c = 0.3 \cdot \sqrt{f_c}$ , with  $f_c$  in [MPa].

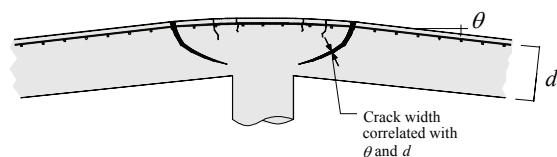


Figure 2.12: Deformations in the zone close to the column and estimate of the width of the critical crack

The control perimeter  $u$  is located at  $0.5 \cdot d$  from the edge of the support (fig. 2.13), according to the Swiss concrete code SIA 262 (SIA 2003b)

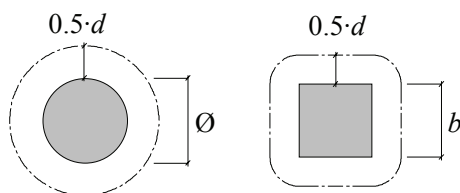


Figure 2.13: Definition of control perimeter for circular and square columns

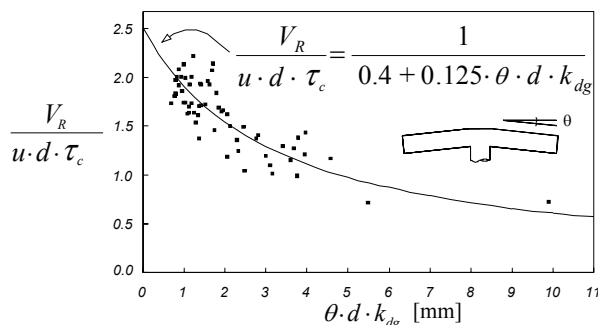


Figure 2.14: Comparison of eq. 2.9 (continuous line) with punching shear tests (Muttoni 2003)

It can be observed that very few punching shear tests are available for large values of  $\theta \cdot d \cdot k_{dg}$ . Indeed, even slabs with low reinforcement ratios will eventually fail in punching shear after a pronounced yielding of the flexural reinforcement. (Guandalini 2005) studied the effect of yielding of flexural reinforcement in the symmetric punching shear strength of slabs without shear reinforcement. He performed several punching shear tests with low reinforcement ratios and concluded that the punching criterion proposed by (Muttoni 2003) remains valid for punching shear failure after yielding of the flexural reinforcement.

## 2.4 Experimental studies

The review of experimental work will focus on the following tests:

- Slab strips without shear reinforcement under one-way shear, failing in shear after yielding of the flexural reinforcement.
- Bridge deck slabs without shear reinforcement under concentrated loads (or similar structures). A larger emphasis is given to full scale structures to limit size effects.



### 2.4.1 Shear strength after yielding of reinforced concrete slab strips

As already mentioned the shear and punching shear failure criteria can be viewed as ductility criteria. Ductility of reinforced concrete slabs was discussed by (Meyboom 2002). He identified and characterized three zones with a distinct behavior regarding ductility:

- Brittle zones. The strength of the slab is dependent on the concrete tensile strength. Zones without shear reinforcement are considered as brittle zones.
- Softening zones. The strength of the slab is dependent on the behavior of concrete in compression. Such zones typically include over-reinforced concrete sections.
- Hardening zones. The strength of the slab is controlled by the properties of the reinforcement. Such zones include all regions where flexural reinforcement yields before the crushing of concrete.

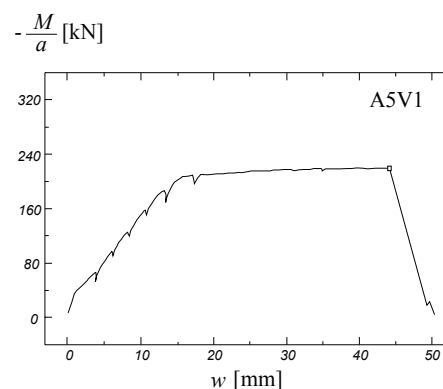
These three categories illustrate well that various ductility limitations can coexist in a given reinforced concrete slab. The slab strips tested in the framework of this dissertation (see chapter 3), that failed in shear after yielding of flexural reinforcement, can be included between the first and third categories.

A very reduced number of slabs strips without shear reinforcement that failed in shear after yielding was found in the literature:

(Jaeger, Marti 2005) performed eight tests on slab strips without shear reinforcement. All specimens without transverse reinforcement underwent a brittle shear failure. Most of the specimens without shear reinforcement failed in shear without yielding of the flexural reinforcement. Test A5V1, shown in fig. 2.15, failed in shear after yielding of the flexural reinforcement. The length of the cantilever is  $a = 0.64$  m, the top reinforcement ratio is  $\rho = 1.06\%$ , the maximum aggregate size  $D_{max} = 16$  mm and the concrete compressive strength  $f_c = 56.7$  MPa.



a) Shear failure of test A5V1



b) Load-displacement curve

Figure 2.15: Test A5V1: shear failure after yielding of flexural reinforcement, adapted from (Jaeger, Marti 2005)

Other tests show that the ductility of the plastic hinge strongly depends on the properties of the reinforcement. (Alvarez et al. 2000) tested three statically indeterminate slab strips without shear reinforcement and with low reinforcement ratios. Test ZP2 shows that the properties of the reinforcement play a crucial role in the deformation capacity of plastic hinges (fig. 2.16).

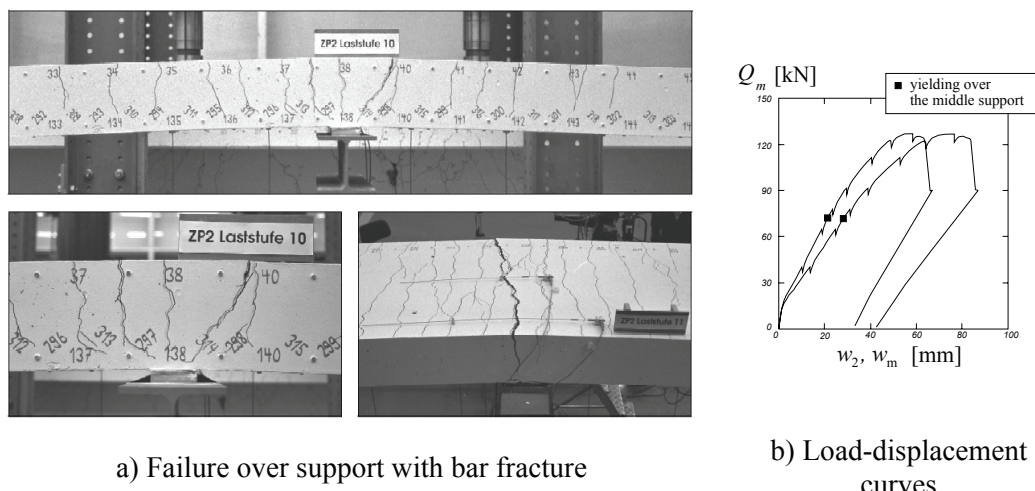


Figure 2.16: Test ZP2: limitation of rotation capacity due to bar fracture, adapted from (Alvarez et al. 2000)

#### 2.4.2 Bridge deck slabs without shear reinforcement

The behavior of bridge deck slabs under concentrated loads is more complex. Several load-carrying mechanisms can develop and coexist, depending on the loading and the geometry of the structure. Two-way shear can become prevalent over one-way shear, but with a flow of inner forces quite different from that of symmetric punching shear. Depending on the loading conditions and the geometry of the structure, yielding of flexural reinforcement can occur before shear or punching shear failure. The following experimental work is related to the shear strength of bridge decks under concentrated loads.

(Miller et al. 1994) performed a destructive test on a 38-year-old decommissioned concrete slab bridge under two concentrated loads (fig. 2.17). The skew bridge had a total length of 31.6 m. The abutments and pier line were skewed at  $30^\circ$  to the roadway. The slab was loaded with two  $1.525 \times 0.690$  m loading blocks simulating the front tandem axle load of a HS20-44 truck (the front tandem has a 144 kN axle load). The bridge failed in shear at  $Q = 3200$  kN, which corresponds to the action of 22 HS20-44 trucks. The theoretical flexural failure load was not reached. Yield was reached only just before failure.

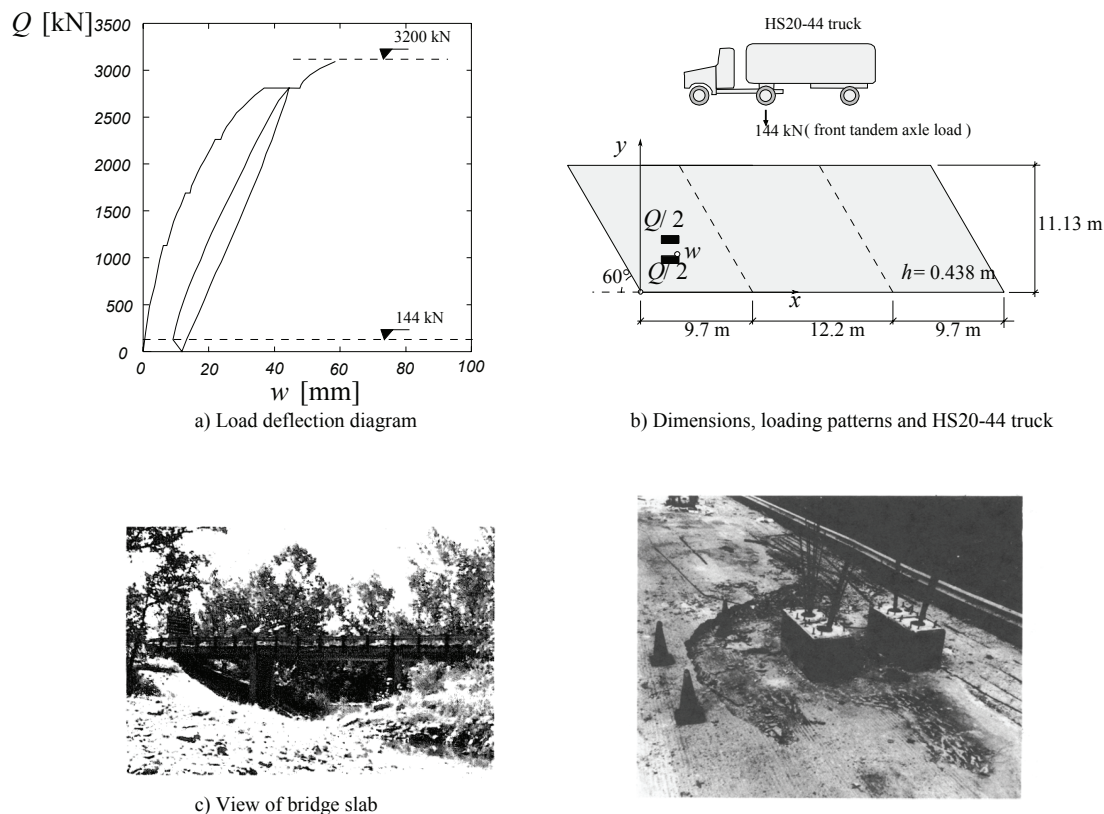


Figure 2.17: Full scale testing of bridge slab, adapted from (Miller et al. 1994)

The following papers focus on the analysis of test results: (Aktan et al. 1992 and Shahrooz et al. 1994).

(Ibell et al. 1999) performed a series of full scale tests on a concrete beam-and-slab bridge deck under concentrated loads. The specimens without stirrups failed in shear with no or limited yielding of the longitudinal reinforcement. It can be observed that for the test shown in fig. 2.18 the shear crack crossed the beam and developed into the slab. No shear reinforcement was present in the slab.

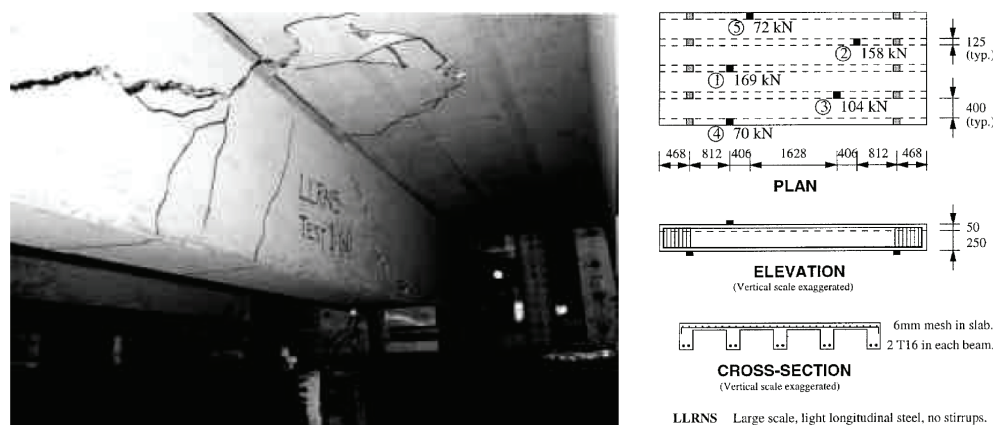


Figure 2.18: Shear failure of full scale beam-and-slab bridge (first test, LLRNS slab, adapted from (Ibell et al. 1999) [mm]

(Lu 2003) performed a series of nine tests on reduced scale cantilevers (fig. 2.19). The tested cantilevers had a relatively small thickness of  $h = 50$  mm to 60 mm. Nevertheless, the behavior of cantilevers under concentrated loads is well represented. The

predominant failure mode is shear. The flexural transverse reinforcement varies from 0.15% to 1.0%. The cantilevers were tested under one or two concentrated loads introduced by means of square loading pads with a side length of 76 mm.

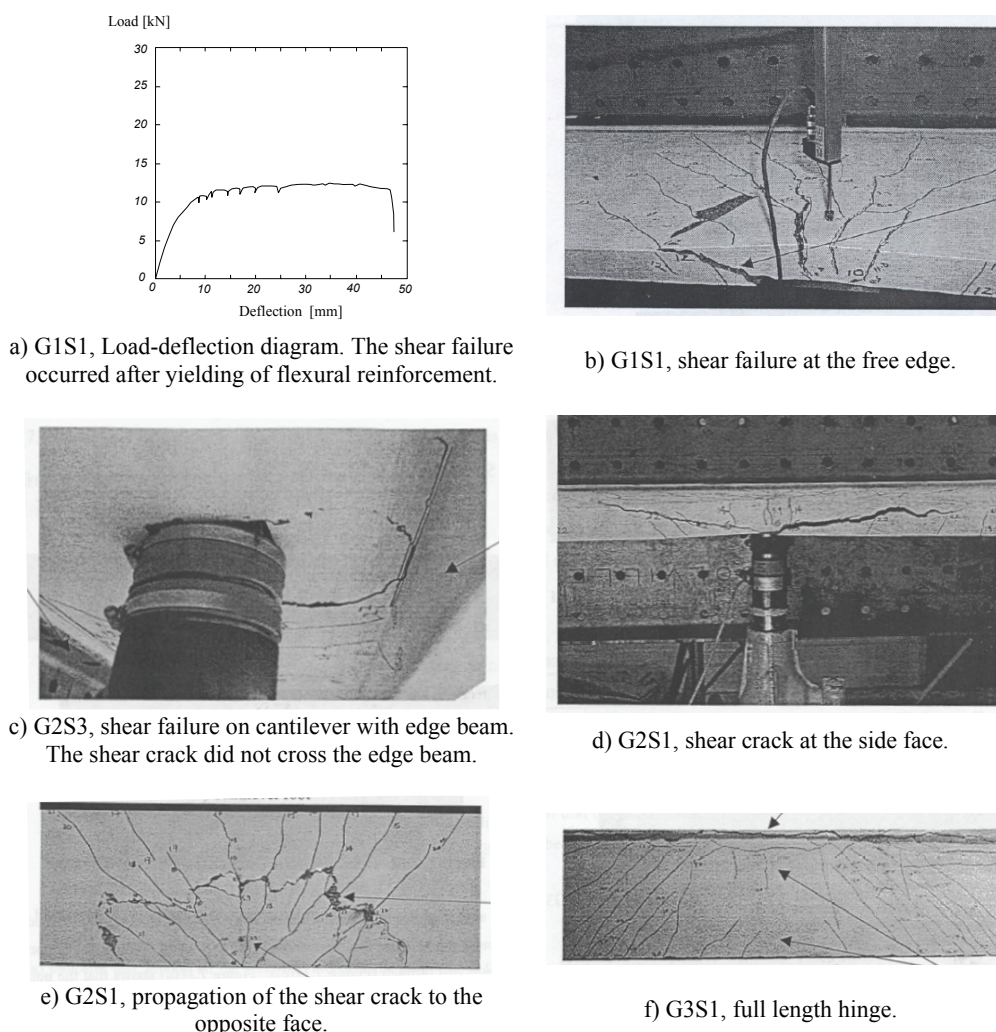


Figure 2.19: Behavior of reduced scale cantilevers under concentrated loads, adapted from (Lu 2003)

Cantilever G1S1 was tested under one concentrated load applied near the free edge. The bending reinforcement ratio was low (0.15%). This cantilever underwent significant ductile deformation before failing in shear (fig. 2.19a). The failure seems to have propagated from the shear cracks in longitudinal direction (fig. 2.19b). Cantilever G2S3, with an edge beam, was tested under a single concentrated load near the free edge (fig. 2.19c). The failure mode was punching shear, but the punching shear crack did not cross the edge beam. The edge beam had a width of 60 mm and an overall depth of 150 mm. Cantilever G2S1 illustrates well the behavior of cantilevers without edge beam subjected to concentrated loads (figs. 2.19d and 2.19e). The shear crack propagates across the thickness to reach the surface opposite to the load introduction. The behavior is brittle (figs. 2.19d and 2.19e). Similar to cantilever G1S1, but subjected to two concentrated loads applied along a line perpendicular to the fixed end, cantilever G3S1 developed a full length hinge (fig. 2.19f).

(Vaz Rodrigues 2002) tested a 1/3 scale model of two cantilevers under concentrated loads applied at the edge. One of the cantilevers has a large edge beam (0.4 x 0.12 m).

The reinforcement ratio was  $\rho = 1\%$  for the transversal top reinforcement over the clamped edge, where the thickness of the slab was  $h = 0.14$  m. The slab thickness at the free edge was  $h = 0.11$  m. The failure mode was a punching shear edge failure, at the free edge without the edge beam (fig. 2.20). The failure load was  $Q = 190$  kN, which corresponds to approximately 75% of the yield line prediction ( $Q_{flex} = 263$  kN).

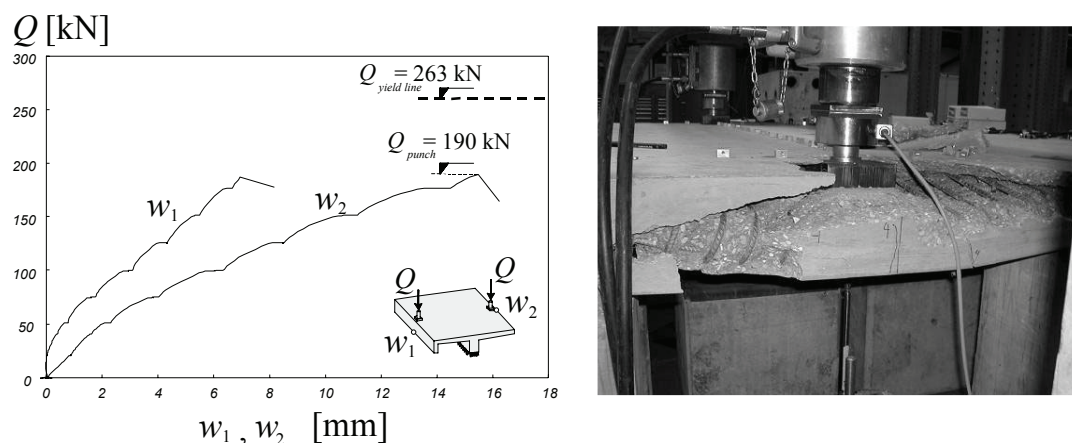


Figure 2.20: Punching shear edge failure of reduced scale cantilever (Vaz Rodrigues 2002)

(Jorgenson, Larson 1976) tested a full scale bridge deck slab subjected to a line load. The line load was applied perpendicularly to the traffic lanes, in the mid-span of a bridge deck slab with a span of 7.6 m between piers and a slab thickness of 0.29 m (fig. 2.21a and b). The theoretical flexural failure load was reached (fig. 2.21c).

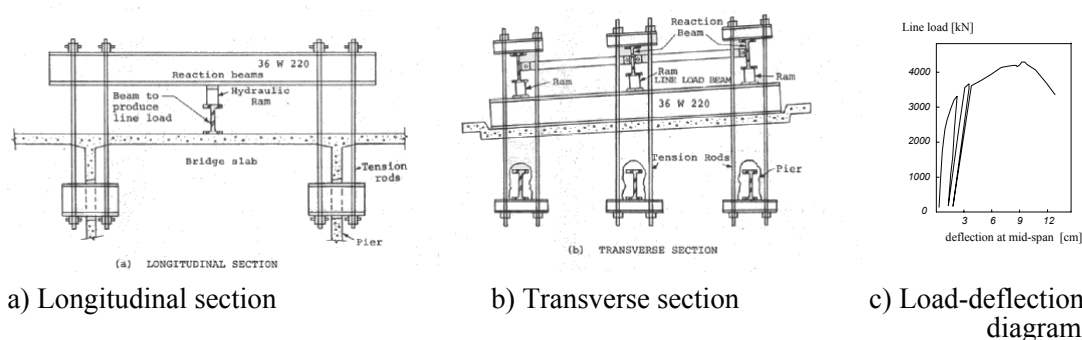


Figure 2.21: Flexural failure of bridge deck under line load (adapted from Jorgenson, Larson 1976)

An extensive review of the available experimental data related to the load capacity of highway bridges is available in (Burdette, Goodpasture 1988).

## 2.5 Flexural failure

The flexural strength can be estimated using classical methods derived from the theory of plasticity. Lower bound methods, such as the discontinuity line analysis or the theory of elasticity lead to lower bound (conservative) estimates of the failure load. Upper bound methods, such as the yield line method, lead to upper bound (unconservative) estimates of the flexural failure load.

Methods based on the theory of plasticity are well adapted for the design of structures that satisfy the requirements of that theory, namely that all sections of the structure

exhibit a ductile behavior. A sufficient ductility is necessary to allow redistributions of inner forces to take place, so that the theoretical ultimate flexural load of statically undetermined structures can be reached.

This section presents a brief description of applicable methods for the calculation of the flexural strength of flat slabs. In particular, applications to cantilever slabs under concentrated loads are highlighted.

### 2.5.1 Lower bound methods

A moment field is considered a lower bound if it is in equilibrium (eq. 2.10) and if the moments at all points of the structure are smaller than the corresponding yielding moments. The load corresponding to that moment field is always smaller or equal than the actual failure load.

$$\frac{\partial^2 m_x}{\partial x^2} + \frac{\partial^2 m_y}{\partial y^2} + 2 \frac{\partial^2 m_{xy}}{\partial x \cdot \partial y} = -q \quad (2.10)$$

The shear forces along direction  $x$  and  $y$  are defined as :

$$v_x = \frac{\partial m_x}{\partial x} + \frac{\partial m_{xy}}{\partial y}, v_y = \frac{\partial m_y}{\partial y} + \frac{\partial m_{yx}}{\partial x} \quad (2.11)$$

While the moments in a slab are represented as a tensor and have two principal directions and moments, the shear forces can be represented as a vector with a single principal direction and principal shear force. The magnitude and direction of the principal shear force is defined as (Marti 1990) :

$$v_{tot} = \sqrt{v_x^2 + v_y^2}, \varphi = \text{atan} \left( \frac{v_y}{v_x} \right) \quad (2.12)$$

There is thus no transmission of shear perpendicularly to the direction of the principal shear force.

### *Elastic analysis*

A particular lower bound is given by the theory of elasticity (Timoshenko, Woinowsky-Krieger 1959). The elastic analysis of thin isotropic slabs is based on the Lagrange equation, a fourth order bi-harmonic differential equation (eq. 2.13):

$$\frac{\partial^4 w}{\partial x^4} + 2 \frac{\partial^4 w}{\partial x^2 \cdot \partial y^2} + \frac{\partial^4 w}{\partial y^4} = \frac{q}{B} \quad (2.13)$$

The plate rigidity is  $B = E \cdot h^3 / 12 \cdot (1 - \nu^2)$ .

The use elastic analysis, which assumes the material to remain linear, elastic and uncracked is well adapted to checking the behavior of the structure at service load, because the amount of cracking and yielding is limited. As these effects become more important, the elastic solution starts to diverge from the actual distribution of inner forces, since no account is made for the non linear behavior of the structure.

The elastic analysis of bridge decks is widespread nowadays by the generalized use linear elastic finite element programs. Any arbitrary geometry and loading can be considered and the inner forces calculated. Nevertheless, finite element analyses can be

time consuming, especially in the conception phase, and prone to errors. Simple equations that allow for hand calculations remain therefore very useful in conception and control of the finite element results.

Bridge deck cantilevers are rather sensitive part of the bridge deck, because they must resist simultaneously to high moments and shear forces induced by loads acting on the cantilevers. The next couple of references are devoted to the elastic methods used in the estimation of the hogging (negative) moment in cantilever slabs.

(Jaramillo 1950) gave the exact elastic solution for an infinitely long (in the longitudinal direction) cantilever plate with a constant thickness and subjected to a concentrated load at any arbitrary position. The bi-harmonic equation (eq. 2.13) was solved and the deflection function was represented by a Fourier integral with eight unknowns that can be calculated by introducing the boundary conditions. Although this is the most rigorous solution, it is not suitable for hand calculations. A computer program to calculate the exact solution is given in (Lu 2003). (Reismann, Cheng 1970) studied the effect of an edge beam with bending and torsional stiffness on the behavior of the cantilever. The exact solution was derived for a cantilever with a constant thickness and an applied concentrated load on top of the edge beam. The solution is not applicable to point loads applied to the slab itself.

(Pucher 1964) developed influence surfaces of moments and shear forces for plates with various boundary conditions. (Homberg, Ropers 1965 and Homberg 1968) extended these influence surfaces to plates with variable thickness (linear and parabolic) and multiple spans, including cantilevers (fig. 2.22). These charts provide practical design tools for the design of plates subjected to concentrated loads.

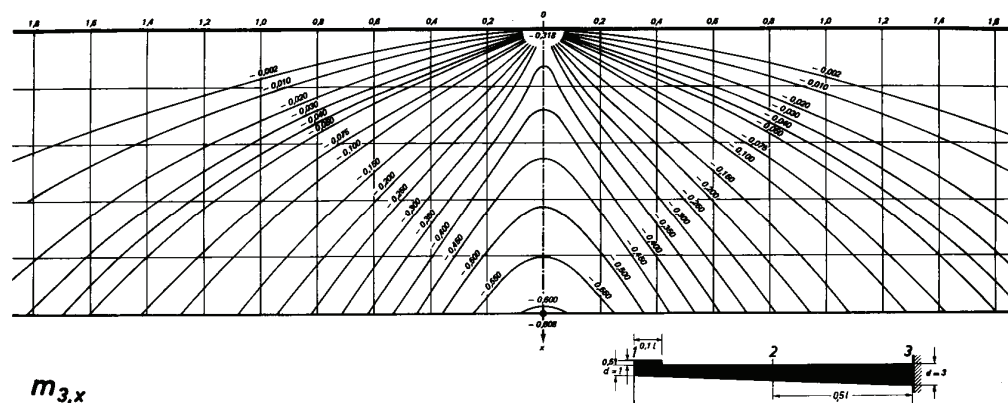


Figure 2.22: Influence surface of variable depth cantilever (Homberg 1968)

(Sawko, Mills 1971) proposed a simplified equation that gives an approximate solution for calculating the transversal hogging (negative) moment at the root of a uniformly thick cantilever slab subjected to a concentrated load applied at any location (eq. 2.14). (Bakht, Holland 1976 and Jaeger, Bakht 1979) modified this equation to calculate the hogging moment at points others than the cantilever root.

$$m_x = -\frac{Q}{\pi} \cdot A' \cdot \frac{1}{\cosh(A' \cdot y/\xi)} \quad (2.14)$$

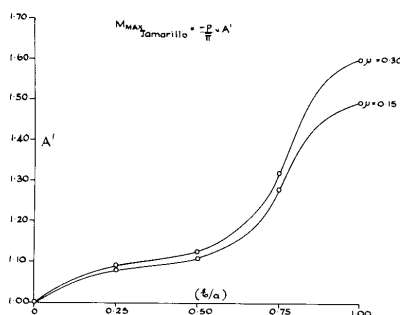


Figure 2.23: Approximate solution for hogging moment at cantilever root (Sawko, Mills 1971)

The width of the cantilever is  $a$ , the transverse distance from the load to the cantilever root is  $\xi$ , the longitudinal distance from the load to the point of interest is  $y$  and  $A'$  is an empirically derived coefficient obtained from finite element analysis.

(Bakht 1981) presented a simplified semi-graphical method for determining transversal moments in edge stiffened cantilever slabs with linearly varying thickness. This author used the grillage analogy method. A method for determining maximum moments in the edge beam is also proposed.

If, as it is in reality, the cantilever is not fully fixed, but rather elastically restrained by the rest of the deck slab and the webs, the maximum negative moment decreases. (Dilger et al. 1990) analyzed the restraining effect of the web and internal deck panels on the hogging transversal moments at the root of the cantilever deck slab. He stated that the assumption of full fixity may lead to a strong overestimation of the acting moments (fig. 2.24).

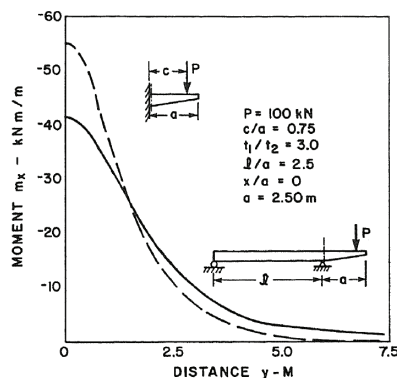


Figure 2.24: Effect of restraining internal deck panels on the maximum hogging moment at the clamped edge of the cantilever (Dilger et al. 1990)

(Mufti et al. 1993) develop a simplified method for analyzing hogging moments in internal deck slab panels of slab-on-girders bridges due to single concentrated loads on the deck slab overhangs. The proposed design charts are derived after finite element analysis.

### Strip method, advanced strip method and discontinuity line method

If torsional moments are neglected ( $m_{xy} = 0$ ), the basic equilibrium equation (eq. 2.10) can still be used to design reinforced concrete slabs, which are then able to carry loads only in the orthogonal directions. This hypothesis serves as the basis to the simple strip method of design, proposed by (Hillerborg 1974). The applied load is equilibrated with



a system of strips that carry loads in bending only. The dimensions of each strip and the portion of the load it carries are chosen by the designer, who is responsible that the system remains in equilibrium. The slab is designed using a grillage of strips that are separated by static discontinuities. The moment fields that are close to elastic solutions are more adequate to ensure serviceability requirements. This method is mostly applicable to slabs supported on linear supports. The advanced strip method (Hillerborg 1982) focuses on the design of more complex slabs, which are partly supported on columns, present re-entrant corners or other point supports or with concentrated loads.

The discontinuity line method (Morley 1986) proposes a particular form of a lower bound solution based on torsionless grillages of closely spaced orthogonal beams. The solution is based on a particular form of discontinuity in the moment fields along the lines of load transfer. The resulting moment patterns are suitable for use with concentrated loads or column reactions.

(Lu 2003) applied the discontinuity line method to cantilevers under concentrated loads. This author proposes discontinuity line patterns for uniformly thick cantilevers under a concentrated load, edge-stiffened cantilevers under a concentrated load and uniformly thick cantilevers under twin loads (fig. 2.25).

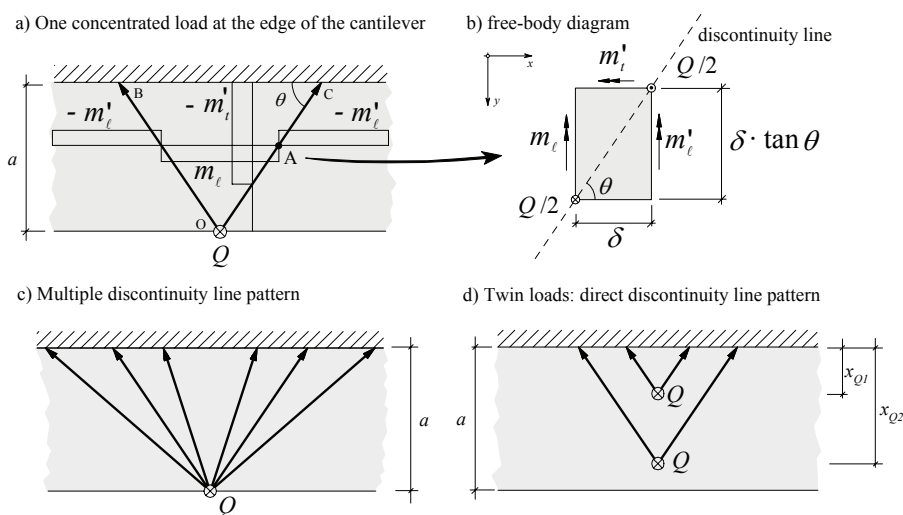


Figure 2.25: Discontinuity line patterns for uniformly thick cantilevers, adapted from (Lu 2003)

The basic principle of the discontinuity line method is illustrated in figure 2.25a). The concentrated load  $Q$  is applied at the free edge of the cantilever. A moment field is in equilibrium with the concentrated load. The transverse hogging yielding moment per unit length of the slab is  $m_t'$ , the longitudinal hogging yielding moment per unit length of the slab is  $m_l'$  and the longitudinal sagging yielding moment per unit length of the slab is  $m_l$ . It should be noted that values of  $m_t'$ ,  $m_l'$  and  $m_l$  are all positive (moment capacities). There are discontinuities in the moment field across lines  $OB$  and  $OC$ . A load of  $Q/2$  is carried along each of these lines. The free body diagram at point  $A$  is indicated in fig. 2.25b). The equilibrium of moments along the  $x$  and the  $y$  axis yields the lower bound estimate of the flexural strength  $Q$  and the angle of the discontinuity lines  $\theta$ .

$$Q = 2 \cdot \sqrt{m_t' \cdot (m_l + m_l')}, \quad \tan \theta = \sqrt{m_t' / (m_l + m_l')} \quad (2.15)$$

The same procedure can be applied to calculate the lower bound estimate of systems with multiple discontinuity line patterns (fig. 2.25c) or several applied loads (fig. 2.25d). This approach seems promising, but the results reported by Lu indicate that the lower bound estimates of the ultimate load only equal 30% of the actual flexural failure load. Equation 2.15 can be compared with the exact solution (eq. 2.20) for an isotropic and uniformly thick cantilever loaded with a concentrated load at the free edge. For this case, eq. 2.15 gives a lower bound estimate that equals 55% of the theoretical flexural failure load (eq. 2.20).

## 2.5.2 Yield line method

Upper bound solutions can be calculated using the yield line theory. The yield line theory was simplified by (Johansen 1962), by restricting the collapse mechanisms to circular, linear and spiral yield lines. He further assumed that close to failure the slab behaves as a system of rigid panels, with the bending curvature concentrated at the yield lines. This assumption correctly describes the actual behavior of slabs failing in bending. The calculation of the upper bound is based on a kinematically admissible displacement field that defines a collapse mechanism. The upper bound load can be calculated using either virtual works or equilibrium methods.

When applying virtual works, the internal work dissipated along the yield lines is set equal to the work done by the applied forces:

$$\sum Q \cdot w = \sum \int m_{nu} \cdot \theta_n ds \quad (2.16)$$

Where  $\theta_n$  is the yield line rotation and  $m_{un}$  the yielding moment along the yield line. The stepped yield line criterion was proposed by Johansen to calculate the capacity of the slab along the yield line. This criterion is derived from equilibrium considerations of moments along the yield line (fig.2.26a). The resistance of the slab along the yield line is:

$$m_{nu} = m_{xu} \cdot \cos^2 \phi + m_{yu} \cdot \sin^2 \phi, \quad m_{mu} = (m_{yu} - m_{xu}) \cdot \sin \phi \cos \phi \quad (2.17)$$

The applied loads will create bending and torsional moments along the yield line of:

$$\begin{aligned} m_n &= m_x \cos^2 \phi + m_y \sin^2 \phi + 2 \cdot m_{xy} \sin \phi \cdot \cos \phi \\ m_m &= (m_y - m_x) \cdot \sin \phi \cdot \cos \phi + m_{xy} \cdot \cos 2\phi \end{aligned} \quad (2.18)$$

Combining equations 2.17 and 2.18 gives the normal yield criterion for slabs:

$$(m_{xu} - m_x) \cdot (m_{yu} - m_y) \geq m_{xy}^2 \quad (2.19)$$

This yield criterion can be represented in terms of a failure surface. The failure surface is represented for an isotropic slab of different amount of reinforcement at top and bottom (fig. 2.26b). The failure surface is defined by two cones, with the axis in the direction AC. The common base of the two cones lies in a plane that passes through BD and is perpendicular to the plane defined by  $m_{xy} = 0$ .

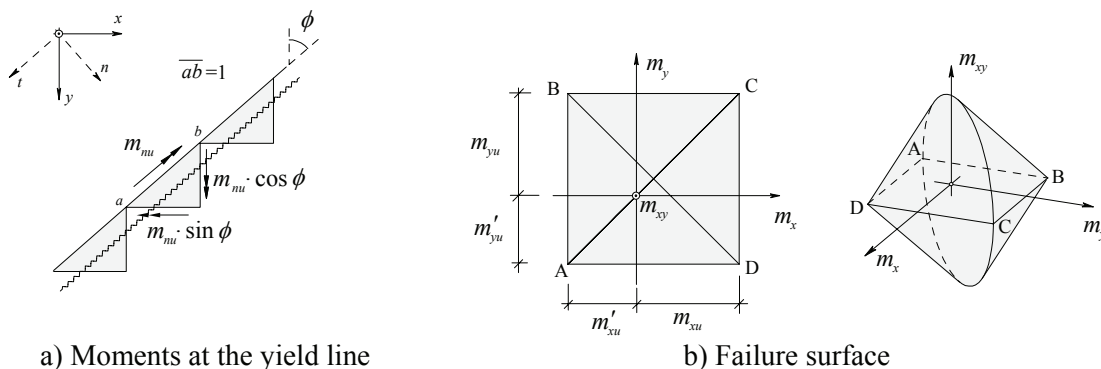


Figure 2.26: Johansen's normal yield criterion

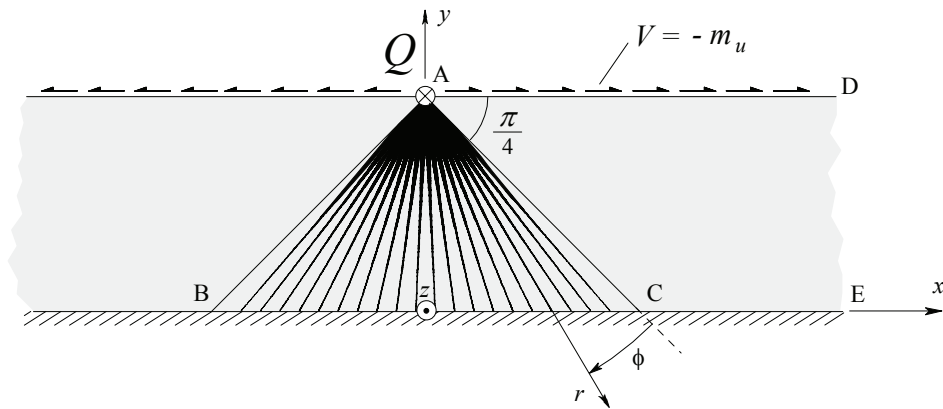
The normal yield criterion is derived only from bending considerations. (Nielsen 1964) and (Marti, Kong 1987) have shown that the normal yield criterion can lead to an overestimation of the flexural strength of the slab, when the principal moment directions deviate considerably from the directions of the reinforcement. The error increases with increasing amounts of reinforcement.

An extensive library of yield line mechanisms is given in (Johansen 1972), including two yield line mechanisms for isotropic cantilevers under concentrated loads at arbitrary positions. (Lu 2003) analyzed other yield line mechanisms for uniform thick cantilevers with isotropic reinforcement under a concentrated load. Actual bridge deck cantilevers can be more complex than isotropic slabs: they are usually orthotropic in both reinforcement layers, present discontinuities in the reinforcement, have a variable thickness and can be loaded with multiple point loads and/or with uniformly distributed loads. The application of yield line theory to this type of structures requires the use of computer programs (Middleton 1993).

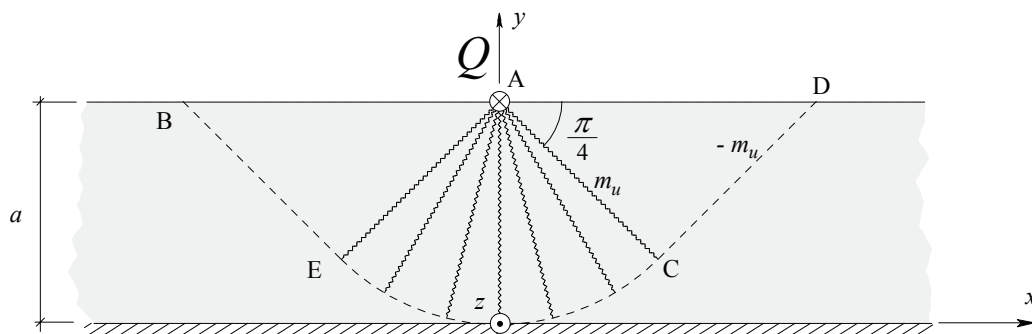
### 2.5.3 Exact solutions for flexural failure

(Nielsen 1964) and (Marti 2003) discussed the exact solution for an infinitely long, isotropic and uniformly thick cantilever subjected to a concentrated load at the free edge (fig. 2.27). The cantilever plate has a transversal width of  $a$ . The slab is isotropic with equal top and bottom reinforcement. Therefore the yielding moment is  $m_u$ , for both positive and negative curvatures, and in all directions. Figure 2.27a) shows the trajectories of principal shear force corresponding to the moment field of the lower bound solution. In region ADCE, the moment field is defined by  $m_x = m_y = 0$  and  $m_{xy} = m_u$ . There is no shear within this region, but a shear force is transmitted along the edge AD,  $V = -m_u$ . In region ABC, the moment field is defined using radial coordinates as  $m_r = -m_\phi = m_u$ . The shear field has principal directions along the  $r$  axis and the magnitude of the principal shear force inside this region is  $v_{tot} = 2 \cdot m_u / r$ . The shear flow trajectories are represented with a variable thickness, proportional to the magnitude of the principal shear force (fig. 2.27a). The thicker lines near the applied load indicate large shear forces. The total shear force carried across region ABC is  $\pi \cdot m_u$ . Vertical equilibrium at point A gives the following lower bound:

$$Q = (2 + \pi) \cdot m_u \quad (2.20)$$



a) Lower bound solution



b) Upper bound solution

Figure 2.27: Exact solution for a cantilever slab under concentrated load  $Q$  at free edge

The analysis of the yield line mechanism is considered in figure 2.27b). For a unit vertical displacement under the load  $Q$ , the energy dissipation is  $\pi \cdot m_u$  for region AEC and  $2 \cdot m_u$  for lines BE and CD. The upper bound failure load is  $Q = (2 + \pi) \cdot m_u$ .

Because both lower and upper bound values are the same, the theoretical flexural failure load is  $Q = (2 + \pi) \cdot m_u$ .

### 3. Summary of experimental results

#### 3.1 Introduction

This chapter describes the main results gained from the experimental campaign carried out in the framework of this dissertation. The first part of the experimental program consisted of six tests performed on two large scale bridge deck cantilevers. The specimens were subjected to various configurations of concentrated forces simulating traffic loads. For all tests, the observed failure mode was shear.

The second part of the experimental program consisted of shear tests on twelve slab strips, with the aim to investigate the influence of plastic hinge rotation on the shear strength. The test results show that the shear strength decreases with increasing plastic hinge rotation. In addition, a punching shear test with a flat jack simulating the action of a pneumatic tire was performed. The aim of this test was to compare the case of a punching shear failure induced by uniformly distributed pressure with the classical case of punching shear induced by a concrete column.

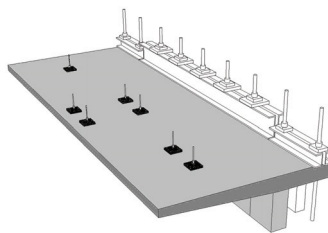
Detailed test results are available in appendices A and B to this dissertation.

#### 3.2 Tests on large scale RC bridge cantilevers (appendix A)

The tested cantilevers are almost full scale specimens that represent the actual behavior of typical and large bridge cantilevers in Switzerland (fig. 3.1a). With a transverse span of 2.78 m and a total length of 10 m, each of the two tested cantilevers was tested three times, with various loading conditions, as shown in figures 3.1b) and 3.2. For slab DR1, the transversal reinforcement of the top layer at the fixed end consisted of 16 mm diameter bars at 75 mm spacing (reinforcement ratio  $\rho = 0.79\%$ ). For slab DR2, the transversal reinforcement of the top layer at the fixed end consisted of 14 mm diameter bars at 75 mm spacing (reinforcement ratio  $\rho = 0.6\%$ ). No shear reinforcement was provided.



a) Bridge girder with cantilever



b) Large scale model under loading patterns



c) Test DR1-a, under four concentrated loads

Figure 3.1: Test concept and load arrangement

Figure 3.2 shows the reinforcement layout and the dimensions of the cantilevers, along with the position of the concentrated loads simulating vehicle wheels. The specimens were conceived as a large scale model (3/4) of a large bridge cantilever (span 3.7 m, thickness varying from 250 to 500 mm). All dimensions, including the layout of the twin axle loads and the size of the load introduction plates were consequently scaled by

3/4. The bottom reinforcement consists of 12 mm diameter bars at 150 mm spacing in both directions for all slabs. The top longitudinal reinforcement consists of 12 mm diameter bars at 150 mm. The concrete cover is 30 mm. The reinforcement steel used at the transversal direction at the top layer is hot rolled, with a yield strength of 515 MPa. Ordinary concrete was used in both slabs with average measured values at the time of testing of compressive strength of  $f_c = 40$  MPa and Young's modulus of  $E_c = 36 \cdot 10^3$  MPa. Maximum aggregate size is 16 mm.

The applied loads for the test DR1-a are the twin axle loads prescribed by Eurocode 1 (Eurocode 1 2003) with all dimensions reduced by 3/4. Subsequent tests were performed using only one or two concentrated load to better focus on shear and punching shear failure modes, as shown in figure 3.2 and summarized in table 3.1. The concentrated loads were applied on the top of the slab using steel plates with dimensions 300 x 300 x 30 mm. The fixed end support was clamped by means of a vertical prestressing (7 MN total force). The concentrated loads were applied through holes ( $\varnothing$  130 mm) in the slab, which allowed to pull directly from the strong floor.

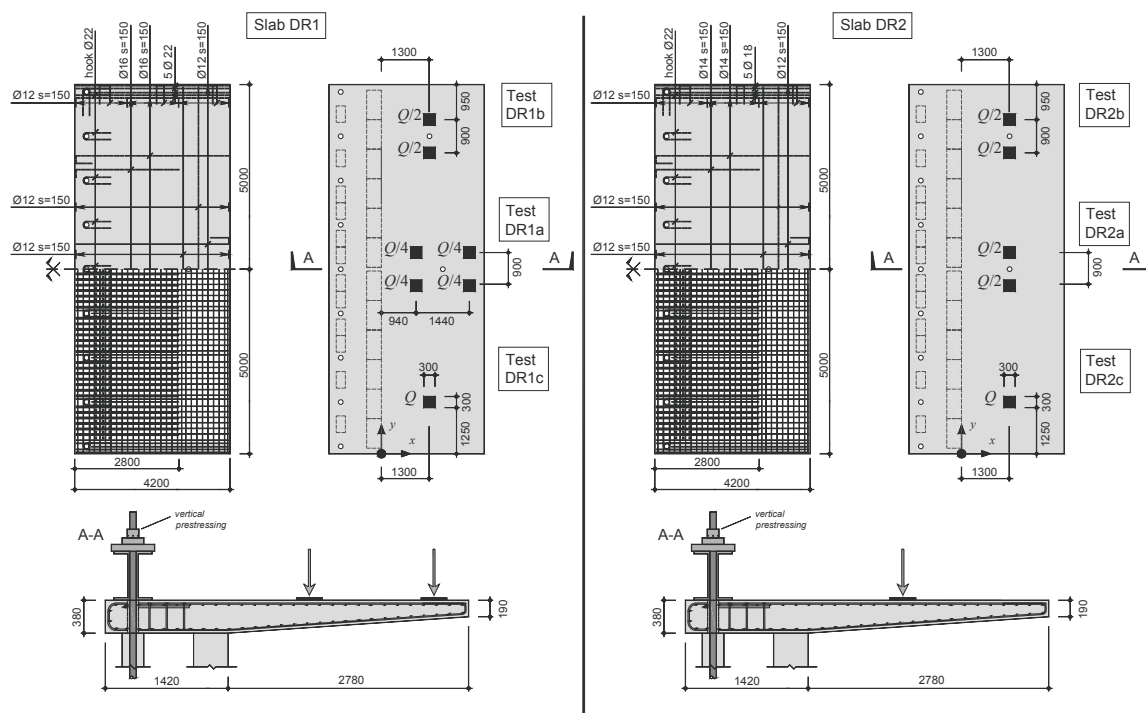


Figure 3.2: Slab dimensions, reinforcement layout and applied loads. Dimensions in mm.

### 3.2.1 Results

Table 3.1: Results of experiments on cantilevers

Test	Number of wheel loads	Failure Load $Q_R$ kN	$Q_{Flex}$ kN	$Q_R/Q_{Flex}$	Failure location	Mode of failure
DR1-a	4	1397	1600	0.87	Cantilever edge	Shear
DR1-b	2	1025	1320	0.78	Fixed end	Shear
DR1-c	1	910	1190	0.77	Fixed end	Shear
DR2-a	2	961	1500	0.64	Fixed end	Shear
DR2-b	2	857	1060	0.81	Fixed end	Shear
DR2-c	1	719	960	0.75	Fixed end	Shear

$Q_{Flex}$ : Theoretical flexural failure load

The results of the 6 tests are summarized in table 3.1. The failure mode for the cantilever under four concentrated loads (DR1-a) was a brittle shear failure at the two loads closest to the free edge (fig. 3.7b and 3.3a). For the other tests, the cantilever also failed in shear, however always between the location of the applied loads and the fixed end of the cantilever (fig. 3.3b and c).

The flexural ultimate load was estimated for each test based on the yield-line method (fig. 3.4). This load was never reached in any of the six tests. The failure load in test DR1-a, with four concentrated loads, is closest to the theoretical yield-line value ( $Q_R/Q_{Flex} = 0.87$ , tab. 3.1). In this case, plastic strains were present both in the top transversal reinforcement at the fixed end and in the bottom longitudinal reinforcement underneath the edge loads. The lowest  $Q_R/Q_{Flex}$  ratio was obtained for test DR2-a, subjected to two concentrated loads.

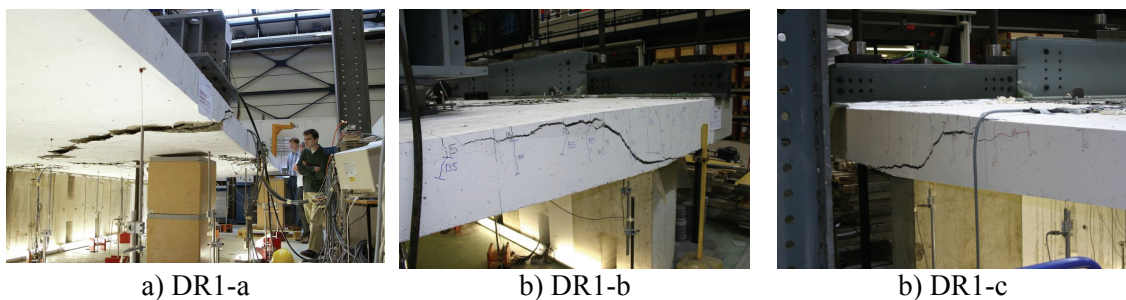


Figure 3.3: Shear failures for slab DR1

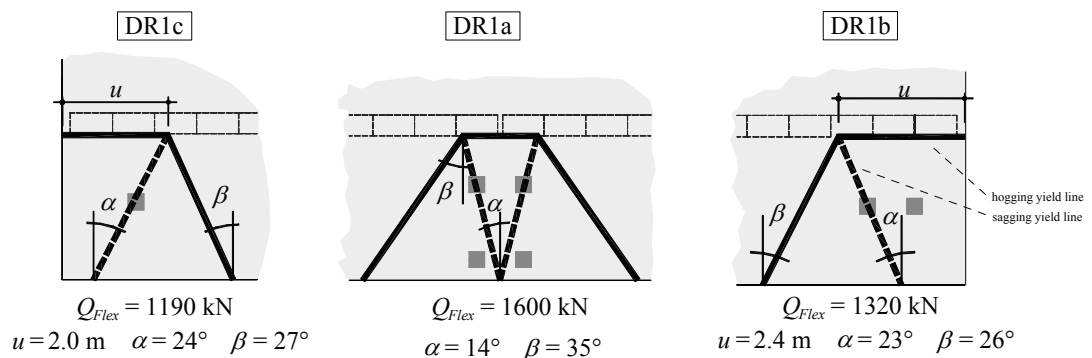


Figure 3.4: Yield-line mechanisms and yield-line failure load for slab DR1 ( $Q_{Flex}$ )

The behavior under service loads was investigated in test DR1-a, under a load of approximately  $Q = 410$  kN and for a limited number of cycles (one hundred cycles). The deflections increased with the number of cycles and tended to stabilize after one hundred cycles (fig. 3.5). This tendency is in agreement with the model proposed by (Muttoni, Fernández Ruiz 2006).

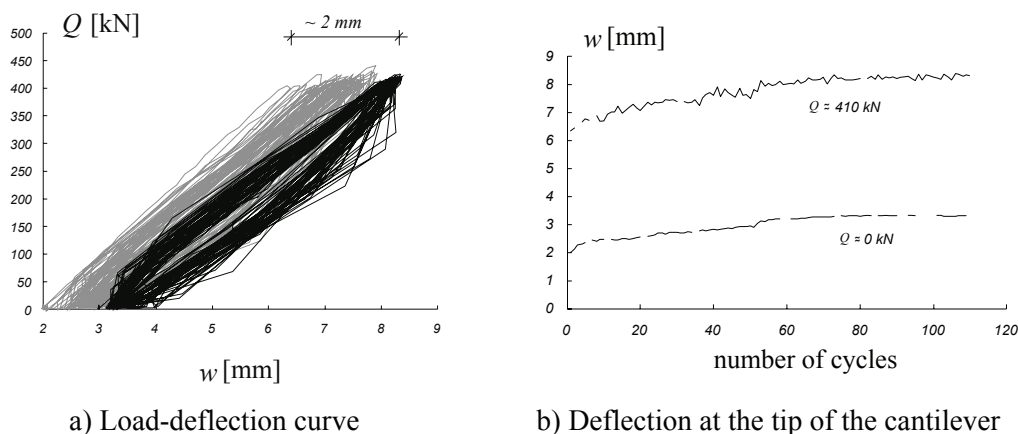


Figure 3.5: Evolution of deflections with the number of cycles for test DR1-a

The load-deflection curves for the six tests are shown in figure 3.6. The deflection  $w$  was measured at the tip of the cantilever, as indicated in figure 3.2.

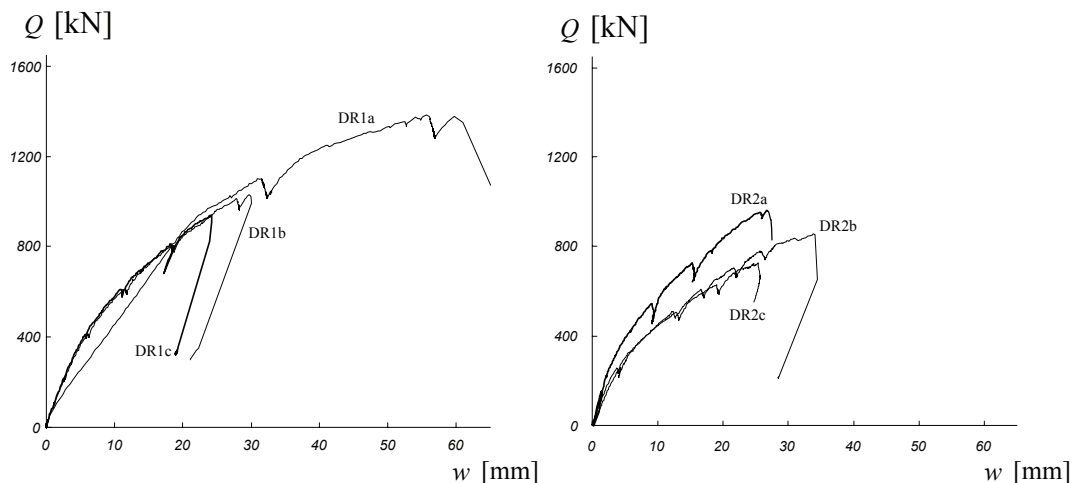
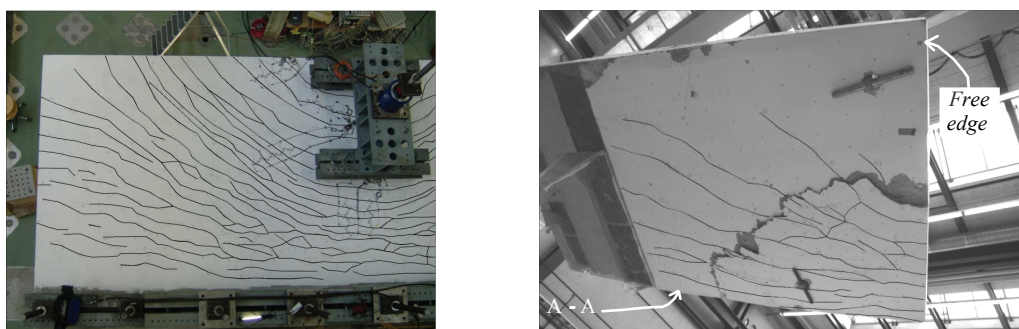


Figure 3.6: Total load – deflection curves for the six tests



a) Cracks at the top face prior to failure

b) Shear failure at edge loads seen from below after cutting of the slab.

Figure 3.7: Crack pattern for test DR1-a

For tests DR1-b and DR1-c (fig. 3.3), the shear crack was clearly visible after failure on the side face of the cantilever and the crack continues inside of the slab. After failure, the slab was cut and the geometry of the critical shear crack was mapped. The location of the shear cracks is shown in figure 3.8 along with the crack pattern on top and bottom surfaces.



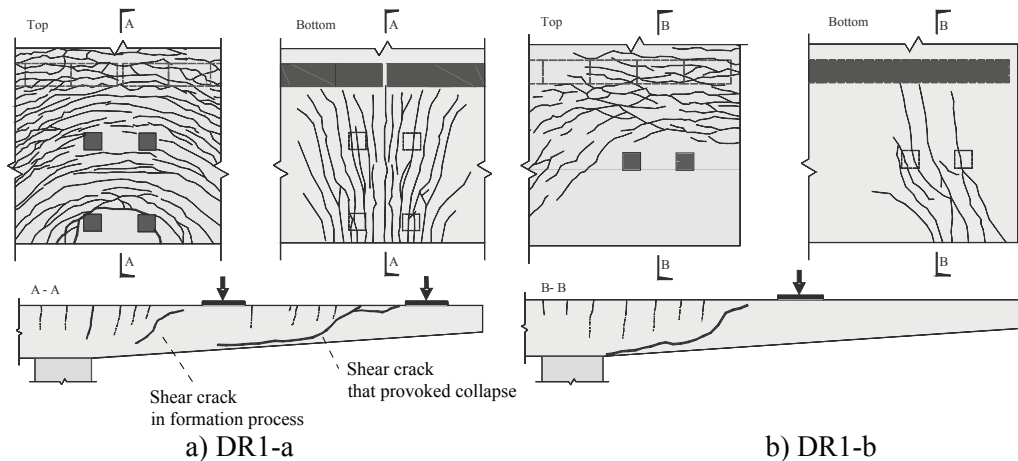


Figure 3.8: Crack pattern on the top and bottom surfaces for tests DR1-a and DR1-b

For test DR1-a, a large shear crack was observed in the region between the fixed end and the applied loads. Since no failure occurred in this region, this suggests that a process of development of the shear crack was under way in this region and that redistributions of the shear flow may have occurred. In order to better follow the development of the shear crack, measurements of the local variation in thickness of the slab, indicative of the vertical shear crack openings within the slab, were performed for slab DR2 (fig. 3.9).

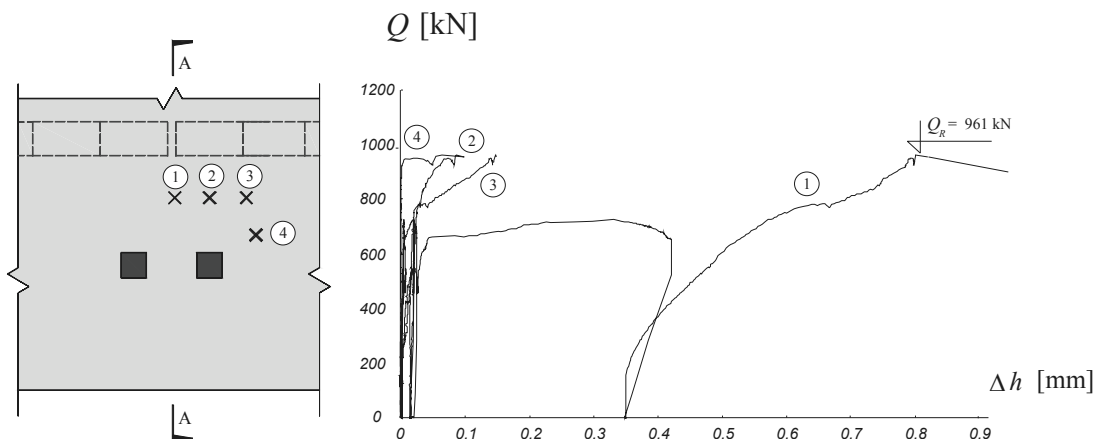


Figure 3.9: Measurements of the variation of slab thickness (test DR2-a)

These measurements confirm that the formation of the critical shear crack is a process that starts at a load level significantly lower than the failure load. For test DR2-a, the shear crack started to grow after  $Q = 660$  kN, whereas the failure took place at  $Q = 961$  kN. The presence of the shear crack probably affected the flow of shear forces, so that redistributions may have occurred after the initiation of the crack.

More detailed results are available in the complete test report, in appendix A.

### 3.3 Tests on RC slab strips without shear reinforcement (appendix B)

A series of eleven slab strips have been tested to investigate the influence of yielding of flexural reinforcement on the shear strength.

#### 3.3.1 Layout of experiments

The tested beams had a constant rectangular section of 0.45 m x 0.25 m and a total length of 8.4 m, as shown in figure 3.10. The top and bottom longitudinal reinforcement consisted of four bars of 16 mm diameter, constant along the beam's length. The reinforcement ratio is 0.79% for both bottom and top bars for all tested beams. The beams were simply supported, with a span of 6.0 m. Two loads,  $Q$  at mid-span, and  $\alpha \cdot Q$  at the tip of the cantilever were applied by two independent hydraulic jacks. The load introduction at mid-span ( $Q$ ) was made by means of a steel plate of 0.1 m x 0.25 x 0.03 m. No shear reinforcement was placed in the measurement zone, but outside of this region stirrups were provided to prevent a shear failure. The ratio  $\alpha$  of the two applied loads was varied between the eleven beams but kept constant during each test, allowing the investigation of various shear forces and shear spans  $a_1$  and  $a_2$  (fig. 3.10).

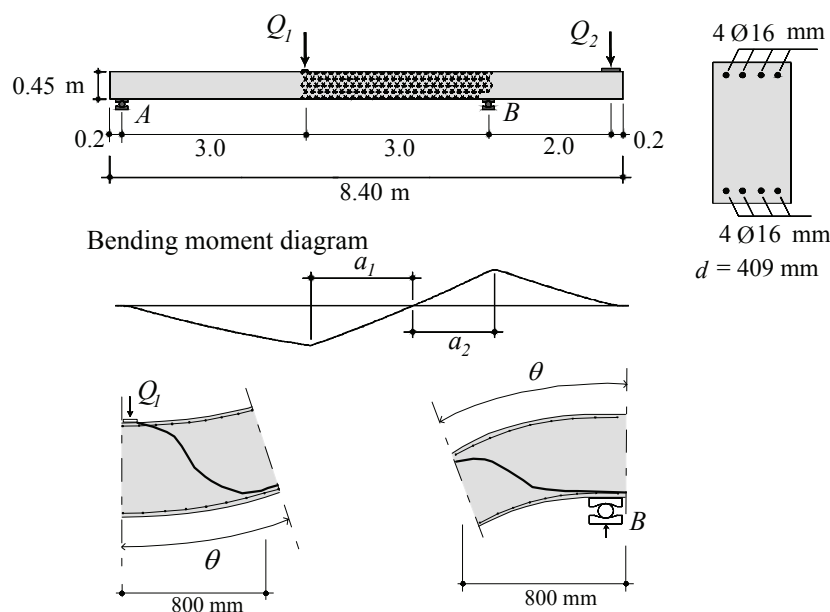


Figure 3.10: Slab strip dimensions, loads, shear spans  $a_1$  and rotation  $\theta$

For slab strips SR2 to SR9, the reinforcement steel used was cold worked with a proportional limit at 0.2% of 515 MPa and a tensile failure strain of 14%. For slab strips SR10 to SR12, the reinforcement steel used was hot rolled with yield strength of 525 MPa.

## 3.3.2 Results

The main results are given in table 3.2 and figures 3.11 and 3.12 for all slab strips.

Table 3.2: Main results for all tested slab strips

Essai	$Q_{1,CR}$	$Q_{2,CR}$	$w_{l,CR}$	$M_R$	$V_R$	$\tau_R$	$f_c$	$\tau_c$	$\tau_R/\tau_c$	$\theta_R$	$a$	$a/d$	Type of failure	Position
	[kN]	[kN]	[mm]	[kN·m]	[kN]	[MPa]	[MPa]	[MPa]		[mrad]	[m]			
SR2	124.1	62.4	19.21	-112.8	-91.8	0.897	43.11	1.970	0.456	3.2	1.46	3.56	V	B
SR3	130.0	27.6	69.52-73.32	161.1	-75.9	0.742	50.62	2.134	0.348	30.1	2.25	5.50	V	Q
SR4	115.2	0.0	110.43	169.9	-59.3	0.580	47.55	2.069	0.280	40.0	2.90	7.09	V	Q
SR5	96.1	-18.7	195.95	163.1	-43.5	0.425	47.64	2.071	0.205	68.1	3.59	8.77	M	Q
SR6	148.0	85.6	56.47	124.2	-104.2	1.019	52.71	2.178	0.468	18.6	1.38	3.37	V	Q
SR7	139.9	71.3	176.43	-128.4	-102.6	1.004	49.11	2.102	0.477	8.6	1.48	3.61	V	B
SR8	107.5	-11.0	133.11	170.8	-51.8	0.506	49.16	2.103	0.241	47.2	3.25	7.96	V	Q
SR9	126.5	43.8	92.07	138.9	-79.5	0.778	52.82	2.180	0.357	29.7	1.90	4.65	V	Q
SR10	101.3	-6.8	140.90	157.7	-50.1	0.490	42.41	1.954	0.251	76.3	3.12	7.62		Q
SR11	130.6	45.1	25.44	-78.7	-89.3	0.873	42.91	1.965	0.444	3.6	1.10	2.68	V	B
SR12	131.5	26.9	148.23	163.9	-76.4	0.747	43.51	1.979	0.378	> 55.8	2.27	5.56		Q

$V_R$ : shear force in the failure section;  $\delta_R$ : mid-span deflection at failure;  $\theta_R$ : rotation in the failure region, integrated along a length of  $1.96 \cdot d$ ; Position: failure location (B: near intermediate support, Q: near applied load at the mid-span)

Beams SR2, SR6, SR7 and SR11 failed in shear, before or at the onset of yielding. Beams SR3, SR9, SR4 and SR8 also failed in shear, but after the formation of the plastic hinge, located below the load  $Q$ . Beam SR5 failed in bending with fracture of the flexural reinforcement in tension. The beams with hot rolled reinforcement underwent larger rotations than those with cold formed steel, when in presence of plastic strains (fig. 3.12). For beams with cold worked reinforcement (SR2 to SR9), the ratio  $V_R / (b \cdot d \cdot 0.3 \cdot f_c^{0.5})$  decreases with increasing rotation  $\theta$ . Figure 3.11 shows the crack pattern after failure for all slab strips. The slab strips are ordered from the lowest to the largest shear strength, for each type of reinforcement. A clear type of failure was not observable for SR10 and SR12, which exhibited yielding of the longitudinal reinforcement. A very large hinge rotation was measured for these two beams (fig. 3.12). For slab strips SR9, SR10 and SR12, the force dropped after failure to about 80% of the failure load and the test was stopped because the crack openings reached several centimeters or the rotations were very large ( $\theta > 50$  mrad,  $2.9^\circ$ ).

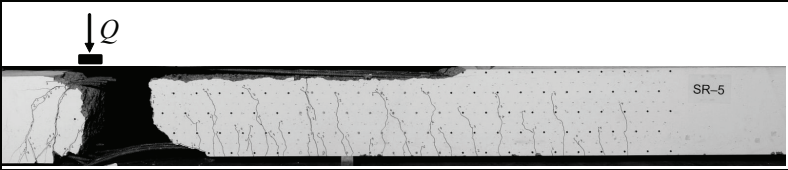
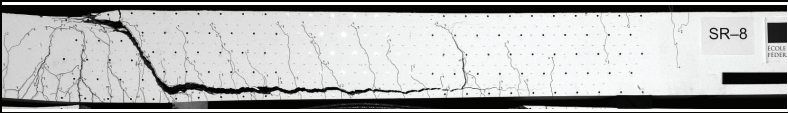
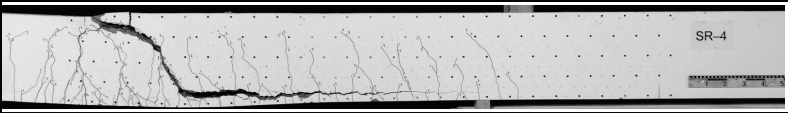
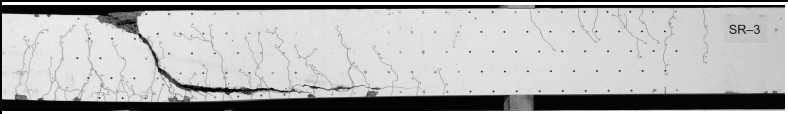
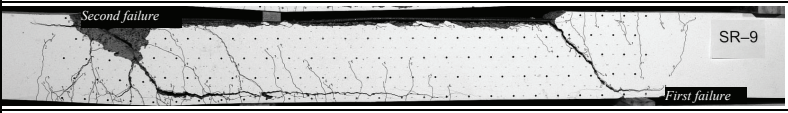
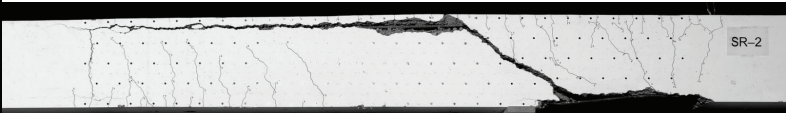
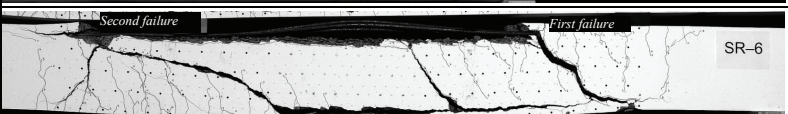
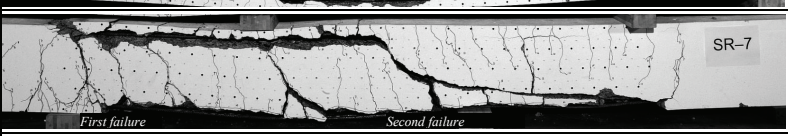
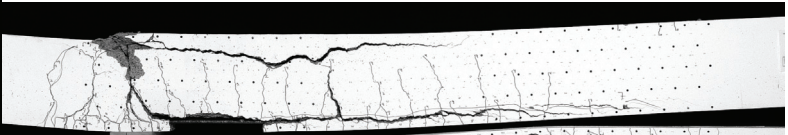
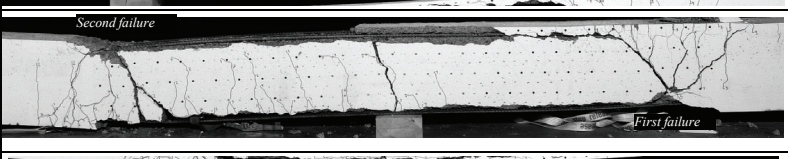
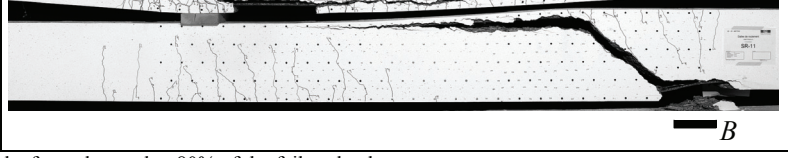
	Failure type	Crack pattern after failure	$\frac{V_R}{b \cdot d \cdot 0.3 \cdot \sqrt{f_c}}$	$\theta$ [mrad]
Cold worked reinforcement type	SR5 Flexural with bar rupture		0.205	68.1
	SR8 Shear with plastic strains		0.241	47.2
	SR4 Shear with plastic strains		0.280	40.0
	SR3 Shear with plastic strains		0.348	30.1
	SR9 Shear with plastic strains		0.357 a), b)	29.7
	SR2 Shear without plastic strains		0.456	3.2
	SR6 Shear with few plastic strains		0.468 b)	18.6
	SR7 Shear without plastic strains		0.477 b)	8.6
Hot rolled reinforcement type	SR10 Undefined failure with plastic strains		0.251 a)	76.3
	SR12 Undefined failure with plastic strains		0.378 a) b)	>55
	SR11 Shear without plastic strains		0.444	3.6
a) After failure the force dropped to 80% of the failure load				
b) The second failure is considered here				

Figure 3.11: Failure type and crack pattern for all slab strips (increasing shear strengths inside each reinforcement type)

The complete test report in appendix B gives detailed description of the test results, including the relative displacements at the shear crack.

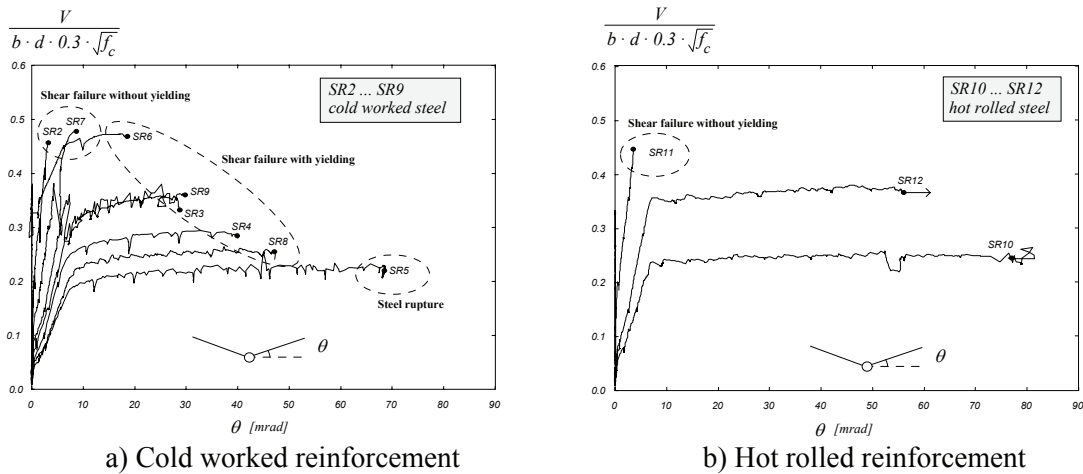


Figure 3.12: Normalized shear stress versus rotation for all tested specimens

### 3.3.3 Analysis of strain fields

The moment-curvature relationships of reinforced concrete cross sections can be easily derived for typical non-prestressed or prestressed cross-sections. The response of a reinforced concrete member can then be calculated by integrating the curvatures along the length of the member. The deflections due to the internal shear forces are usually neglected for slender elements.

In the case of reinforced concrete slab strips without shear reinforcement, a shear crack may form and increase the deflections. Figure 3.13 shows schematically three possible types of cracks and the corresponding evolution of the shear strains ( $\gamma$ ) and vertical strains ( $\epsilon_z$ ). The average strains in each cross section are indicated along the represented length of the member. A pure flexural crack (fig. 3.13a) does not cause any shear or vertical strains. The inclined straight shear crack (fig 3.13b) whose opening is governed by a rotation around point  $d$  causes the shear and vertical strains to increase. A bilinear shear crack is illustrated in figure 3.13c). In this case, the shear strains are concentrated above the horizontal part of the crack. The relative displacements between the lips of the inclined part of the crack are vertical.

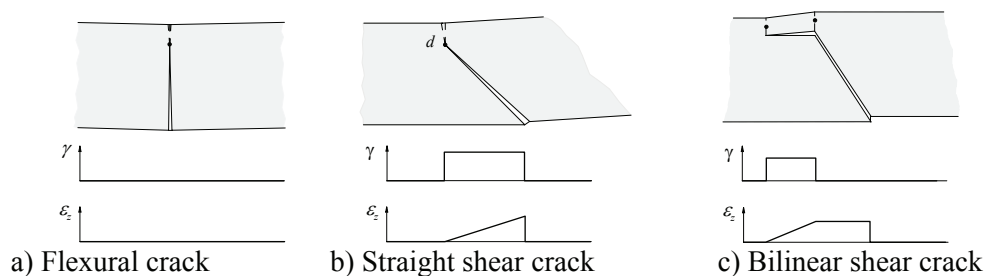


Figure 3.13: Shear strains ( $\gamma$ ) and vertical strains ( $\epsilon_z$ ) for three types of cracks

As the opening of the shear crack increases until failure, the shear strains ( $\gamma = V / (G \cdot B)$  in equation 3.1) increase and the contribution of this term might become relevant. The general virtual work equation that considers the contribution of the shear force for beam elements is:

$$\bar{1} \cdot \delta = \int \bar{V} \cdot \frac{V}{GB} dx + \int \bar{M} \cdot \frac{M}{EI} dx \quad (3.1)$$

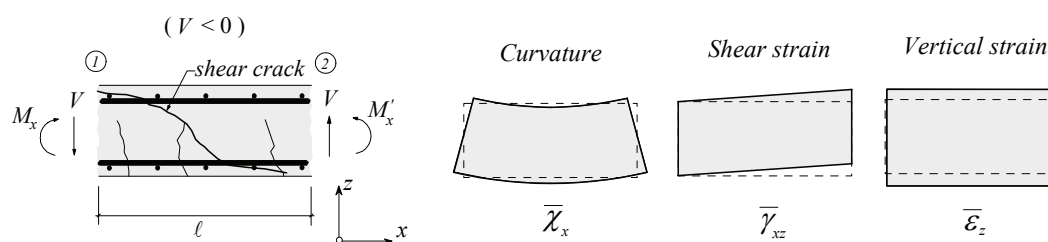
where  $EI$  is the flexural stiffness and  $GB$  is the shear stiffness.

This reduction of the shear stiffness is not only important for calculating the deflections of slab strips with shear cracks, but it also could play a role in the investigation of redistributions in the flow of shear forces in slabs that may occur after cracking.

The objectives of this subsection are:

- To quantify the reduction of shear stiffness for slab strips that fail in shear
- To understand the role of yielding of flexural reinforcement on the reduction of the shear stiffness

Figure 3.14a) shows a typical cross-section of a reinforced concrete slab strip without shear reinforcement. The shear force is carried along the  $x$  axis, from section ① to section ②. It always acts simultaneously with a bending moment, which is variable along the length  $\ell$ . Flexural and shear cracks appear under increasing loads. Failure can occur by the propagation of a diagonal shear crack. The following contributions to the deformations can be identified: curvatures ( $\chi$ ), shear strains ( $\gamma_{xz}$ ) and vertical strains ( $\epsilon_z$ ). The physical interpretation of these contributions is given in figure 3.14b).

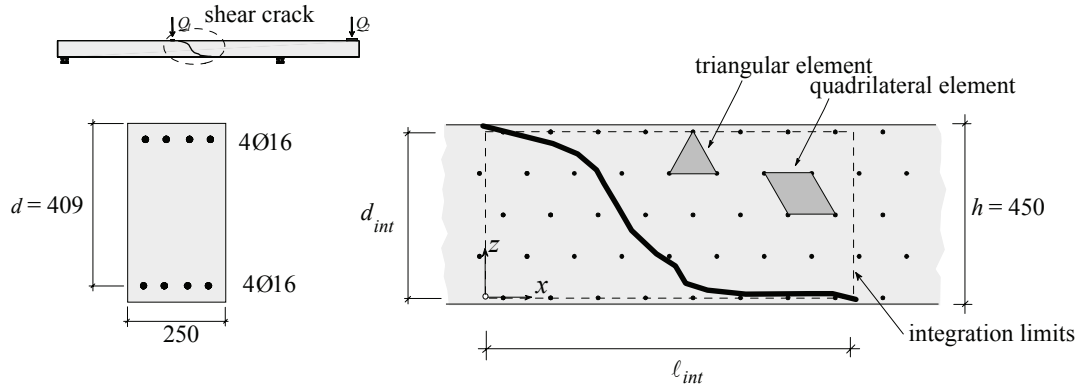



a) Slab strip and notations

b) Modes contributing to the deformations

Figure 3.14: Slab without shear reinforcement under one-way shear


It is possible to identify the individual contributions from these three modes on the basis of measurements of the web strains performed on the slab strips without shear reinforcement. Figure 3.15 shows a detail of a slab strip, with the measuring grid and the shear crack. The relative displacements between the points of the grid have been measured during the test. From these values, the absolute displacements can be reconstructed at each vertex of the grid, as explained in chapter 4 of appendix B to this dissertation. Strains can be calculated from the displacements of the grid vertexes using triangular and quadrilateral elements (Hughes 1987). The equations of the displacement fields (eqs. 3.2 and 3.3) and the strain fields (eqs. 3.4 and 3.5) are given in figure 3.15.



quadrilateral element 

$$\begin{bmatrix} u_x \\ u_z \end{bmatrix} = \begin{bmatrix} a_x & b_x & c_x & d_x \\ a_z & b_z & c_z & d_z \end{bmatrix} \times \begin{bmatrix} x \\ z \\ x \cdot z \\ 1 \end{bmatrix} \quad (3.2)$$

$$\begin{aligned} \varepsilon_z &= \frac{\partial u_z}{\partial z} = b_z + c_z \cdot x \\ \varepsilon_x &= \frac{\partial u_x}{\partial x} = a_x + c_x \cdot z \\ \gamma_{xz} &= \frac{\partial u_x}{\partial z} + \frac{\partial u_z}{\partial x} = b_x + c_x \cdot x + a_z + c_z \cdot z \end{aligned} \quad (3.4)$$

triangular element 

$$\begin{bmatrix} u_x \\ u_z \end{bmatrix} = \begin{bmatrix} e_x & f_x & g_x \\ e_z & f_z & g_z \end{bmatrix} \times \begin{bmatrix} x \\ z \\ 1 \end{bmatrix} \quad (3.3)$$

$$\begin{aligned} \varepsilon_z &= \frac{\partial u_z}{\partial z} = f_z \\ \varepsilon_x &= \frac{\partial u_x}{\partial x} = e_x \\ \gamma_{xz} &= \frac{\partial u_x}{\partial z} + \frac{\partial u_z}{\partial x} = b_x + a_z \end{aligned} \quad (3.5)$$

(3.6)

average curvature

$$\bar{\chi} = \left[ \int_{x=0}^{x=\ell} (\varepsilon_{x(z=d_{int})} - \varepsilon_{x(z=0)}) / d_{int} dx \right] / \ell$$

(3.7)

average distortion

$$\bar{\gamma} = \left[ \int_{x=0}^{x=\ell_{int}} \int_{z=0}^{z=d_{int}} \gamma_{xz} dz dx \right] / (d_{int} \cdot \ell)$$

(3.8)

average vertical strain

$$\bar{\varepsilon}_z = \left[ \int_{x=0}^{x=\ell_{int}} \int_{z=0}^{z=d_{int}} \varepsilon_z dz dx \right] / (d_{int} \cdot \ell)$$

Figure 3.15: Slab strips, elements and definition of average strains [mm]

Averages values of curvatures, shear strains and vertical strains can be calculated by integrating the strain fields (eqs. 3.6, 3.7 and 3.8). As the zone in which the critical shear crack develops is rather well delimited, the domain of integration is a rectangle, with a length  $\ell_{int} \approx 1.5 \cdot d$  and depth  $d_{int} \approx d$  centered on the critical crack. The integrals are numerically evaluated for triangular and quadrilateral elements (fig. 3.16c).

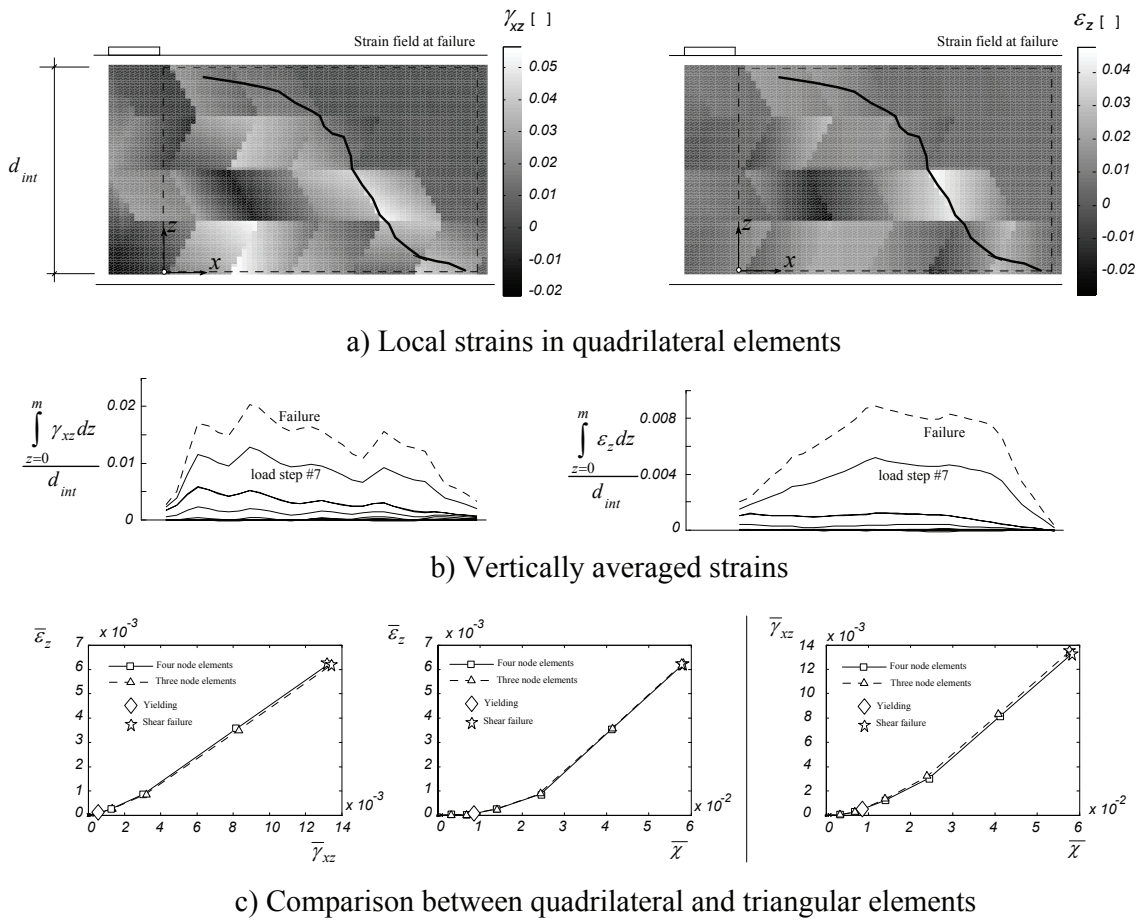
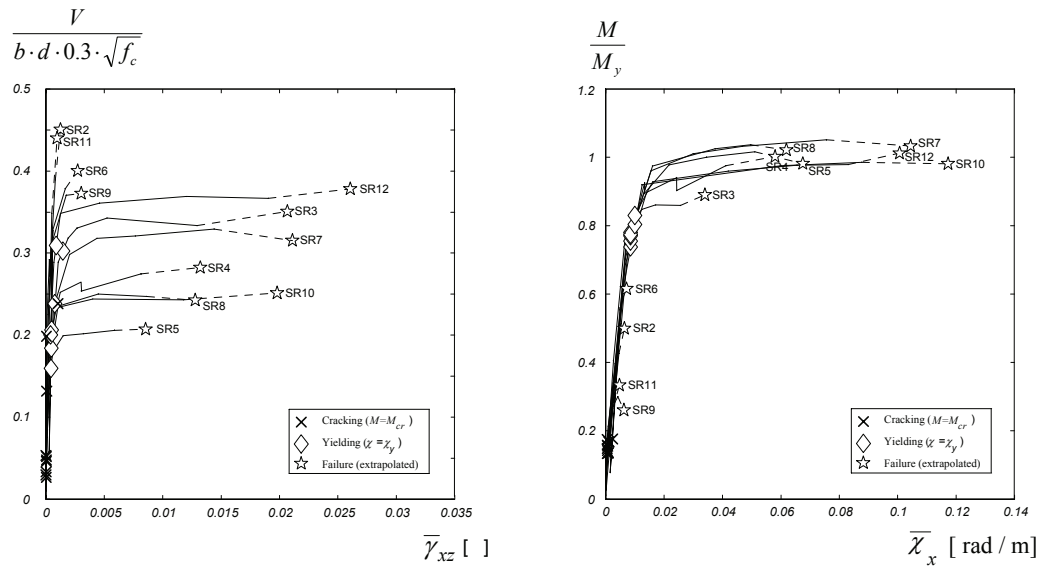


Figure 3.16: Integration of strain fields for slab strip SR4

Fig. 3.16a) shows the strain fields for the shear strains  $\gamma_{xy}$  and vertical strains  $\epsilon_z$  in the vicinity of the critical shear crack for quadrilateral elements, in which strains vary linearly. Fig. 3.16b) shows the vertically averaged values of the same strains along the  $x$  axis. Figure 3.16c) shows various representations of the strains integrated over the entire domain for increasing load levels. Note that the relationship between shear strains and curvature is not linear. It can also be observed that results for quadrilateral and triangular elements are very similar. This observation is also valid for the other slab strips. The strain distributions along the  $x$  axis are integrated to calculate the average strains within the domain of integration. The average shear strains and the average vertical strains significantly increase after yielding for slab strip SR4.

Figure 3.17 shows additional representations of these results: figure 3.17a) shows the relationship between the nominal shear stress  $\tau = V / (b \cdot d)$  normalized by the nominal shear strength  $\tau_c = 0.3 \cdot (f_c)^{0.5}$  and the average shear strains within the integration domain; figure 3.17b) shows the relationship between the flexural moment  $M$  normalized by the flexural yielding moment  $M_y$  of the slab strips and the average curvatures within the integration domain. The shear force  $V$  and the flexural moment  $M$  are calculated at the center of the integration domain (at  $x = \ell / 2$ ). The inner forces are always well known because the slab strips are statically determined.





a) Shear force-shear strain diagrams                      b) Moment-curvature diagrams  
 Figure 3.17: Normalized diagrams for shear force-shear strain and moment-curvature for all tested slab strips

It can be observed that:

- Slab strips SR2, SR6, SR9 and SR11 failed without yielding of the flexural reinforcement. The other slabs failed after yielding of the reinforcement.
- Shear strains significantly increase after yielding of the longitudinal reinforcement. This corresponds to an important reduction of the shear stiffness.
- Beams that failed in shear without yielding of the reinforcement did not exhibit a significant loss in shear stiffness.
- The shear stiffness is less affected by the cracking of the section than the flexural stiffness.

The average shear strain within the integration domain therefore essentially depends on the intensity of the nominal shear stresses and on the intensity of the average bending curvatures.

### 3.4 Punching shear test with simulation of vehicle wheel (appendix A)

Punching shear of deck slabs is different from the classical case of punching of a flat slab by a column. One of the main differences is that the load is not introduced by a very stiff element (a concrete column or the head plate of a steel column), but rather by a pneumatic wheel load. It was thus decided to take the opportunity of a research work under way at the Structural concrete laboratory at the time of the present research to conduct a limited study of that specific behavior. To that end, a punching shear test with distributed support reactions simulating the effect of a vehicle wheel was carried out.

The dimensions, reinforcement layout and concrete properties are similar to that of the test PG-10 (Guandalini, Muttoni 2004). The slab was square with 3.0 x 3.0 m and a thickness of 0.25 m. The top reinforcement consisted of orthogonally disposed bars of Ø 10 mm spaced at 115 mm. The effective depth of the top layer was  $d = 210$  mm. The reinforcement ratio of the top layer was  $\rho = 0.33\%$ . The concrete compressive strength

at the time of testing was  $f_c = 35$  MPa ( $f_c = 28.5$  MPa for the reference slab PG-10). The concrete tensile strength was  $f_{ct} = 2.2$  MPa for both tests. The Young's modulus of concrete was  $E_c = 31.8$  GPa ( $E_c = 29.5$  GPa for slab PG-10). The maximum size of the aggregate was  $d_g = 16$  mm for both slabs. The reinforcement was hot rolled with yielding strength  $f_{sy} = 570$  MPa and a tensile strength  $f_{su} = 650$  MPa for both slabs.

The loads were introduced at eight locations around the perimeter of the slabs (two for each side) for both tests. Instead of a stiff loading plate (260 x 260 mm) for the reference slab, the central support of test PR1 consisted of a circular flat jack consisting of a flexible copper sheet envelope filled with water, with nominal diameter  $\varnothing = 446$  mm. This allows the contact pressure between the slab and the jack to be approximately uniform. The water volume was kept constant during the test. The effective contact surface can be derived from the measured water pressure and the support force  $V$ . The effective contact diameter increased from  $\varnothing = 445$  mm at the beginning of the test to  $\varnothing = 472$  mm at failure.

The diameter of the flat jack was selected to be representative of a vehicle wheel. According to the Eurocode 1 (Eurocode 1 2003) the concentrated load of a vehicle is represented by a square surface of 400 x 400 mm (0.16 m<sup>2</sup>). The diameter selected for the circular flat jack corresponds to a nominal surface of 0.156 m<sup>2</sup>.

Figure 3.18 shows the relationships between the normalized shear stress ( $\tau / \tau_c$ ) and  $\theta \cdot d \cdot k_{dg}$  for tests PG-10 and PR1. The punching shear failure criterion proposed by (Muttoni 2003) is also represented.

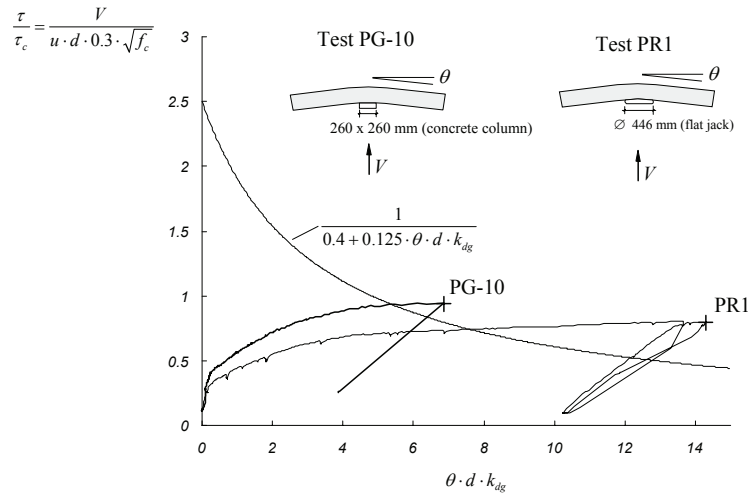


Figure 3.18: Comparison of punching shear tests with failure criterion (Muttoni 2003), considering the total rotation  $\theta$

Slab PR1 failed at a  $V_R = 600$  kN and  $\theta = 44.9$  mrad. Slab PG-10 failed at  $V_R = 540$  kN and  $\theta = 21.7$  mrad. It can be observed that slab PR1 had a more ductile behavior than slab PG-10. The punching shear cone and the flexural cracks are shown in figure 3.19.

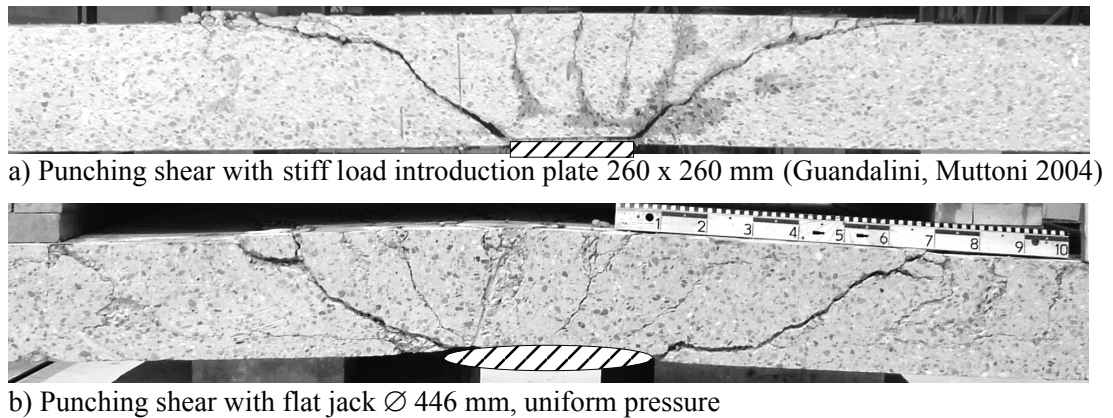


Figure 3.19: Comparison of punching shear cracks

One of the reasons for the large rotations of slab PR1 is the significant opening of the flexural cracks directly above the flat jack. Permanent plastic deformations are clearly visible in this area after cutting of the slab (fig. 3.19b). These cracks are not in the critical region, i.e. their openings and the rotations they cause are not the direct cause of the punching shear failure. Therefore, the contribution of these cracks to the rotation  $\theta$  should be discarded.

In both tests PR1 and PG-10 the rotations measured along the N-S axis were larger than the rotations measured along the W-E axis. This can be explained because of the difference between the effective depths in both directions. Please note that the average rotation between both directions is represented in fig. 3.18, for both slabs. In the case of test PR1, an important part of the rotations along the N-S is concentrated in the flexural crack that developed along the W-E direction (fig. 3.20). Directly above the support, the measured crack width near failure is approximately of  $u = 10$  mm. The rotation  $\theta_{flex}$  associated with this crack opening is:

$$\theta_{flex} = \frac{1}{2} \cdot \frac{u}{d-x} = \frac{1}{2} \cdot \frac{10}{0.21-0.012} = 25 \text{ mrad} \quad (3.2)$$

Where  $x$  is the estimated depth of the compression zone, calculated at yielding of the bending reinforcement. The influence of that rotation on the abscissa of figure 3.18 is  $\theta_{flex} \cdot d \cdot k_{dg} = 7.9$ .

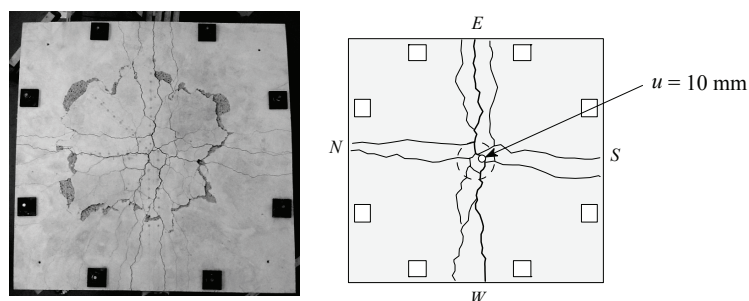


Figure 3.20: Major flexural cracks after failure of slab PR1

In the case of slab PG-10, the crack pattern was similar. The maximum crack width near failure over the concrete column is estimated from measurements by surface-mounted extensometers to  $u = 3.5$  mm. As in the other case, this component of the rotation associated with these cracks should not be considered. For slab PG-10, this component

is  $\theta_{flex} = 9$  mrad ( $\theta_{flex} \cdot d \cdot k_{dg} = 2.8$ ). Figure 3.21 compares the failure criterion with the rotation at failure in the critical region ( $\theta - \theta_{flex}$ ) instead of the total rotation  $\theta$ .

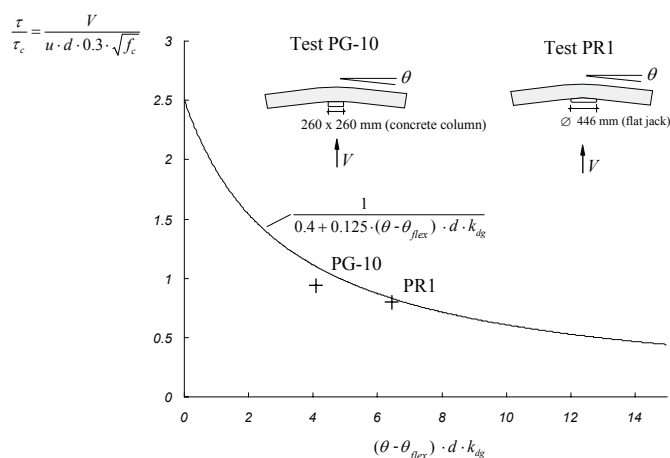


Figure 3.21: Comparison of punching shear tests with failure criteria (Muttoni 2003), considering the rotation in the critical region ( $\theta - \theta_{flex}$ )

It can be concluded that the criterion proposed by (Muttoni 2003) correctly predicts the load and deformation of test PR1, if only the rotation in the critical region is considered. In case PG-10, because the non critical component of the rotation ( $\theta_{flex}$ ) is small, either ( $\theta_{flex}$ ) or ( $\theta - \theta_{flex}$ ) values give correct results.

The differences between tests PR1 and PG-10 can be explained by the following factors:

- Axial stiffness of the support: a uniform pressure distribution (slab PR1) seems to delay the progression of the critical shear crack into the compression zone. Punching shear with a vehicle wheel thus seems to be a more ductile phenomenon than punching shear with a concrete column.
- Shape of the support: shapes with sharp corners induce strong stress concentrations and localization of curvatures in the corners of the support. This leads to a less ductile behavior.

### 3.5 Conclusions

This chapter describes the main results obtained from the experimental campaign:

Conclusions from the tests on bridge cantilevers:

- Punching shear failure was the governing failure mode for all tested bridge cantilevers.
- The ultimate flexural load predicted by the yield-line method was not reached for any of the six tests ( $Q_R / Q_{Flex} = 0.64 - 0.87$ ).
- The measured shear failure load decreases with the reinforcement ratio, for tests performed under the same number of loads.
- The measurements made of the slab thickness in the zone of shear failure indicate possible redistributions of the internal shear flow, with the progressive formation of shear cracks until equilibrium is no longer possible.

- The deflections, strains and crack openings tend to increase in the first hundred cycles under service load.

Conclusions of tests on slab strips without shear reinforcement:

- The rotation capacity of slab strips with cold worked reinforcement is governed by shear failure or flexural failure.
- The rotation capacity of slab strips with cold worked reinforcement decreases with increasing shear force.
- Slab strips with cold worked reinforcement exhibit less ductility after yielding of the longitudinal reinforcement than slab strips with hot rolled reinforcement.

Conclusions of the punching shear test with vehicle wheel:

- The stiffness and shape of the support influence the rotation capacity of reinforced concrete slabs without shear reinforcement.
- The punching shear criterion proposed by (Muttoni 2003) correctly predicts the load and deformation of test PR1, if only the rotation in the shear critical region is considered.

Detailed information is available in the complete test reports in appendices A and B of this dissertation.



## 4. Mechanical model for the shear failure of plastic hinges

### 4.1 Problem statement

Figure 4.1 shows the schematic behavior of ordinary reinforce concrete slabs without shear reinforcement. The theoretical flexural failure ( $Q_{Flex}$ ) load can be estimated using upper bound solutions such as an adequate configuration of yield-lines (Johansen 1972) and lower bound solutions such as moment fields or linear or non-linear finite element solutions. For statically indeterminate structures, the load continues to increase after the first yielding, and a certain rotation capacity is required. Bridge deck slabs or cut-and-cover tunnels are examples of such structures. Ductility of reinforced concrete structures is a major concern in structural engineering. A certain amount of rotation capacity is usually required to activate the ultimate strength of a statically indeterminate structure. The rotation capacity of the yielded regions may be limited by the bending failure modes (CEB 1998) or by a shear failure.

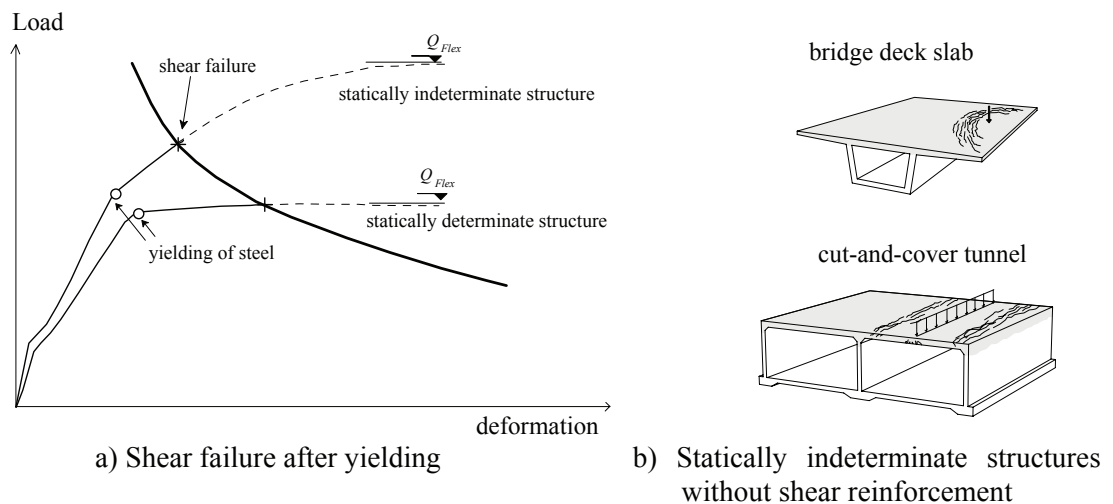
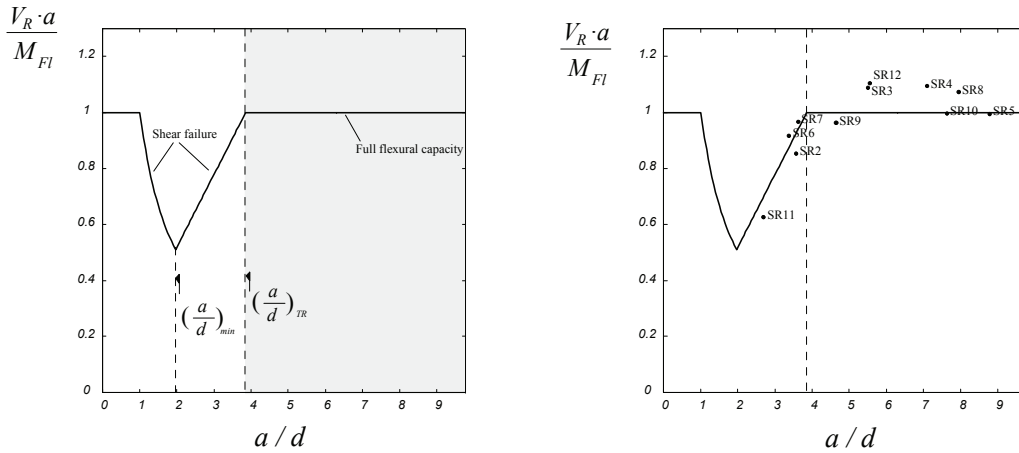


Figure 4.1: Behavior of reinforced concrete slabs

The shear strength of beams without shear reinforcement has been described as a function of the ratio  $a/d$  between the shear span  $a$  and the effective depth  $d$  of beams without shear reinforcement (Kani 1964, Kani et al. 1979). Figure 4.2a) shows the valley of shear failure. The test series on slender beams (section 3.3) is in good agreement with the predictions of Kani's theory (fig. 4.2b). The differences in the region of  $(a/d) > (a/d)_{TR}$  can be explained by the hardening behavior of the flexural reinforcement.

The region of interest of the present study is located at values of  $a/d$  higher than  $(a/d)_{TR}$ . It is shown that a shear failure of the plastic hinge can occur in this region, for a given plastic hinge rotation. In other words the maximal allowable rotation depends on the intensity of the shear force in the plastic hinge.

A mechanical model is proposed in this chapter to predict the shear strength as a function of the plastic hinge rotation. The shear force  $V$  will be assumed to be internally equilibrated by a shear force carried across the shear crack ( $V_{agg}$ ), and a shear force carried by the compression chord ( $V_{comp}$ ).



a) Valley of shear failure (Kani et al. 1979)

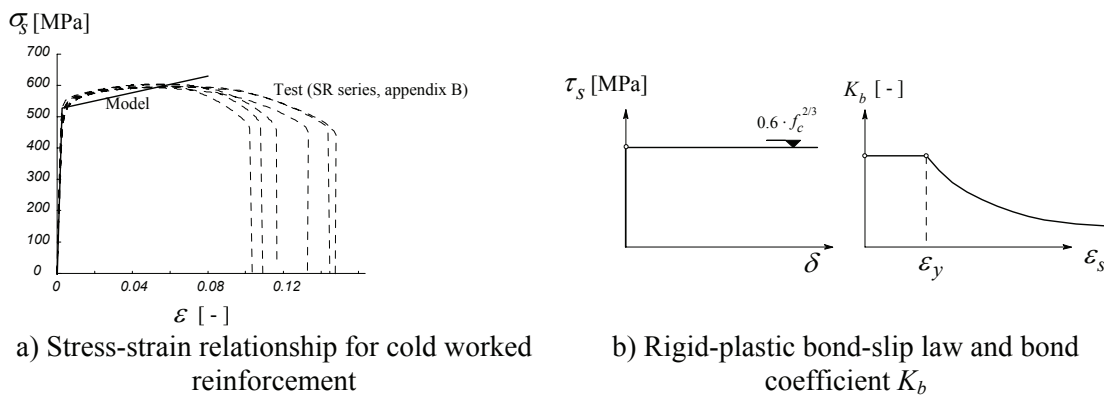
b) Comparison of Kani's model with the results of tests (appendix B).

Figure 4.2: Valley of shear failure

## 4.2 Post-yield behavior of the tension tie

The location of cracks and their openings at the level of tensile longitudinal reinforcement plays a major role in the behavior of the plastic hinge and in the formation of shear cracks. A bond model describing the post-yielding behavior of reinforcement is necessary to calculate the strain profile in the reinforcement.

A model that includes the pre- and post-yield behavior of concrete is proposed by (Fernández Ruiz et al. 2006). This model is used to calculate the actual strain profile in the tensile reinforcement, after the measurements on the concrete surface, at the tensile reinforcement level, on the test series of appendix B. Figure 4.3a) shows the bilinear law for modeling the stress-strain relationship of the reinforcement and the rigid-plastic bond-slip law for concrete (fig. 4.3b). Fernández Ruiz introduced a bond coefficient  $K_b$  to account for the effect of the longitudinal strain state of the bar ( $\epsilon_s$ ) on the local response of bond, so that bond stresses are expressed as  $\tau(\delta, \epsilon_s) = \tau_s(\delta) \cdot K_b(\epsilon_s)$ .



a) Stress-strain relationship for cold worked reinforcement

b) Rigid-plastic bond-slip law and bond coefficient  $K_b$

Figure 4.3: Model for reinforcement and bond

Figure 4.4 shows the position of the cracks at failure for slab strip SR4 with cold worked reinforcement. The calculated distribution of the reinforcement strains  $\epsilon_s$  and reinforcement stresses  $\sigma_s$  is also indicated, along with the crack openings  $w$ . The



performed measurements are represented in the figure as average strains (“measured strains at the concrete surface”). Each step in this diagram corresponds to a measurement between the points fixed to the concrete surface. The actual distribution of strains in the reinforcement is not constant, because of the cracks and bond between reinforcement and concrete. The strain profile in the reinforcement is calculated by imposing equality between the calculated crack openings and the measured crack openings, for each measurement zone along the tension tie. This corresponds to solving a set of non linear equations. The calculated crack openings, for a given crack, correspond to the integral of the strain profile between the points with lowest strain, at left and right of the peak (points *a* and *b* for the largest crack in fig. 4.4). This corresponds to neglecting the contribution of concrete in tension. The measured crack opening is estimated from the strain measurements, also neglecting concrete in tension. The set of non-linear equations can be solved numerically, which gives the calculated strain profile indicated in fig. 4.4. Since no measurements are available at failure ( $Q_R$ ), the measurements were linearly extrapolated from the known values of the vertical deflection below the load  $Q_I$ .

The maximal opening of cracks is approximately located below the load (2.5 mm). As the rotation increases to failure, the crack openings tend to increase near the critical shear crack (1.5 mm at failure). This might be explained because close to failure the shear force is carried by an inclined strut and thus the stresses in the reinforcement in the region of the critical shear crack increases.

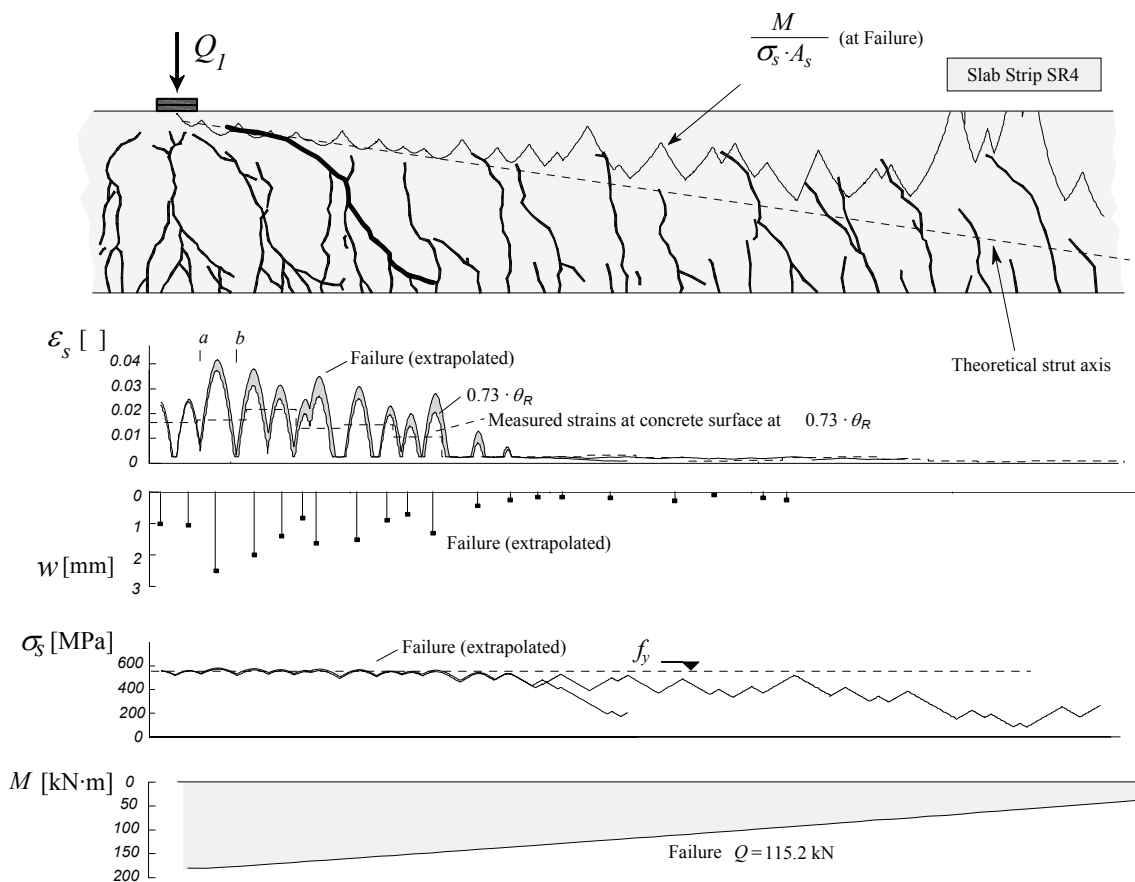


Figure 4.4: Behavior of tension tie along plastic hinge length (slab strip SR4)

The analysis of test SR4 shows that yielding of reinforcement occurs from the point of application of the load to approximately  $1.5 \cdot d$  from the load. The internal lever arm

calculated from the bending moment and the reinforcement stresses is also shown, ( $z = M / (A_s \cdot \sigma_s)$ ). In the yielded regions, the position of the internal lever arm coincides with the position of the inclined theoretical strut.

The deformations are distributed among many cracks rather than localized in a single crack. This evidence is confirmed by the analysis of the average curvatures within the plastic hinge, for other slab strips with yielding of flexural reinforcement (fig. 4.5). It should be noted that for slabs strips with hot rolled reinforcement the critical crack tends to form below the applied load rather than at a distance from the load  $Q_I$ , as it occurs for slab strips with cold worked reinforcement.

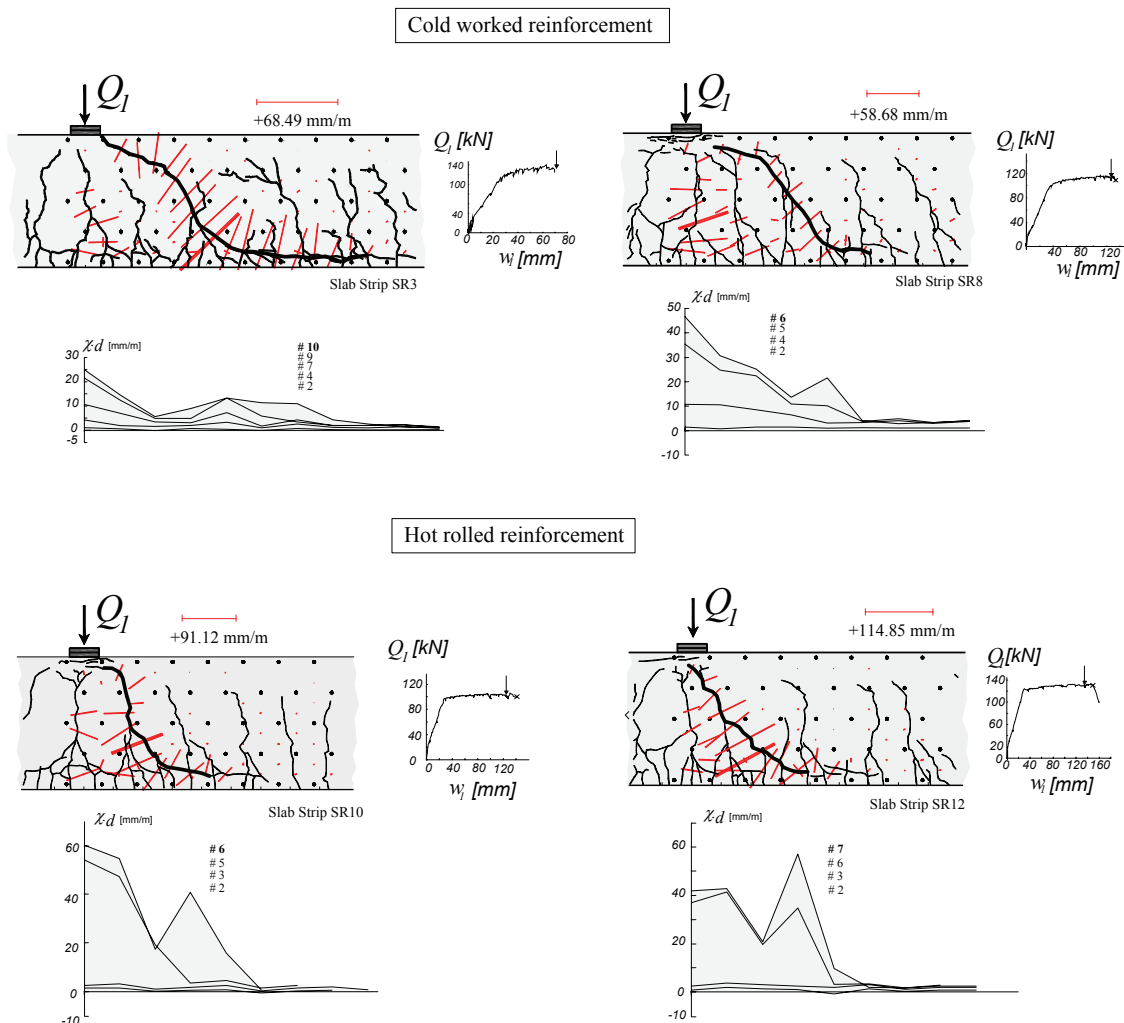


Figure 4.5: Distribution of average curvatures along the length of the plastic hinge and location of the critical shear crack for cold worked and hot rolled reinforcement

### 4.3 Aggregate interlock action

From the analysis of the kinematics of a shear crack, the vector representing the relative displacement between the lips of a crack can be identified (figs. 4.6b and c). Shear transfer across an open crack with a crack width  $u$  requires a slip  $v$  between the lips. This is necessary to activate contact between the aggregates protruding from the crack surface (fig. 4.6a).

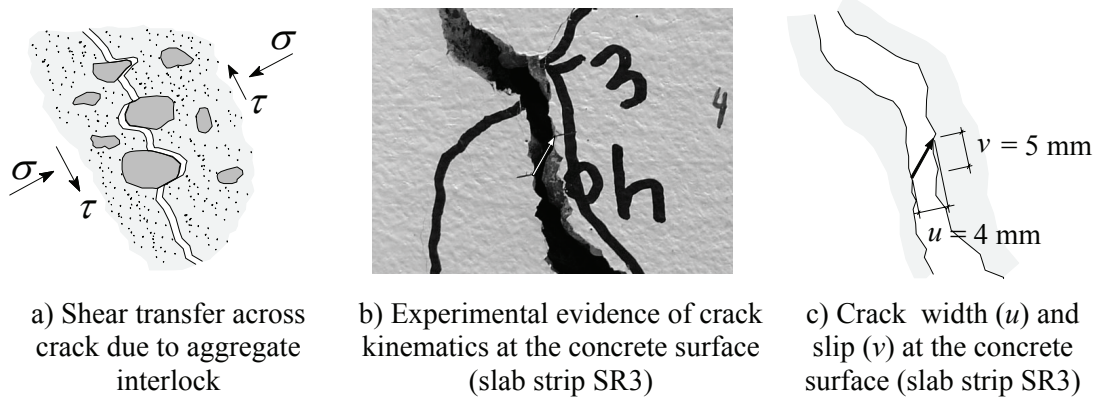


Figure 4.6: Aggregate interlock action

The action of aggregate interlock across cracks has been recognized as an important mode of shear transfer across cracks (Fenwick, Paulay 1968). Hamadi and Regan performed an important experimental work on interface shear and developed a tooth model that consider the interface shear (Hamadi, Regan 1980). Reineck proposed a mechanical model based on a truss model with concrete tensile struts that also considers friction at the interface (Reineck 1991). This model includes constitutive relationships for friction in the cracks and dowel action. The model matches with the test results as well as with those of empirical formulas.

Walraven developed a mathematical model that allows the calculation of the crack interface shear and normal stresses from the crack width and crack slip (Walraven 1980, Walraven 1981). The model is based on the behavior at the particle level, considering the deformation of the hardened cement matrix and frictional forces between the aggregate particles and the matrix during sliding. The structure of the crack surface is established from a statistical analysis. The results of the mathematical model are in agreement with numerous tests. The shear and normal stresses at the crack interface can be explicitly calculated through the numerical evaluation of a number of integrals. A routine was implemented in this dissertation to compute the shear and normal stresses using Walraven's model. An example of such computations is shown in fig. 4.7, for a concrete with compressive strength  $f_c = 40$  MPa, maximum aggregate size  $D_{max} = 16$  mm, coefficient of friction between aggregates and matrix  $\mu = 0.4$  and relative aggregate volume fraction  $p_k = 0.75$ .

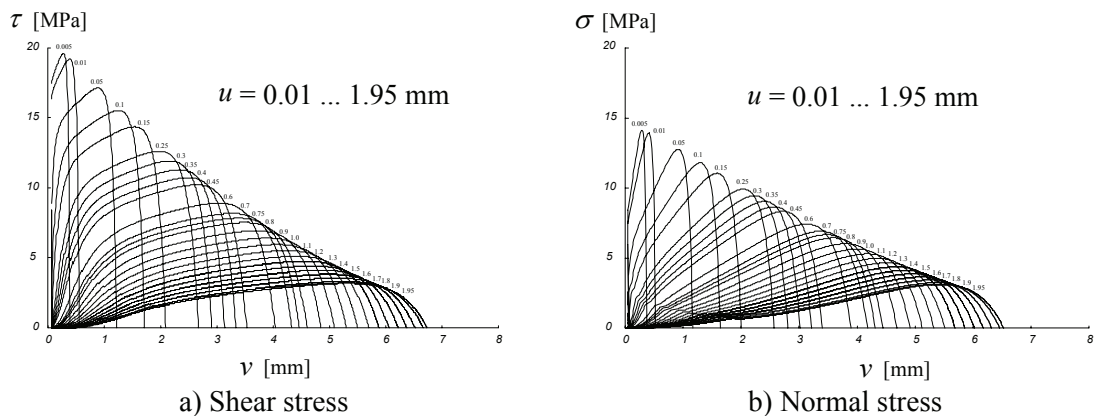


Figure 4.7: Shear and normal stresses across crack calculated from the crack width ( $u$ ) and crack slip ( $v$ ), after the model proposed by (Walraven 1980)

Measurements of the web displacements were systematically made on the surface of the web of the slab strips (appendix B). From the performed measurements it is possible to calculate the relative displacements between the two lips of the crack. The relative displacements are calculated at points along the length of the critical shear crack. The critical shear crack is the crack where failure occurs. Figure 4.8 shows the relative displacements for slab strip SR4. The normal directions to the crack are also represented. In a first stage, the relative displacements tend to be perpendicular to direction of the crack (up to about fifty percent of the measured rotation at failure). In a second stage, near failure, the tangential relative displacements increase. This point is progressively moving towards the load introduction plate. The web displacements have been extrapolated to failure from the measurements of the last load step prior to failure and the continuously measured deflections. At failure, the rotation point is located approximately at the top edge of the crack.

From the measured relative displacements, it is possible to calculate the crack openings  $u$  and crack slide  $v$  along the length of the shear crack. This is done by projection of the relative displacements in directions tangential and normal to the shear crack.

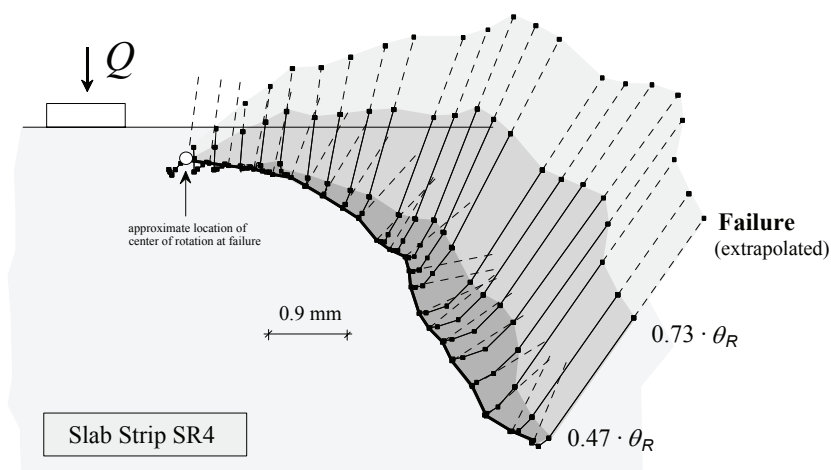
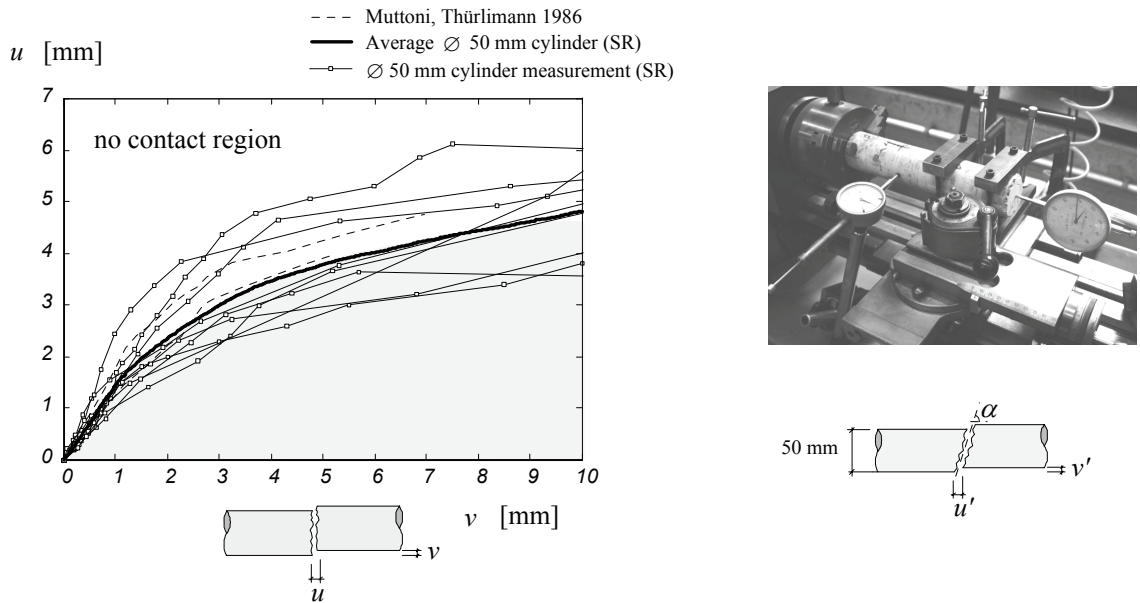


Figure 4.8: Relative displacement between the lips of the critical shear crack [mm]

Additional tests on  $\varnothing 50$  mm cylinders were performed to better understand the relationship between the relative displacements and stresses across the critical shear crack. Nine  $\varnothing 50$  mm cylinders were drilled from non damaged zones of the slab strips. The specimens were broken into two parts with three point bending. The relative displacements  $u'$  and  $v'$  were measured using the test set-up shown in figure 4.9b). The test begins with the two lips of the crack completely in contact. A small opening  $u'$  is then imposed. The value of  $v'$  is adjusted until contact is reached and the two values are recorded. The average angle of the crack  $\alpha$  was used to calculate the relative displacements at crack,  $u$  and  $v$  (fig. 4.9a). This was made by applying a rotation transformation to the measured displacements  $u'$  and  $v'$ . The measured relationships between  $u$  and  $v$  are valid when the two lips of the crack are in contact. It can be seen that there is no contact between the crack lips, for high values the crack opening  $u$ . In this region the transmission of force across the crack is limited or not possible. The measured average relative displacements are in good agreement with the measured relative displacements by (Muttoni, Thürlimann 1986), using a concrete with a compressive strength of about 30 MPa and with the same aggregate size (16 mm).



a) Relative displacements at crack      b) Test set-up and measured displacements

Figure 4.9: Tests on Ø 50 mm drilled cylinders

Figure 4.10a) shows the measured relative displacements at the crack that provoked the failure for all the eleven slab strips. The average measured values with the drilled Ø 50 mm cylinders are also represented, along with the extreme values, median and second and fourth quartiles. This line will be referred to as the average contact line. It can be seen that most of the points are located in the region where there is no contact between the two lips, or very close to the contact line.

The model proposed by Walraven is used to estimate the stresses transferred across the crack. A friction coefficient of  $\mu = 0.4$  is used, as recommended by (Walraven 1981). The ratio between the volume of aggregate and the volume of concrete is  $p_k = 0.75$ .

Figure 4.10b) shows the intensity of calculated tangential  $\tau$  and normal stresses  $\sigma$  for all points along the critical cracks of all slab strips. The diameter of the represented circles is proportional to the square root of the sum of squares of  $\tau$  and  $\sigma$ . The predictions of the model agree very well with the performed measurements on drilled cylinders. For points near the contact line, the stresses tend to increase. The stress increase is more significant for points below the contact line. The largest circle corresponds to the compressive stresses  $\sigma = 4.18$  MPa and tangential stresses  $\tau = 4.79$  MPa.

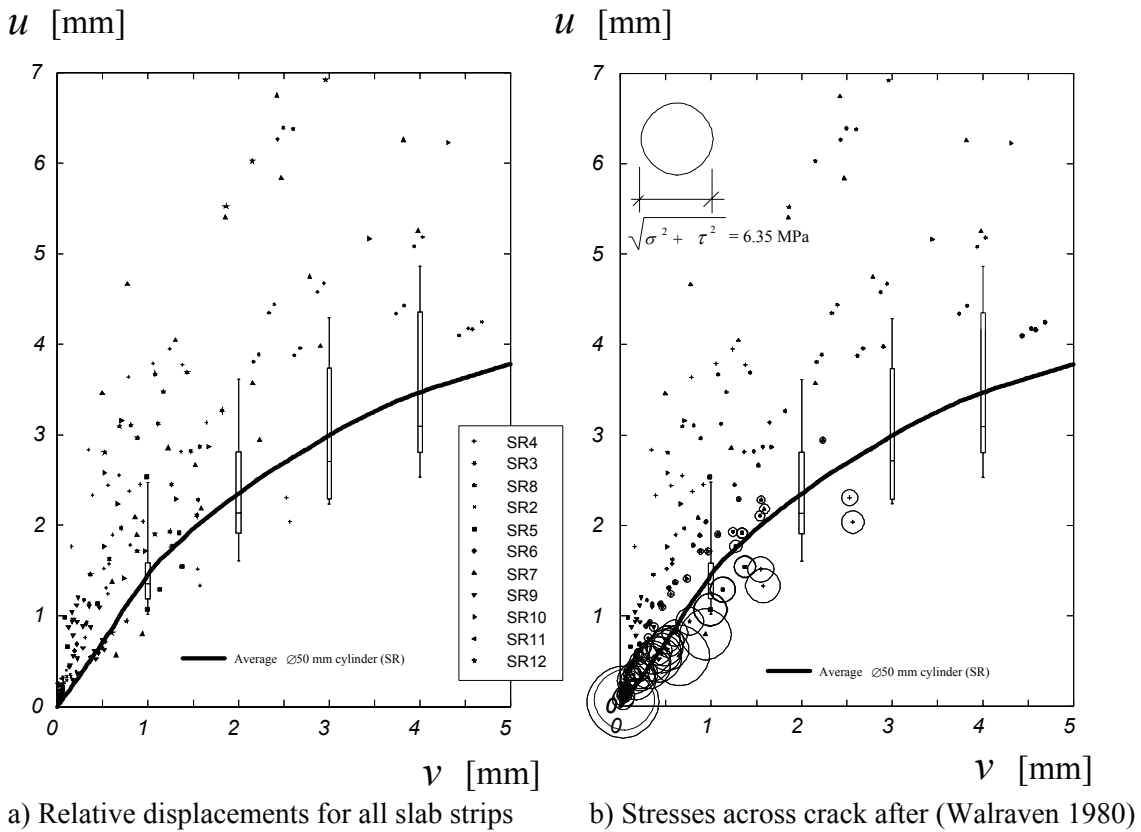


Figure 4.10: Relative displacements and stresses across the critical shear crack

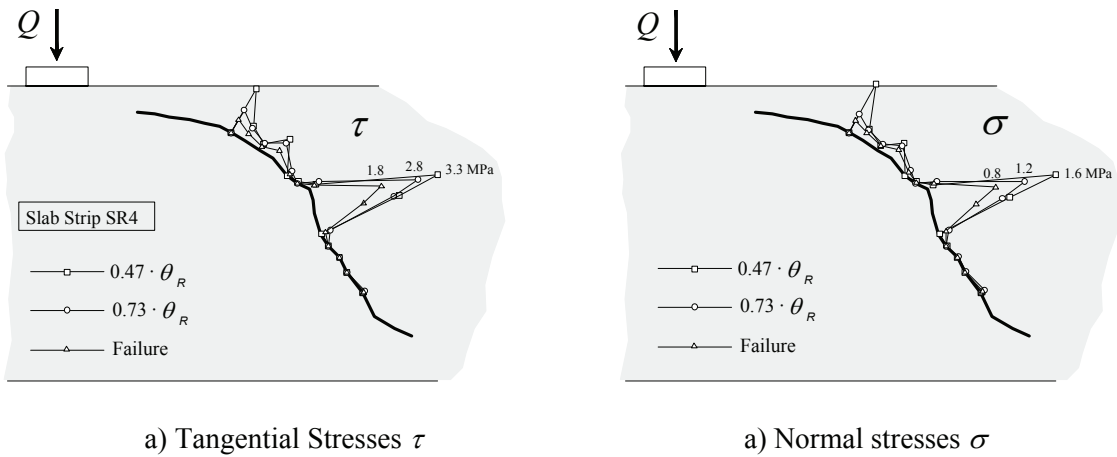


Figure 4.11: Distribution of tangential and normal stresses along the critical shear crack [MPa], test SR4

Figure 4.11 shows the distribution of  $\tau$  and  $\sigma$  along the shear crack for slab strip SR4. The vertical component of the stresses is calculated and multiplied by the width of the slab strip to obtain the transmitted shear force per unit length the crack ( $V'$  in fig. 4.12a). The shear force transmitted across the crack ( $V_{agg}$ ) is calculated by integration along the length of the crack. It can be observed that the shear force is concentrated in the more or less vertical part of the shear crack. The percentage of the shear force transferred across the crack is indicated for different hinge rotations. The amount of shear transferred across the crack decreases with increasing hinge rotation, for slab strip SR4. This tendency is confirmed by the other slab strips that failed in shear (fig. 4.12b).

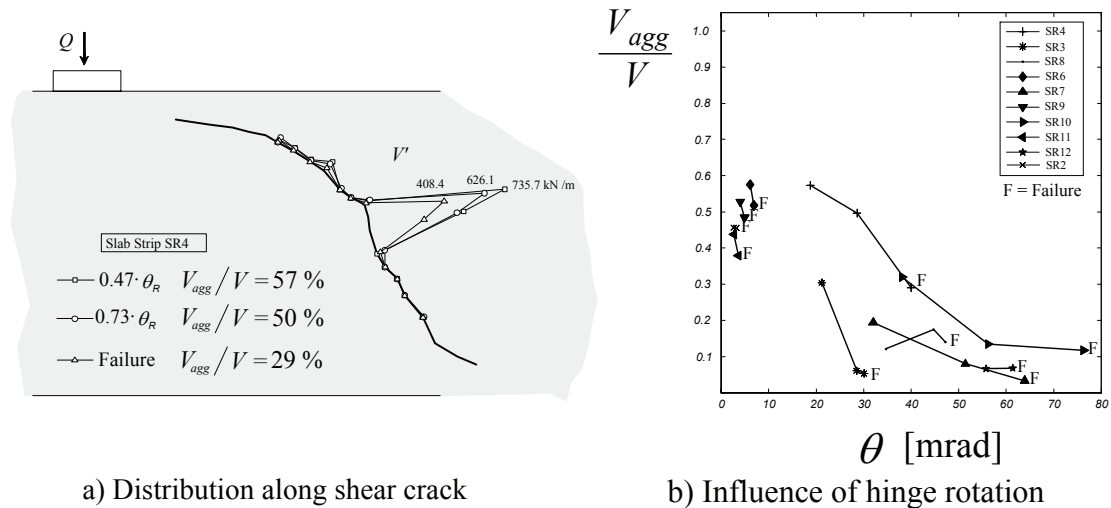


Figure 4.12: Shear force transmitted across shear crack

#### 4.4 Compression zone action

The depth of the compression chord  $x$  in a zone without shear cracks can be calculated by simple bending analysis. The analysis is performed using the compressive stress-strain relationship for concrete according to (Thorenfeldt et al. 1987). The complete calculated diagram is compared to the measured values in figure 4.13a). The compressive stress-strain relationship for concrete according to (Popovics 1970) is also indicated. The behavior of concrete in tension, including tension stiffening, is considered according to (Prakhya, Morley 1990, fig. 4.13b). The behavior of concrete in tension is linear until the tensile strength is reached. The behavior of cold worked reinforcement in tension and compression is considered according to (Cosenza et al. 1993). The complete calculated diagram is compared to the measured values in figure 4.14, for both cold worked and hot rolled reinforcement types.

There is a very good agreement between the stress-strain relationships proposed by (Cosenza et al. 1993) and the tensile tests for cold worked and hot rolled reinforcement type (fig. 4.14).

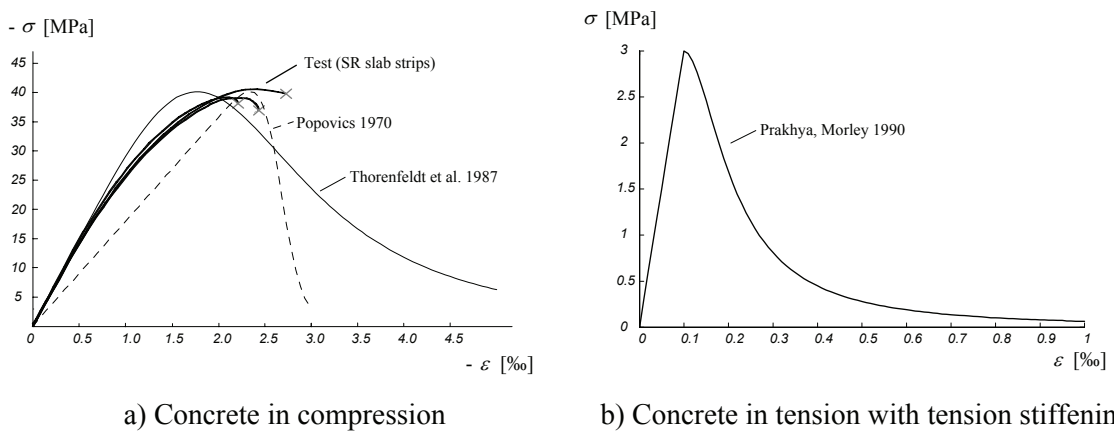


Figure 4.13: Modelling of concrete in compression and tension

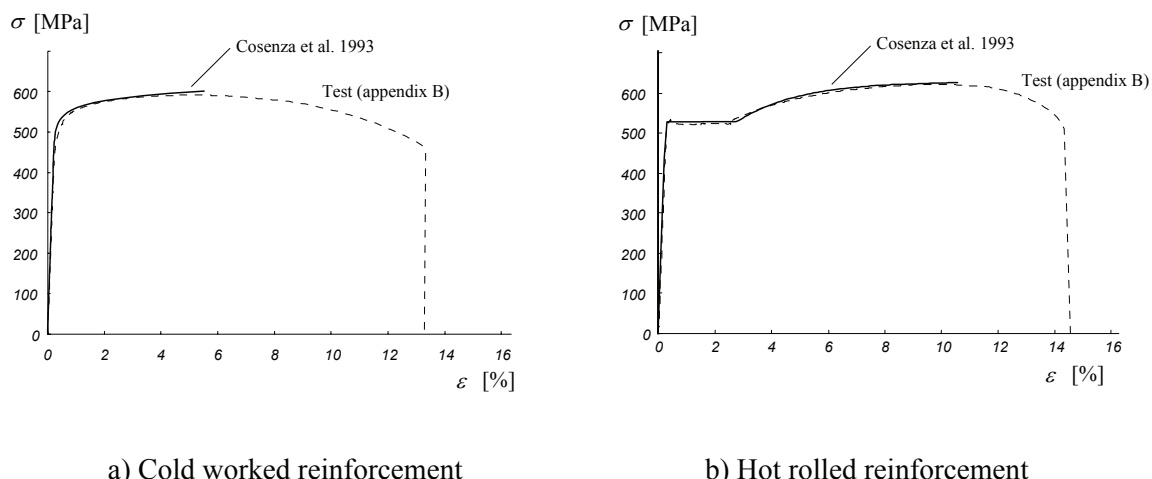


Figure 4.14: Comparison between tests and analytical stress-strain relationships

The moment-curvature diagram of the overall section for slab strips is indicated in figure 4.15. It can be observed that the moment increases after yielding ( $\epsilon_s = \epsilon_{sy}$ ) until the fracture of the reinforcement ( $\epsilon_s = \epsilon_{su}$ ). This corresponds to the strain hardening of reinforcement. The depth of the compression chord decreases in an initial stage after yielding, to stabilize at constant values until failure of the tensile reinforcement ( $x = 0.05$  m). The analysis confirms the obtained results for slab strip SR5, which failed with the fracture of the reinforcement in tension. Figure 4.17 shows the internal axial forces at yielding and at fracture of tensile reinforcement.

The reinforcement in the compression zone plays an important role in ensuring the rotation capacity of the cross-section subjected to bending. At yielding of the tensile reinforcement, concrete carries 80% of the compressive forces (fig. 4.17a). The remainder is carried by reinforcement in compression. At fracture of tensile reinforcement, concrete carries 45% and the reinforcement 55% of the compression force (fig. 4.17b).

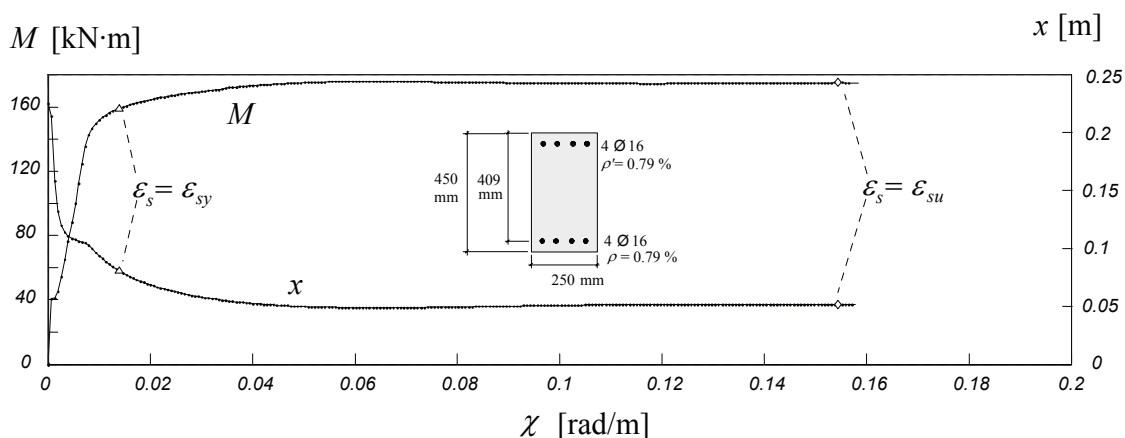


Figure 4.15: Moment-curvature diagram and evolution of depth of compression chord

A comparative analysis of the same cross-section is made with smaller amounts of reinforcement in the compression chord (fig. 4.16). For compression reinforcement ratios that are less than about  $0.5 \cdot \rho$ , the rotation capacity is limited by the failure of concrete in compression. In this case, the failure strain of the tensile reinforcement ( $\epsilon_{su}$ ) is not reached and the moment decreases.



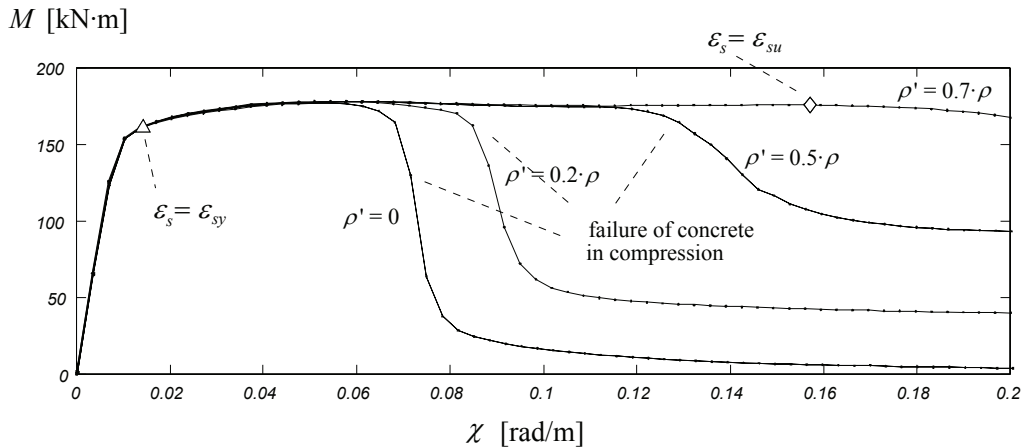


Figure 4.16: Limitation of the rotation capacity due to the failure of concrete in compression

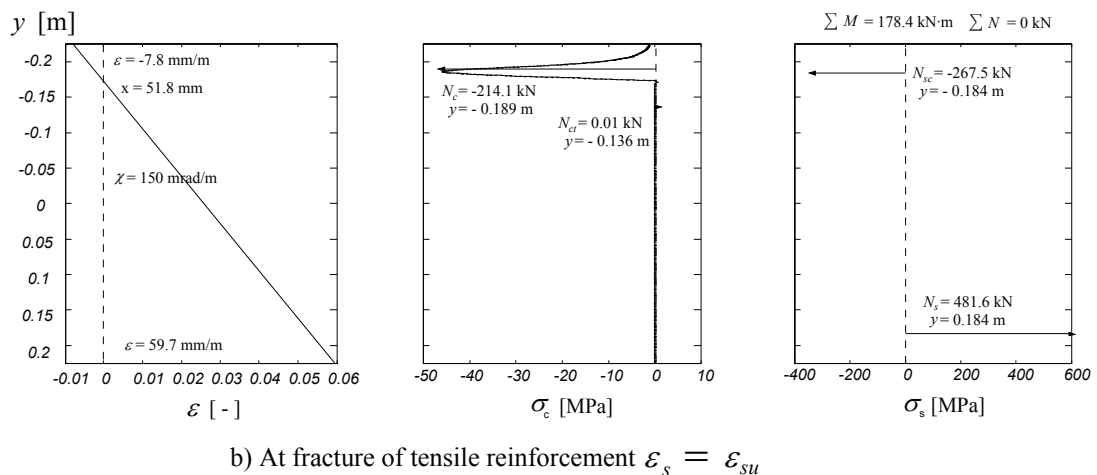
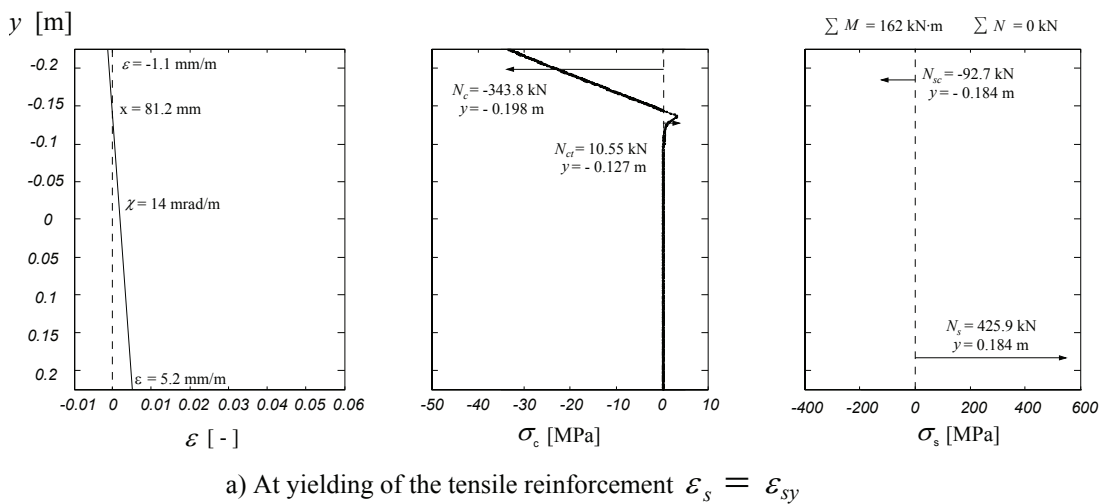


Figure 4.17: Internal forces after bending analysis, at yielding and fracture of reinforcement

The shear force transferred by the compression chord ( $V_{comp}$ ) is estimated for the tested slab strips. A simplified structural model is assumed (fig. 4.18a). The chord is assumed to behave as a clamped beam (with full fixity) at both edges, under constant compression axial force. The considered structural model is considered only valid near failure. The length of the chord  $\ell_c$  is measured according to figure 4.18b) and is indicated in figure 4.18d) for each slab strip. The depth of the compression chord

( $x = 55$  mm) is estimated from bending analysis of the section. This value is assumed to be equal for all slab strips in which reinforcement yielded. The compression force ( $N_c = -426$  kN =  $f_{sy} \cdot A_s$ ) is calculated at yielding of the longitudinal tensile reinforcement. The contribution of concrete in tension is neglected.

The calculated moment-curvature relationship of the compression chord is indicated in figure 4.18c). For positive curvatures, the section fails by crushing of concrete. For negative curvatures the compression reinforcement yields and the behavior is more ductile. The shear force transferred by the compression chord is calculated by imposing the measured displacement  $\delta$  (fig. 4.18d) at the edge of the chord (fig. 4.18a). A simplified moment-curvature diagram (fig. 4.18c) is used for the calculation of the member response. The curvatures are integrated to obtain the shear force carried by the compression chord under the imposed displacement (fig. 4.18e).

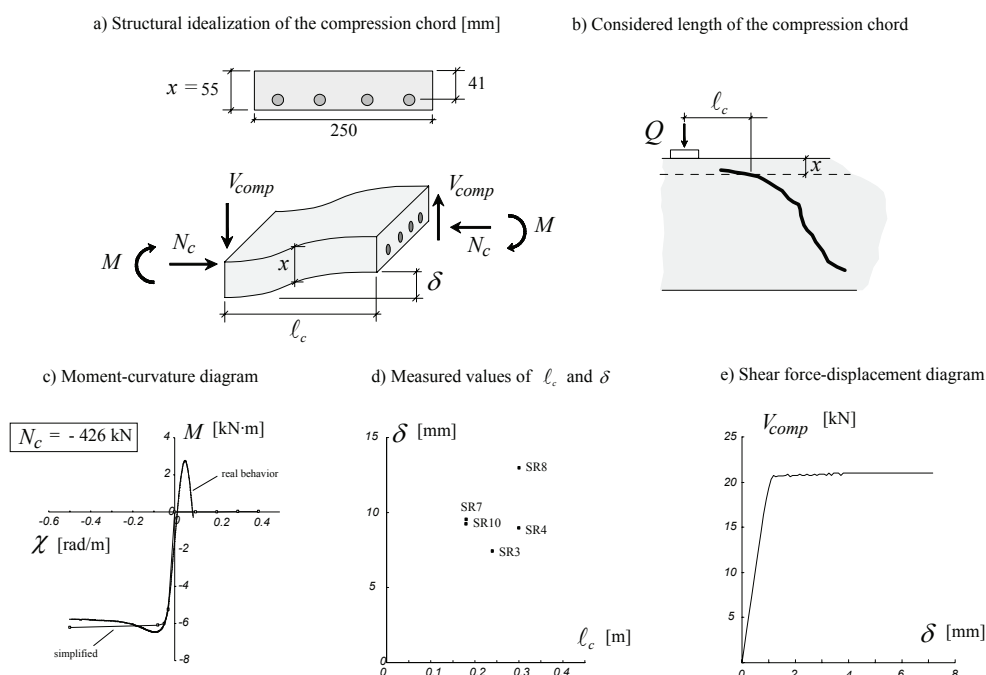


Figure 4.18: Estimation of the shear force carried by the compression chord at failure

Only the slab strips that failed in shear with plastic strains are considered. For slab strips SR6, SR9 and SR12, the length of the compression chord (fig. 4.18b) was not clearly defined. The simplified analysis shows that the percentage of shear force in the compression chord increases with the hinge rotation (fig. 4.19). The same analysis was performed using  $0.9 \cdot l_c$  and  $1.1 \cdot l_c$  for the length of the compression chords. The calculated values are not significantly affected by small variations of  $l_c$ .

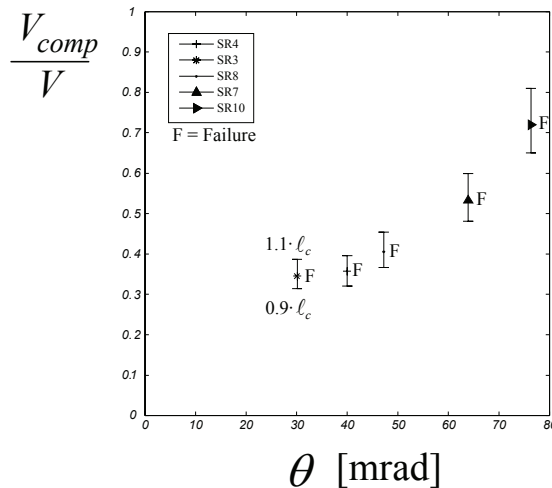


Figure 4.19: Evolution of shear force in the compression chord with increasing hinge rotation

#### 4.5 Dowel action

Figure 4.20 illustrates the crack pattern of slab strip SR3 prior to failure. It can be observed that a horizontal crack forms near the tensile reinforcement. The crack is located above the tensile reinforcement. Similar cracks were observed for slab strips that failed in shear with plastic strains. A crack opening of 3 mm was measured prior to failure for slab strip SR3 (figure 4.20). The measured crack openings strongly limit the transmission of vertical forces across the tensile reinforcement. Dowel action can thus be neglected. It should also be noted that when the shear failure occurs without plastic strains in the tensile reinforcement this hypothesis is not necessarily valid.

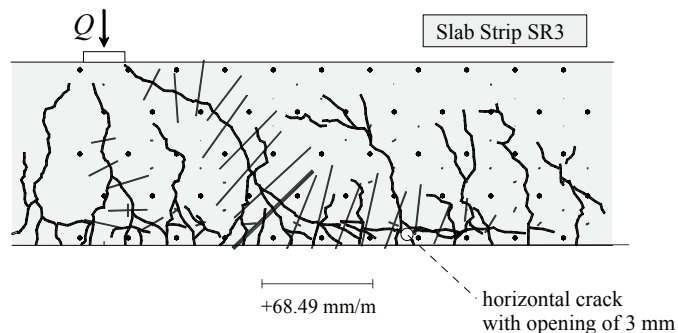


Figure 4.20: Horizontal crack along tensile flexural reinforcement

#### 4.6 Model for the internal shear distribution

A mechanical model is derived to estimate the internal distribution of the shear force at failure. The shear force  $V$  is assumed to be internally equilibrated by:

- A shear force carried across the shear crack ( $V_{agg}$ )
- A shear force carried by the compression chord ( $V_{comp}$ )
- A shear force carried by dowel action ( $V_{dow}$ )

The model is used to estimate the internal distribution of the shear force at failure, neglecting the contribution of dowel action.

A schematic view of the plastic hinge is illustrated in figure 4.21. Only half of the plastic hinge is represented. The plastic hinge is subjected to shear force  $V$  and a rotation  $\theta$ .

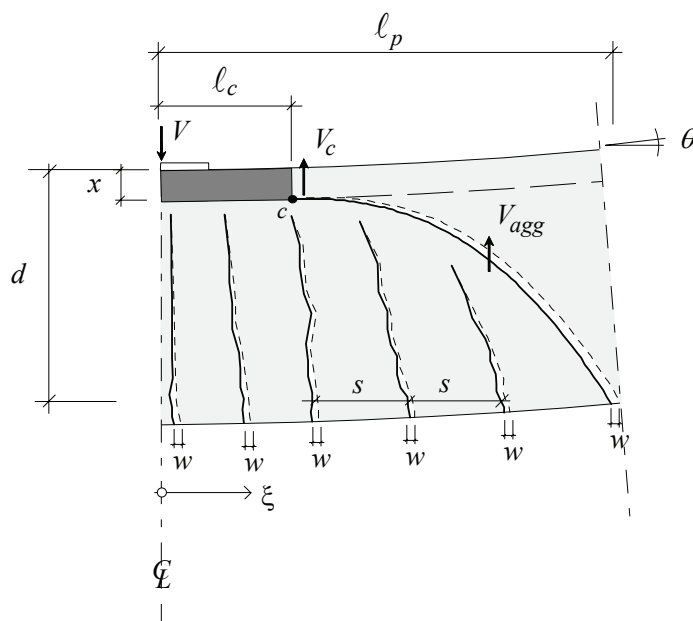


Figure 4.21: Calculation of internal distribution of the shear force

The rotation  $\theta$  affects the internal distribution of the forces (figs. 4.12b and 4.19). The following assumptions are made:

- The half plastic hinge is assumed to have a length of  $l_p$ . The rotation  $\theta$  is measured between  $\xi = 0$  and  $\xi = l_p$ .
- The depth of the compression zone  $x$  is calculated from bending analysis, admitting constant curvatures inside the plastic hinge  $\chi = \theta / l_p$ . Concrete in compression is modeled according to (Thorenfeldt et al. 1987, fig. 4.13a). Concrete in tension and tension stiffening is modeled according to (Prakhya, Morley 1990, fig. 4.13b). Reinforcement in tension and compression is modeled according to (Cosenza et al. 1993) for cold worked and hot rolled reinforcement (fig. 4.14).
- The total elongation of the tension tie, from  $\xi = 0$  and  $\xi = l_p$  and at tensile reinforcement level, is assumed to be  $\Delta u = \theta \cdot (d - x)$ .
- The elongation of the tension tie  $\Delta u$  is assumed to be equally distributed among the crack openings  $w$ . The measured distribution of the crack openings inside the plastic hinge is nearly uniform at failure (fig. 4.4). The contribution of concrete in tension is neglected. A similar hypothesis is assumed by (Bachmann 1967).
- The cracks are assumed equally spaced. The crack spacing is assumed to be  $s = 3 / 16 \cdot (1 - \rho') / \rho' \cdot \varnothing$ , with  $\rho' = 5 \cdot \rho \cdot (d / h)$ . These expressions are derived from a simplified analysis of the tension tie (Muttoni, Burdet 2004).
- A discrete shear crack is considered to calculate the contribution of shear transmitted by aggregate interlock. The center of rotation of the shear crack is at point  $c$ , located at  $\xi = l_c$  and at a distance of  $x$  from top of the slab strip. The

relative displacements along the length of the crack are calculated by imposing the crack opening  $w$  at the lower edge of the crack.

- The model proposed by (Walraven 1981) is used to calculate the distribution of normal and tangential stresses along the shear crack. The component of the shear force transmitted across the shear crack  $V_{agg}$  is calculated by integration of the stresses along the shear crack. The integration is performed from point  $c$  to the lower edge of the shear crack. The remainder shear force is assumed to be entirely carried by the compression chord ( $V_c = V - V_{agg}$ ).
- The results of the model depend on: the length of the compression chord  $l_c$ , the length of half of the plastic hinge  $l_p$  and the shape of the crack. These parameters were calculated by means of a calibration with the test data. Values of  $l_c = 0.5 \cdot d$  and  $l_p = 1.5 \cdot d$  are used. A power law is used to model the shape of the crack ( $\zeta = \eta^c$ ). A similar power law is described in (CEB 1997) to consider the discrete shear crack for slender beams without plastic strains. Figure 4.22 shows the comparison between the theoretical and real shapes of the discrete shear crack, and the lengths  $l_p$  and  $l_c$ , after calibration. It can be observed that the calibrated shape of the crack is rather close to the shape of shear cracks of tests SR3, 8 and 4, that correspond to considerable yielding of the reinforcement. Furthermore the half length of the plastic hinge ( $l_p$ ) is close to the measured yielded length (fig. 4.4).

The results of calculated shear force transmitted across the shear crack ( $V_{agg}$ ) are compared to the test results in figure 4.23.

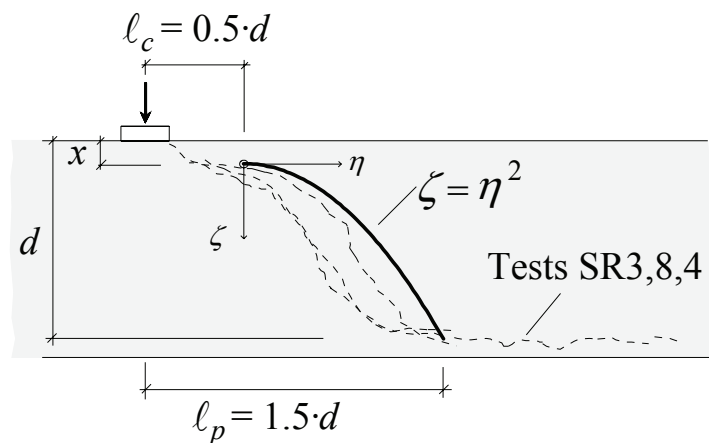


Figure 4.22: Comparison between calibrated and observed crack shapes ( $c = 2$ )

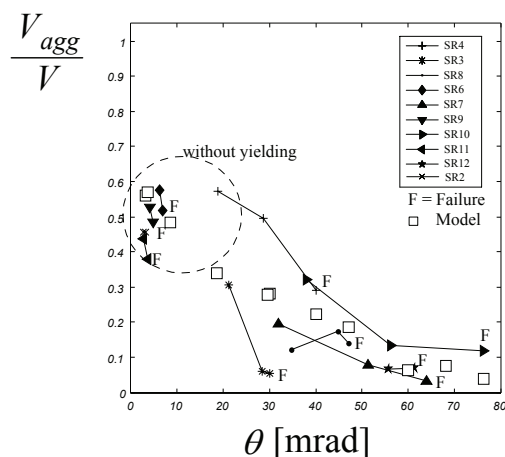


Figure 4.23: Model predictions for the shear force transferred across the shear crack

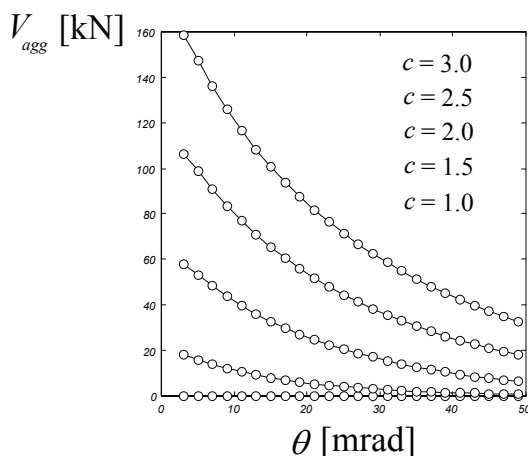


Figure 4.24: Sensitivity analysis on the form of the critical shear crack

A sensitivity analysis on the parameters of the model was performed. It was found that the shape of the crack considerably influences the results. A straight crack (corresponding to a power of  $c = 1.0$  instead of  $c = 2.0$  in fig. 4.22) is expected not to carry any shear force, which is confirmed by the analysis (figs. 4.24 and 4.25). This is because there is no sliding but only openings between the lips of the crack. The other values of the model considered in figure 4.24 are  $d = 0.409$  m,  $h = 0.45$  m,  $x = 0.05$  m,  $\ell_p = 1.5 \cdot d$ ,  $\ell_c = 0.5 \cdot d$  and  $f_c = 47$  MPa. The amount of shear forces carried across the shear crack increases with the exponent  $c$  (fig. 4.24 and 4.25) and decreases with the hinge rotation.

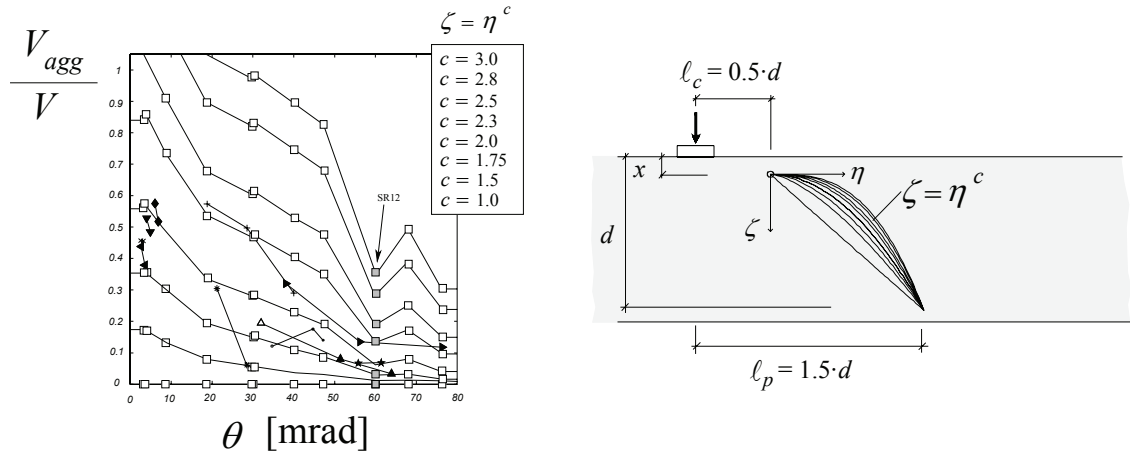


Figure 4.25: Sensitivity analysis on the form of the critical shear crack ( $\zeta = \eta^c$ ,  $l_c = 0.5 \cdot d$ ,  $l_p = 1.5 \cdot d$ ) and comparison with measured values

The case of slab strip SR12 is highlighted in figure 4.25. When compared to slab strip SR3, which failed under the same shear force, SR12 allowed larger hinge rotations up to failure (fig. 3.12). For this reason, the ratio  $V_{agg} / V$  is lower than for slabs strips that failed at equal hinge rotations. This case illustrates well the fact that the position of the crack relative to the theoretical compression strut plays a major role in controlling the shear failure (fig. 4.26).

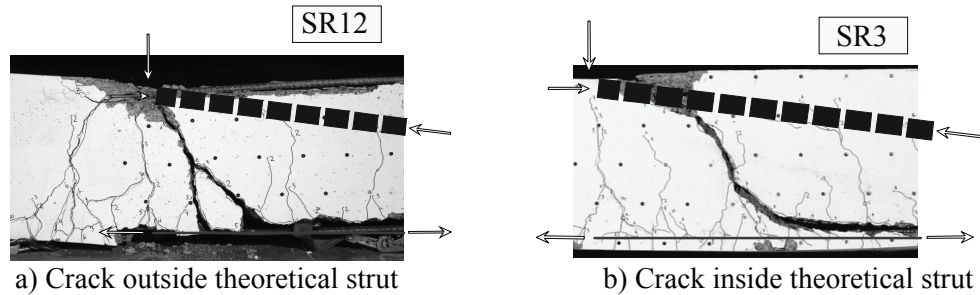


Figure 4.26: Comparison of slab strips SR12 and SR3

## 4.7 Formulation of the shear failure criterion

The considerations of the previous section allow to calculate the repartition of the shear forces between the compression chord and the critical shear crack. Under a constant applied shear force  $V$ , the repartition between the compression chord and the critical shear crack depends of the rotation of the plastic hinge  $\theta$ . With increasing  $\theta$ , more shear is carried by the compression zone.

To define a shear failure criterion, the following assumption is introduced:

The shear failure of the entire section occurs when the shear force in the compression chord ( $V_{comp}$ ) reaches its maximal allowable value ( $V_{comp,R}$ )

The resistant shear force  $V_R$  is therefore the sum of the maximal allowable shear in the compression chord  $V_{comp,R}$  and the shear force carried across the shear crack  $V_{agg}$  :

$$V_R = V_{comp,R} + V_{agg} \quad (4.1)$$

The shear force carried across the shear crack  $V_{agg}$  decreases with increasing rotation  $\theta$ . The calculation procedure for  $V_{agg}$  is explained in the previous section. Figure 4.27 schematically shows the behavior of four plastic hinges with different intensities of the applied shear force ( $V$ ).

The shear failure occurs for three cases when the loading curves reach the shear failure criterion. For the case with the lowest shear force there is no shear failure because  $V < V_{comp,R}$ . In the cases where the shear failure occurs, the shear force in the compression chord reaches at failure the maximal allowable shear in the compression chord ( $V_{comp,R}$ ). The model gives a rational explanation for the reduction of the resistant shear force with increasing hinge rotation. The reduction of the shear capacity is related to the reduction of the shear forces carried across the critical crack by aggregate interlocking.

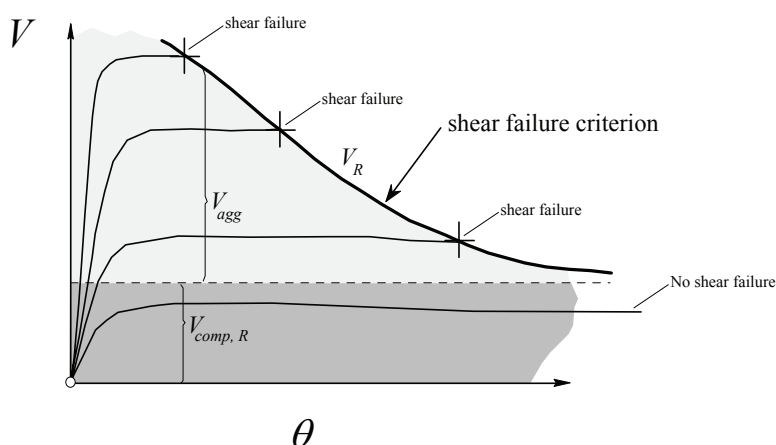


Figure 4.27: Shear failure criterion

Figure 4.28 shows the crack pattern after failure of three tested slab strips. All slab strips failed in shear after yielding of the flexural reinforcement at different levels of hinge rotation. The presence of a crack at the top of the compression chord is clearly visible after failure. The decompression of the top compressed fiber was visible in the strain measurements prior to failure.

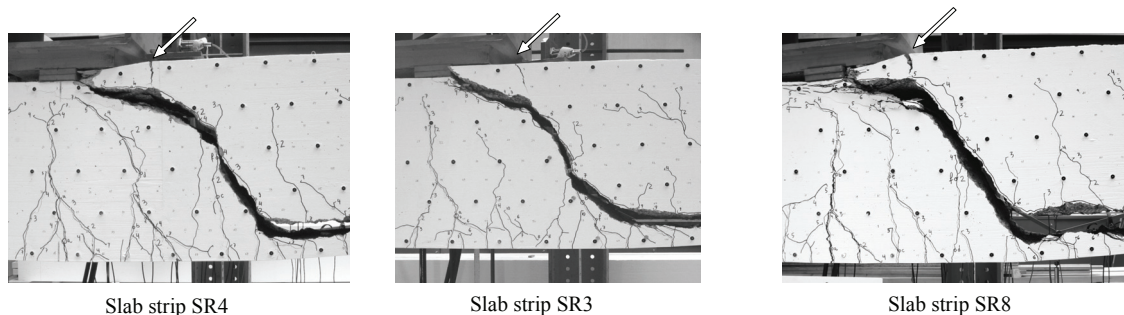


Figure 4.28: Crack in the top of the compression chord after failure

The decompression of the top compression fiber was observed in other tests (Muttoni, Thürlimann 1986). The explanation for this fact is given in this figure 4.29b) with a stress field (Muttoni, Schwartz 1991). The propagation of the shear crack into the compression zone causes the compression strut to deviate. The tension tie in the top fiber is necessary to equilibrate the stress field.



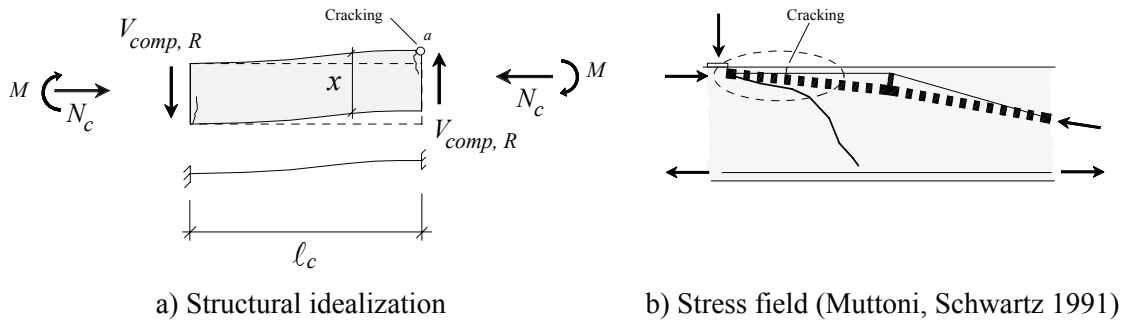


Figure 4.29: Strength of compression chord

The compression chord is idealized as an axially compressed beam clamped at both edges (figure 4.29a). The following assumption is made for the calculation of the maximal allowable shear in the compression chord ( $V_{comp,R}$ ):

- The maximal allowable shear in the compression chord is reached when the axial stresses in the compression chord reach the tensile strength of concrete at point  $a$  (fig. 4.29a).

Based on the previous assumption, the following expression is derived for the maximal allowable shear force in the compression chord:

$$V_{comp,R} = \frac{x^2}{3 \cdot \ell_c} \cdot \left( f_{ct} + \frac{\sigma_s \cdot A_s}{b \cdot x} \right) \cdot b \quad (4.2)$$

A linear elastic behavior of the compression chord is assumed until just before failure. This assumption might not be verified, depending on the amount, strength and position of compression reinforcement (fig. 4.18). Nevertheless, eq. 4.2 gives adequate results and a non linear calculation of the compression chord does not appear to be necessary. This simplification of the compression chord provides a clear physical interpretation of the mechanics involved but the compatibility with the displacement field of the hinge is not necessarily guaranteed.

The length of the compression chord is assumed to be  $\ell_c = 0.5 \cdot d$ , according to figure 4.22. The compression force is assumed  $N_c = \sigma_s \cdot A_s$ , where  $A_s$  is the area of tensile reinforcement. This corresponds to neglecting the contribution of concrete in tension. The compression force  $N_c$  is assumed to act at the middle of the compression chord.

The height of the compression chord  $x$  is calculated from bending analysis assuming an average curvature  $\chi = \theta / \ell_p$ .

## 4.8 Comparison with the test data

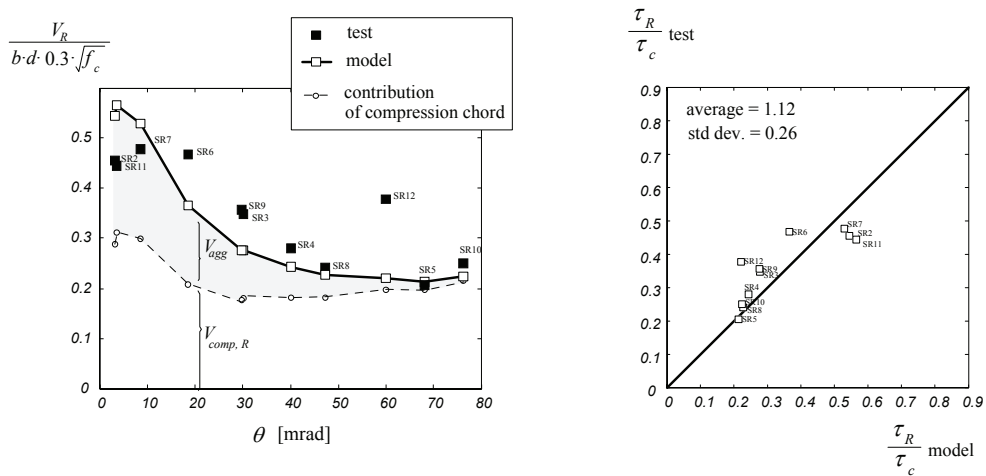
The model predictions for the shear force carried by aggregate interlock  $V_{agg}$  are compared to the test data (appendix B) in figure 4.23. The model correctly reproduces the tendency of the internal distribution of shear forces.

The model predictions for the shear strength are shown in figure 4.30. The following observations can be made:

- The model accurately predicts the shear strength of the slab strips that failed after yielding of the reinforcement.

## Chapter 4

- For slab strip SR12 the position and form of the shear crack considerably deviates from the form and location assumed in the model.



- a) Evolution of shear strength with increasing hinge rotation      b) Model predictions and test results

Figure 4.30: Comparison between calculated and measured shear strength

## 4.9 Parametric analysis

A parametric study was performed to evaluate the influence of the following parameters:

- The effective depth of the slab ( $d = 0.2 \dots 0.45 \dots 0.8 \dots 1.2$  m).
- The tensile reinforcement ratio ( $\rho = A_s / (b \cdot d) = 0.4 \dots 0.75 \dots 1.0 \dots 1.5$  %).
- The maximum size of the aggregate ( $k_{dg} = 8 \dots 16 \dots 32$  mm).

The reinforcement ratio in the compression chord is considered equal to the reinforcement ratio in tension. This is assumed in order to avoid the failure of concrete after yielding of the reinforcement (fig. 4.16). The same parametric analysis was made with lower (and more common) values of the compression reinforcement. The results do not significantly change for beams which are not controlled by failure of concrete in compression.

Other properties are considered as constant values:  $f_c = 47$  MPa,  $f_{ct} = 3$  MPa,  $E_c = 30000$  MPa,  $f_{sy} = 530$  MPa and  $f_{su} = 600$  MPa,  $\varepsilon_{su} = 5\%$ ,  $E_s = 205000$  MPa, cold worked reinforcement is considered and  $\varnothing = 16$  mm.

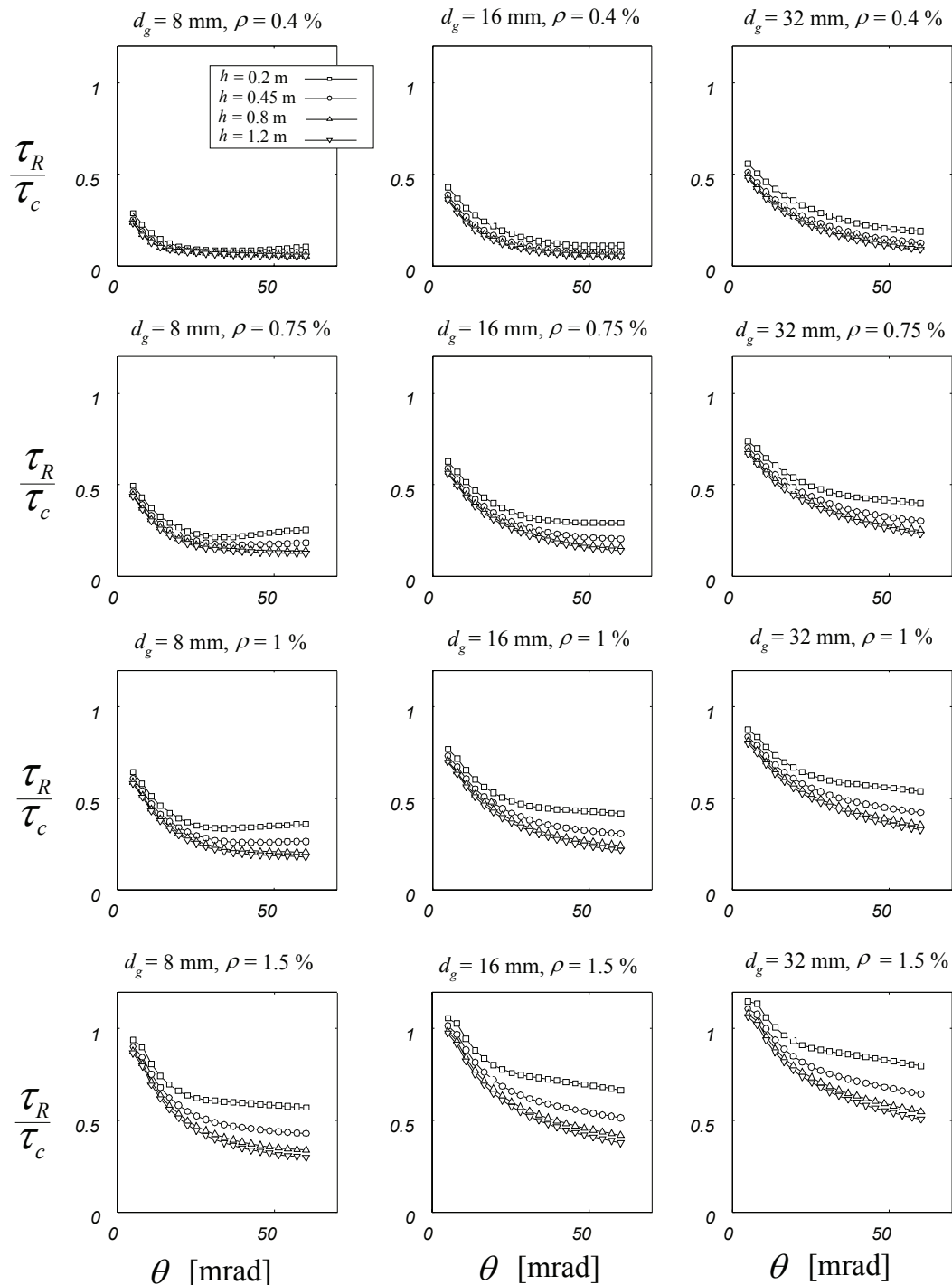


Figure 4.31: Parametric analysis

It can be seen from the parametric analysis that:

- The mechanical model correctly reproduces the tendency of size effect. An increase in the effective depth of the slab strips induces a reduction in the calculated shear strength.
- An increase in the maximum size of the aggregate induces an increase in the shear strength.
- An increase in the ratio of flexural tensile reinforcement increases the shear strength. This is explained because the depth of the compression chord increases.

- For beams of depth  $h = 0.2$  m and size of the aggregate  $d_g = 8$  mm, the model predicts a small increase in the shear strength with increasing rotations. This effect is unrealistic and can be explained because the depth of the compression chord increases after the crushing of concrete.

#### 4.10 Simplified equation

A simplified equation was derived to estimate the shear strength of members with usual reinforcement ratios. The results of the parametric analysis (retaining only the points with  $\rho = 0.75\%$ ) are used to fit a simplified equation:

$$\frac{\tau_R}{\tau_c} = \frac{1}{1.7 + 0.07 \cdot \theta \cdot d \cdot k_{dg}} \quad (4.3)$$

The variables of equation 4.3 are defined as follows:

- $\tau_R = V_R / (b \cdot d)$  is the nominal shear strength
- $\tau_c = 0.3 \cdot (f_c)^{0.5}$  is the nominal shear strength of concrete, with  $f_c$  in MPa
- $k_{dg} = 48 / (16 + d_{dg})$ , with  $d_{dg}$  in [mm]
- $d$  is effective depth, in [m]
- $\theta$  is the hinge rotation (fig. 4.32) in [mrad]

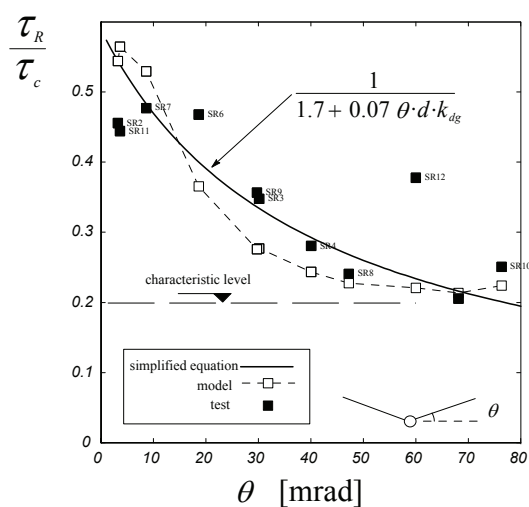


Figure 4.32: Comparison of simplified equation with model and test results

Figure 4.32 compares the predictions of the simplified model with the test results and the full mechanical model.

The characteristic value of all the slab strips that failed in shear can also be determined. This value can be used as a first estimate of the shear strength in the presence of yielding. By assuming that the distribution is normal (fig. 4.33) the shear strength that has a probability of 95% of being exceeded is  $\tau_R / \tau_c = 0.20$ .

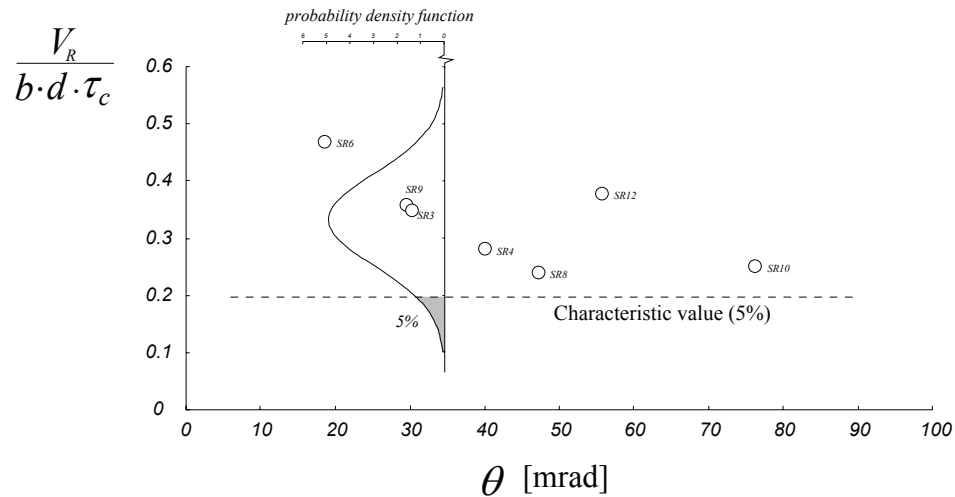


Figure 4.33: Characteristic shear strength of all beams that failed in shear with plastic strains

#### 4.11 Conclusions

The following conclusions can be made:

- The acting shear force is essentially resisted by the compression chord and by aggregate interlock.
- The reduction of the shear strength with increasing hinge rotation is explained by the reduction of aggregate interlock action.
- The strength of the compression chord plays a crucial role in triggering the shear failure. This fact is integrated in the proposed mechanical model by means of a physical formulation of the strength of the compression chord.
- The measured distribution of the shear force, as well as the measured shear strengths can be adequately predicted by the proposed mechanical model. A simplified equation is proposed, derived from the results of the mechanical model.



## 5. Shear assessment of bridge deck slabs under concentrated loads

### 5.1 Introduction

Reinforced concrete bridge deck slabs without shear reinforcement tend to fail in shear when subjected to groups of concentrated loads. This is confirmed by the following experimental evidence on large scale bridge decks without shear reinforcement:

- (Miller et al. 1994) performed one destructive test on a 38-year-old decommissioned concrete slab bridge under two concentrated loads. The failure mode was shear. The theoretical flexural failure load was not reached.
- (Vaz Rodrigues 2006) performed six large scale tests on two bridge deck cantilevers under groups of concentrated loads. All the cantilevers failed in shear and the theoretical flexural failure load was not reached. (see test report in appendix A of this dissertation).
- (Lu 2003) performed a series of nine tests on reduced scale cantilevers. The predominant failure mode was shear.

The shear assessment of reinforced concrete bridge decks will be performed using the punching shear and one-way shear criteria proposed by Muttoni (Muttoni 2003), explained in detail in chapter 2.

The punching shear criterion is applied to zones where the flow of shear forces is strongly two dimensional. This occurs near the applied concentrated loads. In order to apply the punching shear criterion to the case of a non symmetrical situation, further assumptions need to be made to compute the length of the critical perimeter  $u$  and the rotation angle  $\theta$ . These assumptions are described in the next section.

In addition, an evaluation of the one-way shear criterion can be performed in the regions of unidirectional flow of forces, such as the region near the clamped edge of cantilevers. Some additional assumptions are made in section 5.3 in order to apply the one-way shear criterion to reinforced concrete slabs with variable depth.

### 5.2 Further assumptions to calculate the punching shear capacity

The application of the failure criterion to reinforced concrete slabs under concentrated loads requires the following considerations:

- Definition of the control perimeter: The control perimeter lies at a distance of  $d/2$  of the edge of the loaded area. The length of the control perimeter  $u$  should take into account the distribution of transverse shear forces. The length of the control perimeter  $u$  is estimated from the following equation (see also fig. 5.1):

$$u = \frac{Q}{v_{\max,el}} \quad (5.1)$$

Where  $Q$  is the total applied load (uniformly distributed over the loaded surface) and  $v_{\max,el}$  is the maximum principal shear force, calculated for all cross sections lying at  $d/2$  of the edge of the loaded surface. According to eq. 5.1, if the slab's effective depth

is constant along the control perimeter, the punching shear failure occurs when the maximal elastic nominal shear stress ( $\tau = v_{\max, \text{el}} / d$ ) reaches the shear strength given by the punching shear failure criterion (eq. 2.9). This choice of  $u$  is therefore based on the elastic distribution of the principal shear forces, and not on purely geometric considerations. It should be noted that the definition of the length of the control perimeter  $u$  is not strictly necessary, because the maximal elastic nominal shear stress is compared to the shear strength to account for failure. Nevertheless, the concept of the control perimeter is currently used in engineering practice and this is why this concept was kept. The linear model used to calculate the distribution of the principal shear force is described in section 5.5.

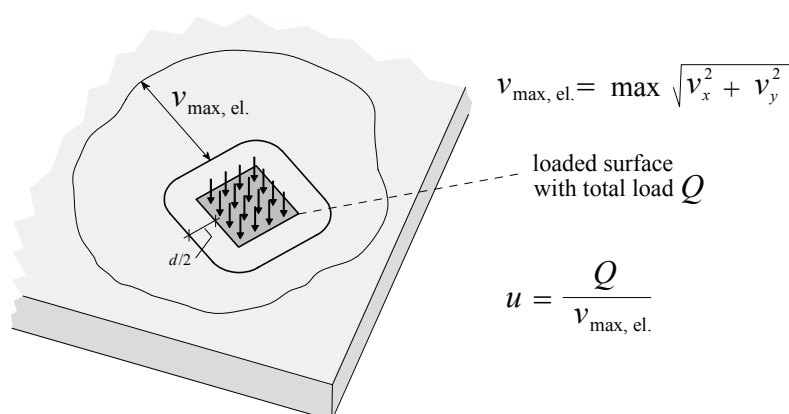


Figure 5.1: Definition of the length of the control perimeter  $u$  in case of single applied concentrated load

- Definition of the rotation  $\theta$ . In the case of symmetric punching shear the rotation is clearly defined (fig. 2.14). In the case of slabs under concentrated loads, the rotation  $\theta$  is considered as the difference between the rotations of the slab at two points. The first point is located at the centroid of the applied load. The second point is chosen so that the maximal relative rotation is obtained. The rotations are calculated along the direction defined by the two points. The definition of the precise location of the points will be illustrated with the available test data. The rotation  $\theta$  is calculated from the results of the non linear analysis, explained in the section 5.6.

### 5.3 Further assumptions to calculate the one-way shear capacity

According to eq. 2.2, the computation of the shear strength at a point of the slab requires the knowledge of the section strains  $\varepsilon$ , calculated from eq. 2.1. The further assumptions are made to estimate the one-way shear strength of reinforced concrete slabs:

- The control sections lie at a distance of  $d/2$  of the edge of the load introduction area.
- The principal shear force (eq. 2.12) is considered to verify the shear failure. The bending moment in the direction of the principal shear force ( $m_\phi$ ) is used to calculate the longitudinal strains ( $\varepsilon$ , equation 2.1).
- The effect of the inclined compressed chord is considered by reducing the principal shear force of  $m_\phi / z \cdot \tan \delta$  as indicated by eq. 5.2. The corrected value of the principal shear force ( $v_{\text{tot}}'$ ) is compared to the shear strength (eq. 2.2) to account for



failure. The angle of the inclined compressed chord with the horizontal plane is  $\delta$ . The angle  $\delta$  is measured in the direction of the principal shear force.

$$v_{tot}' = v_{tot} - m_{\phi} \cdot \tan \delta \quad (5.2)$$

A different criterion should be used when the moment in the direction of the principal shear force exceeds the yielding moment in the same direction. In this case the shear strength is given by the eq. 4.3.

## 5.4 Representation of the flow of transverse shear forces

A useful representation of the shear flow will be used in this dissertation. The direction and magnitude of the principal shear forces can be represented in one diagram to provide an immediate insight of the flow of the inner forces. The thickness of the shear flow trajectories is made to be proportional to the magnitude of the principal shear force (eq. 2.12).

This representation is illustrated after two closed-form limit analysis solutions given by (Nielsen 1964) and discussed by (Marti 1990). The first example considers a corner supported square slab that is subjected to uniformly distributed load. In this case the moment and shear fields are defined as:

$$m_x = m_0 \cdot \left(1 - \frac{4 \cdot x^2}{\ell^2}\right), \quad m_y = m_0 \cdot \left(1 - \frac{4 \cdot y^2}{\ell^2}\right), \quad m_{xy} = m_0 \cdot \frac{4 \cdot x \cdot y}{\ell^2} \quad (5.3)$$

$$v_x = -m_0 \cdot \frac{4 \cdot x}{\ell^2}, \quad v_y = -m_0 \cdot \frac{4 \cdot y}{\ell^2} \quad (5.4)$$

Where  $m_0 = q \cdot \ell^2 / 8$ . According to equation 5.4 the shear flow trajectories radiate from the center of the slab (fig. 5.2). It can also be observed that the magnitude of the principal shear force linearly increases with the distance from the center of the slab, as indicates the varying thickness of the shear flow trajectories. This representation shows that the loads are radially transferred to the edges of the slab along which they are carried (indicated by arrows running parallel to the edge) before being introduced into the corner supports.

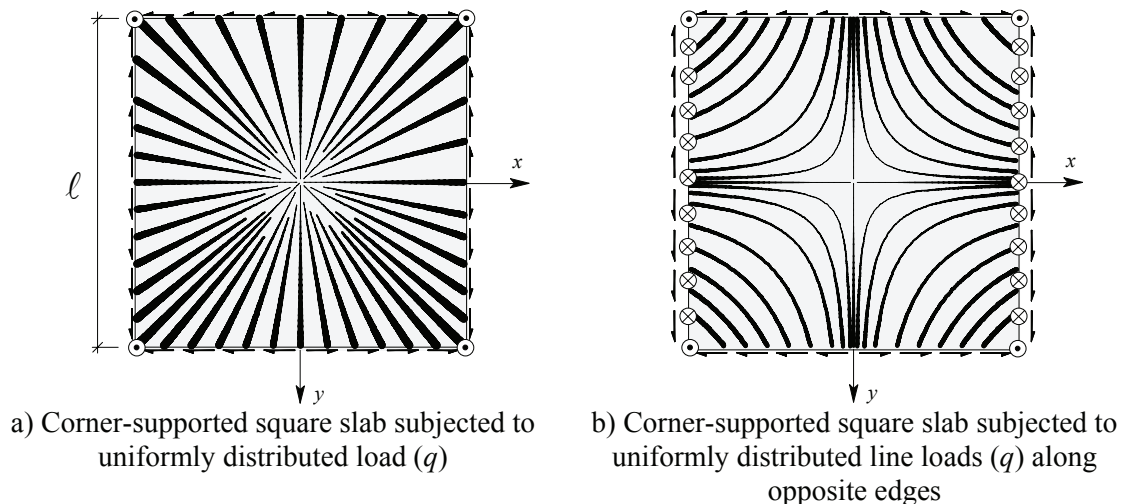


Figure 5.2: Representation of the magnitude and direction of principal shear forces

The second case considers a corner supported square slab that is subjected to uniformly distributed line loads along opposite edges. In this case the moment and shear fields are defined as:

$$m_x = 0, \quad m_y = m_0 \cdot \left(1 - \frac{4 \cdot y^2}{\ell^2}\right), \quad m_{xy} = m_0 \cdot \frac{4 \cdot x \cdot y}{\ell^2} \quad (5.5)$$

$$v_x = m_0 \cdot \frac{4 \cdot x}{\ell^2}, \quad v_y = -m_0 \cdot \frac{4 \cdot y}{\ell^2} \quad (5.6)$$

Where  $m_0 = q \cdot \ell^2 / 8$ . One-half of the line load is directly carried to the closest support along the edge of the slab. The other half is transmitted along hyperbolic lines crossing the interior of the slab before reaching the adjacent edge, along which they are introduced in the closest support.

The proposed representation allows a direct visualization of the transfer of shear forces inside a slab, including load paths and magnitude.

Another representation is used for the evolution of the shear force along the control perimeters. The magnitude of the principal shear force is represented perpendicularly to the control perimeter (fig. 5.1).

## 5.5 Linear model for calculation of inner forces

Linear elastic finite element analysis is performed to calculate the maximal principal shear force along the control perimeter. An example of such computations is indicated in figure 5.3, for the case of three reinforced concrete bridge deck slabs with a span of 4.5 m, a thickness of 0.5 m at the clamped edge and 0.25 m at the free edge. The applied loads are the twin axle loads prescribed by the Eurocode 1 (Eurocode 1 2003) and SIA 261 (SIA 2003), with dimensions 2.0 x 1.2 m (between the centroids of each concentrated load). The load introduction plates are square with a side of 0.4 m. The shear flow is shown for the three cases, using the representation proposed in the last section. A load of  $Q/4 = 150$  kN is applied on each 0.4 x 0.4 m loaded surface. The contribution of the self-weight is not included and full fixity is imposed at the clamped edge.

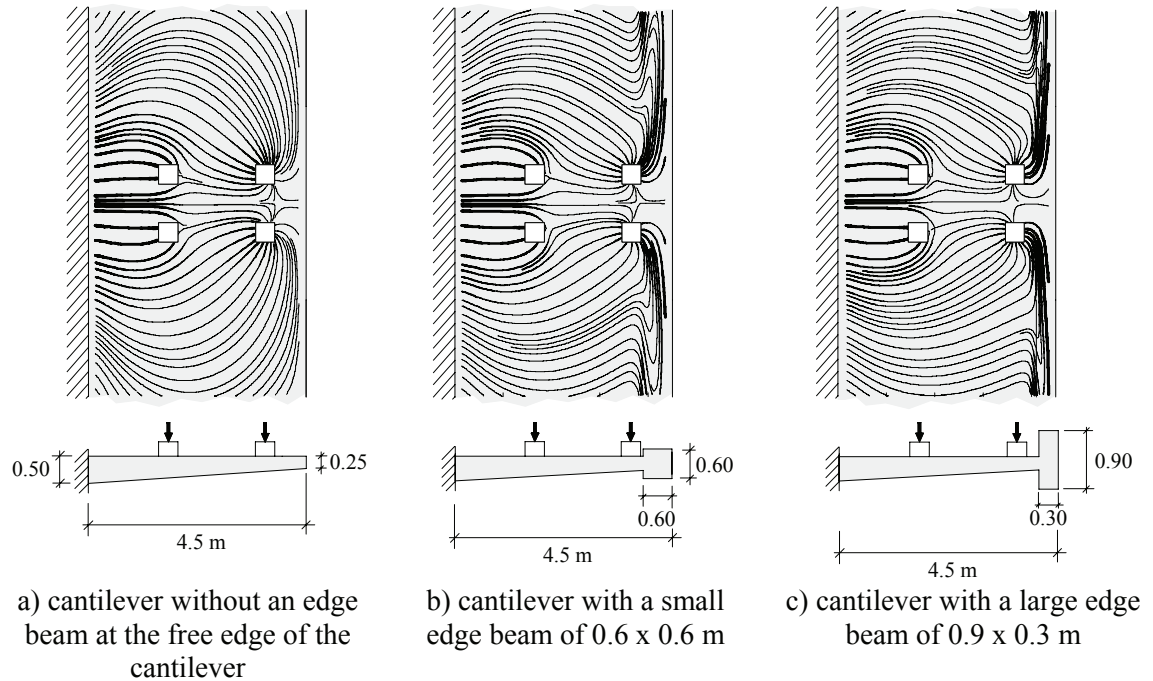


Figure 5.3: Effect of edge beam's inertia on the elastic flow of inner forces at cantilever slabs under four concentrated loads (for  $Q = 600 \text{ kN}$ )

From the analysis of the shear flow it can be seen that the stiffening effect of the edge beam is associated with its load carrying function. A stronger edge beam carries more loads parallel to the cantilever root, in the longitudinal sense, thus contributing to a wider diffusion of the shear forces inside the cantilever slab. This corresponds to a reduction of 15% of the maximal hogging moment, calculated at  $0.5 \cdot d$  from the cantilever root (fig. 5.4d), if cases a) and c) are considered. The distribution of the principal shear force near the clamped edge (fig. 5.4a and b) is less affected by the dimensions of the edge beam. On the contrary the distribution of shear forces is strongly disturbed in the control perimeter around the concentrated loads at the free edge. The shear force is represented along a control perimeter that encircles the two edge loads (fig. 5.4c). The perimeter is located at  $0.5 \cdot d$  from the edge of the applied loads and continues towards the edge of the slab to cross the edge beam.

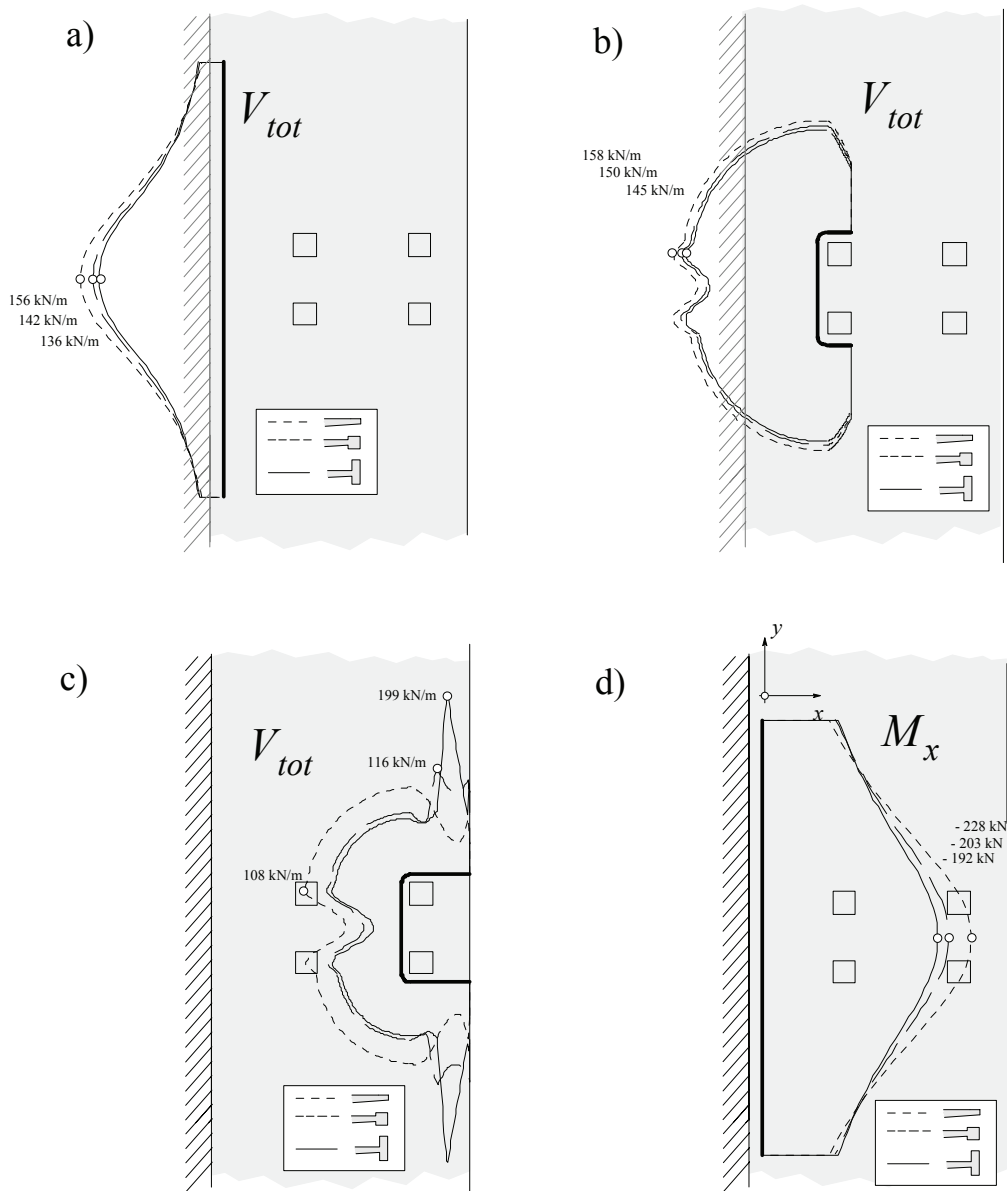


Figure 5.4: Effect of edge beam's inertia on the magnitude of principal shear force [kN/m] at various control perimeters and moments [kN-m/m] near the clamped edge (control perimeters at  $d/2$  from the edge of the applied loads and fixed end, and for  $Q = 600$  kN)

A stiff edge beam attracts the shear forces, causing a “stream” of shear forces of high magnitude to flow from the edge loads to the edge beam (fig. 5.3c). Before being introduced in the edge beam, the shear forces are carried across the region of the slab located between the edge loads and the edge beam, where the slab's thickness is normally small and therefore the shear strength is rather small. This can lead to a local punching shear failure in this region, as shown in figure 2.19c). In this case the shear crack does not cross the edge beam. Despite the high shear forces in the edge beam (fig. 5.4c), the nominal shear stresses are reduced because of the important depth of the edge beam. Furthermore, vertical shear reinforcement is normally present in the edge beam and this strongly limits the possibility of a shear failure in this member. Another effect to consider is the transmission of shear forces by direct support for loads near the edge beam (or the clamped edge). This effect locally increases the shear strength.

The results of the linear analysis for other cantilevers with various spans and thicknesses are summarized in a design chart (fig. 5.5). Several linear elastic analysis were performed and the obtained results used to fit the indicated curves. The maximum transverse hogging moment at the clamped edge (point A) is  $M$ . Two situations are considered: with and without a strong edge beam. The moments and shear forces are calculated for various thicknesses  $h$  at the cantilever clamped edge. The charts only include the effect of the four concentrated loads, with  $Q = 600$  kN. The effects of the self-weight and uniformly distributed traffic loads are not considered. The length of the cantilever is  $a$ . The two exterior concentrated loads are always located at 0.5 m from the edge of the cantilever, the most unfavorable location for the bending moment. Full fixity is assumed at the clamped edge. The two regimes found in chart correspond to the case of two and four concentrated loads over the cantilever. The increase of the slab's thickness at the fixed end of the cantilever causes the bending moment to increase. Inversely, the edge beam causes the maximum hogging moment to decrease.

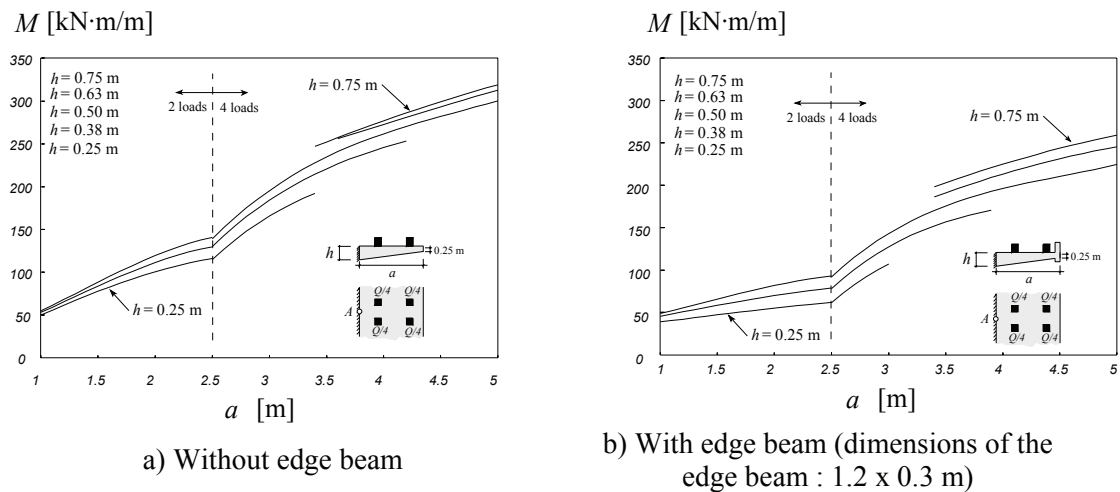


Figure 5.5: Elastic analysis of maximal transverse hogging moment at the cantilever fixed end (point A). The action of four concentrated loads (SIA 261 and Eurocode 1) with  $Q = 600$  kN is considered at the most unfavorable position, the self-weight of the slab is not considered

## 5.6 Non linear model for calculation of rotations and displacements

The deflections and rotations of the slab are computed using a non linear model of the slab. Only the variation of the flexural stiffness and the in-plane shear stiffness is considered in calculating the response of the structure. The non linear calculation can be seen as a procedure that consists of a series of linear elastic analysis until convergence is reached (fig. 5.6). At each iteration the flexural stiffness ( $EI^*$ ) is updated for each element according to the moment-curvature relationships (fig. 5.6). These relationships are defined as a function of the geometry, reinforcement at arbitrary orthogonal directions, and for positive and negative moments. Figure 5.6a) shows only the positive part of the diagrams. The first iteration uses the properties of uncracked concrete. The iterative scheme is indicated in figure 5.6c) The pre-processing of the data, the iterative scheme and post-processing of the results were entirely developed and implement during this dissertation. A different component (Ansys 2004) is used for the solver part. The element used is the four node element isoparametric shell181. The stress-strain matrix of this element is indicated in figure 5.6b).

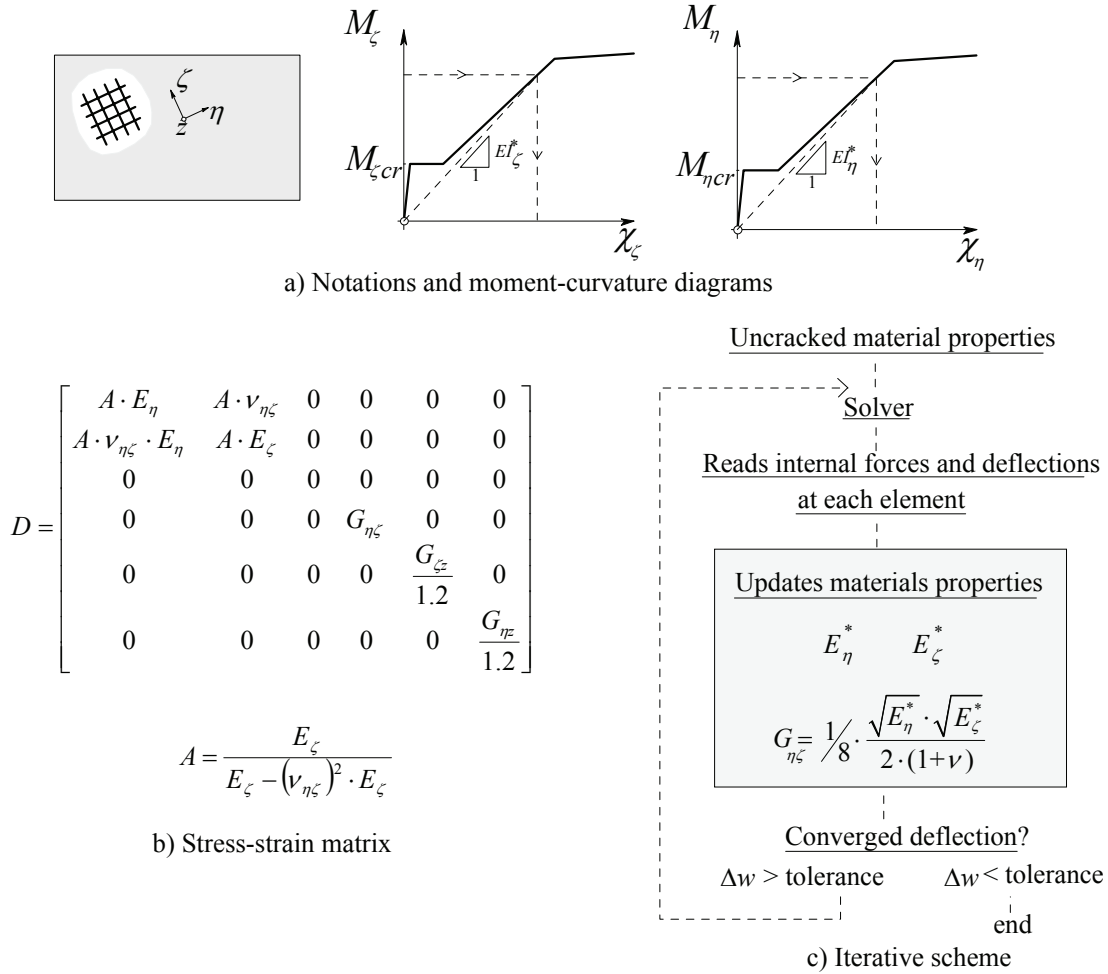


Figure 5.6: Moment-curvature diagrams and iterative scheme

At each iteration the shear modulus in the plane of the slab is reduced to  $G_{\eta\zeta} = \frac{1}{8} \cdot \sqrt{E_\eta^*} \cdot \sqrt{E_\zeta^*} / 2 \cdot (1+\nu)$ . This reduction is only applied if the moment is larger than the cracking moment at one of the reinforcement directions ( $M_\eta > M_{\eta,cr}$  or  $M_\zeta > M_{\zeta,cr}$ ). If the element is not cracked then  $G_{\eta\zeta} = \sqrt{E_\eta^*} \cdot \sqrt{E_\zeta^*} / 2 \cdot (1+\nu)$ . The coefficient of 1/8 takes into account the reduction of the in-plane shear stiffness after the cracking of the section. Torsion tests on reinforced concrete beams show that the ratio between the uncracked and cracked torsional stiffness varies between 0.1 and 0.25 for usual reinforcement ratios (Leonhardt, Schelling 1974). A factor of 1/8 gives good agreement between the calculated and the measured values. The shear modulus in the  $\eta z$  plane is  $G_{\eta z} = E_c / 2 \cdot (1+\nu)$  and the shear modulus in the  $\zeta z$  plane is  $G_{\zeta z} = E_c / 2 \cdot (1+\nu)$ . This corresponds to not considering a decrease in the shear stiffness in both directions. The reduction of the Young's modulus  $E_\eta$  and  $E_\zeta$  can cause the stress-strain matrix to become negative semidefinite. To prevent this, the Poisson ratio is considered equal to zero in all the analysis. A sensitivity analysis shows that the Poisson ratio seems to have a very reduced influence on the deflections of the structure, in particular after cracking.

The iterative procedure is stopped when the difference between the deflections at the same point becomes very small. The number of required iterations is generally small. Figure 5.7 illustrates the evolution of the deflection  $w$  with increasing iterations. The selected control point is the point of maximal deflection.

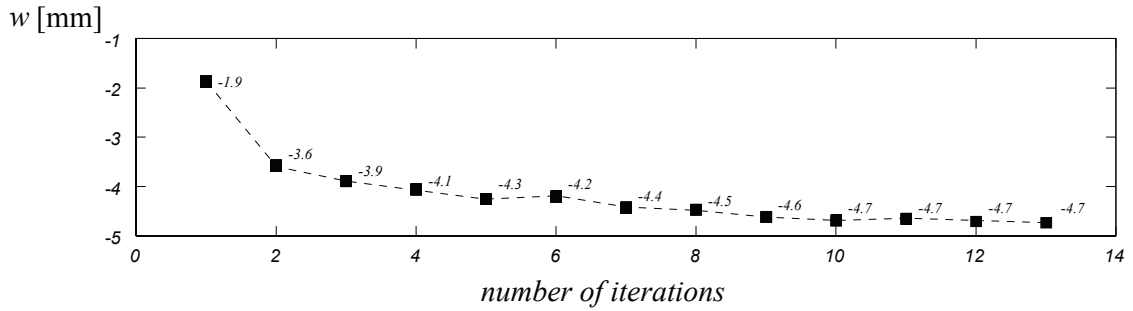


Figure 5.7: Example of converged solution

The following material properties are considered in the moment-curvature diagrams:

- Concrete in uniaxial compression is modeled according to (Thorenfeldt et al. 1987).
- Concrete in uniaxial tension is considered linear until the tensile strength is reached ( $\sigma = E_c \cdot \varepsilon$  for  $\varepsilon \leq f_{ct} / E_c$  and  $\sigma = 0$  for  $\varepsilon > f_{ct} / E_c$ ).
- The stress-strain relationships for cold formed and hot rolled reinforcement are considered according to (Cosenza et al. 1993).
- Tension stiffening is considered according to (Muttoni, Burdet 2004) (eq. 5.7).

$$\Delta\chi_{ts} = \frac{3}{40} \cdot \frac{f_{ct} \cdot h}{a_s \cdot E_s \cdot (h-x)} \quad (5.7)$$

A complete calculation of a moment-curvature diagram is shown in figure 5.8. The following properties are used:  $h = 0.38$  m,  $b = 1$  m,  $d = 0.342$  m,  $d' = 0.04$  m,  $f_c = 45$  MPa,  $f_{ct} = 3.0$  MPa,  $E_c = 30000$  MPa,  $\rho = 0.8\%$ ,  $\rho' = 0.4\%$ ,  $f_{sy} = 530$  MPa,  $f_{su} = 600$  MPa,  $E_s = 205000$  MPa,  $\varepsilon_{sh} = 3\%$ ,  $\varepsilon_{su} = 10\%$  (reinforcement is hot rolled).

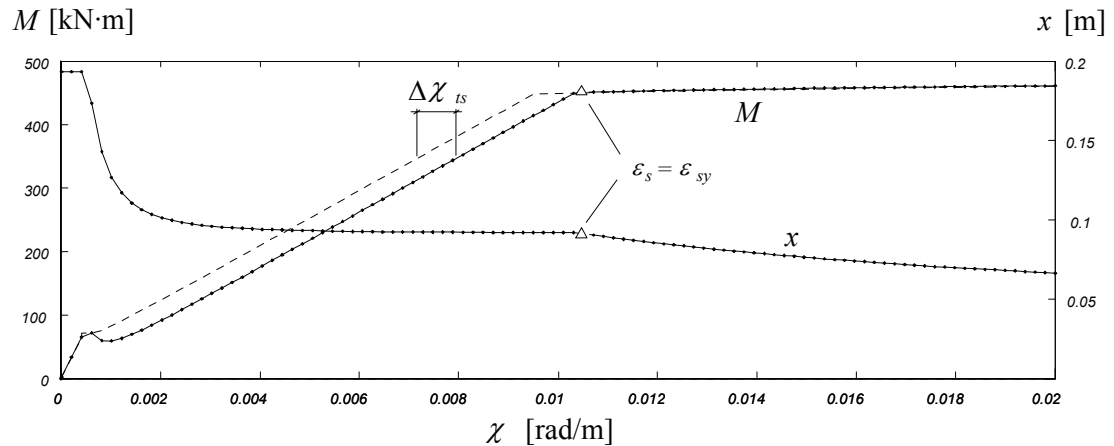


Figure 5.8: Moment curvature diagram and evolution of the depth of compression zone ( $x$ )

A correct modeling of the supports is important to reproduce the actual structural behavior. The vertical stiffness of a simply supported region is introduced using non linear springs. In this case the axial stiffness of the support is equally distributed among the nodes inside the region of the support. The spring is non linear because it has zero stiffness when the slab is lifting (fig. 5.9).

The correct introduction of loads is also important. Concentrated loads that are uniformly distributed over a reduced area of the slab (for example a wheel load) are divided into groups of statically equivalent concentrated loads. Each of these loads is

distributed into four statically equivalent loads that are directly applied in the nodes of the element. This procedure ensures that the applied loads at the nodes and the distributed loads on the structure are statically equivalent (fig. 5.9).

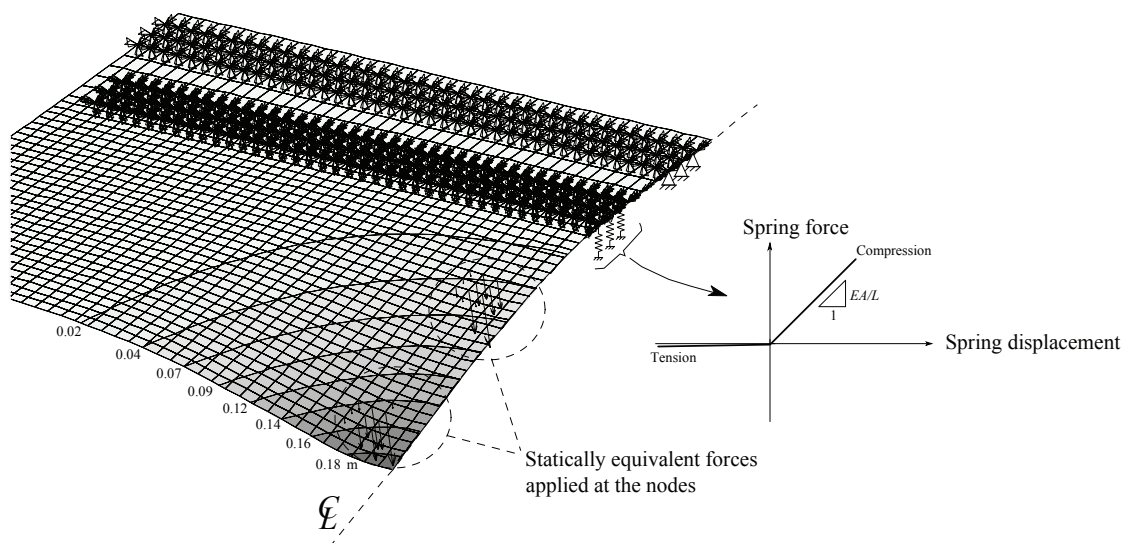


Figure 5.9: Modeling details and converged deformed shape (for  $Q = 1600$  kN), test DR1-a

## 5.7 Comparison with large scale tests

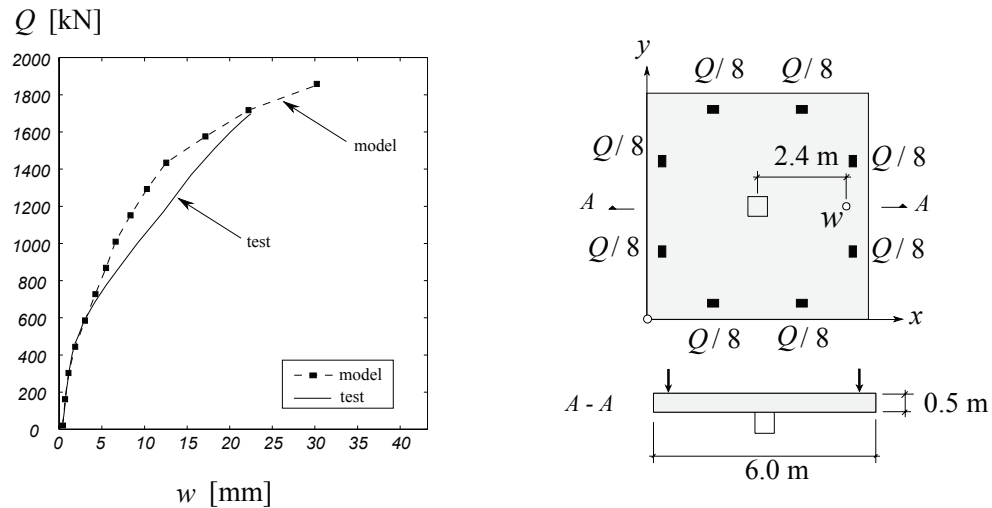
The following tests are considered:

- One large scale punching shear test
- One full scale test of a decommissioned slab bridge
- Six large scale tests of bridge deck cantilevers under concentrated loads (see test report in appendix A).

### 5.7.1 Punching shear test

(Guandalini 2005 and Guandalini, Muttoni 2004) tested a full scale slab under a concentrated load. The slab is square with a side of 6.0 m and thickness of 0.5 m. The slab is supported by a square concrete column with a side of 0.520 m. The loads are introduced near the edge of the slab at eight metallic plates (fig. 5.10b). The top reinforcement is of  $\varnothing$  16 mm bars spaced at 0.135 m for both directions. The effective depth is of 0.464 m for bars along  $x$  and 0.448 m for bars along  $y$ . The central support is modeled using non linear springs. The vertical stiffness in compression of the concrete column is distributed among the nodes inside the column. The springs have zero stiffness in tension.





a) Calculated and measured load-deflection curves    b) Notations and dimensions [m]

Figure 5.10: Test PG3: calculated and measured load-deflection curves

The calculated and measured deflections are indicated in fig. 5.10a). The deflections are calculated by the non linear analysis. The calculated and measured deflections are compared along  $y = 3.0$  m (fig. 5.11). There is good agreement between the calculated and measured values.

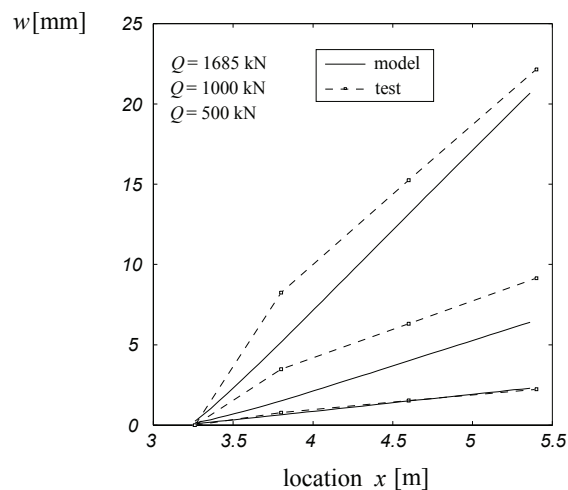
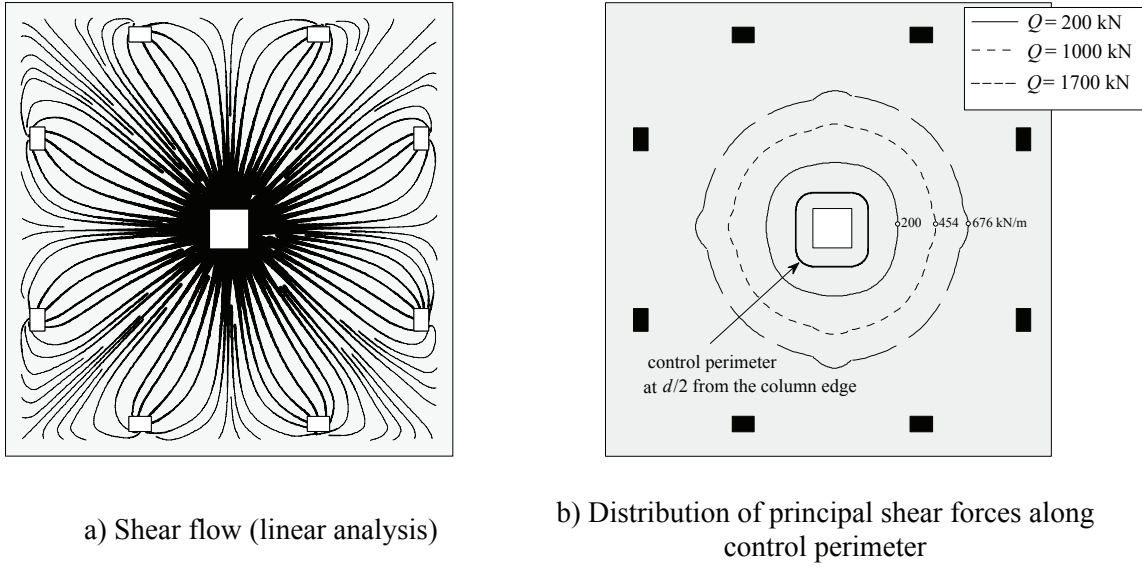


Figure 5.11: Test PG3: comparison of calculated and measured deflections (along  $y = 3.0$  m)

The shear flow is represented in figure 5.12a) using the shear forces calculated by the linear analysis. After being introduced in the slab, the shear forces are carried along lines that radiate from the center of the column. The magnitude of the principal shear forces strongly increases near the column.



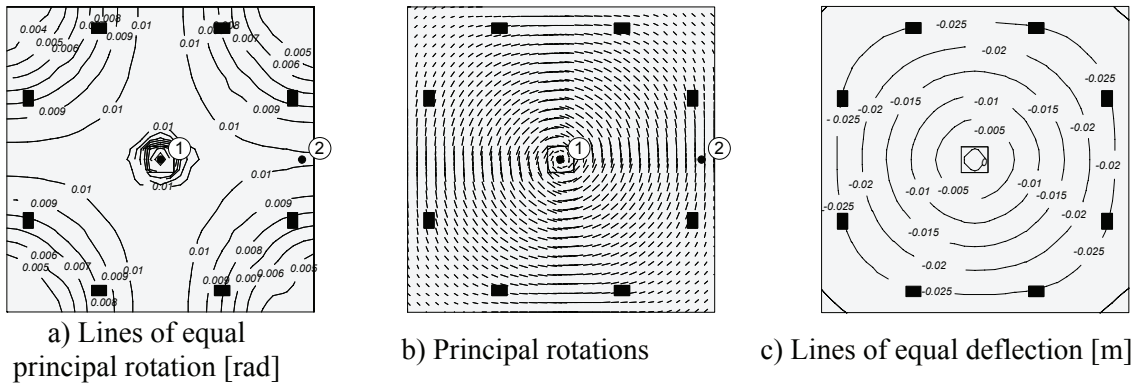
a) Shear flow (linear analysis)

b) Distribution of principal shear forces along control perimeter

Figure 5.12: Test PG3: transverse shear forces

The elastic distribution of the principal shear force along the control perimeter is shown in figure 5.12b). The maximal principal shear force along the control perimeter is  $v_{tot,el} = 676 \text{ kN/m}$ , at  $Q = 1700 \text{ kN}$  and considering the contribution of the self-weight. The force in the central column is  $V = Q + 450 \text{ kN}$ . According to eq. 5.1 the length of the control perimeter is  $u = (1700 + 450) / 676 = 3.18 \text{ m}$ . If the shear force would be uniformly distributed over the geometric perimeter at  $d/2 = 0.228 \text{ m}$ , the maximal shear force would be  $v_{tot} = 2150 / 3.51 = 612 \text{ kN/m}$ .

Figure 5.13c) shows the lines of equal deflection. The line of zero deflection does not coincide with the edge of the column because the axial stiffness of the support is considered. Figure 5.13a) and b) show that the principal rotation is nearly axisymmetric. The rotation  $\theta$  is the difference between the rotation at point ① and the rotation at point ②. The rotation  $\theta$  is calculated and measured along the line defined by the two points.



a) Lines of equal principal rotation [rad]

b) Principal rotations

c) Lines of equal deflection [m]

Figure 5.13: Test PG3: location of points for calculation of the rotation  $\theta$  (from non linear analysis at  $Q=1700 \text{ kN}$ )

The response of the structure can be expressed in terms of  $\tau / \tau_c$  (the contribution of the self weight,  $450 \text{ kN}$ , is added to the total applied load  $Q$ ):

$$\frac{\tau}{\tau_c} = \frac{Q + 450}{u \cdot d \cdot 0.3 \cdot \sqrt{f_c}} \quad (5.8)$$

and  $\theta \cdot d \cdot k_{dg}$ , bearing in mind that  $\theta$  is the relative rotation between points ① and ② (fig. 5.13). The calculated and measured diagrams are compared in figures 5.14 and 5.15, for two different values of  $u$ . The response in figure 5.14 is calculated using the length of the control perimeter of eq. 5.1,  $u = 3.18$  m. The response in figure 5.15 is calculated from the geometric length of the control perimeter  $u = 4 \cdot 0.52 + \pi \cdot 0.456 = 3.51$  m. The rotations corresponding to the lines marked with “Test” were measured with inclinometers. The average effective depth along the control perimeter (fig. 5.12b) is  $d = 0.456$  m. The calculated failure load ( $Q_R$ ) corresponds to the intersection of the calculated response with the punching shear failure criterion. The calculated failure loads are  $Q_{R, calc, punch} = 1648$  kN and  $Q_{R, calc, punch} = 1697$  kN, respectively with  $u = 3.18$  m and  $u = 3.51$  m. The measured failure load is  $Q_{R, test} = 1703$  kN.

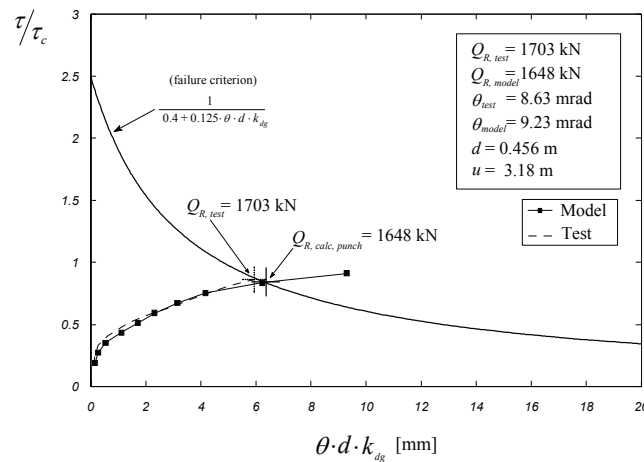


Figure 5.14: Test PG3: evaluation of punching shear criterion, considering the length of the control perimeter given by equation 5.1,  $u = V / v_{max,el} = 3.18$  m

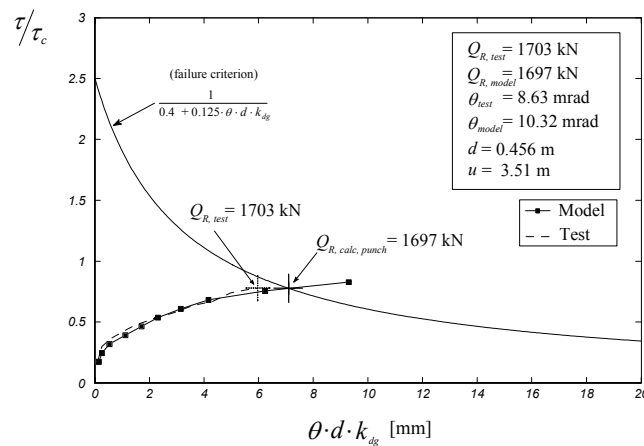


Figure 5.15: Test PG3: evaluation of punching shear criterion, considering the geometric length of the control perimeter given by  $u = 4 \cdot 0.52 + \pi \cdot 0.456 = 3.51$  m

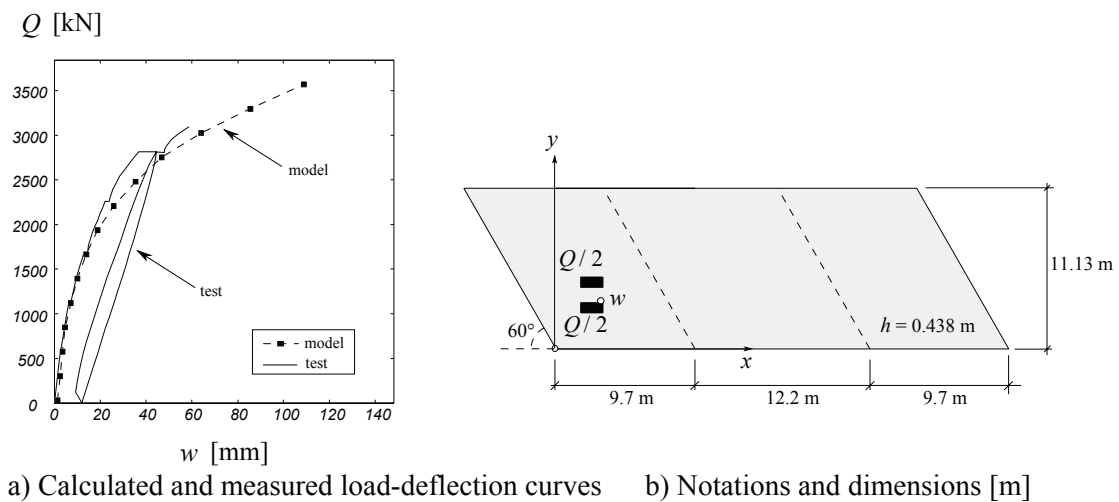
This case shows that equation 5.1 can be used to calculate the length of the control perimeter  $u$ , leading to a good estimation of the punching shear failure load.

Despite the shear flow being strongly two dimensional, the one-way shear criterion can be investigated to predict the punching shear failure load, according to the additional assumptions made. The calculated failure load using this criterion is of about 50% of the actual punching shear failure load. This illustrates that the use of the one-way shear

criterion should be restricted to zones where the flow of forces is essentially unidirectional.

### 5.7.2 Test of decommissioned slab bridge

(Miller et al. 1994) conducted a destructive test on a 38-year-old deteriorated concrete skew slab bridge. The skew bridge had a total length of 31.6 m (fig. 5.16b). The abutments and pier line were skewed at  $30^\circ$  to the roadway. The slab was loaded with two  $1.525 \times 0.690$  m loading blocks simulating the front tandem axle load of a HS20-44 truck. The bridge failed in shear at  $Q = 3200$  kN. The bending stiffness of the piers is considered in the model. The measured and calculated deflections are shown in figs. 5.16a) and 5.17. The model predicts a more flexible behavior at loads higher than  $Q = 2000$  kN.



a) Calculated and measured load-deflection curves    b) Notations and dimensions [m]  
 Figure 5.16: Test of decommissioned slab bridge: calculated and measured load-deflection curves

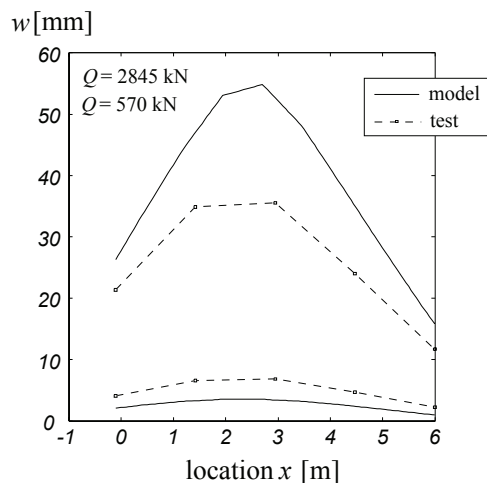


Figure 5.17: Test of decommissioned slab bridge: comparison of calculated and measured deflections (along  $y = 3.355$  m)

From the analysis of the shear flow (fig. 5.18a), two zones can be identified: a zone of strong one-way shear, where forces flow perpendicularly to the center line of the pier; and a zone of two-way shear around the two concentrated loads. Therefore, the one-way and punching shear criteria are respectively used to calculate the failure loads.

Considering the punching shear criterion, the control perimeter is located around the two concentrated loads, at  $d/2 = 0.194$  m from their edge. At  $Q = 3197$  kN, the maximal principal shear is  $v_{tot} = 587$  kN/m. The length of the control perimeter is therefore (eq. 5.1):

$$u = \frac{3197 \text{ kN}}{587 \text{ kN/m}} = 5.45 \text{ m} \quad (5.9)$$

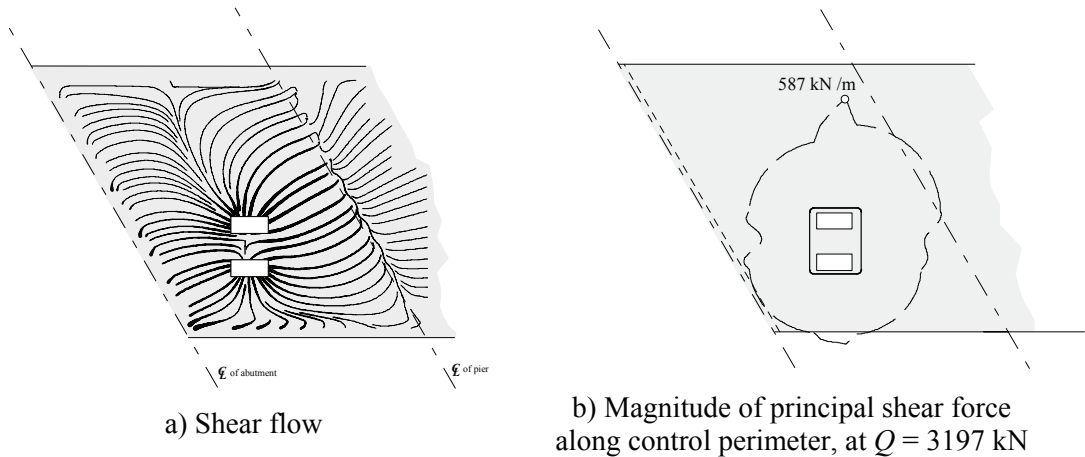


Figure 5.18: Test of decommissioned slab bridge: transverse shear forces (elastic solution)

Figure 5.19 illustrate the locations of points between which the relative rotation is computed. The chosen location of point 2 approximately corresponds to the maximal relative rotation between the two points.

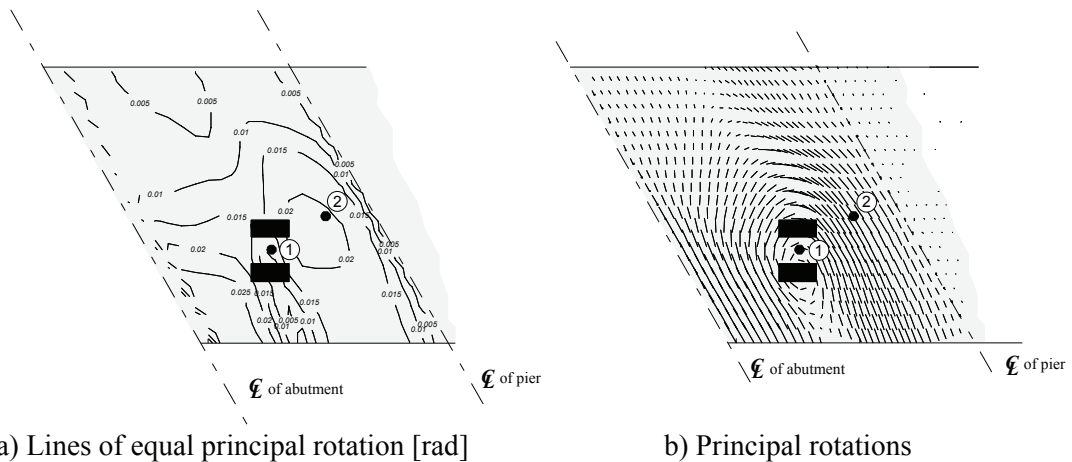


Figure 5.19: Test of decommissioned slab bridge: location of points for calculation of the rotation  $\theta$  (from non linear analysis at  $Q = 3197$  kN)

Figure 5.20 compares the calculated and measured shear failure loads. The predicted failure load is  $Q = 3260$  kN and the measured failure load is  $Q = 3200$  kN.

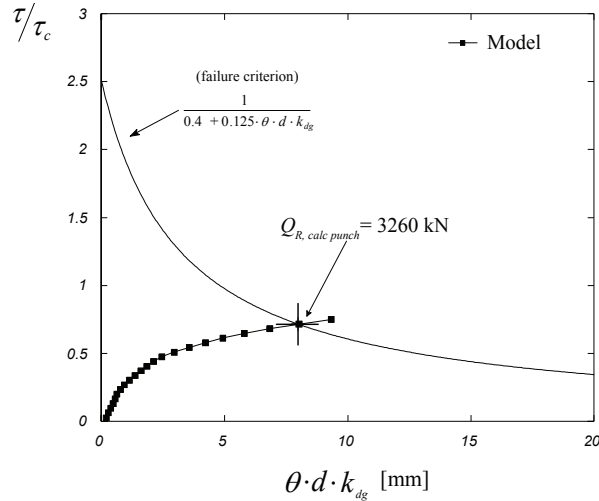


Figure 5.20: Test of decommissioned slab bridge: evaluation of punching shear criterion

The one-way shear criterion is evaluated along the line at  $0.5 \cdot d$  from the center line of the pier. The determining point for the one-way shear failure is located at  $x = 6.49$  m and  $y = 5.23$  m. The calculated failure load according with this criterion is  $Q_{R, calc, shear} = 3304$  kN. At this load level the principal shear force equals the shear strength at point *a* in figure 5.21a).

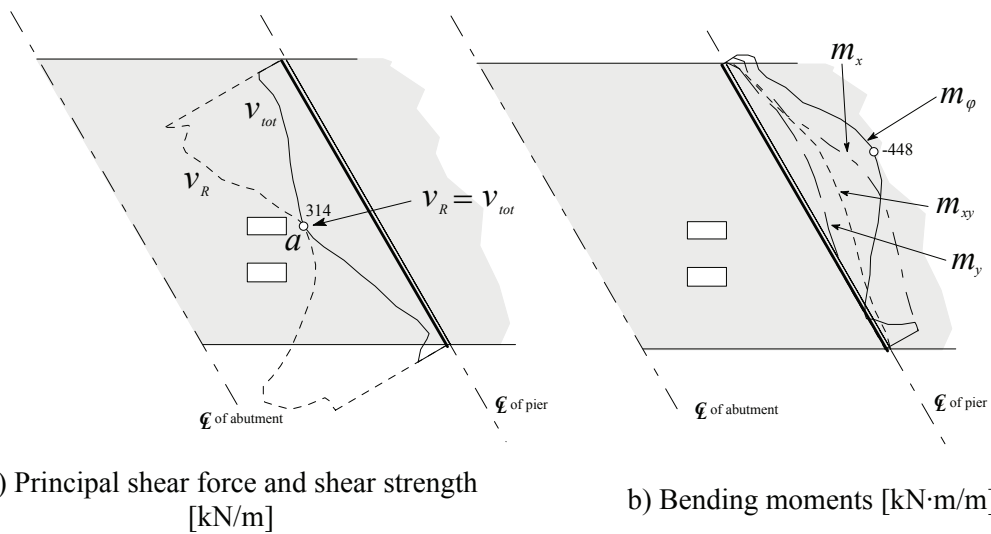


Figure 5.21: Test of decommissioned slab bridge: evaluation of one-way shear failure criterion ( $Q_{R, calc, shear} = 3304$  kN)

The calculation procedure is described as follows:

At  $Q = 3304$  kN, the principal shear force at point *a* is  $v_{tot} = 314$  kN/m and the direction of the principal shear force (eq. 2.12) is  $\varphi = 40^\circ$  (fig. 5.18a). The bending moments are  $m_x = -373$  kN·m/m,  $m_y = -92$  kN·m/m and  $m_{xy} = -195$  kN·m/m. Therefore the bending moment in the direction of the principal shear force is  $m_\theta = -448$  kN·m/m. The principal reinforcement (bars along *x*, top layer) is  $a_s = 4014$  mm<sup>2</sup>/m with an effective depth of  $d = 0.387$  m. From the values of  $m_\theta$ ,  $d$ , and  $a_s$  the strains  $\varepsilon = 0.702$  mm/m are calculated from eq. 2.1, using the measured value of the Young's modulus of  $E_c = 32$  GPa and  $E_s = 205$  GPa. Because the direction of the principal shear force considerably deviates from the direction of the principal reinforcement (in this case, top bars along *x*), the strains should be multiplied by the factor given by eq. 2.8 ( $\varepsilon' = 1.943 \cdot \varepsilon = 1.363$  mm/m). Using this strain as input, the nominal shear strength  $\tau_R / \tau_c = 0.367$  is calculated from

the shear failure criterion (eq. 2.2.), with  $k_{dg} = 1.5$  ( $D_{max} = 16$  mm). From this value and knowing that  $f_c = 54$  MPa, the calculated shear strength is  $v_R = 314$  KN/m. This value equals the principal shear force in the determining point.

This solution was found using an iterative procedure, in which for each load step the points along the linear control perimeter are controlled for failure using the described procedure. The solution is found when the nominal shear stress first reaches the predicted shear strength by the failure criterion (fig. 5.22).

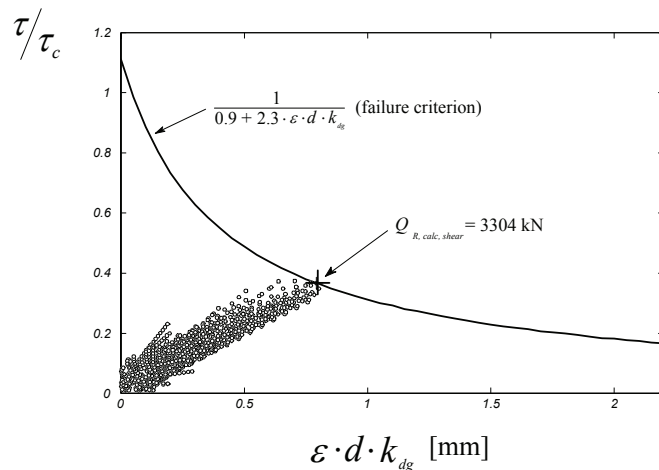


Figure 5.22: Test of decommissioned slab bridge: evaluation of one-way shear failure criterion at points along control perimeter, until failure

### 5.7.3 Tests on bridge deck cantilevers

This section compares the measured results of tests on large scale bridge deck cantilevers described in chapter 3 and appendix A with the calculated responses. A short summary of the measured results is given in table 5.1.

Table 5.1: Overview of tests on bridge deck cantilevers

Test	Reinforcement ratio <sup>*)</sup>	Location of loads (along y)	Number of loads	Failure Load ( $Q_R$ ) [kN]	Failure location	Mode of failure
DR1-a	0.78 %	Center	4	1397	Cantilever edge	Shear
DR1-b		North edge	2	1025	Fixed end	Shear
DR1-c		South edge	1	910	Fixed end	Shear
DR2-a	0.60%	Center	2	961	Fixed end	Shear
DR2-b		North edge	2	857	Fixed end	Shear
DR2-c		South edge	1	719	Fixed end	Shear

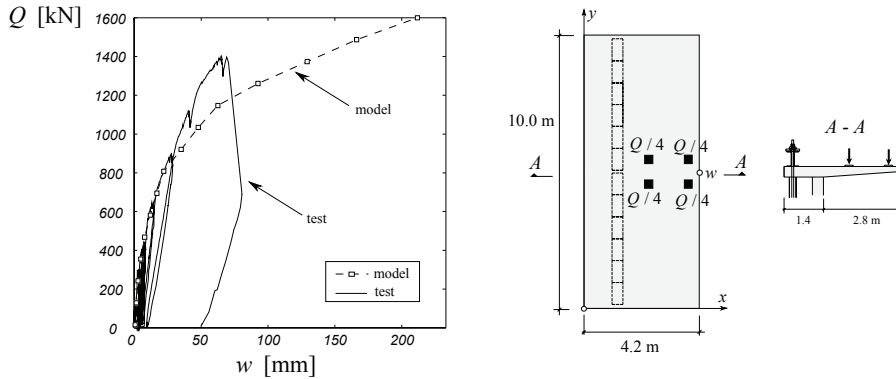
<sup>\*)</sup> At the top transversal reinforcement (bars along x) at the clamped edge

The rotations (compared with the calculated responses of the slabs) were measured by inclinometers. It can be observed that a good agreement is obtained between the calculated responses (in terms of  $\tau / \tau_c$  and  $\theta \cdot d \cdot k_{dg}$ ) for tests DR1-b (fig. 5.33), DR1-c (fig. 5.39), DR2-a (fig. 5.45), DR2-b (fig. 5.51) and DR2-c (fig. 5.57).

The detailed description of the computations is only explained in detail for test DR1-a. For the other tests on cantilevers, the application of the calculation procedure is basically the same, and therefore only the resulting diagrams are shown. The results of all the analysis are summarized in the end of this chapter (conclusions).

Test DR1-a

Test DR1-a was performed under four concentrated loads simulating twin axle loads (fig. 5.23b). Figure 5.23a) shows the comparison between the calculated and measured deflections at the tip of the cantilever. The non linear analysis predicts a more flexible behavior, in particular for high load levels. Prior to loading the cantilever to failure, it was subjected to about two hundred load cycles from  $Q = 0$  to  $Q = 400$  kN. This might have influenced the response of the structure.



a) Calculated and measured load-deflection curves      b) Notations and dimensions [m]

Figure 5.23: Test DR1-a: calculated and measured load-deflection curves

The deflections are also compared along the lines at  $y = 5.0$  m and  $x = 4.18$  m (fig.5.24).

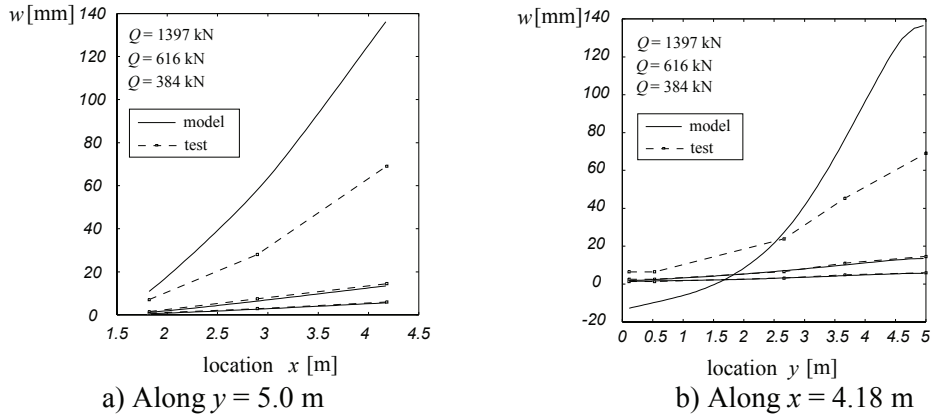


Figure 5.24: Test DR1-a: comparison of calculated and measured deflections

The elastic solution of the shear flow is indicated in fig. 5.25a), for  $Q = 1600$  kN. At this load level, the applied load by each wheel is 400 kN (fig. 5.23b). Therefore, the estimation of the length of the control perimeter 1 and 2 is performed by applying equation 5.1:

$$u_2 = \frac{400 \text{ kN}}{391 \text{ kN/m}} = 1.02 \text{ m} \quad , \quad u_1 = \frac{400 \text{ kN}}{576 \text{ kN/m}} = 0.69 \text{ m} \quad (5.10)$$



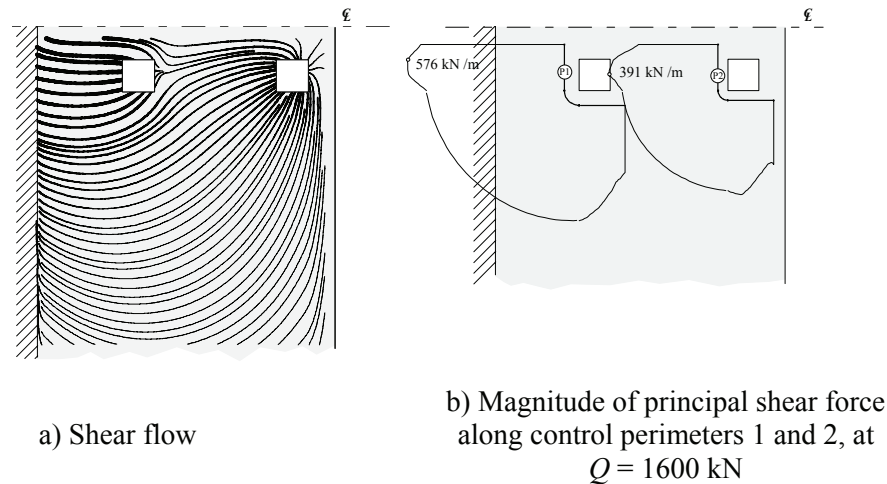


Figure 5.25: Test DR1-a: transverse shear forces (elastic solution)

The rotations of the slab are shown in figure 5.26. The difference of rotations between points ② and ① is used for control perimeter 2. The difference of rotations between points ③ and ② is used for control perimeter 1.

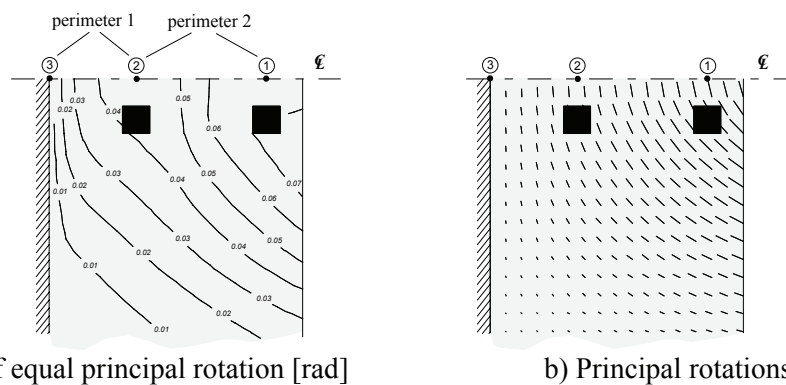


Figure 5.26: Test DR1-a: location of points for calculation of the rotation  $\theta$  (from non linear analysis at  $Q=1400 \text{ kN}$ )

Using the above calculated lengths of control perimeters and locations for calculation of rotations, an evaluation is made of the punching shear capacity of each perimeter (fig. 5.27). The failure load of each perimeter corresponds to the intersection points of the calculated response of the structure with the failure criterion. The perimeter with the lowest calculated failure load is perimeter 1, between the inner loads and the clamped edge ( $Q_{R, calc, punch} = 1118 \text{ kN}$  for perimeter 1 and  $Q_{R, calc, punch} = 1362 \text{ kN}$  for perimeter 2). According to the computations the determining control perimeter is thus the perimeter 1. This contradicts the experimental evidence, because the actual failure occurred at perimeter 2, for the loads near the free edge, at an actual failure load of  $Q_{test} = 1397 \text{ kN}$ . Nevertheless, an important shear crack was identified at control perimeter 1, after cutting the slab along the center line (fig. 3.8a). The presence of this shear crack indicates that the shear failure was impending and would have occurred after a small load increment. Furthermore, it indicates possible redistributions of the shear forces due to the progressive formation of the shear crack (as discussed in chapter 3).

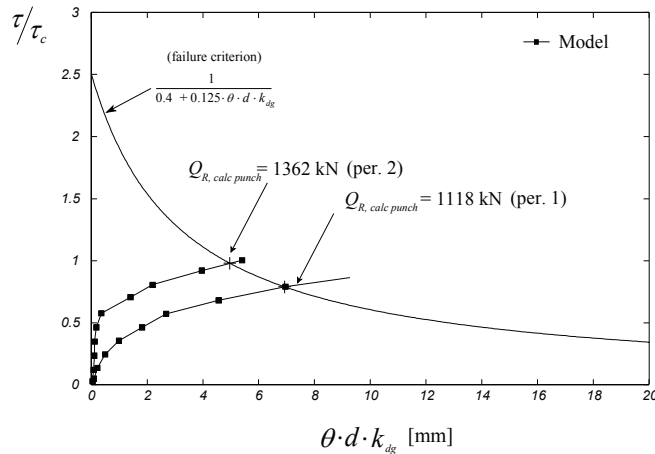
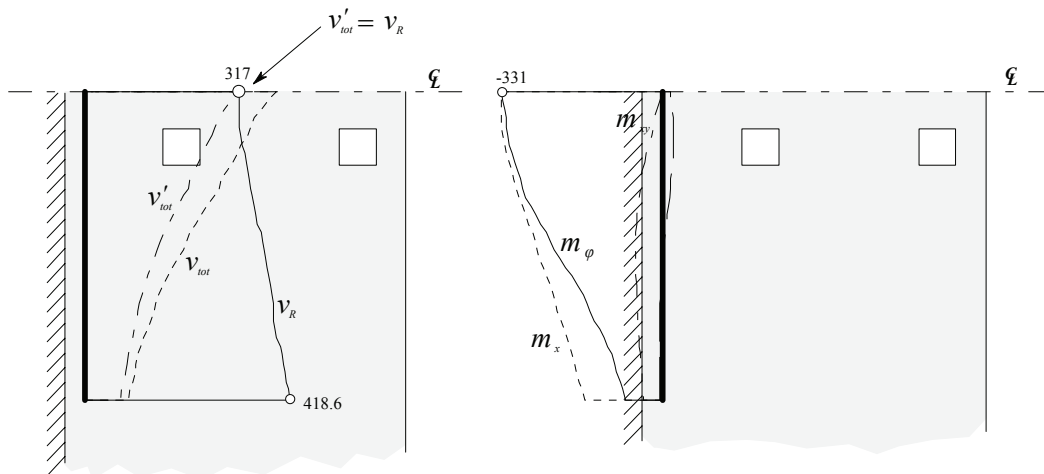


Figure 5.27: Test DR1-a: evaluation of punching shear criterion

The one-way shear criterion is evaluated along the line at  $0.5 \cdot d$  from the fixed end. The determining point for the one-way shear failure is located at intersection between this line and the center line ( $y = 5.0$  m). The calculated failure load according with this criterion is  $Q_{R,calc, shear} = 1053$  kN (fig. 5.28). The calculation procedure is basically the same as described for the decommissioned slab bridge, with the exception that the inclined compression chord carries a shear force. Therefore at the determining point  $v_{tot}'$  is equal to the shear strength  $v_R$ , with  $v_{tot}'$  given by equation 5.2.

The calculated failure load using the elastic distribution (fig. 5.28) equals 75% of the actual failure load. This ratio is rather low and can be explained because the redistributions due to flexural cracking are not considered in the elastic inner forces. The use of the non linear solution of inner forces would therefore predict a higher failure load.

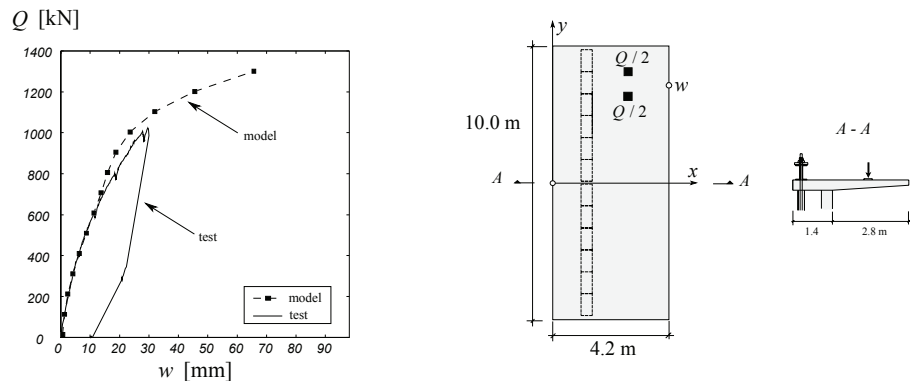


a) Principal shear force and shear strength [kN/m]      b) Bending moments [kN·m/m]

Figure 5.28: Test DR1-a: evaluation of one-way shear failure criterion ( $Q_{R,calc, shear} = 1053$  kN)

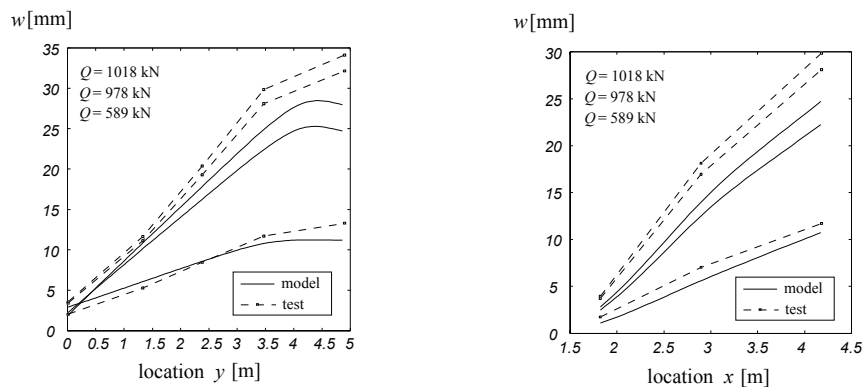
Test DR1-b

Test DR1-b was performed under two concentrated loads at the edge of the cantilever (fig. 5.29b). The two loads simulate half of the twin axle loads. There is an adequate agreement between the calculated and measured deflections (figs. 5.29a) and 5.30). The edge of the slab has an additional amount of flexural reinforcement (along  $x$ ). The edge stiffening effect is visible in the calculated deflections (fig. 5.30a).



a) Calculated and measured load-deflection curves    b) Notations and dimensions [m]

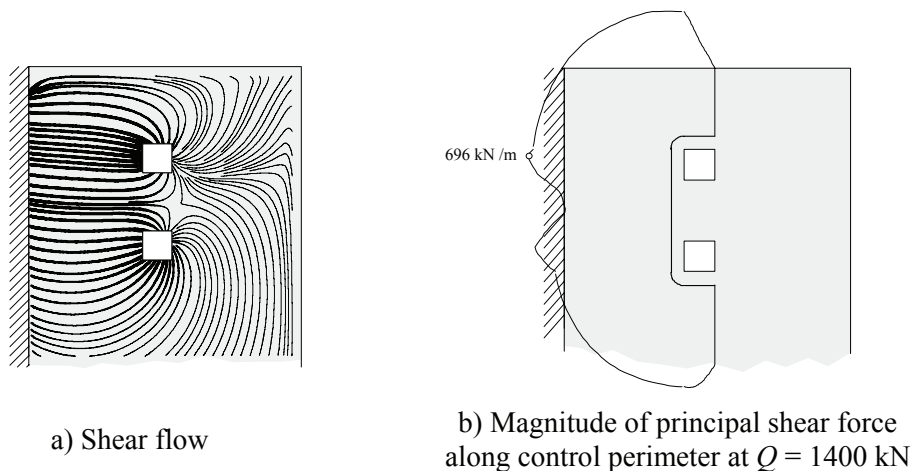
Figure 5.29: Test DR1-b: calculated and measured load-deflection curves



a) Along  $x = 4.18$  m

b) Along  $y = 3.45$  m

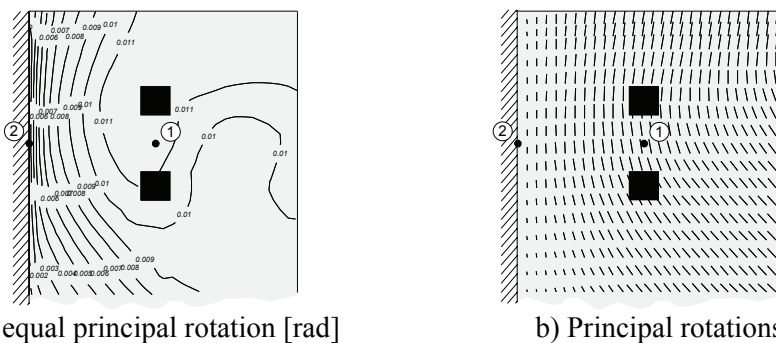
Figure 5.30: Test DR1-b: comparison of calculated and measured deflections



a) Shear flow

b) Magnitude of principal shear force along control perimeter at  $Q = 1400$  kN

Figure 5.31: Test DR1-b: transverse shear forces (elastic solution)



a) Lines of equal principal rotation [rad]      b) Principal rotations  
 Figure 5.32: Test DRI-b: location of points for calculation of the rotation  $\theta$  (from non linear analysis at  $Q=1025$  kN)

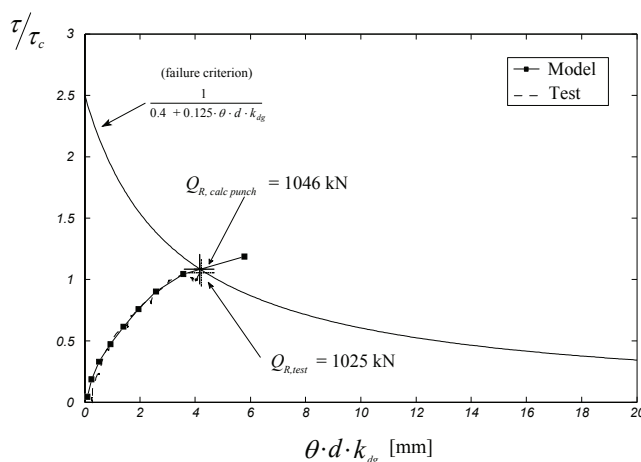
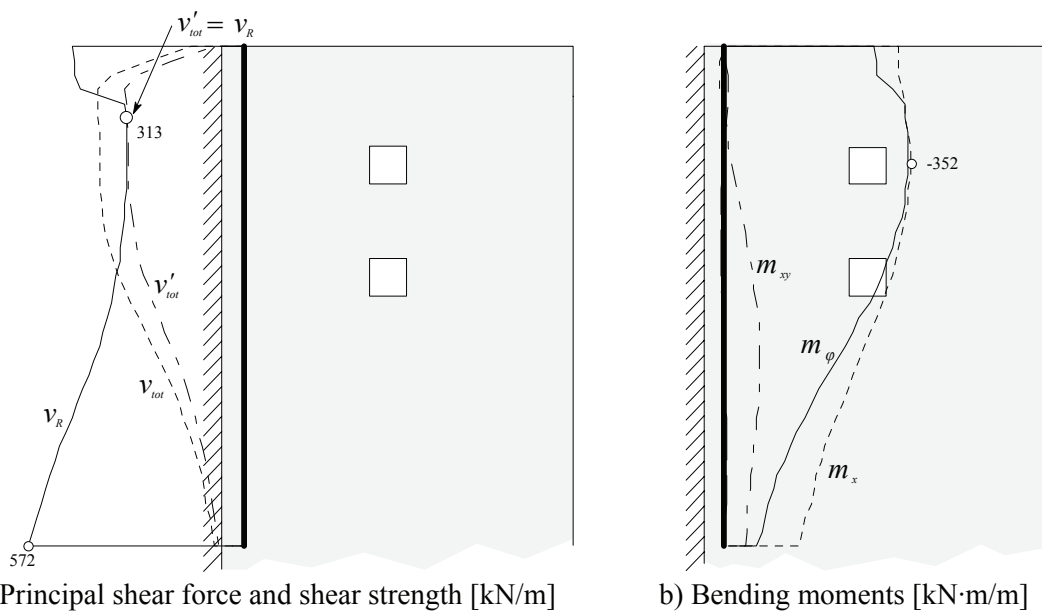


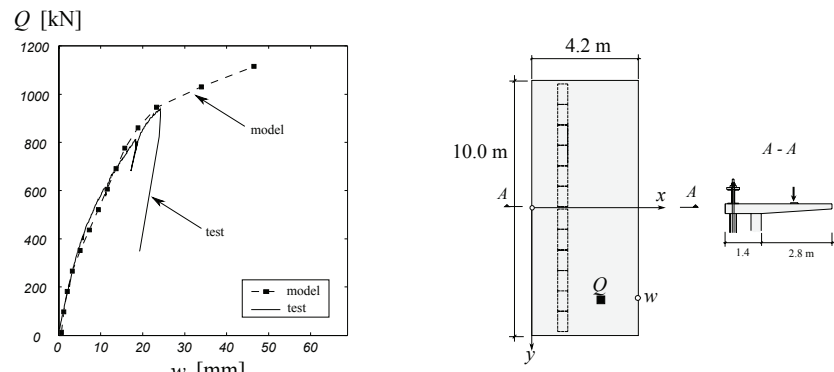
Figure 5.33: Test DRI-b: evaluation of punching shear criterion



a) Principal shear force and shear strength [kN/m]      b) Bending moments [kN·m/m]  
 Figure 5.34: Test DRI-b: evaluation of one-way shear failure criterion ( $Q_{R,calc,shear} = 965$  kN)

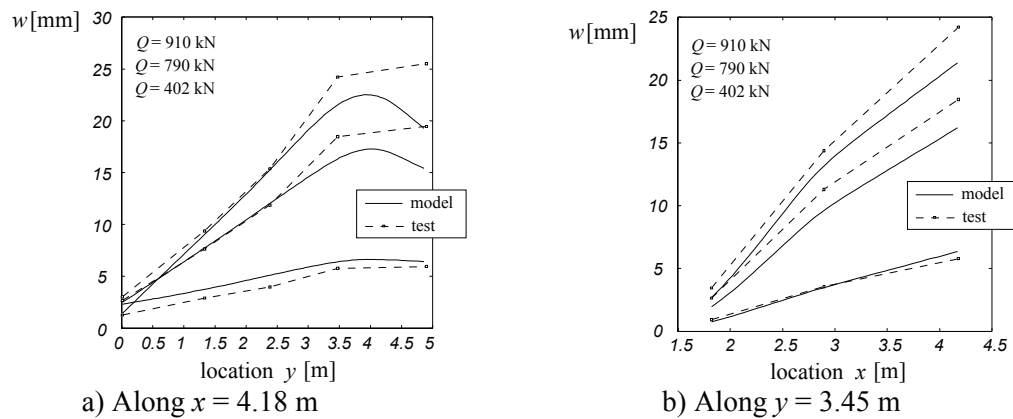
Test DR1-c

Test DR1-c was performed under one concentrated load at the edge of the cantilever (fig. 5.35b). The non linear analysis predicts a slightly more flexible behavior (figs. 5.35a) and 5.36). The edge of the slab has an additional amount of flexural reinforcement (along  $x$ ). The edge stiffening effect is visible in the calculated and measured deflections (fig. 5.36a).



a) Calculated and measured load-deflection curves      b) Notations and dimensions [m]

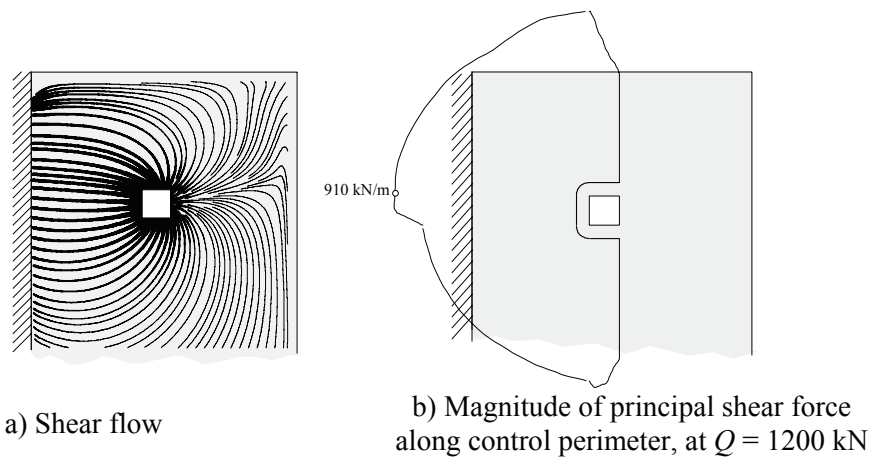
Figure 5.35: Test DR1-c: calculated and measured load-deflection curves



a) Along  $x = 4.18$  m

b) Along  $y = 3.45$  m

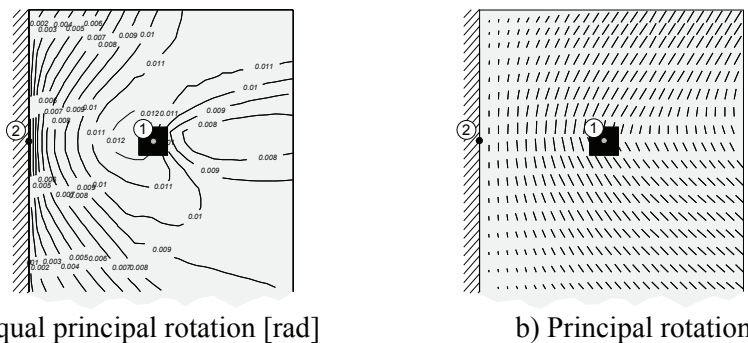
Figure 5.36: Test DR1-c: comparison of calculated and measured deflections



a) Shear flow

b) Magnitude of principal shear force along control perimeter, at  $Q = 1200$  kN

Figure 5.37: Test DR1-c: transverse shear forces (elastic solution)



a) Lines of equal principal rotation [rad]                      b) Principal rotations  
 Figure 5.38: Test DR1-c: location of points for calculation of the rotation  $\theta$  (from non linear analysis at  $Q=910$  kN)

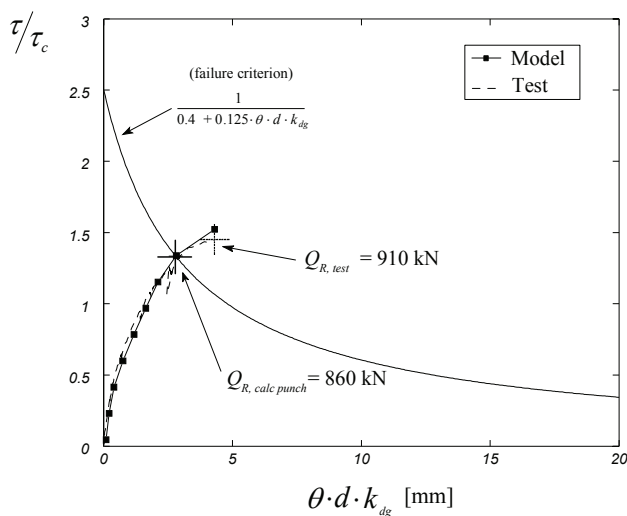
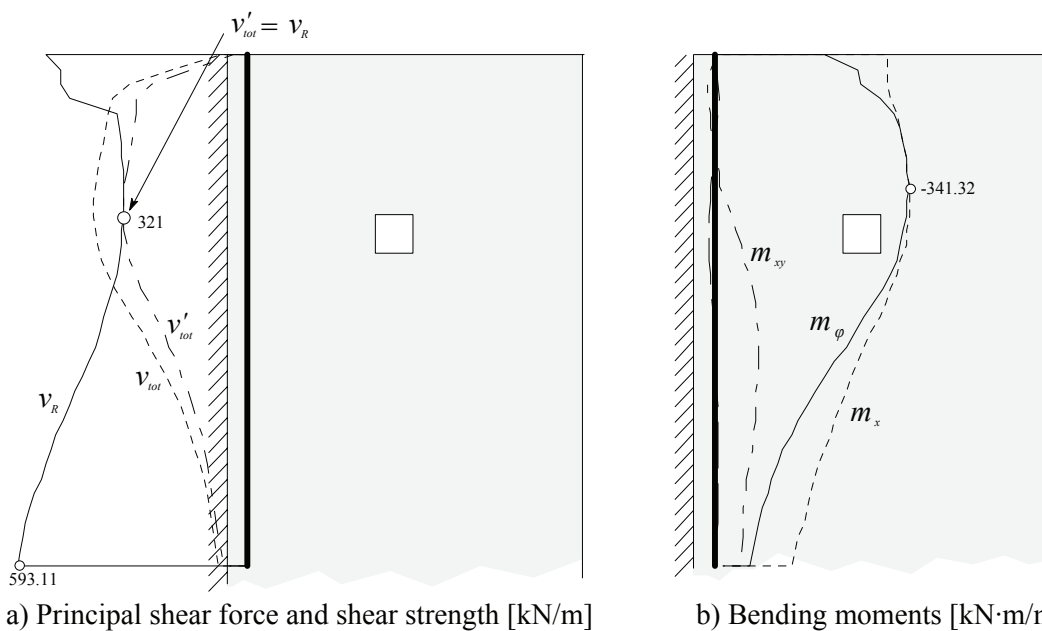


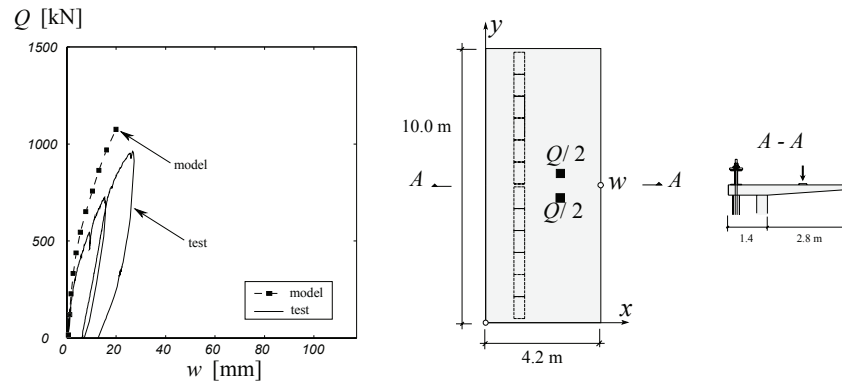
Figure 5.39: Test DR1-c: evaluation of punching shear criterion



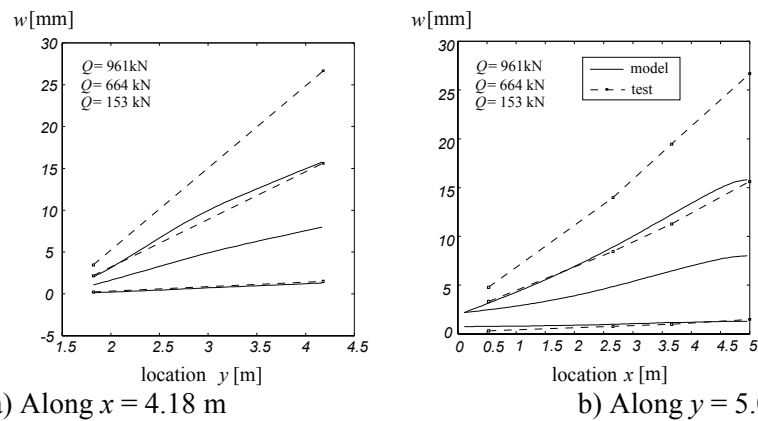
a) Principal shear force and shear strength [kN/m]                      b) Bending moments [kN·m/m]  
 Figure 5.40: Test DR1-c: evaluation of one-way shear failure criterion ( $Q_{R,calc,shear} = 910$  kN)

Test DR2-a

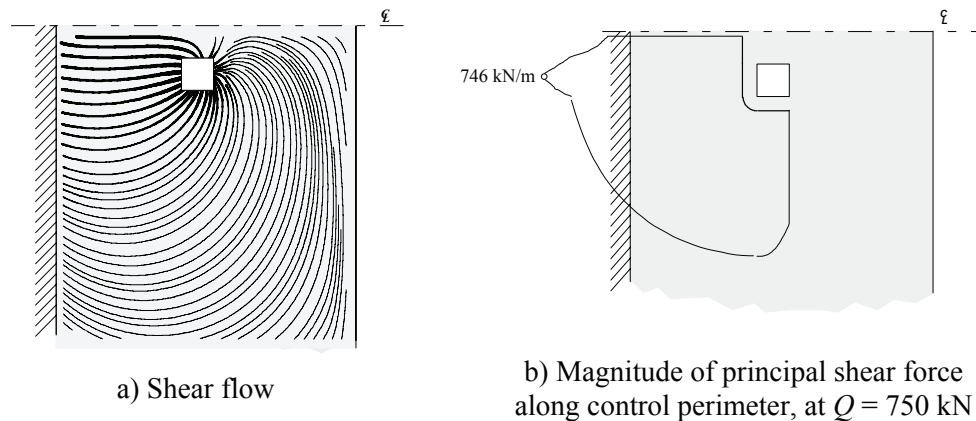
Test DR2-a was performed under two concentrated loads at the center of the cantilever (fig. 5.41b). The two loads simulate half of the twin axle loads. The calculated and measured deflections are compared in figures 5.41a) and 5.42.



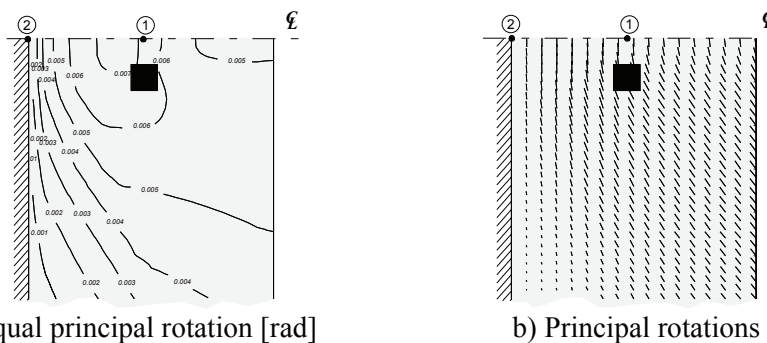
a) Calculated and measured load-deflection curves      b) Notations and dimensions [m]  
 Figure 5.41: Test DR2-a: calculated and measured load-deflection curves



a) Along  $x = 4.18$  m      b) Along  $y = 5.0$  m  
 Figure 5.42: Test DR2-a: comparison of calculated and measured deflections



a) Shear flow      b) Magnitude of principal shear force along control perimeter, at  $Q = 750$  kN  
 Figure 5.43: Test DR2-a: transverse shear forces (elastic solution)



a) Lines of equal principal rotation [rad]      b) Principal rotations  
 Figure 5.44: Test DR2-a: location of points for calculation of the rotation  $\theta$  (from non linear analysis at  $Q=961$  kN)

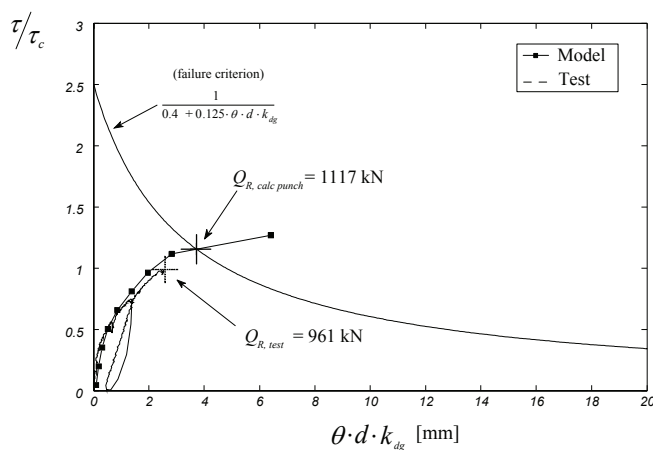
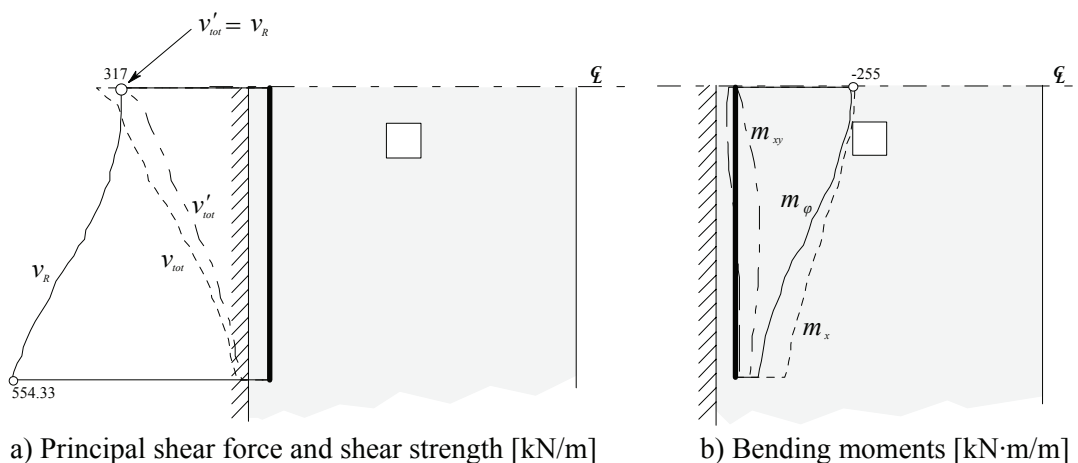


Figure 5.45: Test DR2-a: evaluation of punching shear criterion

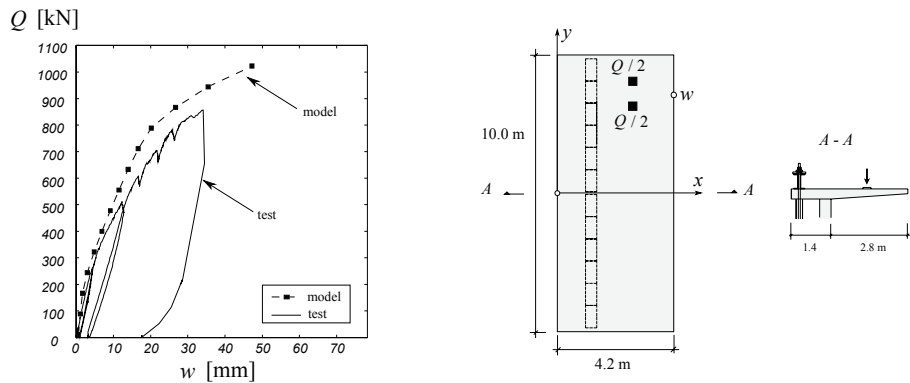


a) Principal shear force and shear strength [kN/m]      b) Bending moments [kN·m/m]  
 Figure 5.46: Test DR2-a: evaluation of one-way shear failure criterion ( $Q_{R,calc,shear} = 920$  kN)



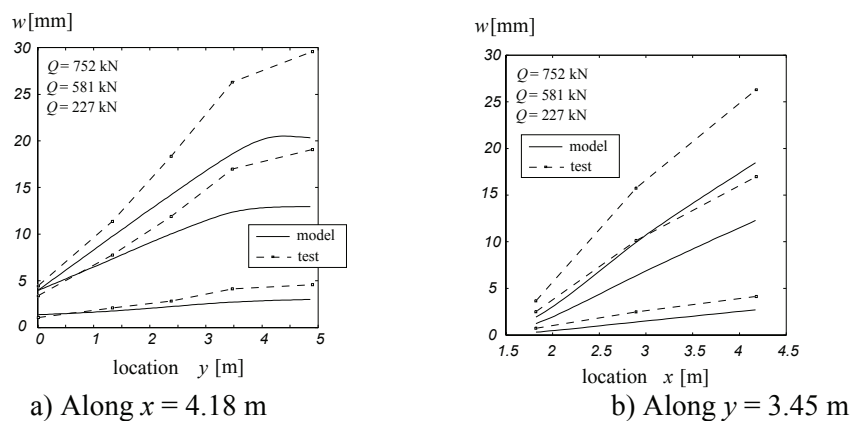
Test DR2-b

Test DR2-b was performed under two concentrated loads at the edge of the cantilever (fig. 5.47b). The calculated and measured deflections are compared in figures 5.47a) and 5.48. The edge of the slab has an additional amount of flexural reinforcement (along  $x$ ). The edge stiffening effect is visible in the calculated deflections (fig. 5.48a).



a) Calculated and measured load-deflection curves    b) Notations and dimensions [m]

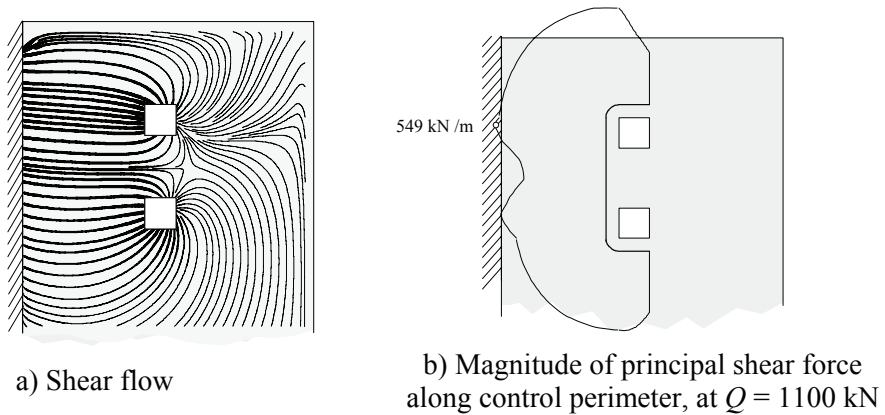
Figure 5.47: Test DR2-b: calculated and measured load-deflection curves



a) Along  $x = 4.18$  m

b) Along  $y = 3.45$  m

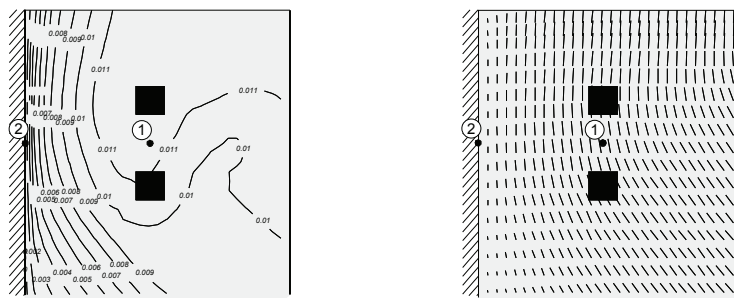
Figure 5.48: Test DR2-b: comparison of calculated and measured deflections



a) Shear flow

b) Magnitude of principal shear force along control perimeter, at  $Q = 1100$  kN

Figure 5.49: Test DR2-b: transverse shear forces (elastic solution)



a) Lines of equal principal rotation [rad]

b) Principal rotations

Figure 5.50: Test DR2-b: location of points for calculation of the rotation  $\theta$  (from non linear analysis at  $Q=857$  kN)

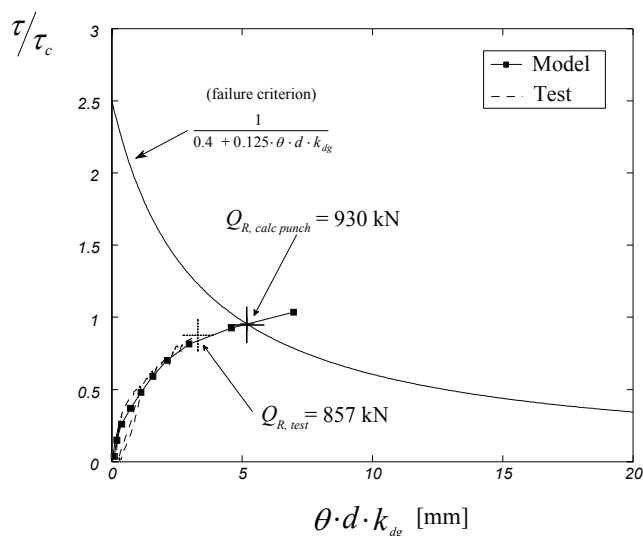
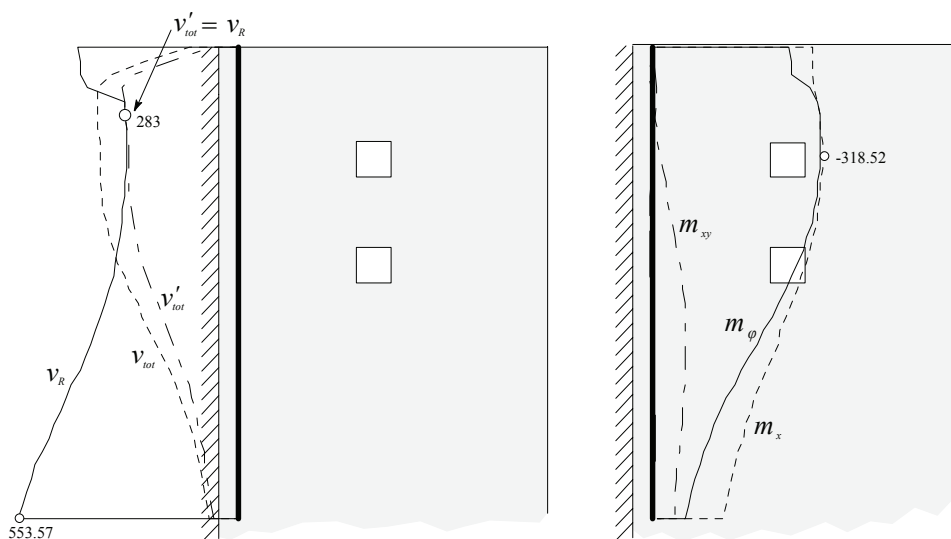


Figure 5.51: Test DR2-b: evaluation of punching shear criterion



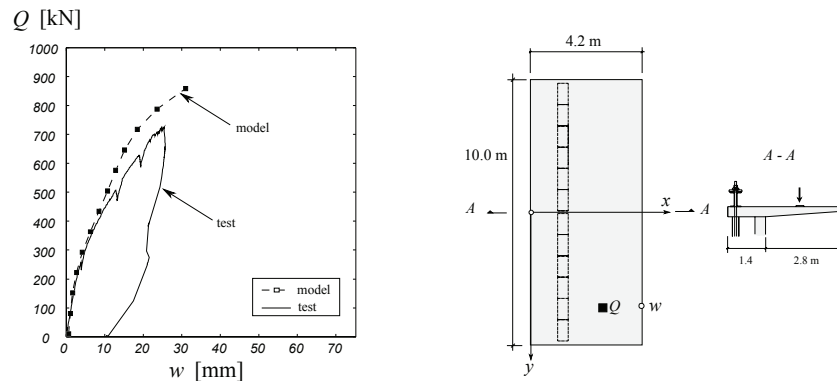
a) Principal shear force and shear strength [kN/m]

b) Bending moments [kN·m/m]

Figure 5.52: Test DR2-b: evaluation of one-way shear failure criterion ( $Q_{R,calc,shear} = 868$  kN)

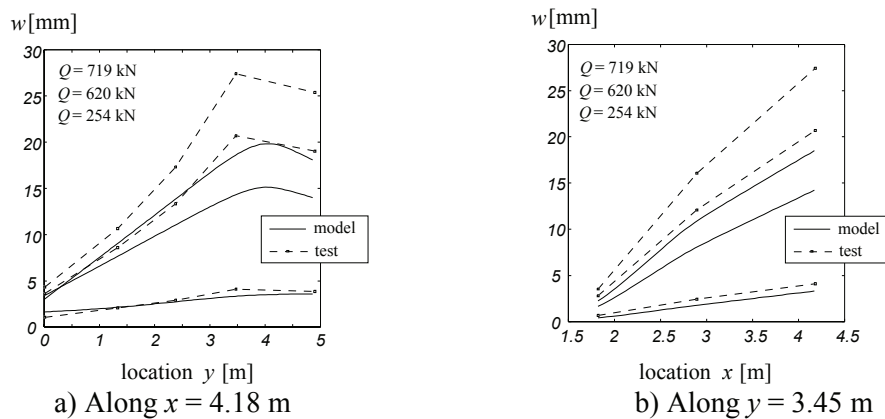
Test DR2-c

Test DR2-c was performed under one concentrated load at the edge of the cantilever (fig. 5.53b). The calculated and measured deflections are compared in figures 5.53a) and 5.54. The edge of the slab has an additional amount of flexural reinforcement (along  $x$ ). The edge stiffening effect is visible in the calculated deflections (fig. 5.54a).



a) Calculated and measured load-deflection curves    b) Notations and dimensions [m]

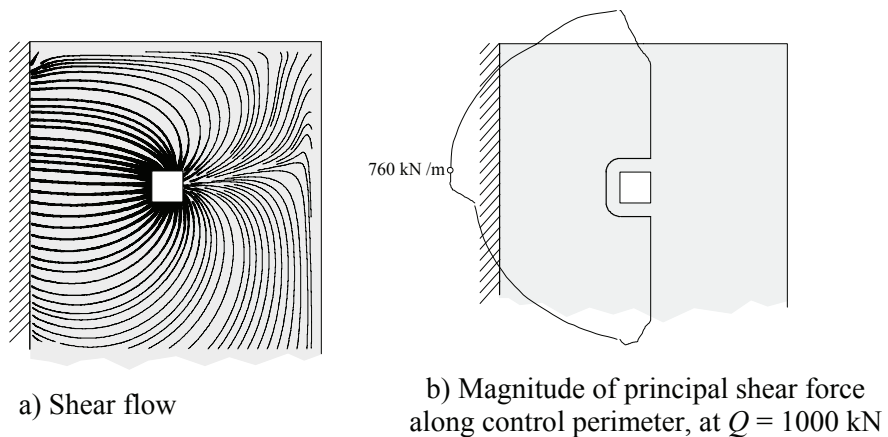
Figure 5.53: Test DR2-c: calculated and measured load-deflection curves



a) Along  $x = 4.18$  m

b) Along  $y = 3.45$  m

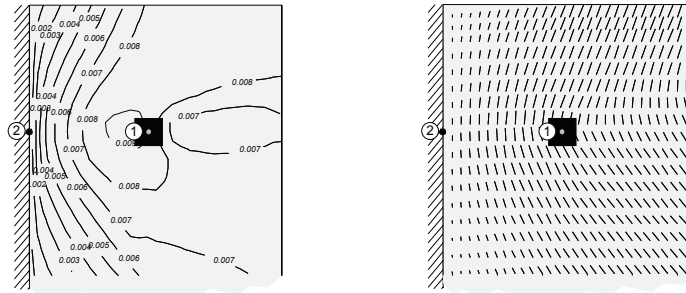
Figure 5.54: Test DR2-c: comparison of calculated and measured deflections



a) Shear flow

b) Magnitude of principal shear force along control perimeter, at  $Q = 1000$  kN

Figure 5.55: Test DR2-c: transverse shear forces (elastic solution)



a) Lines of equal principal rotation [rad]

b) Principal rotations

Figure 5.56: Test DR2-c: location of points for calculation of the rotation  $\theta$  (from non linear analysis at  $Q=719$  kN)

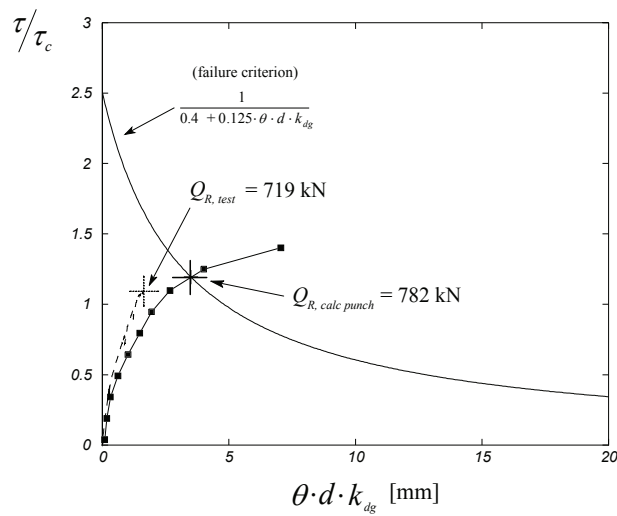
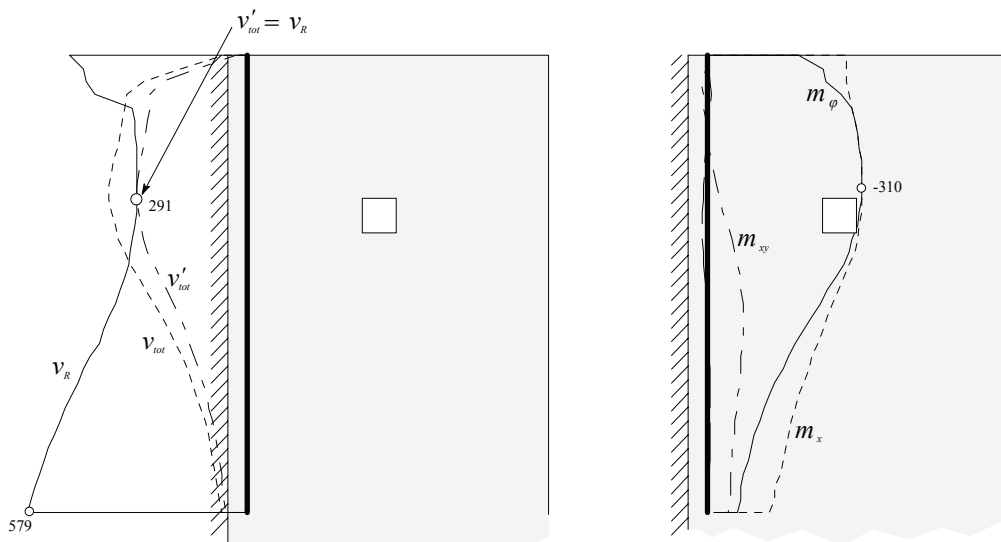


Figure 5.57: Test DR2-c: evaluation of punching shear criterion



a) Principal shear force and shear strength [kN/m]

b) Bending moments [kN·m/m]

Figure 5.58: Test DR2-c: evaluation of one-way shear failure criterion ( $Q_{R,calc,shear} = 822$  kN)

## 5.8 Conclusions

Figure 5.59 compares the calculated and measured failure loads for all tests. The results are also indicated in table 5.2.

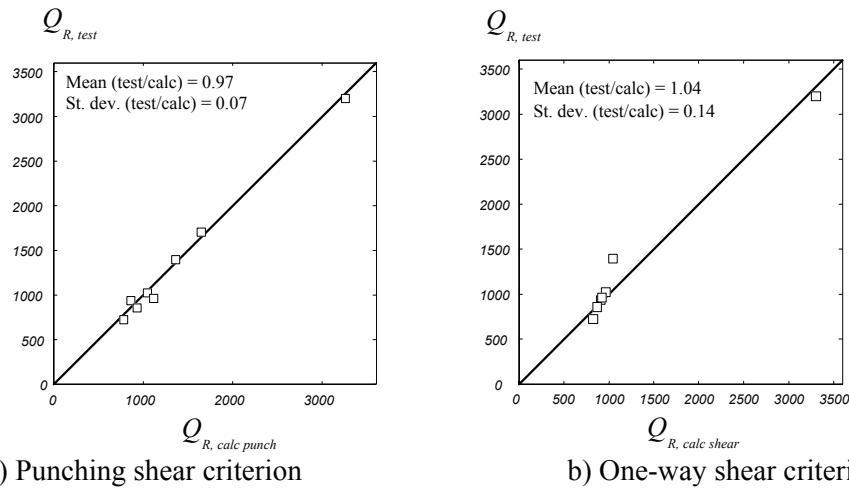


Figure 5.59: Comparison of calculated and measured failure loads with failure criteria

Table 5.2: Calculated and measured failure loads

Test	Measured failure load	Calculated failure load (Punching criterion)	Calculated failure load (One-way shear criterion)		
	$Q_{R, test}$ [kN]	$Q_{R, calc, punch}$ [kN]	$Q_{R, test} / Q_{R, calc, punch}$ [-]	$Q_{R, calc, shear}$ [kN]	$Q_{R, test} / Q_{R, calc, shear}$ [-]
DR1a	1397	1362	1.03	1053	1.33
DR1b	1025	1046	0.98	965	1.06
DR1c	910	860	1.06	910	1.00
DR2a	961	1117	0.86	920	1.04
DR2b	857	930	0.92	868	0.99
DR2c	719	782	0.92	822	0.87
Miller	3200	3260	0.98	3304	0.97
PG3	1703	1648	1.03	N/A	
		Average	0.97	Average	1.04
		Standard deviation	0.07	Standard deviation	0.14
		Coef. variation	0.07	Coef. variation	0.14

The considered perimeter in test DR1-a is the actual failure perimeter (perimeter 2). If perimeter 1 is used, the calculated punching shear failure load is  $Q = 1118$  kN and the coefficient of variation is 0.12. If the minimum of the calculated shear and punching shear capacities is considered, a coefficient of variation of 0.12 is obtained.

The following conclusions can be made:

- A non linear model was developed to predict the response of reinforced concrete slabs. Only the variations of the bending stiffness and of the in-plane shear stiffness are considered. The model correctly predicts the measured deflections and rotations of the slabs.
- The shear failure load of bridge decks is accurately predicted using the punching shear and one-way shear criteria proposed by (Muttoni 2003), together with the proposed assumptions for the length of the control perimeter and the rotation of the slab.

## Chapter 5

- The obtained results confirm that the observed failures of bridge decks are hybrid situations between shear and punching shear failures and therefore both approaches give good results for the analyzed cases.

Under wheel loads with pneumatic pressure the component of the rotation inside the loaded area does not affect the punching shear strength (chapter 3). For all the considered tests in this chapter, the load was applied with rigid plates. Therefore, the applied loads were treated as in the case of rigid supports. However, in the assessment of actual bridge decks under wheel loads with pneumatic pressure the component of the rotation inside the loaded area can be deduced from the total rotation.

The positive effect of the inclined compression chord (eq. 5.2) was clearly considered in the evaluation of the one-way shear capacity of the cantilevers. However, in the evaluation of the punching shear criterion this effect was not considered. This effect is expected to be small in the cantilevers under one or two concentrated loads (all except perimeter 1 of test DR1-a), because the hogging bending moment is small near the loads. In the case of perimeter 1 of DR1-a, the inclined compression chord is expected to have some effect because of the high hogging moment near the applied inner loads, mainly caused by the outer loads. Therefore a higher calculated load for this perimeter would be obtained if this effect is considered.

The developed non linear model for the calculation of rotations was used to predict the punching shear failure load of cantilevers under concentrated loads. The proposed approach can also be used to estimate the punching shear capacity of flat slabs supported by columns.

## 6. Conclusions

### 6.1 Synthesis of contributions and conclusions

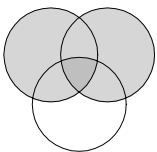
The aim of this work is to investigate the strength and the structural behavior of reinforced concrete bridge deck slabs without shear reinforcement.

Bridge deck slabs are subjected to various types of loading, mainly concentrated loads and distributed loads. The strength of a slab does not depend only on the type of applied loads but also on its geometry and dimensions, its reinforcement ratio and on other mechanical properties. Also, yielding of the flexural reinforcement has a significant influence on the shear strength of slabs without shear reinforcement. Depending on these parameters, three possible failure modes may develop in reinforced concrete deck slabs without shear reinforcement: one-way shear failure, punching shear (or two-way shear) failure and flexural failure.

This work investigates the role of each failure mode in actual bridge deck slabs as well as their interaction. Several contributions to the current state of knowledge have been produced. The following points summarize these contributions, indicating their scope by the conceptual scheme of figure 1.3 (page 2).

#### 1. Full scale shear tests on slab strips without shear reinforcement

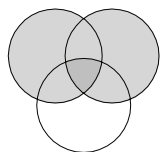
The one-way shear strength of bridge deck slabs is currently estimated using models developed from test data on beams without shear reinforcement and in which the flexural reinforcement remains in the elastic domain. However, yielding of flexural reinforcement may occur at the ultimate limit state.



There are only a few experimental and theoretical contributions on the influence of yielding of the flexural reinforcement on the one-way shear strength of reinforced concrete members. A test series of eleven slab strips without shear reinforcement (8.4 m length) was therefore performed within the scope of the present dissertation. The results show that the development of plastic strains in the flexural reinforcement can reduce the shear strength of up to 50 % in comparison with elements in which the flexural reinforcement remains elastic. The reduction of the shear strength increases with increasing plastic strains. Because plastic strains are associated with the formation of a plastic hinges, the observed results can also be formulated as a reduction of rotation capacity with increasing shear force.

#### 2. Mechanical model for the shear strength of plastic hinges

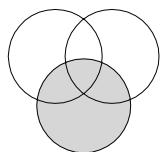
Based on the results of the experimental campaign on slab strips, a mechanical model is proposed in this work to investigate the shear strength of this type of elements. The systematic analysis of the measured web displacements of the slab strips allows to determine the relative displacement between the lips of the shear critical crack. Thus, the shear force carried across the shear crack can be estimated using the model proposed by (Walraven 1980). The results clearly show that the percentage of the shear force carried across the shear crack decreases with increasing hinge rotation. For large hinge



rotations, the amount of shear force carried across the shear crack tends to zero, but the slab strips still have a remaining shear strength. This strength is attributed to the shear force carried by the compression zone, for which a physical model is developed with the aim of estimating its contribution to the shear strength. Prior to failure, the widths of horizontal cracks in the vicinity of the flexural reinforcement were generally large. Consequently, the contribution of dowel action to the shear strength can be neglected. This way, the shear strength is formulated as a function of the opening of the shear crack and of the strength of the compression zone.

The results of the mechanical model are used to develop a simplified equation. The simplified equation is in good agreement with the test results and can be used as an extension of one-way shear models to consider the effect of yielding.

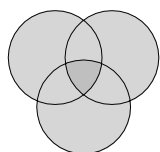
### 3. Punching shear strength of slabs subjected to pneumatic loading and of slabs supported by rigid supports



The punching shear strength of bridge deck slabs subjected to pneumatic loads is currently treated in the same manner as that of slabs supported by concrete columns. No full scale tests of slabs without shear reinforcement under concentrated loads simulating the state of stress created by a pneumatic load were found in the literature. In the case of a pneumatic load, the vertical stress distribution between the slab and the wheel tends to be uniform. On the contrary, in the case of punching shear with a concrete column, stress concentrations arise near the column edges and corners. A large scale punching shear test on a 3.0 x 3.0 m slab with a thickness of 0.25 m was performed to investigate this effect. The pneumatic load was simulated by a circular flat jack consisting of a copper sheet envelope filled with a constant water volume. It was possible to compare this test with another test of a similar slab, tested with a stiff support simulating a concrete column (Guandalini 2005). It was observed that, in the case of punching shear with pneumatic loading, cracks tends to be distributed throughout the zone where the load is introduced, rather than to be concentrated near the edges of the load (where the shear critical region is located), as is the case for punching shear with a stiff support. Thus, for a given crack opening in the critical shear region, larger rotations result for slabs subjected to pneumatic loading.

To account for this effect in the use of the punching shear failure criterion (Muttoni 2003), the part of the rotation associated with the flexural cracks directly above the wheel load should be deducted from the total rotation of the slab. As a result, it can be concluded that the punching shear criterion (Muttoni 2003) developed for concrete columns gives conservative estimates of the punching shear strength for pneumatic loading and thus can be used for practical purposes.

### 4. Large scale tests on bridge deck cantilevers under concentrated loads



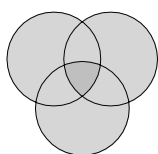
An important experimental program was carried out to investigate the behavior of bridge deck cantilevers without shear reinforcement, loaded to failure under groups of concentrated loads. Six tests were performed on two cantilevers, with a span of 2.8 m, a total length of 10.0 m and a variable thickness ranging from 0.38 m at the fixed end to 0.19 m at the free edge, with usual reinforcement ratios. These tests appear to be the first of their kind to be performed on full scale bridge deck cantilevers.



The experimental results show that the failure mode is always brittle, with a two-way shear failure. The theoretical flexural failure load, estimated by the yield line method, was not reached in any of the tests.

### 5. Estimation of the shear strength of reinforced concrete slabs

As observed in the tests performed on actual bridge cantilevers, two-way shear governs failure for bridge deck slabs subjected to concentrated loading. This phenomenon was investigated by a non linear finite element model developed for the calculation of the rotations and displacements up to failure of reinforced concrete slabs. The mechanical properties of the slab are introduced by the moment-curvature relationships at all locations. This way, it is possible to consider the non linear behavior of concrete (in tension and compression), the distribution of reinforcement and bond. The non linear model correctly reproduces the measured displacements and rotations of the tested cantilevers, as well of other full scale slabs tested to failure, including one full scale punching shear test (Guandalini, Muttoni 2004) and one in situ destructive test of a reinforced concrete bridge deck under two concentrated loads (Miller et al. 1994).



The punching shear strength is estimated by using the punching shear failure criterion defined in (Muttoni 2003). To apply this model to bridge decks, two additional assumptions have been introduced. The first one is related with the choice of the control perimeter  $u$ . It is proposed that the critical perimeter is equal to  $u = Q / v_{max,el}$ , where  $v_{max,el}$  is the elastically calculated maximal principal shear force along the control perimeter, located at a distance  $0.5 \cdot d$  from the surface of introduction of the concentrated load, and  $Q$  is the applied load. The second assumption is related to the choice of points for computation of the rotation  $\theta$ . It is proposed that the first point be located at the centroid of the concentrated load, and the location of the second point is chosen so that the maximal relative rotation results.

The comparison of the measured and calculated failure loads shows that the non linear model, used together with the one-way shear and punching shear criteria proposed by (Muttoni 2003), can be used to predict with a good accuracy the shear strength of bridge deck slabs subjected to concentrated loads.

## 6.2 Recommendations for future research

The following propositions of research should be considered for future research:

Theoretical work:

- The test results and the theoretical work have shown that shear and punching shear are closely related phenomena. On this basis, it is anticipated that a unified model for shear and punching shear design can be developed.
- The non linear model for the computation of the deflections and rotations needs to be improved. In particular, the reduction of the in-plane shear stiffness is so far based on empirical considerations. A more rational approach could be implemented, considering the top and bottom layers as membrane elements (Kaufmann, Marti 1998).
- Rationally derived shear stress–shear strain relationships could be incorporated in the finite element code. This way, the shear failure load would be directly obtained

## Chapter 6

from the non linear finite element analysis and it would be possible to account for eventual redistributions of the shear flow due to the propagation of the shear crack.

Experimental work:

- More tests on bridge decks slabs with yielding of the flexural reinforcement are required to further verify the applicability of the simplified equation derived in chapter 5 to statically indeterminate structures such as slabs with yielded regions.
- A new test series should investigate the effect of the edge beams on the shear and punching shear strengths of bridge deck cantilevers.
- The shear force carried by the inclined compression chord should be investigated in detail by means of an experimental campaign.

Simplified method for practical design:

- The proposed method for estimating the punching shear strength requires the calculation of the rotation of the slab  $\theta$  by means of a non-linear analysis. A simplification of this procedure is desirable, so that the rotation  $\theta$  can be estimated without requiring a non linear calculation.
- According to the proposed method, the length of the control perimeter needs to be determined by linear elastic finite element analysis. A practical rule for the determination of  $u$  is desirable.

## Bibliography

**Aktan A. E., Zwick M., Miller R. and Shahrooz B. M.** , *Nondestructive and Destructive Testing of Decommissioned Reinforced Concrete Slab Highway Bridge and Associated Analytical Studies*, Transportation Research Board, Transp. Res. Record No. 1371, pp. 142-153, Washington D.C., **1992**.

**Alvarez M. and Marti P.** , *Versuche zum Verbundverhalten von Bewehrungsstahl bei plastischen Verformungen*, Birkhäuser, September, **1996**.

**Alvarez M., Köppel S. and Marti P.** , *Rotation capacity of reinforced concrete slabs*, ACI Structural Journal, 97, No. 2, pp. 235-242, **2000**.

**Ansys Inc.** , *Ansys 8.1 user manual*, **2004**.

**Azad A. K., Baluch M. H., Al-Mandil M. and Al-Sawaiyan M.** , *Static and fatigue tests of simulated bridge decks*, Journal of the British soc. for strain measurement, pp. 30-41, Boston, October, **1986**.

**Azad A. K., Baluch M. H., Al-Mandil M., Sharif A. M. and Kareem K.** , *Loss of punching capacity of bridge deck slabs from crack damage*, ACI Structural Journal, 90, pp. 37-41, January-February, **1993**.

**Azizinamini A., Boothby T. E., Shekar Y. and Barnhill G.** , *Old Concrete Slab Bridges. I: Experimental Investigation*, ASCE Journal of Structural Engineering, Vol. 120, No. 11, pp. 3284-3304, November, **1994**.

**Azizinamini A., Shekar Y., Boothby T. E. and Barnhill G.** , *Old Concrete Slab Bridges. II. Analysis*, ASCE Journal of Structural Engineering, Vol. 120, No. 11, pp. 3305-3319, November, **1994**.

**Bachmann H.** , *Zur plastizitätstheoretischen Berechnung statisch unbestimmter Stahlbetonbalken*, IBK Bericht, Bericht Nr. 13, 188 p., Zürich, Switzerland, July, **1967**.

**Bailey S. F.** , *Basic principles and load models for the structural safety evaluation of existing bridges*, PhD dissertation, EPFL, 1467, Lausanne, Switzerland, **1996**.

**Bakht B.** , *Simplified Analysis of Edge Stiffened Cantilever Slabs*, ASCE Journal of the Structural Division, Vol. 107, No. ST3, pp. 535-550, March, **1981**.

**Bakht B. and Holland D. A.** , *A manual method for the elastic analysis of wide cantilever slabs of linearly varying thickness*, Canadian Journal of Civil Engineering, Vol. 3, pp. 523-530, **1976**.

**Batchelor B. and Tissington I. R.** , *Shear strength of two-way bridge slabs*, ASCE, Proceedings, V. 102, ST12, pp. 2315-2331, Dec., **1976**.

**Batchelor B., Hewitt B. E. and Csagoly P. ,** *An investigation of the fatigue strength of deck slabs of composite/concrete bridges*, Transportation Research Board, National Research Council, V. 1, No. 664, pp. 153-161, **1978**.

**Batchelor B., Hewitt B. E., Csagoly P. and Holowka M. ,** *Investigation of the ultimate strength of deck slabs of composite steel/concrete bridges*, Transportation Research Board, National Research Council, No. 664, pp. 162-170, **1978**.

**Beal D. B. ,** *Load capacity of concrete bridge decks*, Journal of the Structural Division, 108, pp. 814-832, April, **1982**.

**Beeby A. W. ,** *Ductility in reinforced concrete: why is it needed and how is it achieved?*, The Structural Engineering, Vol. 75, No. 18, pp. 311-318, September, **1997**.

**Bentz E. C. ,** *Empirical Modeling of Reinforced Concrete Shear Strength Size Effect for Members without Stirrups*, ACI Structural Journal, V. 102, No. 2, pp. 232-241, USA, March, **2005**.

**Bentz E. C., Vecchio F. J. and Collins M. P. ,** *Simplified Modified Compression Field Theory for Calculating Shear Strength of Reinforced Concrete Elements*, ACI Structural Journal, V. 103, No. 4, pp. 614-624, August, **2006**.

**Bigaj A. J. and Walraven J. C. ,** *Size Effects in Plastic Hinges of RC Members*, Heron, Vol. 47 n°1, p. 53-75, Delft, Holland, **2002**.

**Burdette E. G. and Goodpasture D. W. ,** *Correlation of bridge load capacity estimates with test data*, Transportation Research Board, National Research Council, Report 306, 75 p., June, **1988**.

**CEB ,** *Concrete Tension and Size Effects*, CEB (Comité euro-international du béton), Thomas Telford Publishing, Bulletin d'information N°237, Lausanne, Switzerland, April, **1997**.

**CEB ,** *Ductility of reinforced concrete structures - Synthesis Report and Individual Contributions*, CEB (Comité euro-international du béton), Bulletin 242, 332 p., Lausanne, Switzerland, May, **1998**.

**CEB ,** *Shear in prestressed concrete members*, CEB Bulletin d'Information, 180, 144 p., Lausanne, Switzerland, **1987**.

**Cope R. J. ,** *Flexural shear failure of reinforced concrete slab bridges*, Proceedings of the Institution of Civil Engineers, Part 2, Vol. 79, pp. 559-583, September, **1985**.

**Cosenza E., Greco C. and Manfredi G. ,** *The Concept of Equivalent Steel*, Comité Euro-International du Béton (CEB), Bulletin d'Information No. 218, pp. 163-183, Lausanne, **1993**.

**Csagoly P., Holowka M. and Dorton R. ,** *The true behaviour of thin concrete bridge slabs*, Transportation research record, No. 664, pp. 171-179, **1978**.

- Denton S.R. and Morley C. T.** , *Limit analysis and strain-softening structures*, International Journal of Mechanical Sciences, Elsevier, 42, pp. 503-522, **2000**.
- Dilger W. H., Tadros G. S. and Chebib J.** , *Bending moments in cantilever slabs*, Developments in Short and Medium Span Bridges: Engineering '90, Canadian Society for Civil Engineering, Vol. 1, pp. 265-276, Montreal, Canada, **1990**.
- Dvorkin E. N. and Bathe K. J.** , *A continuum mechanics based four-node shell element for general non-linear analysis*, Engineering Computations, Vol. 1, pp. 77-88, USA, March, **1984**.
- Eurocode 1** , *Actions on structures – Part 2: Traffic loads on bridges*, EN 1991-2, September, **2003**.
- Fang I. K., Tsui C. K. T., Burns N. H. and Klingner R. E.** , *Load capacity of isotropically reinforced, cast-in-place and precast panel bridge decks*, PCI Journal, pp. 104-113, **1990**.
- Fenwick R. C. and Paulay T.** , *Mechanism of shear resistance of concrete beams*, Journal of the Structural Division, Proceedings of the American Society of Civil Engineers, Vol. 94, No. ST10, pp. 2325-2350, October, **1968**.
- Fernández Ruiz M. and Muttoni A.** , *On the Development of Suitable Stress Fields for Structural Concrete*, ACI, Structural Journal, Farmington Hills, USA, to be published, **2006**.
- Fernández Ruiz M. and Muttoni A.** , *Plain concrete behaviour under uniaxial compression*, IS-BETON, **2005**.
- Fernández Ruiz M., Muttoni A. and Gambarova P.** , *Analytical modelling of the pre- and post-yield behaviour of bond in reinforced concrete*, ASCE Journal of Structural Engineering, Reston, USA, to be published, **2006**.
- FIB** , *Punching of structural concrete slabs*, fib bulletin 12, 307 p., Lausanne, Switzerland, April, **2001**.
- Greifenhagen C.** , *Seismic behavior of lightly reinforced concrete squat shear walls*, Thèse EPFL, N. 3512, Lausanne, Switzerland, **2006**.
- Guandalini S.** , *Poinçonnement symétrique des dalles en béton armé*, PhD dissertation, N. 3380 (2005), 289 pp., Lausanne, Switzerland, December, **2005**.
- Guandalini S. and Muttoni A.** , *Essais de poinçonnement symétrique des dalles en béton armé sans armature à l'effort tranchant*, Rapport d'essai, Lausanne, Switzerland, **2004**.
- Hamadi Y. D. and Regan P. E.** , *Behaviour in Shear of Beams with Flexural Cracks*, Magazine of Concrete Research, Vol. 32, No. 111, UK, June, **1980**.
- Hillerborg A.** , *Strip method of design*, A Viewpoint Publication, **1974**.

- Hillerborg A.** , *The advanced strip method - a simple design tool*, Magazine of Concrete Research, Vol.34, No.121, pp. 175-181, December, **1982**.
- Homberg H.** , *Farhrbahnplatten mit veränderlicher Dicke; Zweiter Band*, Springer-Verlag, **1968**.
- Homberg H. and Ropers W.** , *Farhrbahnplatten mit veränderlicher Dicke; Erster Band*, Springer-Verlag, **1965**.
- Hughes T. J. R.** , *Finite Element Method - Linear and Dynamic Finite Element Analysis*, Prentice-Hall, 803 pp., **1987**.
- Ibell T. J., Morley C. T. and Middleton C. R.** , *An upper-bound plastic analysis for shear*, Magazine of Concrete Research, 50, No. 1, pp. 67-73, March, **1998**.
- Ibell T. J., Morley C. T. and Middleton C. R.** , *Strength and Behavior in Shear of Concrete Beam-and-Slab Bridges*, ACI Structural Journal, V. 96, No 3, pp. 386-392, May, **1999**.
- Jaeger L. G. and Bakht B.** , *Rationalization of simplified methods of analysing cantilever slabs*, Canadian Journal of Civil Engineering, Vol. 6, No. 2, pp. 865-867, June, **1979**.
- Jaeger T. and Marti P.** , *Versuche zum Querkraftwiderstand und zum Verformungsvermögen von Stahlbetonplatten*, IBK Bericht, 294, December, **2005**.
- Jaramillo T. J.** , *Deflections and moments due to a concentrated load on a cantilever plate of infinite length*, Trans, ASME, Journal of Applied Mechanics, Vol. 72, No. 1, pp. 67-72, March, **1950**.
- Johansen K.W.** , *Yield-line formulae for slabs*, Cement and Concrete Association, **1972**.
- Johansen K.W.** , *Yield-line Theory*, Cement and Concrete Association, 181 p., **1962**.
- Jorgenson J. L. and Larson W.** , *Field Testing of a Reinforced Concrete Highway Bridge to Collapse*, Transportation Research Board, 607, pp. 66-71, USA, **1976**.
- Kani G. N. J.** , *The riddle of shear failure and its solution*, ACI Journal, USA, April, **1964**.
- Kani M. W., Huggins M. W. and Wittkopp R. R.** , *Kani on Shear in Reinforced Concrete*, 226 pp., Toronto, Canada, **1979**.
- Kaufmann W. and Marti P.** , *Structural concrete: cracked membrane model*, Journal of Structural Engineering, vol. 124 n° 12, pp 1467-1475, USA, December, **1998**.
- Kinnunen S. and Nylander H.** , *Punching of Concrete Slabs Without Shear Reinforcement*, Transactions of the Royal Institute of Technology, N°158, 112 p, Stockholm, Sweden, **1960**.

**Leonhardt F. and Schelling G.** , *Torsionsversuche an Stahlbetonbalken*, Deutscher Ausschuss für Stahlbeton, Heft 239, 122 p, Berlin, Germany, **1974**.

**Lu H.-Y.** , *Behaviour of Reinforced Concrete Cantilevers Under Concentrated Loads*, PhD dissertation, University of Cambridge, Girton College, 244 p., October, **2003**.

**Ludescher H.** , *Berücksichtigung von dynamischen Verkehrslasten beim Tragsicherheitsnachweis von Strassenbrücken*, PhD dissertation, EPFL - ENAC - IS - MCS, 2894, 259 p., Lausanne, Switzerland, **2004**.

**Maillart R.** , *Eine schweizerische Ausführungsform der unterzugslosen Decke. Pilzdecke.*, Geneva, Switzerland, **1926**.

**Malvar L. J.** , *Punching Shear Failure of a Reinforced Concrete Pier Deck Model*, ACI Structural Journal, Vol. 89, No. 5, pp. 569-576, USA, September, **1992**.

**Marti P.** , *Design of Concrete Slabs for Transverse Shear*, ACI Structural Journal, Vol. 87 No 2, pp. 180-190, Detroit, USA, March, **1990**.

**Marti P.** , *Kraftfluss in Stahlbetonplatten*, Beton- und Stahlbetonbau, Heft 2, pp. 85-93, Berlin, **2003**.

**Marti P. and Kong K.** , *Response of Reinforced Concrete Slab Elements to Torsion*, Journal of the Structural Division - ASCE, Vol. 113, No. ST5, pp. 976-993, May, **1987**.

**Meyboom J.** , *Limit Analysis of Reinforced Concrete Slabs*, IBK Bericht, Nr. 276, Zürich, November, **2002**.

**Middleton C. R.** , *Strength and safety assessment of concrete bridges*, University of Cambridge PhD dissertation, Cambridge, England, **1993**.

**Miller R., Aktan A. E. and Shahrooz B. M.** , *Destructive Testing of Decommissioned Concrete Slab Bridge*, ASCE Journal of Structural Engineering, Vol. 120 No 7, pp. 2176-2198, Reston, USA, July, **1994**.

**Mirzaei Y. and Muttoni A.** , *Tests on the post-punching behavior of reinforced concrete flat slabs*, IS-BETON, Switzerland, December, **2006**.

**Morley C. T.** , *Equilibrium design solutions for torsionless grillages or Hillerborg slabs under concentrated loads*, Proc. Institution of Civil Engineers, Part 2, pp. 447-460, September, **1986**.

**Morley C. T. and Denton S.R.** , *Modified Plasticity Theory for Reinforced Concrete Slab Structures of Limited Ductility*, Structural Engineering, Mechanics and Computation, Vol. 2, pp. 1523-1530, **2001**.

**Mörsch E.** , *Der Eisenbetonbau - Seine Theorie und Anwendung*, Verlag von Konrad Wittwer, 3. Aufl. 1908, 4. Aufl. 1912, 5. Aufl. 1.Bd., 1. Hälfte, 1920, 2. Hälfte, Stuttgart, **1922**.

**Mufti A. A., Bakht B. and Jaeger L. G.**, *Moments in Deck Slabs Due to Cantilever Loads*, Journal of Structural Engineering, ASCE, Vol. 119, No. 6, pp. 1761-1777, USA, June, **1993**.

**Muttoni A.**, *Die Anwendbarkeit der Plastizitätstheorie in der Bemessung von Stahlbeton*, Birkhäuser Verlag, Institut für Baustatik und Konstruktion ETH Zürich, 176, Basel, Switzerland, **1990**.

**Muttoni A.**, *Schubfestigkeit und Durchstanzen von Platten ohne Querkarfbewehrung*, Beton- und Stahlbetonbau, Vol. 98, No 2, pp. 74-84, Berlin, Germany, Feb., **2003**.

**Muttoni A. and Burdet O.**, *Conception et dimensionnement des éléments de structures, béton armé*, EPFL - IS-BETON, Polycopié cours 5ème semestre, Lausanne, Switzerland, **2004**.

**Muttoni A. and Fernández Ruiz M.**, *Concrete Cracking in Tension Members and Application to Deck Slabs of Bridges*, ASCE Journal of Bridge Engineering, USA, **2006**.

**Muttoni A. and Fernández Ruiz M.**, *Shear strength of members without transverse reinforcement as a function of the critical shear crack width*, ACI Structural Journal, under review, Farmington Hills, USA, **2006**.

**Muttoni A. and Schwartz J.**, *Behavior of Beams and Punching in Slabs without Shear Reinforcement*, IABSE Colloquium, Vol. 62, pp. 703-708, Stuttgart, Germany, **1991**.

**Muttoni A. and Thürlimann B.**, *Schubversuche an Balken und Flachdecken ohne Schubbewehrung*, Institute of Structural Engineering, ETH, unpublished report, **1986**.

**Muttoni A., Schwartz J. and Thürlimann B.**, *Bemessung von Betontragwerken mit Spannungsfeldern*, Birkhäuser, Design of Concrete Structures with Stress Fields, 145 pp, Basel, Switzerland, **1997**.

**Nielsen M. P.**, *Limit Analysis of Reinforced Concrete Slabs*, Acta Polytechnica Scandinavica, Civil Engineering and Building Construction Series, No. 26, 167 p., Helsinki, **1964**.

**Pérez Caldentey A., Padilla P. and Corres Peiretti H.**, *Análisis de piezas sometidas a cortante con bajas cuantías de armadura longitudinal. Estudio teórico de elementos estructurales con estas características y definición de un programa experimental de investigación*, Hormigón y Acero, 233, pp. 103-118, Espagne, febrero, **2004**.

**Polak M. A. and Vecchio F. J.**, *NonLinear Analysis of Reinforced-Concrete Shells*, ASCE Journal of Structural Engineering, Vol. 119, No. 12, pp. 3439-3462, December, **1993**.

**Popovics S.**, *A Review of Stress-Strain Relationships for Concrete*, ACI Journal, 67, pp. 243-248, March, **1970**.



- Prakhya G. K. V. and Morley C. T.** , *Tension-stiffening and moment-curvature relations of reinforced concrete elements*, ACI Structural Journal, V.87, N°5, pp 597-605, USA, September, **1990**.
- Pucher A.** , *Einflussfelder elastischer Platten - Influence Surfaces of Elastic Plates*, 3rd Edition, Springer, 127p., Vienna, Austria, **1964**.
- Reineck K.-H.** , *Ultimate Shear Force of Structural Concrete Members without Transverse Reinforcement Derived from Mechanical Model*, ACI Structural Journal, Vol. 88, pp. 592-602, September, **1991**.
- Reismann H. and Cheng S. H.** , *The edge reinforced cantilever plates strip*, Publs int. Ass. Bridge struct. Engng, Vol. 30, pp. 149-162, **1970**.
- Sawko F. and Mills J. H.** , *Design of cantilever slabs for spine beam bridges*, Proceedings at the Cardiff Conference on Developments in bridge design and construction, Crosby Lockwood and Son Ltd, London, England, **1971**.
- Schlaefli M.** , *Ermüdung von Brückenfahrbahnplatten aus Stahlbeton (Fatigue behaviour of reinforced concrete deck slabs)*, PhD dissertation, EPFL, No.1998, 113 p., Lausanne, Switzerland, **1999**.
- Shahrooz B. M., Ho I. K., Aktan A. E., de Borst R., Blaauwendraad J., van der Veen C., Iding R. H. and Miller R. A.** , *Nonlinear Finite Element Analysis of a Deteriorated RC Slab Bridge*, ASCE Journal of the Structural Division, Vol. 120, No. 2, pp. 422-440, USA, February, **1994**.
- Sherwood E. G., Lubell A. S., Bentz E. C. and Collins M. P.** , *One-way shear strength of thick slabs and wide beams*, ACI Structural Journal, Vol. 103 No 6, pp. 794-802, USA, November, **2006**.
- SIA** , *SIA 261 – Actions on Structures*, Swiss Society of Engineers and Architects, 114p., Zurich, Switzerland, **2003**.
- SIA** , *SIA 262 – Concrete Structures*, Swiss Society of Engineers and Architects, 90 p., Zurich, Switzerland, **2003**.
- SIA** , *SIA D 0182 – Construction en béton, Introduction à la norme SIA 262, D 0182*, 127 pp., Zürich, Switzerland, **2003**.
- Thorenfeldt E., Tomaszewics A. and Jensen J. J.** , *Mechanical properties of high-strength concrete and application in design*, Proceeding on Utilisation of High Strength Concrete, Stavanger, Norway, **1987**.
- Timoshenko S. and Woinowsky-Krieger S.** , *Theory of Plates and Shells*, McGraw-Hill., Second Edition, 580 p., **1959**.
- Tong P. Y. and Batchelor B.** , *Compressive membrane enhancement in two-way bridge slabs, Cracking, Deflection, and Ultimate Load of Concrete Slab Systems*, ACI, SP-30, pp. 271-286, Detroit, **1971**.

**Vaz Rodrigues R.** , *Essai d'un porte-à-faux de pont sous charge concentrée*, EPFL - IS-BETON, Lausanne, **2002**.

**Vaz Rodrigues R.** , *Shear Strength of RC Bridge Deck Cantilevers*, 6th International PhD Symposium in Civil Engineering, IBK Publikation SP-015, pp. 160-161, August, **2006**.

**Vaz Rodrigues R. and Muttoni A.** , *Influence des déformations plastiques de l'armature de flexion sur la résistance à l'effort tranchant des poutres sans étriers. Rapport d'essai*, IS-BETON, Lausanne, **2004**.

**Vaz Rodrigues R. and Muttoni A.** , *Large Scale Tests on Reinforced Concrete Bridge Deck Slabs. Test report*, IS-BETON, Lausanne, **2006**.

**Vaz Rodrigues R., Burdet O. and Muttoni A.** , *Experimental investigation of the shear capacity of plastic hinges*, fib Symposium, Budapest 2005, vol. 2, pp. 651-656, Budapest, Hungary, May, **2005**.

**Vaz Rodrigues R., Muttoni A. and Burdet O.** , *Large Scale Tests on Bridge Slabs Cantilevers Subjected to Traffic Loads*, Proceedings of the 2nd fib Congress, vol.1, pp. 232, Naples, **2006**.

**Walraven J. C.** , *Aggregate interlock: a theoretical and experimental analysis*, Delft University of Technology, Faculty of Civil Engineering, 197 p., Delft, Holland, **1980**.

**Walraven J. C.** , *Fundamental Analysis of Aggregate Interlock*, ASCE Journal of Structural Engineering, Vol. 107 No 11, pp. 2245-2270, USA, **1981**.

**Zararis P. D., Papadakis G. C.** , *Diagonal Shear Failure and Size Effect in RC Beams without Web Reinforcement*, ASCE Journal of Structural Engineering, Vol. 127, No. 7, pp.733-742, USA, July, **2001**.

## Notation

### Roman capital letters

<i>A</i>	point; area
<i>B</i>	plate rigidity; reduced area
<i>C</i>	point; constant
<i>D</i>	diameter of aggregates
<i>E</i>	modulus of elasticity
<i>F</i>	indicates failure
<i>G</i>	shear modulus
<i>I</i>	inertia
<i>M</i>	moment
<i>Q</i>	concentrated load
<i>V</i>	shear force

### Roman small letters

<i>a</i>	shear span; cantilever span
<i>b</i>	width
<i>d</i>	effective depth
<i>f</i>	material strength
<i>h</i>	height; slab thickness
<i>k</i>	constant
<i>ℓ</i>	span; length
<i>m</i>	unit moment
<i>n</i>	coordinate axis normal to yield-line
<i>p</i>	fraction
<i>q</i>	distributed load
<i>r</i>	reduction factor
<i>s</i>	crack spacing
<i>t</i>	coordinate axis parallel to yield-line
<i>u</i>	crack width; length of control perimeter
<i>v</i>	unit shear force; crack slide
<i>w</i>	deflection; crack width
<i>x</i>	depth of compression zone
<i>x</i>	coordinate axis; coordinate
<i>y</i>	coordinate axis; coordinate
<i>z</i>	coordinate axis; coordinate

### Greek letters

$\mu$	friction coefficient
-------	----------------------

$\rho$	geometric reinforcement ratio
$\phi$	polar coordinate; angle
$\xi$	local coordinate axis; coordinate
$\eta$	local coordinate axis; coordinate
$\alpha$	ratio between forces
$\gamma$	partial safety factor; shear strain
$\Delta$	difference
$\delta$	relative displacement; angle
$\varepsilon$	strain
$\zeta$	local coordinate axis; coordinate
$\theta$	angle
$\nu$	Poisson's ratio
$\sigma$	normal stress
$\tau$	shear stress
$\varphi$	angle
$\chi$	curvature

### Subscripts






$\eta$	local coordinate axis
<i>0,1,2</i>	particular value
<i>agg</i>	aggregate interlock
<i>b</i>	bond
<i>c</i>	concrete; compression
<i>comp</i>	compression zone
<i>cr</i>	cracking
<i>d</i>	design
<i>dow</i>	Dowel effect
<i>Flex</i>	flexion
<i>k</i>	characteristic value
<i>max</i>	maximum
<i>min</i>	minimum
<i>calc</i>	calculated value
<i>p</i>	plastic
<i>Q</i>	concentrated load
<i>R</i>	strength
<i>r</i>	polar coordinate
<i>s</i>	steel
<i>t</i>	tensile; transversal direction
<i>test</i>	measured value
<i>tot</i>	principal
<i>TR</i>	transition

$ts$	tension stiffening
$u$	ultimate
$v$	constant
$x$	coordinate axis
$y$	yielding; coordinate axis
$\zeta$	local coordinate axis
$\theta$	angle
$l$	longitudinal direction

### Superscripts

'	negative bending; alternative value; per unit length
*	secant value
—	average value

### Special symbols

$\varnothing$	bar diameter; column diameter
$\mathcal{L}$	center line
	clamped edge
	free edge
	simply supported edge
	force, up
	force, down





# Large Scale Tests on Reinforced Concrete Bridge Deck Slabs

## Essais à grande échelle sur des Dalles de Roulement des Ponts en Béton Armé



Ecole Polytechnique Fédérale de Lausanne  
Institut de Structures  
Laboratoire de Construction en Béton (IS-BETON)

Rui Vaz Rodrigues  
Prof. Dr Aurelio Muttoni

9 mai 2006

This research is funded by the Swiss Federal Roads Authority (OFROU)



and by the Portuguese Foundation for Science and Technology (FCT)

**FCT** Fundação para a Ciência e a Tecnologia  
MINISTÉRIO DA CIÊNCIA, TECNOLOGIA E ENSINO SUPERIOR Portugal



## Table of contents

<b>A-1 Introductory remarks.....</b>	<b>1</b>
A-1.1 Aim .....	1
A-1.2 Acknowledgements.....	1
<b>A-2 Description of the slabs .....</b>	<b>3</b>
A-2.1 Test concept and overview .....	3
A-2.2 Geometry and reinforcement .....	4
A-2.3 Construction of specimens.....	7
A-2.4 Material properties.....	8
Concrete .....	8
Reinforcement .....	11
<b>A-3 Experimental set-up and procedure .....</b>	<b>13</b>
A-3.1 Reaction frames and load application.....	13
A-3.2 Preparation of slabs.....	18
A-3.3 Continuous measurements .....	19
A-3.4 Demountable deformer measurements .....	23
A-3.5 Test procedure .....	24
<b>A-4 Results .....</b>	<b>27</b>
A-4.1 Analysis and presentation of data .....	27
A-4.2 Test DR1-a.....	29
A-4.3 Test DR1-b.....	37
A-4.4 Test DR1-c.....	40
A-4.5 Test DR2-a.....	43
A-4.6 Test DR2-b.....	51
A-4.7 Test DR2-c.....	56
A-4.8 Test PR1.....	61
<b>A-5 Conclusions.....</b>	<b>63</b>
A-5.1 Tests on bridge deck cantilevers.....	63
A-5.2 Punching shear test with simulation of vehicle wheel.....	66
<b>Bibliography .....</b>	<b>67</b>



## **A-1 Introductory remarks**

### **A-1.1 Aim**

The main objective of the tests on bridge cantilevers is to study the actual behavior of bridge deck cantilevers without shear reinforcement, under concentrated loads. The application of failure criteria for shear and punching shear (Muttoni 2003, and others) is investigated for the obtained test results.

From the obtained results of cantilevers failing in shear or punching shear, practical rules such as the location of control perimeters should be proposed. This could contribute to a more accurate assessment of bridge deck slabs failing in shear or punching shear.

Measurements of the surface strains, rotations, deflections, variation of slab thickness and geometry of the critical crack were made. These measurements can be used to compare with results from non linear finite element analysis or other models.

The tests were performed at full scale, without size-effect.

The objective of the punching shear test is to compare the case of punching shear with a vehicle wheel with the case of punching shear with a concrete column.

### **A-1.2 Acknowledgements**

This research was performed at the Structural Concrete Laboratory (IS-BETON) of the Ecole Polytechnique Fédérale de Lausanne, under the supervision of Prof. Dr. Aurelio Muttoni, to whom I would like to express my gratitude for his advice and encouragement provided.

The financial support granted by the Swiss Federal Roads Authority (FEDRO) and by the Portuguese Foundation for Science and Technology (FCT / BD 13259 / 2003) is gratefully acknowledged.

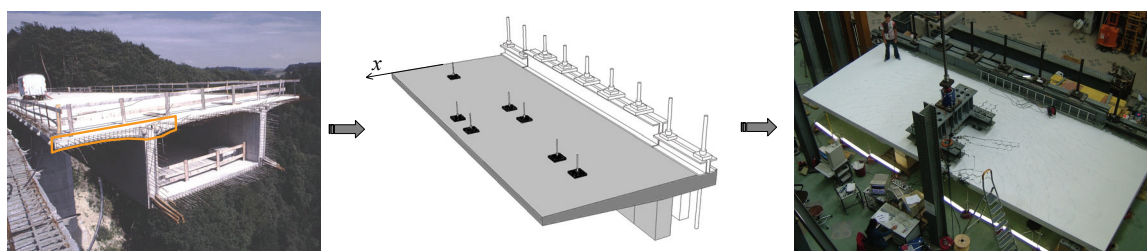
I wish to thank to all the field staff of the Structures Laboratory of the Ecole Polytechnique Fédérale de Lausanne for their support provided to the experimental activities.



## A-2 Description of the slabs

### A-2.1 Test concept and overview

The cantilevers are full scale models of part of a reinforced concrete bridge box girder, as shown in figure A-2.1. Two slabs (DR1 and DR2) were tested under loading patterns of one, two and four concentrated loads. Table A-2.1 shows the main parameters for the tests on cantilevers. The reinforcement ratio is calculated at the clamped edge, for the top bars at the transversal direction (bars along  $x$  axis).



a) Bridge girder with cantilever

b) Full scale model under loading patterns

c) Test DR1a, under four concentrated loads

Figure A-2.1: Test concept and load arrangement for the bridge cantilevers

Table A-2.1: Parameters for tests on cantilevers

Slab	Test	Number of concentrated loads	Reinforcement ratio for top bars along $x$ at the clamped edge
DR1	DR1-a	4	0.78%
	DR1-b	2	
	DR1-c	1	
DR2	DR2-a	2	0.60%
	DR2-b	2	
	DR2-c	1	

The reinforcement ratio of slab DR1 is representative of an elastically dimensioned reinforced concrete cantilever using the traffic loads prescribed by the Eurocode 1 (2003). The reinforcement ratio of the slab DR2 was reduced to validate the models described by (Muttoni 2003) for lower reinforcement ratios. None of the slabs has an edge beam.

The applied loads for test DR1-a are the twin axle loads prescribed by the Eurocode 1 (2003) with all dimensions reduced by 3/4. The subsequent tests were performed using only two or one concentrated loads to better focus on shear and punching shear failure modes.

Concerning the punching shear test, figure A-2.2 compares two types of punching shear tests. Both slabs have the same reinforcement layout and similar concrete properties. The central support for case a) at figure A-2.2 is a flat jack. The flat jack is made of a copper sheet envelope with water inside. The schematic distribution of the contact

pressure is indicated. For case a) the contact pressures at the interface  $a-b$  are approximately constant up to the failure of the slab. For case b) the central support is a concrete column. The contact pressures are not uniform and tend to increase near the column edge as the deflection of the slab increases. Guandalini (Guandalini 2005) tested a reinforced concrete slab with a concrete column as a central support (PG-10). This report presents only the results of the punching shear test with a flat jack (test PR1).

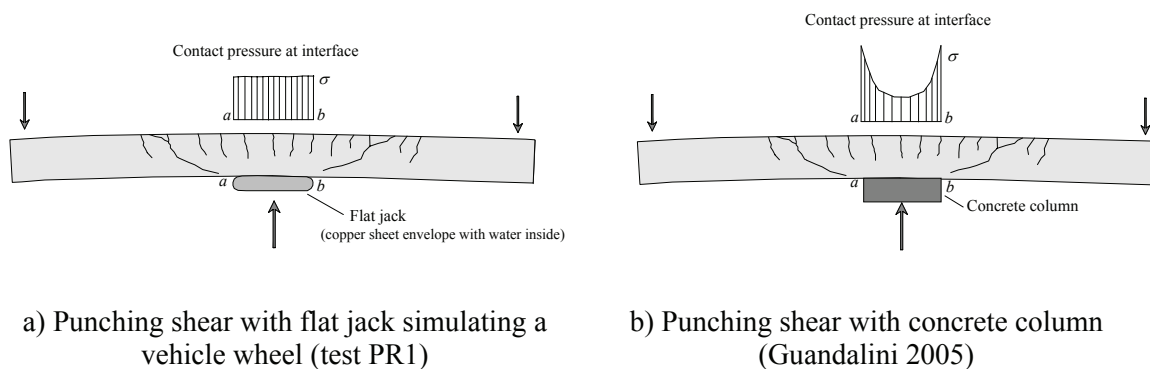


Figure A-2.2: Two punching shear experiments

The reinforcement ratio at the top layer in both directions for slab PR1 and PG-10 is equal to 0.33%. This value is representative of the bottom reinforcement at both directions for cantilevers, at the region near the cantilever edge.

## A-2.2 Geometry and reinforcement

The figures A-2.3 and A-2.4 illustrate the dimensions, the reinforcement layout and the applied loads for slabs DR1 and DR2. The cantilevers have a span of 2.78 meters (distance from the fixed end to the tip of the cantilever) and a total length of 10.00 meters. The thickness of the cantilevers is 0.19 meters at the free edge and 0.38 meters at the fixed end. For slab DR1, the transversal reinforcement of the top layer at the fixed end consists of 16 mm diameter bars at 75 mm spacing (reinforcement ratio  $\rho = 0.78\%$ ). The top transversal reinforcement is reduced to 16 mm diameter bars at 150 mm spacing at halfway of the span. For slab DR2, the transversal reinforcement of the top layer at the fixed end consists of 14 mm diameter bars at 75 mm spacing (reinforcement ratio  $\rho = 0.6\%$ ). The top transversal reinforcement is reduced to 14 mm diameter bars at 150 mm spacing at halfway of the span. No vertical shear reinforcement was provided between the free edge and the fixed end. The bottom reinforcement in both directions and the top longitudinal reinforcement consists of 12 mm diameter bars at 150 mm spacing for both slabs DR1 and DR2. An edge reinforcement consisting of 12 mm diameter bars at 150 mm spacing was added along the side edges ( $y = 0$  and  $y = 10.0$  m). The concrete cover is 30 mm.

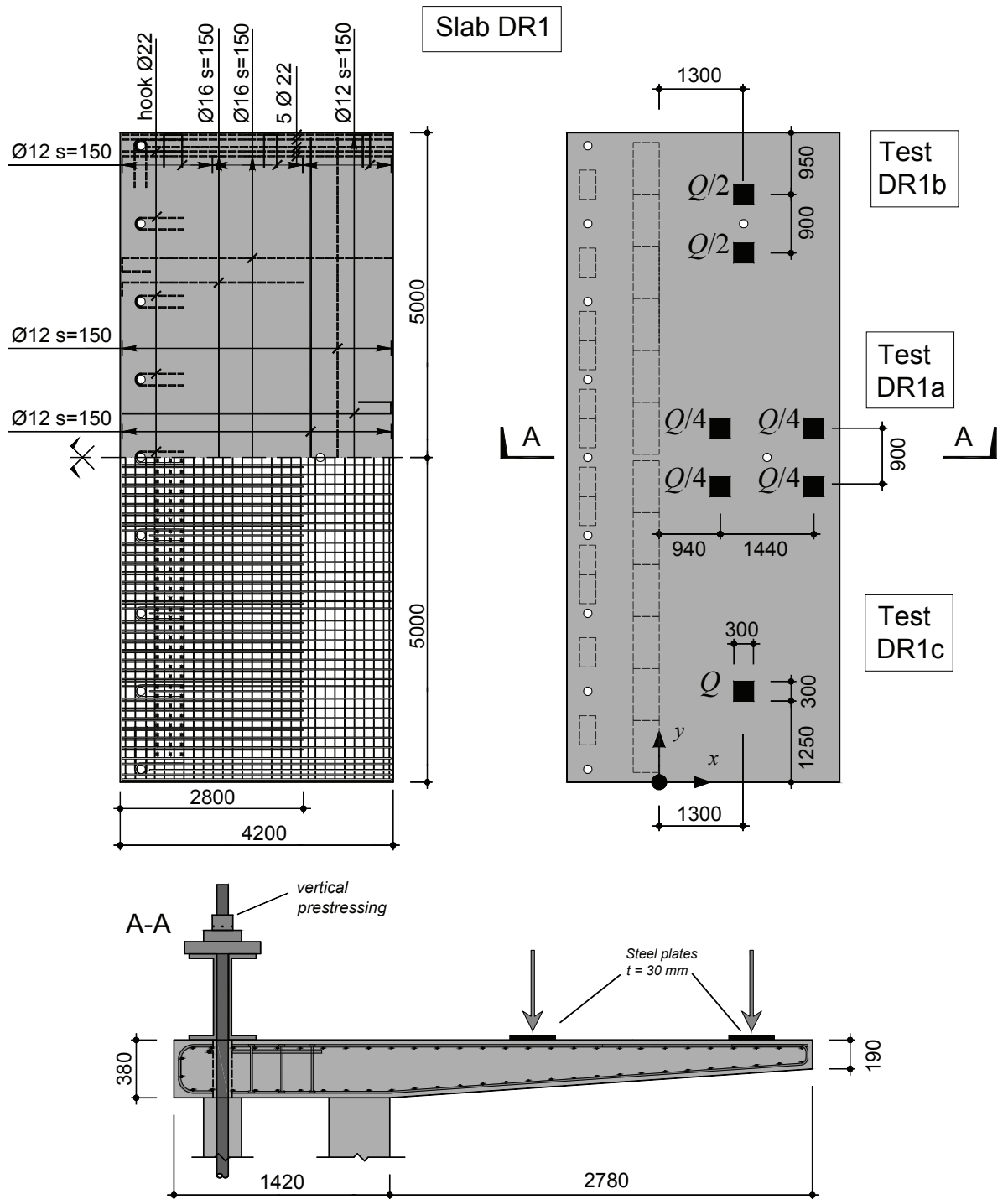


Figure A-2.3: Slab DR1. Dimensions, reinforcement layout and applied loads [mm]

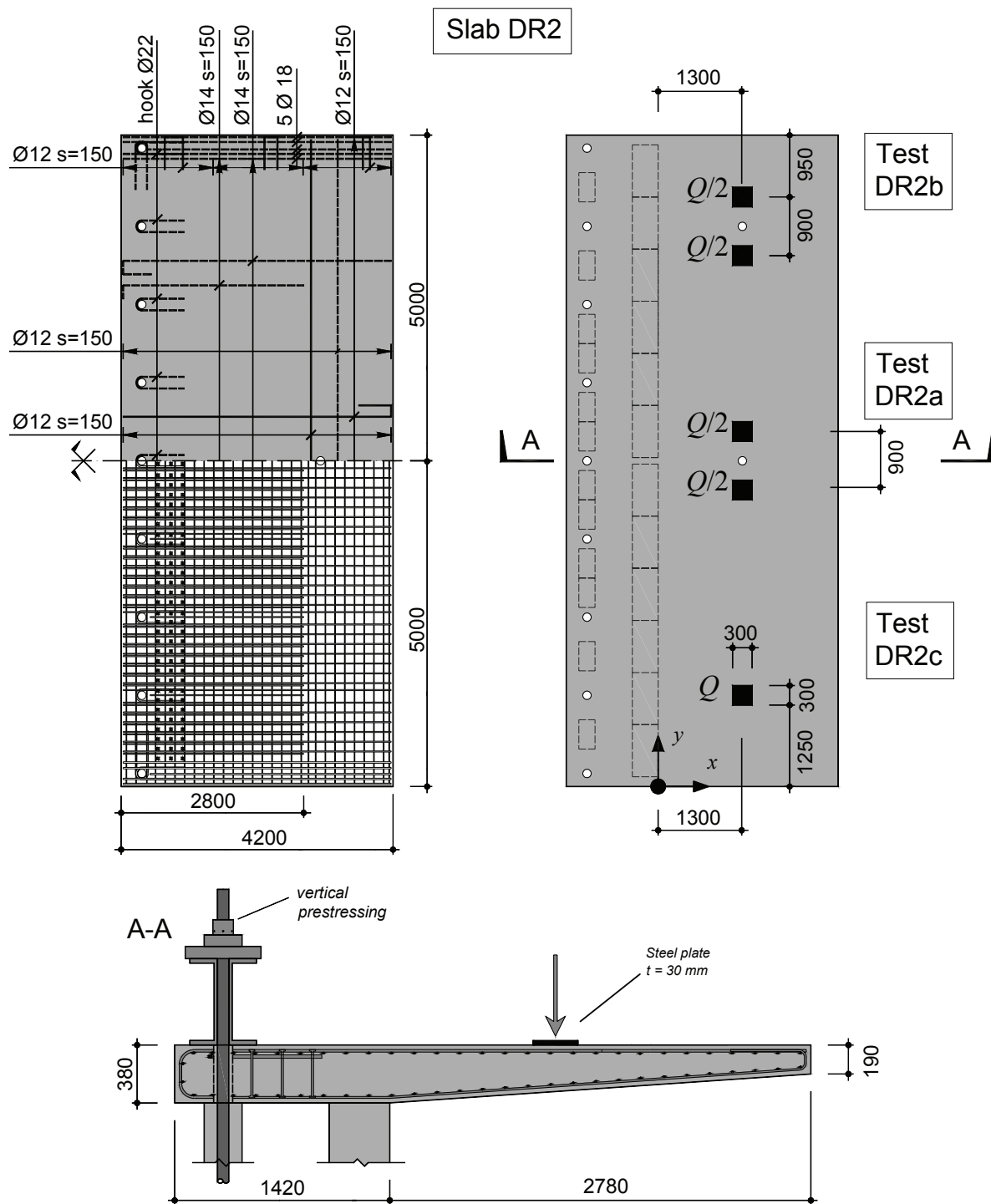


Figure A-2.4: Slab DR2. Dimensions, reinforcement layout and applied loads [mm]

Figure A-2.5 shows the reinforcement layout and geometry of slab PR1. The reinforcement at the top layer consists of 10 mm diameter bars at 115 mm spacing for both directions (reinforcement ratio  $\rho = 0.33\%$ ). The average effective depth between both directions at the top layer is 210 mm. The reinforcement at the bottom layer



consists of 8 mm diameter bars at 115 mm spacing for both directions. The concrete cover is 30 mm. The central support consists of a circular flat jack with a nominal surface of  $0.156 \text{ m}^2$ . No vertical shear reinforcement was provided.

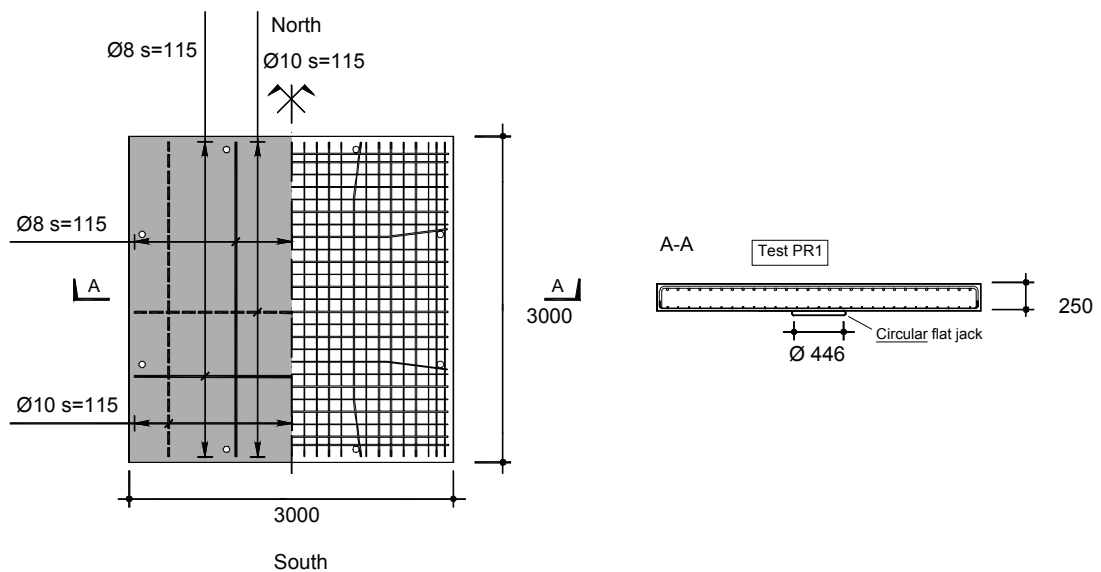


Figure A-2.5: Slab PR1. Dimension and reinforcement layout [mm]

### A-2.3 Construction of specimens

Figure A-2.6 shows some steps of the construction of slabs DR1 and DR2. Both slabs were cast at the Laboratory of Structures of the Ecole Polytechnique Fédérale de Lausanne. The plywood formwork surface in contact with concrete was impregnated with mould oil prior to the setting of reinforcement. Metallic hollow cylinders were fixed to the bottom of the formwork to create the holes required to apply loads on the cantilever. The casting of each slab required approximately 14 square meters of concrete. The concrete was made at a factory outside of the Structures Laboratory and was transported by a concrete mixer truck. Three shuttle trips were required to cast each slab. A conveyor belt was used to efficiently dispose the concrete in the formwork (fig. A-2.6 c). Two concrete vibrators were used to correctly place the concrete. The slump and flow table tests were performed before the casting of the slab. The table A-2.2 shows the results of the slump and flow table tests. About thirty concrete cylinders were cast for each slab using the same batch of concrete. The surface of the slab was leveled and smoothed with the help of a ruler and a mason's mortar board. After casting, the slab was covered with a plastic sheet to maintain a moist environment. Water was sprayed onto the slab during the period of curing.

Slab DR1 was cast on the 27<sup>th</sup> of April of 2005 and slab DR2 was cast on the 4<sup>th</sup> of October of 2005. The formwork was partially removed two weeks after casting to allow the vertical prestressing of the fixed end (figs. A-2.3 and A-2.4). A total prestress force of 7 MN ensured that the fixed end was well clamped. Three weeks after casting the entire formwork was removed.

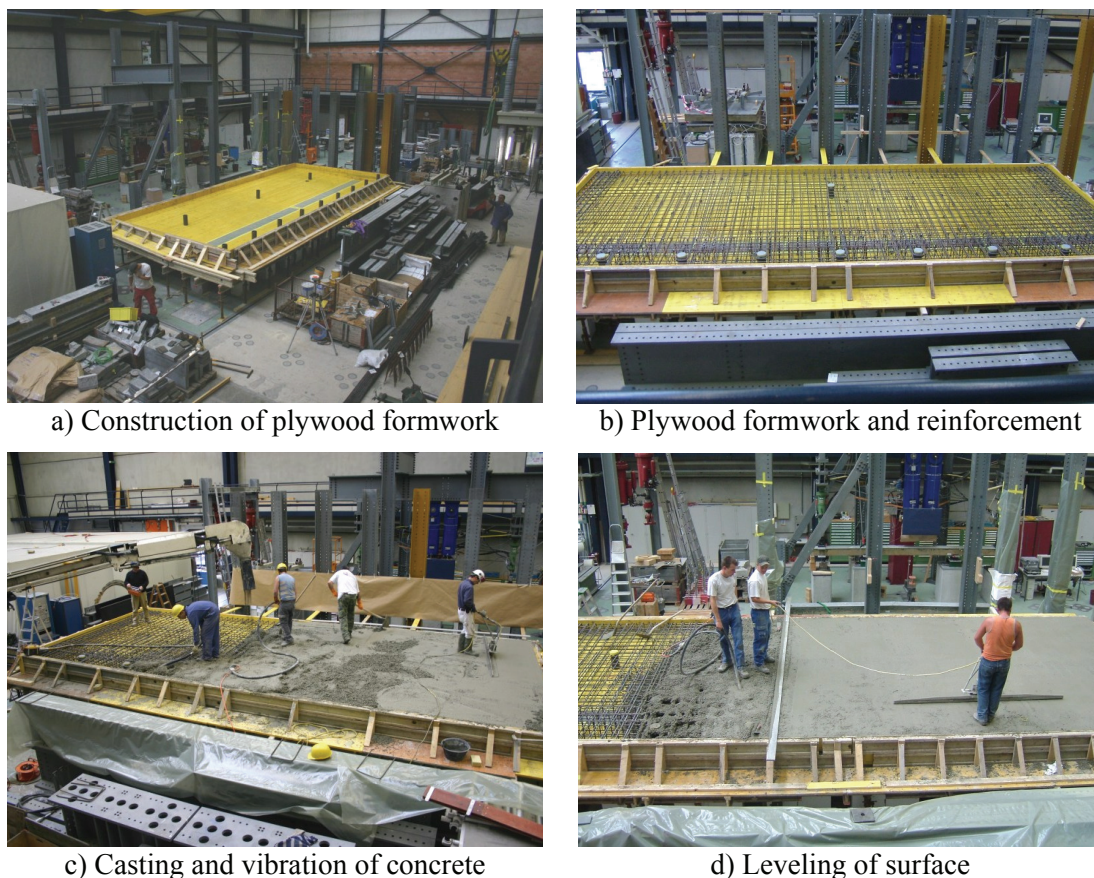


Figure A-2.6: Construction of slabs DR1 and DR2

## A-2.4 Material properties

### Concrete

The composition of concrete used for slabs DR1 and DR2 is indicated in table A-2.2. The water-cement ratio is 0.54 for both slabs. The maximum size of the aggregate is 16 mm. Concrete cylinders were cast for each slab using the same batch of concrete. Each concrete cylinder had a diameter  $\varnothing = 159$  mm and height of  $h = 320$  mm. The mechanical properties were measured with tests on concrete cylinders. The tests were performed at the Laboratory of Construction Materials (LMC) of the Ecole Polytechnique Fédérale de Lausanne. The measured properties are the concrete compressive strength, the tensile strength, the Young's modulus and the apparent density. Tables A-2.4, A-2.5 and A-2.6 show the results of tests on concrete cylinders for slabs DR1, DR2 and PR1, respectively. The mechanical properties at the time of testing are calculated using fitted equations of form  $a \cdot \text{days}^b + c$ . Figure A-2.7 (1) shows the time evolution of the concrete compressive strength ( $f_c$ ), the concrete tensile strength ( $f_{ct}$ ) and the Young's modulus ( $E_c$ ). Figure A-2.7 (2) shows the measured stress-strain curve in compression for concrete of slab DR1, after (Fernández Ruiz 2005). The table A-2.3 indicates the average value and the coefficient of variation of the mechanical properties at the time of failure.

Table A-2.2: Composition of 1 cubic meter of concrete and results of tests on fresh concrete

Slab	Sand 0-4	Gravel 4-8	Gravel 8-16	Cement	Water	Slump test [mm]	Flow table test [mm]
	[kg]	[kg]	[kg]	[kg]	[kg]		
DR1	753	604	661	325	174	20	360
	37%	30%	33%		W/C = 0.54		
DR2	753	604	661	325	174	15	320
	37%	30%	33%		W/C = 0.54		

Table A-2.3: Concrete properties at the time of failure (average value and coefficient of variation)

Test	Date	Number of days	Compressive strength	Tensile strength	Young's modulus
			( $f_c$ ) [MPa]	( $f_{ct}$ ) [MPa]	( $E_c$ ) [GPa]
DR1-a	12.07.2005	76	39.11	2.94	36.03
			3.3%	8.3%	4.2%
DR1-b	28.07.2005	92	39.91	3.02	36.09
			5.1%	8.3%	4.3%
DR1-c	19.08.2005	114	40.82	3.11	36.16
			7.6%	8.3%	4.6%
DR2-a	09.12.2005	66	38.92	3.13	36.26
			4.8%	4.9%	0.8%
DR2-b	17.01.2006	105	41.98	3.14	37.39
			15.5%	0.0%	4.0%
DR2-c	24.01.2006	112	42.42	3.14	37.54
			4.3%	0.0%	3.8%
PR1	24.05.2004	47	35.17	2.23	31.84
			4.3%	5.2%	4.0%

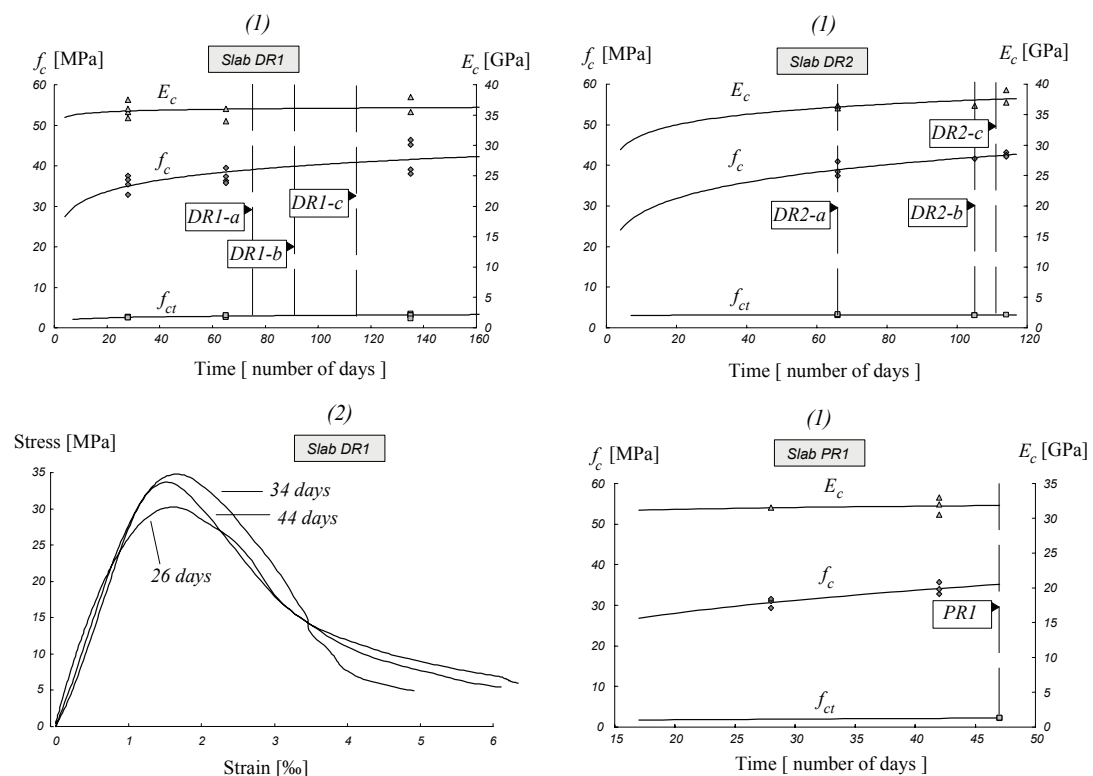


Figure A-2.7: (1) Evolution of mechanical properties of concrete with time for slabs DR1, DR2 and PR1; (2) Stress-strain curve of concrete in compression after tests performed by (Fernández Ruiz 2005)

## Chapter A-2

Table A-2.4: Results of tests on concrete cylinders (slab DR1)

Report	Date	Number of days	Compressive strength ( $f_c$ ) [MPa]	Tensile strength ( $f_{ct}$ ) [MPa]	Young's modulus ( $E_c$ ) [GPa]	Apparent density [t/m <sup>3</sup> ]
Casting	27.04.2005	0	0.00	0.00	0.00	-
124/05/LMC	25.05.2005	28	35.40		35.50	2.43
124/05/LMC	25.05.2005	28	37.50		36.00	2.45
124/05/LMC	25.05.2005	28	36.60		34.50	2.44
124/05/LMC	25.05.2005	28	32.90		37.50	2.45
125/05/LMC	25.05.2005	28		2.60		2.44
125/05/LMC	25.05.2005	28		2.70		2.44
125/05/LMC	25.05.2005	28		2.50		2.45
125/05/LMC	25.05.2005	28		2.50		2.45
171/05/LMC	01.07.2005	65	36.30		34.00	2.44
171/05/LMC	01.07.2005	65	37.40		36.00	2.44
172/05/LMC	01.07.2005	65		2.70		2.45
172/05/LMC	01.07.2005	65		3.00		2.43
172/05/LMC	01.07.2005	65		2.60		2.44
172/05/LMC	01.07.2005	65		3.10		2.45
170/05/LMC	01.07.2005	65	39.50			2.44
170/05/LMC	01.07.2005	65	35.70			2.42
227/05/LMC	09.09.2005	135		3.50		2.44
227/05/LMC	09.09.2005	135		3.00		2.44
227/05/LMC	09.09.2005	135		3.10		2.43
227/05/LMC	09.09.2005	135		2.20		2.43
226/05/LMC	09.09.2005	135	46.30			2.44
226/05/LMC	09.09.2005	135	39.10			2.45
224/05/LMC	09.09.2005	135	45.10		38.00	2.44
224/05/LMC	09.09.2005	135	38.00		35.50	2.42

Table A-2.5: Results of tests on concrete cylinders (slab DR2)

Report	Date	Number of days	Compressive strength ( $f_c$ ) [MPa]	Tensile strength ( $f_{ct}$ ) [MPa]	Young's modulus ( $E_c$ ) [GPa]	Apparent density [t/m <sup>3</sup> ]
Casting	04.10.2005	0	0.00	0.00	0.00	-
299/05/LMC	09.12.2005	66		3.10		2.44
299/05/LMC	09.12.2005	66		3.00		2.45
299/05/LMC	09.12.2005	66		3.30		2.44
298/05/LMC	09.12.2005	66	38.40		36.50	2.44
298/05/LMC	09.12.2005	66	41.00		36.50	2.44
298/05/LMC	09.12.2005	66	37.40		36.00	2.44
004/06/LMC	17.01.2006	105	41.60		36.50	2.44
005/06/LMC	17.01.2006	105		3.1		2.45
005/06/LMC	17.01.2006	105		3.1		2.44
006/06/LMC	26.01.2006	114	43.20		39.00	2.44
006/06/LMC	26.01.2006	114	42.50		37.00	2.43
007/06/LMC	26.01.2006	114		3.20		2.43
008/06/LMC	26.01.2006	114	42.20			2.43

Table A-2.6: Results of tests on concrete cylinders (slab PR1)

Report	Date	Number of days	Compressive strength ( $f_c$ ) [MPa]	Tensile strength ( $f_{ct}$ ) [MPa]	Young's modulus ( $E_c$ ) [GPa]	Apparent density [t/m <sup>3</sup> ]
Casting	07.04.2004	0	0.00	0.00	0.00	-
099/04/LMC	05.05.2004	28	31.00		31.50	2.43
098/04/LMC	05.05.2004	28	31.60			2.43
098/04/LMC	05.05.2004	28	29.40			2.43
112/04/LMC	19.05.2004	42	32.80		33.00	2.43
112/04/LMC	19.05.2004	42	33.90		30.50	2.42
112/04/LMC	19.05.2004	42	35.70		32.00	2.44
115/04/LMC	24.05.2004	47		2.30		2.43
115/04/LMC	24.05.2004	47		2.10		2.43
115/04/LMC	24.05.2004	47		2.30		2.43

## Reinforcement

The reinforcement bars were tested in tension at the Laboratory of Mechanical Metallurgy of the Ecole Polytechnique Fédérale de Lausanne. The stress-strain curves are shown in figure A-2.8, along with the surface of the reinforcement bars and the dimension of the ribs. All the bars are of type B500B accordingly with the Swiss code SIA 262 (2003). The mechanical properties are indicated in table A-2.7. All the bars are hot-rolled except for bars with 12 mm of diameter for slab DR2. Table A-2.8 indicates the detailed results for each tensile test. The strains were measured using extensometers with a measurement length of 150 mm. The loading speed was 10 MPa/s.

Table A-2.7: Mechanical properties of reinforcement

Slab	Diameter (Ø) [mm]	Yield Strength ( $f_y$ ) [MPa]	Tensile strength ( $f_t$ ) [MPa]	Deformation under maximum load ( $\epsilon_u$ ) [%]	$f_t/f_y$	Steel type
DR1	16	499 4.2%	600 2.0%	10.73 6.0%	1.20 2.2%	hot-rolled
	12	541 0.4%	629 0.2%	9.05 6.1%	1.16 0.5%	hot-rolled
	22	534 0.2%	644 0.3%	10.91 12.8%	1.21 0.5%	hot-rolled
DR2	14	505 3.1%	591 4.1%	11.11 28.4%	1.17 1.5%	hot-rolled
	12	469* 6.0%	580 1.2%	5.19 15.2%	1.24 4.8%	cold formed
	18	541 -	639 -	11.54 -	1.18 -	hot-rolled
PR1	10	566 -	648 -	9.66 -	1.15 -	hot-rolled
	12	566 0.3%	622 0.4%	8.80 8.6%	1.10 0.1%	hot-rolled

\* Offset yield-point at 0.2% strain

Table A-2.8: Results of tests on reinforcement

Test	Nominal Diameter (Ø) [mm]	Yield Strength ( $f_y$ ) [MPa]	Tensile strength ( $f_t$ ) [MPa]	Deformation under maximum load ( $\epsilon_u$ ) [%]	$f_t/f_y$	Distance between anchorages [mm]	Measurement length with extensometer [mm]
DR1_16_1	16	519	612	10.53	1.18	670	150
DR1_16_2	16	516	610	9.92	1.18	670	150
DR1_16_3	16	480	590	11.39	1.23	670	150
DR1_16_4	16	482	590	11.09	1.22	670	150
DR1_12_1	12	542	628	9.04	1.16	790	150
DR1_12_2	12	539	630	8.51	1.17	790	150
DR1_12_4	12	543	630	9.61	1.16	790	150
DR1_22_1	22	536	644	10.33	1.20	660	150
DR1_22_2	22	533	646	12.50	1.21	660	150
DR1_22_3	22	534	642	9.90	1.20	660	150
DR2_14_1	14	517	600	16.30	1.16	500	150
DR2_14_2	14	502	592	10.10	1.18	470	150
DR2_14_3	14	501	588	9.45	1.17	470	150
DR2_14_4	14	500	585	8.59	1.17	470	150
DR2_12_1	12	500*	588	5.95	1.18	525	150
DR2_12_3	12	461*	576	5.25	1.25		150
DR2_12_4	12	445*	575	4.38	1.29		150
DR2_18_1	18	541	639	11.54	1.18	660	150
PR1_10_2	10	566	648	10.53	1.15	595	150
PR1_12_1	12	565	621	9.92	1.10	625	150
PR1_12_2	12	568	624	11.39	1.10	810	150

\* Offset yield-point at 0.2% strain

## Chapter A-2

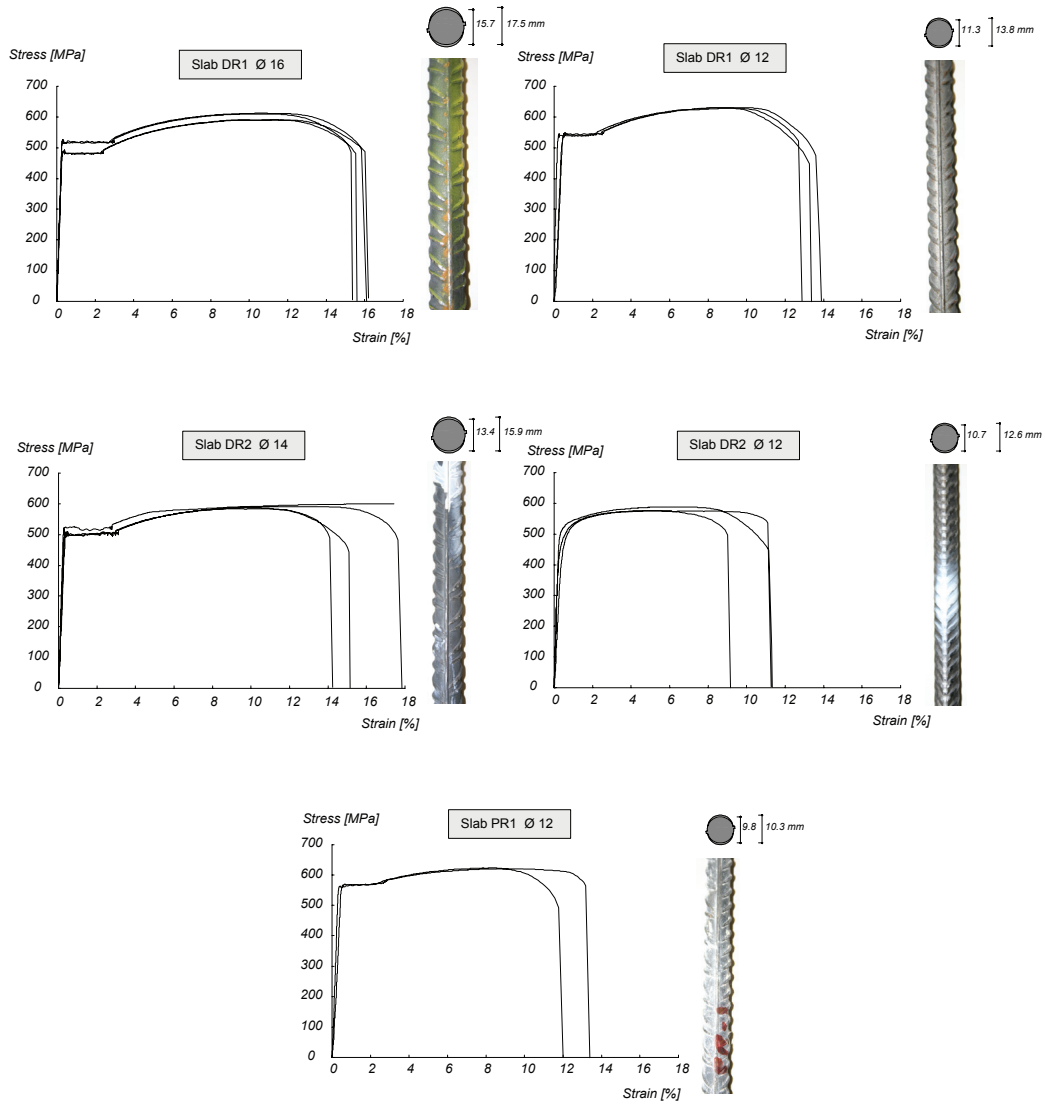


Figure A-2.8: Stress-strain curves for steel bars

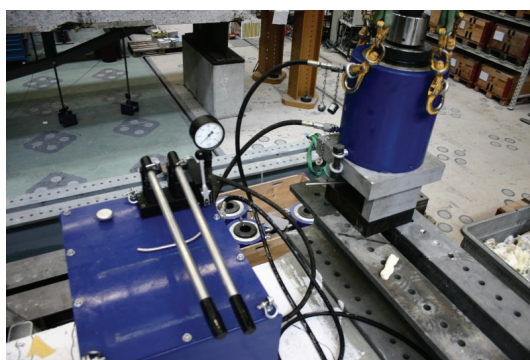
### A-3 Experimental set-up and procedure

All tests have been performed at the Structural Laboratory of the Ecole Polytechnique Fédérale de Lausanne.

#### A-3.1 Reaction frames and load application

Figure A-3.2 shows the test set-up for test DR1-a. Four concentrated loads were applied using square steel plates of 300 x 300 x 30 mm. The distance between the center points of the loads is of 1440 mm in the transversal direction and 900 mm in the longitudinal direction. These dimensions correspond to 3/4 of the dimensions of the twin axle loads prescribed by Eurocode 1 (2003). A hollow hydraulic jack introduced a self-equilibrated stress state in the system. The load was transmitted to the concentrated loads by one steel beam in the transversal direction and four channels in the longitudinal direction. Steel bars of 75 mm of diameter were anchored below the strong floor and above the hydraulic jack. A cylindrical opening of 120 mm of diameter was created in the center of the slab. Spherical nuts and washers were used to accommodate rotation at the anchorage point of the steel bars. The forces were measured at the four applied loads and at the bar above the hydraulic jack. This allowed for redundancy in the system and to know the effective force at each of the four concentrated loads. A hand pump was used in all tests.

A total prestress force of 7 MN was applied at the nine bars behind the fixed end to ensure that the slab was properly clamped. The prestress was applied three weeks after casting. Figure A-3.1 shows the prestressing set-up used to clamp the fixed end of the cantilever.



a) Prestressing set-up



b) Detail of bench and nut

Figure A-3.1: Prestressing of the fixed end of cantilevers DR1 and DR2

Figure A-3.3 illustrates the test set-up for test DR1-b. Only two concentrated loads were applied. The distance between the concentrated loads is of 900 mm in the longitudinal direction. This loading pattern corresponds to half of the loading pattern prescribed by the Eurocode 1 (2003), with dimensions reduced by 3/4.

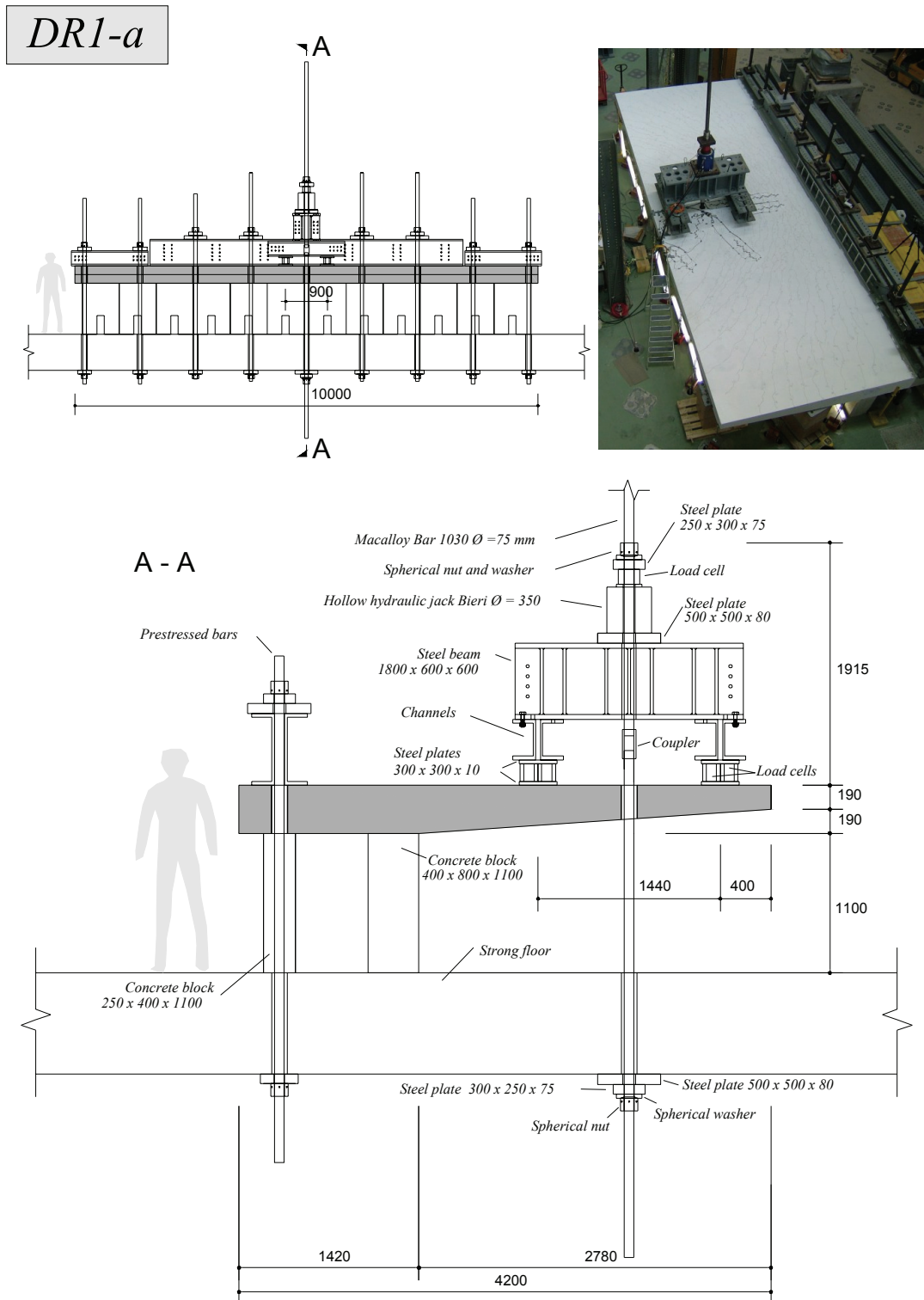


Figure A-3.2: Test set-up for test DR1-a [mm]



DR2-a

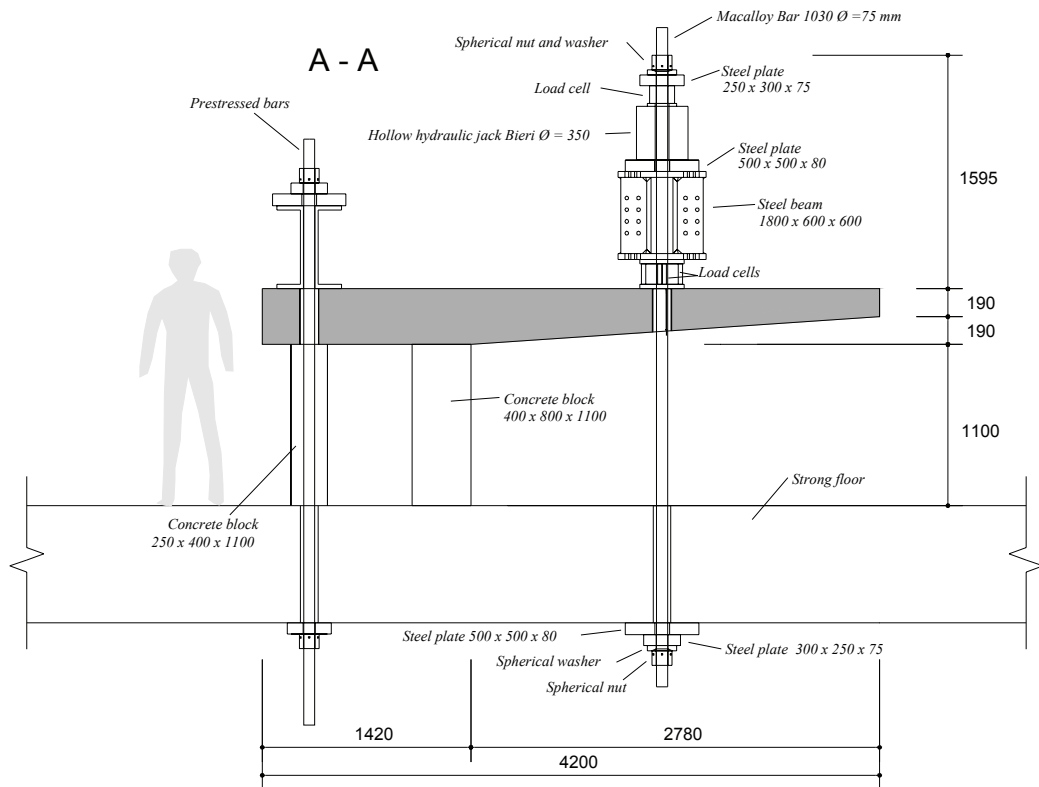
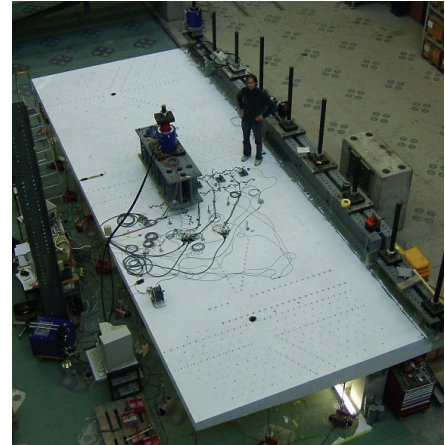
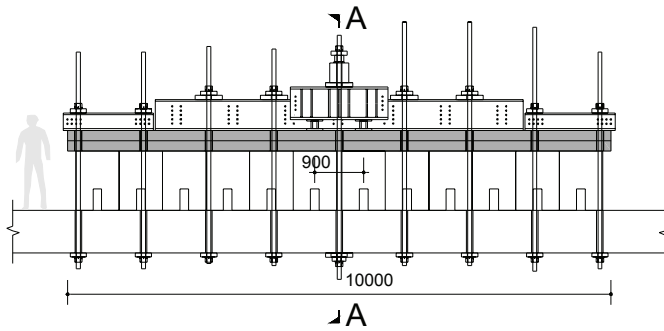


Figure A-3.3: Test set-up for test DR2-a [mm]

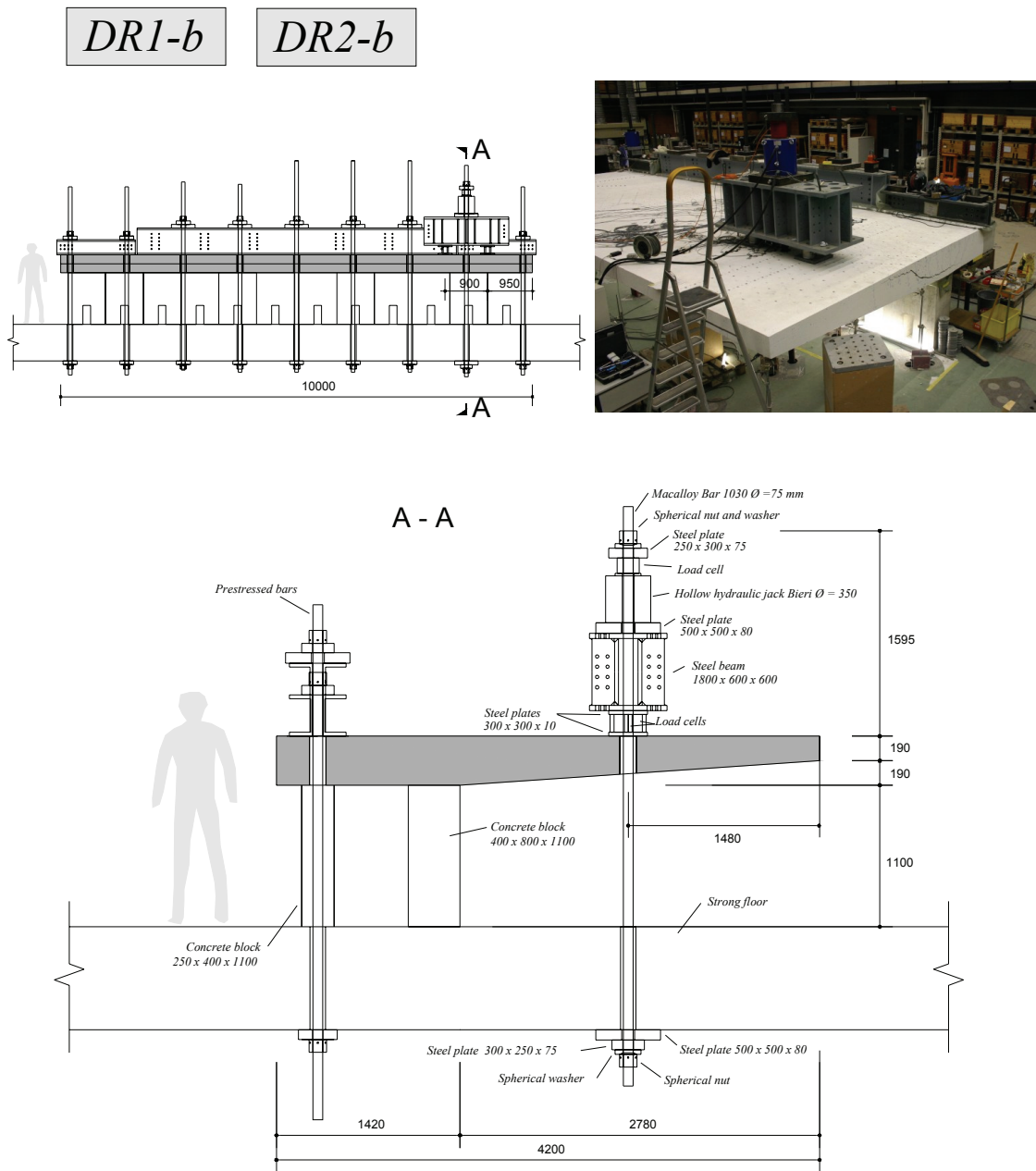


Figure A-3.4: Test set-up for tests DR1-b and DR2-b [mm]

Figure A-3.4 illustrates the test set-up for test DR1-b and DR2-b. Only two concentrated loads were applied, as in the case of test DR2-a. The loads were applied near the short free edge of the cantilever.

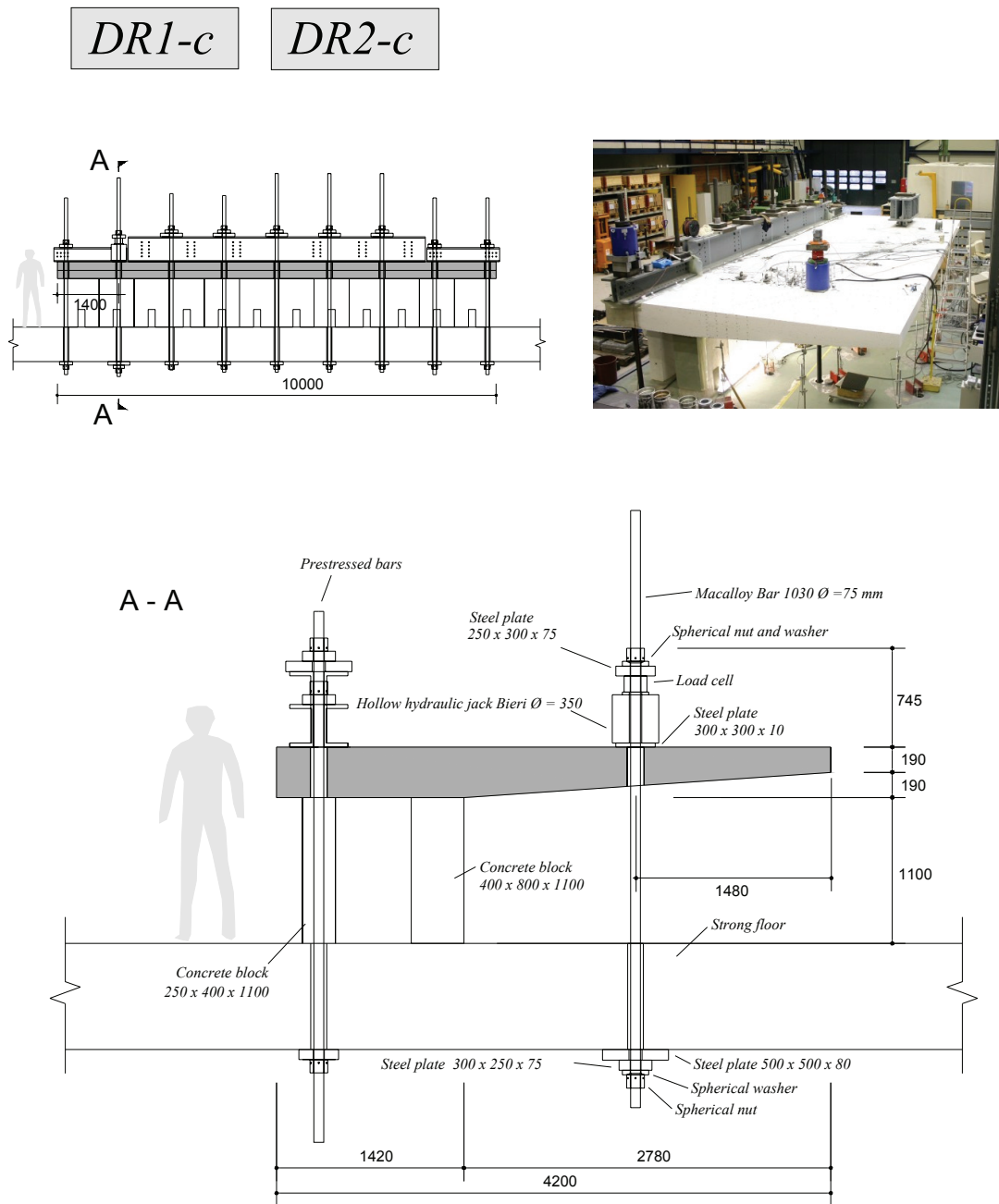


Figure A-3.5: Test set-up for tests DR1-c and DR2-c [mm]

Figure A-3.5 illustrates the test set-up for test DR1-c and DR2-c. Only one concentrated load was applied near the short free edge of the cantilever.

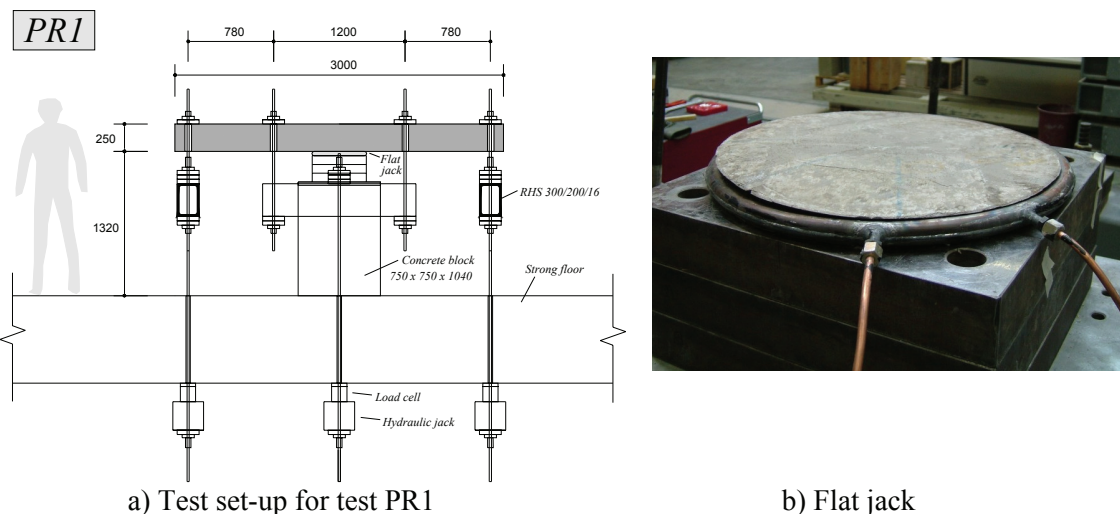


Figure A-3.6: Test set-up for test PR1 [mm]

Figure A-3.6 shows the test set-up for test PR1. The loads were applied using four hydraulic jacks below the strong floor. The force was measured using four load cells between the jacks and the strong floor. At each of the four sides of the slab, two openings were created to allow the introduction of the forces. The central support was a flat jack. The flat jack is made of a copper sheet envelope with water inside. The nominal surface is 0.156 m<sup>2</sup> and the nominal diameter 446 mm. Before the test the flat jack was completely filled with water. During the test the water volume was kept constant.

The self-weight of the steel elements of the test rig is indicated in table A-3.1. For the tests on cantilevers, only the elements in the cantilever part are considered.

Table A-3.1: Self-weight of the test rig

Test	Self-weight [kN]
DR1-a	32.2
DR1-b, DR2-b, DR2-a	22.1
DR1-c, DR2-c	6.7
PR1	16.8

### A-3.2 Preparation of slabs

After the introduction of the prestressing behind the fixed end to ensure that the slabs DR1 and DR2 were properly clamped, the sensors were installed for each test. The following procedure was used to install the sensors:

- The entire cantilever was painted using dispersion white paint.
- The measuring grids (fig. A-3.13) and the position of all sensors were printed on full scale paper of the size of the slab and marked on the bottom and top surfaces.
- The surface was cleaned with compressed air and smoothed with a sanding block at the locations of the sensors.
- The aluminum measuring targets of the demountable deformer grid were glued to the concrete surface using synthetic rapid hardening glue.

- The aluminum supports of the omega-shaped extensometers were glued to the concrete surface using a two component glue, X60.
- The slab was perforated along the cantilever thickness with a 8 mm drill at the measuring locations (only for slab DR2, fig. A-3.9).
- The positions of the demountable deformer were numbered.
- The omega-shaped extensometers, the LVDTs and the inclinometers were installed along with their cables.
- Three computers were installed, one for the omega-shape extensometers, LVDTs and load cells, one for the measurements of the demountable deformer and one for the inclinometers.
- All measuring devices were tested by individually moving them and controlling the response on the computer.
- All measuring devices were zeroed.
- A light load of about 50% of cracking was applied to ensure that all measures were properly saved in the results file.

### A-3.3 Continuous measurements

The following values were continuously measured during the tests:

- The forces were measured using load cells (figs. A-3.2 to A-3.6).
- The deflections were measured using LVDTs (figs. A-3.7 and A-3.11).
- The strains on the concrete surface were measured using omega-shaped extensometers (figs. A-3.8, A-3.9 and A-3.11).
- The rotations of slab were measured using inclinometers (figs. A-3.8, A-3.9 and A-3.11).
- The variation of the thickness of the slab was measured using LVDTs (fig. A-3.9).
- The time was measured with the clock of the computers.

The minimum time interval between two measures is of 10 seconds. The oil pressure was measured for all tests as a redundant value. The figure A-3.10 illustrates the top surface of slab DR2 during test DR2-c.

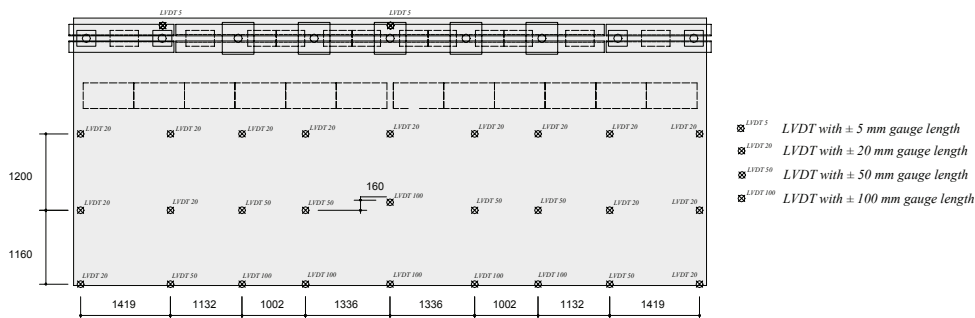


Figure A-3.7: Deflection measurements for all tests on cantilevers (DR1-a, DR1-b, DR1-c, DR2-a, DR2-b and DR2-c) [mm]

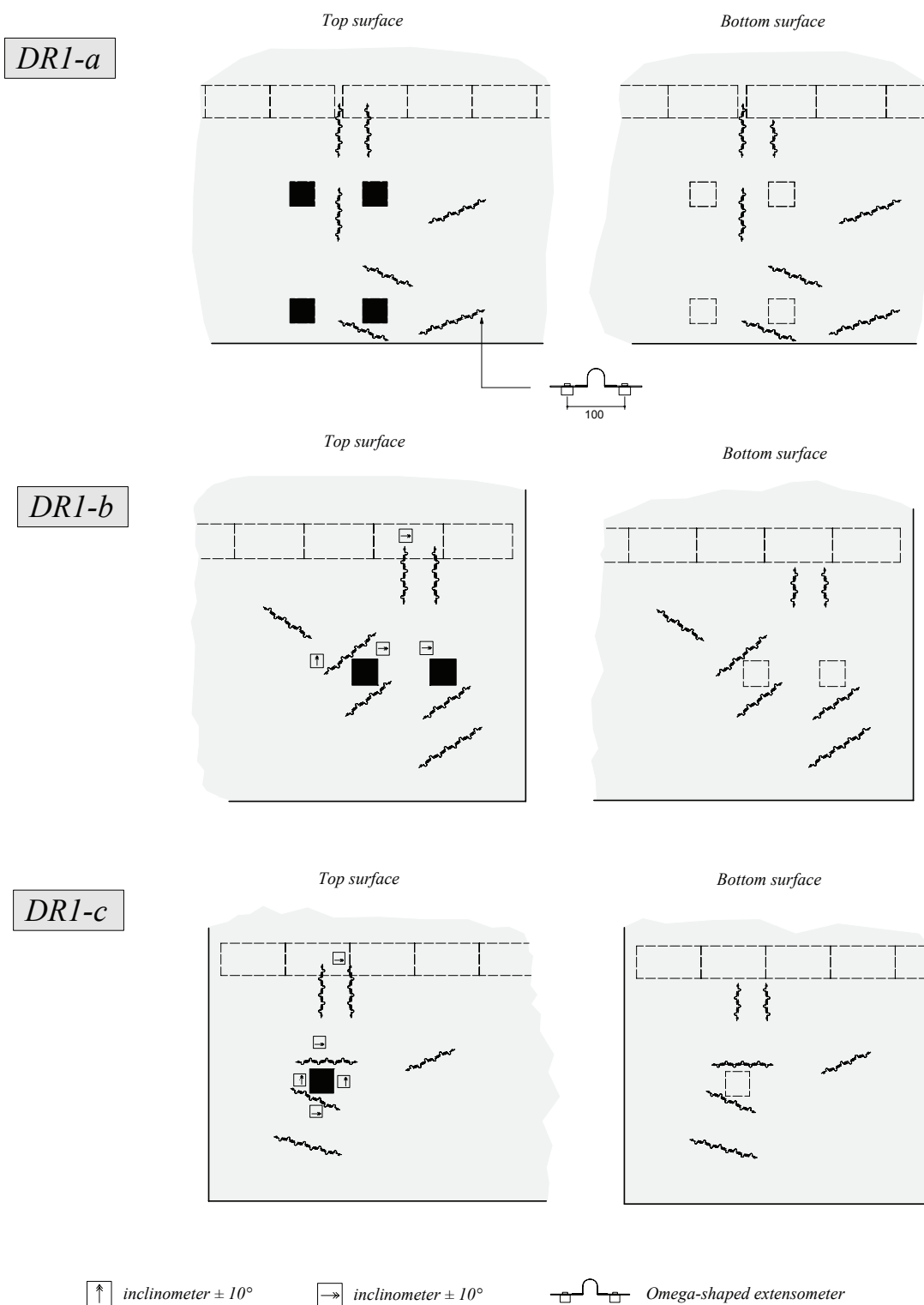


Figure A-3.8: Inclinometers and omega-shaped extensometers for tests DR1-a, DR1-b and DR1-c [mm]

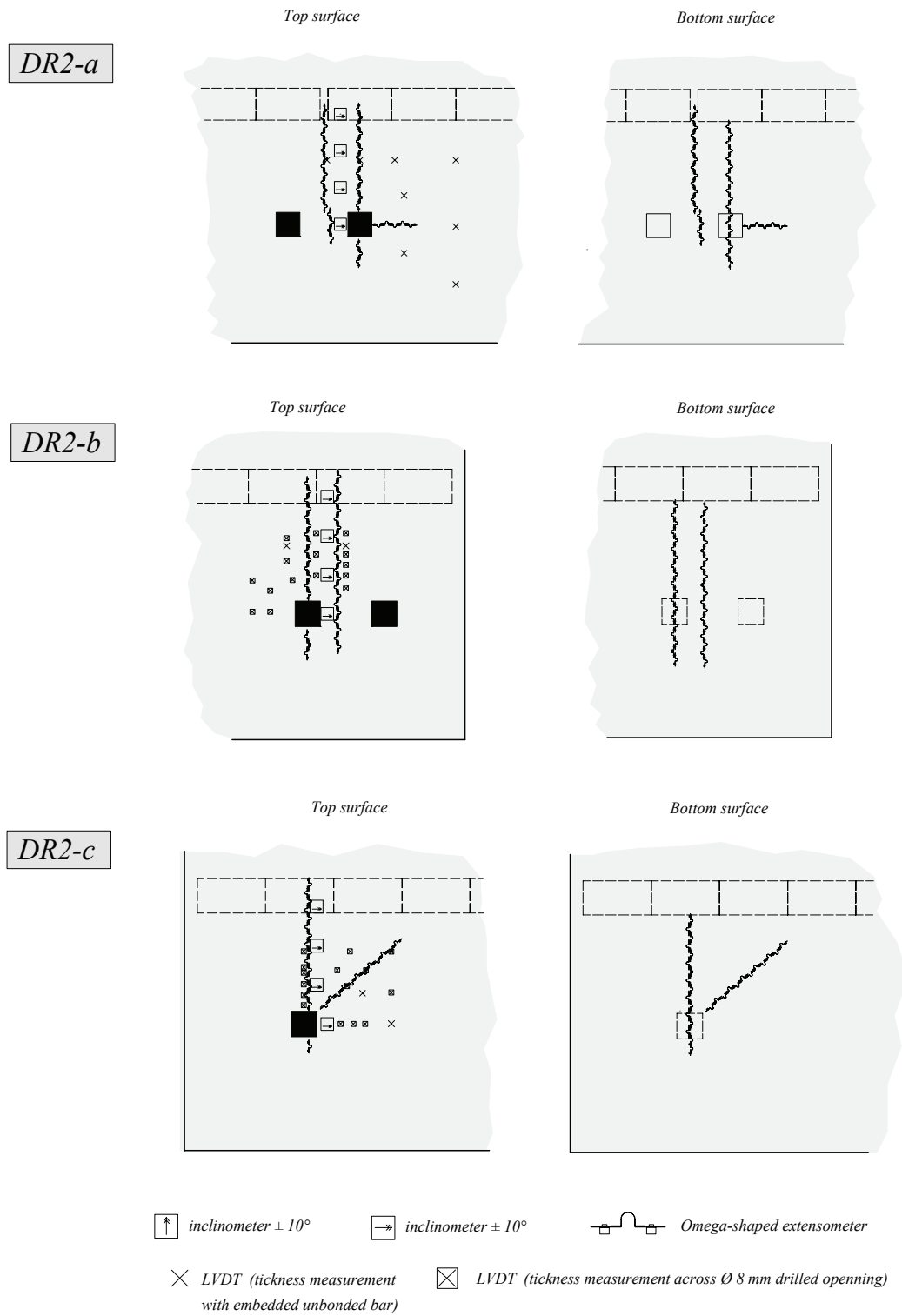


Figure A-3.9: Inclinometers, omega-shaped extensometers and LVDTs used to measure the variation of the tickness of the cantilever (tests DR2-a, DR2-b and DR2-c)

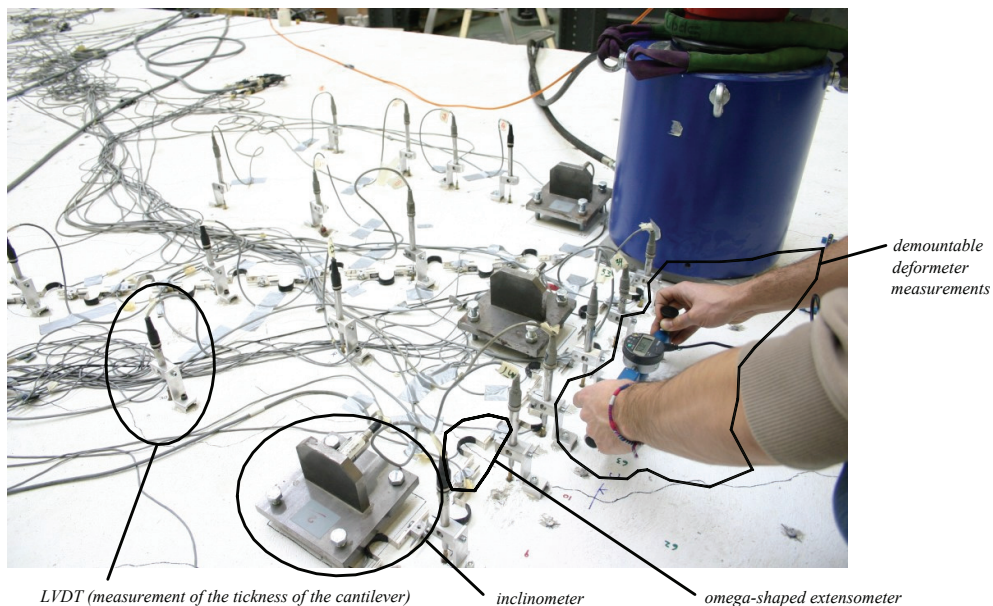


Figure A-3.10: Top surface of slab DR2 during test DR2-c

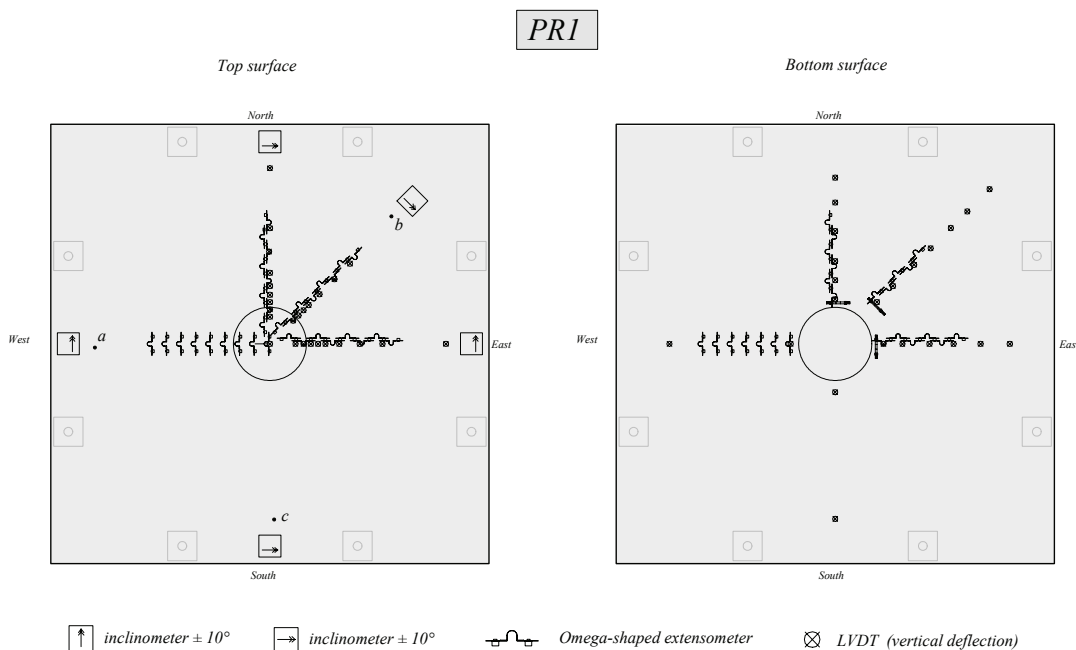


Figure A-3.11: Inclinometers, omega-shaped extensometers and LVDTs for test PR1

For the tests performed on slab DR1, the omega-shaped extensometers were placed in the zones where the largest flexural strains were expected. For tests performed on slab DR2, the omega-shaped extensometers were placed almost exclusively in the region between the concentrated loads and the clamped edge. For slab PR1, the omega-shaped extensometers were placed in the radial direction along three lines and in the tangential direction along one line (fig. A-3.11).

The LVDTs for tests on slabs DR1 and DR2 were arranged in a grid and measured the deflection from the strong floor (fig. A-3.7). Each LVDT was fixed to a structure that was prestressed to the strong floor. This prevented the LVDT to be accidentally



displaced during the tests. Two LVDTs were placed behind the clamped edge. The maximum deflection measured at these locations was of 0.17 mm for test DR1-a at the failure load. This value represents only 0.3% when compared with the measured deflection at the tip of the cantilever. For slab PR1, the LVDTs measured the deflection of the slab at both top and bottom surfaces (fig. A-3.11). The LVDTs on the top surface were fixed to a rigid aluminum structure. The points *a*, *b*, and *c* in figure A-3.11 are the bearing points of the aluminum structure.

The LVDTs were also used to measure the variation of the thickness of the slab for the tests on slab DR2 (fig. A-3.9). Two systems were used. The idea of the first system consists of using a vertical metallic bar of small diameter that is not bonded to concrete (fig. A-3.12a). There is a plastic duct around the metallic bar. A small circular plate is welded in the bottom end of the bar. This point is where the bar is anchored to concrete. The displacements between the top end of the bar and the top surface of the concrete slab are measured using LVDTs. If a shear crack forms, the top end of the bar will be vertically displaced. The value of this displacement is equal to the variation of the thickness of the slab. The metallic bars have to be fixed to the formwork before casting. The second system (fig. A-3.12b) is simpler and consists of using a LVDT that directly measures the displacements across small cylindrical openings, between the top and bottom surfaces of the slab. A drill of 8 mm of diameter and a length of about 450 mm was used to perform the cylindrical openings. The measurements using the first system (fig. A-3.12a) are sensible to the friction between the metallic bar and the plastic duct.

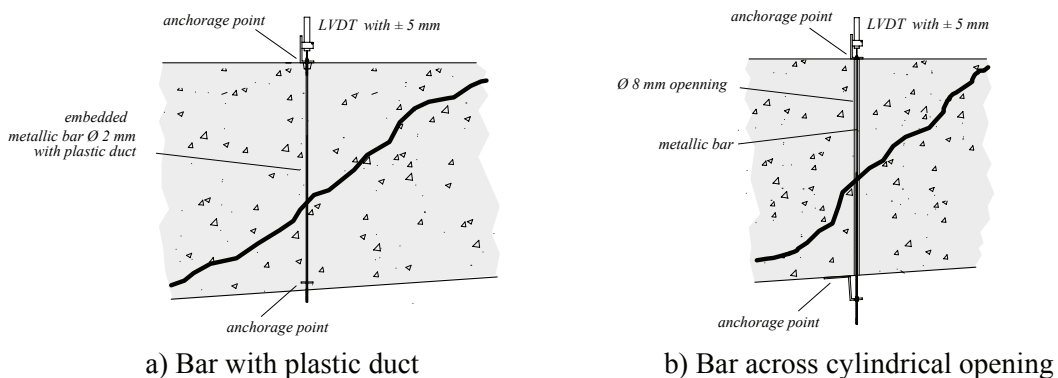


Figure A-3.12: Two systems for measuring the variation of the thickness of the slab

The rotations were measured using inclinometers. The rotation vector is indicated in figs. A-3.8, A-3.9 and A-3.11 at each inclinometer. For the tests on cantilevers, inclinometers were placed between the concentrated loads and the fixed end (figs. A-3.8 and A-3.9). For slab PR1, inclinometers were placed along the perimeter of a circle with diameter of 1380 mm (fig. A-3.11).

For test PR1, the water pressure in the flat jack was measured at each load step (fig. A-3.6).

### A-3.4 Demountable deformer measurements

Figure A-3.13 shows the measuring grids used to determine the in-plane deformations of both top and bottom surfaces of the cantilevers. The measurements with demountable deformers were only made for tests DR1-a, DR2-a, DR2-b and DR2-c. Each line in the grid drawings represents a measurement. The measuring grid represents a highly redundant truss. The redundancy allows the random measuring errors to be distributed, as explained in chapter 4. Three measuring lengths were used ( $500 \pm 5$  mm,  $300 \pm 5$  and

100 ± 5 mm) and two demountable deformeters with accuracy of 5 µm. Measurements of an invar standard were taken approximately every twenty measurements. These measurements were used to account for the temperature changes and drift in the demountable deformeter.

### A-3.5 Test procedure

The operations related to demountable deformeter readings are only applicable to tests DR1-a, DR2-a, DR2-b and DR2-c.

The measuring grid was measured two times at undeformed position. These measurements correspond to load stage 0 and load stage 1.

During the test the sequence of the procedures is controlled using a check-list. Any unexpected event is registered in the lab journal. For each load stage the order of the procedures is the following:

- The frequency of continuous measurements is increased prior to increasing the load.
- At the end of the loading of the structure the pressure is locked-off in the hydraulic cylinders.
- The cracks are drawn and numbered using a heavy marker.
- The openings of the cracks are measured using a magnifying glass.
- Photographs are taken of the crack pattern and of other interesting aspects.
- A complete set of demountable deformeter readings is taken, recorded and controlled in the computer. At this point of load stage the deflections of the slab were stable.

For test DR1-a, the cantilever was subjected to one hundred load cycles at a load level of about 410 kN. The cantilever was afterwards taken to failure.

After failure the slabs were cut into two or more parts and the geometry of the critical shear crack was mapped. For tests DR1-b, DR1-c, DR2-a, DR2-b and DR2-c the geometry of the critical shear crack was three dimensionally mapped. This was performed by isolating the upper part of the slab (separated from the lower part by the surface defined by the shear crack). The distances from the ground to the failure surface were then measured using an optical laser and a measuring grid with about six hundred measuring positions.

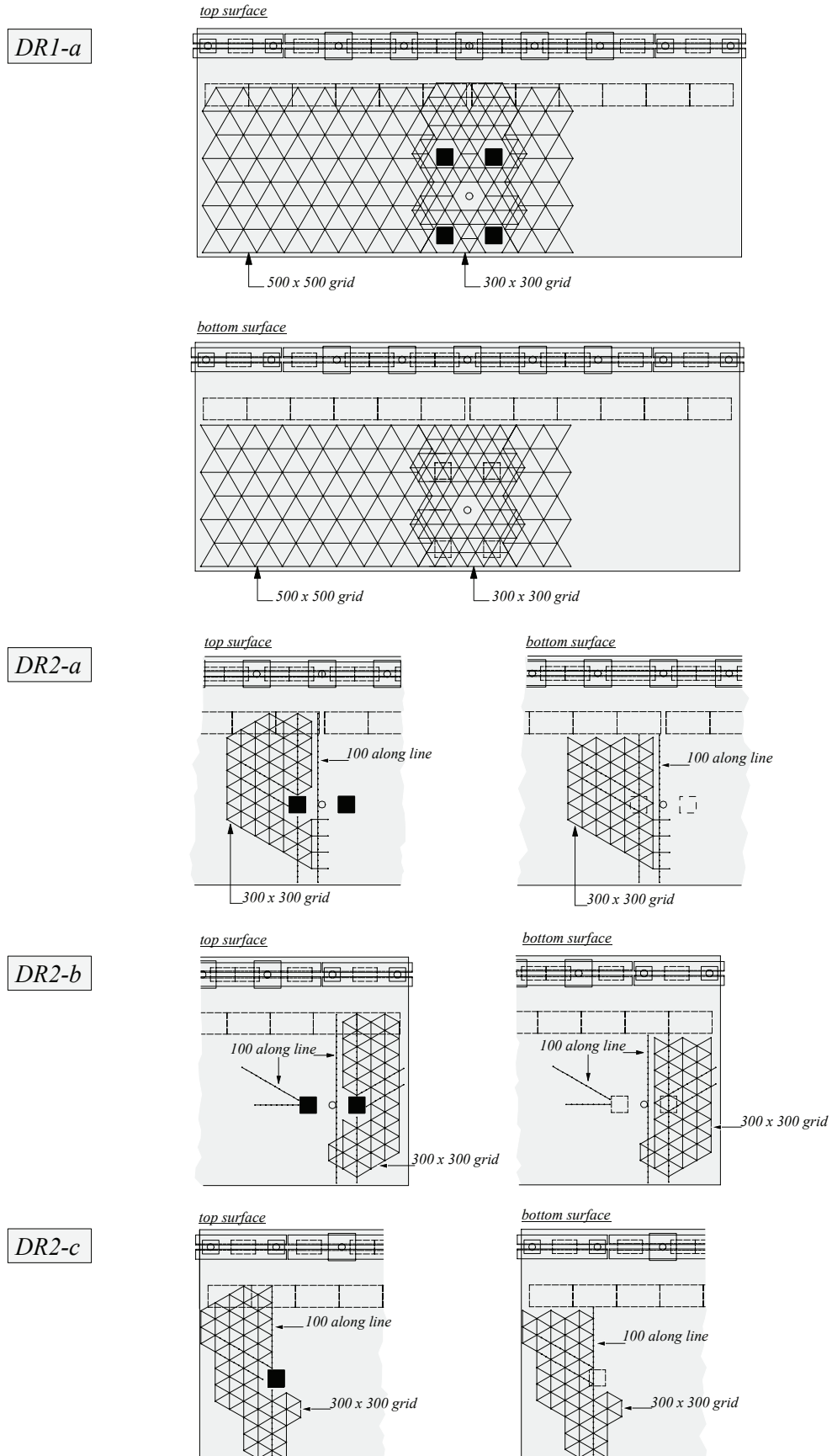


Figure A-3.13: Measuring grids for demountable deformaters (bottom surface as seen from above) [mm]



## A-4 Results

### A-4.1 Analysis and presentation of data

The values of the applied forces were measured simultaneously at load introduction plates and at the  $\varnothing$  75 mm steel bar for tests DR1-a (fig. A-3.2), DR1-b (fig. A-3.4), DR2-a (fig. A-3.3) and DR2-b (fig. A-3.3). The same force value should be obtained for the sum of the measured forces at the load introduction plates and for the measured force at the  $\varnothing$  75 mm steel bar. Very small differences are obtained. For slab DR1a the differences are less than 3%, for slab DR1b less than 1%, for slab DR2a less than 1.5% and for slab DR2b less than 1%. The measured forces at the load introduction plates are only used to calculate the distribution of the total force among the point loads.

The principal strains are calculated from the demountable deformer measurements of the measuring grid (fig. A-3.13). The highly redundant measuring grid allows the measured values to be corrected. The calculations of the corrections and principal strains are described in (Vaz Rodrigues, Muttoni 2004). These procedures were adapted to the grid dimensions used in the present experiments. The stiffness of the truss bars with gross errors was reduced to zero. The correct value of the measurement was determined from the truss analysis. Very few gross errors were found. Tables A-4.1 and A-4.2 show the standard deviation of the corrections for each test and for each load stage. The standard deviation is calculated without consideration of the gross errors.

Table A-4.1: Standard deviation of corrections for demountable deformer readings, for load stages of test DR1-a

Grid	# 0	# 1	# 2	# 3	# 4	# 5	# 6	# 8	# 10	# 11	# 12	# 13	# 14	# 15	# 16	Average
	[ $\mu\text{m}$ ]	[ $\mu\text{m}$ ]	[ $\mu\text{m}$ ]	[ $\mu\text{m}$ ]	[ $\mu\text{m}$ ]	[ $\mu\text{m}$ ]	[ $\mu\text{m}$ ]	[ $\mu\text{m}$ ]	[ $\mu\text{m}$ ]	[ $\mu\text{m}$ ]	[ $\mu\text{m}$ ]	[ $\mu\text{m}$ ]	[ $\mu\text{m}$ ]	[ $\mu\text{m}$ ]	[ $\mu\text{m}$ ]	[ $\mu\text{m}$ ]
300 bottom	4.0	4.9	5.0	2.9	2.6	3.0	5.7	3.5	3.5	3.3	3.7	3.1	3.6	4.7	3.7	3.8
300 top	3.0	2.7	2.5	2.3	2.7	2.5	2.8	2.3	2.5	3.1	2.8	3.7	2.6	6.3	4.6	3.1
500 bottom	13.3	3.1	3.9	5.4	7.1		2.7	3.7	3.4	5.8	3.2	5.5	3.3	7.3	3.3	5.0
500 top	7.1	7.1	7.1	7.6	7.3	10.9	7.9	8.2	7.2	8.4	8.3	7.5	6.6	8.3	7.6	7.8
Average of all grids																4.9

Table A-4.2: Standard deviation of corrections for demountable deformer readings, for load stages of tests DR2-a, DR2-b and DR2-c

Grid	# 0	# 1	# 2	# 3	# 4	# 5	# 6	Average	
	[ $\mu\text{m}$ ]	[ $\mu\text{m}$ ]	[ $\mu\text{m}$ ]	[ $\mu\text{m}$ ]	[ $\mu\text{m}$ ]	[ $\mu\text{m}$ ]	[ $\mu\text{m}$ ]	[ $\mu\text{m}$ ]	
DR2-a 300 bottom	7.4	2.5	1.8	6.8	2.0			4.1	
DR2-a 300 top	1.7	1.3	0.9	1.2	4.6			1.9	
DR2-b 300 bottom	5.4	5.7	2.5	2.9	2.6	3.6	2.8	3.7	
DR2-b 300 top	2.1	2.6	1.4	1.4	1.5	1.3	1.4	1.7	
DR2-c 300 bottom	4.4	4.1	2.2	5.5	3.4			3.9	
DR2-c 300 top	1.7	1.2	1.2	1.5	1.6			1.4	
Average of all grids									2.8

For test DR1-a the standard deviation of the corrections applied to the 300 mm measuring grid are smaller than those applied to the 500 mm measuring grid (table A-4.1). For the other measuring grids (table A-4.2), the standard deviation of measurements made from the bottom side is always larger than the standard deviation from the top side. This can be explained because of the uncomfortable measuring position (upside-down). Figure A-4.1 shows the dispersion of the corrections for two

extreme cases. The normal distribution is represented using the average and standard deviation of the corresponding load stage. The average standard deviation of the corrections is  $4.2 \mu\text{m}$  (0.01 ‰) for all grids and tests.

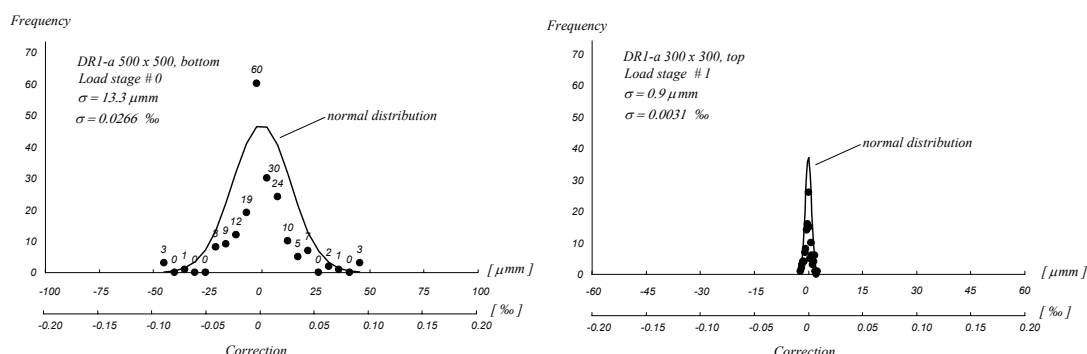


Figure A-4.1: Two load stages with large and small dispersion of corrections

The following results are presented for the tests:

- Force-deflection curves and force-time curves. The force  $Q$  is the measured on the  $\varnothing 75$  mm steel bar that applied the total load, above the hollow hydraulic jack. The self weight of the slab and test rig is not included in the diagrams.
- Tables with force values and deflection values at key locations, at the beginning of the load stage, at the end of the demountable deformer measurements and at the end of the load stage.
- The principal strains on top and bottom surfaces, with the cracks on background, for three representative chosen load stages (only for tests DR1-a, DR2-a, DR2-b and DR2-c).
- A photo of the failure.
- A sectional view of the cantilever showing the position of the shear cracks. The evolution of the surface strains measured on the concrete surface with the omega-shaped extensometers is also represented. The evolution of the rotations is represented from the measurements of the inclinometers.
- Level curves of the shear failure surface (only for tests DR1-b, DR1-c, DR2-a, DR2-b and DR2-c).
- Plots showing the variation of thickness of slab until failure (only for tests DR2-a, DR2-b and DR2-c).

The behavior under service loads was investigated in test DR1-a, under a total load of approximately 410 kN and at a low number of cycles (one hundred cycles). Magnified photos of the crack openings under and without load are shown. A diagram is provided with the evolution of the residual and under load crack openings and deflection under increasing cycles.

A-4.2 Test DR1-a

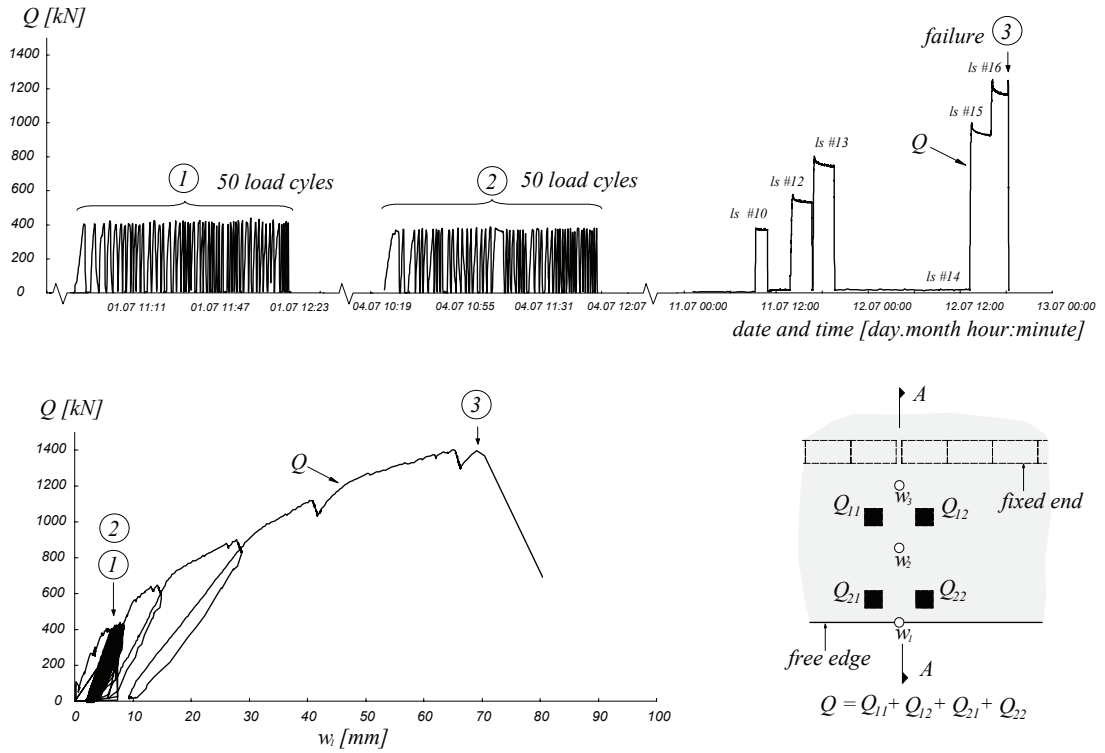


Figure A-4.2: Test DR1-a: Load history and load-deflection curve

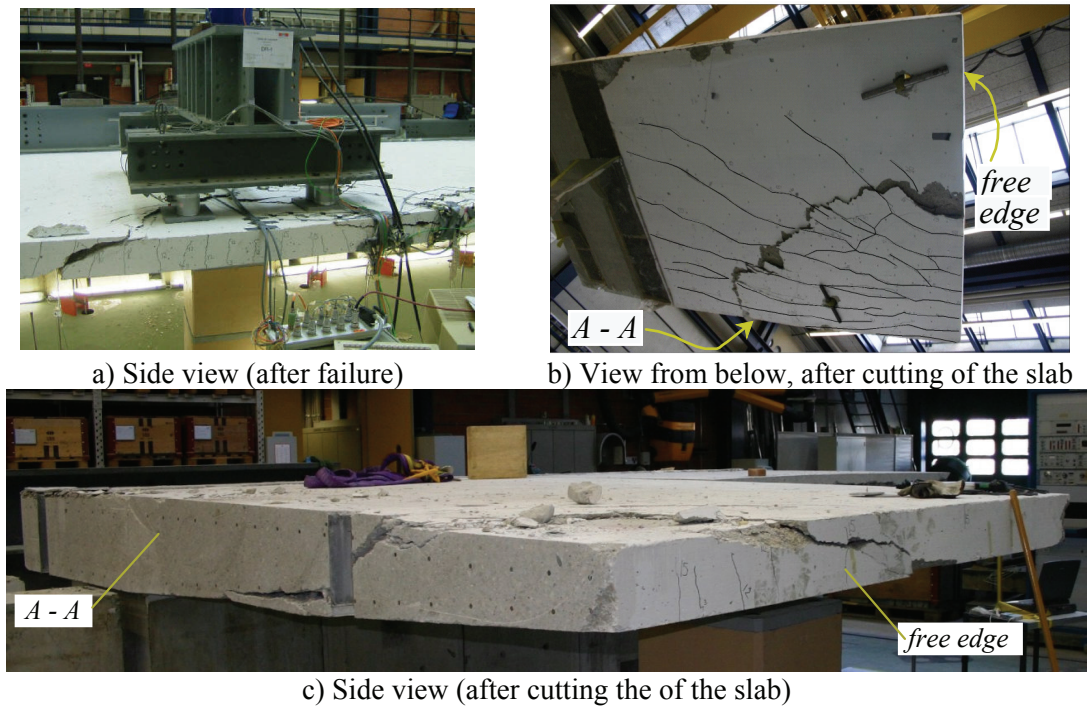


Figure A-4.3: Test DR1-a: Shear failure

Table A-4.3: Test DR1-a: Evolution of some measured values

Load stage	$Q$	$Q_{11}/Q$	$Q_{12}/Q$	$Q_{21}/Q$	$Q_{22}/Q$	$w_1$	$w_2$	$w_3$	$Q/Q_{FL}$	Remark
	[kN]	-	-	-	-	[mm]	[mm]	[mm]	%	
#0	4.1	15.3%	40.0%	20.0%	24.8%	0.1	0.0	0.0		
#1	10.8	15.8%	37.4%	17.8%	29.0%	0.1	0.1	0.0		
#2	278.7	17.1%	34.3%	32.0%	16.6%	3.5	1.8	0.5	20%	B
	265.3	17.0%	34.6%	32.1%	16.4%	3.5	1.8	0.5	19%	M
	258.7	16.8%	34.7%	32.2%	16.2%	3.5	1.7	0.5	19%	E
#3	399.6	18.7%	32.6%	30.6%	18.1%	5.9	2.9	0.8	29%	B
	383.8	18.5%	32.8%	30.7%	18.0%	6.0	2.9	0.8	27%	M
	373.5	18.4%	32.9%	30.8%	17.9%	6.1	2.9	0.8	27%	E
	1.0					2.1	1.5	0.2	0%	B
#4	0.2					2.1	1.5	0.2	0%	M
	1.1					2.0	7.1	0.2	0%	E
	413.0	19.0%	31.7%	30.4%	18.9%	8.0	5.0	1.0	30%	B
#5	411.7	19.0%	31.7%	30.4%	18.9%	8.0	5.0	1.0	29%	M
	406.0	18.9%	31.8%	30.5%	18.8%	8.0	5.0	1.0	29%	E
	5.4					3.0	1.7	0.3	0%	B
#6	3.8					3.0	1.7	0.4	0%	M
	2.7					3.0	1.6	0.4	0%	E
	406.1	19.0%	31.7%	30.5%	18.9%	8.2	4.1	1.0	29%	B
#7	402.2	18.9%	31.7%	30.5%	18.9%	8.2	4.1	1.0	29%	M
	386.9	18.8%	31.9%	30.6%	18.7%	8.1	4.1	1.0	28%	E
	413.0	19.1%	31.5%	30.4%	19.1%	8.5	4.4	1.0	30%	B
#8	412.0	19.0%	31.5%	30.4%	19.1%	8.5	4.4	1.0	29%	M
	399.7	18.9%	31.7%	30.5%	18.9%	8.4	4.4	1.0	29%	E
	6.2					3.4	2.0	0.4	0%	B
	4.0					3.4	2.0	0.3	0%	M
#9	6.6					3.3	1.9	0.3	0%	E
	422.0	19.0%	31.6%	30.2%	19.1%	8.4	4.5	0.9	30%	B
	420.9	19.0%	31.7%	30.2%	19.1%	8.4	4.4	0.9	30%	M
#10	411.2	18.9%	31.7%	30.4%	19.0%	8.4	4.7	1.0	29%	E
	14.3					3.5	2.4	0.4	1%	B
	19.0					3.4	2.4	0.4	1%	M
	20.2					3.4	2.7	0.4	1%	E
#11	629.0	20.9%	30.1%	28.4%	20.6%	14.5	7.5	1.5	45%	B
	616.4	20.9%	30.2%	28.4%	20.6%	14.6	7.5	1.5	44%	M
	597.7	20.9%	30.1%	28.2%	20.7%	14.8	6.9	1.6	43%	E
#12	871.5	22.2%	28.6%	27.3%	21.9%	28.2	12.2	2.7	62%	B
	862.7	22.2%	28.7%	27.3%	21.8%	28.3	12.2	2.7	62%	M
	841.9	22.1%	28.7%	27.3%	21.8%	28.6	12.3	2.8	60%	E
#13	19.5					9.4	4.2	0.8	1%	B
	17.1					9.4	4.2	0.9	1%	M
	17.5					9.4	4.2	0.9	1%	E
#14	1084.2	22.7%	27.8%	26.9%	22.6%	41.3	17.7	4.0	78%	B
	1073.2	22.7%	27.9%	26.9%	22.5%	41.4	17.6	4.0	77%	M
	1047.4	22.7%	27.9%	26.9%	22.5%	41.6	17.4	4.0	75%	E
#15	1361.9	24.1%	26.1%	25.6%	24.3%	65.7	27.2	6.7	97%	B
	1328.7	24.2%	26.0%	25.5%	24.4%	66.0	27.2	6.8	95%	M
	1303.5	24.2%	26.0%	25.4%	24.3%	66.3	27.1	6.8	93%	E
ML	1397.2	24.4%	25.7%	25.3%	24.6%	69.1	28.1	7.1	100%	ML
FL	1397.2	24.4%	25.7%	25.3%	24.6%	69.1	28.1	7.1	100%	FL

B : Beginning of load stage ; M : End of demountable deformer measurements ; E : End of load stage ; ML : Maximum load ; FL : Failure Load



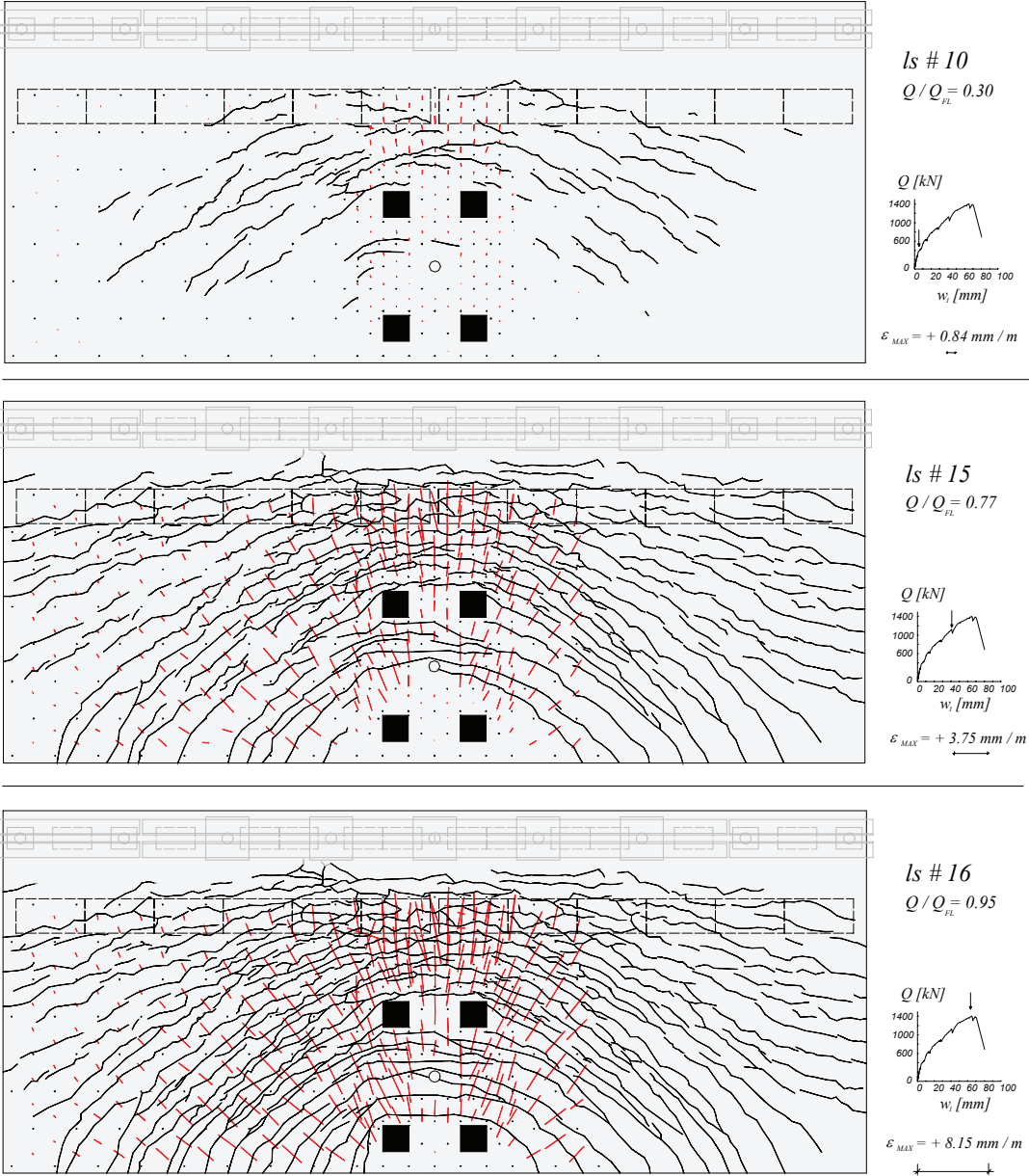


Figure A-4.4: Test DR1-a: Crack pattern and tensile principal strains on the top surface

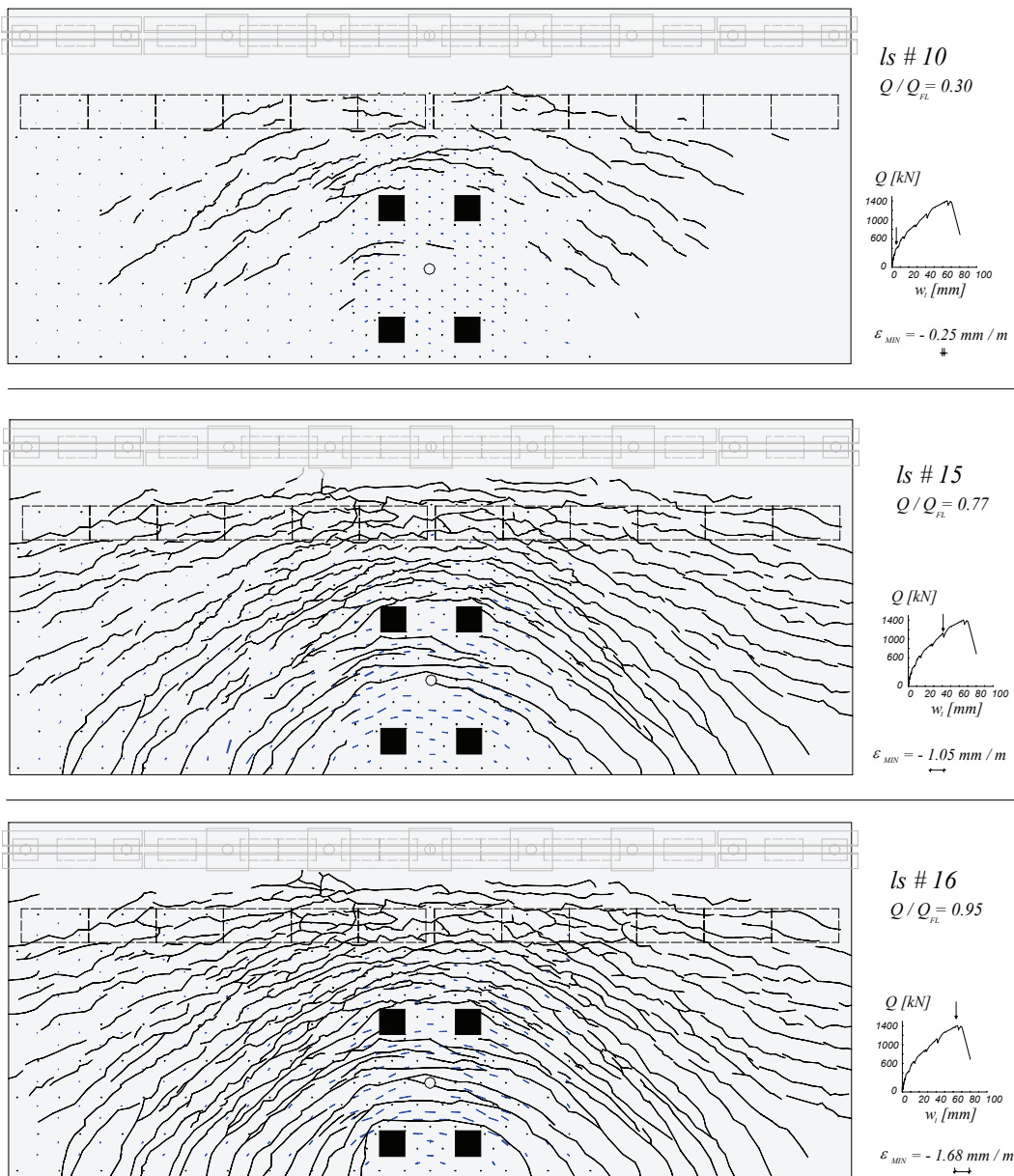


Figure A-4.5: Test DR1-a: Crack pattern and compressive principal strains on the top surface

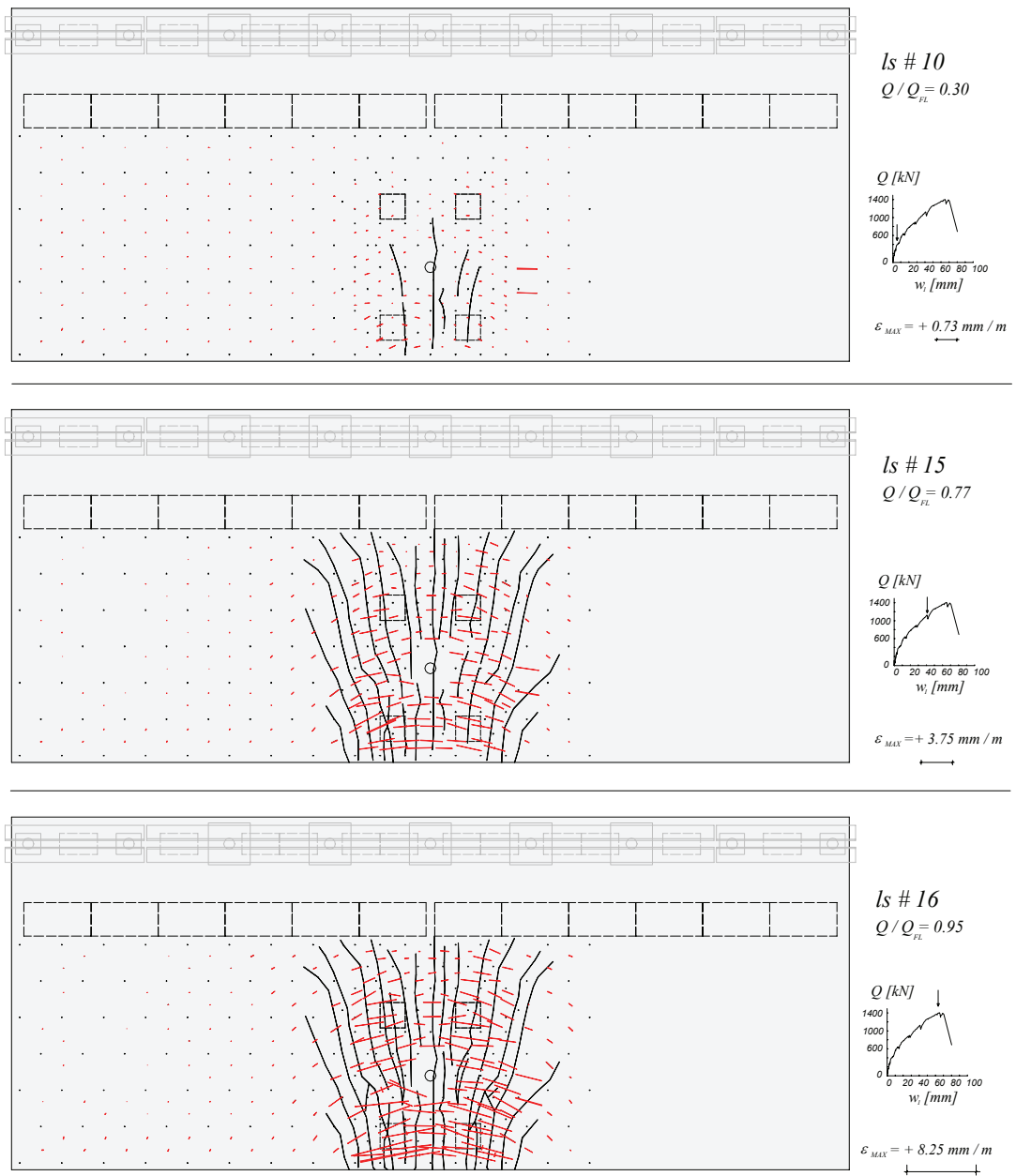


Figure A-4.6: Test DR1-a: Crack pattern and tensile principal strains on the bottom surface (as seen from above)

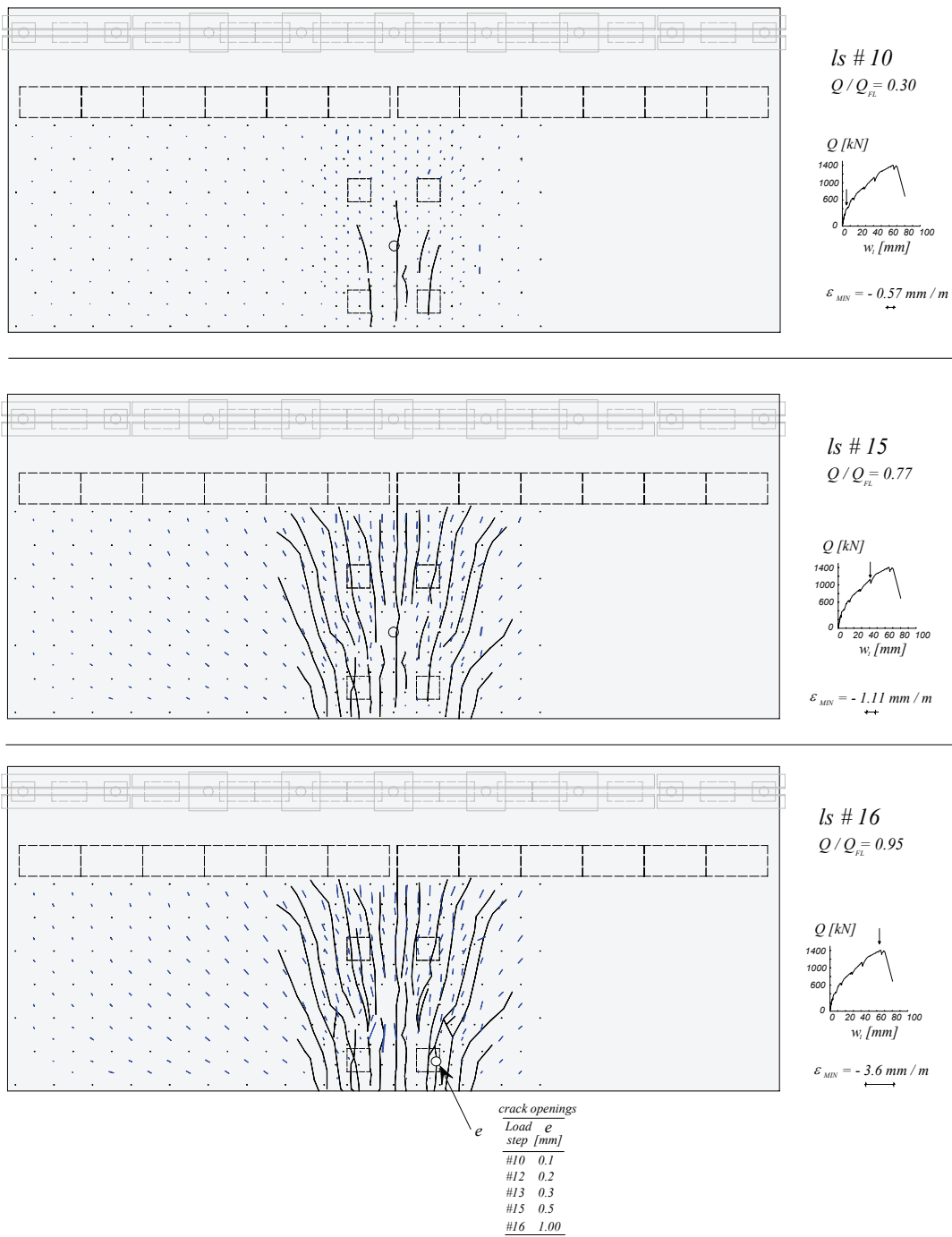


Figure A-4.7: Test DRI-a: Crack pattern and compressive principal strains on the bottom surface (as seen from above)

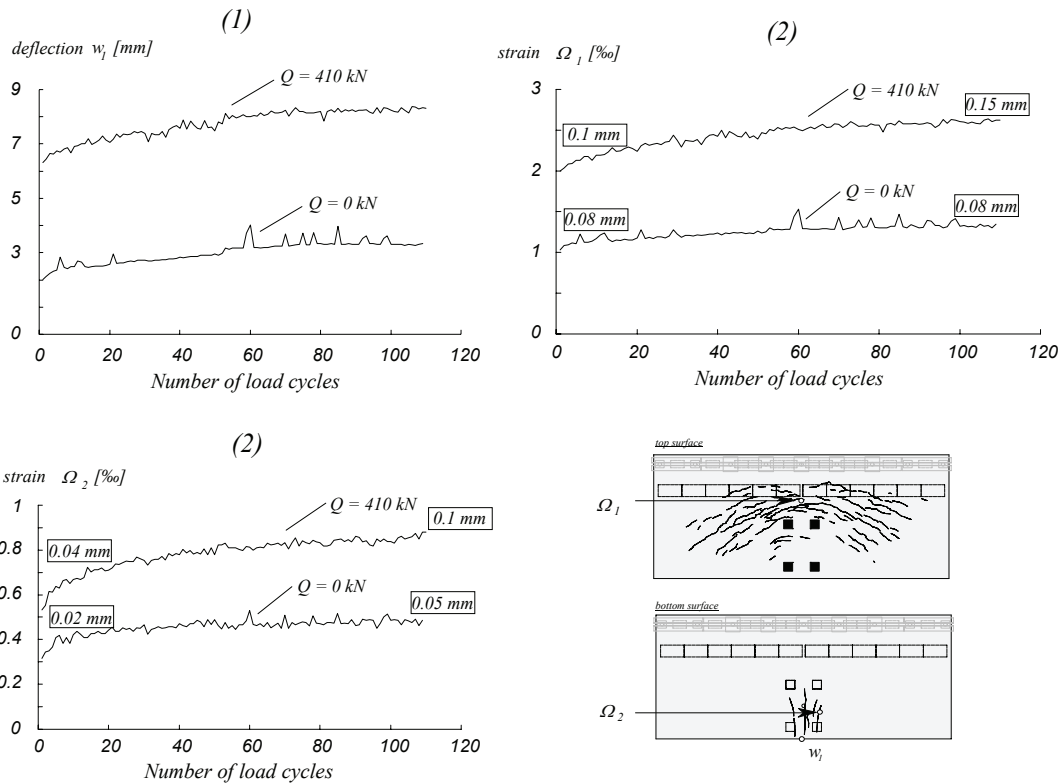
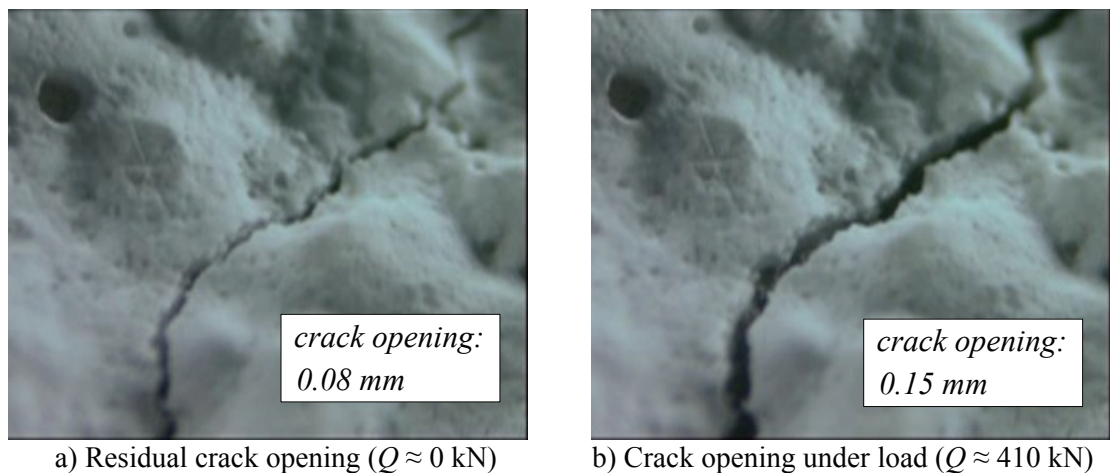


Figure A-4.8: Test DRI-a: (1) Evolution of the deflection with number of load cycles; (2) Evolution of maximal strains measured with omega-shaped extensometers on the concrete surface (length of measurement: 100 mm). The associated crack openings are indicated



a) Residual crack opening ( $Q \approx 0 \text{ kN}$ )

b) Crack opening under load ( $Q \approx 410 \text{ kN}$ )

Figure A-4.9: Test DRI-a: Maximal crack openings at the top surface of the cantilever after the load cycles

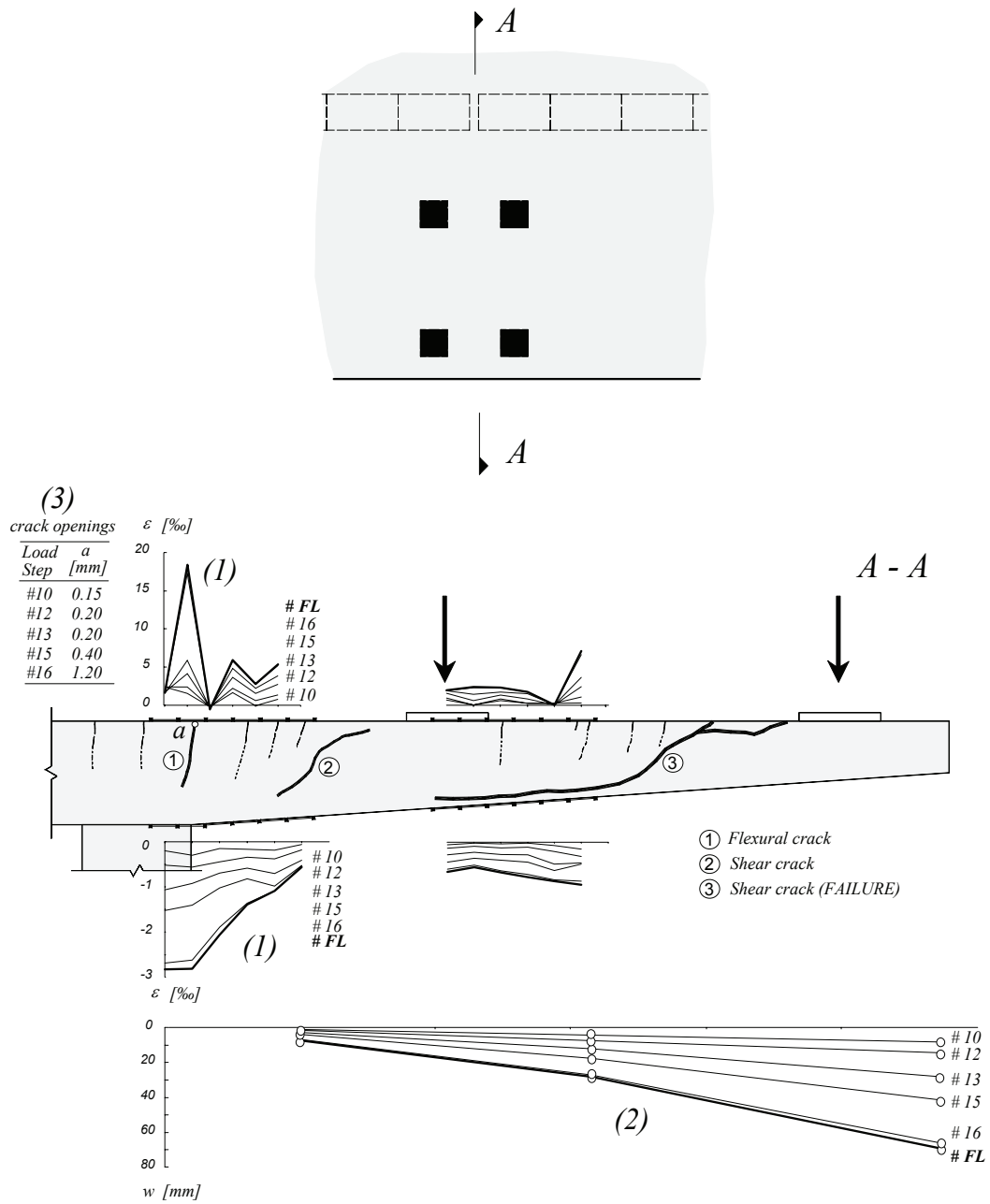


Figure A-4.10: Test DR1-a: (1) Strains measured on the surface of the slab with omega-shaped extensometers (100 mm length) ; (2) Deflections measured with LVDTs; (3) Crack openings measured with magnifying glass

A-4.3 Test DR1-b

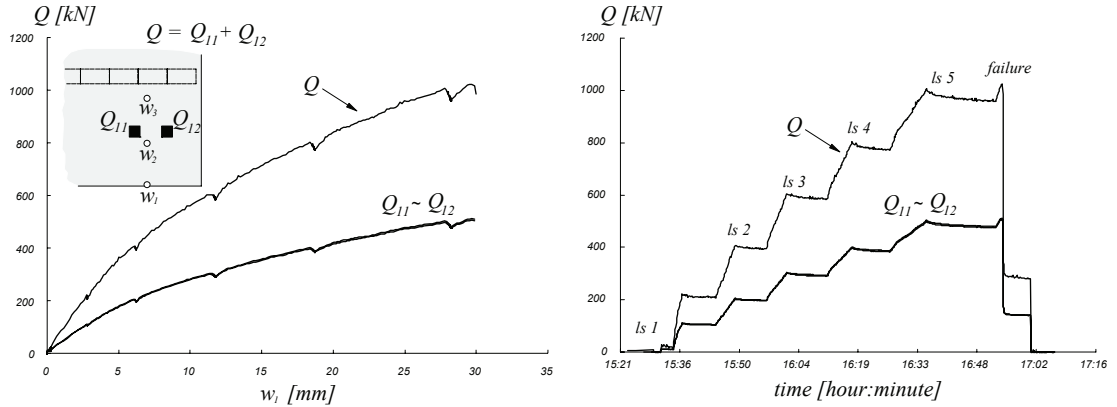


Figure A-4.11: Test DR1-b: Load history and load-deflection curve

Table A-4.4: Test DR1-b: Evolution of some measured values

Load stage	Q [kN]	Q <sub>11</sub> / Q	Q <sub>12</sub> / Q	w <sub>1</sub> [mm]	w <sub>2</sub> [mm]	w <sub>3</sub> [mm]	Q / Q <sub>FL</sub> [%]	Remark
#1	6.5	39.0%	61.0%	0.0	0.0	0.0		
#2	403.0	50.3%	49.7%	6.2	3.8	1.0	39%	
#3	595.9	50.3%	49.7%	11.7	7.0	1.7	58%	
#4	790.1	50.3%	49.7%	18.6	11.2	2.6	77%	
#5	984.4	50.3%	49.7%	28.1	17.0	3.7	96%	
ML	1030.0	50.2%	49.8%	29.7	18.0	3.9	101%	ML
FL	1024.5	50.2%	49.8%	29.9	18.1	3.9	100%	FL

ML : Maximum load ; FL : Failure Load

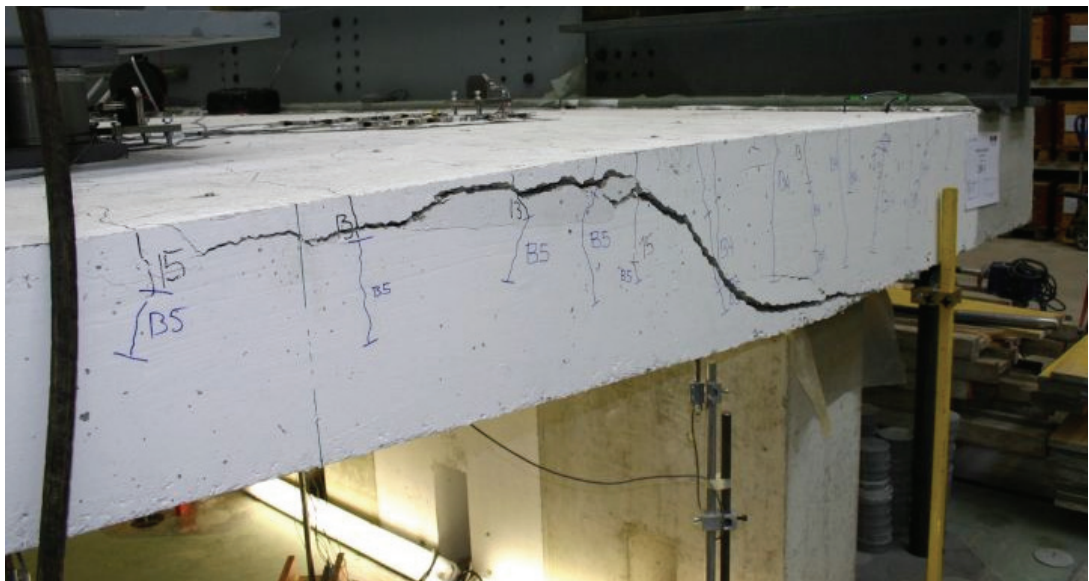


Figure A-4.12: Test DR1-b: Side view of the shear crack after failure

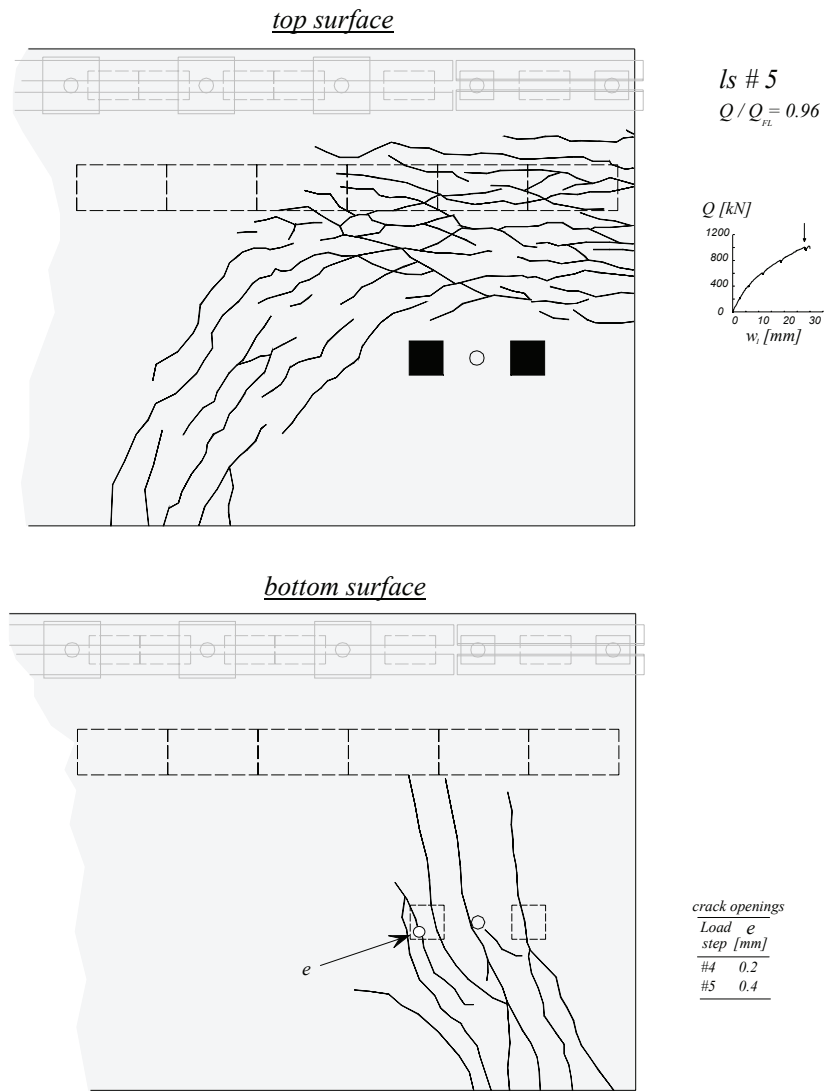


Figure A-4.13: Test DR1-b: Crack pattern



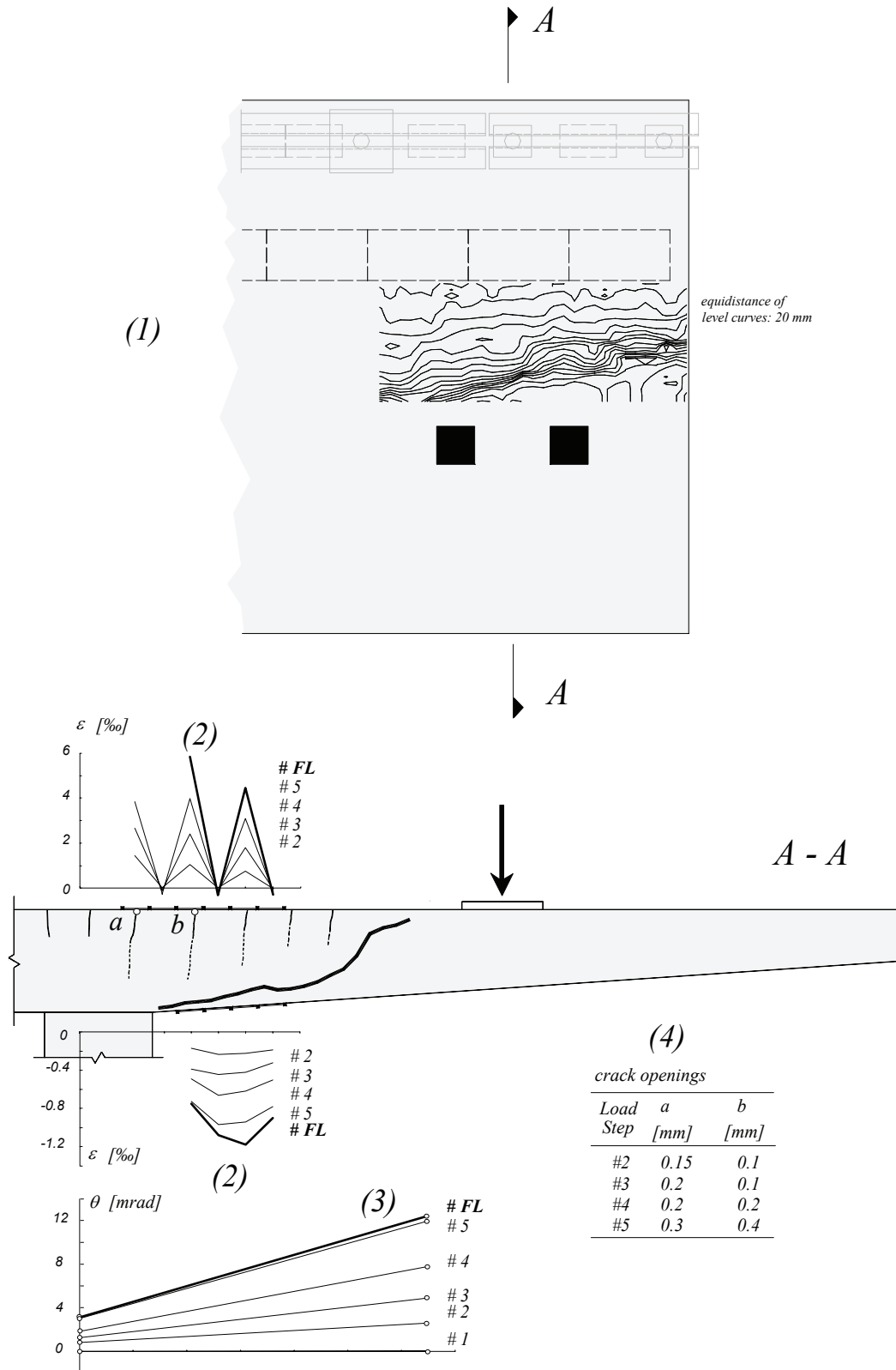


Figure A-4.14: Test DR1-b: (1) Level curves of the shear crack; (2) Strains measured on the surface of the slab with omega-shaped extensometers (100 mm length); (3) Rotations measured with inclinometers; (4) Crack openings measured with magnifying glass

A-4.4 Test DR1-c

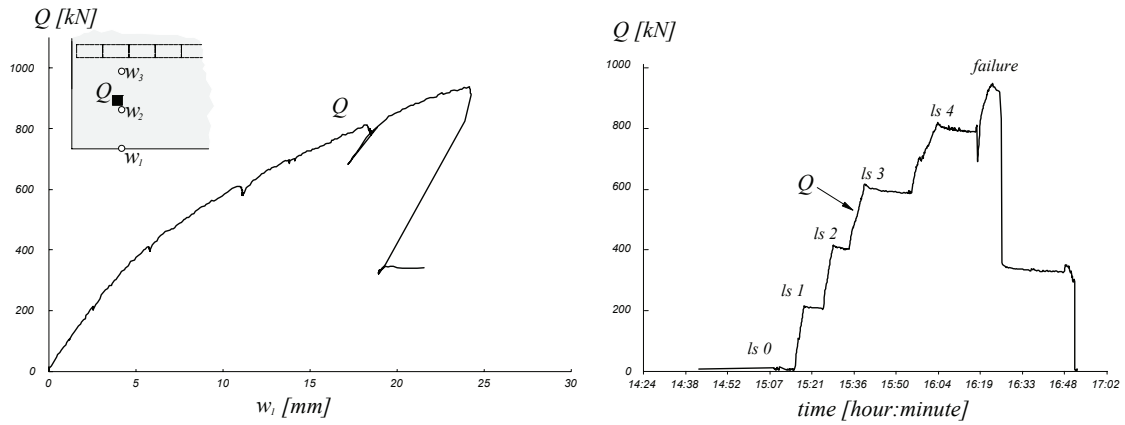


Figure A-4.15: Test DR1-c: Load history and load-deflection curve

Table A-4.5: Test DR1-c: Evolution of some measured values

Load stage	Q [kN]	w <sub>1</sub> [mm]	w <sub>2</sub> [mm]	w <sub>3</sub> [mm]	Q / Q <sub>FL</sub> [%]	Remark
#0	4.4	0.0	0.0	0.0		-
#1	208.3	2.5	1.6	0.4	23%	
#2	401.7	5.8	3.6	0.9	44%	
#3	586.7	11.1	6.9	1.7	64%	
#4	789.6	18.5	11.3	2.7	87%	
ML	938.0	24.2	14.3	3.4	103%	ML
FL	910.0	24.2	14.4	3.5	100%	FL

ML : Maximum load ; FL : Failure Load

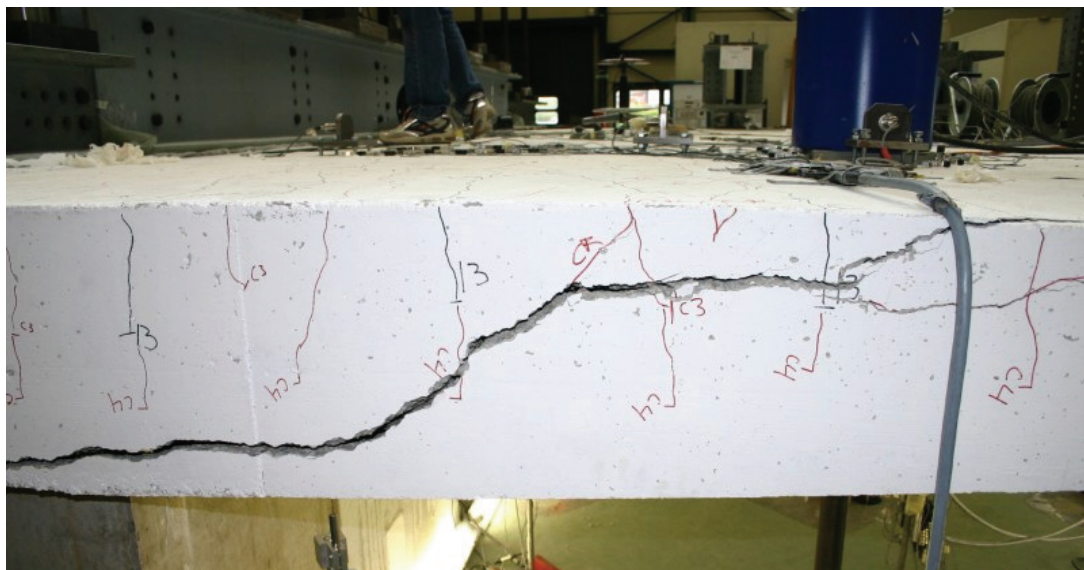


Figure A-4.16: Test DR1-c: Side view of the shear crack after failure

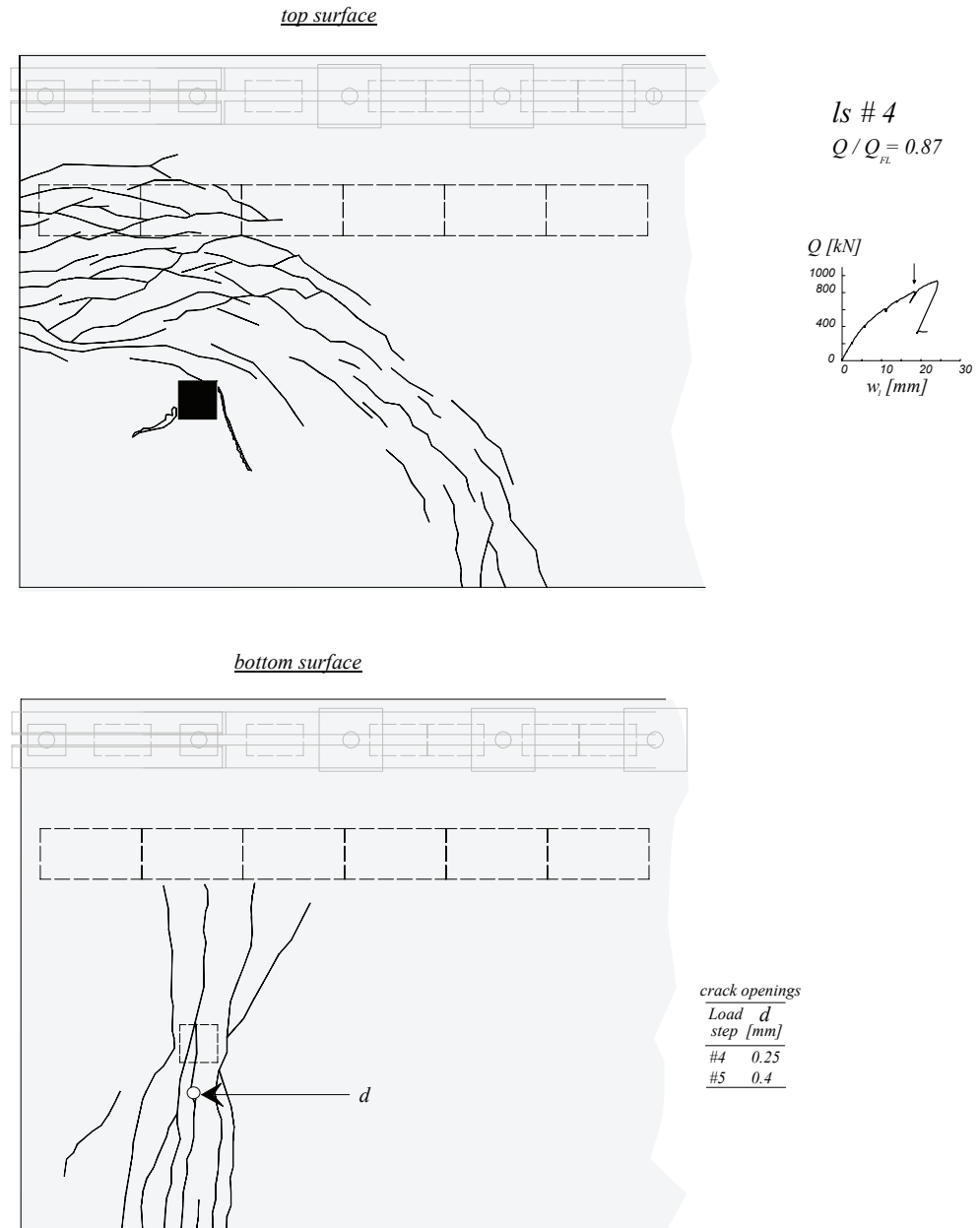


Figure A-4.17: Test DR1-c: Crack pattern

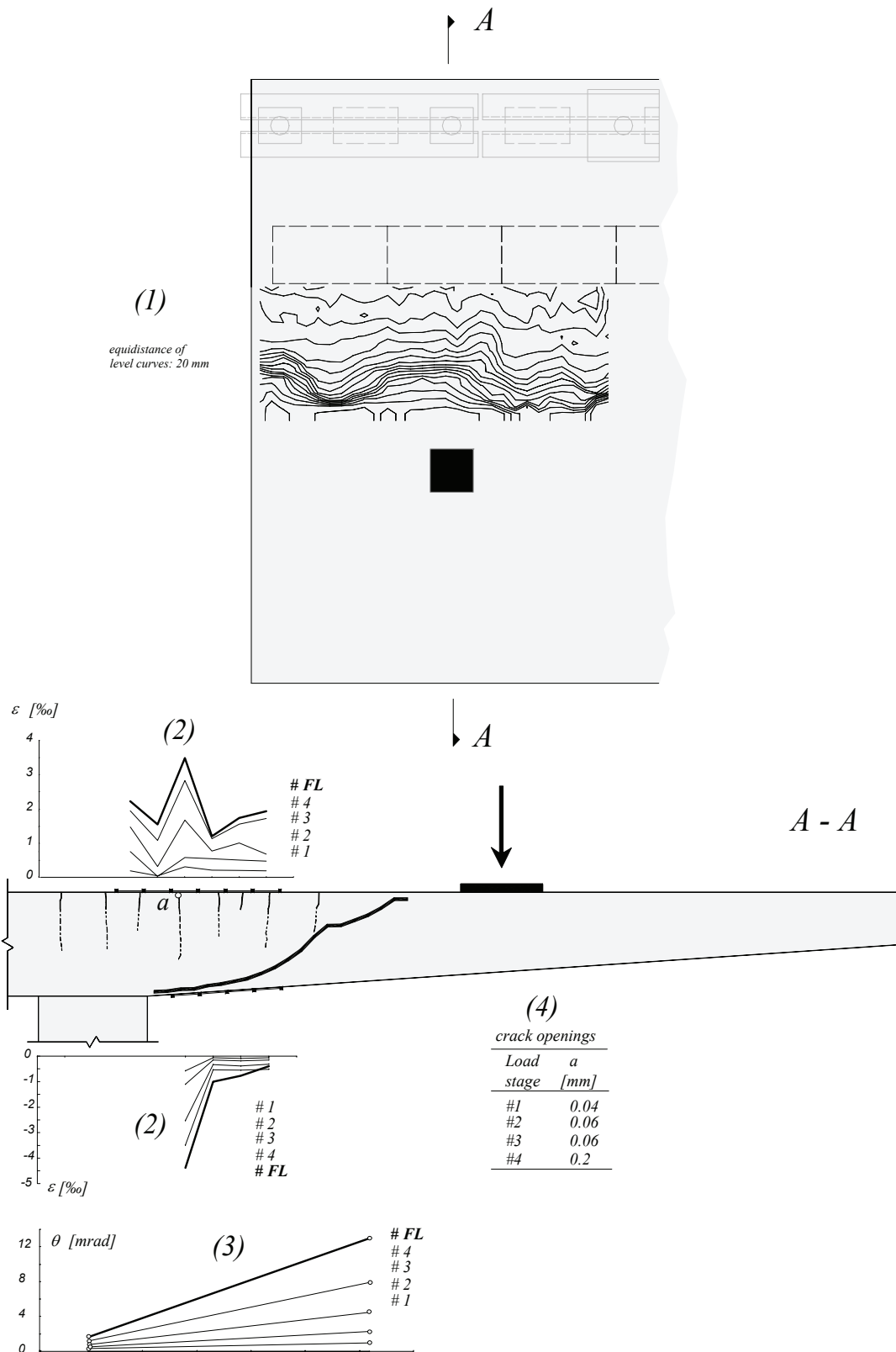


Figure A-4.18: Test DR1-c: (1) Level curves of the shear crack; (2) Strains measured on the surface of the slab with omega-shaped extensometers (100 mm length); (3) Rotations measured with inclinometers; (4) Crack openings measured with magnifying glass

## A-4.5 Test DR2-a

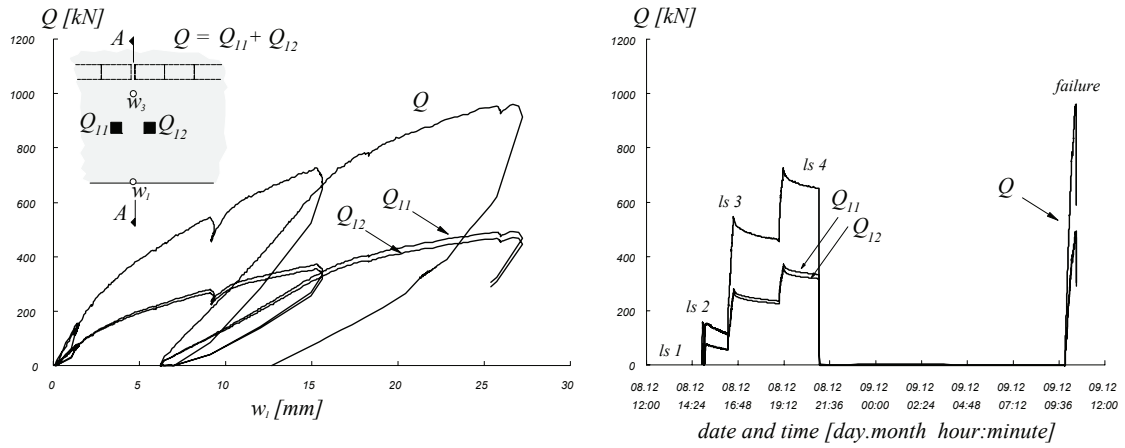


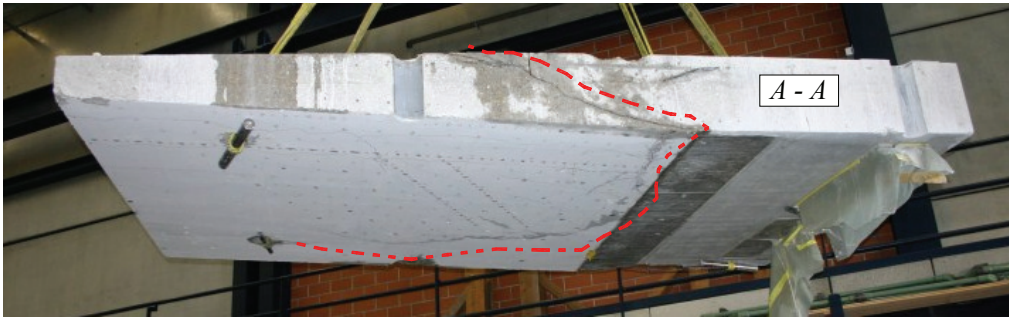
Figure A-4.19: Test DR2-a: Load history and load-deflection curve

Table A-4.6: Test DR2-a: Evolution of some measured values

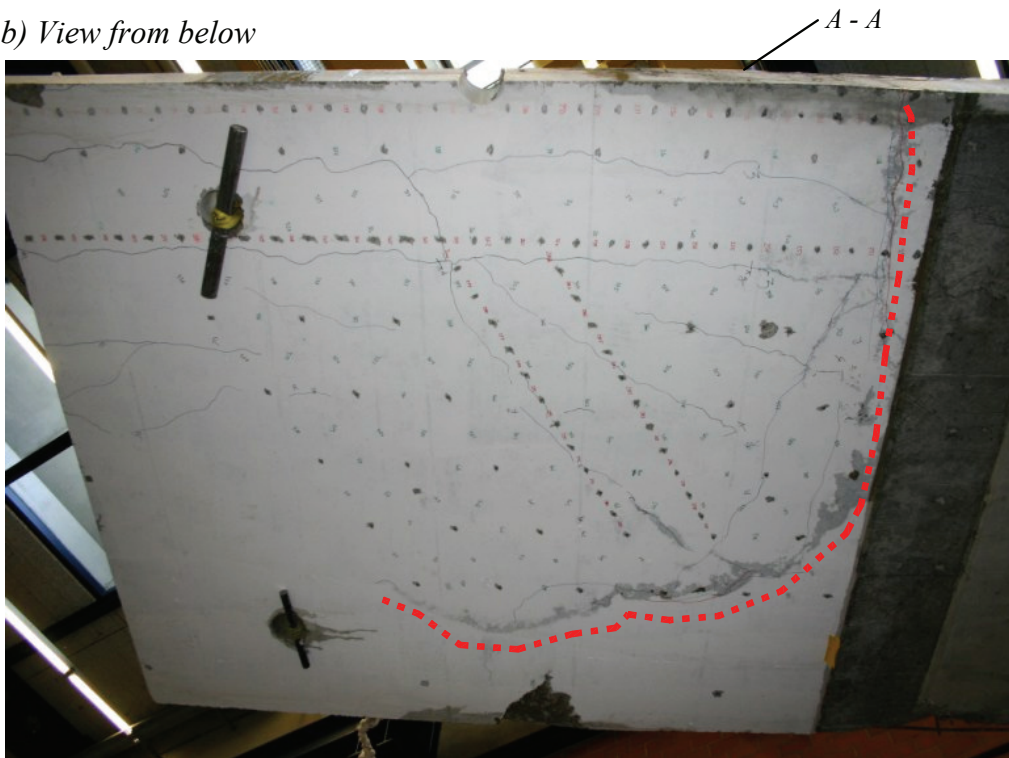
Load stage	$Q$ [kN]	$Q_{11}/Q$ -	$Q_{12}/Q$ -	$w_1$ [mm]	$w_3$ [mm]	$Q/Q_{FL}$ [%]	Remark -
#1	2.1			0.1	0.0	0%	
#2	153.5	50.7%	49.3%	1.5	0.2	16%	B
	153.0	50.7%	49.3%	1.5	0.2	16%	M
	117.9	50.7%	49.3%	1.3	0.2	12%	E
#3	535.8	51.1%	48.9%	9.2	1.3	56%	B
	474.5	51.1%	48.9%	9.2	1.3	49%	M
	462.7	51.1%	48.9%	9.2	1.3	48%	E
#4	698.6	51.2%	48.8%	15.5	2.2	73%	B
	664.1	51.2%	48.8%	15.6	2.2	69%	M
	650.8	51.2%	48.8%	15.6	2.2	68%	E
ML	961.4	51.2%	48.8%	26.7	3.5	100%	ML
FL	961.4	51.2%	48.8%	26.7	3.5	100%	FL
AFT	359.3	51.2%	48.8%	22.1	14.5	37%	AFT

B : Beginning of load stage ; M : End of demountable deformer measurements ; E : End of load stage ; ML : Maximum load ; FL : Failure Load; AFT: After Failure

a) Sectional view



b) View from below



c) View of the internal failure surface (upper lip of the shear crack)



Figure A-4.20: Test DR2-a: Views of the shear crack after cutting the slab

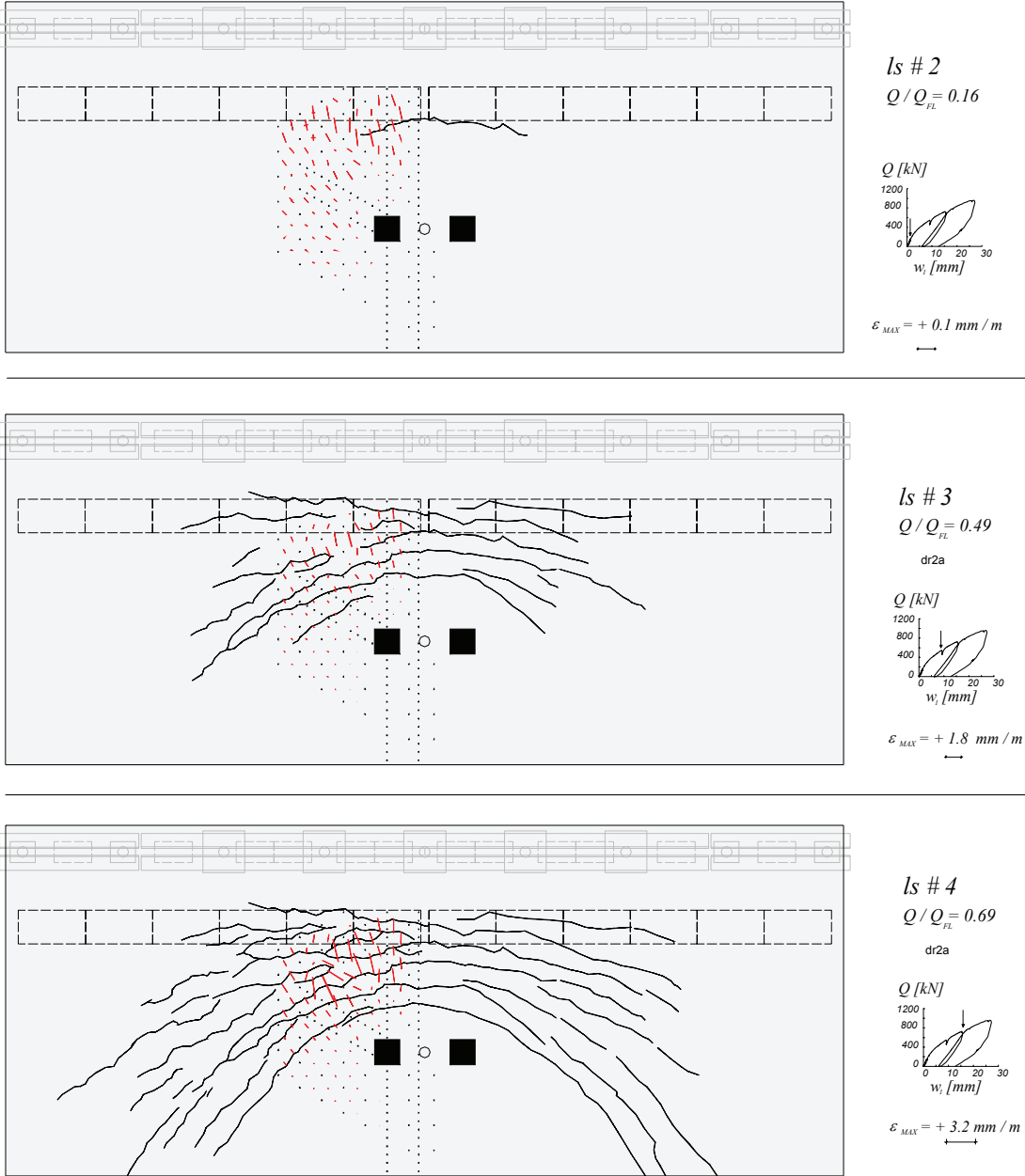


Figure A-4.21: Test DR2-a: Crack pattern and tensile principal strains on the top surface

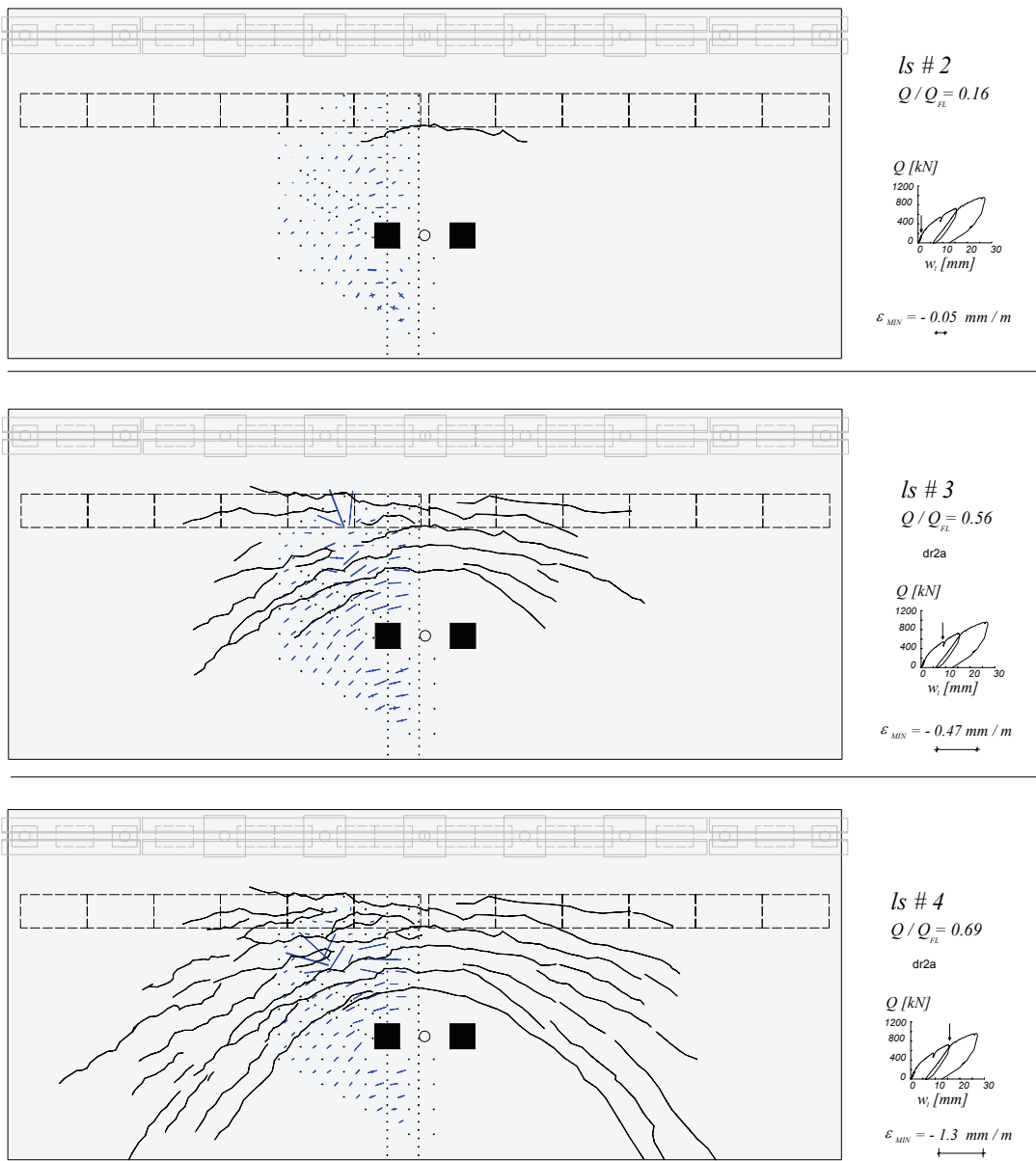


Figure A-4.22: Test DR2-a: Crack pattern and compressive principal strains on the top surface



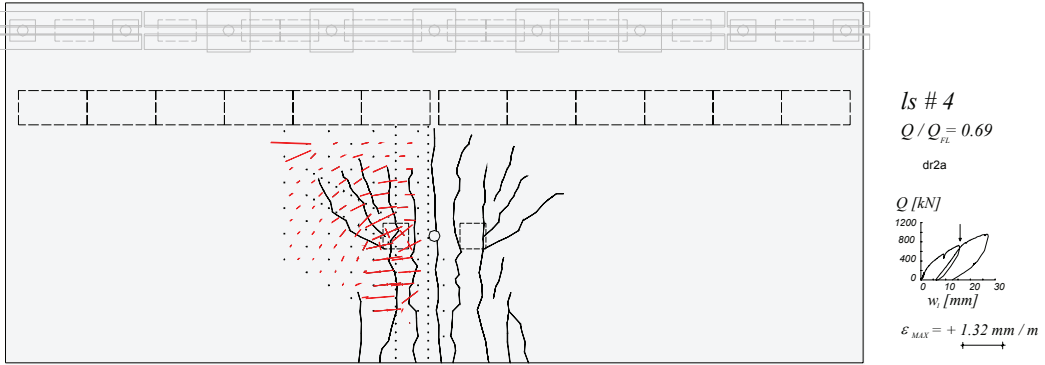
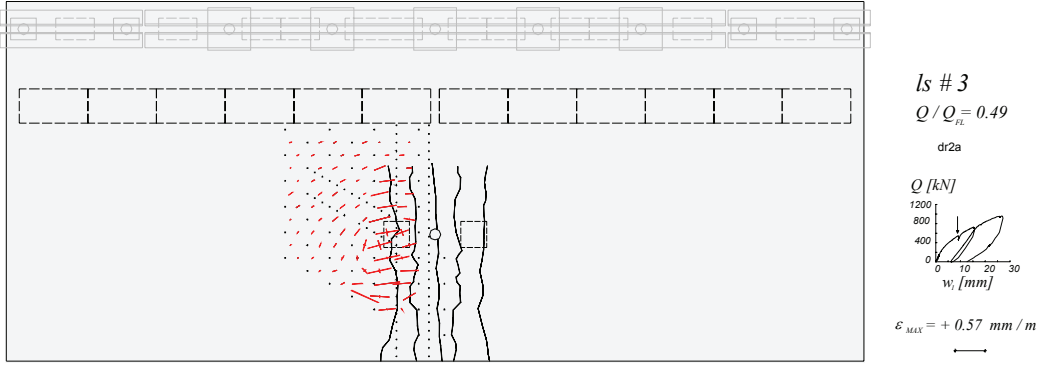
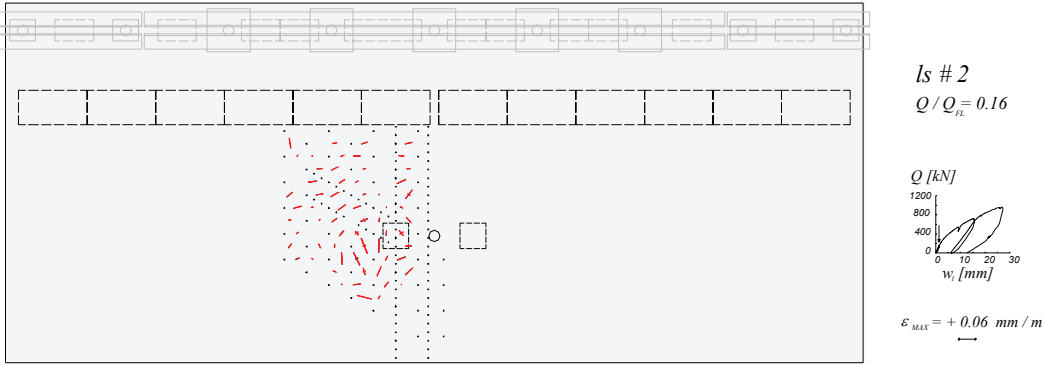


Figure A-4.23: Test DR2-a: Crack pattern and tensile principal strains on the bottom surface (as seen from above)

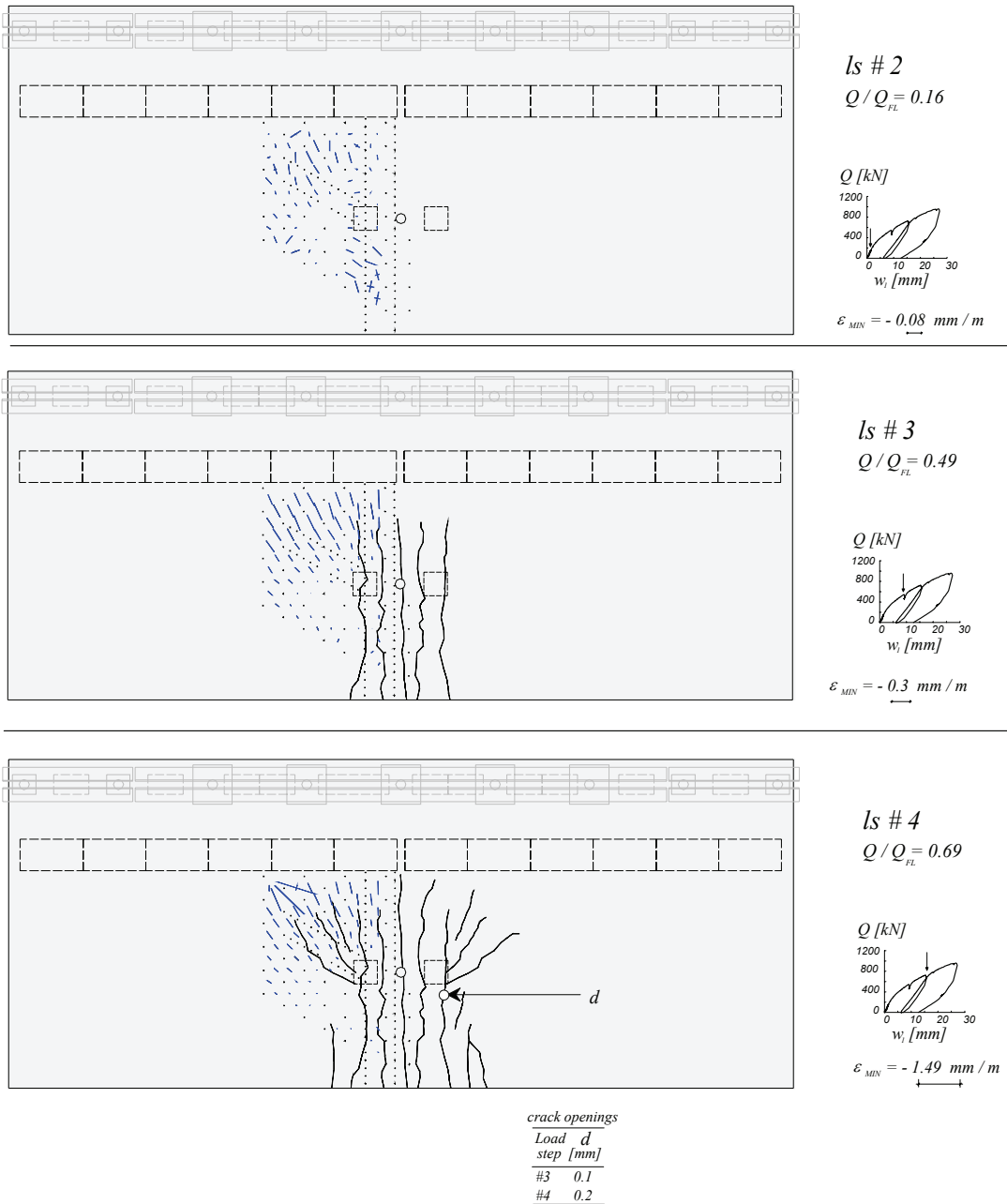


Figure A-4.24: Test DR2-a: Crack pattern and compressive principal strains on the bottom surface (as seen from above)

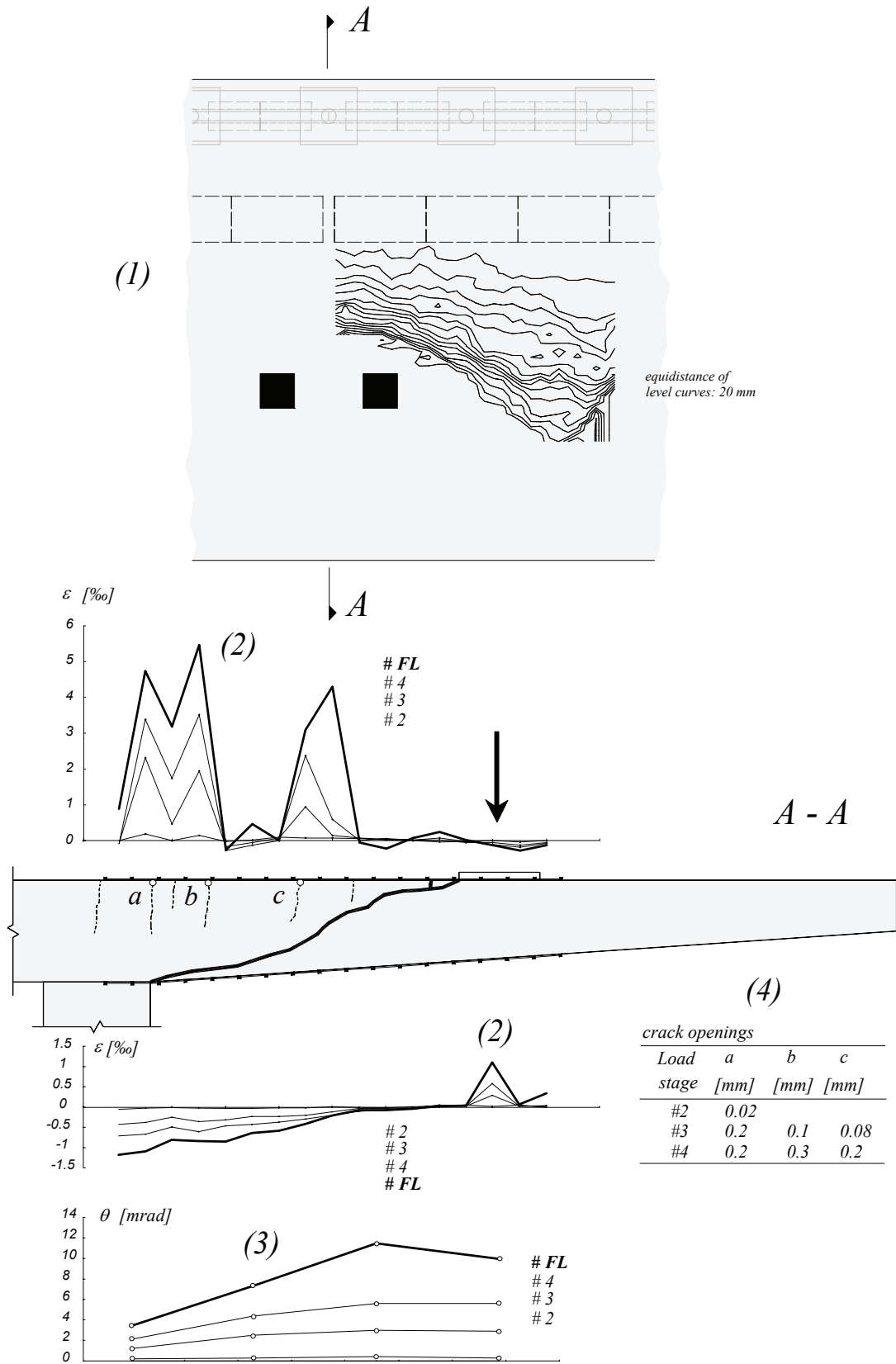


Figure A-4.25: Test DR2-a: (1) Level curves of the shear crack; (2) Strains measured on the surface of the slab with omega-shaped extensometers (100 mm length); (3) Rotations measured with inclinometers; (4) Crack openings measured with magnifying glass

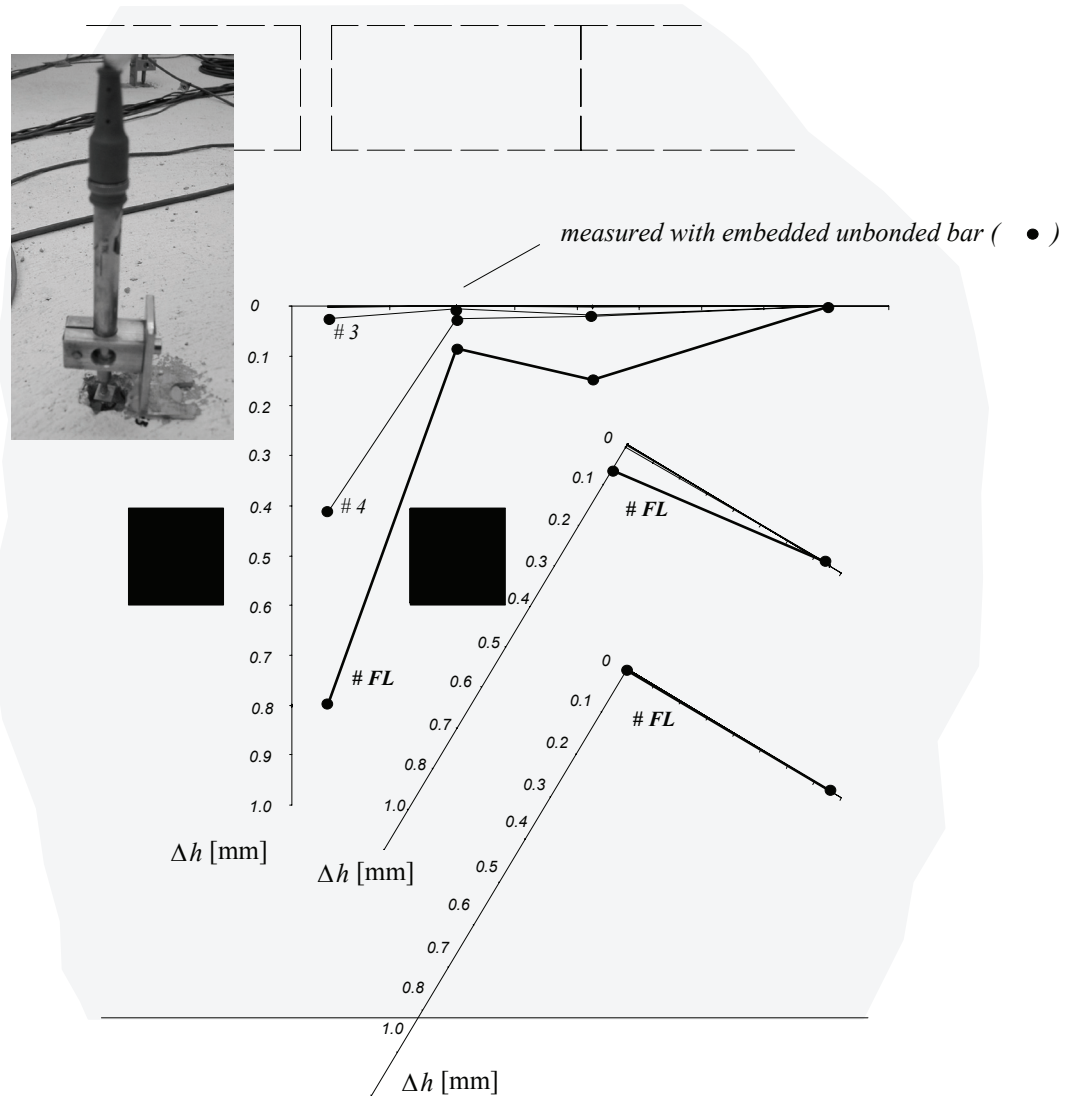


Figure A-4.26: Test DR2-a: Measurements of the variation of the thickness of the slab

A-4.6 Test DR2-b

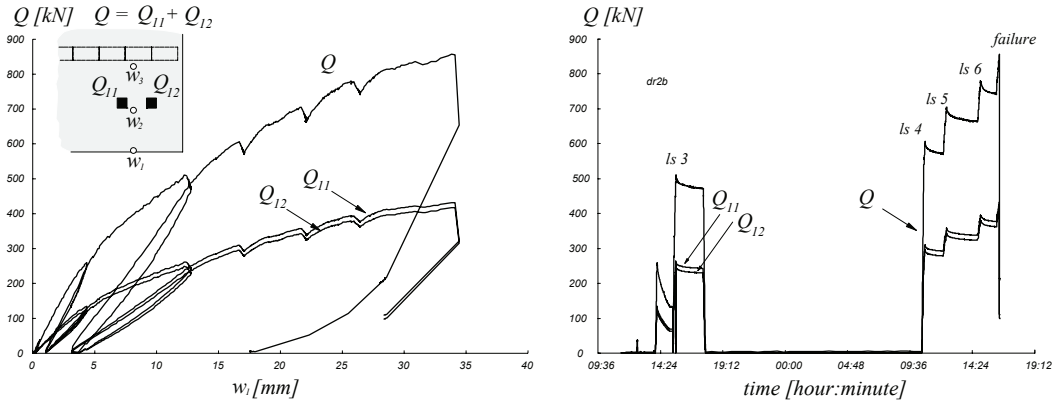


Figure A-4.27: Test DR2-b: Load history and load-deflection curve

Table A-4.7: Test DR2-b: Evolution of some measured values

Load Stage	Q [kN]	Q <sub>11</sub> /Q	Q <sub>12</sub> /Q	w <sub>1</sub> [mm]	w <sub>2</sub> [mm]	w <sub>3</sub> [mm]	Q/Q <sub>FL</sub> [%]	Remark
#1	1.4	-	-	0.0	0.0	0.0	0%	-
#2	247.6	52.0%	48.0%	4.3	2.6	0.8	29%	B
	226.6	52.0%	48.0%	4.1	2.5	0.7	26%	M
	141.2	52.4%	47.6%	3.1	1.9	0.6	16%	E
#3	495.1	51.3%	48.7%	12.6	7.5	1.9	58%	B
	476.4	51.4%	48.6%	12.7	7.6	1.9	56%	M
	471.3	51.4%	48.6%	12.8	7.6	1.9	55%	E
#4	603.2	51.2%	48.8%	16.7	10.0	2.5	70%	B
	581.5	51.2%	48.8%	17.0	10.1	2.5	68%	M
	570.8	51.2%	48.8%	17.1	10.2	2.5	67%	E
#5	696.7	51.1%	48.9%	21.8	13.0	3.1	81%	B
	667.3	51.1%	48.9%	22.1	13.2	3.1	78%	M
	665.4	51.1%	48.9%	22.1	13.2	3.1	78%	E
#6	773.8	51.0%	49.0%	26.0	15.6	3.6	90%	B
	752.2	51.0%	49.0%	26.3	15.8	3.7	88%	M
	743.0	51.0%	49.0%	26.4	15.8	3.7	87%	E
ML	856.6	50.9%	49.1%	33.8	20.3	4.6	100%	ML
FL	856.6	50.9%	49.1%	33.8	20.3	4.6	100%	FL

B : Beginning of load stage ; M : End of demountable deformer measurements ; E : End of load stage ; ML : Maximum load ; FL : Failure Load

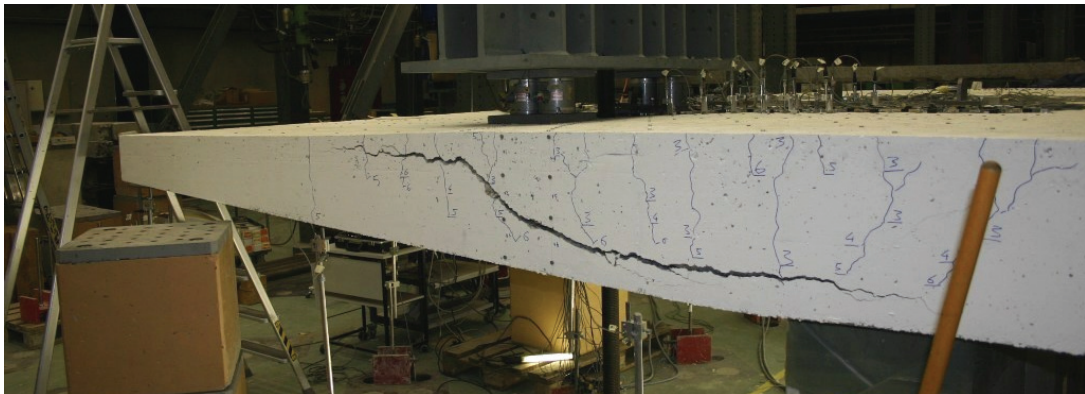


Figure A-4.28: Test DR2-b: Side view of the shear crack after failure

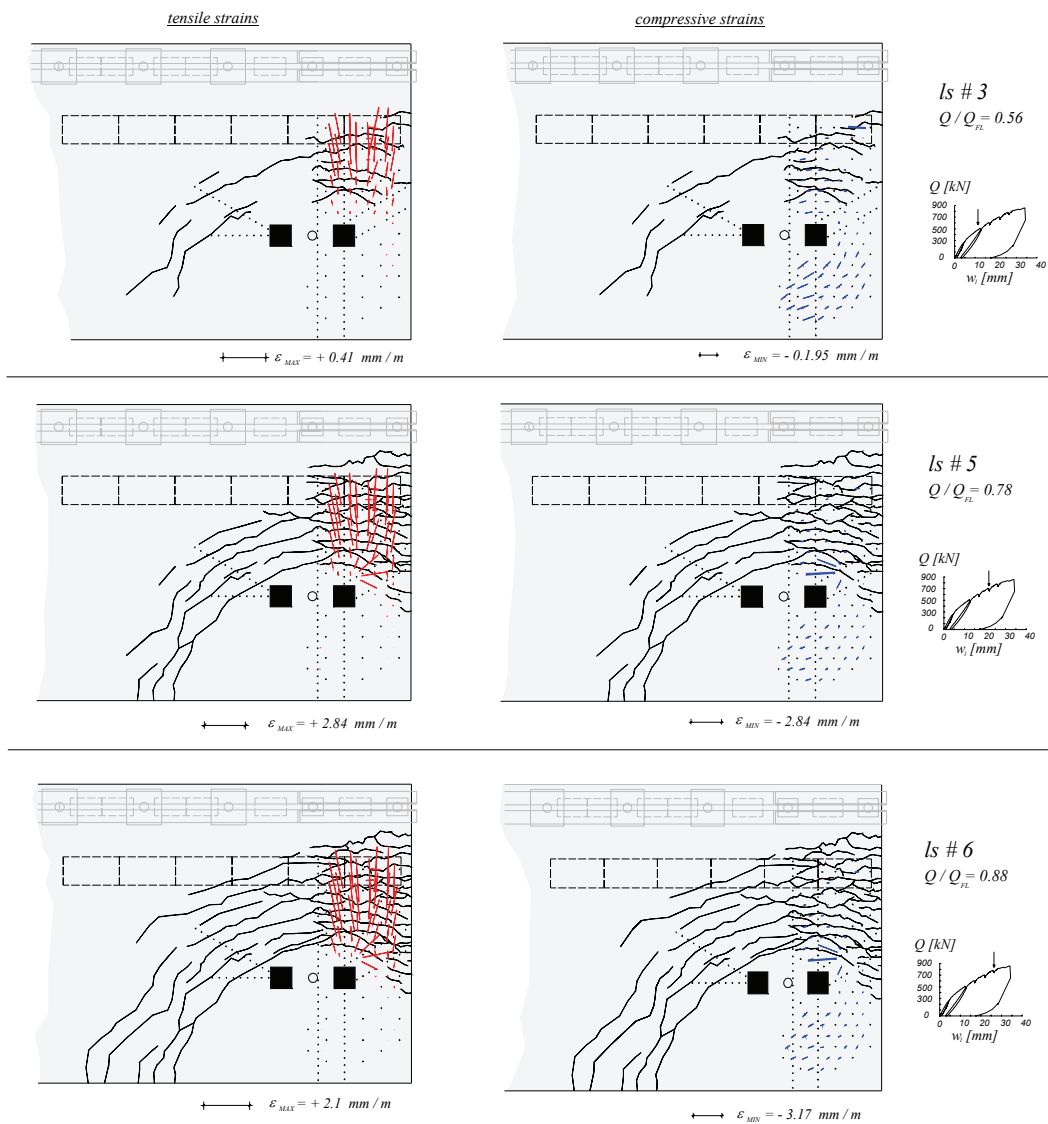


Figure A-4.29: Test DR2-b: Crack pattern and principal strains on the top surface

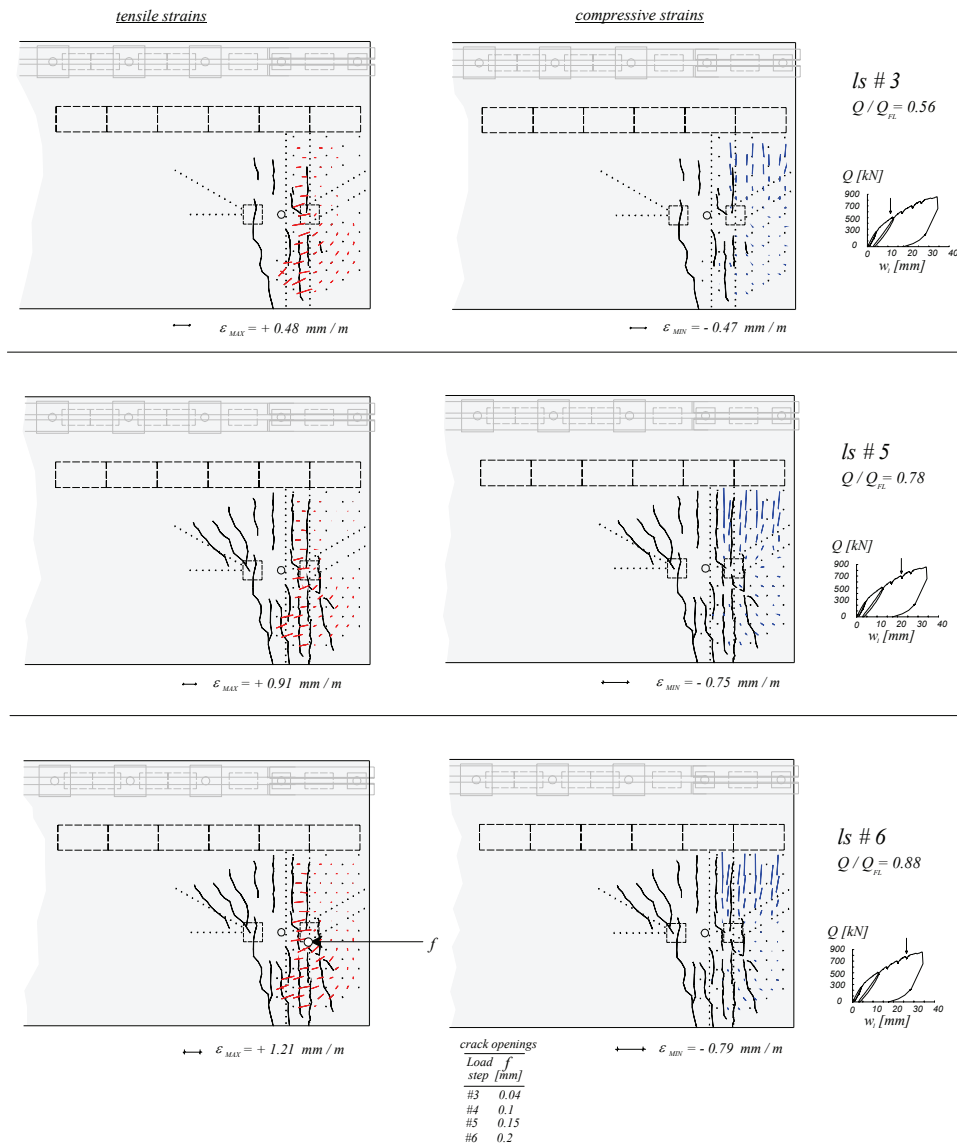


Figure A-4.30: Test DR2-b: Crack pattern and principal strains on the bottom surface (as seen from above)

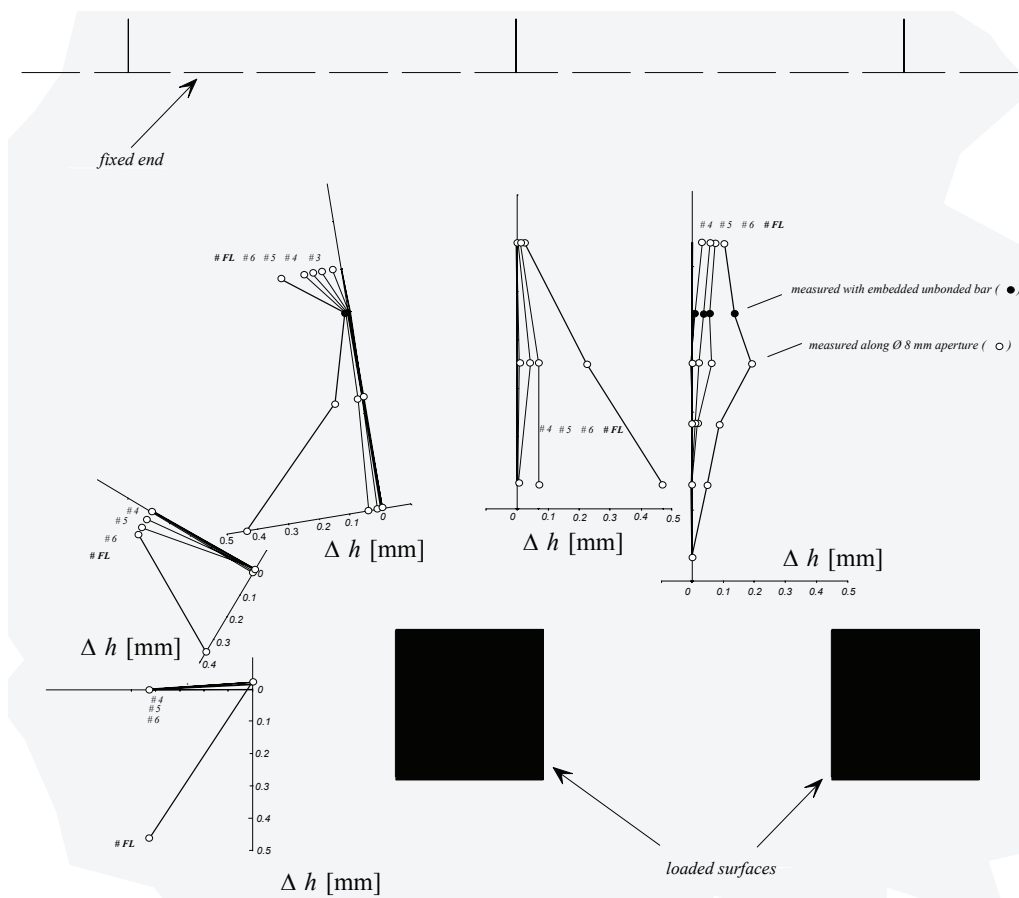


Figure A-4.31: Test DR2-b: Measurements of the variation of the thickness of the slab

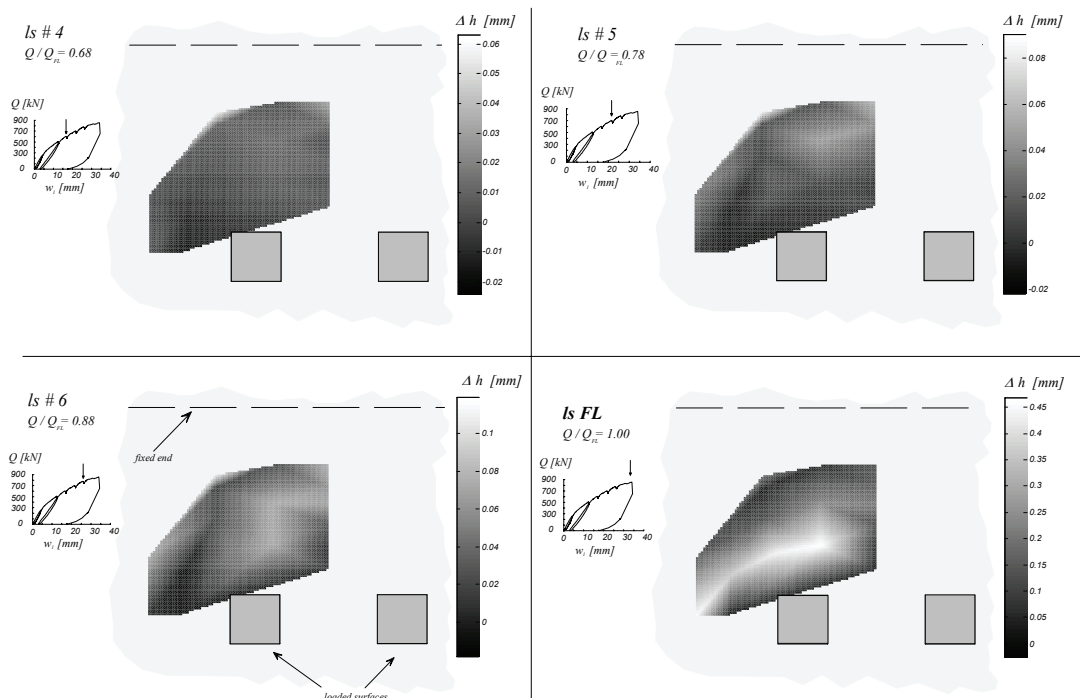


Figure A-4.32: Test DR2-b: Measurements of the variation of the thickness of the slab (interpolated values on all points inside the measurement zone)



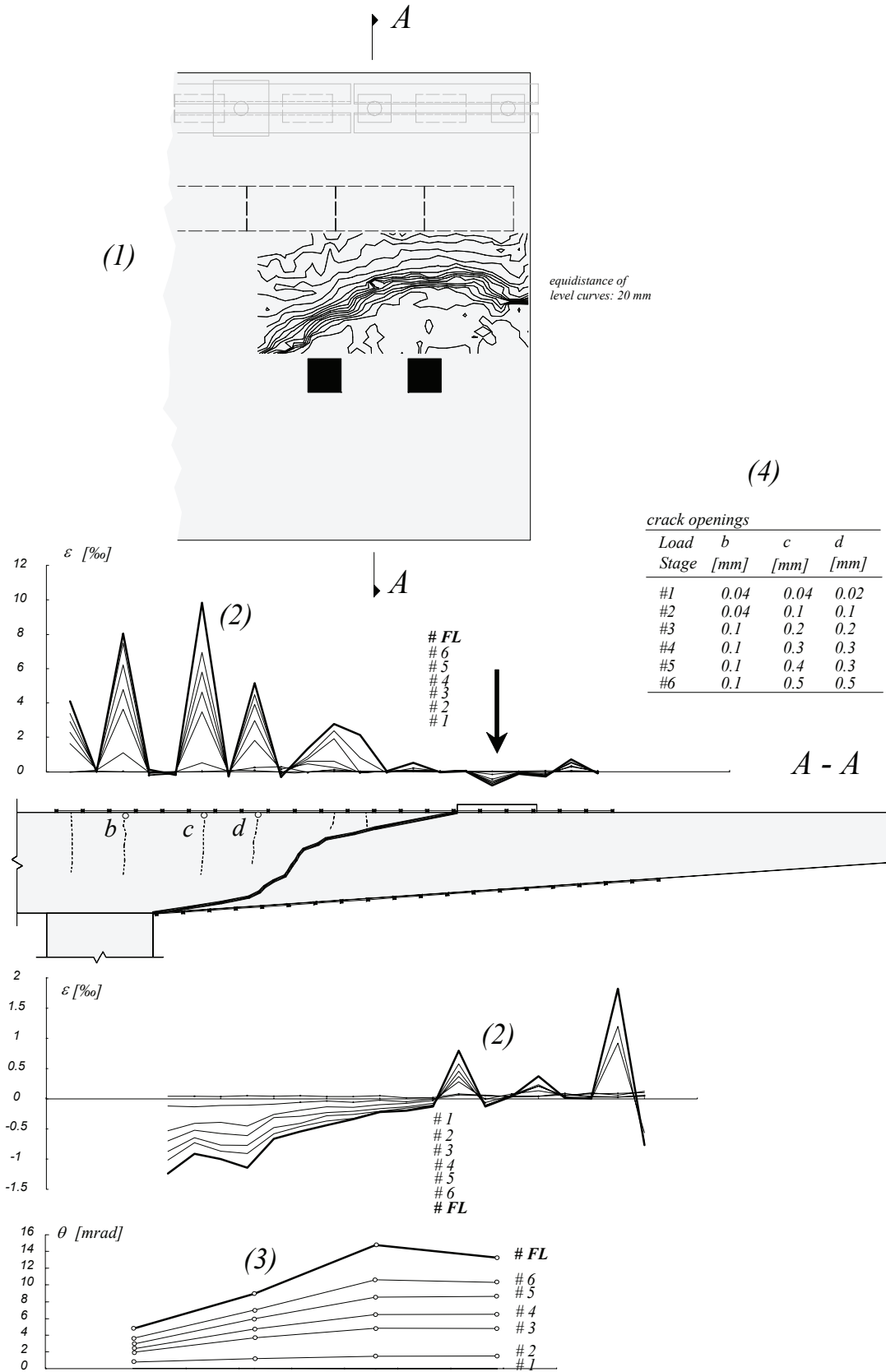


Figure A-4.33: Test DR2-b: (1) Level curves of the shear crack; (2) Strains measured on the surface of the slab with omega-shaped extensometers (100 mm length); (3) Rotations measured with inclinometers; (4) Crack openings measured with magnifying glass

A-4.7 Test DR2-c

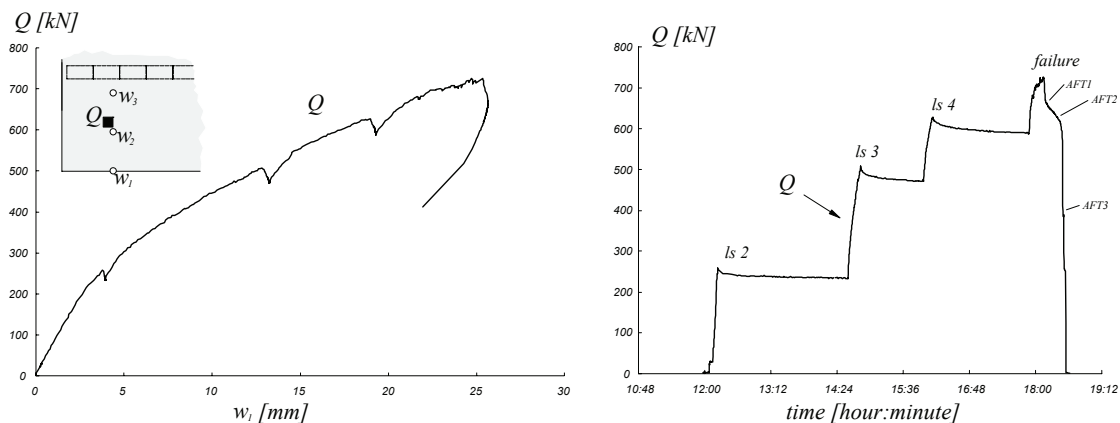


Figure A-4.34: Test DR2-c: Load history and load-deflection curve

Table A-4.8: Test DR2-c: Evolution of some measured values

Load stage	$Q$ [kN]	$w_1$ [mm]	$w_2$ [mm]	$w_3$ [mm]	$Q/Q_{FL}$ [%]	Remark -
#1	3.8	0.0	0.0	0.0	1%	
#2	254.4	3.8	2.4	0.7	35%	B
	240.2	3.9	2.5	0.7	33%	M
	237.1	3.9	2.5	0.7	33%	E
#3	498.9	13.0	8.1	2.0	69%	B
	480.3	13.2	8.2	2.0	67%	M
	471.3	13.2	8.3	2.0	66%	E
#4	620.5	19.0	12.1	2.8	86%	B
	594.3	19.3	12.2	2.8	83%	M
	589.8	19.3	12.3	2.8	82%	E
ML	726.1	25.4	16.1	3.5	101%	ML
FL	719.4	25.4	16.1	3.5	100%	FL
AFT1	664.4	25.7	16.4	3.4	92%	AFT1
AFT2	596.5	25.2	16.5	3.2	83%	AFT2
AFT3	384.6	21.3	16.5	34.6	53%	AFT3

B : Beginning of load stage ; M : End of demountable deformer measurements ; E : End of load stage ; ML : Maximum load ; FL : Failure Load ; AFT1, 2, 3 : After failure



Figure A-4.35: Test DR2-c: Side view of the shear crack after failure

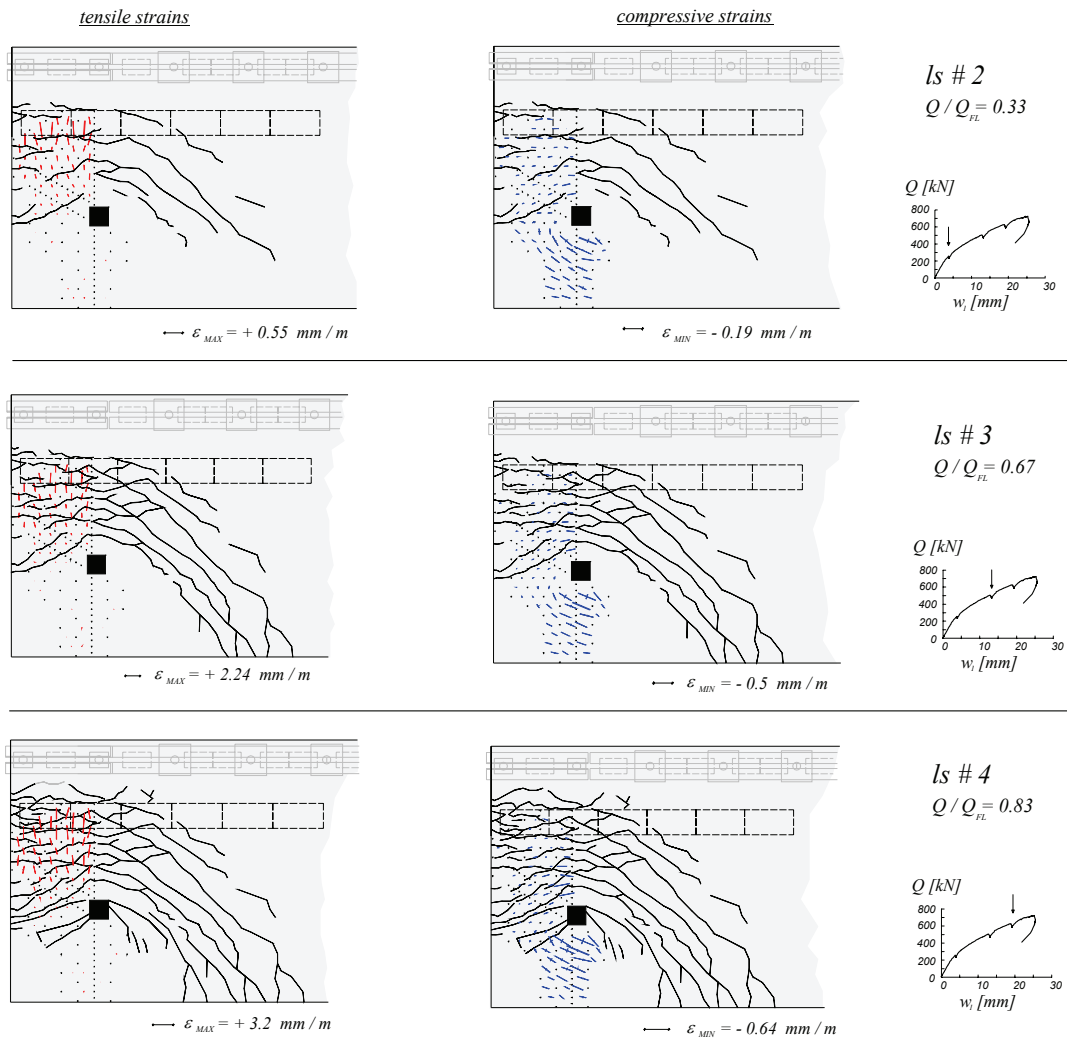


Figure A-4.36: Test DR2-c: Crack pattern and principal strains on the top surface

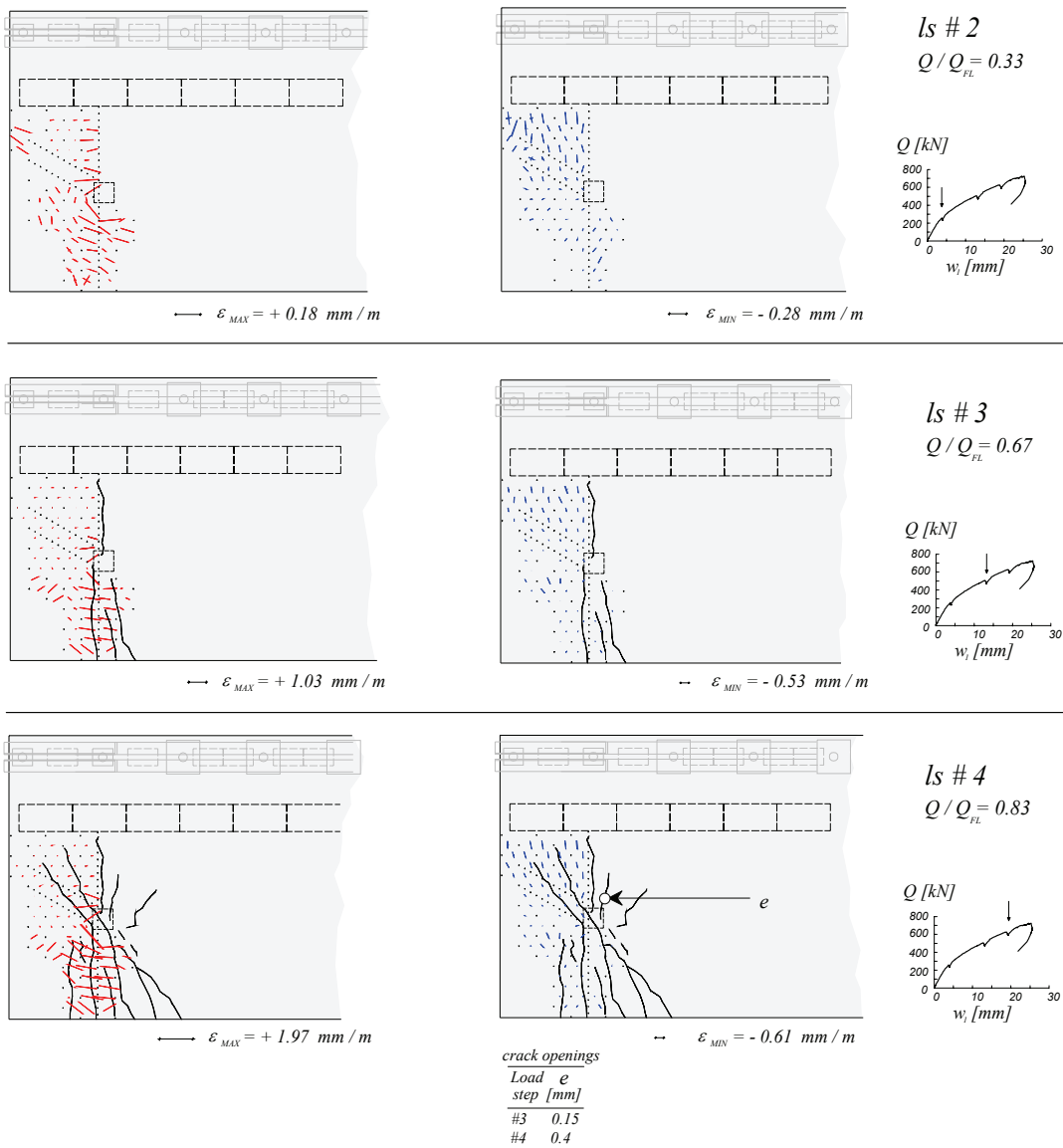


Figure A-4.37: Test DR2-c: Crack pattern and principal strains on the bottom surface (as seen from above)

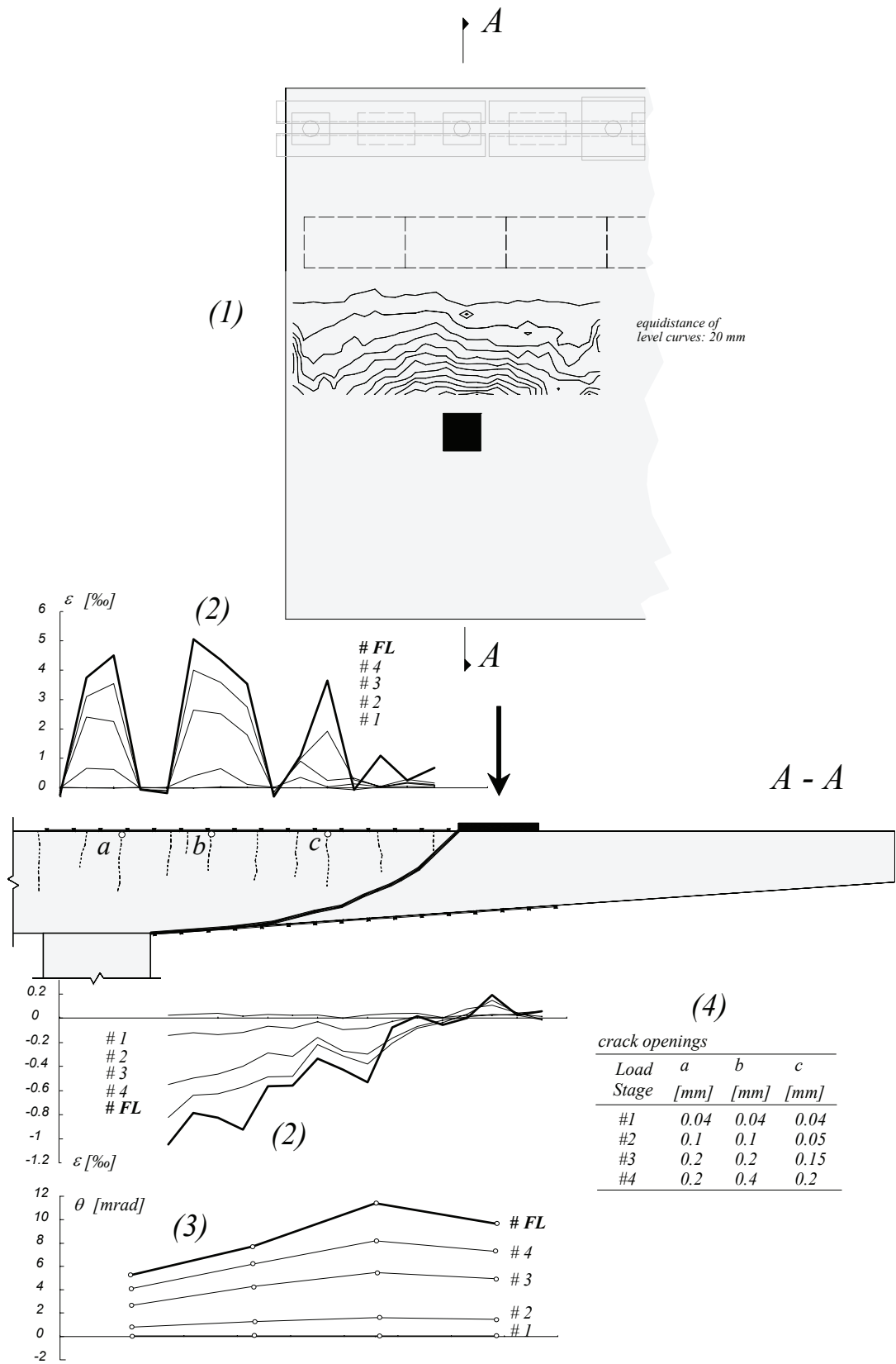


Figure A-4.38: Test DR2-c: (1) Level curves of the shear crack; (2) Strains measured on the surface of the slab with omega-shaped extensometers (100 mm length); (3) Rotations measured with inclinometers; (4) Crack openings measured with magnifying glass

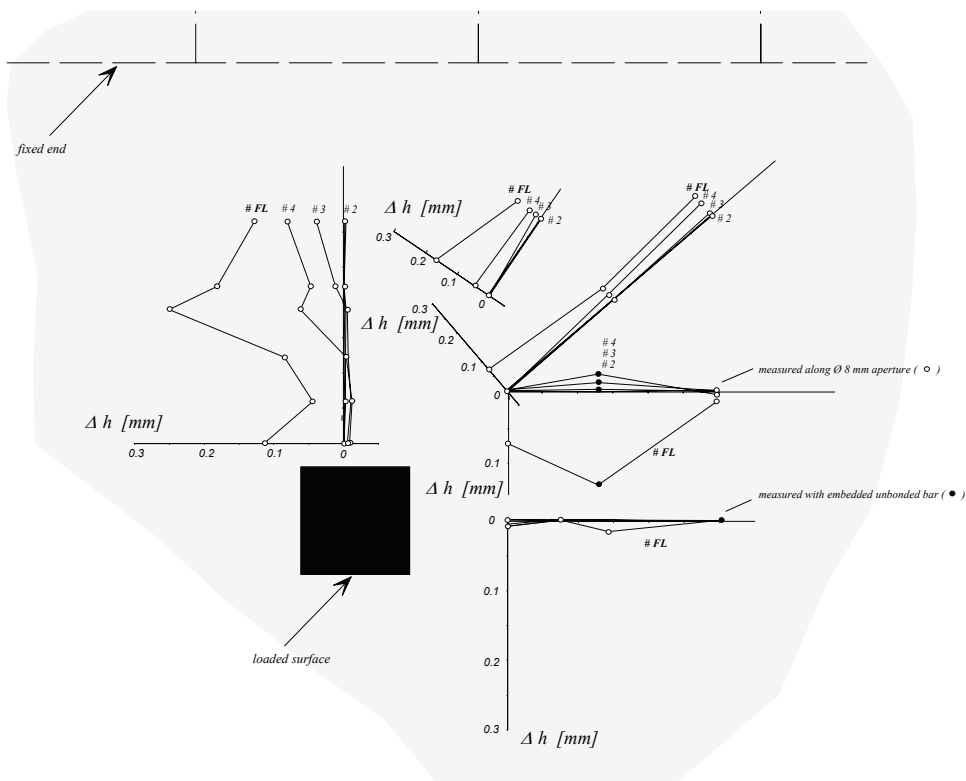


Figure A-4.39: Test DR2-c: Measurements of the variation of the thickness of the slab

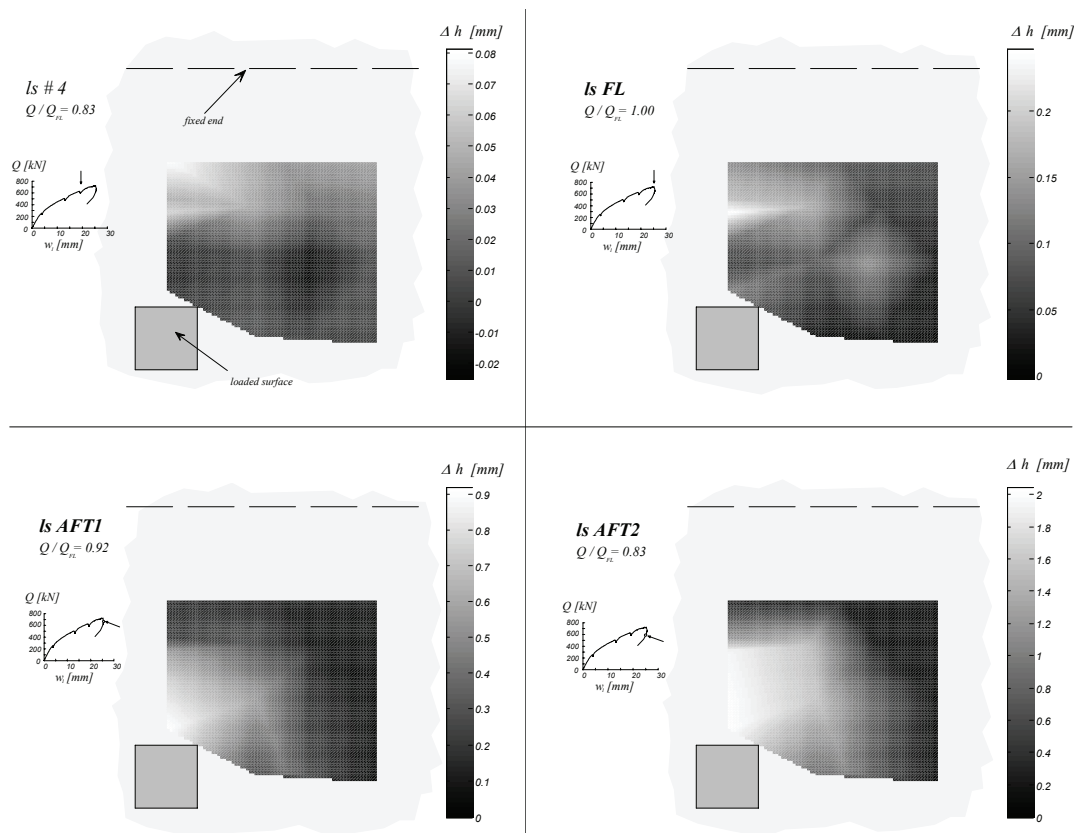


Figure A-4.40: Test DR2-c: Measurements of the variation of the thickness of the slab (interpolated values on all points inside the measurement zone)

A-4.8 Test PR1

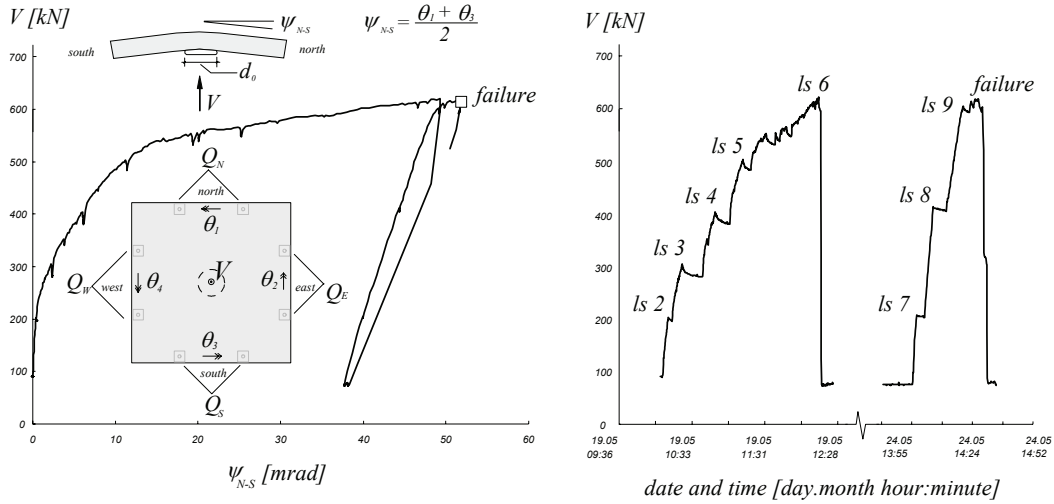


Figure A-4.41: Test PR1: Load history and load-deflection curve

The force on the central support is  $V$ .  $V$  is equal to the sum of the forces applied by the jacks ( $Q_N$ ,  $Q_S$ ,  $Q_W$  and  $Q_E$ ) with the self weight of the slab and test rig (about 73 kN). The rotations  $\theta_1$ ,  $\theta_2$ ,  $\theta_3$ ,  $\theta_4$  are measured with the inclinometers. The pressure  $p$  was measured at each load stage with a pressure gauge. The diameter  $d_0$  is calculated from the force  $V$  and the pressure  $p$  at each load stage:  $d_0 = \sqrt{4 \cdot V / (\pi \cdot p)}$ . The rotation  $\psi_{N-S}$  is the average of the rotations  $\theta_1$  and  $\theta_3$  and the rotation  $\psi_{E-W}$  is the average of the rotations  $\theta_2$  and  $\theta_4$ . Very large rotations were obtained near failure (fig. A-4.41).

Table A-4.9: Test PR1: Evolution of some measured values

Load stage	$Q$	$V$	$p$	$d_0$	$Q_N/Q$	$Q_S/Q$	$Q_W/Q$	$Q_E/Q$	$\theta_1$	$\theta_2$	$\theta_3$	$\theta_4$	$\psi_{NS}$	$\psi_{EW}$	$Q/Q_{FL}$	Rem.
	[kN]	[kN]	[bar]	[mm]	-	-	-	-	[mrad]	[mrad]	[mrad]	[mrad]	[mrad]	[mrad]	[%]	-
#0	15.8	88.8	5.7	445	19%	22%	30%	29%	0.0	0.0	0.0	0.0	0.0	0.0		
#1	126.3	199.3	13.7	430	24%	25%	26%	25%	0.1	2.0	0.7	-1.3	0.4	0.3	24%	
#2	226.4	299.4	20.0	437	25%	25%	26%	24%	3.5	6.2	1.0	-2.3	2.3	1.9	43%	
#3	319.9	392.9	25.3	445	24%	25%	26%	25%	8.9	13.5	3.1	-3.0	6.0	5.3	61%	
#4	420.9	493.9	31.1	450	25%	25%	26%	25%	13.3	23.0	9.4	-3.2	11.3	9.9	80%	
#5	469.1	542.1	33.7	453	24%	25%	26%	25%	21.1	30.0	17.4	-1.1	19.3	14.5	89%	
#6	547.0	620.0	35.0	475	25%	25%	26%	24%	49.3	42.9	49.1	31.7	49.2	37.3	104%	
#7	129.1	202.1	12.0	463	24%	25%	26%	25%	46.8	48.5	33.0	10.0	39.9	29.2	25%	
#8	331.1	404.1	23.6	467	25%	25%	25%	25%	53.6	56.3	35.1	10.1	44.3	33.2	63%	
#9	521.2	594.2	34.0	472	25%	25%	25%	25%	61.4	63.7	36.8	11.0	49.1	37.4	99%	
ML	541.5	614.5			25%	25%	25%	25%	64.1	64.7	39.0	12.9	51.6	38.8	103%	ML
FL	526.1	599.1			25%	25%	25%	25%	64.2	64.4	38.9	12.4	51.5	38.4	100%	FL

ML : Maximal load ; FL : Failure Load

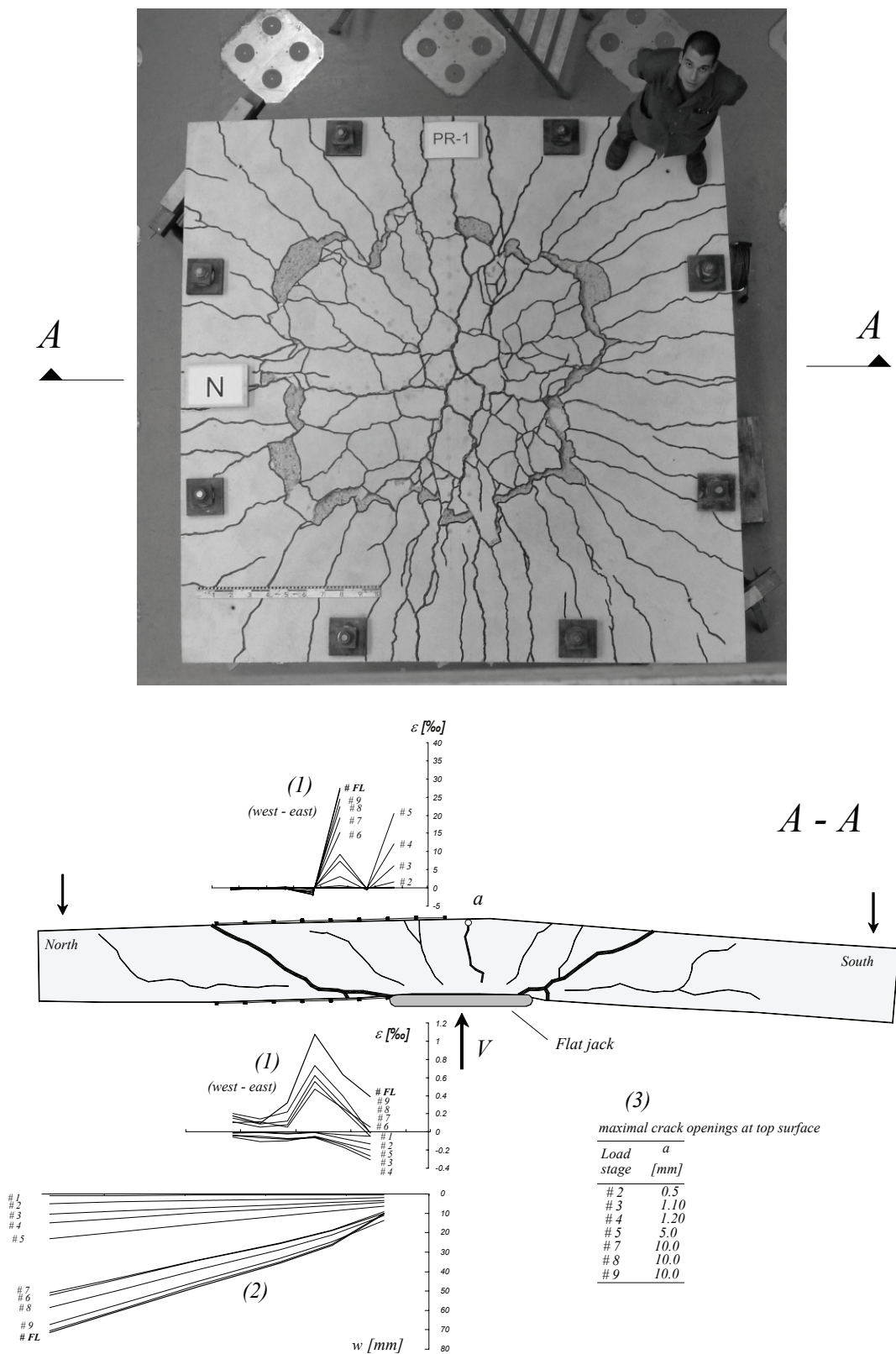


Figure A-4.42: Test PR1: Crack pattern on the top surface; (1) Strains measured on the surface of the slab with omega-shaped extensometers (100 mm length); (2) Deflections measured with LVDTs; (3) Crack openings measured with magnifying glass



## A-5 Conclusions

### A-5.1 Tests on bridge deck cantilevers

Table A-5.1 summarizes the obtained results on all tests on bridge deck cantilevers. Figure A-5.1 shows the load-deflection curves for all the six tests. Note that the self-weight of the test rig (table A-3.1) is not included in the force values. Test DR1-a had the highest failure load and the largest deflection  $w$ , measured at the tip of the cantilever. The measuring location of the deflection  $w$  is indicated in the same figure. The shape of the shear crack is indicated in figure A-5.2 for all tests on cantilevers, for the sectional view  $A - A$ , as explained in figure A-5.1. The strains on the concrete and the rotations are represented using the same scale for all tests. For test DR1-a, the rotations were not measured. The deflections are indicated instead.

Table A-5.1: Summary of the obtained results

Test	Reinforcement ratio <sup>*)</sup>	Location of loads (along $y$ )	Number of loads	Failure Load ( $Q_R$ ) [kN]	Failure location	Mode of failure
DR1-a	0.78 %	Centre	4	1397	Cantilever edge	Shear
DR1-b		North edge	2	1025	Fixed end	Shear
DR1-c		South edge	1	910	Fixed end	Shear
DR2-a	0.60%	Centre	2	961	Fixed end	Shear
DR2-b		North edge	2	857	Fixed end	Shear
DR2-c		South edge	1	719	Fixed end	Shear

<sup>\*)</sup> At the top transversal reinforcement (bars along  $y$ ) at the clamped edge

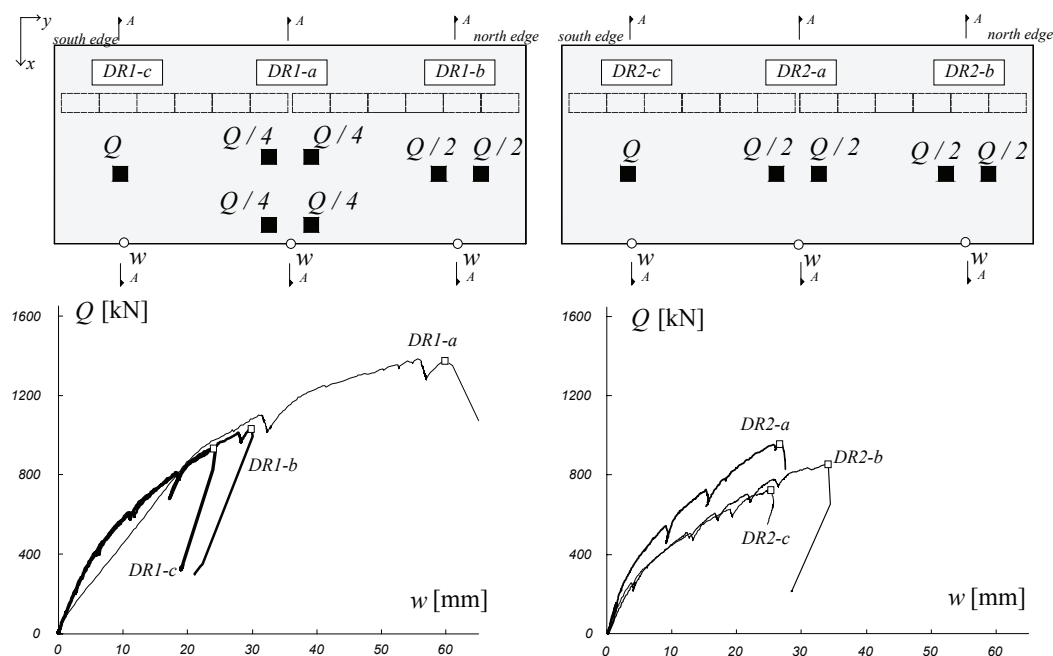


Figure A-5.1: Force-deflection curves for all tests on cantilevers

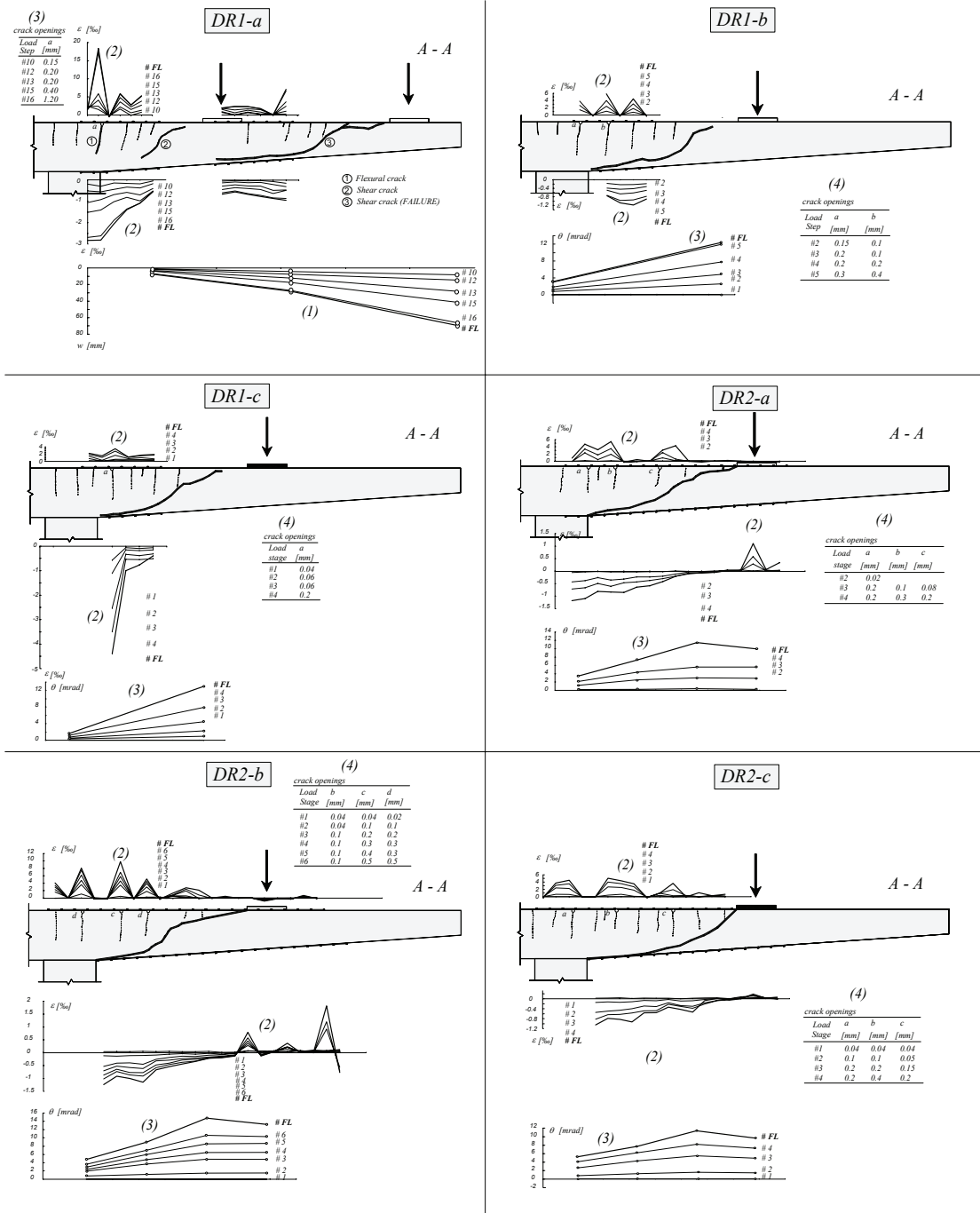


Figure A-5.2: Sectional views of all tests on bridge deck cantilevers: (1) Deflections measured with LVDTs; (2) Strains measured on the concrete surface with omega-shaped extensometers (100 mm length); (3) Rotations measured with inclinometers; (4) Crack openings measured with magnifying glass

The following conclusions can be drawn for the performed tests on cantilevers:

### 1. Behavior at failure

- The cantilevers always failed in shear, in a non ductile manner.
- The location of the shear failure was always in the region between the loads and the clamped edge. For test DR1-a the failure took place at the concentrated loads near the cantilever edge.
- For the tests performed on the same slab, the failure load increases with the number of applied loads (one, two or four).
- For tests performed with the same number of loads, the failure load decreases with the reinforcement ratio.
- For test DR1-a the shear crack that provoked the failure is indicated (DR1-a, ③ in fig. A-5.2). Besides from this crack, an important shear crack was found in the region between the clamped edge and the concentrated loads (DR1-a, ② in fig. A-5.2). It appears that a process of formation of the shear crack in this region was in progress, without leading to a shear failure.
- The critical shear cracks do not seem to form from the existing flexural cracks (fig. A-5.2).
- The surface defined by the failure crack resembles for all tests to a flat truncated conical surface.

### 2. Formation and openings of flexural cracks

- The first flexural crack has always appeared on the top surface at the clamped edge (cracks along  $y$ ).
- The maximal crack openings on the top surface, at failure, range from 0.3 mm for test DR1-c to 1.8 mm for test DR1-a. The cracks with maximal openings at the top surface are always located at the clamped edge (cracks along  $y$ ).
- The maximal crack openings measured on the bottom surface, at the load stage prior to failure, range from 0.2 mm for test DR2-b and DR2-a to 1.0 mm for test DR1-a. The cracks with maximal openings at the bottom surface are always located below the applied loads. These cracks are normally oriented along the cantilever span (cracks along  $x$ ).

### 3. Yielding of flexural reinforcement

Based on the analysis of the crack openings, omega-shaped extensometers and measurements with demountable deformer, it can be concluded that:

- For test DR1-a, significant yielding occurred in top and bottom reinforcement, namely over the clamped edge and under the applied loads. At failure, the crack openings at the clamped edge for top bars along  $x$  was of 1.8 mm. For bottom bars along  $y$  under the edge loads, the crack opening at failure was of 1.0 mm.
- No or very limited yielding occurred for the other tests, with crack openings at failure smaller than 0.6 mm at all locations and for all load levels.

#### 4. Variation of slab thickness and propagation of shear crack

- For test DR2-a, the thickness of the slab has increased after load stage # 3 ( $Q = 0.49 \cdot Q_{FL}$ ). At maximal load, the maximal variation of thickness was of about + 0.8 mm. The increase of thickness was more pronounced at the section A – A, between the load and the clamped edge.
- For test DR2-b the thickness of the slab has increased after load stage # 3 ( $Q = 0.56 \cdot Q_{FL}$ ). At maximal load, the maximal variation of thickness was of about + 0.5 mm. The increase of thickness concentrated in half-circular region around the concentrated load.
- For test DR2-c the thickness of the slab has increased after load stage # 3 ( $Q = 0.67 \cdot Q_{FL}$ ). At maximal load, the maximal variation of thickness was of about + 0.25 mm. The increase was more pronounced at section A – A, between the load and the clamped edge. After the maximal load was attained, the shear failure produced in a rather slow way. The variation of the slab thickness was recorded during the decrease of the load after failure. At load step AFT2 ( $Q = 0.83 \cdot Q_{FL}$ ) the maximal variation of the thickness was of about 2 mm. The increase of thickness was approximately distributed around the applied load, however with larger values at section A – A.

#### 5. Behavior under service load

A cyclical loading of the cantilever took place under the loading patterns of test DR1-a before going to failure. About one hundred cycles ranging from  $Q = 0$  to 410 kN were performed. The following conclusions can be drawn:

- The deflection at the tip of the cantilever increased from 6.3 mm to 8.3 mm (about 30%) after the cyclic loading.
- An increase due to load cycles was also observed in the maximal crack openings at the clamped edge, of 0.1 mm to 0.15 mm. At the bottom surface under the applied loads an increase was observed in the maximal and residual crack openings respectively of 0.04 to 0.1 and 0.02 to 0.05 mm.

### A-5.2 Punching shear test with simulation of vehicle wheel

The following conclusions can be drawn for the punching shear test PR1, with simulation of a vehicle wheel with pneumatic pressure:

- Slab PR1 failed in punching shear in presence of very large crack openings directly above the loaded surface (crack opening of 10.0 mm).
- A very large plateau is observed in the force-rotation diagram.
- Tensile stresses have appeared on the radial direction on the bottom side of the slab, near the central support. This was observed at very large rotations, near failure.
- The diameter of the contact surface between the flat jack and the concrete slab is calculated for each load step from the values of the force and pressure. The diameter sensibly increases along the load stages.

**Bibliography**

**Eurocode 1** , *Actions on structures – Part 2: Traffic loads on bridges*, EN 1991-2, September, **2003**.

**Fernández Ruiz M., Muttoni A.** , *Plain concrete behaviour under uniaxial compression*, IS-BETON, **2005**.

**Guandalini S.** , *Poinçonnement symétrique des dalles en béton armé*, Thèse de doctorat, N. 3380 (2005), 289 pp., Lausanne, Suisse, décembre, **2005**.

**Guandalini S., Muttoni A.** , *Essais de poinçonnement symétrique des dalles en béton armé sans armature à l'effort tranchant*, Rapport d'essai, Lausanne, Switzerland, **2004**.

**Muttoni A.** , *Schubfestigkeit und Durchstanzen von Platten ohne Querkarftbewehrung*, Beton- und Stahlbetonbau, Vol. 98, No 2, pp. 74-84, Berlin, Germany, Feb., **2003**.

**SIA** , *SIA 261 - Actions sur les structures porteuses*, 114p., Zurich, Suisse, **2003**.

**Vaz Rodrigues R.** , *Essai d'un porte-à-faux de pont sous charge concentrée*, EPFL - IS-BETON, Lausanne, **2002**.

**Vaz Rodrigues R.** , *Shear Strength of RC Bridge Deck Cantilevers*, 6th International PhD Symposium in Civil Engineering, IBK Publikation SP-015, pp. 160-161, August, **2006**.

**Vaz Rodrigues R.** , *Shear Strength of Reinforced Concrete Bridge Deck Slabs*, IS-BETON, PhD thesis, n° 3739, Lausanne, Switzerland, January, **2007**

**Vaz Rodrigues R., Muttoni A.** , *Influence des déformations plastiques de l'armature de flexion sur la résistance à l'effort tranchant des poutres sans étriers. Rapport d'essai*, IS-BETON, Lausanne, **2004**.









# Influence des déformations plastiques de l'armature de flexion sur la résistance à l'effort tranchant des poutres sans étriers. Rapport d'essai

## Shear strength without stirrups after yielding of RC slab strips. Test report



Ecole Polytechnique Fédérale de Lausanne  
Institut de Structures  
Laboratoire de Construction en Béton (IS-BETON)

Rui Vaz Rodrigues  
Prof. Dr Aurelio Muttoni

1<sup>er</sup> octobre 2004

Cette recherche a été soutenue par l'Office Fédéral des Routes (OFROU)



et par la Fondation Portugaise pour la Science et Technologie (FCT)

**FCT** Fundação para a Ciência e a Tecnologia

MINISTÉRIO DA CIÊNCIA, TECNOLOGIA E ENSINO SUPERIOR Portugal

## Table des matières

<b>B-1 Introduction.....</b>	<b>1</b>
B-1.1 But.....	1
B-1.2 Remerciements.....	1
<b>B-2 Bandes de dalle.....</b>	<b>3</b>
B-2.1 Géométrie et armature.....	3
B-2.2 Paramètres d'essai.....	5
B-2.3 Fabrication.....	6
B-2.4 Matériaux.....	7
Béton.....	7
Acier.....	12
<b>B-3 Banc d'essai et instrumentation.....</b>	<b>15</b>
B-3.1 Banc d'essai.....	15
B-3.2 Instrumentation.....	16
Mesures manuelles.....	16
Mesures en continu.....	18
B-3.3 Préparation et déroulement de l'essai.....	20
<b>B-4 Résultats.....</b>	<b>21</b>
B-4.1 Dépouillement des mesures.....	21
Forces.....	21
Mesures manuelles au déformètre.....	23
B-4.2 Poutre SR2.....	28
B-4.3 Poutre SR3.....	32
B-4.4 Poutre SR4.....	36
B-4.5 Poutre SR5.....	40
B-4.6 Poutre SR6.....	44
B-4.7 Poutre SR7.....	48
B-4.8 Poutre SR8.....	52
B-4.9 Poutre SR9.....	56
B-4.10 Poutre SR10.....	60
B-4.11 Poutre SR11.....	64
B-4.12 Poutre SR12.....	68
<b>B-5 Comparaison des essais.....</b>	<b>73</b>
<b>Références bibliographiques.....</b>	<b>77</b>



## **B-1 Introduction**

### **B-1.1 But**

Les essais ont pour principal but d'étudier la résistance à l'effort tranchant des dalles sans étriers, en particulier l'effet des déformations plastiques de l'armature de flexion dans la zone tendue sur la résistance à l'effort tranchant. Les grandeurs principales mesurées sont donc les déformations à la fibre supérieure et à la fibre inférieure et les forces appliquées qui permettront de calculer les sollicitations dans la section de rupture. Onze bandes de dalle (poutres) ont été essayées et testées en laboratoire. Le système statique choisi est isostatique. Les déformations dans le plan de l'âme ont aussi été mesurées.

### **B-1.2 Remerciements**

Cette recherche a été réalisée au Laboratoire de construction en béton (IS-BETON) de la faculté ENAC, section de Génie Civil de l'Ecole Polytechnique Fédérale de Lausanne, sous la direction du Professeur A. Muttoni. Je tiens à lui exprimer mes plus sincères remerciements pour ses conseils, sa grande disponibilité et son enthousiasme pour la recherche mis à disposition.

Pour la réalisation des essais en laboratoire je remercie Messieurs S. Demierre, N. Frey, G. Guignet, R. Gysler, F. Perrin, G. Pidoux et H. Reist.

Au niveau financier, ce travail a été rendu possible grâce au soutien de l'Office Fédéral des Routes (OFROU) et de la Fondation Portugaise pour la Science et Technologie (FCT / BD 13259 / 2003).



## **B-2 Bandes de dalle**

### **B-2.1 Géométrie et armature**

Les bandes de dalle ont 8.4 mètres de longueur et une section rectangulaire de 450 mm de hauteur par 250 mm de largeur, constante sur toute la longueur. Les dimensions des poutres sont indiquées en coupe et élévation à la figure B-2.1.

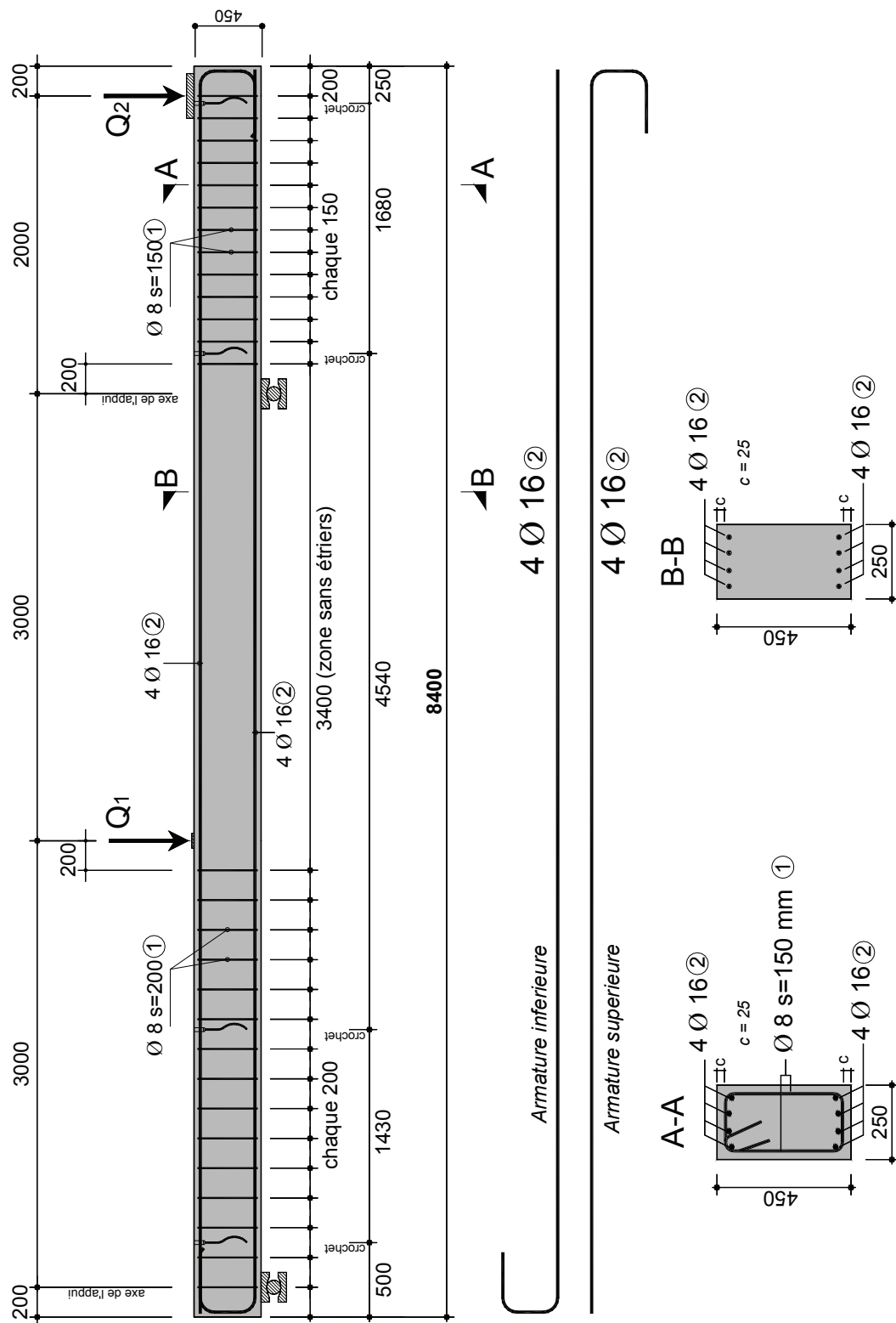


Figure B-2.1: Dimensions des bandes de dalle et armature [mm]



## B-2.2 Paramètres d'essai

Le taux d'armature choisi pour la flexion ( $\rho = 0.79\%$ ) est jugé représentatif pour des éléments en porte-à-faux des dalles de roulement de pont, au niveau de l'encastrement.

Les dimensions de la portée principale et du porte-à-faux ont été choisies de façon à investiguer l'effet des déformations plastiques de l'armature de flexion sur la résistance à l'effort tranchant sans étriers. Selon le modèle de résistance à l'effort tranchant sans étriers défini dans (Muttoni03), la résistance à l'effort tranchant vaut :

$$\tau_R = \frac{0.3 \cdot \sqrt{f_c}}{0.9 + 2.3 \cdot \varepsilon \cdot d \cdot k_{dg}} \quad (\text{B-2.1})$$

Où

- $f_c$  [MPa] est la résistance à la compression du béton
- $d$  [mm] est l'hauteur utile
- $k_{dg} = 48/(d_g+16)$
- $d_g$  [mm] est le diamètre maximal des agrégats
- $\varepsilon$  est la déformation axiale de la poutre, calculée avec la section fissurée à  $0.6 \cdot d$  du bord comprimé et à une section située à  $0.5 \cdot d$  du bord de la charge concentrée (dans ce cas, la charge  $Q_1$ ).

Pour l'armature et les dimensions données à la figure B-2.1, on a  $\rho = 0.79\%$ ,  $d = 409$  mm et  $b = 250$  mm. Les propriétés suivantes sont admises pour les matériaux:  $E_c = 30$  kN/mm<sup>2</sup>,  $E_s = 210$  kN/mm<sup>2</sup>,  $f_c = 50$  MPa,  $f_y = 550$  MPa (limite d'écoulement de l'acier),  $d_g = 16$  mm. On considère aussi l'hypothèse que le comportement en stade homogène est négligeable et que le comportement est parfaitement plastique après que le moment résistant de la section soit atteint. La figure B-2.2 indique la position de la section critique située à  $0.5 \cdot d$  de la force  $Q_1$  et l'évolution de l'effort tranchant sollicitant  $V_s$  (au cours de l'essai) avec l'effort tranchant résistant  $V_R = \tau_R \cdot b \cdot d$  ( $\tau_R$  selon l'équation B-2.1.) pour différents rapports  $Q_2/Q_1$ .

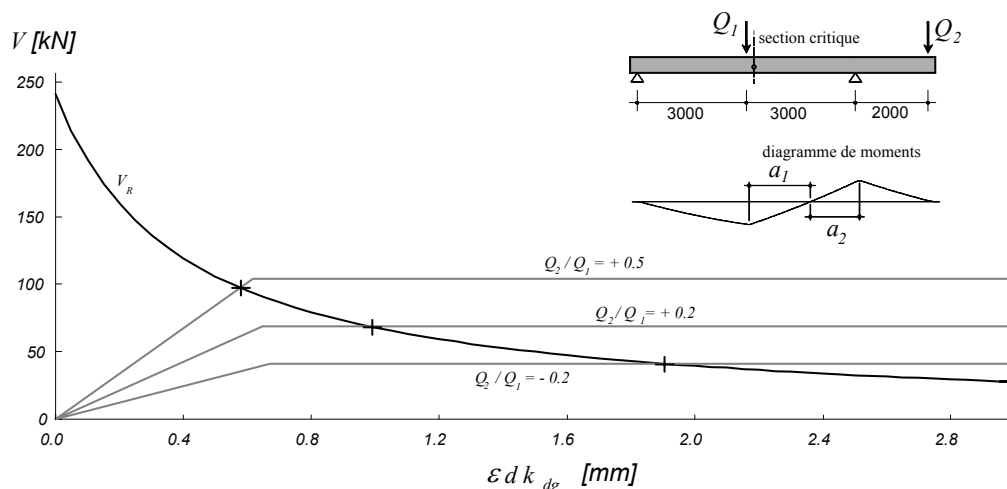


Figure B-2.2: Comportement des poutres et critère de rupture (Muttoni03)

Le comportement illustré à la figure B-2.2 montre que, pour  $Q_2/Q_1 = +0.5$  la rupture à l'effort tranchant se produit alors que la poutre se trouve à la fin de la phase élastique fissuré, avant que le plateau plastique soit atteint. Les déformations plastiques à la rupture augmentent lorsque les valeurs du rapport  $Q_2/Q_1$  diminuent. La ductilité de l'acier de l'armature joue un rôle important : si l'acier n'est pas suffisamment ductile une rupture précoce des barres d'armature se produit avant la rupture par effort tranchant.

En variant le rapport  $Q_2/Q_1$ , on fait varier l'effort tranchant sollicitant à la rupture, mais aussi (selon le critère énoncé à la figure B-2.2) les déformations plastiques à la rupture. Ceci permet donc d'investiguer l'effet des déformations plastiques sur la résistance à l'effort tranchant sans étriers.

Le rapport  $Q_2/Q_1$  a été choisi entre -0.20 et +0.5. La force de réaction à l'appui intermédiaire est nulle pour  $Q_2/Q_1 = -0.375$ . Le rapport  $Q_2/Q_1 = +0.5$  correspond à la formation d'une rotule plastique sur l'appui intermédiaire avec mécanisme de porte-à-faux. Le tableau B-2.1 résume les paramètres des poutres. Les distances  $a_1$  et  $a_2$  sont indiquées à la figure B-2.2.

Tableau B-2.1: Paramètres des poutres d'essai

Essai	$Q_2/Q_1$	$a_1$ [m]	$a_2$ [m]	Type d'acier
SR-2	0.50	1.50	1.50	} Etiré à froid
SR-3	0.20	2.29	0.71	
SR-4	0.00	3.00	0	
SR-5	-0.20	3.92	-	
SR-6	0.60	1.28	1.72	
SR-7	0.10	2.63	0.37	
SR-8	-0.10	3.43	-	
SR-9	0.35	1.87	1.14	
SR-10	-0.10	3.43	-	
SR-11	0.35	1.87	1.14	
SR-12	0.20	2.29	0.71	

### B-2.3 Fabrication

Les bandes de dalle ont été fabriquées dans l'usine de préfabrication d'éléments en béton armé GRAM, à Villeneuve FR, Suisse. La figure B-2.3 montre quelques étapes du processus de fabrication. Les bétonnages ont été effectués en 3 gâchées, le lundi 9 février 2004 (gâchée 1, G1) et le lundi 16 février 2004 (gâchée 2, G2) et le lundi 31 janvier 2005 (gâchée 3, G3).

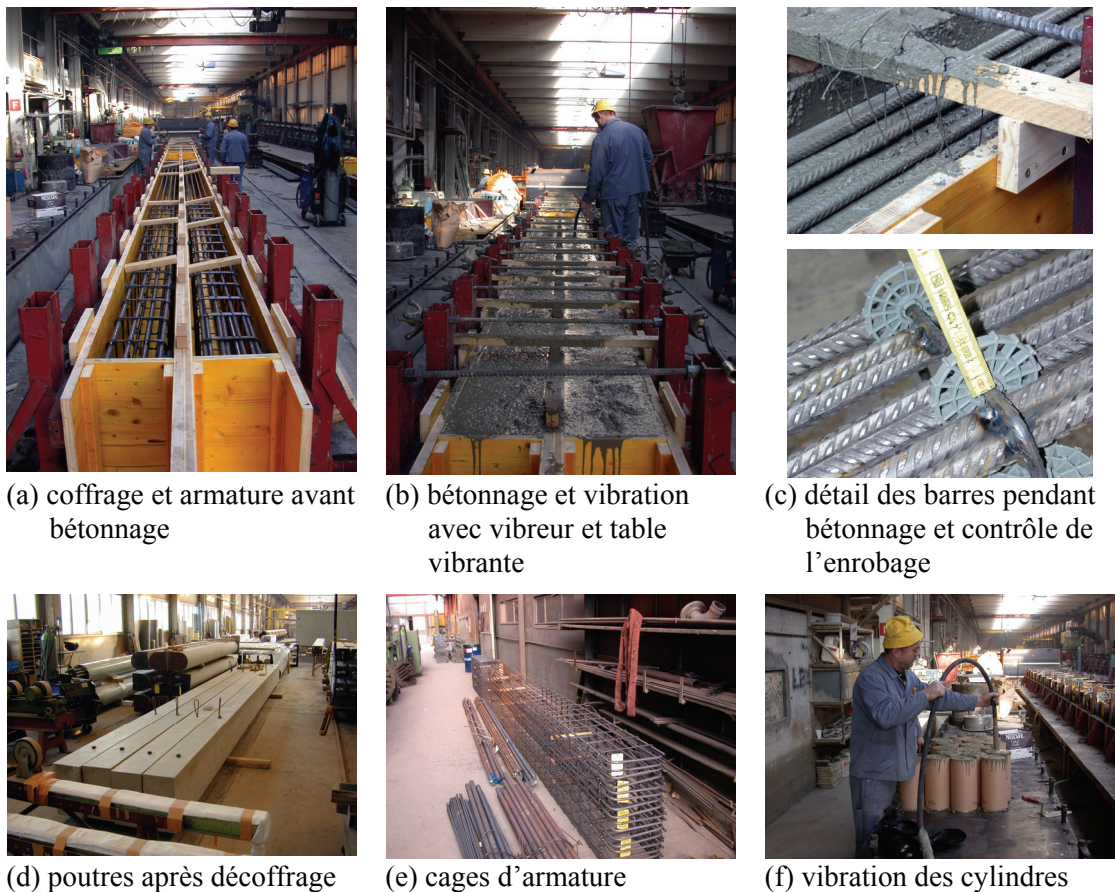


Figure B-2.3: Fabrication des poutres

## B-2.4 Matériaux

### Béton

Lors de la fabrication, des éprouvettes cylindriques de diamètre  $\varnothing = 159$  mm et hauteur  $h = 320$  mm ont été réalisées simultanément en vue de la détermination des propriétés du béton.

Les résultats des essais de compression et de traction sur cylindres sont présentés au tableau B-2.4 pour la gâchée G1, au tableau B-2.5 pour la gâchée G2, et au tableau B-2.6 pour la gâchée G3. Les propriétés mécaniques le jour des essais sont déterminées sur la base de courbes de la forme  $a \cdot \text{jours}^b + c$  ajustées, dont les constantes  $a$ ,  $b$  et  $c$  sont déterminées par les moindres carrés. Les valeurs des propriétés mécaniques le jour des essais sont indiquées au tableau B-2.3. L'évolution des propriétés mécaniques est représentée graphiquement à la figure B-2.4 pour la gâchée G1, à la figure B-2.5 pour la gâchée G2 et à la figure B-2.6 pour la gâchée G3.

La composition par mètre cubique de béton est indiquée au tableau B-2.2. La figure B-2.8 montre les agrégats utilisés.

## Chapitre B-2

Tableau B-2.2: Composition de 1 m<sup>3</sup> de béton

Sable 0/4	Gravier 4/8	Gravier 8/16	Ciment	Eau
929 kg	1337 kg	1858 kg	440 kg	190 kg
23%	32%	45%		E/C = 0.43

Tableau B-2.3: Propriétés du béton le jour des essais (moyenne et coefficient de variation)

Essai	Date	Jours	Résistance à la compression ( $f_c$ )	Résistance à la traction ( $f_{ct}$ )	Module d'élasticité ( $E_c$ )
			[MPa]	[MPa]	[GPa]
SR2	16.03.2004	37	43.11	2.82	30.98
	17.03.2004		± 2.4%	± 2.0%	± 1.7%
SR3	27.04.2004	79	50.62	3.00	31.94
	28.04.2004		± 4.9%	± 2.3%	± 1.8%
SR4	27.05.2004	102	47.55	2.56	33.06
	28.05.2004		± 5.1%	± 2.9%	± 2.8%
SR5	01.06.2004	107	47.64	2.59	33.07
	02.06.2004		± 5.4%	± 2.9%	± 2.8%
SR6	22.11.2004	288	52.71	3.32	33.63
	23.11.2004		± 3.9%	± 3.4%	± 2.5%
SR7	02.12.2004	291	49.11	3.18	32.63
	03.12.2004		± 5.7%	± 3.1%	± 3.2%
SR8	10.12.2004	299	49.16	3.20	32.61
	11.12.2004		± 7.9%	± 3.1%	± 3.2%
SR9	15.12.2004	311	52.82	3.34	33.82
	16.12.2004		± 8.5%	± 3.5%	± 2.5%
SR10	05.05.2005	95	42.41	2.49	31.66
	06.05.2005		± 1.4%	± 6.03%	± 2.40%
SR11	17.05.2005	106	42.91	2.67	31.85
	17.05.2005		± 0.8%	± 4.0%	± 2.4%
SR12	31.05.2005	121	43.51	2.91	32.08
	01.06.2005		± 4.4%	± 3.4%	± 0.9%

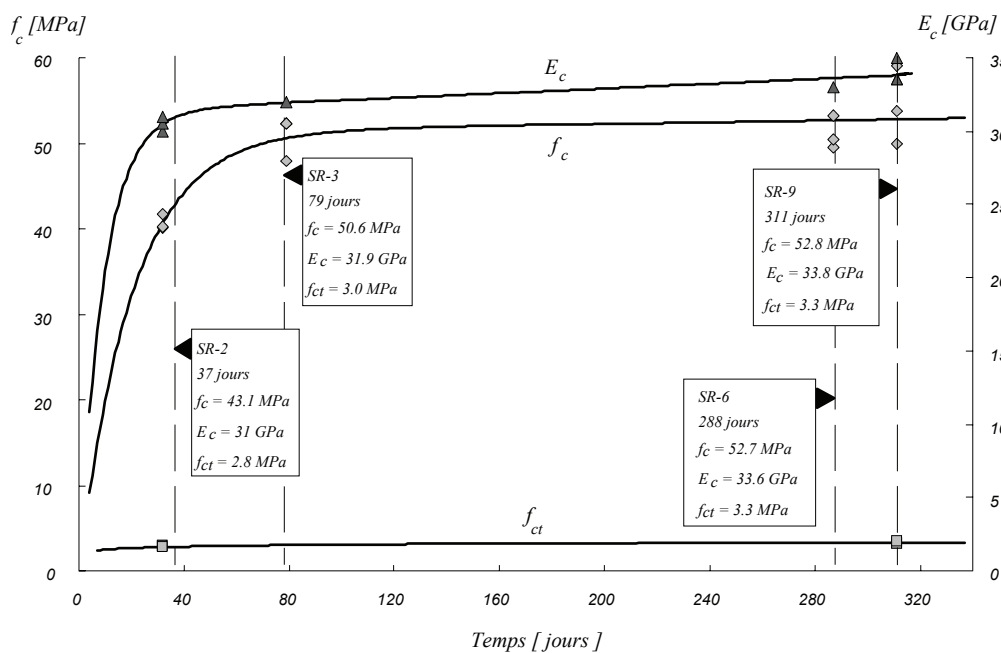


Figure B-2.4: Evolution des propriétés mécaniques (G1)

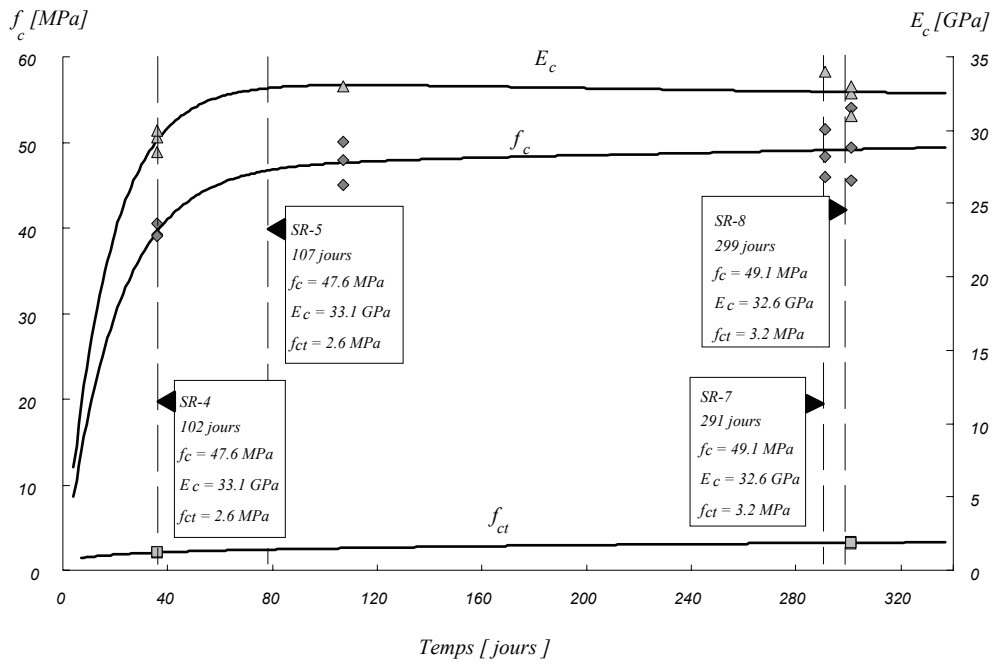


Figure B-2.5: Evolution des propriétés mécaniques (G2)

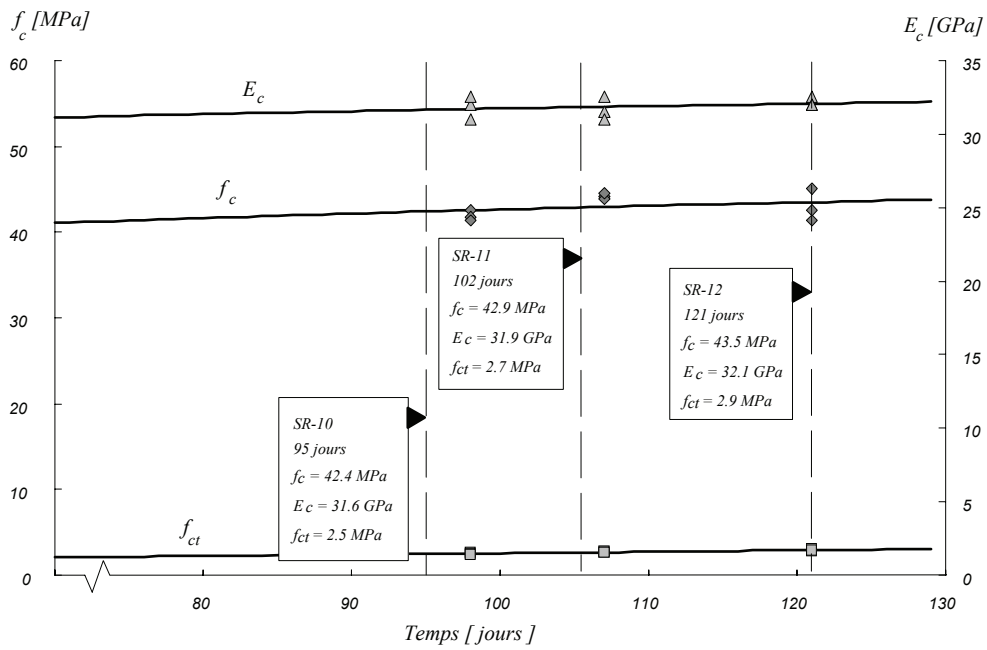


Figure B-2.6: Evolution des propriétés mécaniques (G3)

## Chapitre B-2

Tableau B-2.4: Résultats des essais sur cylindres, (G1)

n°PV	Date	Jours	Résistance à la compression ( $f_c$ ) [MPa]	Résistance à la traction ( $f_{ct}$ ) [MPa]	Module d'élasticité ( $E_c$ ) [GPa]	Masse volumique apparente [t/m <sup>3</sup> ]	
(Fabrication)	09.02.2004	0	-	-	-	-	
047/04/LMC	12.03.2004	32		2.9		2.38	
047/04/LMC	12.03.2004	32		2.9		2.37	
047/04/LMC	12.03.2004	32		2.8		2.37	
046/04/LMC	12.03.2004	32	40.1		30.0	2.36	a)
046/04/LMC	12.03.2004	32	41.7		30.5	2.38	a)
046/04/LMC	12.03.2004	32	40.3		31.0	2.38	a)
089/04/LMC	28.04.2004	79	48.0			2.37	
089/04/LMC	28.04.2004	79	52.3			2.37	
090/04/LMC	28.04.2004	79	52.3		32.0	2.38	
334/04/LMC	22.11.2004	287	49.50			2.37	
334/04/LMC	22.11.2004	287	50.50			2.37	
333/04/LMC	22.11.2004	287	53.20		33.00	2.36	
370/04/LMC	16.12.2004	311	53.80		33.50	2.34	
370/04/LMC	16.12.2004	311	49.90		35.00	2.36	
370/04/LMC	16.12.2004	311	59.10		33.50	2.37	
371/04/LMC	16.12.2004	311		3.20		2.37	
371/04/LMC	16.12.2004	311		3.20		2.36	
371/04/LMC	16.12.2004	311		3.40		2.36	

a) Avec diagramme contrainte-déformation

Tableau B-2.5: Résultats des essais sur cylindres, (G2)

n°PV	Date	Jours	Résistance à la compression ( $f_c$ ) [MPa]	Résistance à la traction ( $f_{ct}$ ) [MPa]	Module d'élasticité ( $E_c$ ) [GPa]	Masse volumique apparente [t/m <sup>3</sup> ]	
(Fabrication)	16.02.2004	0	-	-	-	-	
071/04/LMC	23.03.2004	36		2.00		-	
071/04/LMC	23.03.2004	36		2.10		-	
071/04/LMC	23.03.2004	36		2.10		-	
070/04/LMC	23.03.2004	36	40.5		29.5	2.38	a)
070/04/LMC	23.03.2004	36	39.2		30.0	2.38	a)
070/04/LMC	23.03.2004	36	39.1		28.5	2.38	a)
124/04/LMC	02.06.2004	107	45.0			2.38	
124/04/LMC	02.06.2004	107	50.1			2.38	
125/04/LMC	02.06.2004	107	47.9		33.0	2.38	
349/04/LMC	03.12.2004	291	51.50			2.37	
349/04/LMC	03.12.2004	291	48.30			2.36	
348/04/LMC	03.12.2004	291	46.00		34.00	2.36	
361/04/LMC	13.12.2004	301	45.60		31.00	2.36	
361/04/LMC	13.12.2004	301	49.40		32.50	2.35	
361/04/LMC	13.12.2004	301	54.00		33.00	2.37	
362/04/LMC	13.12.2004	301		3.10		2.36	
362/04/LMC	13.12.2004	301		3.30		2.36	
362/04/LMC	13.12.2004	301		3.20		2.37	

a) Avec diagramme contrainte-déformation

Tableau B-2.6: Résultats des essais sur cylindres, (G3)

n°PV	Date	Jours	Résistance à la compression ( $f_c$ ) [MPa]	Résistance à la traction ( $f_{ct}$ ) [MPa]	Module d'élasticité ( $E_c$ ) [GPa]	Masse volumique apparente [t/m <sup>3</sup> ]
(Fabrication)	31.01.2005	0	0.00	0.00	0.00	-
102/05/LMC	09.05.2005	98	42.50		32.00	2.39
102/05/LMC	09.05.2005	98	41.80		32.50	2.38
102/05/LMC	09.05.2005	98	41.30		31.00	2.37
103/05/LMC	09.05.2005	98		2.70		2.36
103/05/LMC	09.05.2005	98		2.50		2.37
103/05/LMC	09.05.2005	98		2.40		2.38
116/05/LMC	18.05.2005	107		2.80		2.38
116/05/LMC	18.05.2005	107		2.60		2.37
116/05/LMC	18.05.2005	107		2.70		2.37
113/05/LMC	18.05.2005	107	44.10		31.50	2.38
113/05/LMC	18.05.2005	107	43.90		32.50	2.37
113/05/LMC	18.05.2005	107	44.50		31.00	2.37
134/05/LMC	01.06.2005	121		3.00		2.37
134/05/LMC	01.06.2005	121		2.80		2.37
134/05/LMC	01.06.2005	121		2.90		2.38
133/05/LMC	01.06.2005	121	41.40		32.50	2.37
133/05/LMC	01.06.2005	121	42.60		32.00	2.37
133/05/LMC	01.06.2005	121	45.10		32.00	2.38

Les essais de compression et traction des cylindres ont eu lieu au Laboratoire de Matériaux de Construction (LMC) de l'EPFL. Les diagrammes contrainte-déformation lors de l'essai de compression pour 6 cylindres sont montrés à la figure B-2.7 (3 cylindres à 32 jours de la gâchée G1 et 3 cylindres à 36 jours de la gâchée G2). Les déformations ont été mesurées à la surface du cylindre jusqu'à la rupture. La base de mesure était de 100 mm, sur le tiers central de la hauteur du cylindre (figure B-2.8 à gauche). L'essai est contrôlé en déplacement à une vitesse de chargement d'environ 0.2 mm/min.

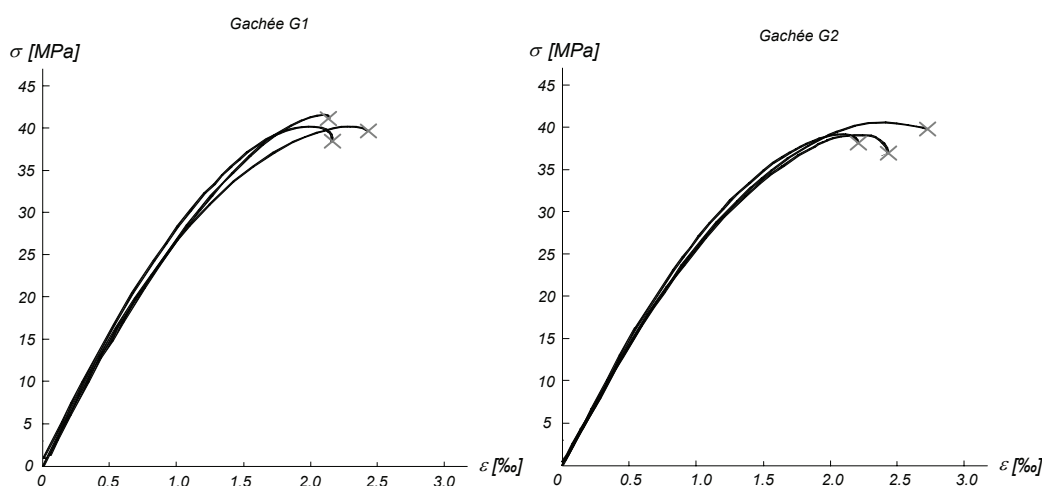


Figure B-2.7: Diagramme contrainte-déformation du béton lors de l'essai de compression, à 32 et 36 jours (G1 et G2, resp.)



Figure B-2.8: Instrumentation de cylindre à la compression (32 jours G1), et dimension maximale de l'agrégat,  $d_g=16$  mm

Les essais de traction pure ont été réalisés à l'aide de 2 plaques collées à la surface du béton. La rupture ne s'est jamais produite aux ancrages collés (figure B-2.9)



Figure B-2.9: Essai de traction à 32 jours (G1) et éprouvettes après rupture

## Acier

L'acier utilisé pour l'armature est de type B500B selon la norme SIA262. Les caractéristiques mécaniques de l'armature en traction ont été mesurées par des tests. Les essais ont eu lieu au Laboratoire de Métallurgie Mécanique (LMM) de l'EPFL. La vitesse de chargement était de l'ordre de 10 MPa/s. Les tableaux B-2.7 et B-2.8 montrent les résultats des propriétés géométriques et mécaniques en traction des barres.

Tableau B-2.7: Caractéristiques mécaniques des barres d'armature en traction (moyenne et coefficient de variation)

Essai	Diamètre nominal ( $\emptyset$ ) [mm]	Limite d'écoulement ( $f_f$ ) [MPa]	Résistance à la traction ( $f_t$ ) [MPa]	Déformation sous charge maximale ( $\epsilon_u$ ) [%]	$f_t / f_y$	Type d'acier
SR2 à SR9	16	530* ±3.1%	600 ±0.8%	5.52 ±14.9%	1.13 ±2.4%	Etiré à froid
SR10 à SR12	16	523 ±0.4%	621 ±0.04	10.57 ±1.2%	1.19 ±0.4%	Laminé à chaud

\* limite conventionnelle d'élasticité à 0.2%.



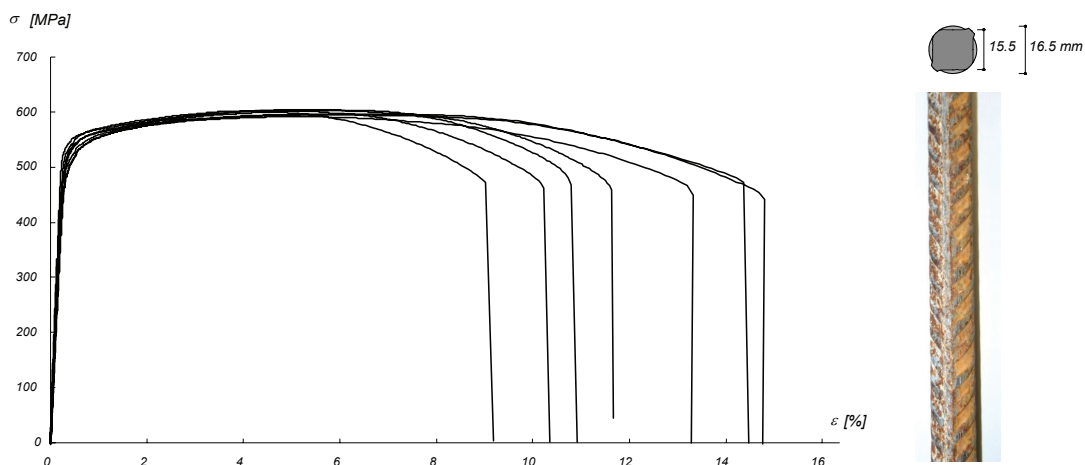


Figure B-2.10: Diagramme contrainte-déformation à la traction (poutres SR2 à SR9)

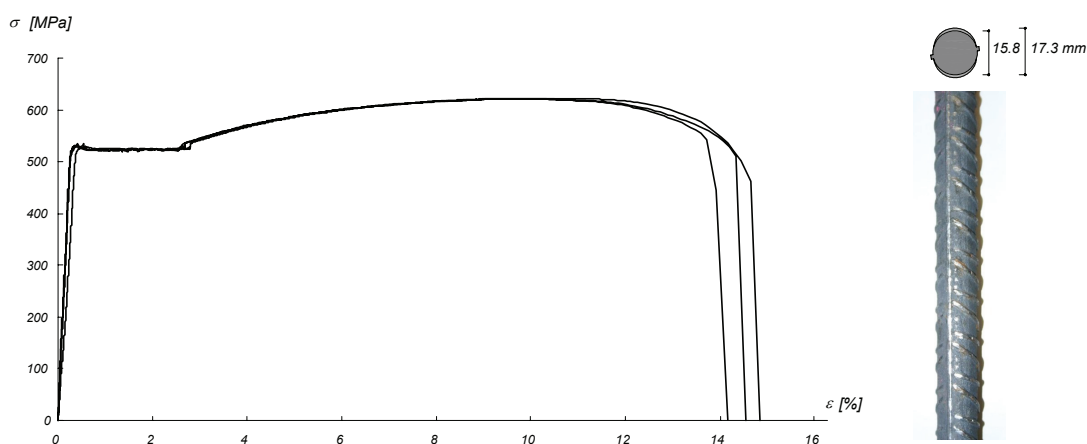


Figure B-2.11: Diagramme contrainte-déformation à la traction (poutres SR10 à SR12)

Les diagrammes contrainte-déformation lors de l'essai de traction sont montrés à la figure B-2.10 et B-2.11 pour les poutres SR2 à SR9 et SR10 à SR12. Les dimensions et la forme des nervures sont illustrées pour chaque type d'acier.

Tableau B-2.8: Résultats d'essais sur barres d'armature

Essai	Diamètre nominal (Ø)	Limite d'écoulement (f <sub>y</sub> )	Résistance à la traction (f <sub>t</sub> )	Déformation sous charge maximale (ε <sub>m</sub> )	f <sub>t</sub> / f <sub>y</sub>	Distance entre ancrages (ℓ <sub>a</sub> )	Longueur de mesure avec extensomètre
	[mm]	[MPa]	[MPa]	[%]		[mm]	[mm]
SR2-9_1	16	539*	603	6.02	1.12	310	150
SR2-9_2	16	548*	602	4.94	1.10	400	150
SR2-9_3	16	545*	601	4.27	1.10	470	150
SR2-9_6	16	540*	605	5.60	1.12	415	150
SR2-9_LM4	16	515*	597	6.82	1.16	~700	200
SR2-9_LM5	16	512*	592	5.18	1.16	~700	200
SR2-9_LM6	16	512*	596	5.81	1.16	~700	200
SR10-12_4	16	521	622	10.71	1.19	755	150
SR10-12_5	16	525	621	10.53	1.18	755	150
SR10-12_6	16	524	622	10.47	1.19	755	150

\* limite conventionnelle d'élasticité à 0.2%.



### B-3 Banc d'essai et instrumentation

Tous les essais des poutres sans étriers ont été exécutés à la halle 2 de l'Institut des Structures (IS) de l'EPFL.

#### B-3.1 Banc d'essai

Le banc d'essai est représenté en élévation à la figure B-3.3, en coupe à la figure B-3.2. La figure B-3.1 montre une vue d'ensemble et une image virtuelle du bâti de charge. Les forces concentrées sont appliquées par le biais de 2 vérins similaires d'une capacité de 500 kN chacun. Les vérins sont équipés d'un capteur de force intégré. La force ou la position verticale du piston des 2 vérins peuvent être réglées ou programmées de manière indépendante, permettant ainsi de charger les différentes éprouvettes de manière variable. A l'extrémité inférieure d'un des vérins (n° 2b à la figure B-3.2), un dispositif permettant de d'appliquer des forces de traction a été ajouté. Il s'agit de 2 plaques qui fixent la poutre en béton à l'aide de 6 tiges filetées précontraintes. La possibilité d'imposer une force de traction avec le vérin situé à l'extrémité de la poutre permet de soumettre les éprouvettes à des modes de chargement variés. Le vérin central (n° 2a à la figure B-3.2) travaille uniquement à la compression. Le type de rupture et le degré de plastification de la poutre dépendront ainsi quasi exclusivement du rapport entre les charges des 2 vérins. A l'extrémité inférieure du vérin central, un profilé métallique (n°8 à la figure B-3.2) et une plaque métallique ont été ajoutés de façon à pouvoir utiliser une grande partie de la course disponible (300 mm). La plaque d'introduction des efforts sous le vérin central a une surface de 100 mm dans le sens de l'axe de la poutre x 250 mm. La poutre s'appuie sur 2 appareils d'appui qui permettent la rotation dans le plan défini par les 2 vérins et le déplacement longitudinal. Ces appareils sont constitués de rotules en acier et leurs axes sont écartés de 6 mètres. Les capteurs de force aux appuis (3 capteurs HBM PRE de 300kN chacun) permettent d'avoir une mesure de la force de réaction pendant l'essai. Le déroulement de l'essai se fait en déplacements contrôlés. Ceci limite les variations des déformations mesurées à chaque palier de charge.



a) Vue d'ensemble



b) Image virtuelle

Figure B-3.1: Bâti de charge (image virtuelle créée par Sylvain Demierre)

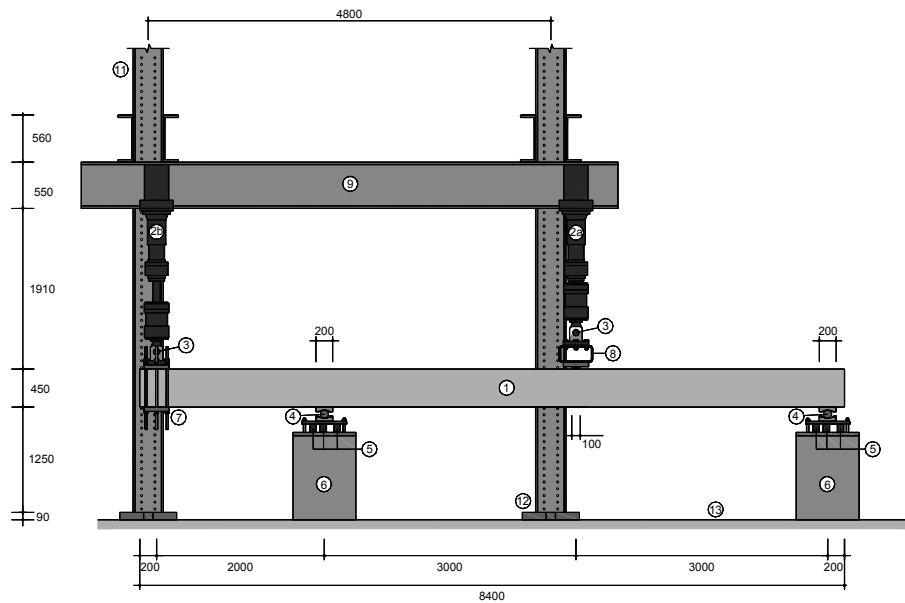


Figure B-3.2: Schéma du bâti de charge (coupe A-A) [mm]

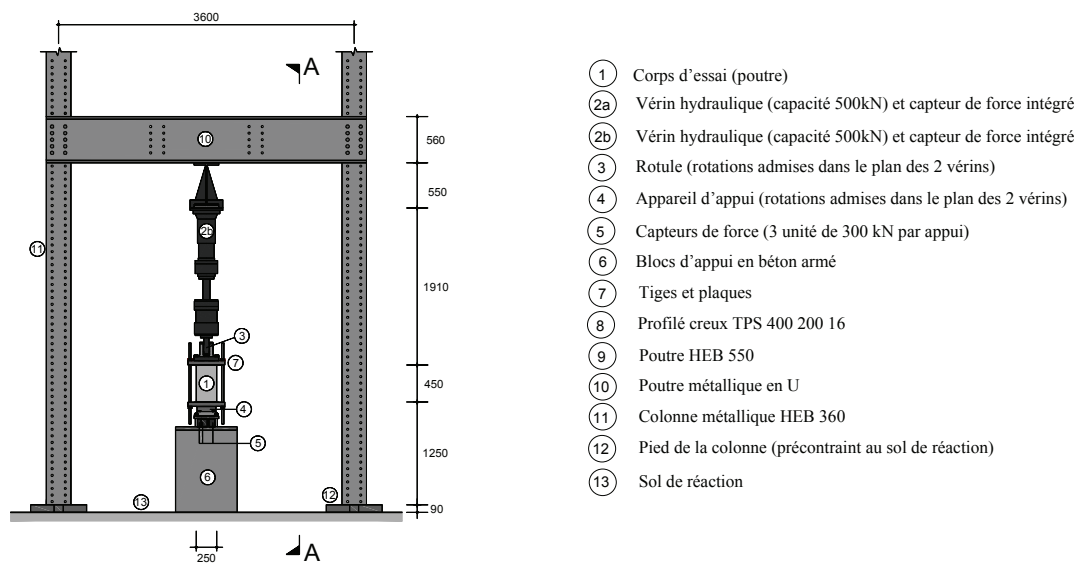


Figure B-3.3: Schéma du bâti de charge (élévation) [mm]

## B-3.2 Instrumentation

### Mesures manuelles

Les mesures de la déformation dans le plan vertical de l'âme de la poutre ont été prises avec le déformètre, sur une zone située entre la charge à mi-travée ( $Q_1$ ) et l'appui intermédiaire. Le réseau de mesure était composé de 131 taquets circulaires en aluminium de 10 mm de diamètre, collés à la surface de la poutre et espacés de 120 mm, définissant ainsi 331 mesures avec un angle de 60 degrés entre eux. Le réseau de mesure est dessiné à la figure B-3.5. Un seul appareil avec une longueur de base de 120 mm et

une plage de mesure de  $\pm 5\text{mm}$  a été utilisé. Afin de contrôler les éventuelles variations de température pouvant se produire durant l'essai, une barre d'invar de 120 mm de longueur était régulièrement mesurée, chaque 16 mesures, au maximum. Les températures étaient également enregistrées au cours de l'essai. Lorsque les déformations locales devenaient très grandes, comme l'a souvent été le cas pour des paliers proches de la rupture, l'appareil de mesure utilisé n'avait pas une course suffisante pour faire la mesure. Dans ce cas, un autre taquet a été collé à côté d'un des taquets originaux de façon à raccourcir la longueur de mesure. La distance entre le nouveau taquet et l'original a ensuite été mesurée.

Le processus de mesure requiert 2 opérateurs. Le premier réalise activement les mesures avec le déformètre alors que le second contrôle à l'ordinateur l'enregistrement de l'écart-type et de la moyenne des valeurs mesurées à chaque position. La mesure complète de tout le réseau dure environ 45 minutes. A noter que les mesures sont toujours prises par la même personne, de façon à éviter des variations probables introduites par différents opérateurs. La séquence suit la numérotation indiquée à la figure B-3.5. Ainsi, 5 régions de mesure existent (mes. 1 à 69, 70 à 134, 135 à 199, 200 à 264 et 265 à 331). A l'intérieur de chaque région la séquence de mesure a été choisie de façon à minimiser les changements de position (figure B-3.4). A la fin de chaque mesure complète du réseau, la déformée de la zone mesurée est calculée et affichée, ceci afin de remarquer les éventuelles mesures manquantes ou autres anomalies et de les corriger en conséquence.

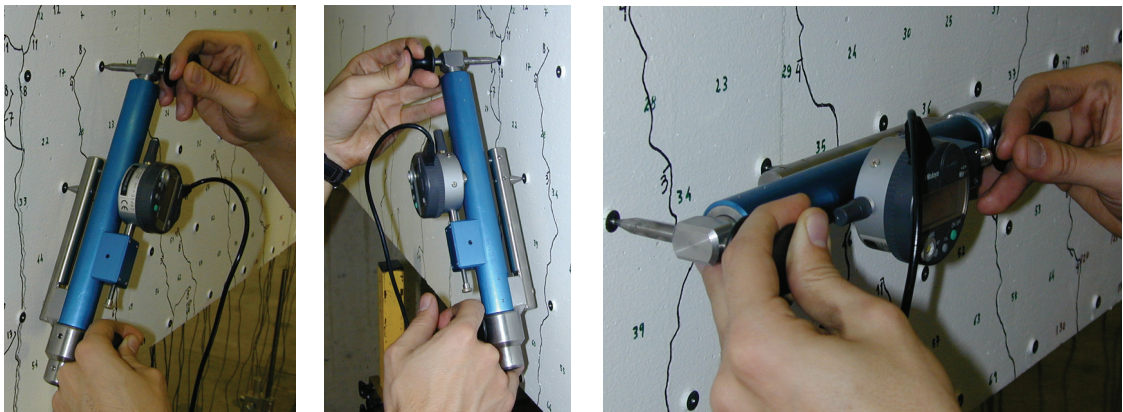


Figure B-3.4: Positions de mesure avec le déformètre

Au cours de l'essai, soit à chaque palier, des ouvertures des fissures ont été systématiquement mesurées en quelques endroits jugés intéressants. En plus, une estimation du glissement entre les 2 lèvres d'une fissure a aussi été réalisée dès que celle-ci était jugée critique.

Des photos à haute résolution ont été prises systématiquement à chaque palier de charge, à gauche de l'appui intermédiaire et à droite du vérin central (force  $Q_1$ ), du côté du réseau de mesure du déformètre. Ces 2 sections ont été jugées critiques. Les photos permettent une bonne documentation de l'histoire de la fissuration à l'appui et en travée et une éventuelle estimation par photogrammétrie des déplacements à la surface. Les taquets du déformètre ont été peints en noir dans ces zones pour améliorer le contraste avec le fond blanc de la poutre et mieux définir les cibles. Des cibles fixées au sol et indépendantes des déplacements de la poutre ont été disposées et permettent de calibrer les photos pour obtenir les déplacements de la poutre.

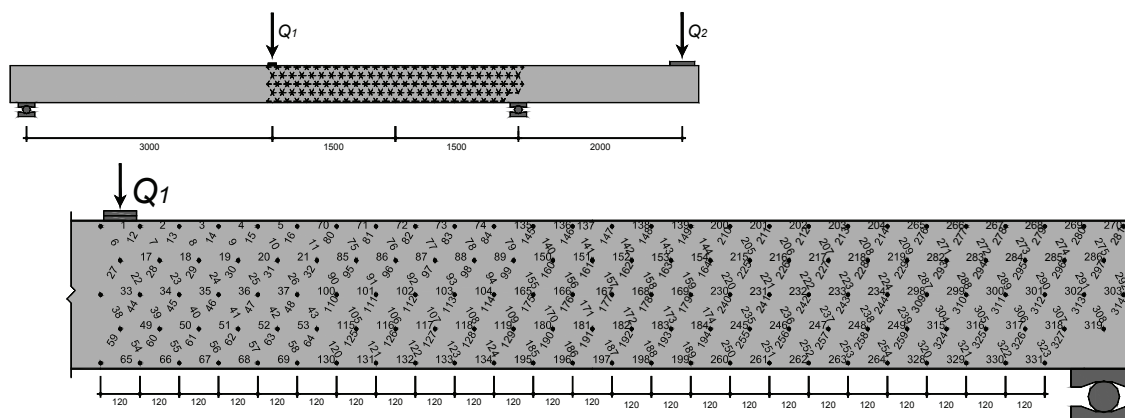


Figure B-3.5: Ordre et numérotation des mesures manuelles (déformètre) [mm]

### Mesures en continu

Les mesures en continu sont de 5 types :

- Mesures des forces dans les vérins ( $Q_1$  et  $Q_2$ ) et des réactions aux appuis
- Mesures des allongements à la surface du béton avec des jauges d'extensiométrie (jauges "oméga"), de différentes longueurs de mesure (fig. B-3.6 et B-3.7)
- Mesures des déplacements verticaux à la surface inférieure de la poutre avec des capteurs inductifs (fig. B-3.8)
- Mesures des rotations de la poutre dans le plan des forces appliquées, avec des inclinomètres (fig. B-3.8)
- Mesures de la température à la surface du béton

Les mesures des forces, des allongements et des déplacements ont été constamment enregistrées automatiquement à l'ordinateur, avec un intervalle d'environ 10 secondes pendant la mise en charge. Durant les paliers, la vitesse de mesure a été diminuée. Pour ces mesures, une unité de mesure de 100 canaux a été utilisée.

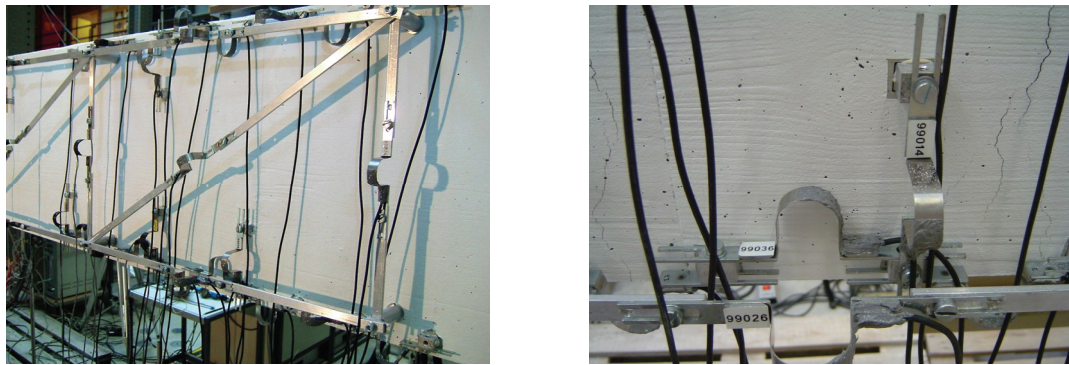
Les jauges "oméga" sont des capteurs constitués d'un support en forme d'oméga au sommet duquel est collé un pont complet de jauges d'extensiométrie qui va mesurer les déformations dudit support. La position des jauges "oméga" utilisées à la surface du béton (jauges isolées et en treillis) est indiquée à la figure B-3.7. L'utilisation d'un treillis en aluminium combiné avec les jauges oméga a permis de mesurer les déformations sur des distances plus grandes. Le tableau B-3.1 résume les numéros des jauges utilisées, leur région de mesure, leur longueur de base utilisée et leur direction de mesure.

Une élévation de la poutre avec la position des inclinomètres et des capteurs inductifs est montrée à la figure B-3.8. Les capteurs inductifs utilisés pour mesurer les déplacements  $w_0$  et  $w_l$  étaient des W200 ( $\pm 200$  mm). Les capteurs inductifs utilisés pour mesurer les autres déplacements étaient des W100 ( $\pm 100$  mm). La présence des déformations plastiques lors de la formation du mécanisme de rupture a imposé de prévoir des grandes plages de mesure.

La visualisation graphique des mesures à l'écran de l'ordinateur pendant la réalisation de chaque essai a permis une meilleure gestion de l'essai. En particulier, il intéressait de

connaître les valeurs des forces des vérins et leur rapport, afin de pour pouvoir régler efficacement leur position. Le rapport entre les forces ( $Q_2 / Q_1$ ) ciblé pour chaque essai a ainsi pu être constamment réglé pendant la mise en charge.

Les jauges d'extensiométrie, les capteurs inductifs et les capteurs de force aux appuis ont été étalonnées avant chaque série d'essais. Les capteurs de force aux vérins sont régulièrement étalonnés par l'EMPA.



a) Réseau de mesure

b) Détail

Figure B-3.6: Mesure des allongements à la surface du béton avec des jauges "omega"

Tableau B-3.1: Organisation des mesures avec des jauges "oméga"

Position	Grandeur	N° de voie / mesure	Nombre	Longueur de mesure [mm]
Travée, supérieur	Allongement horizontal	35, 38, 41, 45, 50, 53, 55, 57	8	100
Travée, inférieur	Allongement horizontal	37, 40, 43, 46, 51, 54, 56, 59	8	100
Appui, supérieur	Allongement horizontal	00, 01, 02, 03, 10, 15, 18, 19	8	100
Appui, inférieur	Allongement horizontal	05, 06, 07, 08, 09, 14, 17, 21	8	100
Inférieur	Allongement vertical	16, 22, 25, 31, 42	5	100
Inférieur	Allongement vertical	20, 27, 30, 36, 44, 52	6	100
Treillis, vertical	Allongement vertical	04, 23, 29, 39, 58	5	370
Treillis, supérieur	Allongement horizontal	11, 24, (32, 47)	4	900, (600)
Treillis, inférieur	Allongement horizontal	13, 28, (34, 49)	4	900, (600)
Treillis, diagonal	Allongement diagonal	12, 26, (33, 48)	4	973, (705)

Total : 60

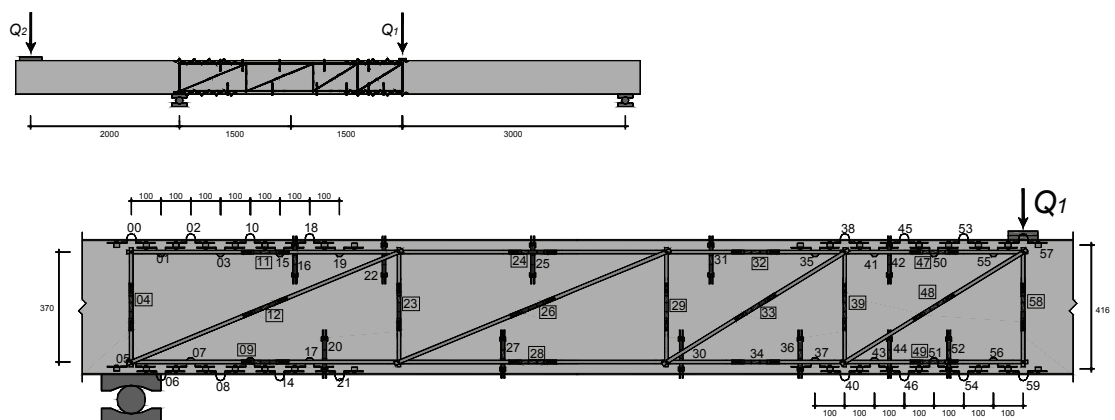


Figure B-3.7: Ordre et numérotation des jauges "oméga" [mm]

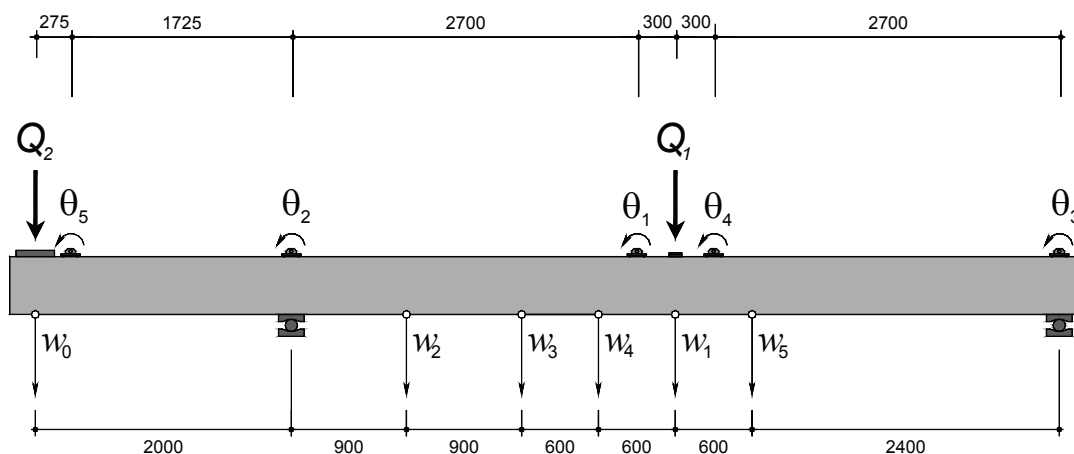


Figure B-3.8: Ordre et numérotation des capteurs inductifs et inclinomètres [mm]

### B-3.3 Préparation et déroulement de l'essai

La préparation intégrale d'une poutre pour l'essai a duré environ 7 jours, y compris les travaux suivants (l'ordre n'est pas respecté) : traçage de la poutre, collage des taquets pour les jauges "oméga" et déformètre, perçage des trous pour le support de la structure en aluminium, peinture de l'élément avec de la dispersion blanche, numérotation du réseau de mesure au déformètre, mise de la poutre sur les appuis, montage des jauges d'extensiométrie, des inclinomètres et capteurs inductifs, assemblage des plaques au vérin  $Q_2$ , mise en place des appareils photo, peinture des cibles en noir.

Une fois que toute l'instrumentation est mise en place, un test est mené pour contrôler le bon fonctionnement des jauges "oméga", des capteurs inductifs et de l'enregistrement des données. Une mise à zéro complète des forces, des jauges "oméga" et des capteurs inductifs est ensuite effectuée. Le réseau du déformètre est intégralement mesuré à deux reprises avant que le début de l'essai.

Pendant l'essai, l'ordre des procédures est contrôlé à l'aide d'une liste. Tout événement non prévu est consigné dans le cahier de l'essai. Pour chaque palier, l'ordre des procédures est la suivante: augmenter la fréquence de mesure de l'enregistrement; activer la caméra de vidéo; relever les forces des vérins, l'heure et le déplacement vertical sous vérin  $Q_1$  avant et après la mise en charge ; désactiver la caméra de vidéo; diminuer la fréquence de mesure; mesurer le réseau du déformètre; enregistrer les valeurs des forces et du déplacement vertical à la fin des mesures du réseau; visualiser les mesures faites du réseau pour le palier effectué; dessiner, numéroter et mesurer les ouvertures des fissures; prendre des photos à haute résolution à l'appui et en travée et vérification de l'enregistrement/stockage; photographier autres aspects intéressants. Chaque palier a duré environ une heure à une heure et demi. Tous les essais ont été réalisés sur une durée de 1 à 2 jours. La poutre a été laissée en charge pendant la nuit (en déplacements contrôlés). La rupture a toujours été filmée en vidéo.



## B-4 Résultats

### B-4.1 Dépouillement des mesures

#### Forces

Les forces des vérins ( $Q_1$  et  $Q_2$ ) et des réactions ( $R_1$  et  $R_2$ ) ont été mesurées pendant l'essai (figure B-4.1). Ceci conduit à une redondance dans les valeurs mesurées qui peut être utile pour corriger les erreurs de mesure éventuelles. En négligeant le moment de torsion, les équations suivantes permettent de corriger des mesures à faire pour les forces et réactions (équations B-4.1 et B-4.2) :

$$Q_i = \tilde{Q}_i + q_i \quad (\text{B-4.1})$$

$$R_i = \tilde{R}_i + r_i, \quad \text{avec } i = 1,2 \quad (\text{B-4.2})$$

$Q_i$  et  $R_i$  sont les valeurs des forces et réactions corrigées. Les conditions  $F_1$  et  $F_2$  à introduire sont (équilibre des forces et moments,  $\gamma_c$  est le poids volumique du béton, en  $\text{kN/m}^3$ ) :

$$F_1 = R_1 + R_2 - Q_1 - Q_2 - 0.945 \cdot \gamma_c = 0 \quad (\text{B-4.3})$$

$$F_2 = 4 \cdot R_1 - Q_1 - 2 \cdot R_2 + 4 \cdot Q_2 = 0 \quad (\text{B-4.4})$$

Et la fonction à minimiser, avec la méthode des multiplicateurs de Lagrange est :

$$q_1^2 + q_2^2 + \omega \cdot (r_1^2 + r_2^2) + \lambda_1 \cdot F_1 + \lambda_2 \cdot F_2 = \min, \quad \text{avec } \omega = 0.2. \quad (\text{B-4.5})$$

La solution s'obtient en dérivant B-4.5 par rapport à  $q_1, q_2, r_1, r_2, \lambda_1$  et  $\lambda_2$ . Ceci donne un système de 6 équations à 6 inconnues à résoudre pour chaque mesure des forces et des réactions. Les forces maximales mesurées par chaque capteur aux appuis sont petites par rapport à leur valeur maximale d'étalonnage, ce qui implique une perte de précision. La valeur de  $\omega$  est la pondération sur les erreurs aux réactions à l'équation B-4.5. La valeur de  $\omega$  a été choisie 5 fois plus petite que celle choisie pour les erreurs sur les forces ( $q_i$ ).

Le poids propre n'est pas pris en compte dans les mesures des forces puisque les capteurs de force ont été mis à zéro avant l'essai alors que la poutre était déjà sur les appuis. Le poids volumique du béton  $\gamma$  est donc pris égal à zéro pour la résolution de l'équation B-4.5. Le tableau B-4.1 résume les résultats obtenus pour les corrections des forces ( $q_1, q_2$ ) et des réactions ( $r_1, r_2$ ). Les valeurs sont des moyennes des corrections effectuées pour les mesures  $R_i$  et  $Q_i$  au cours de chaque essai. Les variations moyennes des valeurs non corrigées sont aussi indiquées.

Tableau B-4.1: Correction des forces et réactions (valeur moyenne et variation moyenne)

Essai	$r_1$ kN	$r_2$ kN	$q_1$ kN	$q_2$ kN
SR2	0.85 4.0%	1.77 2.7%	-0.07 -0.1%	-0.10 -0.4%
SR3	2.11 6.1%	2.08 3.7%	-0.10 -0.1%	-0.10 -0.7%
SR4	0.92 1.6%	1.61 3.7%	-0.06 -0.1%	-0.09 -
SR5	1.67 2.9%	0.71 4.4%	-0.06 -0.1%	-0.02 0.2%
SR6	1.48 5.6%	3.49 3.2%	-0.50 -0.5%	-0.83 -1.6%
SR7	3.47 6.7%	3.12 3.7%	-0.66 -0.5%	-0.60 -3.7%
SR8	1.22 1.8%	0.12 0.0%	-0.13 -0.1%	0.05 -0.7%
SR9	1.27 2.8%	2.06 2.3%	-0.33 -0.3%	-0.46 -1.6%
SR10	1.35 3.3%	-0.80 -2.6%	-0.06 -0.1%	0.30 -4.4%
SR11	0.24 0.8%	1.88 4.2%	-0.21 -0.3%	-0.48 -1.9%
SR12	1.80 4.2%	1.80 2.2%	-0.36 -0.3%	-0.36 -1.6%

La moyenne des corrections en pourcentage à appliquer aux forces  $Q_i$  pour tous les essais est inférieure à 1%. Le calcul des efforts et des réactions  $R_i$  est fait à partir des valeurs non corrigées des forces des vérins  $Q_1$  et  $Q_2$ . La figure B-4.1 montre le diagramme des efforts tranchants et le diagramme des moments de flexion de la poutre sollicitée par les forces  $Q_1$  et  $Q_2$ . Les équations des courbes correspondantes sont indiquées au tableau B-4.2.

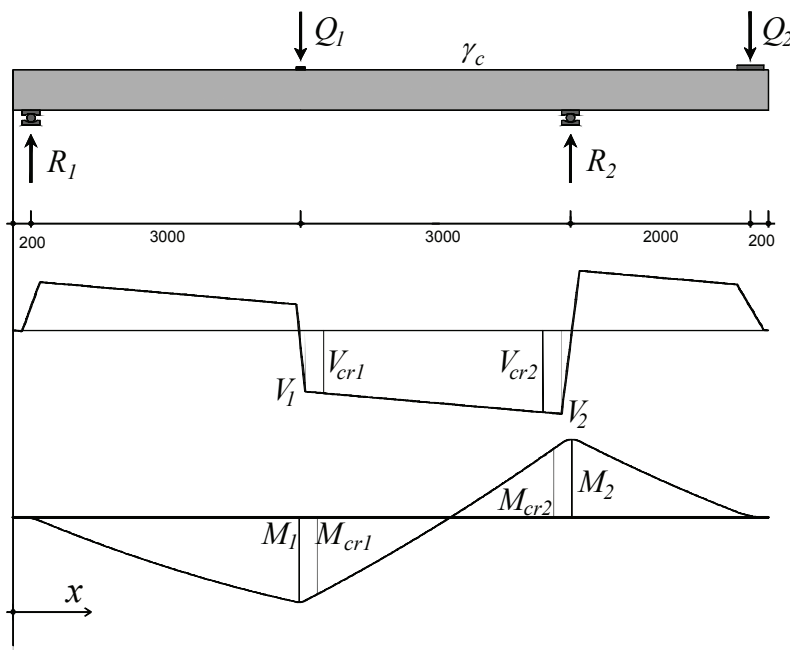


Figure B-4.1: Système statique et diagrammes d'efforts tranchants et des moments de flexion [mm]

Toutes les forces et réactions sont considérées dans le calcul comme étant uniformément réparties sur la longueur d'introduction correspondante. La position de 2 sections critiques selon [Muttoni03] pour la rupture à l'effort tranchant est aussi connue. La section critique se situe à une distance de  $0.5 \cdot d$  de l'axe de la force appliquée  $Q_1$  ou de la force de réaction  $R_2$ . La position de la section critique par rapport à l'extrémité gauche de la poutre (fig. B-4.1) vaut respectivement  $x = 3.405$  m et  $x = 5.996$  m, en travée et en appui.

Tableau B-4.2: Equations des diagrammes des efforts tranchants et moments de flexion dus à  $Q_1$  et  $Q_2$ ,  $m = Q_2/Q_1$ ,  $Q_1$  en [kN],  $x$  en [m]

Position $x$ [m]	Effort tranchant ( $V$ ) [kN]	Moment de flexion ( $M$ ) [kN·m]
0.1 .. 0.3	$(-5/3 \cdot m \cdot x + 1/6 \cdot m + 5/2 \cdot x - 1/4) \cdot Q_1$	$(-5/6 \cdot m \cdot x^2 + 1/6 \cdot m \cdot x - 1/120 \cdot m + 5/4 \cdot x^2 - 1/4 \cdot x + 1/80) \cdot Q_1$
0.3 .. 3.15	$(-1/3 \cdot m + 1/2) \cdot Q_1$	$(1/15 \cdot m - 1/10 - 1/3 \cdot m \cdot x + 1/2 \cdot x) \cdot Q_1$
3.15 .. 3.25	$(-10 \cdot x + 32 - 1/3 \cdot m) \cdot Q_1$	$(-5 \cdot x^2 + 32 \cdot x - 1/3 \cdot m \cdot x + 1/15 \cdot m - 3977/80) \cdot Q_1$
3.25 .. 6.1	$(-1/3 \cdot m - 1/2) \cdot Q_1$	$(1/15 \cdot m + 31/10 - 1/3 \cdot m \cdot x - 1/2 \cdot x) \cdot Q_1$
6.1 .. 6.3	$(20/3 \cdot m \cdot x - 41 \cdot m + 5/2 \cdot x - 63/4) \cdot Q_1$	$(10/3 \cdot m \cdot x^2 - 41 \cdot m \cdot x + 5/4 \cdot x^2 - 63/4 \cdot x + 1241/10 \cdot m + 49.6125) \cdot Q_1$
6.3 .. 8.05	$m \cdot Q_1$	$(\alpha \cdot x - 41/5 \cdot m) \cdot Q_1$
8.05 .. 8.35	$(-10/3 \cdot m \cdot x + 167/6 \cdot m) \cdot Q_1$	$(-5/3 \cdot m \cdot x^2 + 167/6 \cdot m \cdot x - 27889/240 \cdot m) \cdot Q_1$

Tableau B-4.3: Equations des diagrammes des efforts tranchants et moments de flexion dus au poids propre,  $\gamma$  en [kN/m<sup>3</sup>],  $x$  en [m]

Position $x$ [m]	Effort tranchant ( $V$ ) [kN]	Moment de flexion ( $M$ ) [kN·m]
0 .. 0.1	$(-2.8125 \cdot x)/25 \cdot \gamma$	$(-1.40625 \cdot x^2)/25 \cdot \gamma$
0.1 .. 0.3	$(36.5625 \cdot x - 3.93750)/25 \cdot \gamma$	$(18.28125 \cdot x^2 - 3.9375 \cdot x + 0.196875)/25 \cdot \gamma$
0.3 .. 6.1	$(-2.8125 \cdot x + 7.875)/25 \cdot \gamma$	$(-1.40625 \cdot x^2 + 7.875 \cdot x - 1.575)/25 \cdot \gamma$
6.1 .. 6.3	$(75.9375 \cdot x - 472.5)/25 \cdot \gamma$	$(37.96875 \cdot x^2 - 472.5 \cdot x + 1463.56875)/25 \cdot \gamma$
6.3 .. 8.4	$(-2.8125 \cdot x + 23.625)/25 \cdot \gamma$	$(-1.40625 \cdot x^2 + 23.625 \cdot x - 99.225)/25 \cdot \gamma$

## Mesures manuelles au déformètre

Chaque mesure faite à la position  $i$  du réseau de mesures au déformètre vaut  $\Delta \ell_i$ . La correction appliquée  $\Delta \ell_{inv,i}$  (équation B-4.6) à chaque mesure permet de supprimer l'effet de la température au cours de l'essai. L'indice  $i$  désigne la position de la mesure ( $\Delta \ell_i$ ,  $\Delta \ell_{inv,i}$  en mm) :

$$\Delta \ell'_i = \Delta \ell_i - \Delta \ell_{inv,i} \quad \text{avec } i=1, \dots, 331. \quad (\text{B-4.6})$$

Chaque correction appliquée  $\Delta \ell_{inv,i}$  est calculée en interpolant linéairement à partir des mesures de la barre d'invar les plus proches dans le temps.

Due à la redondance du réseau de mesure, une minimisation et une correction des erreurs de mesure peuvent être menées. Ceci est fait par le biais de l'analogie du treillis à l'aide d'un calcul automatique. Les valeurs mesurées et déjà corrigées de l'influence de la température ( $\Delta \ell'_i$ ), sont introduites comme des déformations imposées  $\varepsilon_{imp,i}$  (équation B-4.7) dans un treillis imaginaire coïncidant avec le réseau de mesure et extérieurement isostatique et dont les longueurs initiales des barres valent 120 mm. Un calcul hyperstatique fournit les valeurs des déformations de chaque barre  $\Delta \varepsilon_i$  (équation B-4.8) qui sont utilisées pour corriger les mesures (équation B-4.9). L'écart-

type des corrections appliquées à chaque palier est indiqué au tableau B-4.4. Pour le calcul hyperstatique, la rigidité axiale  $EA/\ell$  est par défaut prise égale à 1 et est identique pour toutes les barres. L'écart-type de chaque mesure a aussi été enregistré et est toujours inférieur à  $2 \mu\text{m}$ . La déformation axiale finale de chaque barre pour chaque palier  $p$  le long de l'essai est donnée à l'équation B-4.10 ( $\Delta\ell_i$ ,  $\Delta\ell_{inv,i}$ ,  $\Delta\ell_i'$  et  $\Delta\ell_i''$  en mm). L'indice  $p$  désigne le numéro du palier :

$$\varepsilon_{imp,i} = \frac{\Delta\ell_i' + 120}{120} \tag{B-4.7}$$

$$\Delta\varepsilon_i = H(\varepsilon_{imp,1}, \dots, \varepsilon_{imp,i}, \dots, \varepsilon_{imp,331}) \tag{B-4.8}$$

$$\Delta\ell_i'' = \Delta\ell_i - \Delta\ell_{inv,i} + \Delta\varepsilon_i \cdot 120 \quad \text{avec } i=1, \dots, 331. \tag{B-4.9}$$

$$\varepsilon_{i,p} = \frac{\Delta\ell_{i,p}'' - \Delta\ell_{i,p=1}''}{120 + \Delta\ell_{i,p=1}''} \tag{B-4.10}$$

Tableau B-4.4: Ecart-type des corrections  $\Delta\varepsilon_i \cdot 120$  pour chaque palier de charge

Essai	# 0	# 1	# 2	# 3	# 4	# 5	# 6	# 7	# 8	# 9	# 10	Ecart-type moyen
	[ $\mu\text{m}$ ]	[ $\mu\text{m}$ ]	[ $\mu\text{m}$ ]	[ $\mu\text{m}$ ]	[ $\mu\text{m}$ ]	[ $\mu\text{m}$ ]	[ $\mu\text{m}$ ]	[ $\mu\text{m}$ ]	[ $\mu\text{m}$ ]	[ $\mu\text{m}$ ]	[ $\mu\text{m}$ ]	[ $\mu\text{m}$ ]
SR2	6.0	2.5	2.1	2.7	2.2	2.4	2.2					2.9
SR3		2.5	2.3	2.6	2.3	2.1	2.4	2.6	2.6	2.3	3.8	2.6
SR4		4.2	3.6	5.5	3.5	4.3	6.0	3.8	0.0	0.0		3.4
SR5		3.4	2.7	3.1	2.4	3.2	2.6	11.9	3.4	3.9		4.1
SR6	4.3	2.7	2.5	2.4	2.4	2.8	2.8	3.6	2.2	2.5		2.8
SR7	4.4	3.2	3.3	3.0	3.2	3.7	2.7	2.9	3.0			3.3
SR8	4.0	2.6	3.1	3.9	3.4							3.4
SR9	4.0	2.6	3.1	3.9	3.4							3.4
SR10	6.8	3.5	3.5	4.0	3.6							4.3
SR11	6.3	4.7	4.0	3.3	5.2							4.7
SR12	4.1	5.5	3.5	5.3	5.3							4.7

Moyenne de tous les essais 3.6  $\mu\text{m}$

A chaque  $\varepsilon_{i,p}$  calculé correspond un angle  $\theta$  dans le référentiel indiqué à figure B-4.2 égal à 0, 60 ou 120°. Les déformations  $\varepsilon_{i,p}$  sont ainsi attribuées aux triangles selon leur angle  $\theta$  et les valeurs de  $\varepsilon_0$ ,  $\varepsilon_{60}$  et  $\varepsilon_{120}$  sont ainsi définies (fig. B-4.2). Ensuite, le calcul des déformations  $\varepsilon_x$ ,  $\varepsilon_y$ ,  $\gamma_{xy}$  et des déformations et directions principales  $\varepsilon_I$ ,  $\varepsilon_{II}$ ,  $\theta_I$  et  $\theta_2$  se fait une fois par triangle, en admettant un état plan de déformation dans le plan  $(x,y)$  et selon les équations B-4.11 à B-4.15.

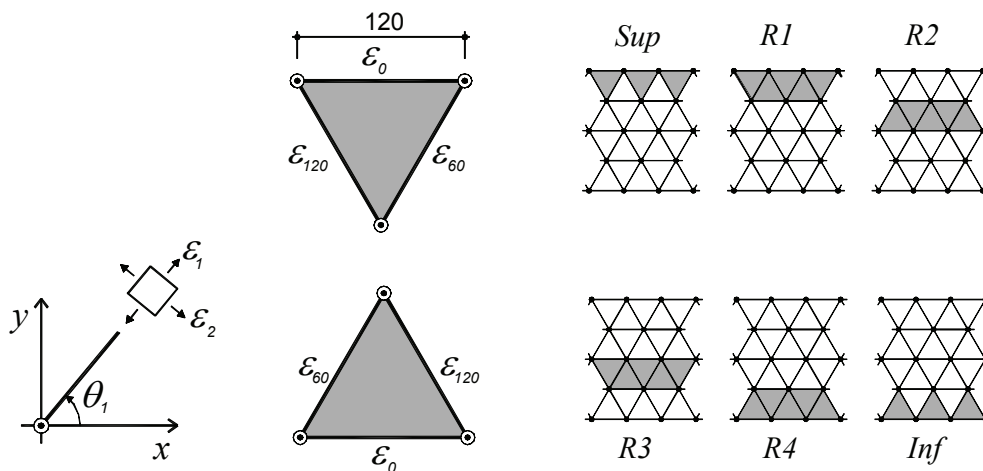


Figure B-4.2: Référentiel avec directions et déformations principales, triangles utilisés pour le calcul des déformations et rangés pour la visualisation des résultats

$$\varepsilon_x = \varepsilon_0 \quad (\text{B-4.11})$$

$$\varepsilon_y = \frac{2}{3} \cdot \varepsilon_{60} + \frac{2}{3} \cdot \varepsilon_{120} - \frac{1}{3} \cdot \varepsilon_0 \quad (\text{B-4.12})$$

$$\gamma_{xy} = 2 \cdot \varepsilon_{xy} = 2 \cdot \varepsilon_{yx} = \frac{2}{\sqrt{3}} \cdot (\varepsilon_{60} - \varepsilon_{120}) \quad (\text{B-4.13})$$

$$\varepsilon_{1,2} = \frac{\varepsilon_x + \varepsilon_y}{2} \pm \sqrt{\left(\frac{\varepsilon_x - \varepsilon_y}{2}\right)^2 + \left(\frac{\gamma_{xy}}{2}\right)^2} \quad (\text{B-4.14})$$

$$\tan \theta_1 = \frac{\varepsilon_1 - \varepsilon_x}{(\gamma_{xy}/2)} \quad \tan \theta_2 = \frac{\varepsilon_2 - \varepsilon_x}{(\gamma_{xy}/2)} \quad (\text{B-4.15})$$

Les déformations calculées sont représentées graphiquement au centre de gravité des triangles correspondants au calcul.

Les courbures peuvent être calculées à partir des  $\varepsilon_x$  des rangés *Sup* et *Inf* (fig. B-4.2):

$$\chi = \frac{\varepsilon_x(\text{Sup}) - \varepsilon_x(\text{Inf})}{h_{rel}} \quad , \text{ avec } h_{rel} = 415.7 \text{ mm} \quad (\text{B-4.16})$$

Le calcul du déplacement relatif entre les 2 lèvres d'une fissure critique [Muttoni91] se fait à chaque fissure jugée critique pour un ensemble de points sur celle-ci. La fissure critique est celle qui provoque la rupture. Pour calculer le déplacement relatif entre 2 points très proches mais situés de part et d'autre de la fissure critique, on procède de la manière suivante: deux champs de déplacements  $w(x,y)$  et  $w'(x,y)$  sont tout d'abord calculés des deux côtés de la fissure (fig. B-4.3). Le champ de déplacements  $w(x,y)$  est calculé à partir des déplacements absolus des points  $P_1$  et  $P_2$ , obtenus auparavant à l'aide d'un calcul informatique (équation B-4.8) en faisant l'hypothèse que la région entre la fissure et une droite définie par  $P_1$  et  $P_2$  est un corps rigide et que l'état de déformation est plan.  $w'(x,y)$  est déterminé de façon similaire de l'autre côté de la fissure. Les déplacements absolus des points  $f$  et  $f'$  sont ensuite calculés à gauche et à droite de la fissure. Le déplacement relatif entre les 2 lèvres de la fissure est la différence entre les déplacements absolus des points  $f$  et  $f'$ . Une condition importante pour que les hypothèses admises soient admissibles est l'absence d'autres fissures importantes à l'intérieur de la région définie par la droite reliant les points  $P_1$  et  $P_2$  et la fissure critique. Si de telles fissures sont présentes, l'hypothèse d'un corps rigide n'est plus valable.

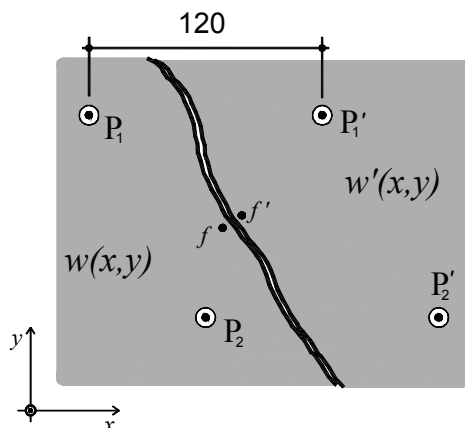


Figure B-4.3: Calcul du déplacement relatif entre les 2 lèvres de la fissure critique [mm]

La forme du champ de déplacements  $w(x,y)$  est donné à l'équation B-4.17.

$$w(x, y) = \begin{cases} w_x = a - e \cdot y \\ w_y = b + e \cdot x \end{cases} \quad (\text{B-4.17})$$

Avec  $a$ ,  $b$  et  $e$  les inconnues, calculées avec l'équation B-4.18.

$$s = (A^T \cdot A)^{-1} \cdot (A^T \cdot c) \quad (\text{B-4.18})$$

$$s = \begin{bmatrix} a \\ b \\ e \end{bmatrix} \quad A = \begin{bmatrix} 1 & 0 & -y_{P_1} \\ 0 & 1 & x_{P_1} \\ 1 & 0 & -y_{P_2} \\ 0 & 1 & x_{P_2} \end{bmatrix} \quad c = \begin{bmatrix} w_{x,P_1} \\ w_{y,P_1} \\ w_{x,P_2} \\ w_{y,P_2} \end{bmatrix}$$

Les coordonnées  $(x_P, y_P)$  et les déplacements absolus  $(w_{x,P}, w_{y,P})$  des points  $P_1$  et  $P_2$  sont connus dans un référentiel  $(x,y)$  (fig. B-4.3). Le déplacement relatif  $\Delta u_{rel}$  du point  $f$  relativement au point  $f'$  vaut :

$$\Delta u_{rel} = w(x_f, y_f) - w'(x_{f'}, y_{f'}) \quad (\text{B-4.19})$$

Pour les calculs,  $x_f = x_{f'}$  et  $y_f = y_{f'}$ , ont été admis. Les coordonnées du point  $f$  sont lues sur la fissure directement à partir des photos (corrigées de la distorsion). Tous les calculs des déformations ont été effectués à l'ordinateur avec un logiciel du type tableur.

Pour chaque poutre, les résultats suivants sont présentés :

- Diagrammes forces-flèche et forces-temps
- Tableau avec l'évolution des forces, moments, efforts tranchants et quelques allongements mesurés pendant les paliers. La contribution du poids propre de la poutre a été mesurée et est prise en compte ( $\gamma = 24.8 \text{ kN/m}^3$ )
- Diagrammes des moments, des efforts tranchants et la déformée des poutres à chaque palier
- Photos de la région de rupture, avant et après la rupture

- Diagrammes du déplacement relatif entre les 2 lèvres des fissures critiques (selon l'équation B-4.19), mesure des déformations longitudinales à la zone tendue et zone comprimée (avec des jauges "oméga") et tableau avec les mesures de l'ouverture des fissures à l'œil nu (ouvertures et glissement)
- Dessin avec les déformations principales de compression et traction pour des paliers choisis et avec le dessin des fissures en arrière plan

### B-4.2 Poutre SR2

La poutre SR2 a été testée avec un rapport  $Q_2/Q_1$  ciblé de +0.5. La rupture observée a été une rupture à l'effort tranchant très fragile (fig. B-4.6), dans la région proche de l'appui intermédiaire avec des ouvertures des fissures très petites. L'ouverture des fissures estimées au palier précédent la rupture est de l'ordre de 0.3 mm (voir figure B-4.7).

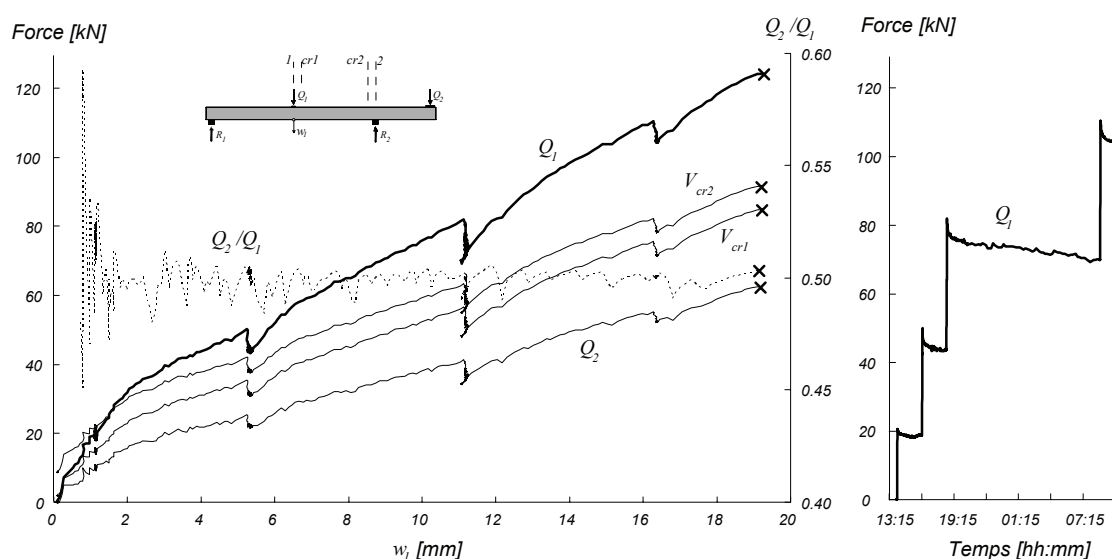


Figure B-4.4: Poutre SR2 : Diagramme charge – flèche et évolution dans le temps

Tableau B-4.5: Poutre SR2: Evolution des valeurs mesurées et calculées

Palier	$Q_1$	$Q_2$	$Q_2/Q_1$	$M_1$	$M_{cr1}$	$M_2$	$M_{cr2}$	$V_1$	$V_{cr1}$	$V_2$	$V_{cr2}$	$\Omega_{11}$	$\Omega_{00}$	$w_1$	$w_0$	$Q_1/Q_{1,CR}$	Rem.	
	[kN]	[kN]	-	[kN·m]	[kN·m]	[kN·m]	[kN·m]	[kN]	[kN]	[kN]	[kN]	[mm]	[mm]	[mm]	[mm]	%	*	
#2	20.3	10.6	0.52	28.8	26.0	-26.9	-23.2	-14.9	-15.4	-22.9	-22.6	0.02	0.01	1.12	0.66	16%	DP	
	18.8	9.72	0.52	27.5	24.8	-25.2	-21.7	-13.9	-14.3	-21.9	-21.6						15%	FD
	19.3	10.1	0.52	27.8	25.1	-26.1	-22.5	-14.3	-14.7	-22.3	-22.0	0.01	0.01	1.17	0.64	16%	FP	
#3	50.2	25.4	0.51	58.4	51.9	-55.7	-48.8	-34.8	-35.2	-42.8	-42.5	0.09	0.20	5.23	2.33	40%	DP	
	43.9	22.18	0.51	52.2	46.5	-49.4	-43.2	-30.6	-31.0	-38.5	-38.2						35%	FD
	44.0	21.9	0.50	52.7	47.0	-49.0	-42.8	-30.6	-31.0	-38.5	-38.2	0.11	0.20	5.39	2.40	35%	FP	
#4	82.0	41.2	0.50	89.9	79.5	-86.3	-76.0	-56.0	-56.4	-63.9	-63.6	0.43	0.35	11.14	5.10	66%	DP	
	76.3	38.33	0.50	84.3	74.6	-80.8	-71.1	-52.2	-52.6	-60.1	-59.8						61%	FD
	74.7	37.1	0.50	83.3	73.7	-78.3	-68.8	-51.0	-51.4	-58.9	-58.6	0.43	0.34	11.18	5.06	60%	FP	
#5	70.6	34.9	0.49	79.2	70.2	-74.1	-65.1	-48.2	-48.6	-56.1	-55.8	0.44	0.34	11.11	5.10	57%	DP	
	70.5	34.83	0.49	79.2	70.2	-74.0	-64.9	-48.1	-48.5	-56.1	-55.8						57%	FD
	69.8	34.3	0.49	78.8	69.9	-72.9	-63.9	-47.6	-48.0	-55.6	-55.3	0.42	0.34	11.07	5.05	56%	FP	
#6	110.6	55.3	0.50	118.3	104.3	-113.8	-100.4	-75.0	-75.4	-82.9	-82.6	0.74	0.51	16.27	7.95	89%	DP	
	105.6	53.07	0.50	113.1	99.8	-109.4	-96.6	-71.7	-72.2	-79.7	-79.4						85%	FD
	104.5	52.3	0.50	112.3	99.0	-108.0	-95.3	-70.9	-71.4	-78.9	-78.6	0.72	0.51	16.40	8.07	84%	FP	
	124.2	62.5	0.50	131.4	115.7	-127.7	-112.9	-84.2	-84.6	-92.1	-91.8	0.86	0.61	19.10	9.42	100%	CM	
	124.1	62.4	0.50	131.4	115.7	-127.5	-112.7	-84.1	-84.5	-92.1	-91.8	0.86	0.61	19.21	9.52	100%	CR	

\* DP : Début du palier ; FD : Fin des mesures avec le déformètre ; FP : Fin du palier ; CM : Charge maximale ; CR : Charge de rupture ;



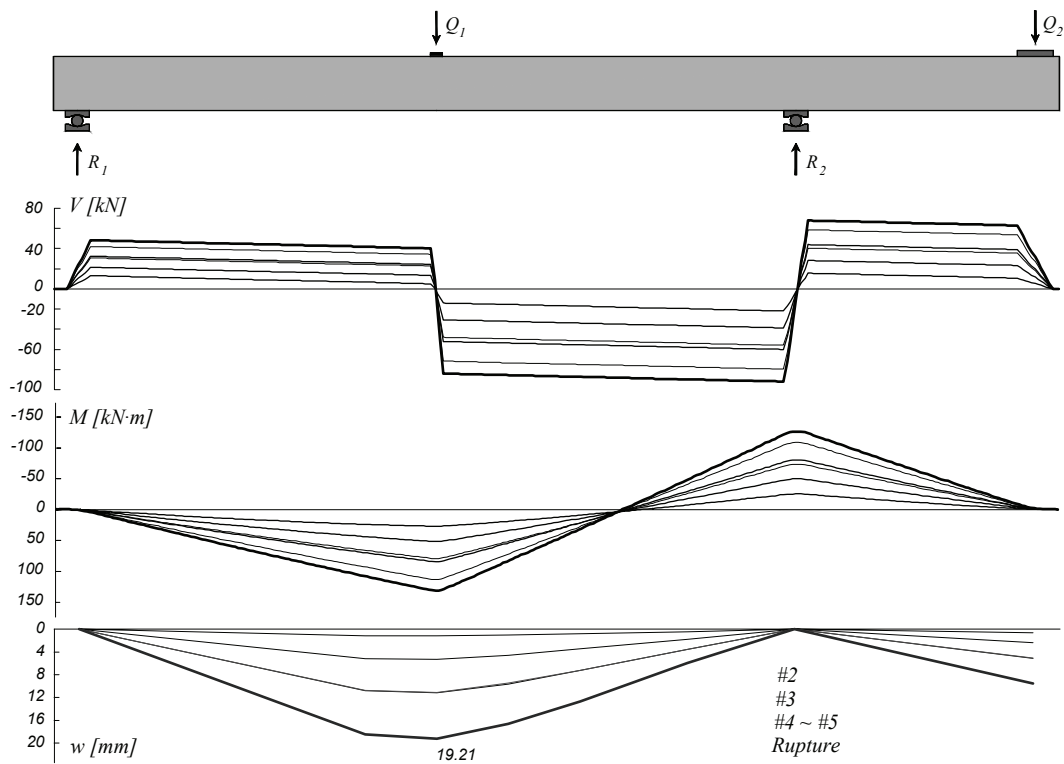


Figure B-4.5: Poutre SR2: Diagramme des efforts tranchants, diagramme des moments de flexion et déformée

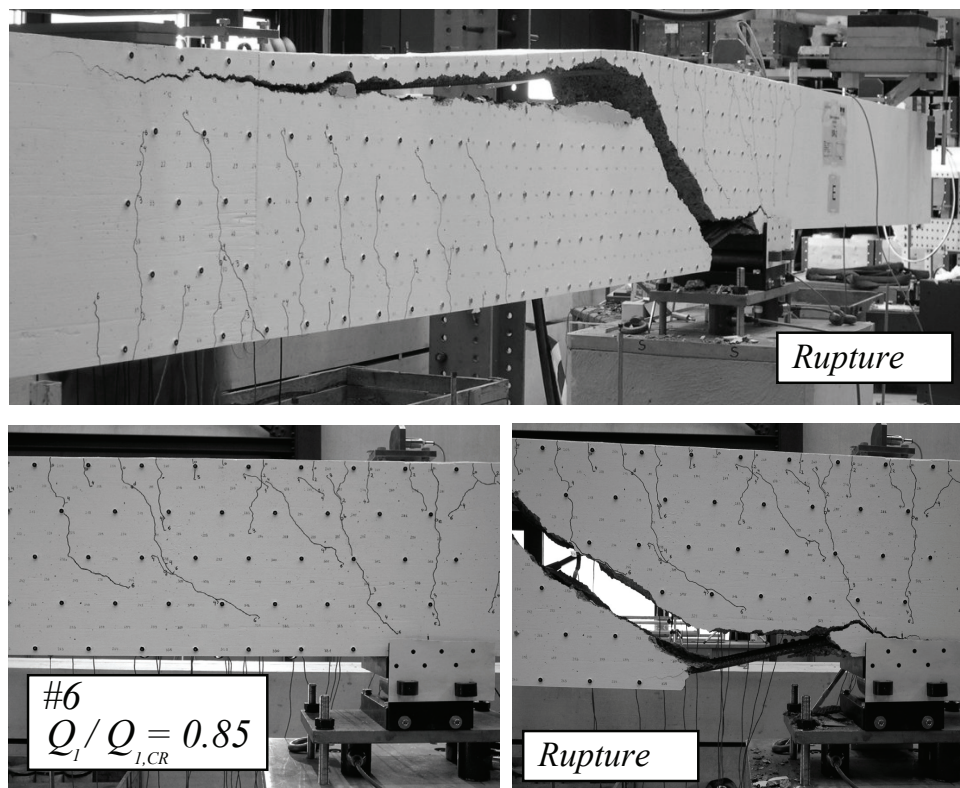


Figure B-4.6: Poutre SR2: Rupture à l'effort tranchant

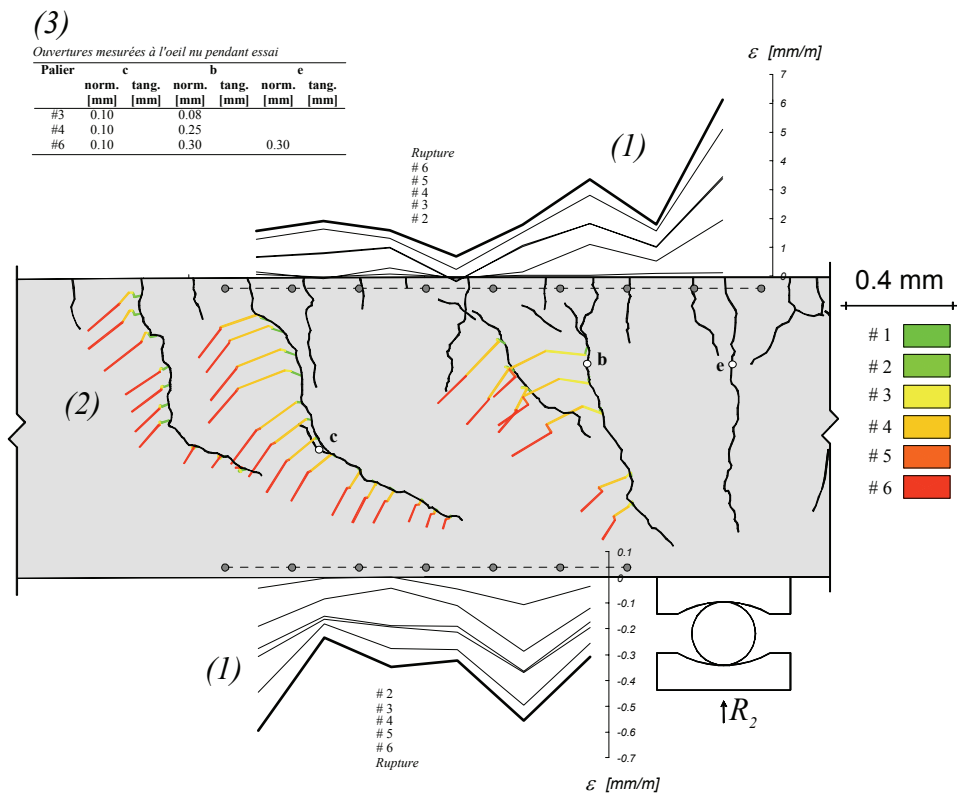
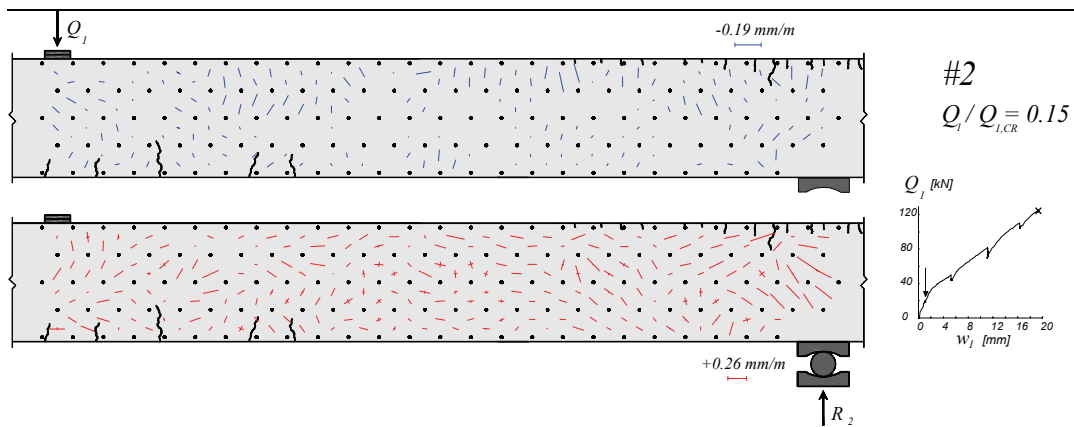


Figure B-4.7: (1) Déformations mesurées avec les jauges “oméga” ;  
 (2) Déplacement relatif entre les 2 lèvres des fissures, calculé avec les mesures au déformètre; (3) Ouvertures mesurées à l'œil nu pendant l'essai



Suite page suivante

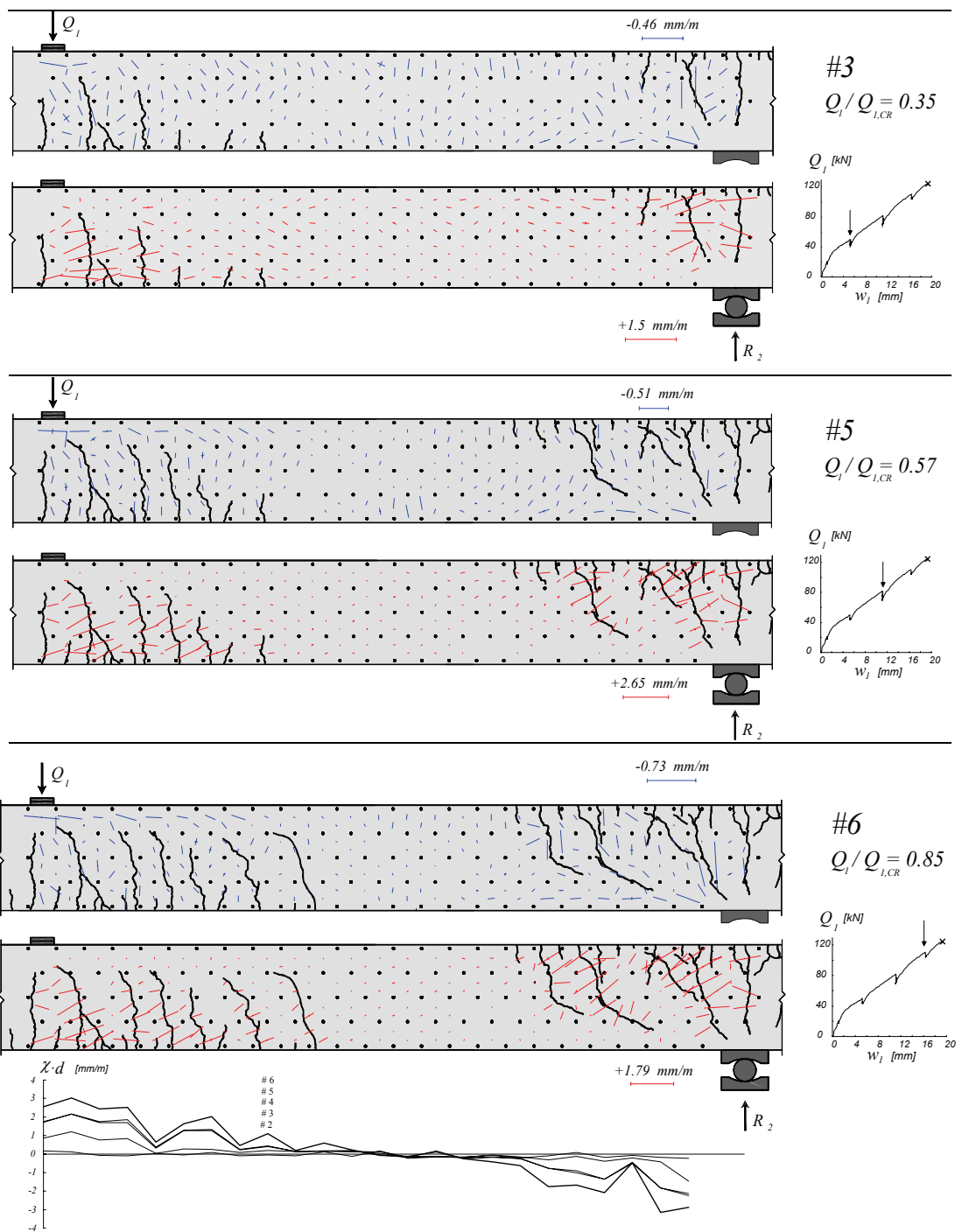


Figure B-4.8: Poutre SR2: déformations principales, fissuration et courbures

### B-4.3 Poutre SR3

La poutre SR3 a été testée avec un rapport  $Q_2/Q_1$  de + 0.2. La rupture est caractérisée par une rupture à l'effort tranchant localisée en travée en présence de déformations plastiques importantes de l'armature de flexion (voir figure B-4.12). Une ouverture et un glissement très importants au droit de la fissure critique ont été observées lors du dernier palier (#10), figure B-4.11.

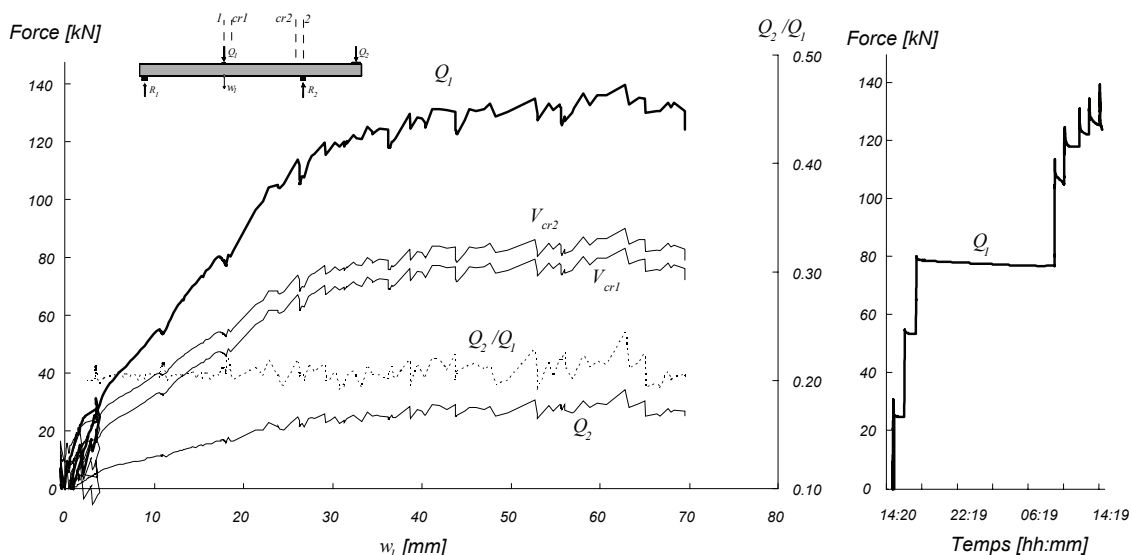


Figure B-4.9: Poutre SR3: Diagramme charge – flèche et évolution dans le temps

Tableau B-4.6: Poutre SR3: Evolution des valeurs mesurées et calculées

Palier	$Q_1$	$Q_2$	$Q_2/Q_1$	$M_1$	$M_{cr1}$	$M_2$	$M_{cr2}$	$V_1$	$V_{cr1}$	$V_2$	$V_{cr2}$	$\Omega_{49}$	$\Omega_{59}$	$w_1$	$w_0$	$Q_1/Q_{1,C}$	Rem.
	[kN]	[kN]	-	[kN·m]	[kN·m]	[kN·m]	[kN·m]	[kN]	[kN]	[kN]	[kN]	[mm]	[mm]	[mm]	[mm]	%	*
#2	25.2	5.0	0.20	41.6	38.7	-16.0	-12.0	-15.5	-16.0	-23.5	-23.2	0.22	0.07	3.32	-2.01	19%	DP
	24.9	5.16	0.21	41.0	38.1	-16.2	-12.3	-15.4	-15.9	-23.4	-23.1					19%	FD
	24.9	5.3	0.21	40.8	38.0	-16.5	-12.6	-15.5	-15.9	-23.4	-23.1	0.23	0.07	3.42	-2.10	19%	FP
#3	55.1	11.2	0.20	79.9	73.9	-27.6	-20.8	-32.5	-32.9	-40.5	-40.2	0.92	0.20	10.59	-6.97	42%	DP
	53.6	11.54	0.22	77.4	71.5	-28.4	-21.7	-31.9	-32.3	-39.9	-39.6					41%	FD
	53.5	11.6	0.22	77.2	71.3	-28.4	-21.7	-31.9	-32.3	-39.8	-39.5	0.95	0.20	11.01	-7.10	41%	FP
#4	80.3	16.5	0.21	112.1	103.4	-37.8	-28.6	-46.9	-47.3	-54.9	-54.6	1.37	0.29	17.32	-11.38	61%	DP
	78.9	16.66	0.21	109.9	101.4	-38.1	-29.0	-46.3	-46.7	-54.2	-53.9					60%	FD
	78.8	16.7	0.21	109.7	101.2	-38.1	-29.0	-46.2	-46.6	-54.2	-53.9	1.40	0.29	17.82	-11.41	60%	FP
#5	77.1	15.9	0.21	107.9	99.6	-36.7	-27.8	-45.1	-45.6	-53.1	-52.8	1.42	0.29	18.03	-11.53	59%	DP
	77.2	15.95	0.21	108.0	99.7	-36.8	-27.8	-45.2	-45.6	-53.1	-52.8					59%	FD
	77.3	16.0	0.21	108.1	99.8	-36.9	-27.9	-45.2	-45.7	-53.2	-52.9	1.42	0.30	18.04	-11.48	59%	FP
#6	111.8	23.4	0.21	152.1	140.2	-51.0	-38.6	-65.0	-65.4	-72.9	-72.6	1.94	0.46	26.28	-16.00	85%	DP
	106.7	21.99	0.21	145.9	134.5	-48.3	-36.4	-61.9	-62.4	-69.9	-69.6					81%	FD
	105.4	21.5	0.20	144.4	133.2	-47.3	-35.6	-61.1	-61.5	-69.1	-68.8	1.95	0.46	26.32	-15.96	80%	FP
#7	121.4	24.5	0.20	165.2	152.3	-53.1	-39.9	-70.1	-70.6	-78.1	-77.8	3.01	0.90	36.25	-22.16	92%	DP
	118.2	24.0	0.20	161.0	148.5	-52.0	-39.1	-68.3	-68.8	-76.3	-76.0					90%	FD
	118.2	24.5	0.21	160.4	147.8	-53.2	-40.2	-68.5	-69.0	-76.5	-76.2	3.02	0.91	36.40	-22.10	90%	FP
#8	126.1	25.3	0.20	171.4	158.1	-54.6	-40.9	-72.7	-73.2	-80.7	-80.4	3.86	1.23	43.77	-26.82	96%	DP
	122.66	25.36	0.21	166.2	153.2	-54.7	-41.3	-71.0	-71.5	-79.0	-78.7					93%	FD
	122.6	25.6	0.21	166.0	152.9	-55.1	-41.7	-71.1	-71.5	-79.0	-78.7	3.91	1.25	44.01	-26.77	93%	FP
#9	131.2	28.7	0.22	175.6	161.6	-61.3	-47.0	-76.5	-76.9	-84.4	-84.1	4.86	1.74	55.57	-33.52	100%	DP=C
	126.38	27.69	0.22	169.5	155.9	-59.2	-45.4	-73.7	-74.1	-81.6	-81.3					96%	FD
	125.7	27.6	0.22	168.6	155.2	-59.0	-45.3	-73.3	-73.7	-81.3	-81.0	4.89	1.76	55.68	-33.47	96%	FP
#10	128.7	26.4	0.21	174.1	160.5	-56.7	-42.7	-74.4	-74.8	-82.3	-82.0	4.46	1.97	69.52	-41.42	98%	DP
#10	124.06	25.26	0.20	168.4	155.3	-54.5	-41.0	-71.7	-72.1	-79.7	-79.4					95%	FD

\* DP : Début du palier ; FD : Fin des mesures avec le déformètre ; FP : Fin du palier ; CM : Charge maximale

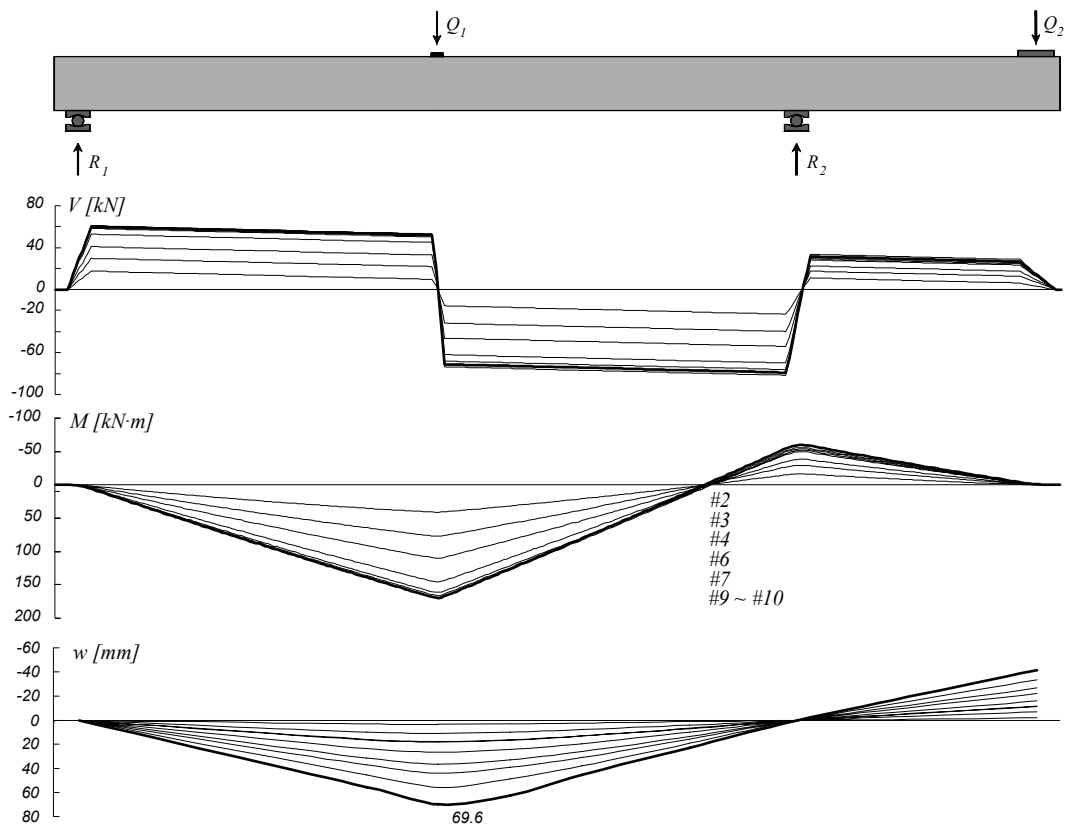


Figure B-4.10: Poutre SR3: Diagramme des efforts tranchants, diagramme des moments de flexion et déformée

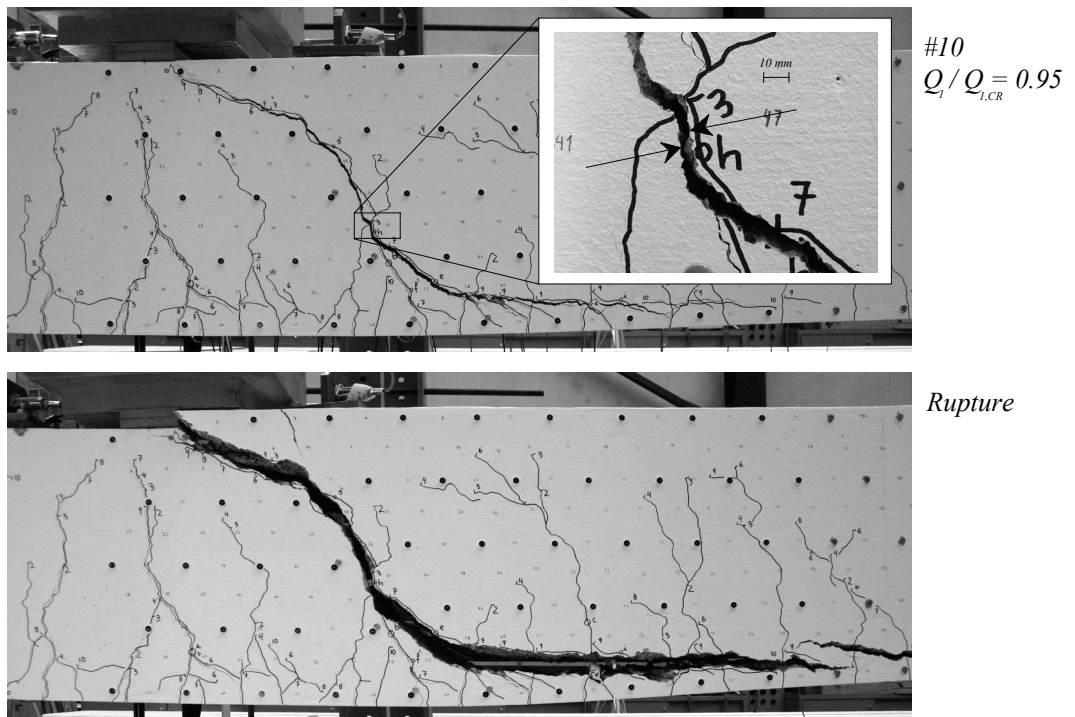


Figure B-4.11: Poutre SR3: Fissuration avant rupture en travée (palier 10) et après rupture

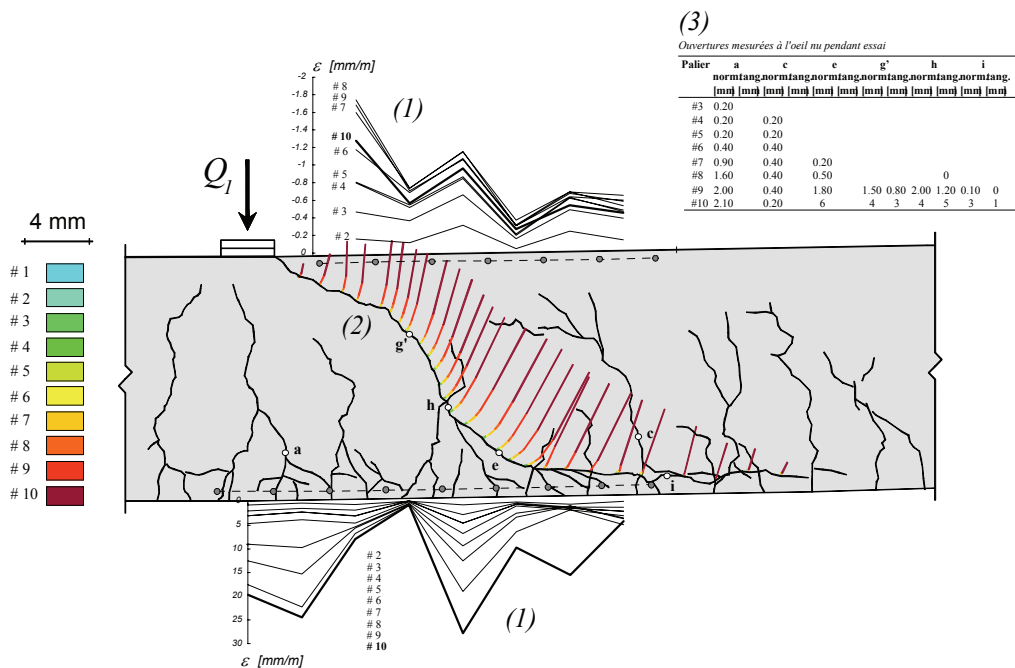
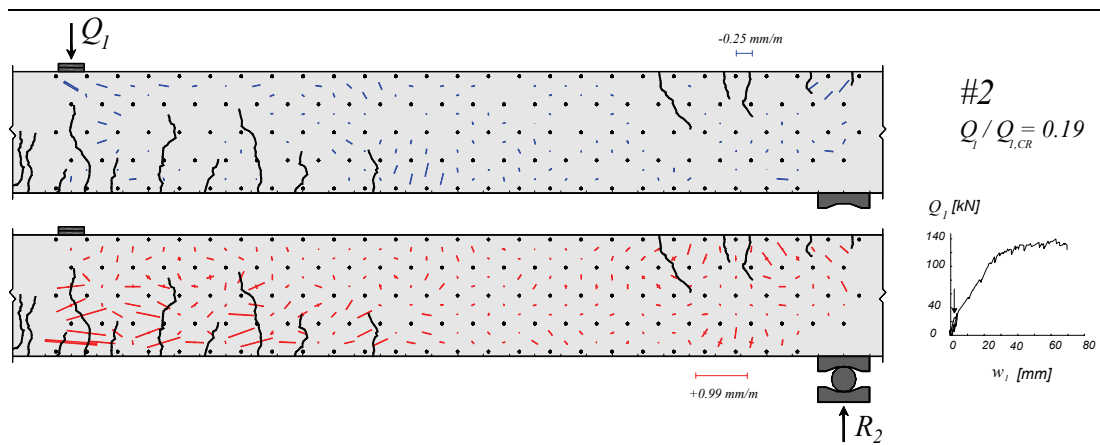


Figure B-4.12: Poutre SR3: (1) Déformations mesurées avec les jauges "oméga" ;  
 (2) Déplacement relatif entre les 2 lèvres des fissures, calculé avec les mesures au déformètre; (3) Ouvertures mesurées à l'œil nu pendant l'essai



Suite page suivante

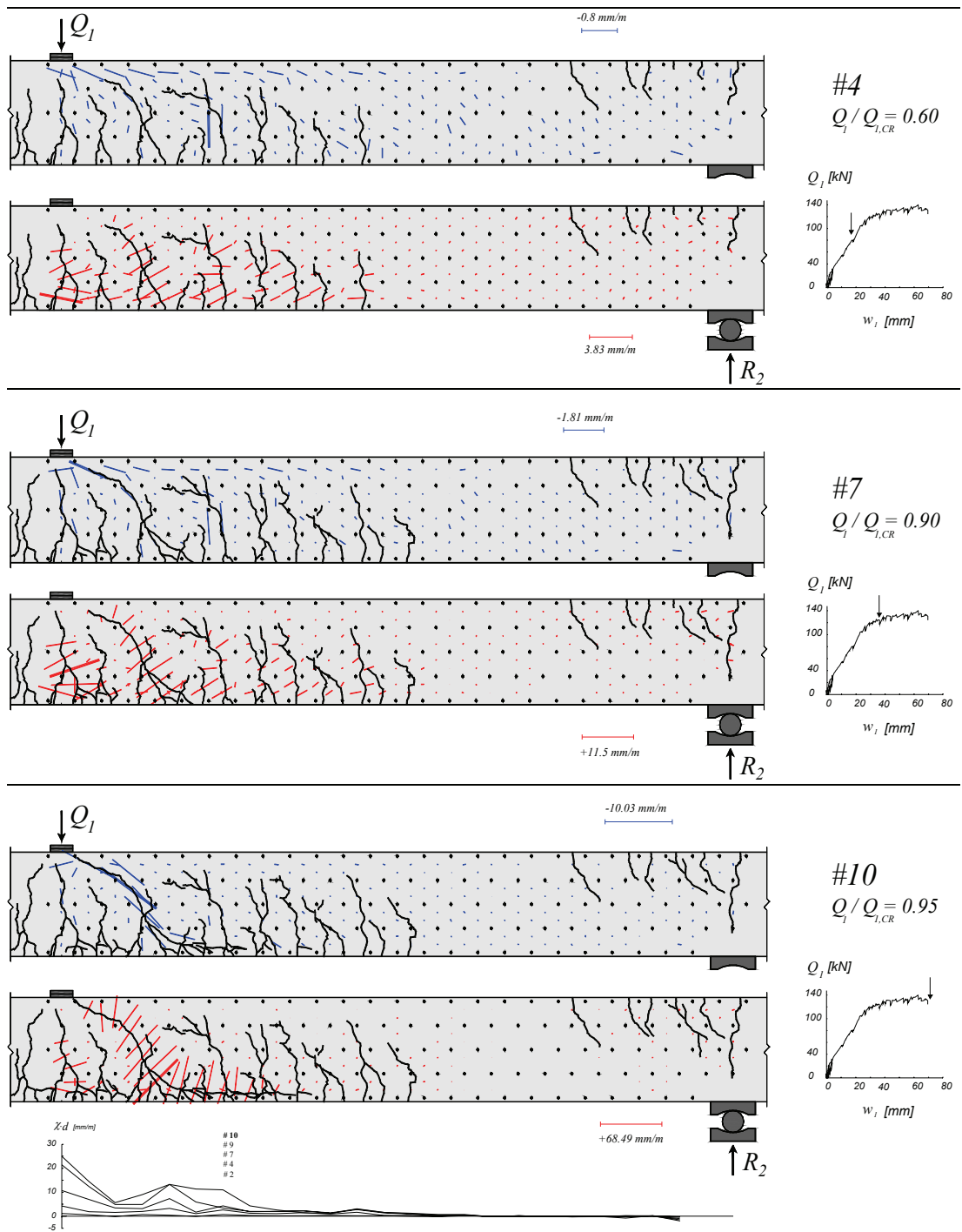


Figure B-4.13: Poutre SR3: déformations principales, fissuration et courbures

### B-4.4 Poutre SR4

La poutre SR4 a été testée avec un rapport  $Q_2/Q_1$  de zéro. La rupture par effort tranchant a été observée en travée en présence des déformations plastiques importantes de l'armature de flexion (voir figure B-4.17).

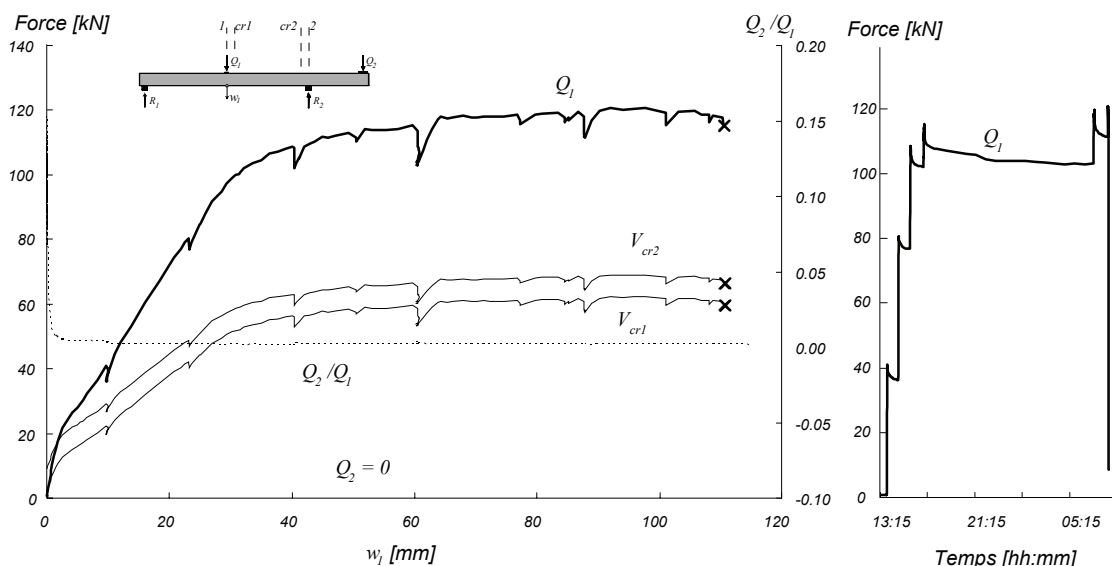


Figure B-4.14: Poutre SR4 : Diagramme charge – flèche et évolution dans le temps

Tableau B-4.7: Poutre SR4: Evolution des valeurs mesurées et calculées

Palier	$Q_1$	$Q_2$	$Q_2/Q_1$	$M_1$	$M_{cr1}$	$M_2$	$M_{cr2}$	$V_1$	$V_{cr1}$	$V_2$	$V_{cr2}$	$\Omega_{49}$	$\Omega_{59}$	$w_1$	$w_0$	$Q_1/Q_{1,c}$	Rem.
	[kN]	[kN]	-	[kN·m]	[kN·m]	[kN·m]	[kN·m]	[kN]	[kN]	[kN]	[kN]	[mm]	[mm]	[mm]	[mm]	%	*
#2	40.0	0.0	0.00	68.6	64.8	-5.9	-0.8	-21.2	-21.7	-29.2	-28.9	0.44	0.11	9.90	-7.49	35%	DP
	36.4	0.0	0.00	63.4	59.8	-5.9	-1.1	-19.5	-19.9	-27.4	-27.1					32%	FD
	36.3	0.0	0.00	63.1	59.5	-5.9	-1.2	-19.4	-19.8	-27.3	-27.0	0.42	0.10	9.72	-7.41	31%	FP
#3	79.9	0.0	0.00	128.0	120.5	-5.4	3.3	-41.2	-41.6	-49.1	-48.9	0.96	0.16	23.15	-18.64	69%	DP
	76.9	0.0	0.00	123.6	116.4	-5.4	3.0	-39.7	-40.2	-47.7	-47.4					67%	FD
#4	76.8	0.0	0.00	123.4	116.2	-5.4	3.0	-39.6	-40.1	-47.6	-47.3	0.96	0.16	23.25	-18.80	67%	FP
	107.0	0.0	0.00	168.2	158.4	-5.0	6.1	-54.7	-55.2	-62.7	-62.4	2.31	0.64	40.32	-31.37	93%	DP
	102.4	0.0	0.00	161.5	152.0	-5.1	5.6	-52.5	-52.9	-60.4	-60.1					89%	FD
#5	102.1	0.0	0.00	161.0	151.5	-5.1	5.6	-52.3	-52.7	-60.2	-59.9	2.34	0.66	40.39	-31.36	89%	FP
	111.6	0.0	0.00	175.2	164.9	-5.0	6.5	-57.1	-57.5	-65.0	-64.7	3.92	1.65	60.51	-43.95	97%	DP
	107.7	0.0	0.00	169.4	159.4	-5.0	6.1	-55.1	-55.6	-63.1	-62.8					94%	FD
#6	107.7	0.0	0.00	169.4	159.4	-5.0	6.1	-55.1	-55.6	-63.1	-62.8	3.92	1.67	60.68	-43.93	94%	FP
	103.0	0.0	0.00	162.4	152.9	-5.1	5.7	-52.8	-53.2	-60.7	-60.4	3.89	1.67	60.41	-43.62	89%	DP
	103.1	0.0	0.00	162.5	153.0	-5.1	5.7	-52.8	-53.2	-60.8	-60.5					90%	FD
#7	103.1	0.0	0.00	162.5	153.0	-5.1	5.7	-52.8	-53.2	-60.8	-60.5	3.89	1.67	60.44	-43.64	90%	FP
	116.2	0.0	0.00	182.0	171.3	-4.9	7.0	-59.4	-59.8	-67.3	-67.0	6.49	1.95	87.72	-60.73	101%	DP
	111.9	0.0	0.00	175.6	165.2	-5.0	6.6	-57.2	-57.6	-65.1	-64.9					97%	FD
CM	111.4	0.0	0.00	174.8	164.5	-5.0	6.5	-56.9	-57.4	-64.9	-64.6	6.47	1.96	87.82	-60.59	97%	FP
	120.8	0.0	0.00	188.8	177.7	-4.9	7.5	-61.6	-62.1	-69.6	-69.3	4.81	2.54	97.70	-66.78	105%	CM
CR	115.20	0.0	0.00	180.5	169.9	-4.9	6.9	-58.9	-59.3	-66.8	-66.5	2.82	3.09	110.43	-73.44	100%	CR

\* DP : Début du palier ; FD : Fin des mesures avec le déformètre ; FP : Fin du palier ; CM : Charge maximale ; CR : Charge de rupture ;



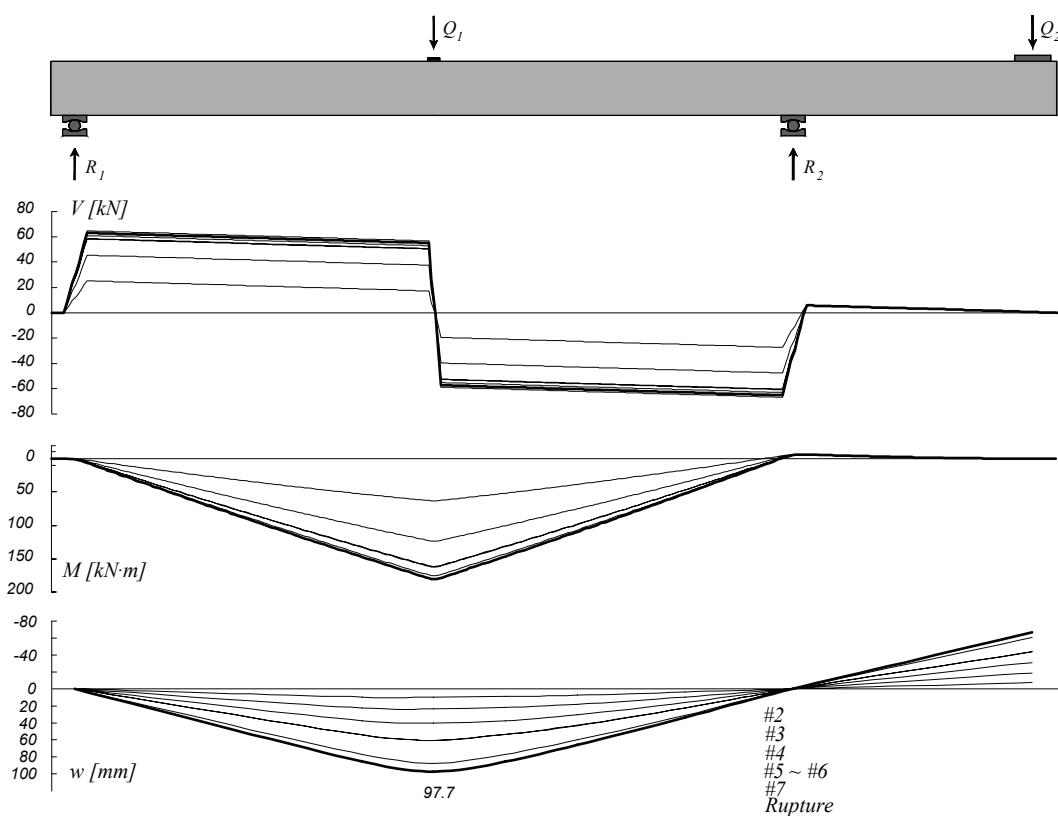


Figure B-4.15: Poutre SR4: Diagramme des efforts tranchants, diagramme des moments de flexion et déformée

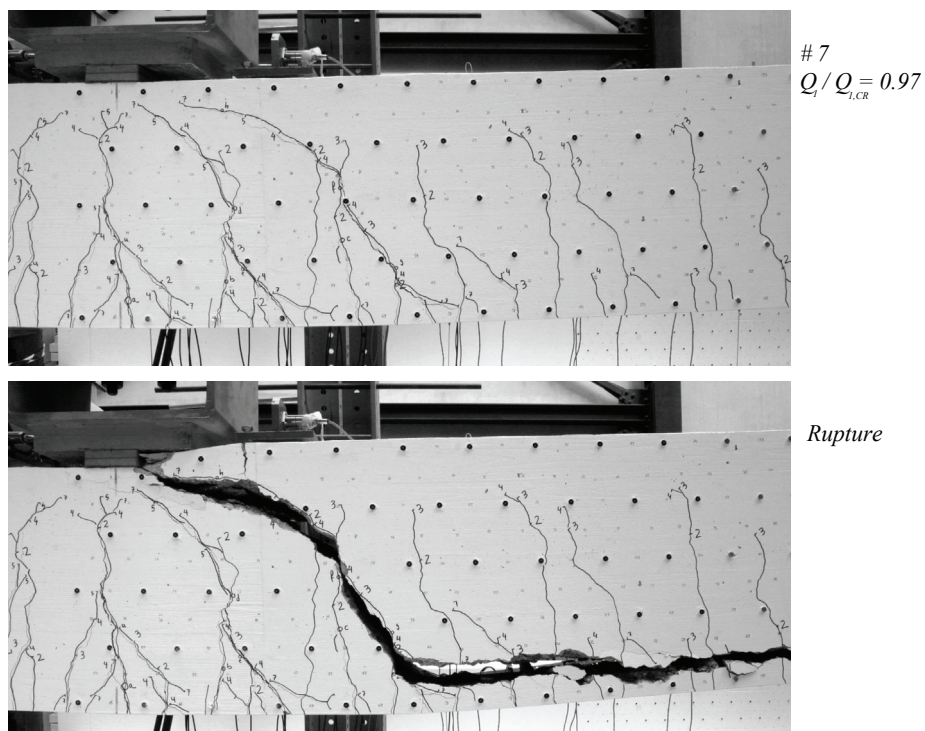


Figure B-4.16: Poutre SR4: Fissuration avant rupture en travée (palier 7) et après rupture

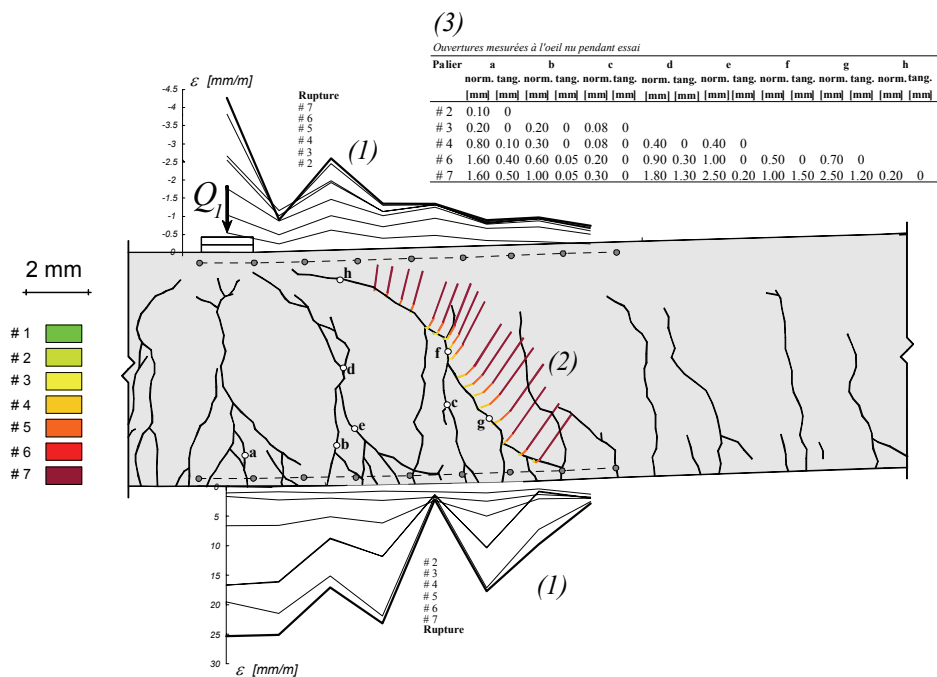
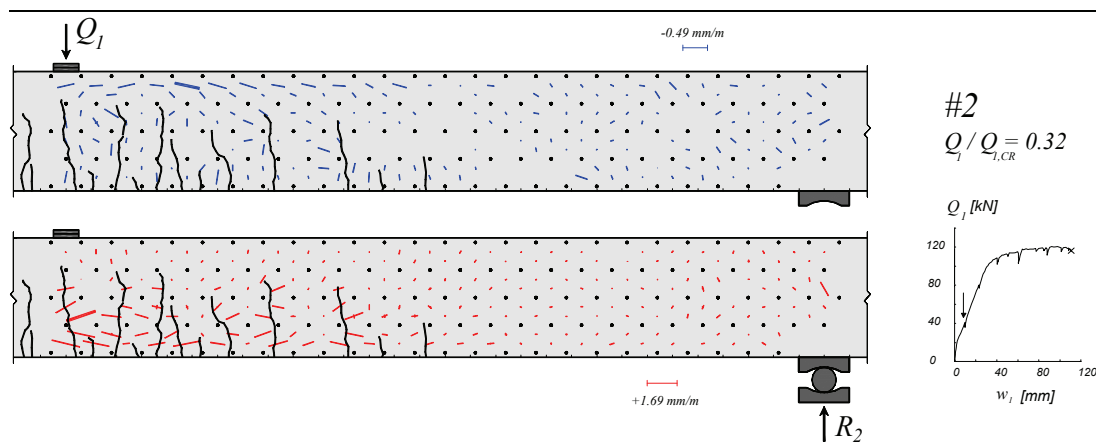


Figure B-4.17: Poutre SR4: (1) Déformations mesurées avec les jauges “oméga” ; (2) Déplacement relatif entre les 2 lèvres des fissures, calculé avec les mesures au déformètre; (3) Ouvertures mesurées à l’œil nu pendant l’essai



Suite page suivante

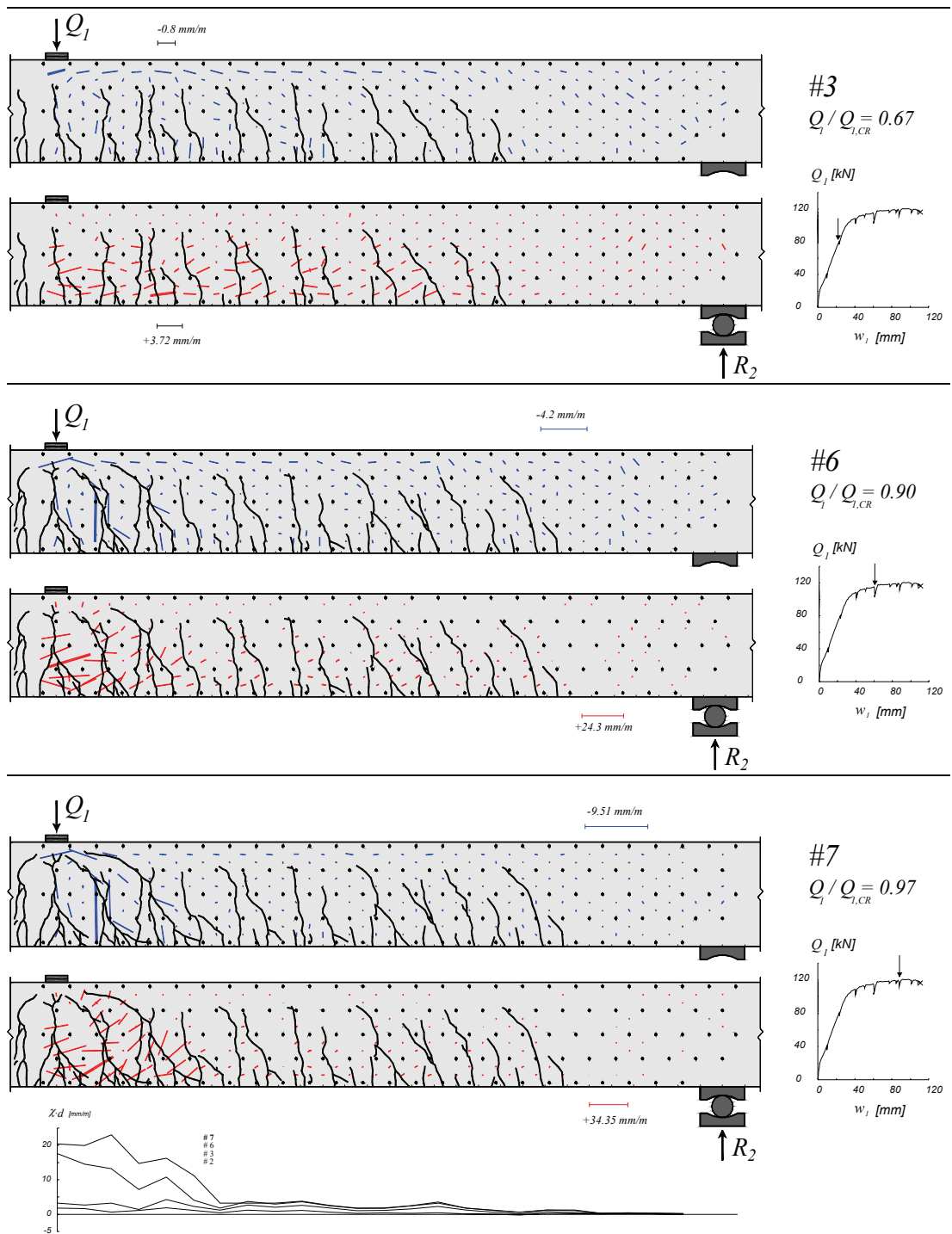


Figure B-4.18: Poutre SR4: déformations principales, fissuration et courbures

### B-4.5 Poutre SR5

La poutre SR5 a été testée avec un rapport  $Q_2/Q_1$  de -0.2. La rupture a été en flexion avec arrachement des barres d'armature (fig. B-4.21).

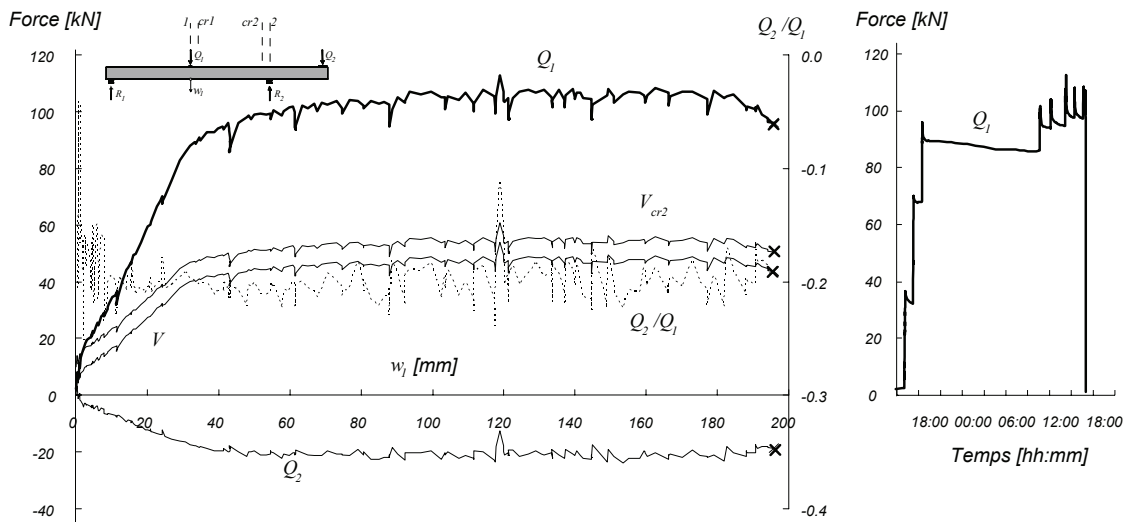


Figure B-4.19: Poutre SR5: Diagramme charge – flèche et évolution dans le temps

Tableau B-4.8: Poutre SR5: Evolution des valeurs mesurées et calculées

Palier	$Q_1$	$Q_2$	$Q_2/Q_1$	$M_1$	$M_{cr1}$	$M_2$	$M_{cr2}$	$V_1$	$V_{cr1}$	$V_2$	$V_{cr2}$	$\Omega_{49}$	$\Omega_{59}$	$w_1$	$w_0$	$Q_1/Q_{1,CR}$	Rem.	
	[kN]	[kN]	-	[kN·m]	[kN·m]	[kN·m]	[kN·m]	[kN]	[kN]	[kN]	[kN]	[mm]	[mm]	[mm]	[mm]	%	*	
2	35.8	-7.4	-0.21	69.9	66.9	8.7	13.2	-16.7	-17.1	-24.6	-24.4	0.49	0.16	11.44	-11.42	37%	DP	
	32.7	-7.29	-0.22	65.1	62.4	8.4	12.6	-15.2	-15.6	-23.1	-22.8						34%	FD
	32.2	-7.3	-0.23	64.4	61.7	8.5	12.6	-14.9	-15.3	-22.9	-22.6	0.48	0.16	11.29	-11.38	33%	FP	
3	69.7	-13.6	-0.19	126.4	120.8	21.2	28.5	-31.6	-32.0	-39.5	-39.2	0.75	0.33	24.24	-25.83	72%	DP	
	67.7	-12.44	-0.18	122.3	116.8	19.0	26.1	-30.9	-31.4	-38.9	-38.6						70%	FD
	68.1	-12.2	-0.18	122.6	117.1	18.5	25.6	-31.2	-31.7	-39.2	-38.9	0.74	0.32	24.29	-25.84	71%	FP	
4	93.4	-20.0	-0.21	168.0	160.7	34.1	43.3	-41.3	-41.7	-49.2	-49.0	1.21	1.13	43.01	-43.99	97%	DP	
	89.1	-19.08	-0.21	160.8	153.8	32.3	41.1	-39.5	-39.9	-47.4	-47.1						93%	FD
	89.3	-18.7	-0.21	160.7	153.7	31.5	40.4	-39.7	-40.1	-47.6	-47.3	1.24	1.15	43.13	-44.01	93%	FP	
5	85.8	-18.5	-0.22	155.3	148.6	31.1	39.6	-38.0	-38.4	-46.0	-45.7	1.25	1.15	43.03	-43.99	89%	DP	
	86.0	-18.18	-0.21	155.3	148.5	30.5	39.0	-38.2	-38.6	-46.2	-45.9						89%	FD
	86.1	-18.1	-0.21	155.3	148.6	30.4	39.0	-38.3	-38.7	-46.2	-45.9	1.24	1.14	43.02	-43.97	90%	FP	
6	99.3	-20.5	-0.21	177.4	169.6	35.2	44.9	-44.1	-44.5	-52.0	-51.7	2.87	2.09	61.42	-58.53	103%	DP	
	94.0	-20.64	-0.22	169.6	162.3	35.4	44.6	-41.4	-41.8	-49.3	-49.0						98%	FD
	94.0	-20.6	-0.22	169.5	162.2	35.3	44.5	-41.4	-41.8	-49.3	-49.0	2.88	2.12	61.54	-58.48	98%	FP	
7	101.0	-21.1	-0.21	180.4	172.5	36.3	46.2	-44.7	-45.2	-52.7	-52.4	3.19	3.48	87.91	-77.77	105%	DP	
	95.8	-21.7	-0.23	173.3	165.8	37.4	46.8	-41.9	-42.3	-49.9	-49.6						100%	FD
	94.7	-21.7	-0.23	171.7	164.4	37.4	46.7	-41.4	-41.8	-49.4	-49.1	3.19	3.50	87.99	-77.75	99%	FP	
8	103.0	-20.6	-0.20	183.0	174.9	35.5	45.5	-45.9	-46.3	-53.8	-53.6	4.89	5.34	121.2	-	107%	DP	
	97.97	-21.19	-0.22	176.1	168.4	36.5	46.1	-43.2	-43.6	-51.1	-50.8						102%	FD
	97.5	-21.2	-0.22	175.4	167.8	36.5	46.0	-43.0	-43.4	-50.9	-50.6	4.88	5.36	121.3	-	101%	FP	
9	101.5	-21.4	-0.21	181.6	173.6	37.0	46.8	-44.9	-45.3	-52.8	-52.6	6.29	7.06	144.6	-	106%	DP	
	97.62	-21.88	-0.22	176.2	168.7	37.9	47.4	-42.8	-43.2	-50.7	-50.4						102%	FD
	97.3	-21.9	-0.22	175.7	168.2	37.9	47.3	-42.6	-43.0	-50.6	-50.3	6.24	7.08	144.7	-	101%	FP	
CM	108.4	-20.3	-0.19	190.8	182.2	35.0	45.5	-48.7	-49.1	-56.7	-56.4	6.53	9.39	162.63	-	113%	CM	
CR	96.1	-18.7	-0.19	170.9	163.2	31.6	41.1	-43.1	-43.5	-51.0	-50.8	6.91	10.00	195.95	-	100%	CR	

\* DP : Début du palier ; FD : Fin des mesures avec le déformètre ; FP : Fin du palier ; CM : Charge maximale ; CR : Charge de rupture ;

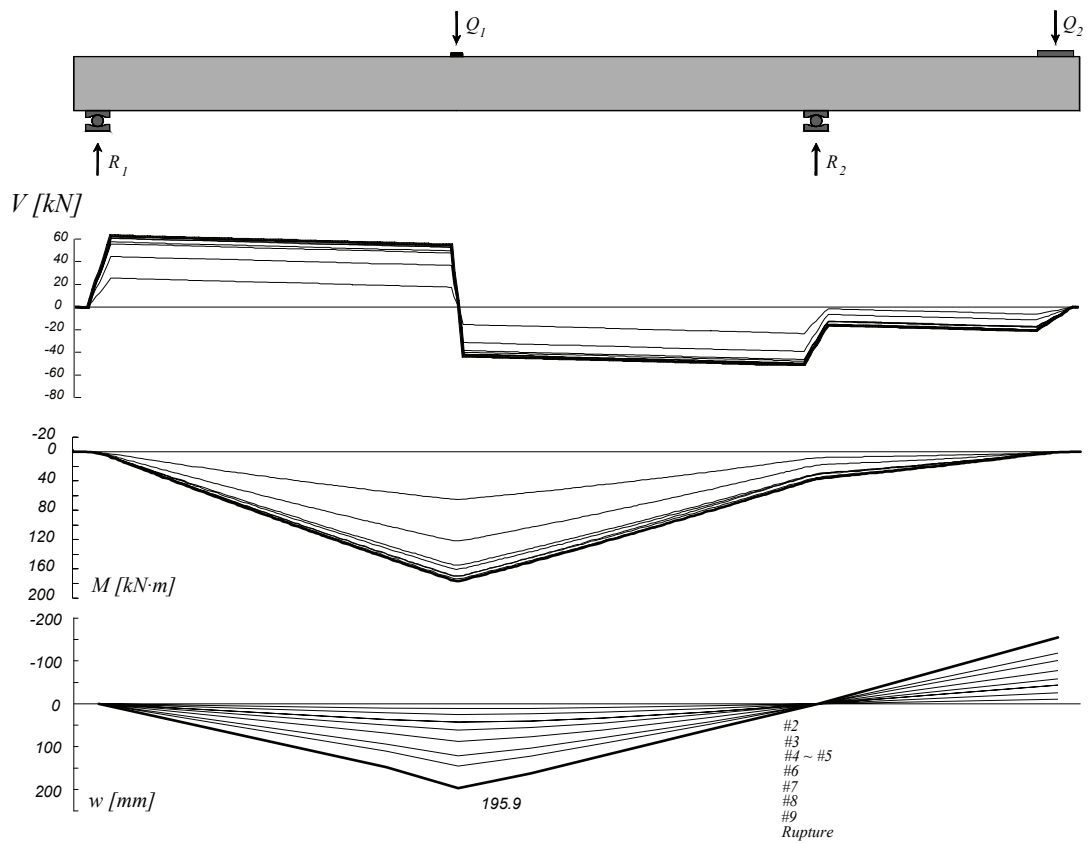


Figure B-4.20: Poutre SR5: Diagramme des efforts tranchants, diagramme des moments de flexion et déformée

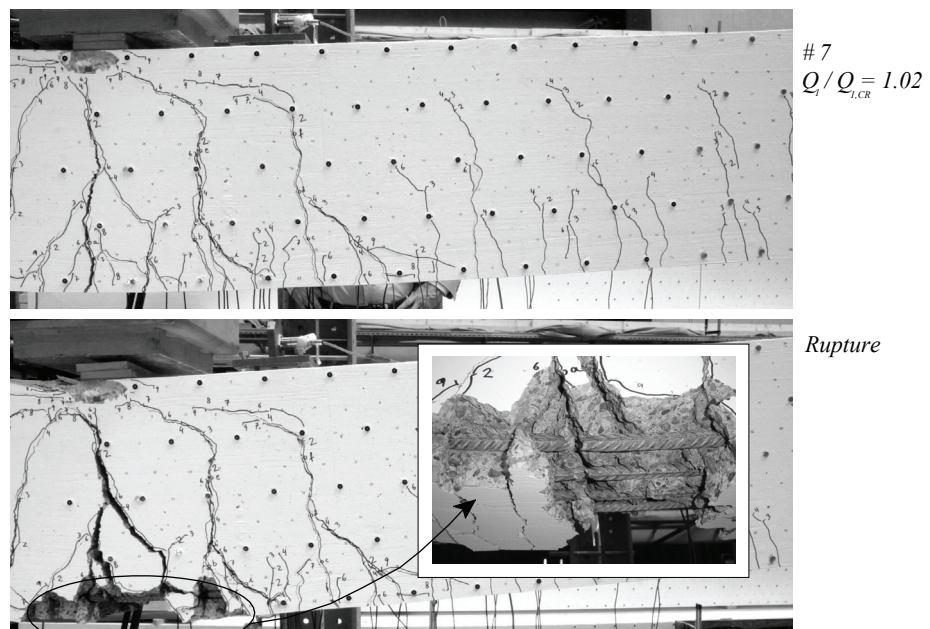


Figure B-4.21: Poutre SR5: Fissuration avant rupture en travée (palier 9) et après rupture

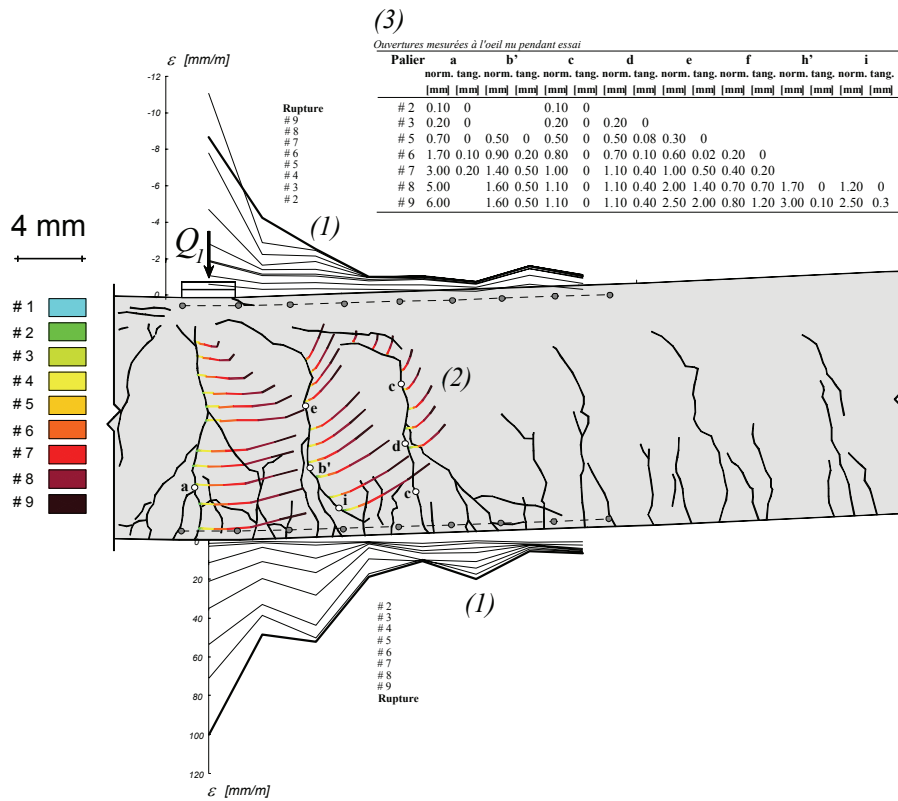
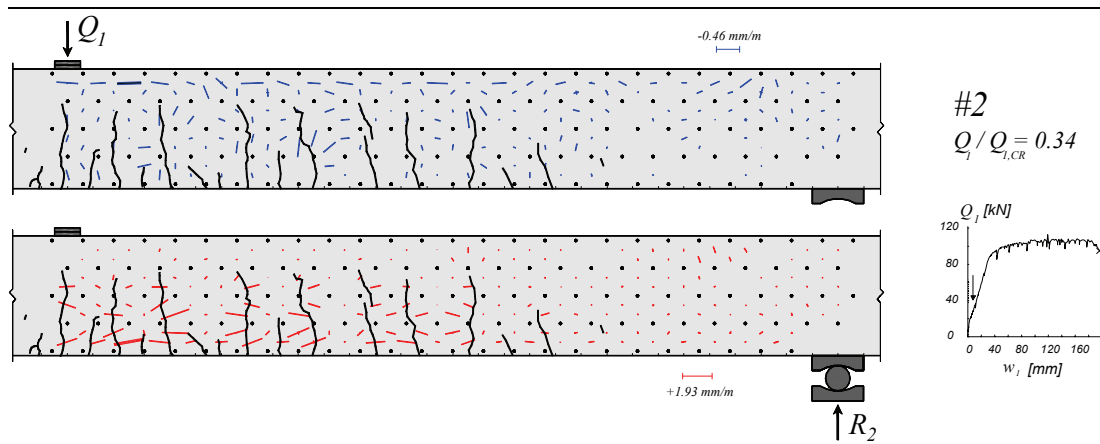


Figure B-4.22: Poutre SR5: (1) Déformations mesurées avec les jauges "oméga" ;  
 (2) Déplacement relatif entre les 2 lèvres des fissures, calculé avec les mesures  
 au déformètre; (3) Ouvertures mesurées à l'œil nu pendant l'essai



Suite page suivante

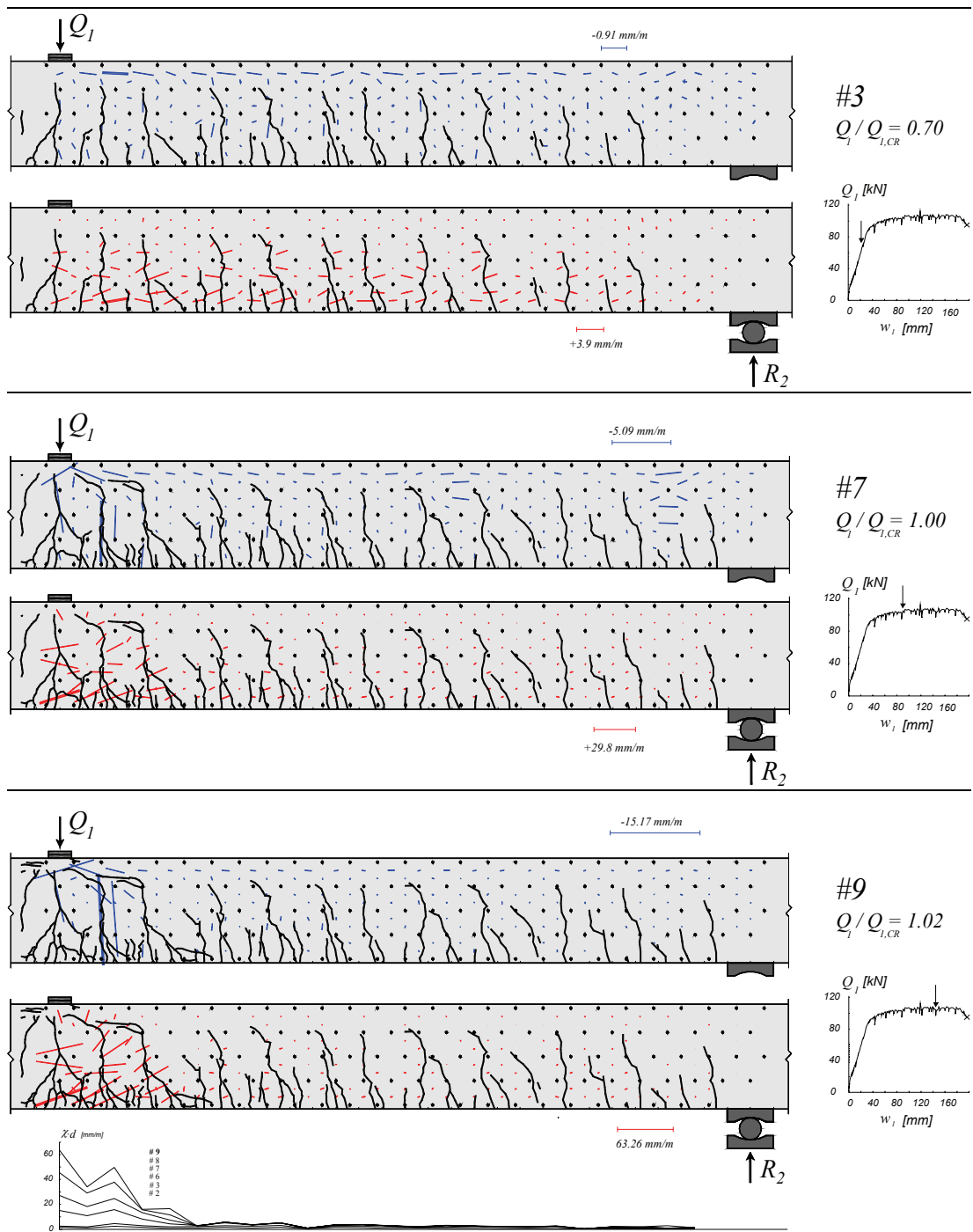


Figure B-4.23: Poutre SR5: déformations principales, fissuration et courbures

### B-4.6 Poutre SR6

La poutre SR6 a été testée avec un rapport  $Q_2/Q_1$  de +0.6. Pour un niveau de charge de  $Q_1 = 117$  kN, une importante fissure d'effort tranchant s'est ouverte au droit de la section  $cr2$ , près de l'appui intermédiaire. Cette fissure n'a pas engendrée la rupture de la poutre, ni la perte totale de la charge appliquée (fig. B-4.26a). Après rechargement, une rupture très fragile s'est produite en travée, pour  $Q_1 = 148$  kN (fig. B-4.26b).

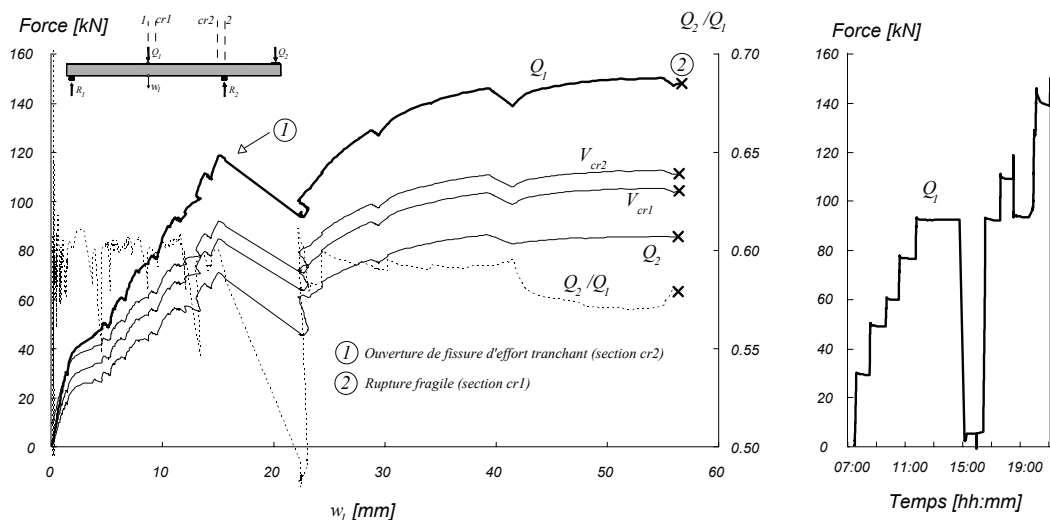


Figure B-4.24: Poutre SR6: Diagramme charge – flèche et évolution dans le temps

Tableau B-4.9: Poutre SR6: Evolution des valeurs mesurées et calculées

Palier	$Q_1$	$Q_2$	$Q_2/Q_1$	$M_1$	$M_{cr1}$	$M_2$	$M_{cr2}$	$V_1$	$V_{cr1}$	$V_2$	$V_{cr2}$	$\Omega_{11}$	$\Omega_{00}$	$w_1$	$w_0$	$Q_1/Q_{1,CR}$	Rem.
	[kN]	[kN]	-	[kN·m]	[kN·m]	[kN·m]	[kN·m]	[kN]	[kN]	[kN]	[kN]	[mm]	[mm]	[mm]	[mm]	%	*
#2	30.0	17.7	0.6	36.1	31.9	-40.8	-36.0	-22.2	-22.6	-30.1	-29.8	0.17	0.11	1.39	1.78	26%	DP
	29.3	17.4	0.6	35.3	31.2	-40.2	-35.5	-21.7	-22.1	-29.7	-29.4					25%	FD
	29.3	17.4	0.6	35.2	31.1	-40.3	-35.6	-21.7	-22.1	-29.6	-29.4	0.17	0.12	1.40	1.85	25%	FP
#3	50.2	30.2	0.6	53.5	46.7	-65.2	-58.1	-36.4	-36.8	-44.4	-44.1	0.55	0.22	4.82	4.54	43%	DP
	49.0	29.7	0.6	52.3	45.6	-64.2	-57.2	-35.7	-36.1	-43.6	-43.3					42%	FD
	49.1	29.7	0.6	52.5	45.8	-64.1	-57.1	-35.7	-36.1	-43.6	-43.4	0.60	0.23	5.10	4.74	42%	FP
#4	60.8	36.5	0.6	63.1	54.9	-77.4	-69.2	-43.8	-44.3	-51.8	-51.5	0.81	0.27	6.28	6.19	52%	DP
	60.0	36.2	0.6	62.2	54.1	-76.8	-68.7	-43.3	-43.8	-51.3	-51.0					51%	FD
	60.0	36.0	0.6	62.4	54.2	-76.5	-68.4	-43.3	-43.7	-51.2	-50.9	0.85	0.27	6.61	6.34	51%	FP
#5	77.4	46.3	0.6	78.1	67.7	-96.4	-86.3	-55.4	-55.8	-63.3	-63.1	1.15	0.32	9.13	8.58	66%	DP
	76.7	45.8	0.6	77.4	67.2	-95.5	-85.5	-54.9	-55.3	-62.8	-62.5					66%	FD
	76.7	45.8	0.6	77.5	67.2	-95.5	-85.6	-54.9	-55.3	-62.9	-62.6	1.18	0.32	9.40	8.69	66%	FP
#6	93.0	56.3	0.6	91.1	78.7	-116.0	-104.2	-66.5	-67.0	-74.5	-74.2	1.49	0.35	11.19	11.42	80%	DP
	92.5	55.9	0.6	90.8	78.4	-115.1	-103.4	-66.1	-66.6	-74.1	-73.8					79%	FD
	92.5	55.8	0.6	90.8	78.5	-115.0	-103.3	-66.1	-66.5	-74.0	-73.8	1.51	0.34	11.50	11.63	79%	FP
#7	5.4	6.4	1.2	10.8	9.6	-18.8	-16.6	-6.1	-6.5	-14.0	-13.7	0.52	0.12	2.67	4.55	5%	DP
	5.4	6.2	1.1	11.0	9.8	-18.5	-16.3	-6.0	-6.5	-14.0	-13.7					5%	FD
	5.4	6.3	1.2	10.9	9.7	-18.6	-16.4	-6.0	-6.5	-14.0	-13.7	0.51	0.12	2.69	4.38	5%	FP
#8	92.8	56.2	0.6	91.0	78.6	-115.8	-104.0	-66.4	-66.9	-74.4	-74.1	1.52	0.34	11.51	11.93	80%	DP
	92.4	56.1	0.6	90.5	78.1	-115.5	-103.8	-66.2	-66.6	-74.1	-73.8					79%	FD
	92.2	56.0	0.6	90.2	77.9	-115.4	-103.7	-66.0	-66.5	-74.0	-73.7	1.53	0.34	11.53	11.99	79%	FP
#9	110.2	65.2	0.6	107.8	93.2	-133.3	-119.6	-78.1	-78.5	-86.0	-85.7	1.92	0.37	14.06	14.22	94%	DP
	109.3	64.8	0.6	106.9	92.4	-132.4	-118.9	-77.5	-77.9	-85.5	-85.2					94%	FD
	109.2	64.7	0.6	107.0	92.5	-132.2	-118.6	-77.4	-77.9	-85.4	-85.1	1.94	0.37	14.34	14.36	94%	FP
CFAP	116.7	68.2	0.6	114.5	99.1	-139.1	-124.7	-82.3	-82.8	-90.3	-90.0	2.42	0.39	15.63	17.10	100%	CFAP
CR	148.0	85.6	0.6	143.6	124.2	-172.9	-155.2	-103.8	-104.2	-111.7	-111.4	2.12	0.57	56.47	57.47	127%	CR

\* DP : Début du palier ; FD : Fin des mesures avec le déformètre ; FP : Fin du palier ; CM : Charge maximale ; CFAP : Ouverture de fissure d'effort tranchant à l'appui ; CR : Charge de rupture ;



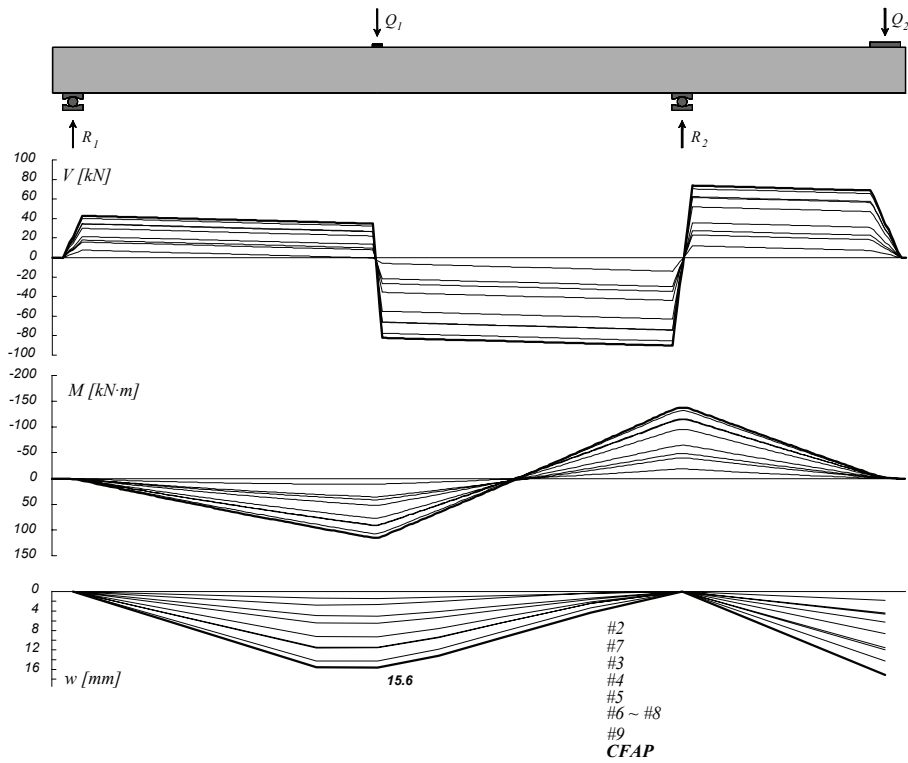


Figure B-4.25: Poutre SR6: Diagramme des efforts tranchants, diagramme des moments de flexion et déformée

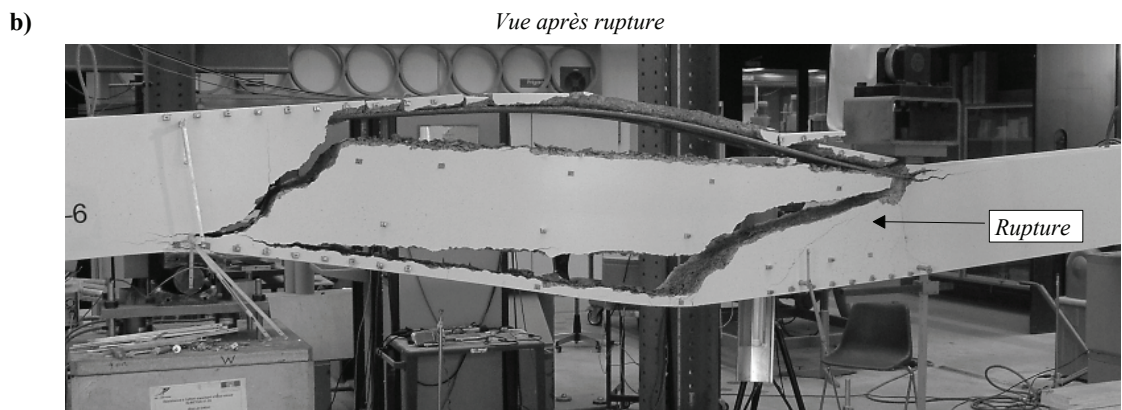
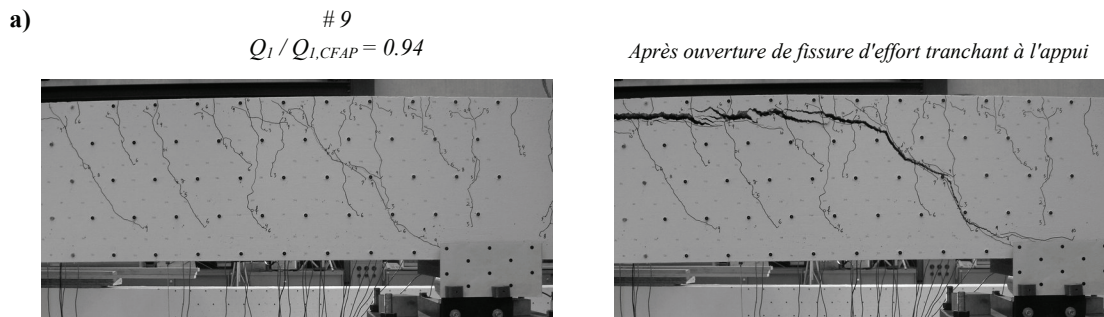


Figure B-4.26: Poutre SR6: a) Ouverture de fissure d'effort tranchant non critique à l'appui; b) rupture fragile en travée

(3)

Ouvertures mesurées à l'œil nu pendant essai

Palier	a	b	c	d	e	f	g	h	i
2	0.02	0							
3	0.2	0	0.2	0	0.1	0	0.05	0	0.08
4	0.2	0	0.3	0	0.2	0	0.05	0	0.2
5	0.2	0	0.3	0	0.2	0	0.08	0	0.2
6	0.2	0	0.4	0	0.2	0	0.1	0.05	0.2
8	0.2	0	0.4	0	0.2	0	0.1	0.08	0.2
9	0.2	0	0.4	0	0.2	0	0.8	0.2	0.05

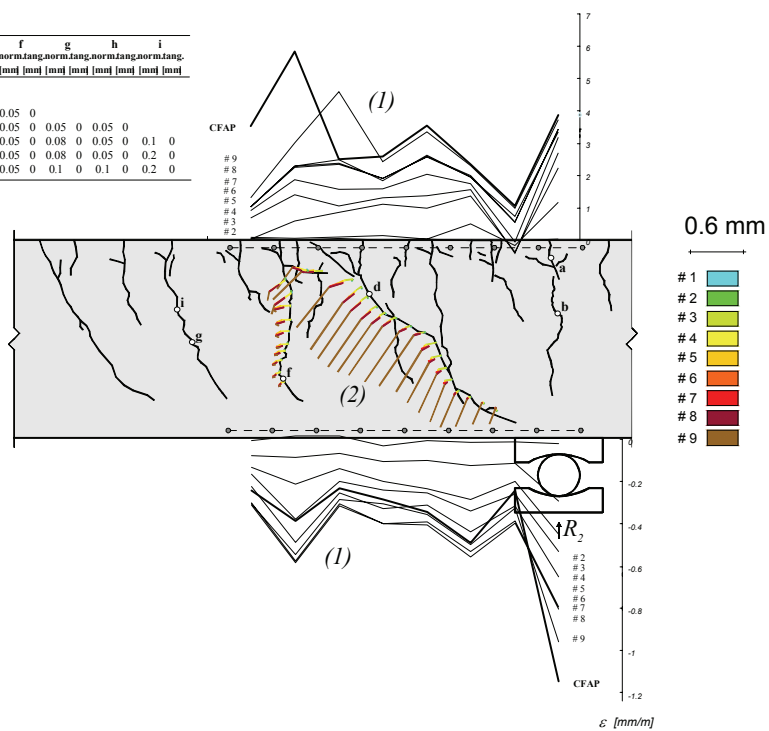
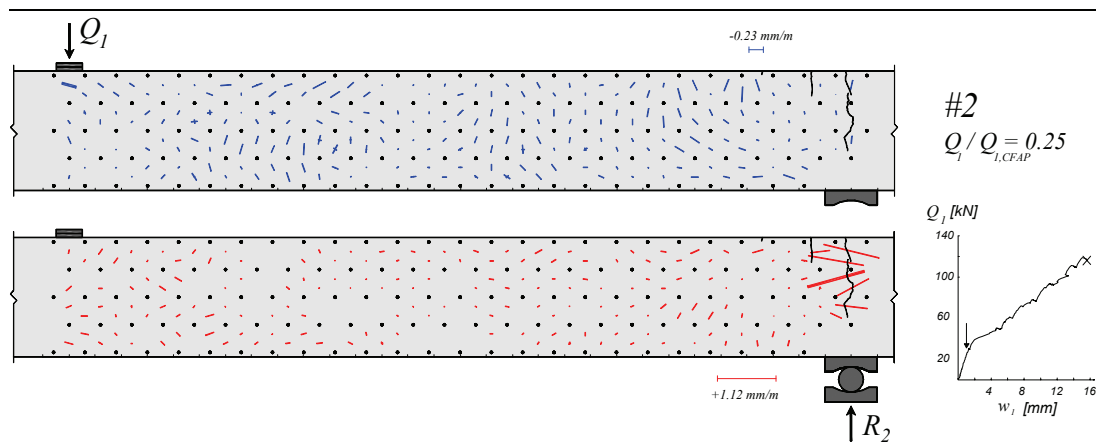


Figure B-4.27: Poutre SR6: (1) Déformations mesurées avec les jauges "oméga" ; (2) Déplacement relatif entre les 2 lèvres des fissures, calculé avec les mesures au déformètre; (3) Ouvertures mesurées à l'œil nu pendant l'essai



Suite page suivante

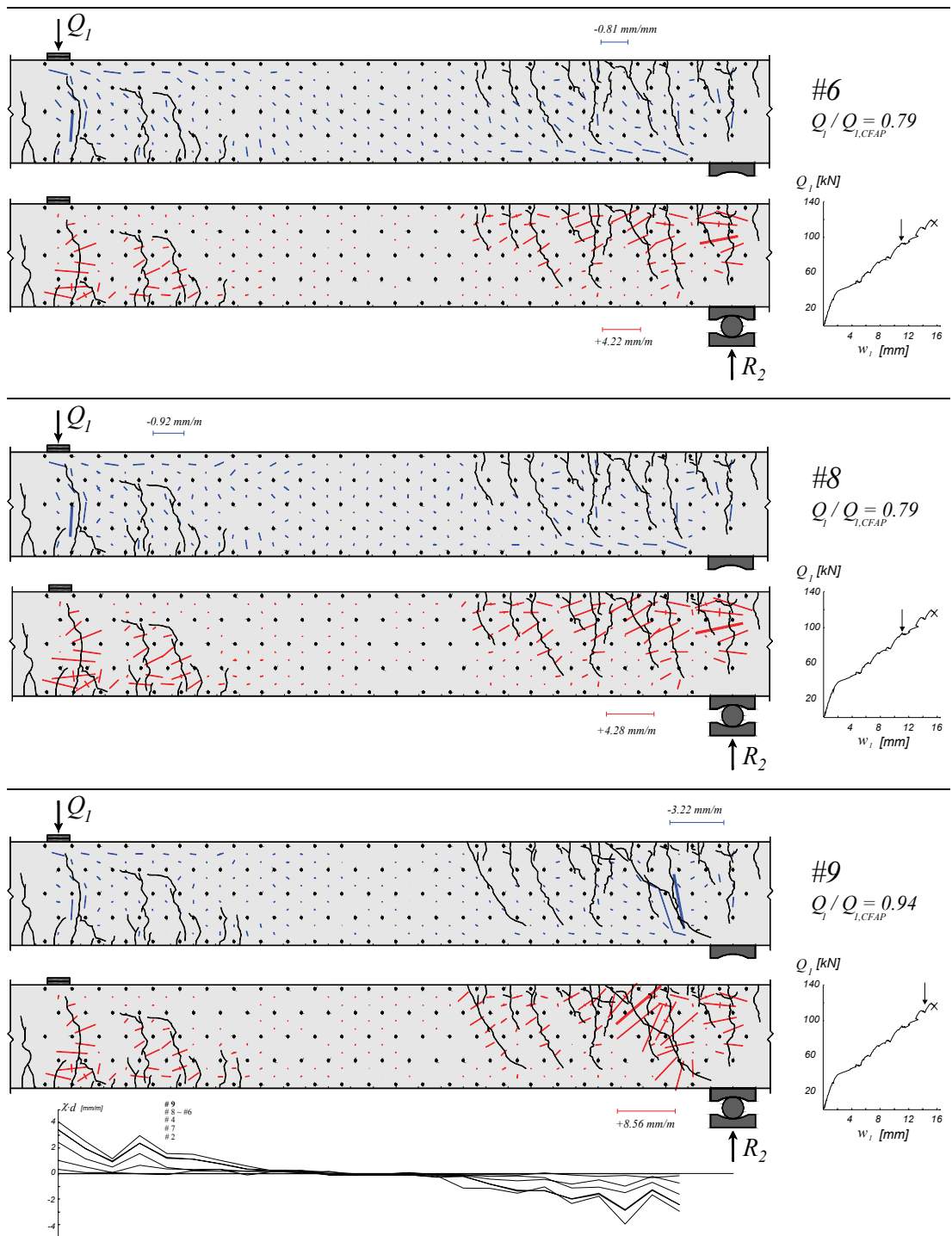


Figure B-4.28: Poutre SR6: déformations principales, fissuration et courbures

### B-4.7 Poutre SR7

La poutre SR7 a été testée avec un rapport  $Q_2/Q_1$  de +0.10 dans la première partie de l'essai. Pour un niveau de charge de  $Q_1 = 123$  kN, une importante fissure d'effort tranchant s'est ouverte au droit de la section  $cr1$ , près de la charge  $Q_1$ . Cette fissure n'a pas engendrée la rupture de la poutre, ni la perte totale de la charge appliquée (fig. B-4.31a). Après rechargement, une rupture très fragile s'est produite, pour  $Q_1 = 140$  kN (fig. B-4.31b) et un rapport  $Q_2/Q_1$  de +0.51.

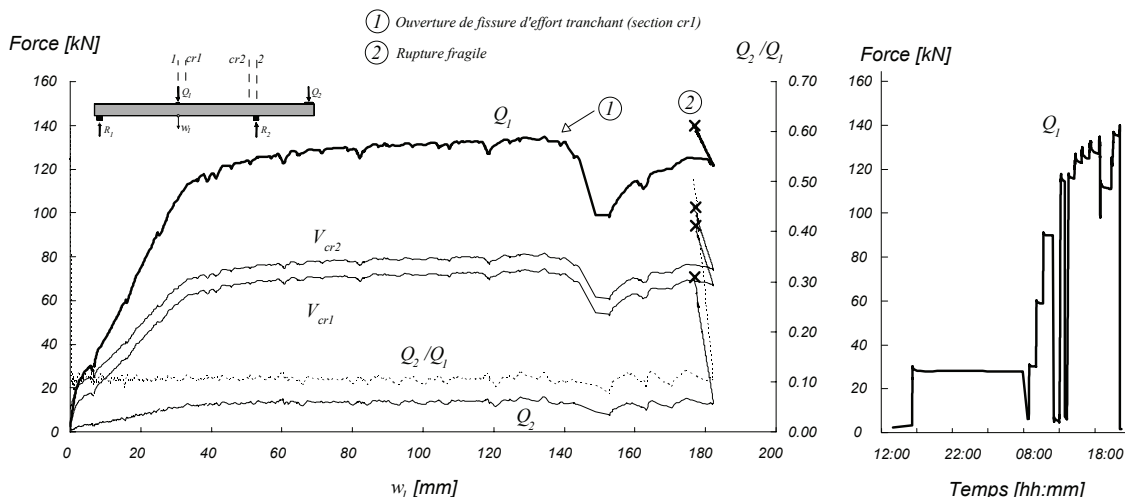


Figure B-4.29: Poutre SR7: Diagramme charge – flèche et évolution dans le temps

Tableau B-4.10: Poutre SR7: Evolution des valeurs mesurées et calculées

Palier	$Q_1$	$Q_2$	$Q_2/Q_1$	$M_1$	$M_{cr1}$	$M_2$	$M_{cr2}$	$V_1$	$V_{cr1}$	$V_2$	$V_{cr2}$	$\Omega_{49}$	$\Omega_{59}$	$w_1$	$w_0$	$Q_1/Q_{1,CR}$	Rem.
	[kN]	[kN]	-	[kN·m]	[kN·m]	[kN·m]	[kN·m]	[kN]	[kN]	[kN]	[kN]	[mm]	[mm]	[mm]	[mm]	%	*
#0	2.9	1.7	0.59	11.8	11.1	-9.7	-7.9	-3.3	-3.7	-11.2	-10.9	0.00	0.00	0.00	0.00	2%	
#1	3.4	1.8	0.53	12.4	11.7	-9.9	-8.0	-3.6	-4.0	-11.5	-11.2	0.00	0.00	0.00	0.00	3%	
#2	29.6	3.4	0.12	49.7	46.5	-12.7	-8.5	-17.2	-17.6	-25.1	-24.8	0.26	0.10	6.00	-4.86	24%	DP
	28.4	3.5	0.12	47.9	44.8	-12.9	-8.7	-16.6	-17.1	-24.6	-24.3	0.27	0.11	6.19	-4.95	23%	FP
#3	30.7	3.3	0.11	51.5	48.2	-12.5	-8.2	-17.7	-18.1	-25.7	-25.4	0.29	0.12	6.69	-5.43	25%	DP
	30.3	3.5	0.12	50.7	47.5	-12.9	-8.5	-17.6	-18.0	-25.5	-25.2	0.29	0.11	6.75	-5.43	24%	FD
	30.3	3.5	0.12	50.7	47.4	-12.9	-8.5	-17.6	-18.0	-25.5	-25.2	0.29	0.11	6.75	-5.43	24%	FP
#4	59.3	6.6	0.11	90.8	84.7	-18.5	-11.5	-33.1	-33.5	-41.0	-40.7	0.70	0.19	16.01	-13.45	48%	DP
	58.9	6.7	0.11	90.1	84.0	-18.8	-11.8	-32.9	-33.4	-40.9	-40.6	0.70	0.19	16.06	-13.50	48%	FD
	58.9	6.7	0.11	90.0	84.0	-18.8	-11.8	-32.9	-33.4	-40.9	-40.6	0.70	0.19	16.06	-13.50	48%	FP
#5	90.7	10.0	0.11	134.0	124.9	-24.9	-14.9	-49.9	-50.3	-57.9	-57.6	1.13	0.26	24.88	-20.80	73%	DP
	89.8	10.3	0.11	132.4	123.4	-25.5	-15.6	-49.6	-50.0	-57.5	-57.2	1.13	0.26	25.15	-20.91	72%	FD
	89.7	10.3	0.11	132.3	123.3	-25.5	-15.6	-49.6	-50.0	-57.5	-57.2	1.13	0.26	25.15	-20.91	72%	FP
#6	116.6	12.8	0.11	169.8	158.2	-30.1	-17.7	-63.9	-64.3	-71.8	-71.5	2.67	0.68	40.94	-32.98	94%	DP
	115.9	13.0	0.11	168.6	157.0	-30.5	-18.1	-63.5	-64.0	-71.5	-71.2	2.71	0.69	41.23	-33.03	93%	FD
	115.7	13.0	0.11	168.2	156.6	-30.5	-18.2	-63.4	-63.9	-71.4	-71.1	2.71	0.69	41.23	-33.03	93%	FP
#7	125.0	14.6	0.12	180.6	168.1	-33.5	-20.2	-68.6	-69.1	-76.6	-76.3	5.80	1.44	59.59	-45.11	101%	DP
	123.2	14.8	0.12	177.6	165.3	-33.9	-20.9	-67.8	-68.2	-75.7	-75.4	5.93	1.48	60.30	-45.21	100%	FD
	122.9	14.8	0.12	177.2	164.9	-34.0	-21.0	-67.7	-68.1	-75.6	-75.3	5.93	1.48	60.30	-45.21	99%	FP
#8	127.3	13.5	0.11	185.1	172.5	-31.3	-17.9	-69.4	-69.9	-77.4	-77.1	9.83	2.49	81.32	-59.43	103%	DP
	125	13.9	0.11	181.3	168.9	-32.1	-18.9	-68.4	-68.9	-76.4	-76.1	9.98	2.53	82.04	-59.62	101%	FD
	124.9	14.0	0.11	181.0	168.6	-32.3	-19.1	-68.4	-68.8	-76.3	-76.0	9.98	2.53	82.04	-59.62	101%	FP
#9	129.0	14.6	0.11	186.5	173.6	-33.5	-19.9	-70.6	-71.1	-78.6	-78.3	4.18	3.77	117.8	-83.30	104%	DP
	128	14.9	0.12	183.9	171.2	-34.1	-20.6	-70.0	-70.4	-77.9	-77.6	4.27	3.79	118.3	-83.41	103%	FD
	127.1	14.9	0.12	183.2	170.5	-34.1	-20.7	-69.8	-70.2	-77.7	-77.4	4.27	3.79	118.3	-83.41	103%	FP
CFTR	123.8	12.2	0.10	181.1	168.9	-28.8	-15.7	-67.2	-67.6	-75.2	-74.9	2.80	3.98	144.25	-98.88	100%	CFTR
CR	139.9	71.3	0.51	146.0	128.3	-144.8	-128.3	-95.0	-95.4	-102.9	-102.6	2.60	3.95	176.43	-73.52	113%	CR

\* DP : Début du palier ; FD : Fin des mesures avec le déformètre ; FP : Fin du palier ; CM : Charge maximale ; CFTR : Ouverture de fissure d'effort tranchant en travée ; CR : Charge de rupture

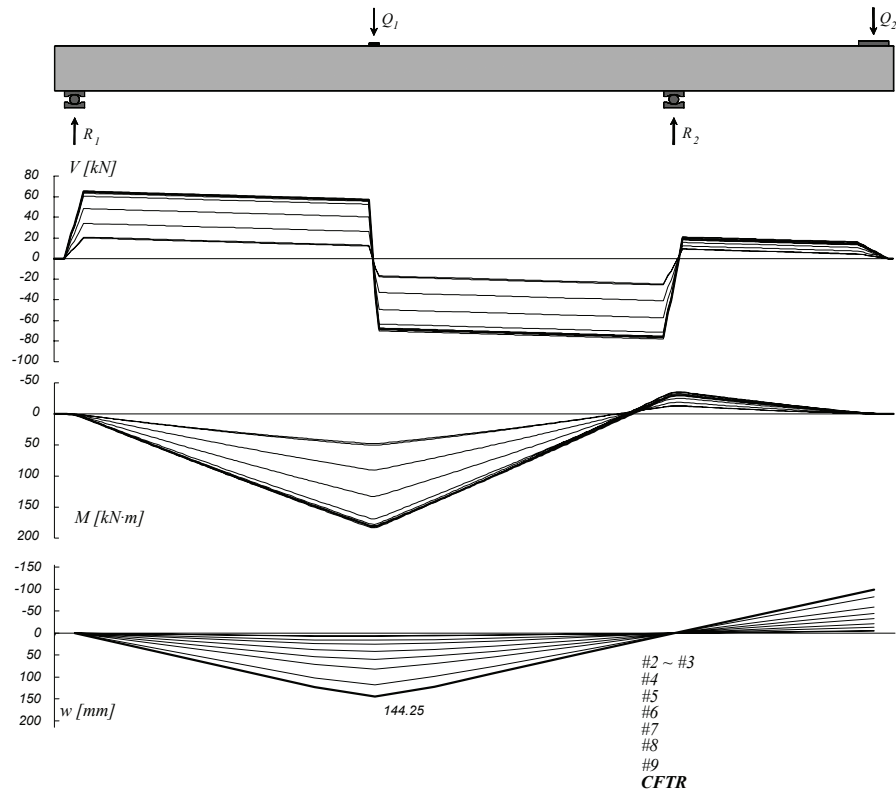


Figure B-4.30: Poutre SR7: Diagramme des efforts tranchants, diagramme des moments de flexion et déformée

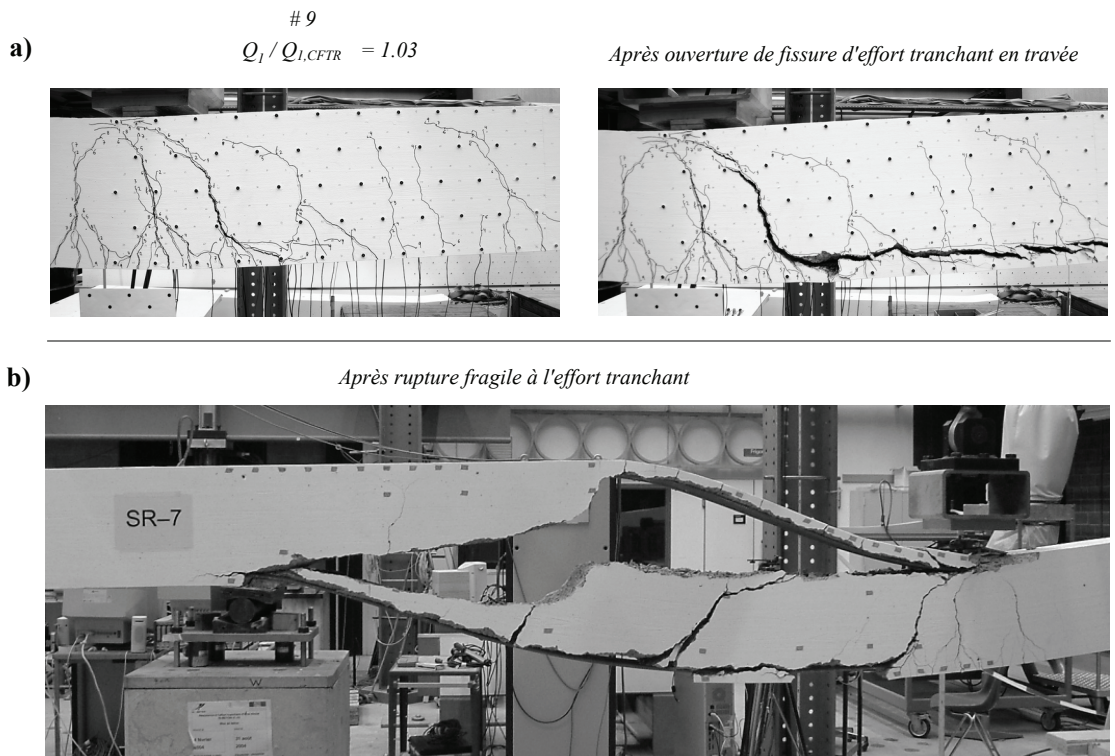


Figure B-4.31: Poutre SR7: a) Ouverture de fissure d'effort tranchant non critique en travée ; b) rupture fragile à l'appui

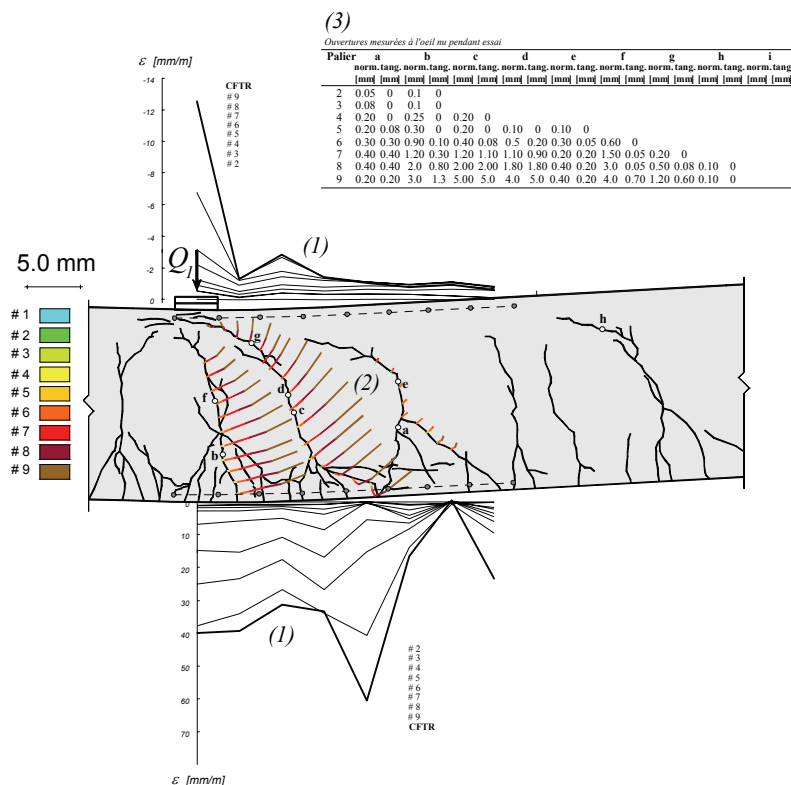
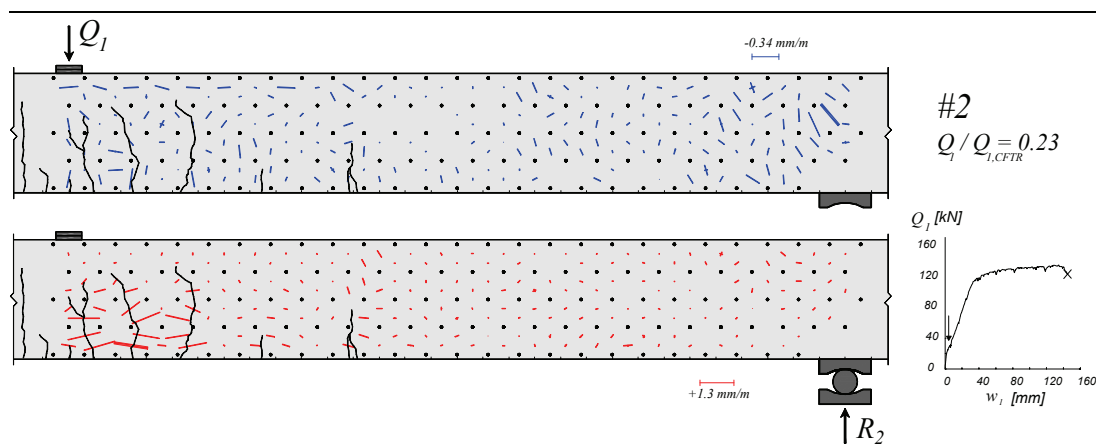


Figure B-4.32: Poutre SR7: (1) Déformations mesurées avec les jauges “oméga” ;  
 (2) Déplacement relatif entre les 2 lèvres des fissures, calculé avec les mesures  
 au déformètre; (3) Ouvertures mesurées à l’œil nu pendant l’essai



Suite page suivante

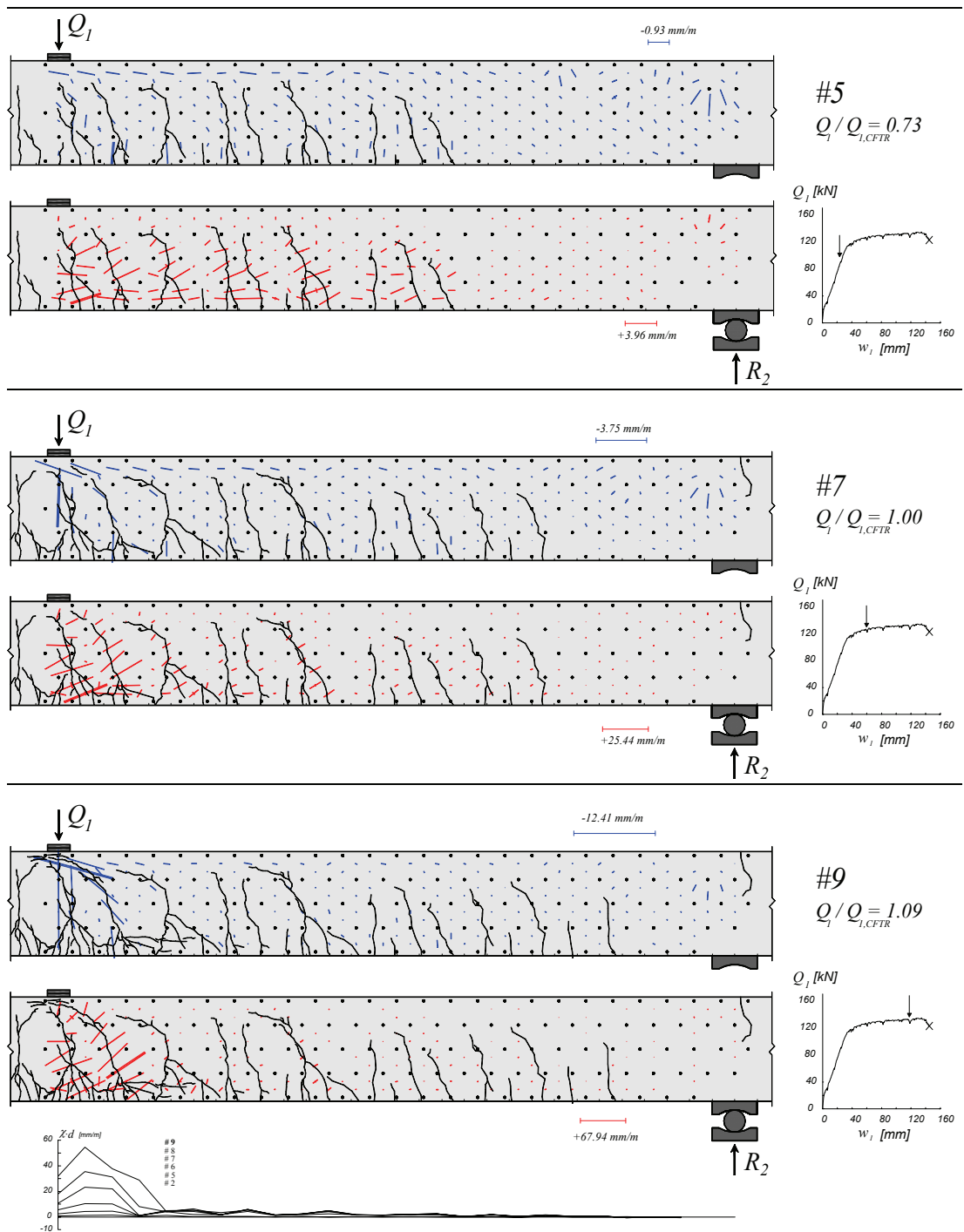


Figure B-4.33: Poutre SR7: déformations principales, fissuration et courbures

### B-4.8 Poutre SR8

La poutre SR8 a été testée avec un rapport  $Q_2/Q_1$  de -0.10. La rupture par effort tranchant a été observée en travée en présence des déformations plastiques importantes de l'armature de flexion (fig. B-4.36).

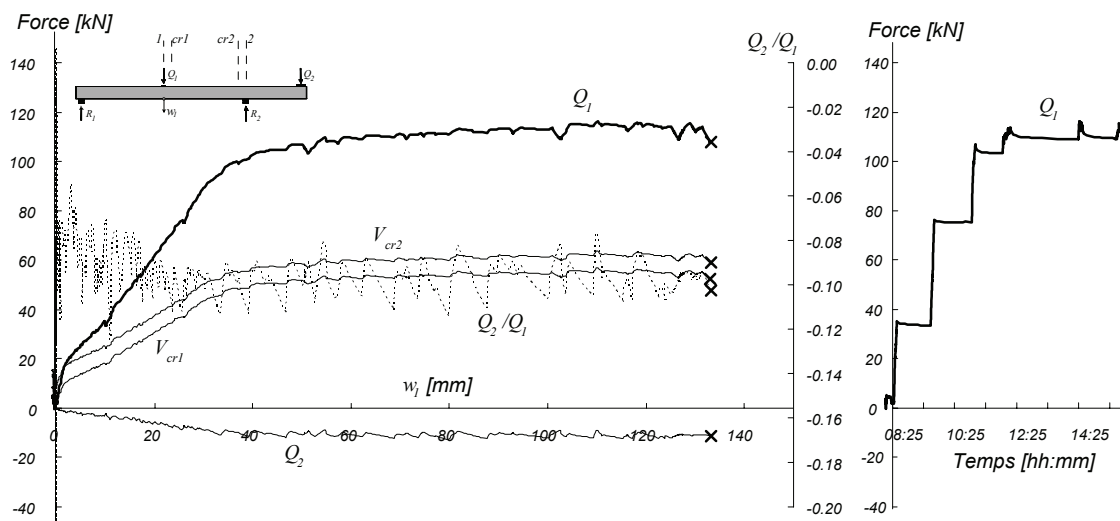


Figure B-4.34: Poutre SR8: Diagramme charge – flèche et évolution dans le temps

Tableau B-4.11: Poutre SR8: Evolution des valeurs mesurées et calculées

Palier	$Q_1$	$Q_2$	$Q_2/Q_1$	$M_1$	$M_{cr1}$	$M_2$	$M_{cr2}$	$V_1$	$V_{cr1}$	$V_2$	$V_{cr2}$	$\Omega_{49}$	$\Omega_{59}$	$w_1$	$w_0$	$Q_1/Q_{1,CR}$	Rem.
	[kN]	[kN]	-	[kN·m]	[kN·m]	[kN·m]	[kN·m]	[kN]	[kN]	[kN]	[kN]	[mm]	[mm]	[mm]	[mm]	%	*
#0	3.3	3.2	0.97	10.9	10.1	-12.6	-10.7	-4.0	-4.4	-11.9	-11.6	0.00	0.00	0.00	0.00	3%	
#1	3.4	3.4	1.00	10.8	10.0	-13.0	-11.1	-4.1	-4.5	-12.0	-11.7	0.00	0.00	0.00	0.00	3%	
#2	34.8	-3.0	-0.08	63.9	60.7	-0.1	4.4	-17.7	-18.1	-25.6	-25.4	0.49	0.16	9.94	-8.51	32%	DP
	33.7	-2.4	-0.07	61.7	58.5	-1.2	3.2	-17.3	-17.7	-25.3	-25.0					31%	FD
#3	33.4	-2.4	-0.07	61.1	58.0	-1.3	3.1	-17.1	-17.6	-25.1	-24.8	0.48	0.16	10.16	-8.68	31%	FP
	75.6	-7.9	-0.10	129.5	123.0	10.2	18.2	-36.4	-36.9	-44.4	-44.1	0.85	0.30	25.89	-25.22	70%	DP
#4	75.2	-7.6	-0.10	128.6	122.1	9.5	17.5	-36.3	-36.8	-44.3	-44.0					70%	FD
	75.3	-7.4	-0.10	128.5	122.0	9.1	17.1	-36.5	-36.9	-44.4	-44.1	0.85	0.30	26.04	-25.35	70%	FP
#5	104.8	-10.0	-0.10	175.1	166.1	14.7	25.2	-50.3	-50.8	-58.3	-58.0	3.30	1.65	50.76	-44.82	98%	DP
	103.3	-9.33	-0.09	172.1	163.2	13.3	23.7	-49.8	-50.2	-57.7	-57.5					96%	FD
#6	103.2	-9.2	-0.09	171.9	162.9	13.1	23.5	-49.8	-50.2	-57.7	-57.4	3.37	1.69	51.35	-45.05	96%	FP
	110.7	-9.6	-0.09	183.5	173.9	14.0	25.0	-53.4	-53.8	-61.4	-61.1	7.88	4.63	101.7	-80.03	103%	DP
#7	109.5	-9.13	-0.08	181.2	171.7	13.0	24.0	-53.0	-53.4	-60.9	-60.6					102%	FD
	109.0	-8.9	-0.08	180.2	170.8	12.5	23.5	-52.8	-53.2	-60.8	-60.5	7.93	4.67	102.4	-79.72	101%	FP
#8	111.3	-11.3	-0.10	186.0	176.5	17.3	28.4	-53.1	-53.6	-61.1	-60.8	8.85	5.87	125.9	-96.19	104%	DP
	109.4	-10.9	-0.10	182.8	173.4	16.4	27.4	-52.3	-52.8	-60.3	-60.0					102%	FD
#9	109.2	-10.7	-0.10	182.3	173.0	16.1	27.1	-52.3	-52.7	-60.2	-59.9	8.95	5.89	126.6	-96.41	102%	FP
	CM	115.4	-11.0	-0.10	191.8	181.9	16.7	28.1	-55.3	-55.7	-63.2	-63.0	9.18	5.94	129.02	-98.24	107%
CR	107.5	-11.0	-0.10	180.1	170.9	16.7	27.4	-51.3	-51.8	-59.3	-59.0	8.53	5.92	133.11	-99.35	100%	CR

\* DP : Début du palier ; FD : Fin des mesures avec le déformètre ; FP : Fin du palier ; CM : Charge maximale ; CR : Charge de rupture ;



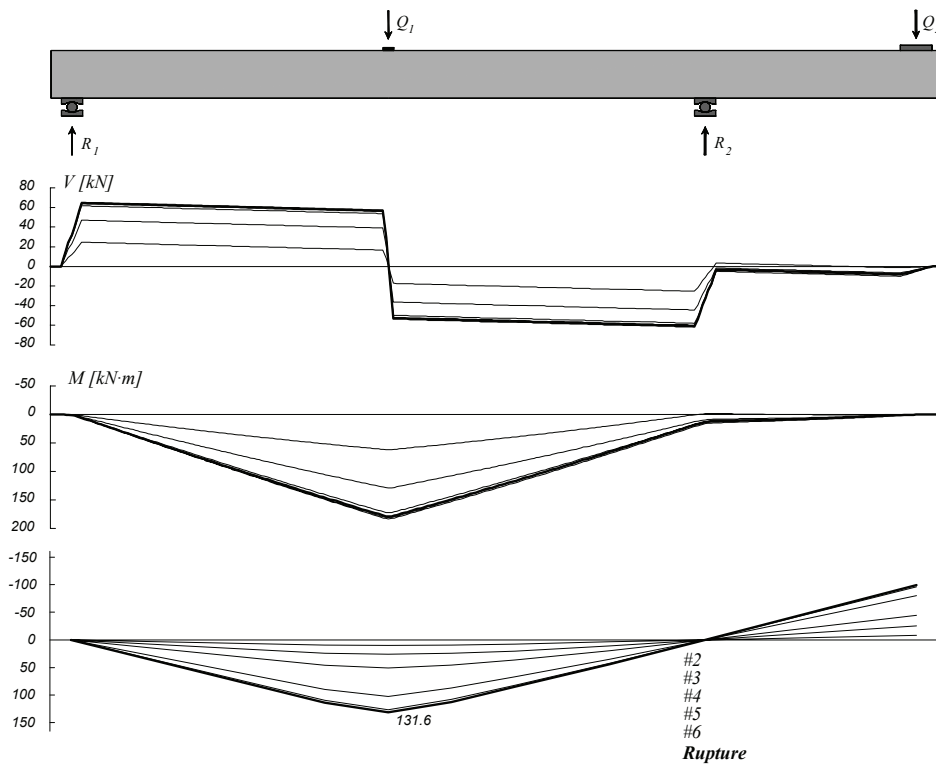
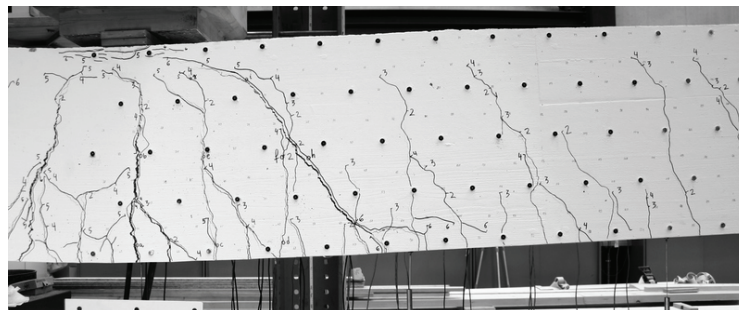
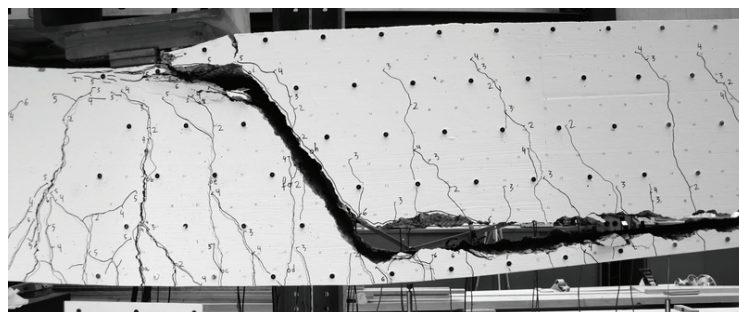


Figure B-4.35: Poutre SR8: Diagramme des efforts tranchants, diagramme des moments de flexion et déformée



# 6  
 $Q_1 / Q_{1,CR} = 0.97$



Rupture

Figure B-4.36: Poutre SR8: Fissuration avant rupture en travée (palier 6) et après rupture

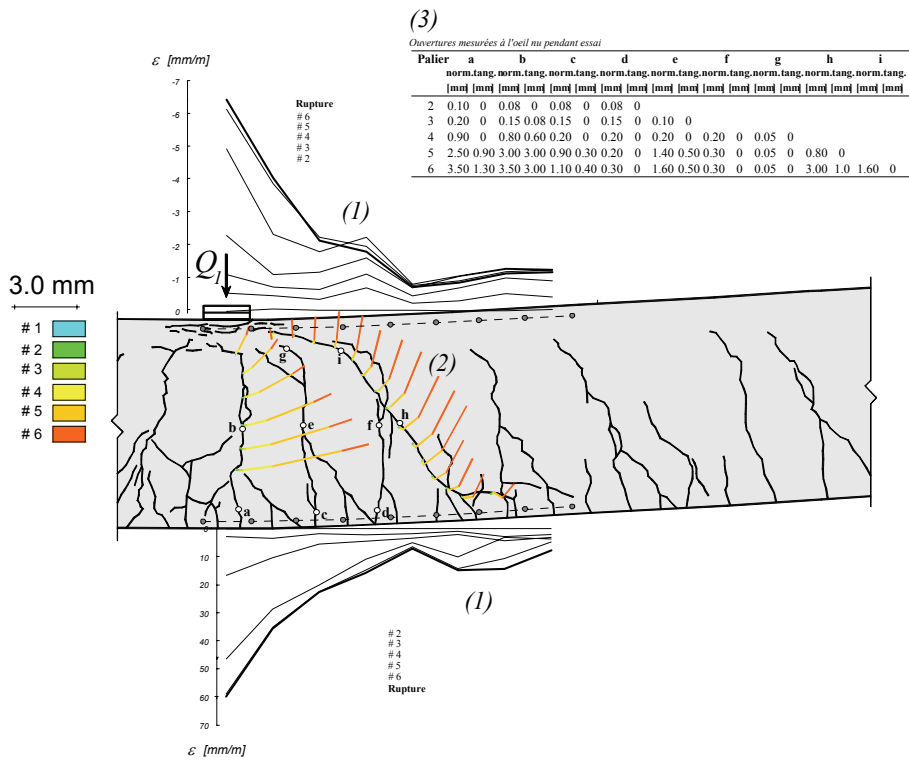
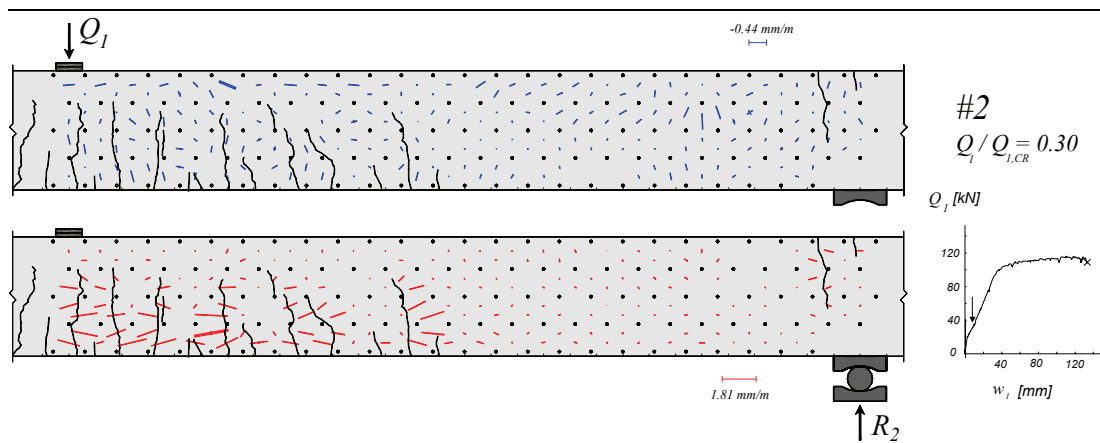


Figure B-4.37: Poutre SR8: (1) Déformations mesurées avec les jauges “oméga” ;  
 (2) Déplacement relatif entre les 2 lèvres des fissures, calculé avec les mesures au déformètre;  
 (3) Ouvertures mesurées à l’œil nu pendant l’essai



Suite page suivante

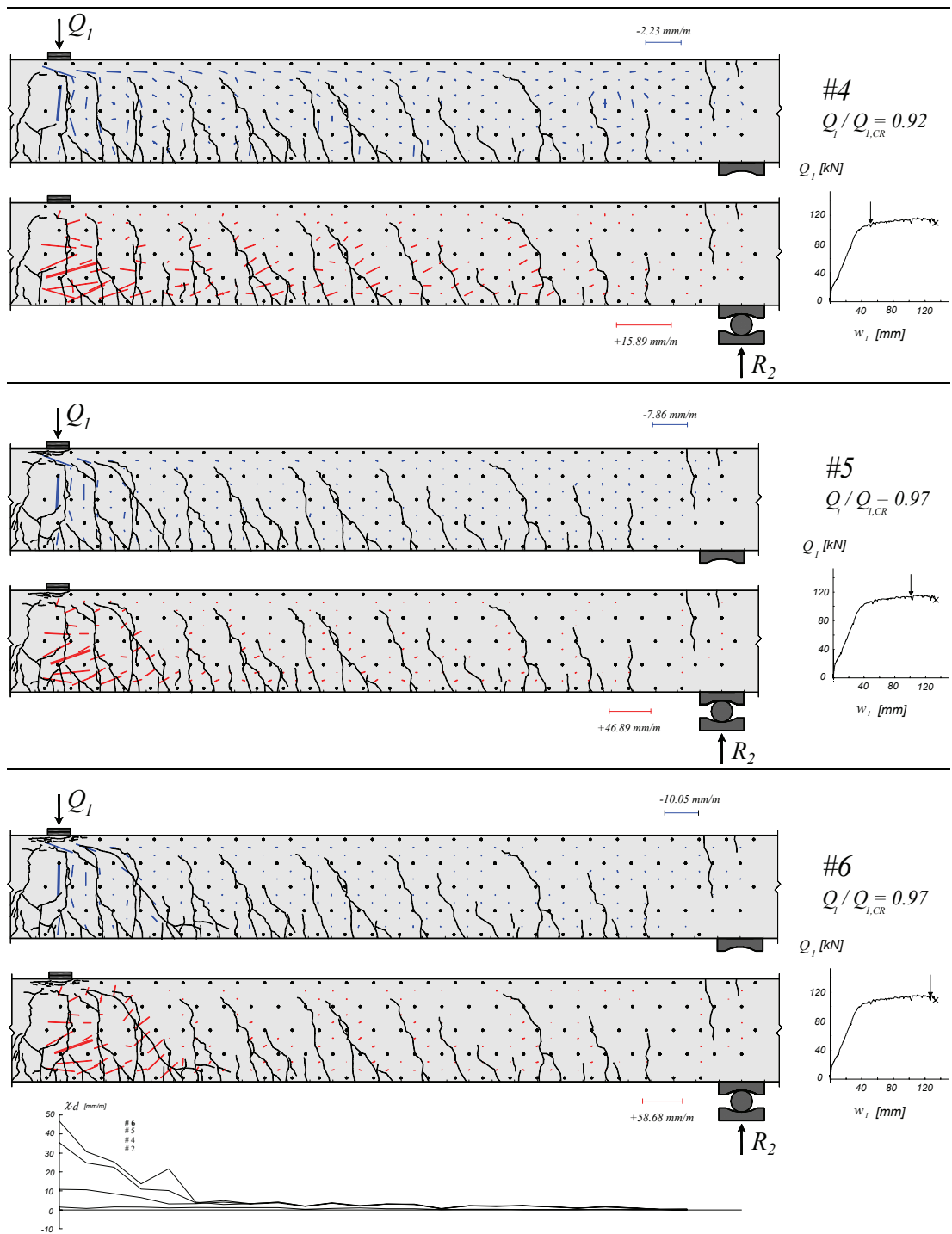


Figure B-4.38: Poutre SR8: déformations principales, fissuration et courbures

### B-4.9 Poutre SR9

La poutre SR9 a été testée avec un rapport  $Q_2/Q_1$  de +0.35. Pour un niveau de charge de  $Q_1 = 125$  kN, une importante fissure d'effort tranchant s'est ouverte au droit de la section  $cr2$ , près de l'appui intermédiaire. Cette fissure n'a pas engendrée la rupture de la poutre, ni la perte totale de la charge appliquée (fig. B-4.41a). Après rechargement, une fissure inclinée s'est créée au droit de la section  $cr1$ , près de la charge  $Q_1$ . Pour  $Q_1 = 125$  kN, cette fissure s'est considérablement ouverte (plusieurs centimètres au niveau de l'armature tendue) et la charge a diminué à  $Q_1 = 85$  kN environ (fig. B-4.41b). La charge de rupture est identifiée à  $Q_1 = 125$  kN.

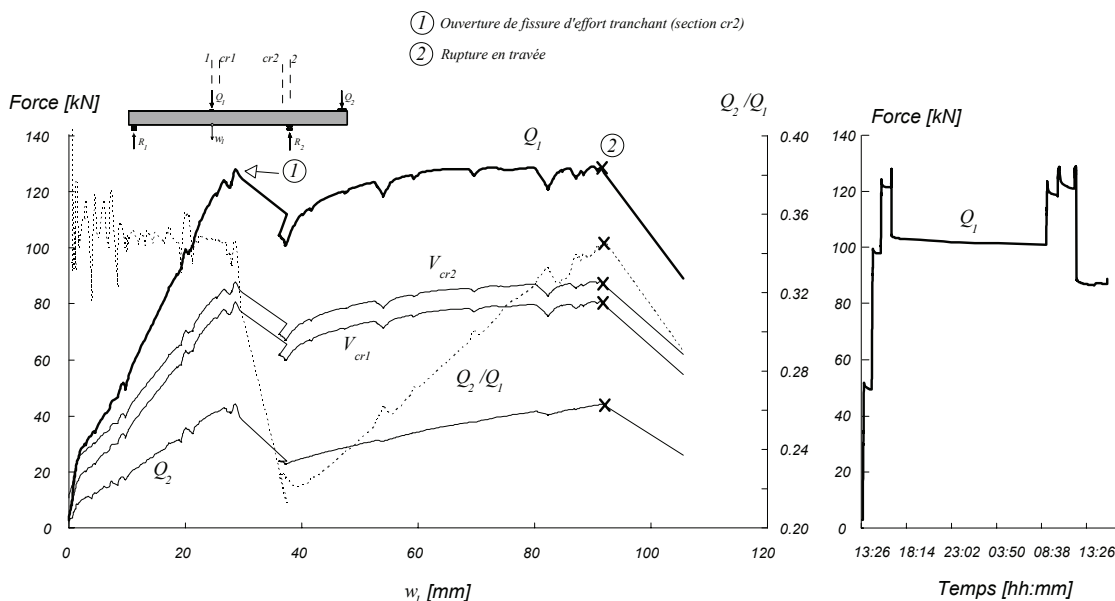


Figure B-4.39: Poutre SR9: Diagramme charge – flèche et évolution dans le temps

Tableau B-4.12: Poutre SR9: Evolution des valeurs mesurées et calculées

Palier	$Q_1$ [kN]	$Q_2$ [kN]	$Q_2/Q_1$ -	$M_1$ [kN·m]	$M_{cr1}$ [kN·m]	$M_2$ [kN·m]	$M_{cr2}$ [kN·m]	$V_1$ [kN]	$V_{cr1}$ [kN]	$V_2$ [kN]	$V_{cr2}$ [kN]	$\Omega_{49}$ [mm]	$\Omega_{59}$ [mm]	$w_1$ [mm]	$w_0$ [mm]	$Q_1/Q_{1,CR}$ %	Rem. *
#0	2.8	1.9	0.68	11.4	10.7	-10.1	-8.3	-3.3	-3.7	-11.2	-10.9	0.00	0.00	0.00	0.00	2%	
#1	3.12	1.9	0.61	11.9	11.2	-10.1	-8.2	-3.4	-3.9	-11.4	-11.1	0.00	0.00	0.00	0.00	3%	
#2	50.6	17.4	0.34	67.1	61.1	-39.9	-33.2	-32.4	-32.8	-40.3	-40.0	0.24	0.08	9.68	-4.43	41%	DP
	49.6	17.2	0.35	65.7	59.8	-39.6	-33.0	-31.8	-32.2	-39.7	-39.4					40%	FD
#3	49.4	17.2	0.35	65.4	59.5	-39.6	-33.0	-31.7	-32.1	-39.6	-39.3	0.25	0.08	9.72	-4.40	40%	FP
	98.9	35.5	0.36	120.8	109.2	-75.0	-63.4	-62.6	-63.0	-70.5	-70.2	0.24	0.14	20.16	-5.08	79%	DP
#4	98.0	35.2	0.36	119.7	108.2	-74.4	-62.9	-62.0	-62.4	-69.9	-69.6					79%	FD
	97.9	35.2	0.36	119.6	108.1	-74.3	-62.8	-61.9	-62.4	-69.9	-69.6	0.24	0.15	20.56	-5.02	79%	FP
CFAP	122.7	41.7	0.34	150.0	135.9	-86.8	-72.8	-76.5	-76.9	-84.5	-84.2	0.25	0.17	27.13	-6.65	99%	DP
	121.5	41.3	0.34	148.6	134.6	-86.1	-72.3	-75.8	-76.2	-83.7	-83.4					98%	FD
CR	121.4	41.3	0.34	148.5	134.5	-86.0	-72.2	-75.7	-76.2	-83.7	-83.4	0.24	0.17	27.65	-6.54	98%	FP
CFAP	124.5	38.3	0.31	156.0	142.0	-80.2	-66.2	-76.3	-76.7	-84.3	-84.0	0.51	0.15	29.71	-4.19	100%	CFAP
CR	126.5	43.8	0.35	153.5	138.9	-90.9	-76.5	-79.1	-79.5	-87.0	-86.7	0.24	0.16	92.07	-5.94	102%	CR

\* DP : Début du palier ; FD : Fin des mesures avec le déformètre ; FP : Fin du palier ; CM : Charge maximale ; CFAP : Ouverture de fissure d'effort tranchant à l'appui ; CR : Charge de rupture ;

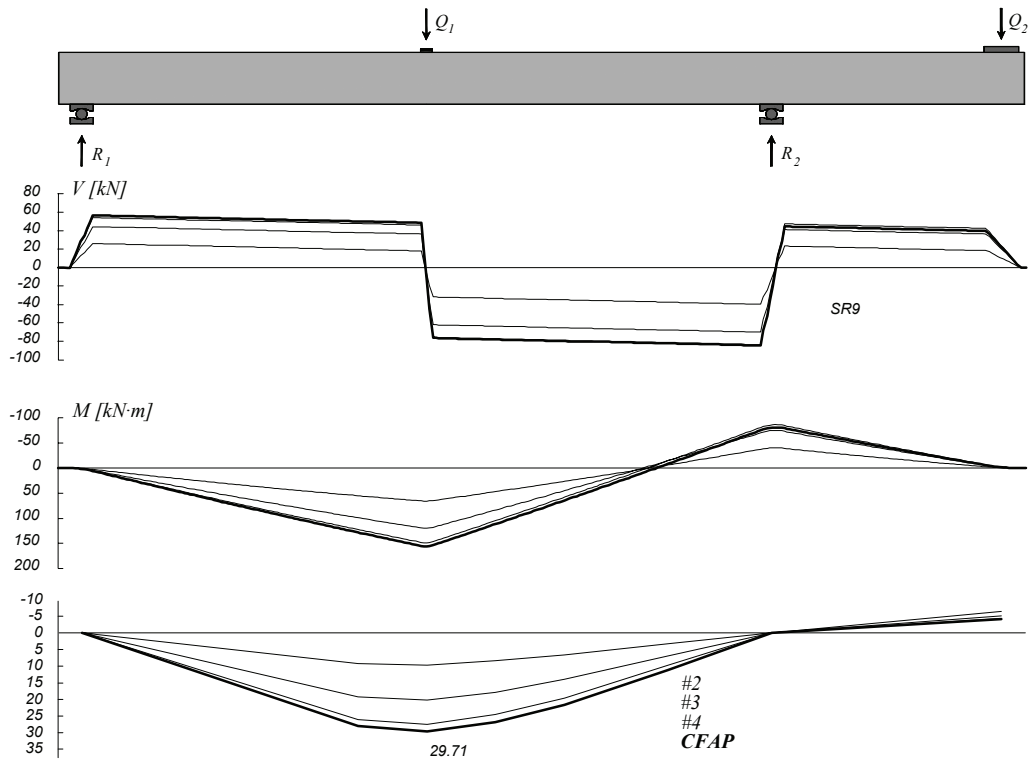


Figure B-4.40: Poutre SR9: Diagramme des efforts tranchants, diagramme des moments de flexion et déformée

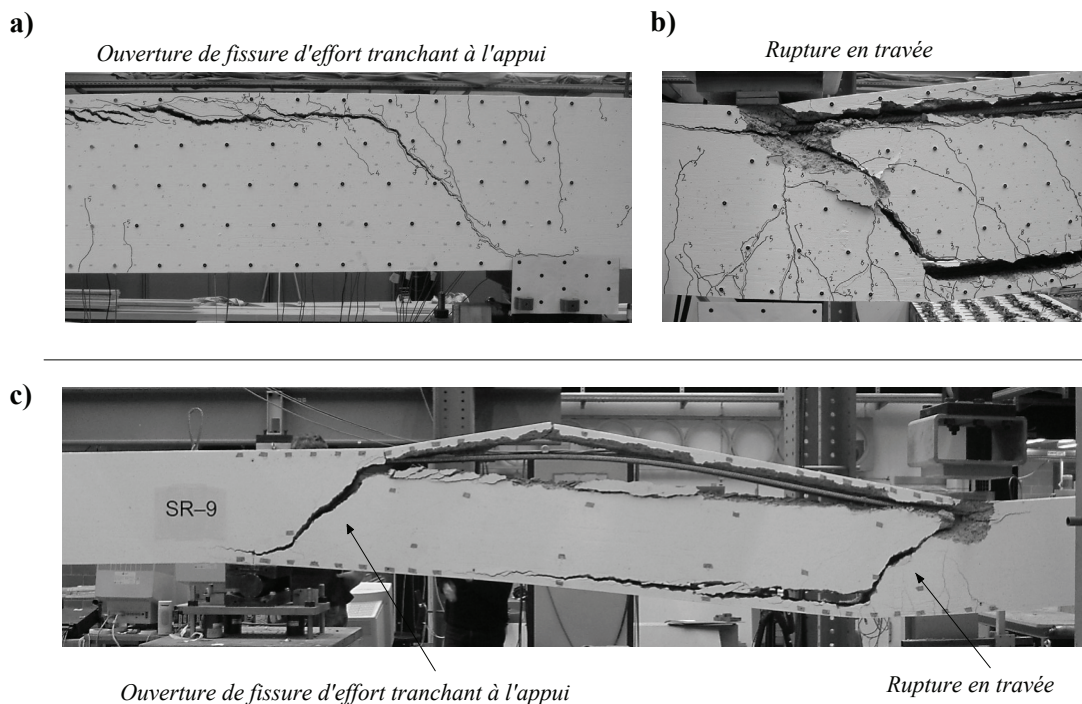


Figure B-4.41: a) Ouverture de fissure d'effort tranchant à l'appui ;  
 b) Rupture en travée ; c) Vue d'ensemble après la fin de l'essai

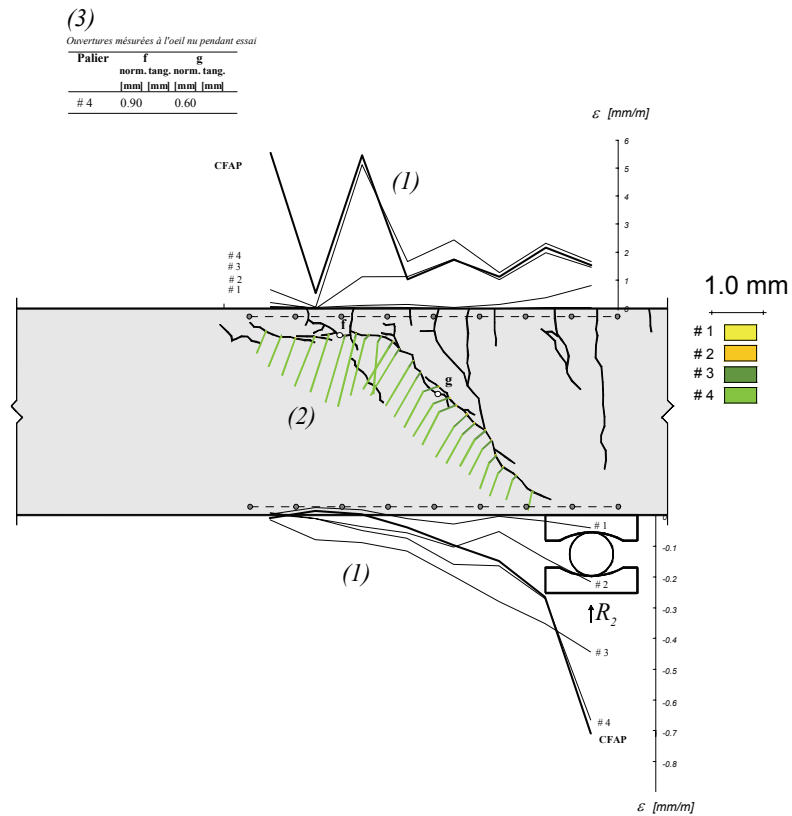
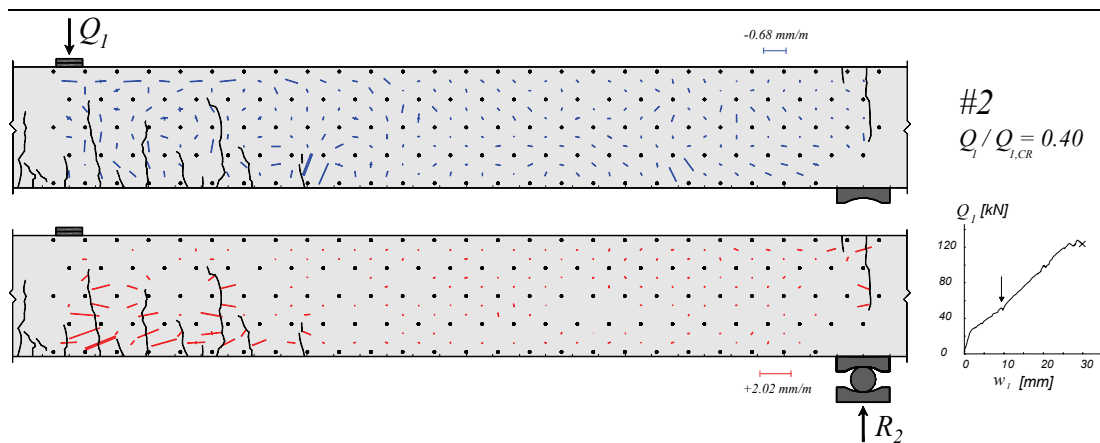


Figure B-4.42: Poutre SR9: (1) Déformations mesurées avec les jauges “oméga” ;  
(2) Déplacement relatif entre les 2 lèvres des fissures, calculé avec les mesures  
au déformètre; (3) Ouverture mesurées à l’œil nu pendant l’essai



Suite page suivante

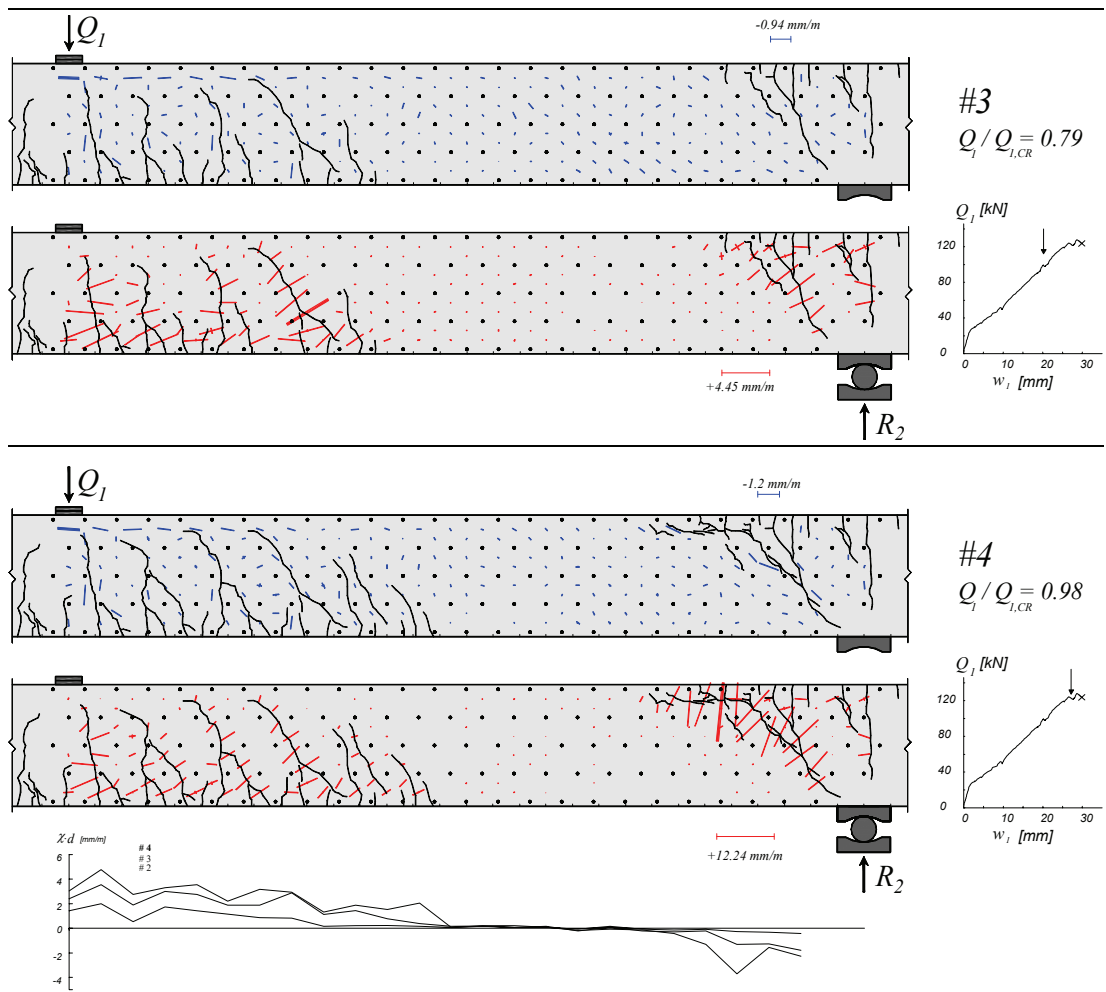


Figure B-4.43: Poutre SR9: déformations principales, fissuration et courbures

### B-4.10 Poutre SR10

La poutre SR10 a été testée avec un rapport  $Q_2/Q_1$  de -0.10. Le type de l'acier était laminé à chaud. Après un très grand plateau plastique, pour un niveau de charge de  $Q_1 = 103$  kN et une flèche de  $w_1 = 140$  mm, une importante fissure s'est ouverte à environ 20 cm de l'axe de la charge  $Q_1$ . Par la suite la charge appliquée a diminuée à  $Q_1 = 80$  kN environ et le béton d'enrobage au niveau de l'armature tendue a éclaté. La fissure n'a pas engendrée la rupture de la poutre, ni la perte totale de la charge appliquée (figs. B-4.44 et B-4.46).

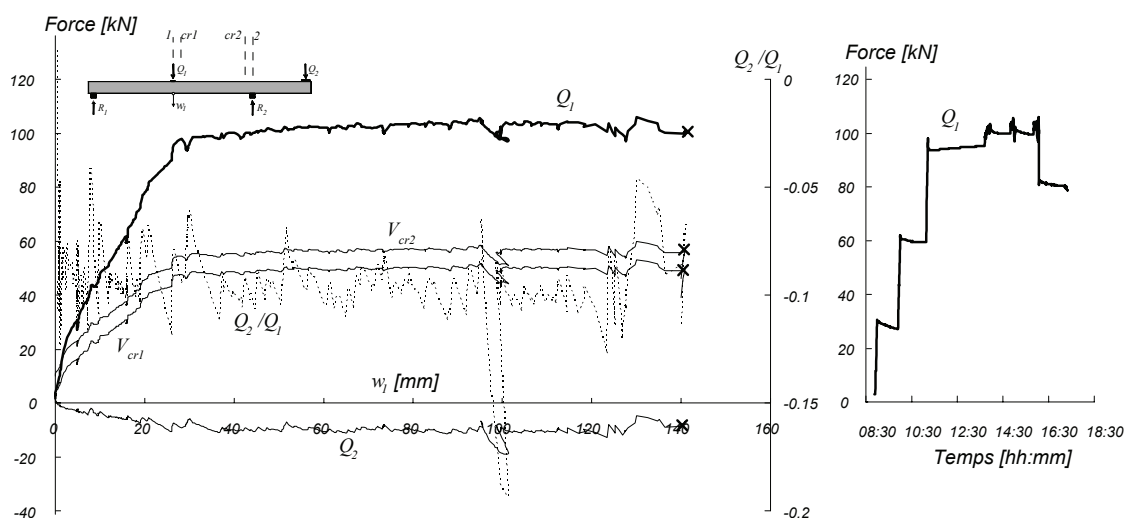


Figure B-4.44: Poutre S10: Diagramme charge – flèche et évolution dans le temps

Tableau B-4.13: Poutre SR10: Evolution des valeurs mesurées et calculées

Palier	$Q_1$ [kN]	$Q_2$ [kN]	$Q_2/Q_1$ -	$M_1$ [kN·m]	$M_{cr1}$ [kN·m]	$M_2$ [kN·m]	$M_{cr2}$ [kN·m]	$V_1$ [kN]	$V_{cr1}$ [kN]	$V_2$ [kN]	$V_{cr2}$ [kN]	$\Omega_{49}$ [mm]	$\Omega_{59}$ [mm]	$w_1$ [mm]	$w_0$ [mm]	$Q_1/Q_{1,CR}$ %	Rem.
#0	1.2	0.5	0.42	10.4	10.0	-7.3	-5.7	-2.0	-2.5	-10.0	-9.7	0.00	0.00	0.00	0.00	1%	
#1	2.1	0.2	0.10	12.1	11.6	-6.7	-5.0	-2.4	-2.8	-10.3	-10.0	0.00	0.00	0.00	0.00	2%	
#2	29.7	-2.3	-0.08	55.6	52.8	-1.4	2.6	-15.3	-15.8	-23.3	-23.0	0.21	0.13	5.51	-5.10	29%	DP
	27.9	-2.73	-0.10	53.4	50.8	-0.6	3.3	-14.3	-14.7	-22.2	-22.0					28%	FD
	27.4	-3.0	-0.11	52.8	50.3	-0.2	3.6	-14.0	-14.4	-21.9	-21.6	0.22	0.13	5.63	-5.39	27%	FP
#3	60.8	-5.7	-0.09	105.2	99.9	5.6	12.3	-29.7	-30.2	-37.7	-37.4	0.72	0.28	17.14	-16.37	60%	DP
	59.5	-6	-0.10	103.7	98.4	6.2	12.8	-29.0	-29.4	-37.0	-36.7					59%	FD
	59.6	-5.9	-0.10	103.7	98.5	6.0	12.7	-29.1	-29.5	-37.0	-36.7	0.68	0.27	17.17	-16.54	59%	FP
#4	94.1	-8.1	-0.09	157.2	149.1	10.8	20.5	-45.6	-46.0	-53.5	-53.2	1.05	1.20	31.26	-29.10	93%	DP
	93.9	-7.2	-0.08	156.0	147.8	9.0	18.6	-45.8	-46.2	-53.8	-53.5					93%	FD
	95.0	-6.0	-0.06	156.6	148.1	6.7	16.5	-46.8	-47.2	-54.7	-54.4	1.05	1.31	32.06	-29.19	94%	FP
#5	100.7	-8.7	-0.09	167.7	159.0	12.1	22.3	-48.7	-49.1	-56.7	-56.4	6.10	4.60	91.79	-69.78	99%	DP
	99.4	-8.3	-0.08	165.3	156.7	11.2	21.3	-48.2	-48.6	-56.1	-55.8					98%	FD
	99.8	-8.1	-0.08	165.7	157.0	10.9	21.1	-48.4	-48.9	-56.4	-56.1	6.11	4.61	92.15	-69.91	99%	FP
#6	101.4	-9.5	-0.09	169.5	160.7	13.6	23.9	-48.8	-49.2	-56.7	-56.4	>10.0	5.07	126.3	-94.46	100%	DP
	99.7	-9.4	-0.09	166.9	158.3	13.4	23.5	-48.0	-48.4	-55.9	-55.6					98%	FD
	99.4	-9.5	-0.10	166.5	158.0	13.6	23.7	-47.8	-48.2	-55.7	-55.4	>10.0	5.08	126.5	-94.57	98%	FP
CM	105.8	-4.9	-0.05	171.5	162.0	4.5	15.4	-52.5	-53.0	-60.5	-60.2	>10.0	5.17	130.2	-	105%	CM
CR	101.3	-6.8	-0.07	166.6	157.7	8.3	18.6	-49.6	-50.0	-57.6	-57.3	>10.0	5.18	140.9	-	100%	CR

\* DP : Début du palier ; FD : Fin des mesures avec le déformètre ; FP : Fin du palier ; CM : Charge maximale ; CR : Charge de rupture ;



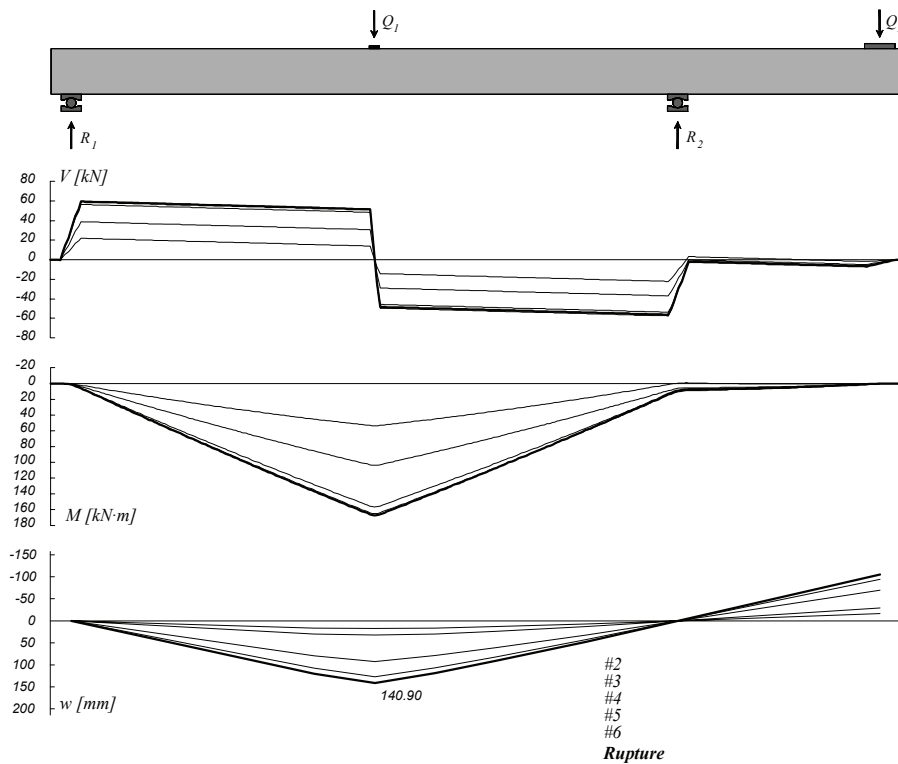
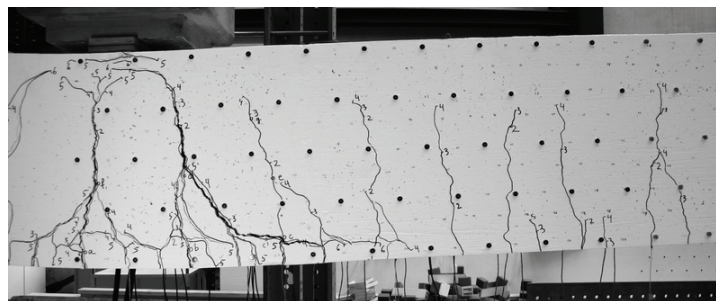
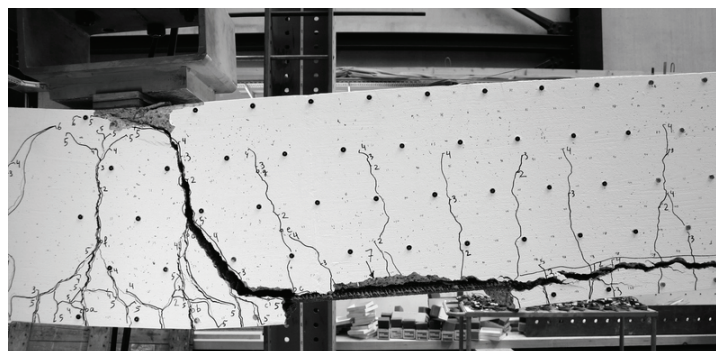


Figure B-4.45: Poutre SR10: Diagramme des efforts tranchants, diagramme des moments de flexion et déformée



# 6  
 $Q_1 / Q_{I,CR} = 0.98$



Rupture

Figure B-4.46: Poutre SR10: Fissuration avant rupture en travée (palier 6) et après rupture

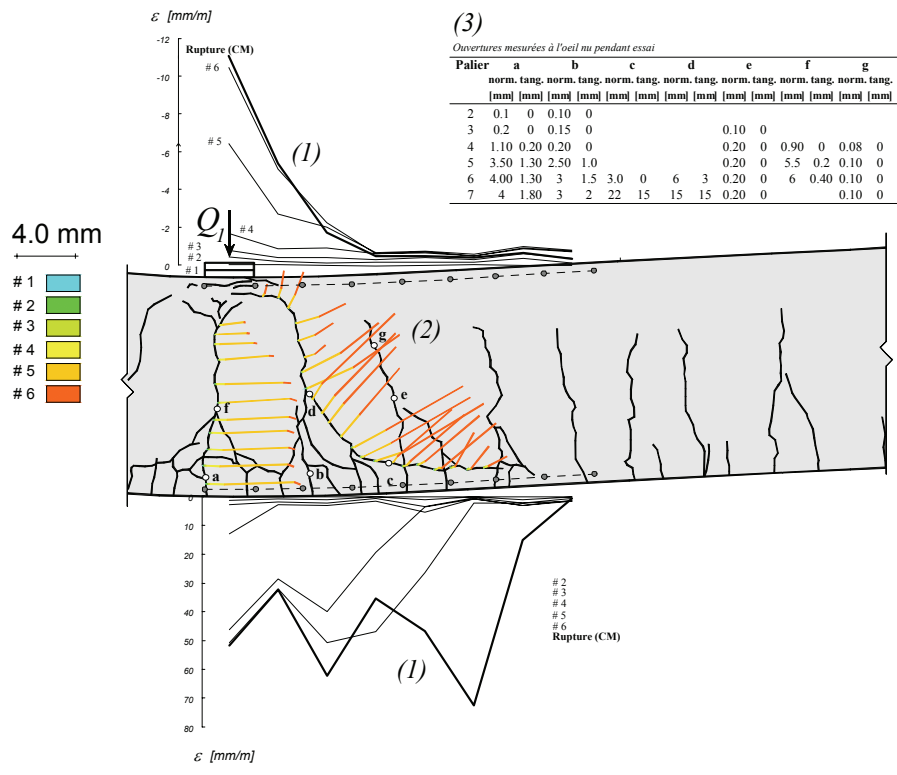
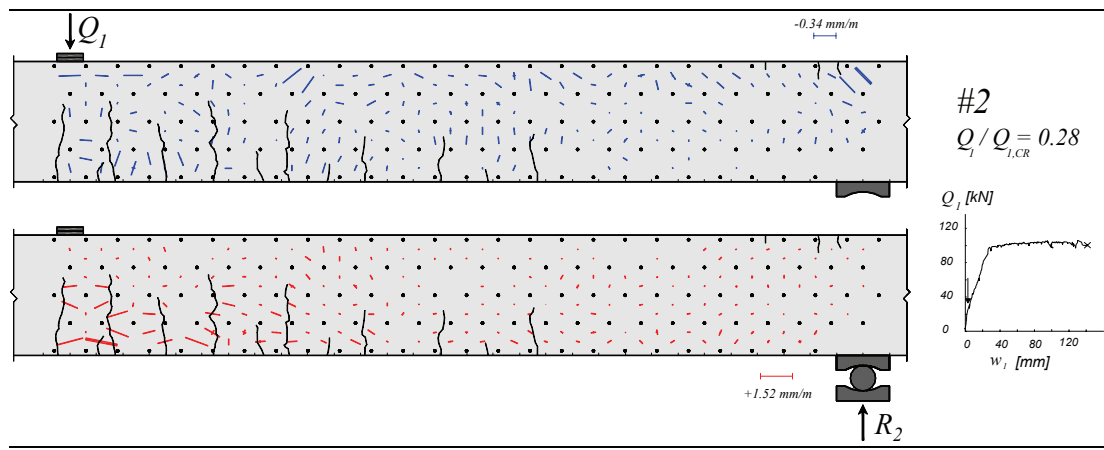


Figure B-4.47: Poutre SR10: (1) Déformations mesurées avec les jauges "oméga" ;  
 (2) Déplacement relatif entre les 2 lèvres des fissures, calculé avec les mesures au déformètre; (3) Ouvertures mesurées à l'œil nu pendant l'essai



Suite page suivante

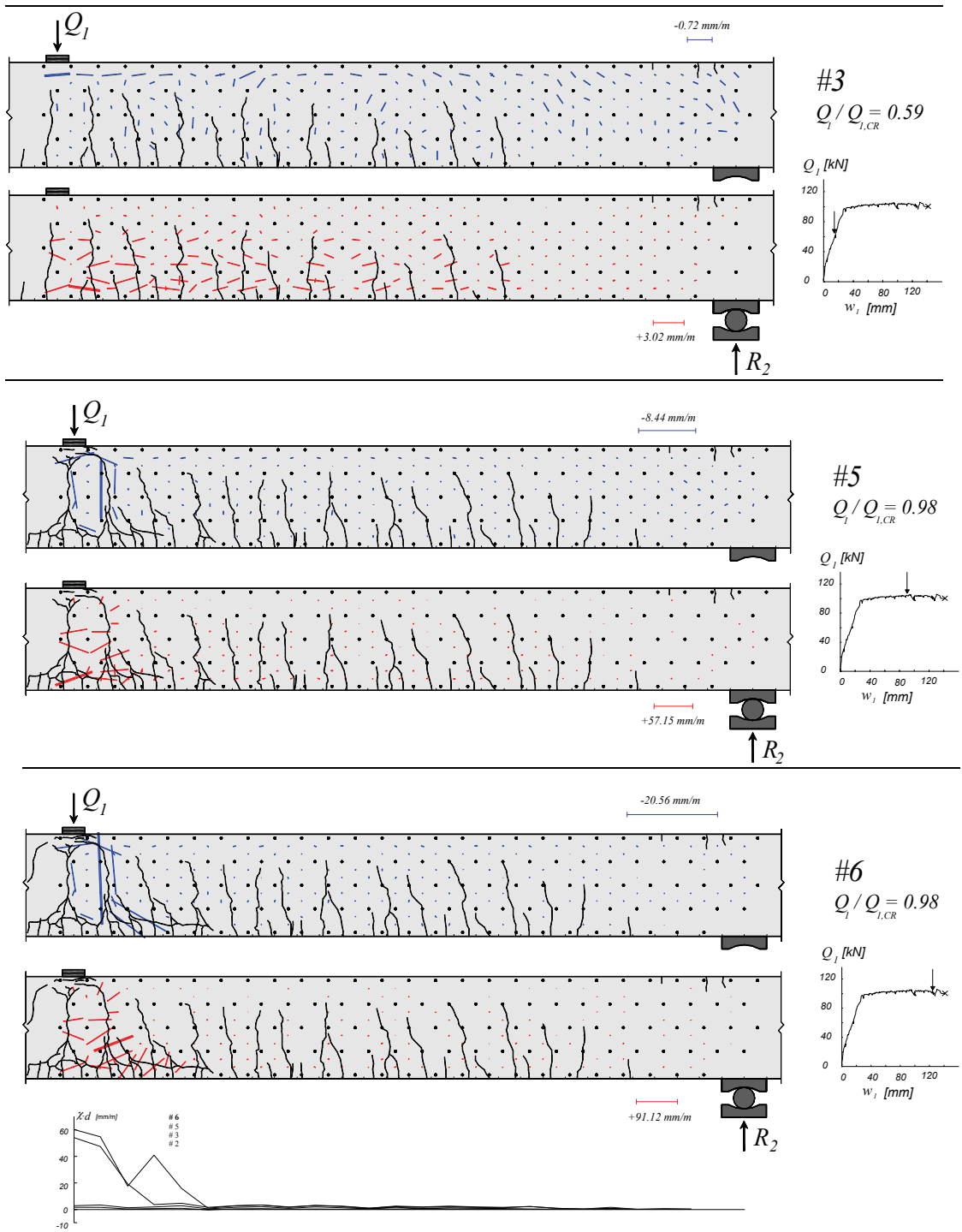


Figure B-4.48: Poutre SR10: déformations principales, fissuration et courbures

### B-4.11 Poutre SR11

La poutre SR11 a été testée avec un rapport  $Q_2/Q_1$  ciblé de +0.35. Le type de l'acier était laminé à chaud. La rupture observée a été une rupture à l'effort tranchant très fragile (fig. B-4.51), dans la région proche de l'appui intermédiaire avec des ouvertures des fissures très petites. L'ouverture des fissures estimées au palier précédent la rupture est de l'ordre de 0.2 mm (voir figure B-4.52). Le comportement observé a été similaire à celui de la poutre SR2.

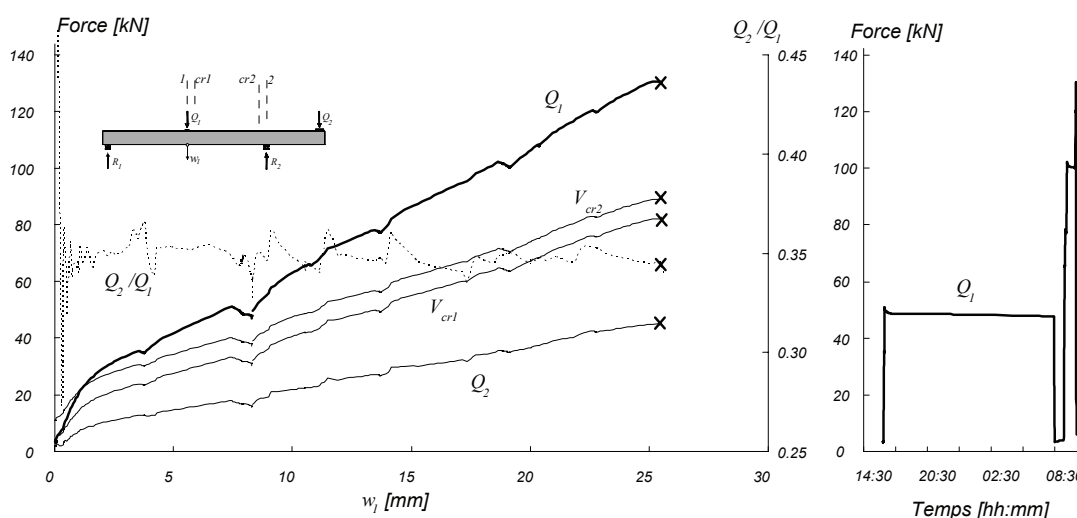


Figure B-4.49: Poutre SR11: Diagramme charge – flèche et évolution dans le temps

Tableau B-4.14: Poutre SR11: Evolution des valeurs mesurées et calculées

Palier	$Q_1$ [kN]	$Q_2$ [kN]	$Q_2/Q_1$ -	$M_1$ [kN·m]	$M_{cr1}$ [kN·m]	$M_2$ [kN·m]	$M_{cr2}$ [kN·m]	$V_1$ [kN]	$V_{cr1}$ [kN]	$V_2$ [kN]	$V_{cr2}$ [kN]	$\Omega_{49}$ [mm]	$\Omega_{59}$ [mm]	$w_1$ [mm]	$w_0$ [mm]	$Q_1/Q_{1,CR}$ %	Rem. *
#0	3.3	1.7	0.52	12.4	11.7	-9.7	-7.8	-3.5	-3.9	-11.4	-11.1	0.00	0.00	0.00	0.00	3%	
#1	3.4	2	0.59	12.2	11.5	-10.3	-8.4	-3.6	-4.1	-11.6	-11.3	0.00	0.00	0.00	0.00	3%	
#2	48.5	16.9	0.35	64.4	58.6	-39.0	-32.6	-31.1	-31.6	-39.1	-38.8	10.00	0.11	7.94	-2.61	37%	DP
	48.6	16.9	0.35	64.5	58.7	-39.0	-32.5	-31.2	-31.6	-39.1	-38.8					37%	FD
	48.5	16.9	0.35	64.4	58.6	-39.0	-32.6	-31.1	-31.6	-39.1	-38.8	10.00	0.11	8.01	-2.63	37%	FP
#3	3.5	1.6	0.45	12.8	12.1	-9.4	-7.5	-3.5	-4.0	-11.5	-11.2	10.00	0.07	3.41	-1.02	3%	DP
	4.0	1.6	0.40	13.5	12.7	-9.5	-7.6	-3.8	-4.2	-11.7	-11.4					3%	FD
	4.0	1.6	0.39	13.5	12.8	-9.4	-7.5	-3.8	-4.2	-11.7	-11.4	10.00	0.07	3.38	-1.05	3%	FP
#4	101.5	35.4	0.35	124.7	112.9	-74.8	-63.0	-63.8	-64.2	-71.8	-71.5	10.00	0.23	18.86	-3.87	78%	DP
	100.4	35.1	0.35	123.4	111.7	-74.1	-62.4	-63.2	-63.6	-71.1	-70.8					77%	FD
	100.2	35.1	0.35	123.1	111.4	-74.1	-62.4	-63.1	-63.5	-71.0	-70.7	10.00	0.23	19.17	-3.74	77%	FP
CM	130.6	45.1	0.35	158.3	143.2	-93.5	-78.7	-81.6	-82.0	-89.5	-89.3	0.34	0.27	25.44	-5.06	100%	CM
CR	130.6	45.1	0.35	158.3	143.2	-93.5	-78.7	-81.6	-82.0	-89.5	-89.3	0.34	0.27	25.44	-5.06	100%	CR

\* DP : Début du palier ; FD : Fin des mesures avec le déformètre ; FP : Fin du palier ; CM : Charge maximale ; CR : Charge de rupture ;

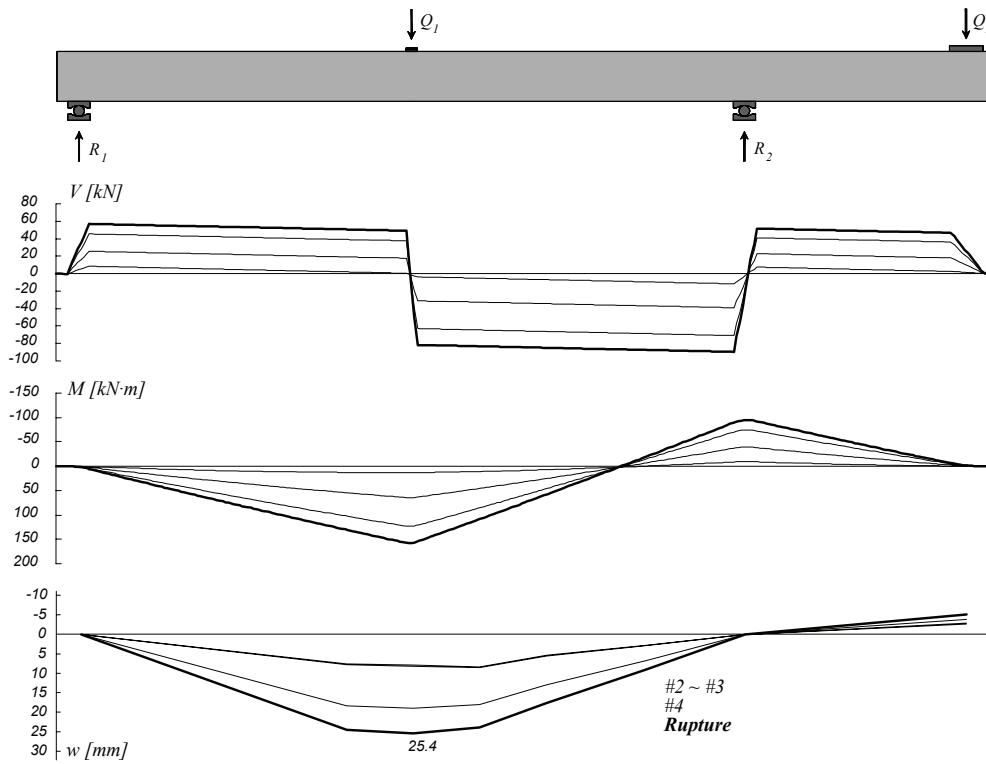
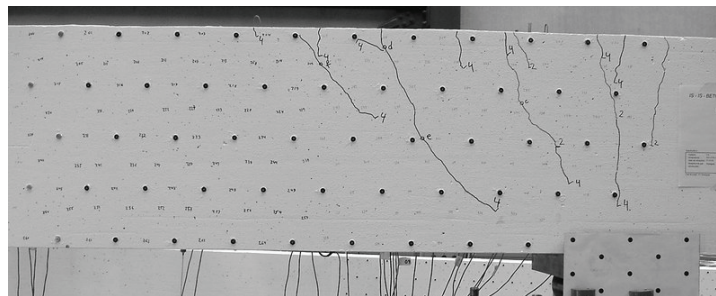
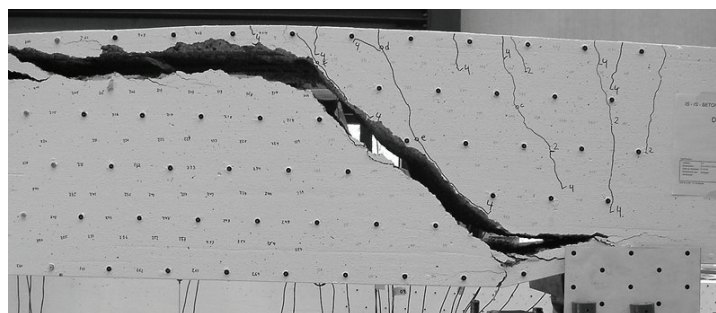


Figure B-4.50: Poutre SR11: Diagramme des efforts tranchants, diagramme des moments de flexion et déformée



# 4  
 $Q_1 / Q_{I,CR} = 0.77$



**Rupture**

Figure B-4.51: Poutre SR11: Fissuration avant rupture à l'appui (palier 4) et après rupture

# Chapitre B-4

(3)

Ouvertures mesurées à l'oeil nu pendant essai

Palier	a		b		c		d		e		f	
	norm.	tang.	norm.	tang.	norm.	tang.	norm.	tang.	norm.	tang.	norm.	tang.
	[mm]	[mm]	[mm]	[mm]	[mm]	[mm]	[mm]	[mm]	[mm]	[mm]	[mm]	[mm]
2	0.10	0	0.10	0	0.05	0						
3	0.05	0	0.02	0	0.02	0						
4	0.20	0	0.15	0	0.20	0	0.20	0	0.20	0	0.10	0

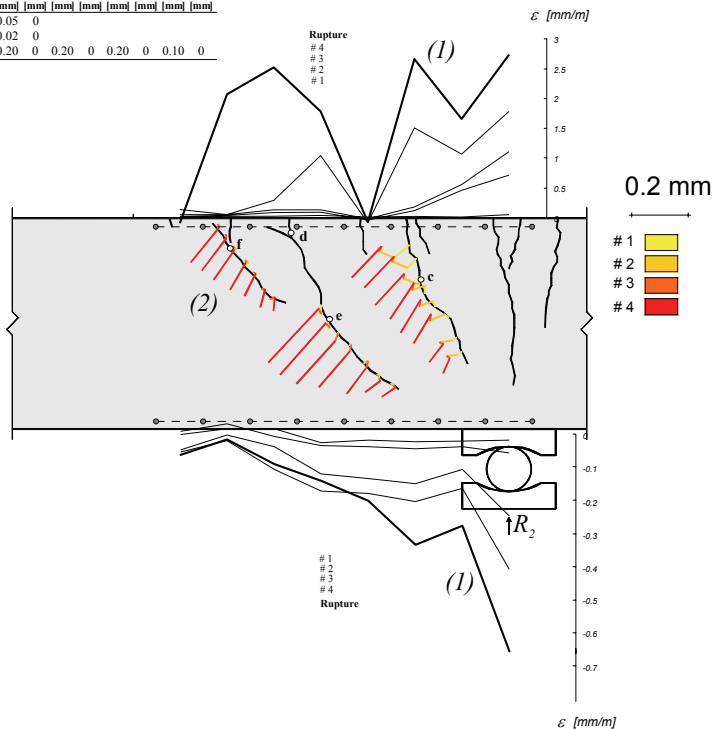
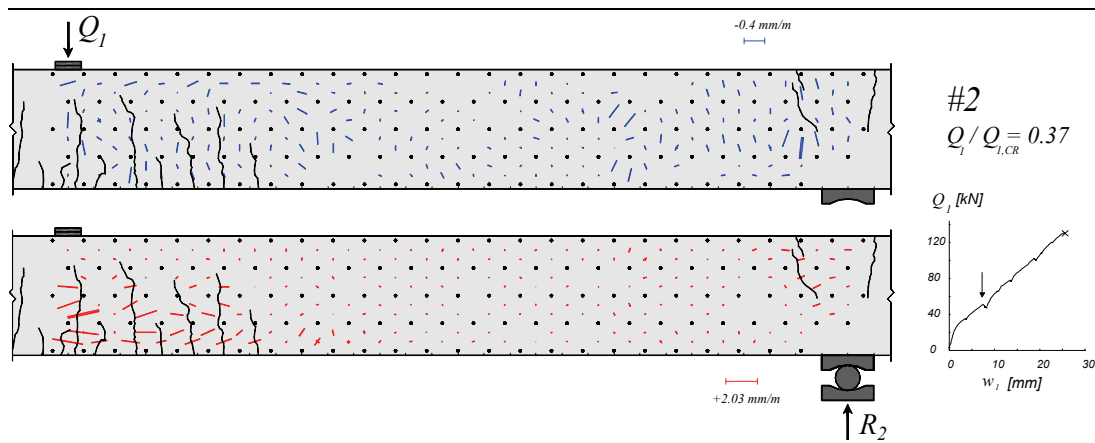


Figure B-4.52: Poutre SR11: (1) Déformations mesurées avec les jauges “oméga” ;  
 (2) Déplacement relatif entre les 2 lèvres des fissures, calculé avec les mesures au déformètre; (3) Ouvertures mesurées à l’œil nu pendant l’essai



Suite page suivante

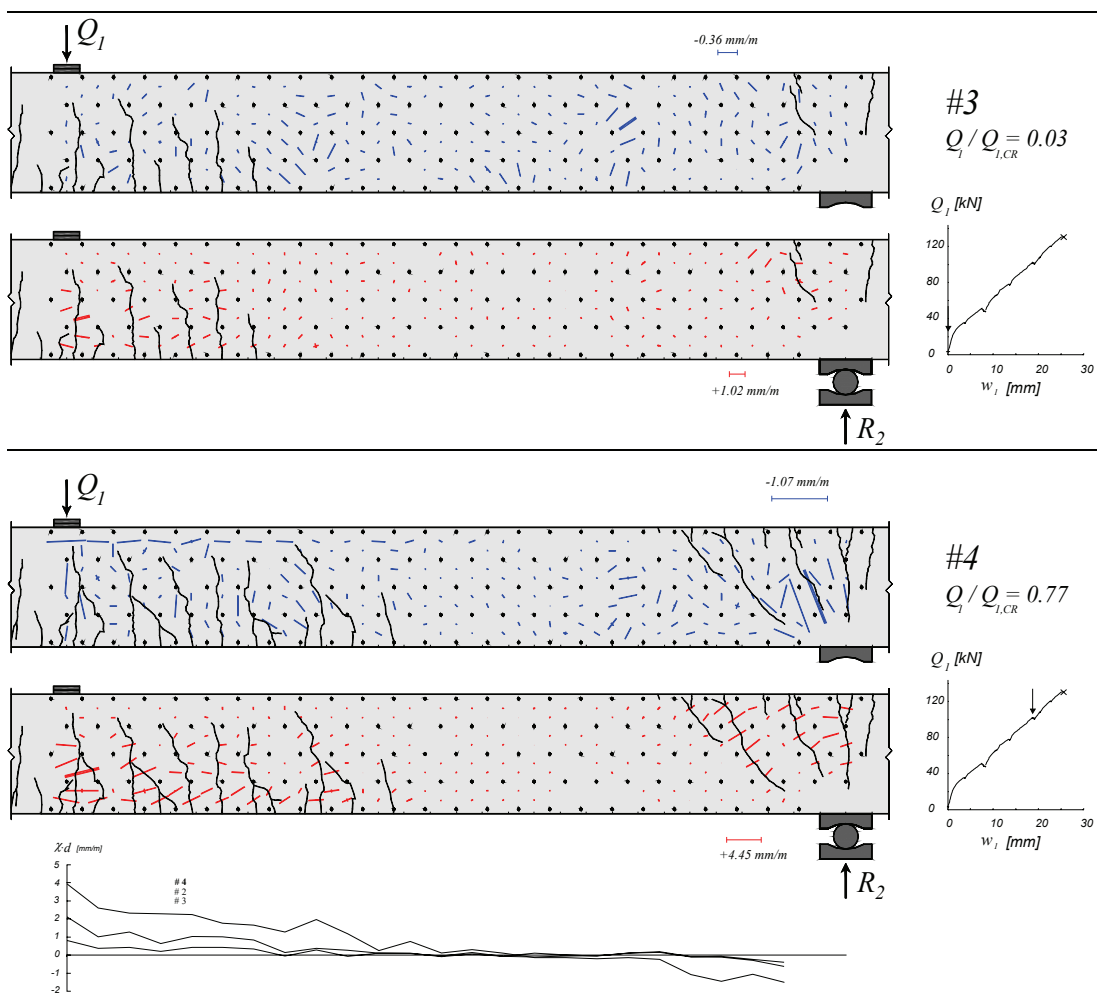


Figure B-4.53: Poutre SR11: déformations principales, fissuration et courbures

### B-4.12 Poutre SR12

La poutre SR12 a été testée avec un rapport  $Q_2/Q_1$  de +0.20. Le type de l'acier était laminé à chaud. Après un très grand plateau plastique, pour un niveau de charge de  $Q_1 = 131$  kN et une flèche de  $w_1 = 150$  mm, une importante fissure s'est ouverte à la proximité de la charge  $Q_1$ . Par la suite la charge appliquée a diminuée à  $Q_1 = 100$  kN environ et le béton d'enrobage au niveau de l'armature tendue a éclaté. La fissure n'a pas engendrée la rupture de la poutre, ni la perte totale de la charge appliquée (figs. B-4.54 et B-4.56).

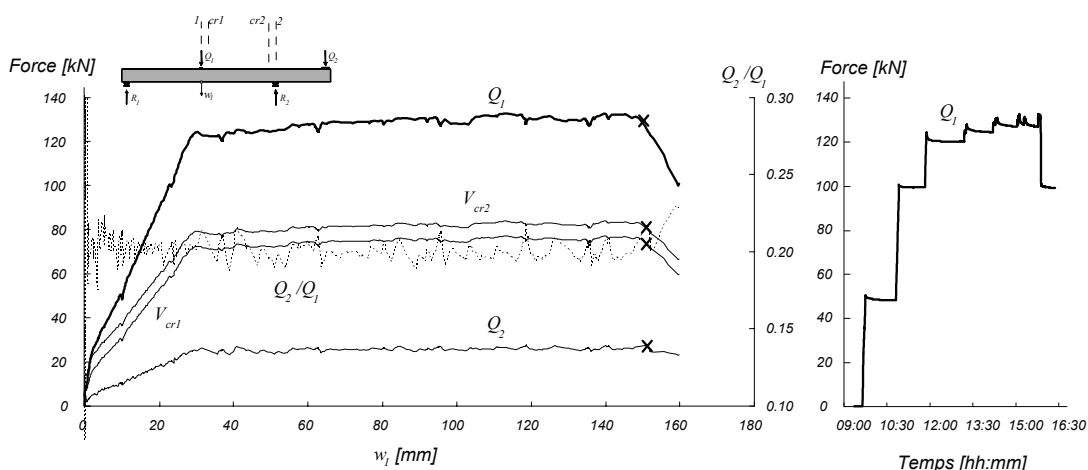


Figure B-4.54: Poutre SR12: Diagramme charge – flèche et évolution dans le temps

Tableau B-4.15: Poutre SR12: Evolution des valeurs mesurées et calculées

Palier	$Q_1$	$Q_2$	$Q_2/Q_1$	$M_1$	$M_{cr1}$	$M_2$	$M_{cr2}$	$V_1$	$V_{cr1}$	$V_2$	$V_{cr2}$	$\Omega_{49}$	$\Omega_{59}$	$w_1$	$w_0$	$Q_1/Q_{1,CR}$	Rem.	
	[kN]	[kN]	-	[kN·m]	[kN·m]	[kN·m]	[kN·m]	[kN]	[kN]	[kN]	[kN]	[mm]	[mm]	[mm]	[mm]	%	*	
#0	2.5	1.8	0.72	11.1	10.4	-9.9	-8.1	-3.1	-3.5	-11.1	-10.8	0.00	0.00	0.00	0.00	2%		
#1	2.8	1.8	0.64	11.5	10.9	-9.9	-8.1	-3.3	-3.7	-11.2	-10.9	0.00	0.00	0.00	0.00	2%		
#2	49.8	10.3	0.21	73.0	67.5	-26.0	-19.7	-29.6	-30.0	-37.5	-37.3	0.61	0.14	9.75	-6.96	38%	DP	
	48.5	10.3	0.21	71.0	65.7	-26.0	-19.8	-28.9	-29.4	-36.9	-36.6						37%	FD
	48.6	10.4	0.21	71.0	65.7	-26.2	-20.0	-29.0	-29.4	-37.0	-36.7	0.60	0.14	9.86	-6.82	37%	FP	
#3	99.9	20.3	0.20	137.5	126.9	-45.0	-33.8	-58.0	-58.4	-65.9	-65.6	1.09	0.27	23.01	-15.19	76%	DP	
	99.5	20.5	0.21	136.7	126.0	-45.4	-34.3	-57.8	-58.3	-65.8	-65.5						76%	FD
	99.6	20.5	0.21	136.7	126.1	-45.5	-34.3	-57.9	-58.3	-65.8	-65.5	1.11	0.27	23.34	-15.13	76%	FP	
#4	121.8	25.1	0.21	165.3	152.3	-54.2	-40.9	-70.5	-71.0	-78.5	-78.2	2.60	2.02	36.29	-22.25	93%	DP	
	120.5	25.2	0.21	163.2	150.4	-54.4	-41.2	-69.9	-70.3	-77.9	-77.6						92%	FD
	120.5	25.3	0.21	163.1	150.3	-54.7	-41.5	-70.0	-70.4	-77.9	-77.6	2.68	2.14	37.01	-22.25	92%	FP	
#5	126.2	26.1	0.21	170.8	157.4	-56.2	-42.4	-73.1	-73.5	-81.0	-80.7	5.97	3.53	62.11	-38.06	96%	DP	
	124.9	26.16	0.21	168.8	155.5	-56.2	-42.6	-72.4	-72.9	-80.4	-80.1						95%	FD
	124.6	26.1	0.21	168.5	155.2	-56.1	-42.5	-72.3	-72.7	-80.2	-79.9	5.72	3.59	62.66	-38.14	95%	FP	
#6	128.4	27.0	0.21	173.1	159.5	-57.9	-44.0	-74.5	-74.9	-82.4	-82.1	8.81	4.40	95.28	-59.61	98%	DP	
	127.6	27.1	0.21	171.9	158.3	-58.1	-44.2	-74.1	-74.5	-82.0	-81.7						97%	FD
	127.2	27.1	0.21	171.3	157.8	-58.0	-44.1	-73.9	-74.3	-81.8	-81.5	8.83	4.43	95.64	-59.64	97%	FP	
#7	128.2	26.1	0.20	173.8	160.2	-56.1	-42.2	-74.1	-74.5	-82.0	-81.7	10.00	4.89	135.2	-86.23	98%	DP	
	127.2	26.3	0.21	172.1	158.6	-56.5	-42.7	-73.6	-74.1	-81.6	-81.3						97%	FD
	127.2	26.3	0.21	172.0	158.5	-56.5	-42.7	-73.6	-74.0	-81.6	-81.3	10.00	4.91	135.5	-86.27	97%	FP	
CM	132.7	27.2	0.21	179.3	165.3	-58.3	-43.9	-76.7	-77.1	-84.6	-84.4	10.00	4.98	139.70	-88.90	101%	CM	
CR	131.5	26.9	0.20	177.8	163.9	-57.7	-43.5	-76.0	-76.4	-83.9	-83.6	10.00	5.18	148.23	-94.37	100%	CR	

\* DP : Début du palier ; FD : Fin des mesures avec le déformètre ; FP : Fin du palier ; CM : Charge maximale ; CR : Charge de rupture ;



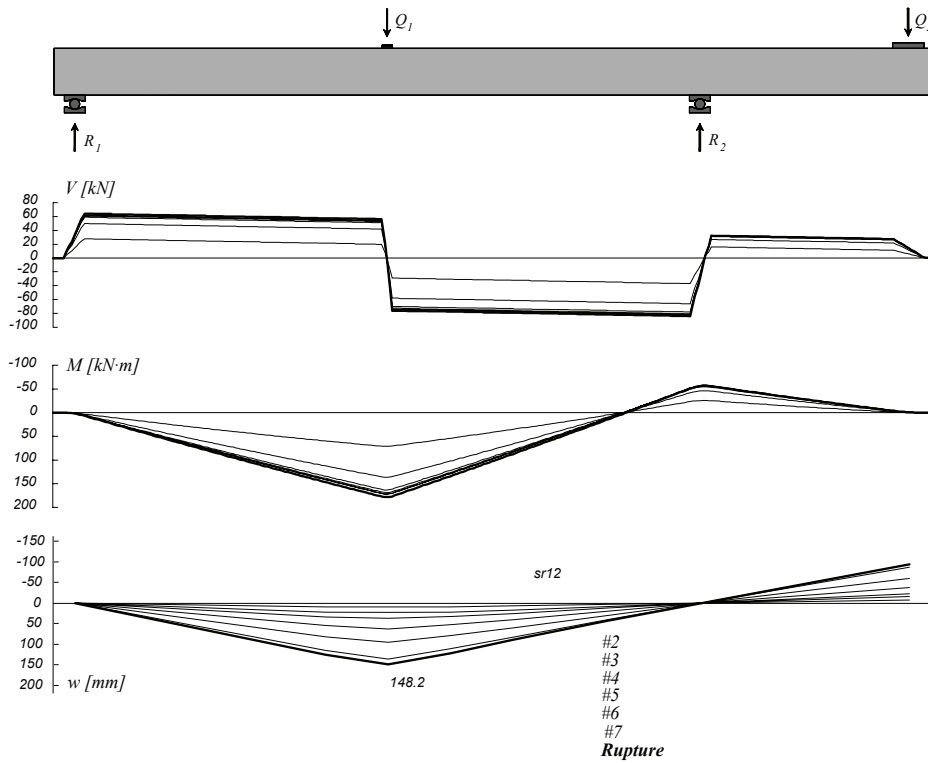
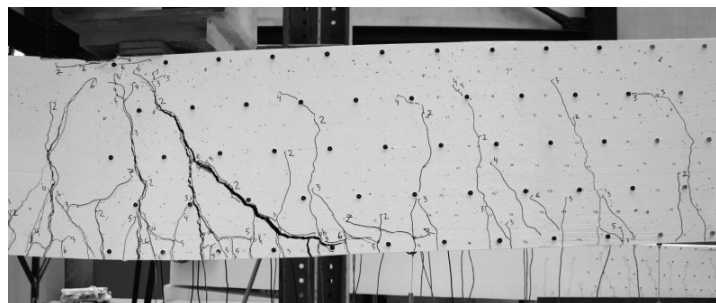
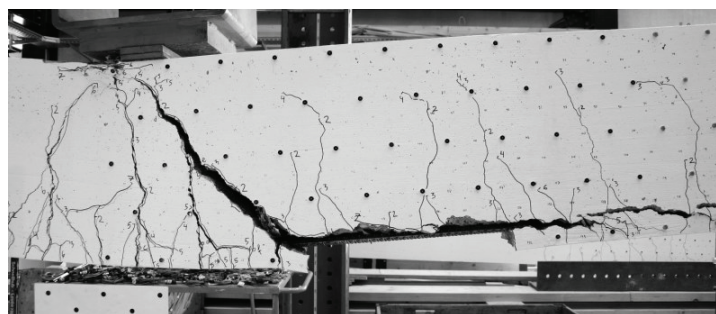


Figure B-4.55: Poutre SR12: Diagramme des efforts tranchants, diagramme des moments de flexion et déformée



# 7  
 $Q_1 / Q_{I,CR} = 0.97$



Rupture

Figure B-4.56: Poutre SR12: Fissuration avant rupture en travée (palier 7) et après rupture

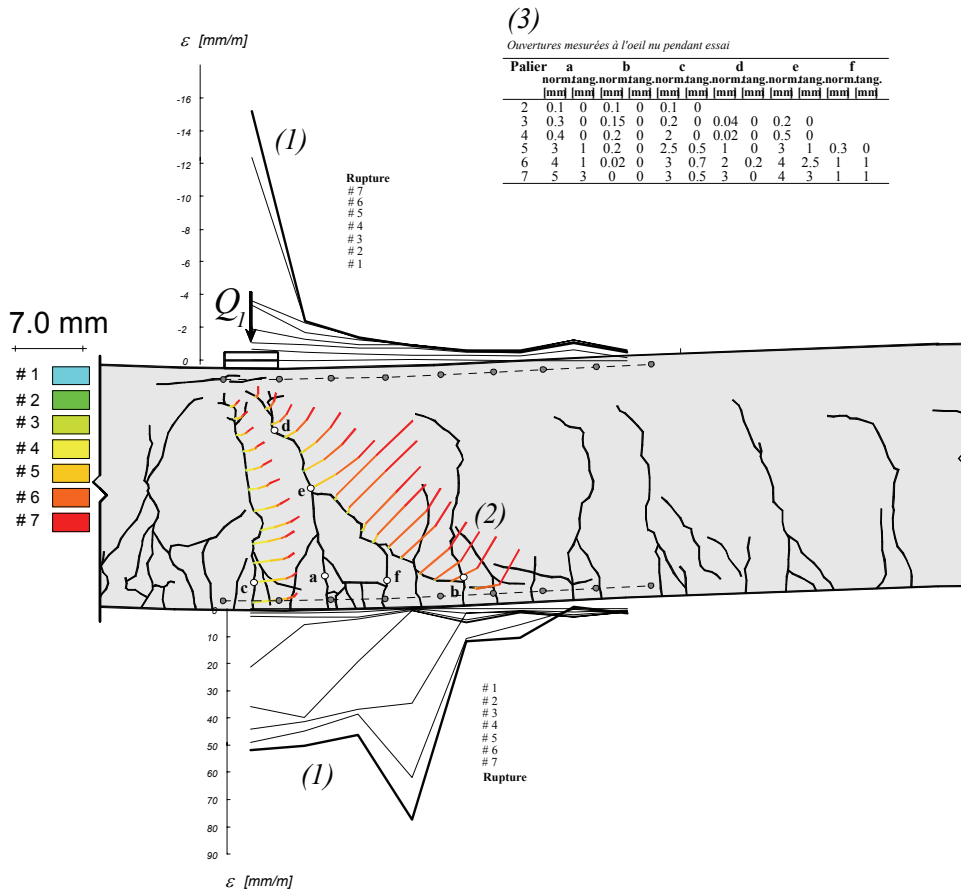
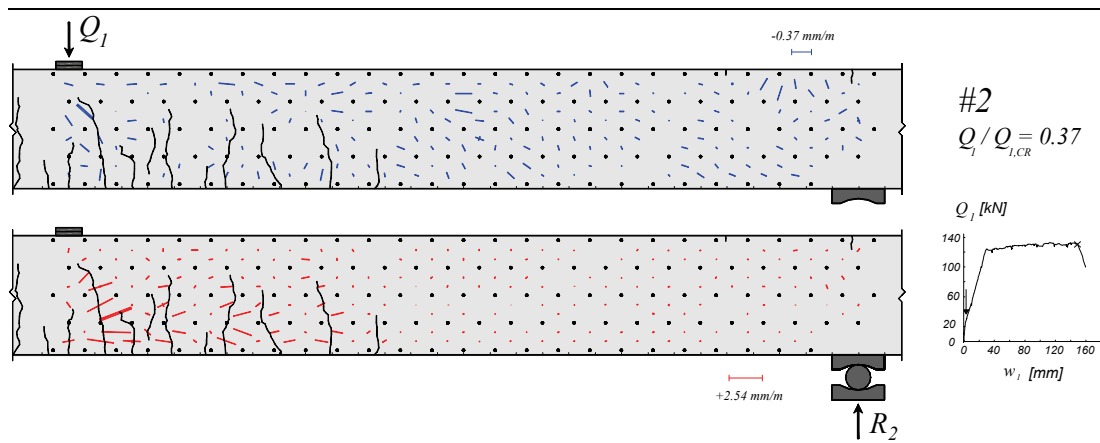


Figure B-4.57: (1) Déformations mesurées avec les jauges "oméga" ;  
 (2) Déplacement relatif entre les 2 lèvres des fissures, calculé avec les mesures au déformètre; (3) Ouvertures mesurées à l'œil nu pendant l'essai



Suite page suivante

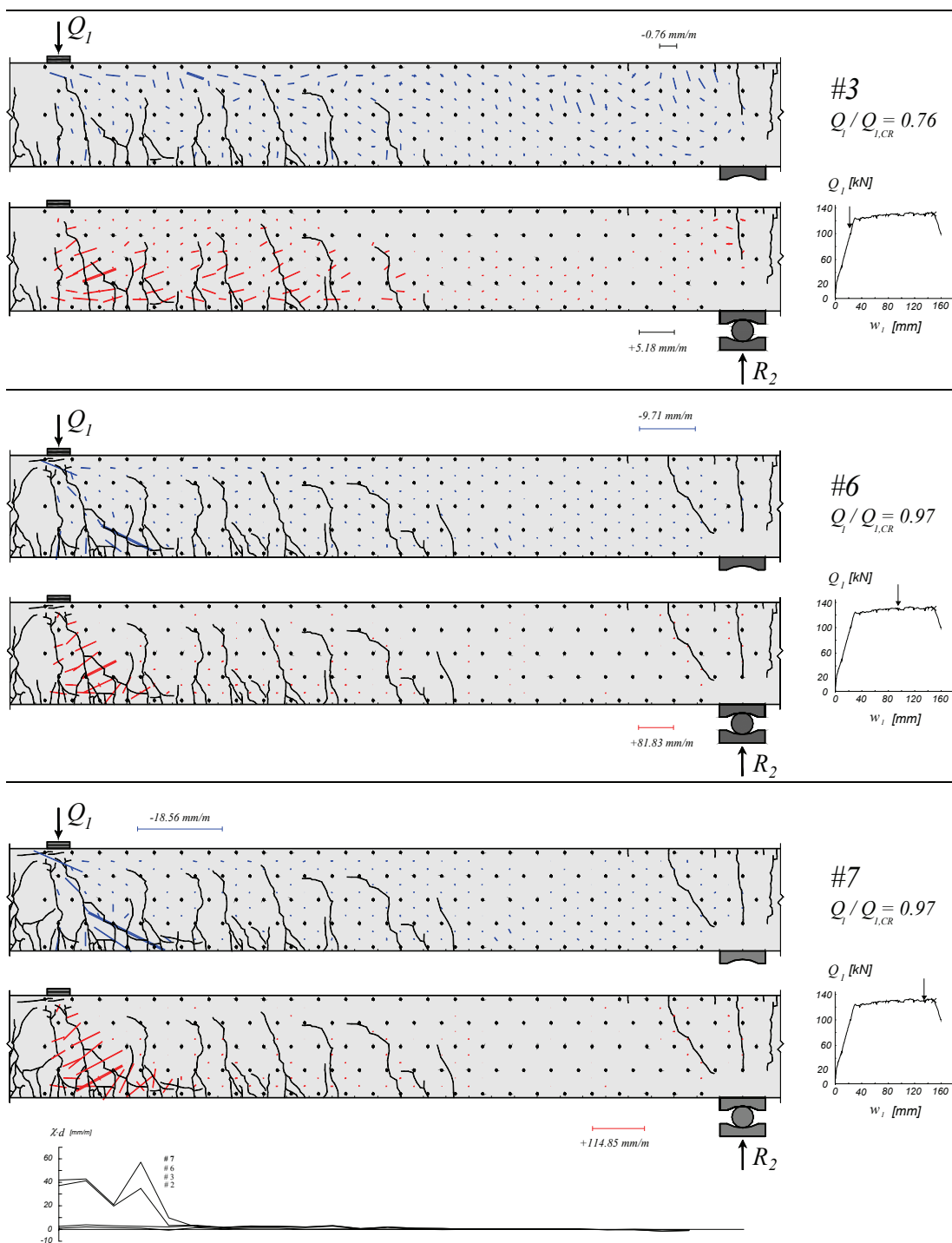


Figure B-4.58: Poutre SR12: déformations principales, fissuration et courbures



## B-5 Comparaison des essais

Une vue d'ensemble de tous les essais réalisés est montrée à la figure B-5.2. Les variables suivantes sont utilisées pour comparer les essais.

- Le rapport entre la résistance à l'effort tranchant ( $\tau_R$ ) et la résistance nominale au cisaillement ( $\tau_c$ ).
- La rotation  $\theta$  de la poutre calculée à la région de rupture (fig B-5.1).

La résistance à l'effort tranchant ( $\tau_R$ ) est définie à l'équation B-5.1 et la résistance nominale  $\tau_c$  est définie à l'équation B-5.2. La comparaison entre poutres avec bétons de différentes résistances à la compression est ainsi possible.

$$\tau_R = \frac{V_R}{b \cdot d} \quad (\text{B-5.1})$$

$$\tau_c = 0.3 \cdot \sqrt{f_c} \quad (\text{B-5.2})$$

L'effort tranchant résistant ( $V_R$ ) dans l'équation B-5.1 est calculé avec la contribution des charges  $Q_1$  et  $Q_2$  et avec la contribution du poids propre. Les sections  $cr1$  et  $cr2$  de calcul de  $V_R$  sont indiquées à la figure B-5.1. La section critique se situe à une distance de  $0.5 \cdot d$  de l'axe de la force  $Q_1$  (section  $cr1$ ) ou de la réaction  $R_2$  (section  $cr2$ ). La section  $cr1$  est utilisée pour des poutres avec rupture en travée et la section  $cr2$  pour des poutres avec rupture en appui.

La rotation  $\theta$  est calculée en intégrant les allongements horizontaux mesurés aux fibres inférieure et supérieure avec les jauges "oméga". Le calcul est fait en travée ou en appui selon la position de la section de rupture. La distance d'intégration vaut 800 mm, soit  $1.96 \cdot d$  (fig. B-5.1).

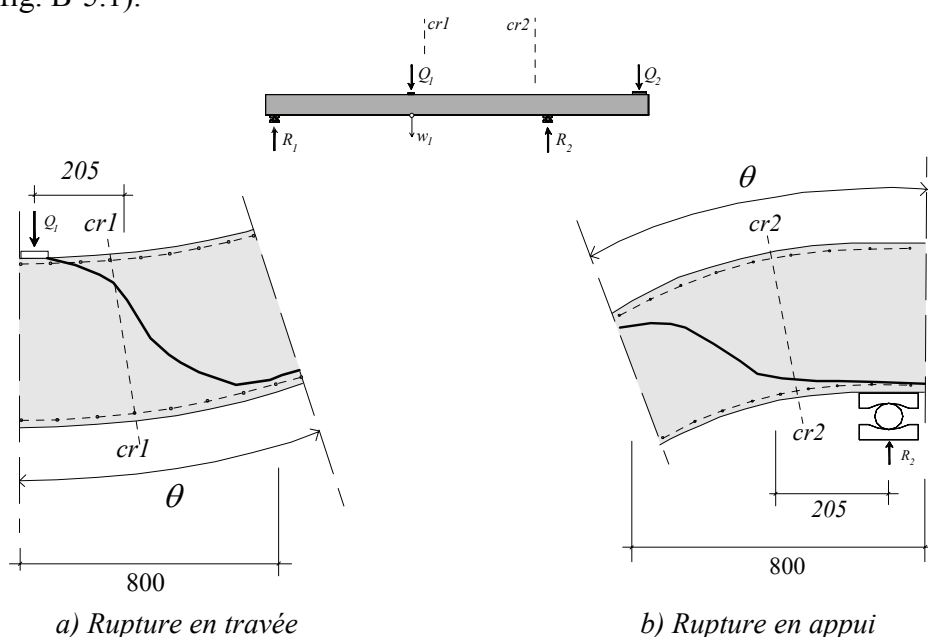


Figure B-5.1: Position de la section de calcul de  $V_R$  et définition de la rotation  $\theta$ , [mm]

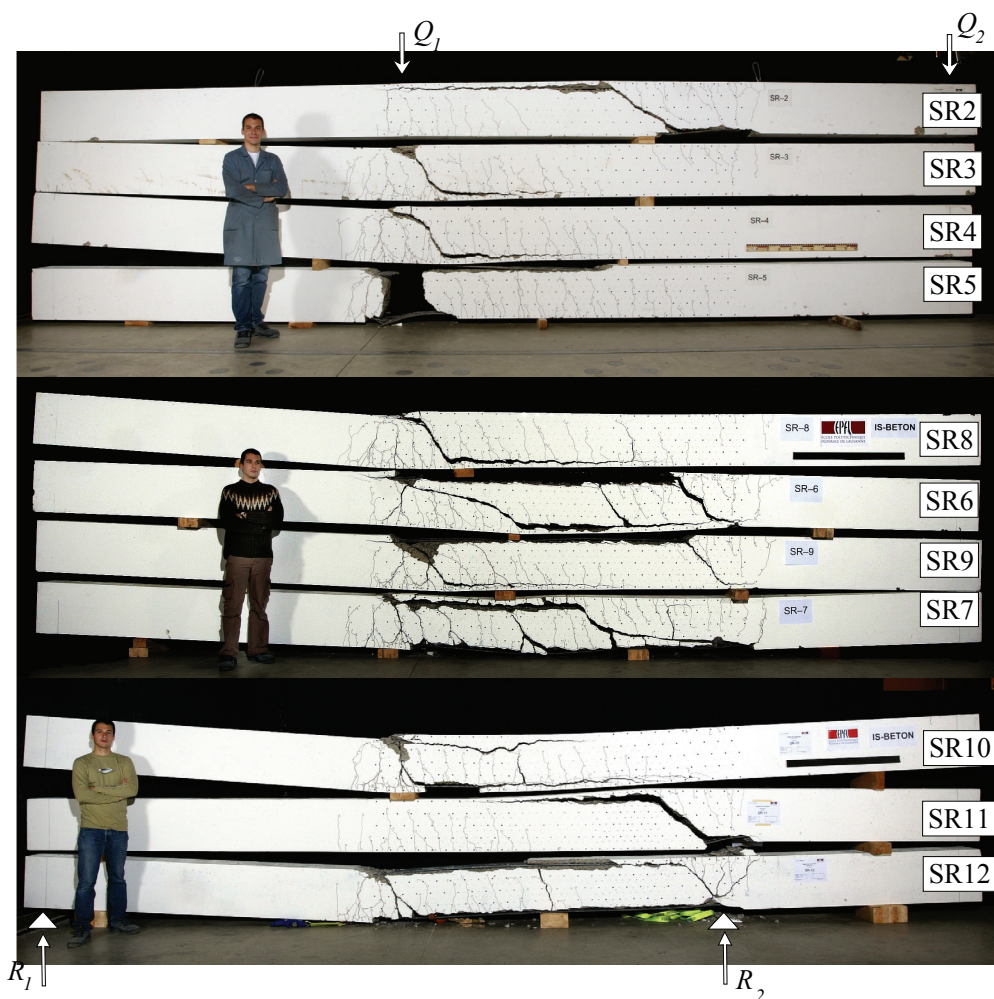


Figure B-5.2: Vue d'ensemble de toutes les poutres testées

Le tableau B-5.1 indique les valeurs à la rupture pour toutes les poutres testées. La flèche  $w_l$  est indiquée à la figure B-5.1. La portée de cisaillement équivalente  $a$  a été calculée avec considération du poids propre et avec les charges  $Q_1$  et  $Q_2$  à la rupture. Le moment  $M_R$  est calculé à la section de rupture avec la contribution des charges  $Q_1$  et  $Q_2$  et la contribution du poids propre (fig. B-5.1).

Tableau B-5.1: Comparaison des essais. Valeurs à la rupture

Essai	$Q_{1,CR}$ [kN]	$Q_{2,CR}$ [kN]	$w_{l,CR}$ [mm]	$M_R$ [kN·m]	$V_R$ [kN]	$\tau_R$ [MPa]	$f_c$ [MPa]	$\tau_c$ [MPa]	$\tau_R/\tau_c$	$\theta_R$ [mrad]	$a$ [m]	$a/d$	Type de Rupture	Endroit de Rupture
SR2	124.1	62.4	19.21	-112.8	-91.8	0.897	43.11	1.970	0.456	3.2	1.46	3.56	V	Appui
SR3	130.0	27.6	69.52-73.32	161.1	-75.9	0.742	50.62	2.134	0.348	30.1	2.25	5.50	V	Travée
SR4	115.2	0.0	110.43	169.9	-59.3	0.580	47.55	2.069	0.280	40.0	2.90	7.09	V	Travée
SR5	96.1	-18.7	195.95	163.1	-43.5	0.425	47.64	2.071	0.205	68.1	3.59	8.77	M	Travée
SR6	148.0	85.6	56.47	124.2	-104.2	1.019	52.71	2.178	0.468	18.6	1.38	3.37	V	Travée
SR7	139.9	71.3	176.43	-128.4	-102.6	1.004	49.11	2.102	0.477	8.6	1.48	3.61	V	Appui
SR8	107.5	-11.0	133.11	170.8	-51.8	0.506	49.16	2.103	0.241	47.2	3.25	7.96	V	Travée
SR9	126.5	43.8	92.07	138.9	-79.5	0.778	52.82	2.180	0.357	29.7	1.90	4.65	V	Travée
SR10	101.3	-6.8	140.90	157.7	-50.1	0.490	42.41	1.954	0.251	76.3	3.12	7.62	V	Travée
SR11	130.6	45.1	25.44	-78.7	-89.3	0.873	42.91	1.965	0.444	3.6	1.10	2.68	V	Appui
SR12	131.5	26.9	148.23	163.9	-76.4	0.747	43.51	1.979	0.378	> 55.8	2.27	5.56	V	Travée

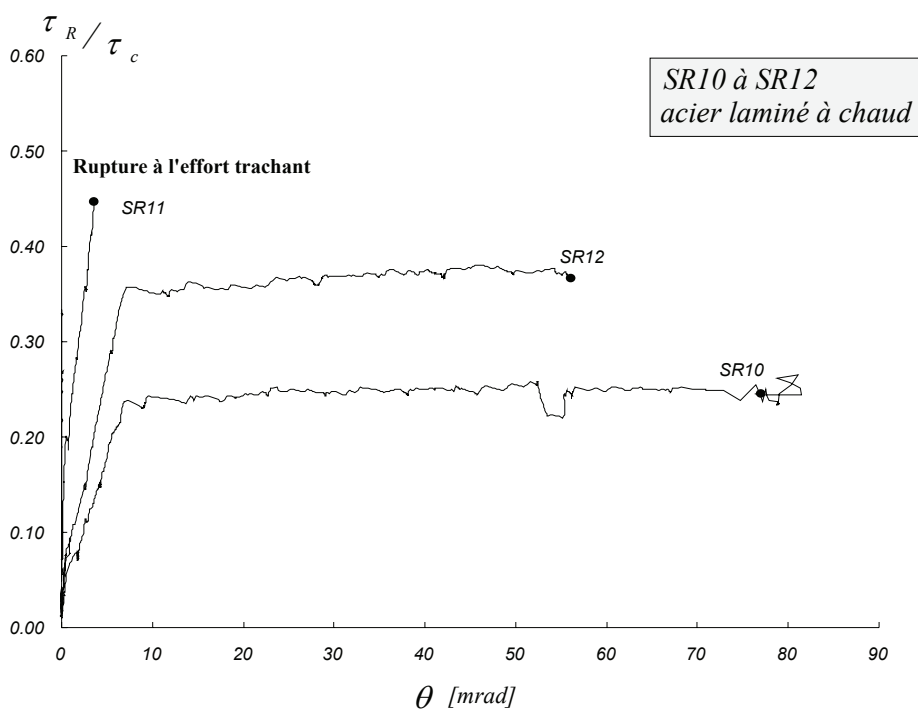
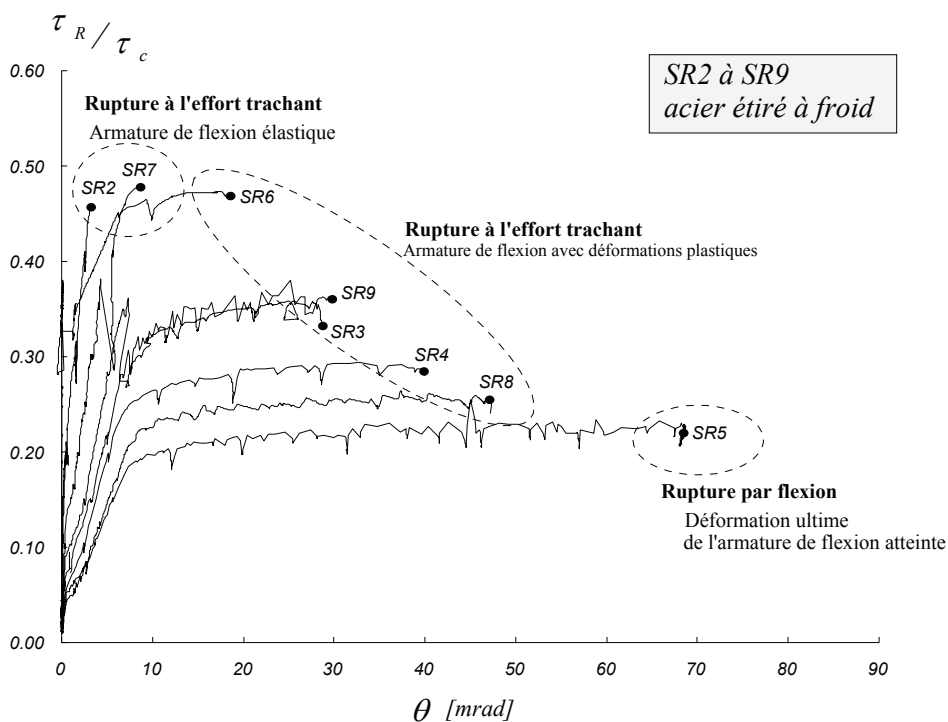


Figure B-5.3: Comparaison des essais

La figure B-5.3 montre l'évolution de la résistance au cisaillement ( $\tau_R / \tau_c$ ) avec la rotation à la région de rupture  $\theta$  pour toutes les poutres testées. Les considérations suivantes peuvent être énoncées :

- La rupture à l'effort tranchant des poutres SR2, SR7 et SR11 s'est produite avant ou au début de la plastification de l'armature de flexion.

## Chapitre B-5

- Pour les poutres SR3, SR4, SR6, SR8 et SR9, la rupture à l'effort tranchant s'est produite en présence d'importantes déformations plastiques de l'armature de flexion.
- Une rupture par flexion a été obtenue pour la poutre SR5. La déformation ultime de l'armature inférieure de flexion a été atteinte.
- La résistance à l'effort tranchant  $\tau_R / \tau_C$  diminue avec l'augmentation de la rotation  $\theta$  à la région de rupture.
- Les poutres avec acier de type laminé à chaud (SR10 et SR12) ont eu plus de ductilité par rapport aux poutres avec acier de type étiré à froid.







# Curriculum Vitae

Rui VAZ RODRIGUES  
Dr. ès sc., Civil engineer

born January 8, 1979  
Lisbon, Portugal  
Portuguese  
Married  
rui.vazrodrigues@gmail.com

## Education

- |             |   |
|-------------|---|
| 2002 – 2006 | Doctorate in Sciences (Ph.D.), Ecole Polytechnique Fédérale de Lausanne, Switzerland.                                     |
| 1997 – 2002 | Civil engineering degree (5 years program), Instituto Superior Técnico, Lisbon, Portugal, grade 17/20, structural branch. |
| 2001 – 2002 | Exchange program at the Ecole Polytechnique Fédérale de Lausanne (EPFL), Switzerland, grade 5.6/6.                        |
| 1994 – 1997 | Secondary school, Oeiras, Portugal, grade 19/20.  |

## Professional Experience

- |             |   |
|-------------|---|
| 2002 – 2006 | Research associate at the Structural Concrete Laboratory at the Ecole Polytechnique Fédérale de Lausanne (EPFL), under the direction of Prof. A. Muttoni: <ul style="list-style-type: none"><li>- Research on the shear strength of RC slabs</li><li>- External consulting in the field of reinforced concrete structures (slabs and bridges)</li><li>- Responsible for the design and execution of numerous full scale tests on RC structures (100 tones of tested elements)</li><li>- Participation on the teaching activities of the research unit</li></ul> |
| 2001        | Student assistant at the Applied Computing and Mechanics Laboratory, EPFL   |

## Publications

**Vaz Rodrigues R.**, *Shear Strength of Reinforced Concrete Bridge Deck Slabs*, IS-BETON, PhD thesis, n° 3739, 264 p., Lausanne, Switzerland, January, **2007**.

**Vaz Rodrigues R.**, *Shear Strength of RC Bridge Deck Cantilevers*, 6th International PhD Symposium in Civil Engineering, IBK Publikation SP-015, pp. 160-161, August, **2006**.

**Vaz Rodrigues R., Muttoni A.**, *Large Scale Tests on Reinforced Concrete Bridge Deck Slabs. Test report*, IS-BETON, Lausanne, **2006**.

**Vaz Rodrigues R., Muttoni A., Burdet O.**, *Large Scale Tests on Bridge Slabs Cantilevers Subjected to Traffic Loads*, Proceedings of the 2nd fib Congress, vol.1, pp. 232, Naples, **2006**.

**Vaz Rodrigues R., Burdet O., Muttoni A.** , *Experimental investigation of the shear capacity of plastic hinges*, fib Symposium, Budapest 2005, vol. 2, pp. 651-656, Budapest, Hungary, May, **2005**.

**Vaz Rodrigues R., Muttoni A.** , *Influence des déformations plastiques de l'armature de flexion sur la résistance à l'effort tranchant des poutres sans étriers. Rapport d'essai*, IS-BETON, Lausanne, **2004**.

**Vaz Rodrigues R.** , *Essai d'un porte-à-faux de pont sous charge concentrée*, EPFL - IS-BETON, Lausanne, **2002**.

## **Professional Affiliation**

Member of the Portuguese Chamber of Engineers, Civil Engineer College (n. 50245)  
*fib*, Fédération Internationale du Béton  
IABSE, International Association for Bridge and Structural Engineering

## **Languages**

Portuguese (mother tongue)  
Very good knowledge of French and English  
Good knowledge of German and Castellan  
Basic knowledge of Italian

## **Computer Skills**

Programming languages: Octave / Matlab, Vba, Lisp, C, Html  
Advanced user of Autocad (including 3d and programming), Ansys, Cubus.  
As a daily user: Windows, MsOffice, Adobe, Ghostscript.

## **Leisure**

Advanced student of classical guitar at Conservatoire de Lausanne  
Sports: Volleyball player, cycling, ski and snowboard, canyoning.

